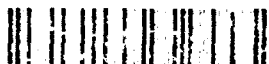


AD-A262 138



Addendum

1992 National Interagency Coordinating Group

2

DTIC
SELECTED
MAR 12 1993
S B D



DISTRIBUTION STATEMENT A
Approved for public release
Distribution Unlimited

15th International Aerospace and Ground Conference
on
Lightning and Static Electricity

Taj Mahal

October 6-8, 1992

Atlantic City, New Jersey, USA

93-05219



93 3 11 050

NOTICE

This document is disseminated under the sponsorship of the U.S. Department of Transportation in the interest of information exchange. The United States Government assumes no liability for the contents or use thereof.

The United States Government does not endorse products or manufacturers. Trade or manufacturers' names appear herein solely because they are considered essential to the objective of this report.

1. Report No. DOT/FAA/CT-92/20 ADD.1	2. Government Accession No.	3. Recipient's Catalog No. (2)
4. Title and Subtitle 1992 INTERNATIONAL AEROSPACE AND GROUND CONFERENCE ON LIGHTNING AND STATIC ELECTRICITY - ADDENDUM	5. Report Date November 1992	6. Performing Organization Code
7. Author(s) Michael S. Glynn	8. Performing Organization Report No. DOT/FAA/CT-92/20 ADD.1	10. Work Unit No. (TRAIS)
9. Performing Organization Name and Address Federal Aviation Administration Technical Center Atlantic International Airport, NJ 08405	11. Contract or Grant No.	13. Type of Report and Period Covered Proceedings October 6-8 1992
12. Sponsoring Agency Name and Address National Interagency Coordinating Group (NICG) of the National Atmospheric Electricity Hazards Protection Program and the Federal Aviation Administration Technical Center	14. Sponsoring Agency Code ACD-230	
15. Supplementary Notes The NICG consists of members from the FAA, U.S. Air Force, U.S. Army, U.S. Navy, NASA and NOAA.		
16. Abstract This report supplements the compilation of papers presented at the 1992 International Aerospace and Ground Conference on Lightning and Static Electricity, held at the Taj Mahal, Atlantic City, NJ, October 6-8, 1992. It includes papers concerning lightning phenomenology, lightning characterization, modeling and simulation, test criteria and techniques, and protection of both airborne and ground systems. This conference was sponsored by the Federal Aviation Administration Technical Center and the NICG, in concert with the Florida Institute of Technology.		
<div data-bbox="223 1339 707 1535" data-label="Text"> <p>DISTRIBUTION STATEMENT A Approved for public release Distribution Unlimited</p> </div> <div data-bbox="883 1339 1247 1585" data-label="Text"> <p>DTIC ELECTE S B D MAR 12 1993</p> </div>		
17. Key Words Phenomenology, Electromagnetics Lightning Standards, Mapping, Modeling P-Static and Corona, Coupling Lightning Simulation, Meteorological	18. Distribution Statement Document is available to the public through the National Technical Information Service, Springfield, Virginia 22161	
19. Security Classif. (of this report) Unclassified	20. Security Classif. (of this page) Unclassified	21. No. of Pages 307
22. Price		

**1992 INTERNATIONAL AEROSPACE AND
GROUND CONFERENCE ON LIGHTNING
AND STATIC ELECTRICITY**

6-8 October 1992
Atlantic City, New Jersey, USA



ADDENDUM

Conference Chairman
Michael S. Glynn
FAA Technical Center
Atlantic City International Airport, New Jersey

Sponsored by
National Interagency Coordinating Group (NICG)

PREFACE

This addendum to the proceedings of the 1992 international conference on lightning and static electricity, contains all those papers which were written for the conference but were not available for the original publication. In addition to the papers, there is an appendix of the attenders with their name, address, organization, phone, and fax. It is anticipated that this will assist in fostering better communication within the lightning community.

I would like to thank the many who made the conference a resounding success. I have personally been associated with the National Interagency Coordination Group (NICG) for eight years, and it was delightful for me to have the opportunity to host this years conference. Having spent considerable time assisting the other members in hosting their conferences, this brought me back to reality as to the effort it takes to host such an event.

To those in the scientific community who contributed to the conference, you made it the forum that attracts the participants that return year after year.

I would like to thank the members of the NICG for their cooperation and tolerance over the past 18 months. Your guidance and cooperation were an inspiration. Especial thanks to Larry Walko, Bill Walker, Felix Pitts and Andy Revay.

To Galaxy Scientific Corporation (GSC) who at a critical time, came to my rescue when Ltc Mike Cupples, conference coordinator, retired from the US Army. In particular, I want to thank Rosemarie McDowall, new conference coordinator, and the numerous other GSC personnel who helped make this a success.

To stage an event like this, one must have an adequate facility. The Trump Taj Mahal and their staff, especially Jon Pappas and Doni Bettis, allowed everything to come together and work like a clock. Everything that was contracted for or requested by my staff was provided on time and with style. A very hearty thanks.

To Heinrich Busse, 1994 chairman, the best of luck in Mannheim. The NICG is here to help and we will endeavor to assist you in any way possible to ensure your conference is a success and a credit to the lightning community.

To all those who contributed and I've not thanked by name, thanks, and we'll see you at the next conference.

DTIC QUALITY INSPECTED 8

Mike Glynn

92 Conference Chairman
NICG Secretariat

Accession For	
NTIS GRA&I	<input checked="checked" type="checkbox"/>
DTIC TAB	<input type="checkbox"/>
Unannounced	<input type="checkbox"/>
Justification	
By	
Distribution/	
Availability Codes	
Dist	Avail and/or Special
A-1	

TABLE OF CONTENTS

ALPHABETICAL LIST OF AUTHORS	xii
------------------------------------	-----

Session 1 - Plenary Session

Lightning Protection Technology for Small General Aviation Composite Material Aircraft	1-1
<i>J. A. Plumer, T. E. Setzer, S. Siddiqi</i>	

Session 2A - Ground/Ship Protection

Andrew S. Podgorski

ARIANE 5—Lightning Protection	2-1
<i>A. Schaffar</i>	
Launch Pad Lightning Protection Enhancement by Induced Streamers	3-1*
<i>J. R. Stahmann, E. R. Bentti</i>	
Evaluation of the Electric Field Mill as an Effective and Efficient Means of Lightning Detection	4-1
<i>Robert Hoefft, Charles Wakefield</i>	

Session 2B - Lightning Phenomenology

David L. Albright

Electrical Forces Applied to Basic Weather Phenomena	5-1
<i>Charles A. Yost</i>	
Lightning Precursor Signatures from Dual-Polarization Radar Measurements of Storms	6-1*
<i>Paul Krehbiel, Tiehan Chen, Stephen McCrary, William Rison, Grant Gray, Marx Brook</i>	
Applications of Triggered Lightning to Space Vehicle Operations	7-1‡
<i>William Jafferis, Rocco Sanicandro, John Rompalla, Richard Wohlman</i>	

* Paper printed in the Addendum

† Camera-ready copy not available

‡ Paper not submitted

Session 3A - Aerospace Vehicles

Kathy L. Giori

Numerical Modelling of Induced Effects of Lightning Strike on an All Composite Helicopter	8-1*
<i>P. Gondot, G. Donnet, P. Trochet</i>	
Aircraft Lightning Strike Interference Fit Fastener for Use in Composites	9-1
<i>L. T. Lemke</i>	
FILAMENT - A Program for Transient Analysis of Interconnected Wires	10-1
<i>Franklin A. Fisher</i>	
Lightning Threat Evaluation on HERMES Shingle Antennas	11-1
<i>D. Gauthier</i>	

Session 3B - Specifications & Standards

Kenneth M. Grachan

The Use of Probability to Define Lightning Strike Zones	12-1*
<i>N. G. Bankston</i>	
Technical Issues Related to Lightning Protection of Facilities	13-1
<i>Richard S. Collier, Rodney A. Perala, Frederick J. Eriksen</i>	
Equipment Testing with Damped Sinewaves Between 1 and 50 MHz	14-1*
<i>C. J. Hardwick, R. E. Baldwin</i>	
Development of a Unified Military E ³ Standard for Army Helicopters	15-1
<i>Gregory J. Rigden</i>	

Session 4A - Simulation

Rodney A. Perala

An Integrated Approach to 300 KV Electrostatic Discharge Application During Component Testing That Will Satisfy MIL-STD-331B Appendix F	16-1*
<i>Monty R. Lehmann, Jack Nial, Mike Whitaker</i>	

* Paper printed in the Addendum

† Camera-ready copy not available

‡ Paper not submitted

Lightning-Induced Currents on a Canonical Test Object Due to Different Configurations of the U.S. Army RTTC Component D (Restrike) Lightning Effects Simulator	17-1
<i>D. B. Elkins, J. D. Craven, T. H. Shumpert, T. E. Roy, R. P. Henderson</i>	

Methods of Producing Simulated Lightning Pulse Waveforms to Satisfy MIL-STD-1757A	18-1‡
<i>Monty R. Lehmann, Mike Whitaker</i>	

Session 4B - Lightning Phenomenology *Christopher C. R. Jones*

Lightning Data Acquisition	19-1*
<i>Rosemarie L. McDowall, J. Anderson Plumer, Michael S. Glynn</i>	
Digitization of Analog Data From In-Flight Lightning Strikes	20-1*
<i>James R. Elliott, Henry S. Weigel</i>	
F106 Lightning Strike Data for FRED	21-1
<i>Poh H. Ng, James R. Elliott</i>	

Session 5A - Aerospace Vehicles *J. Anderson Plumer*

Electric Space Charges and Explosion Hazards in Aviation Fuel Systems	22-1
<i>I. I. Inculet, J. LoVetri, E. J. Weckman</i>	
A Procedure for Defining Lightning Risk to Air Vehicles—Summary	23-1*
<i>D. Beeman, N. Morita</i>	
Parameters Influencing the Hot-Spot Ignition of Aviation Fuel/Air and Ethylene/Air Mixtures	24-1*
<i>S. J. Haigh, C. J. Hardwick</i>	
Detection of Sparks in Fuel Tanks	25-1
<i>J. L. Emanuely, J. P. Clerc, B. Puybras</i>	

* Paper printed in the Addendum
† Camera-ready copy not available
‡ Paper not submitted

Session 5B - Electrostatics & P-Static

Lawrence C. Walko

Frictional Electrification Between Ice and Metals (withdrawn) . . 26-1
Hisashi Shio

Comparison of the Electrical Charging and Discharging Environments of
Multiple Aircraft-borne Electric-field Measurement Systems 27-1*
K. L. Giori, J. E. Nanevich

Standardization of Precipitation Static Test Methods and Equipment for
the Navy 28-1
Matthew R. Maier

Royal Australian Navy S-70B-2 P-Static Test Results Using Commercial Test
Equipment 29-1
R. Wayne Devereux

Session 6A - Lightning Phenomenology

Andrew W. Revay

Simultaneous Optical Observations of NO₂ and O₃ During Thunderstorms 30-1
D. B. Jadhav, S. Bose

Observation of Radiation From Lightning Discharges by LPATS 31-1*
M. Ishii, J. Hojo, T. Yamamoto, E. Zaima, J. Sawada, N. Fukiyama

Parameters and Spectra of Lightning Radiated Electric Fields in the Short
Distance Range 32-1
Christian Hopf

Session 6B - Simulation

Felix Pitts

Simulation of the High Current Steepness of Negative Subsequent Strokes
Using Exploding Wires 33-1
W. J. Zischank

* Paper printed in the Addendum

† Camera-ready copy not available

‡ Paper not submitted

Laboratory Lightning Simulation Testing	34-1
<i>Jon B. Jolly, A. J. Mauriello, John J. Reilly</i>	

A Lightning Impulse Simulator With Easily Variable Current, Risetime and Fall-Time	35-1
<i>V. Carboni, C. Eichenberger, I. Smith, D. Serafin, A. Bazin</i>	

Session 7A - Ground/Ship Protection
William Jafferis

A System to Measure Lightning-Induced Transients on Spacecraft Umbilical Lines	36-1*
<i>Jeffrey C. Brown, Noel B. Sargent, Carl J. Wenzler</i>	

RF Antenna and Lightning Grounding Solutions for Climatic and Geologic Extremes Based on Extensive Measurements and TDR Models	37-1†
<i>Burt J. Bittner</i>	

The Early Streamer Emission Lightning Rod Conductor	38-1
<i>Gérard Berger</i>	

Lightning Protection by Way of Thunderstorm Sensing and Automatic Electrical Isolation	39-1
<i>Leon G. Byerley III, Jim Reed</i>	

Session 7B - Aerospace Vehicles
Nathaniel G. Bankston

Testing Thin Composite Skins for Punch Through	40-1
<i>B. J. C. Burrows, J. Wilson</i>	

A Computational Approach to Predicting the Extent of Arc Root Damage in CFC Panels	41-1*
<i>N. Jennings, C. J. Hardwick</i>	

Lightning Protection for Electrical and Electronic Equipment . . . (withdrawn) . .	42-1
<i>Olaf Spiller</i>	

* Paper printed in the Addendum;
† Camera-ready copy not available
‡ Paper not submitted

Comparison of the Damage for Various Types of Fibre Reinforced Composites Due to Different Lightning Test Standards (MIL-STD-1757 A, German Military VG-Standard 96903)	43-1*
<i>J. Wiedmann, J.-U. Roth, A. Kern</i>	

Session 8A - Lightning Phenomenology
E. Philip Krider

Lightning Characteristics in the North-East Part of Japan Observed by a Magnetic Direction-Finder Network	44-1*
<i>N. Honma, H. Komuro, M. Ishii, J. Hojo</i>	
Image Processing Analysis of Multiple Flash Characteristics on the Streak Photograph of the Artificially Triggered Lightning	45-1
<i>Yuki Nagamori, Masakazu Wada, Kouichi Nakamura, Kenji Horii, Shin-ichi Sumi, Mototaka Sone</i>	
Three-Dimensional Time Domain Modelling of Stratospheric Lightning	46-1
<i>Andrew S. Podgorski, Elizabeth M. Podgorski</i>	

Session 8B - Lightning Phenomenology
Sam Frazier

Fractal Determination of Parameters in Lightning and ESD Model	47-1*
<i>G. Vecchi, D. Labate, F. Canavero</i>	
A Model for Positive Return Strokes	48-1
<i>Vernon Cooray</i>	
Detection of Thunderstorms Near Surface Stations by Lightning Data	49-1
<i>Ronald M. Reap</i>	

Session 9A - Aerospace Vehicles
Charles King

Zoning of Aircraft by Electric Field Modelling	50-1*
<i>C. J. Hardwick, V. K. Thompson</i>	

* Paper printed in the Addendum
† Camera-ready copy not available
‡ Paper not submitted

Rocket-Triggered Lightning Test of an Earth-Covered Munitions Storage Bunker	51-1
<i>George H. Schnetzer, Richard J. Fisher</i>	
Lightning Phenomenology Bases for Full Threat Return Stroke Occurrence Following Extended Leader Sweep at Flight Altitudes	52-1*
<i>J. A. Plumer</i>	
Computer Optimized Design of π Type Surge Protective Circuits	53-1
<i>Yinggang Tu</i>	

Session 9B - Lightning Phenomenology

Samuel K. Frick

Triggering Lightning Flashes at Beijing Lightning Trigger Laboratory	54-1
<i>Hongfei Chen, Xinzhong Liu</i>	
Positive Cloud-to-Ground Flashes in Severe Storms	55-1*
<i>Donald R. MacGorman, Donald W. Burgess, Carolyn D. Morgenstern</i>	
On the Electromagnetic Fields and Power Radiated by Lightning Return Strokes	56-1
<i>E. P. Krider</i>	
On the Characteristics of Winter Lightning and Thundercloud	57-1
<i>Y. Goto, K. Narita, H. Komuro, N. Honma</i>	

Session 10A - Lightning Mapping

Ronald L. Holle

A Comparative Analysis of the Temporal Variability of Lightning Observations and GOES Imagery	58-1
<i>P. B. Roehr, T. H. Vonder Haar</i>	
U.S.A. National Lightning Data Service	59-1
<i>Bill Cook, Paul Casper</i>	
Real Time Monitor of Thunderstorm Activities in Japan by SAFIR	60-1
<i>Z-I. Kawasaki, K. Matsuura, P. Richard</i>	

* Paper printed in the Addendum

† Camera-ready copy not available

‡ Paper not submitted

Session 10B - Lightning Phenomenology

John Reed

- Lightning Environment at the Toronto 553 M AGL CN Telecommunications
Tower Under Severe Weather Conditions 61-1
*Jer-Shih Chang, W. Janischewskyj, A. M. Hussein, W. A. Chisholm,
P. Dziurewicz, Z-I. Kawasaki, K. Matsuura*
- The Coupling of a Current Channel to a Uniaxially Anisotropic Composite Skin . 62-1
Poh H. Ng, Paul M. McKenna
- Study of Atmospheric Electrical Events Above Complex Terrain 63-1*
Oscar Troncoso-Lozada

Session 11A - Ground/Ship Protection

Brian J. C. Burrows

- Evidence of Oscillations in Calculated Fields and Currents Induced by
Lightning in the Space Shuttle Launch Pad Structure 64-1
Frederick J. Eriksen, Richard S. Collier
- Coaxial Lightning/EMP Protective Device Characteristics 65-1
J. F. Fischer
- Cloud-to-Ground Lightning Related to Deaths, Injuries, and Property
Damage in Central Florida 66-1
*Ronald L. Holle, Raul E. Lopez, Robert Ortiz, Andrew I. Watson, Daniel
L. Smith, Dennis M. Decker, Charles H. Paxton*
- Breakdown Gradient of the Soil Under Lightning Discharge Conditions 67-1
Abdul M. Mousa

Session 11B - Aerospace Vehicles

William Walker

- Applications of Stress Envelope Concepts to Aircraft EMP and Lightning
Survivability 68-1*
Sam Frazier

- * Paper printed in the Addendum
† Camera-ready copy not available
‡ Paper not submitted

Integrating Army Avionics Hardening 69-1‡
Robert A. Pfeffer

ES-3A Lightning Qualification Test; Test Results Summary 70-1
Kurt Sebacher, Mike Whitaker

High Current Pulse Injection Test on an F-16/Lantirn Aircraft . . . (withdrawn) . . 71-1
John C. Horwath, Lawrence C. Walko, Steven Coffman, Jane White

Session 12A - Lightning Phenomenology *Vernon Cooray*

A Theory of Bead Lightning 72-1
T. S. Lee

Lightning Frequency and Associated Climatic Processes 73-1‡
J. K. Patnaik

Development of Models for Predicting the Triggering of Lightning by Launch
Vehicles 74-1*
Rodney A. Perala, Terence H. Rudolph, Calvin C. Easterbrook, Dale A. Steffen

Session 12B - Lightning Mapping *Donald R. MacGorman*

Detection Efficiency Losses of Networks of Direction Finders Due to Flash
Signal Attenuation With Range 75-1
Raul E. Lopez, Ronald L. Holle, Robert Ortiz, Andrew I. Watson

A Single-Point Warning System for Thunderstorms and Electric Fields 76-1*
W. T. Neumann, K. L. Cummins, E. P. Krider

Severe Thunderstorm Nowcasting 77-1
P. Richard

Poster Papers

An Empirical Approach to Dissipation Array® Systems Design P1-1
Roy B. Carpenter, Jr, Yinggang Tu

* Paper printed in the Addendum

† Camera-ready copy not available

‡ Paper not submitted

Human Body Responses to Step Voltages Due to Ground Currents in Lightning Attachments	P2-1
<i>J. C. Chai</i>	
Evaluating Groundpoint Equalization During Lightning Strikes	P3-1
<i>Donald R. Covington</i>	
Investigation of Aircraft Discharging Circuits	P4-1
<i>B. F. Evteev</i>	
Laboratory Produced Ball Lightning	P5-1
<i>Robert K. Golka, Jr.</i>	
Some Radiation Characteristics of Return Stroke Lightning	P6-1
<i>S. P. Gupta</i>	
Comparative Study of K-Pulses and Return Stroke Lightning	P7-1
<i>S. P. Gupta</i>	
Ball Lightning	P8-1
<i>M. A. Honnell, Thomas H. Shumpert</i>	
Finite-Difference Analysis of a Buried Munitions Storage Bunker Subject to Direct Lightning and Comparison with Experiment	P9-1
<i>K. O. Merewether, M. E. Morris</i>	
Acoustic-Based Real Time Discharge Channel Reconstruction of Triggered Lightning Using DSP-PC System	P10-1
<i>K. Nakamura, K. Horii</i>	
Inspection of Cable Shields In-Situ Without Disconnection	P11-1
<i>John E. B. Tuttle</i>	
Lightning: A View from the space Shuttle Payload Bay TV Cameras	P12-1
<i>Otha H. Vaughan, Jr.</i>	
Commercial Precipitation Static (P-Static) Test Equipment	P13-1
<i>R. Wayne Devereux</i>	
Comparative Performance of Lightning Air Terminals Under Natural Storm Conditions	P14-1*
<i>J. R. Gumley, Philip J. Jones</i>	

* Paper printed in the Addendum

† Camera-ready copy not available

‡ Paper not submitted

Alternative Equipment Test Procedures for Simultaneous Current Injection on Multiple Cable Bundles	P15-1*
<i>C. J. Hardwick, S. J. Haigh, R. E. Baldwin</i>	

LIST OF ATTENDERS

* Paper printed in the Addendum
† Camera-ready copy not available
‡ Paper not submitted

ALPHABETICAL LIST OF AUTHORS

Baldwin, R. E.	14*, P15*	Elliott, James R.	20*, 21
Bankston, N. G.	12	Emanuely, J. L.	25
Bazin, A.	35	Eriksen, Frederick J.	13, 64
Beeman, D.	23*	Evteev, B. F.	P4
Bentti, E. R.	3*		
Berger, Gérard	38	Fischer, J. F.	65
Bittner, Burt J.	37†	Fisher, Franklin A.	10
Bose, S.	30	Fisher, Richard J.	51
Brook, Marx	6*	Frazier, Sam	68*
Brown, Jeffrey C.	36*	Fukiyama, N.	31*
Burgess, Donald W.	55*		
Burrows, B. J. C.	40	Gauthier, D.	11
Byerley III, Leon G.	39	Giori, K. L.	27*
		Glynn, Michael S.	19*
Canavero, F.	47*	Golka, Jr., Robert K.	P5
Casper, Paul	59	Gondot, P.	8*
Carboni, V.	35	Goto, Y.	57
Carpenter, Jr, Roy B.	P1	Gray, Grant	6*
Chai, J. C.	P2	Gumley, J. R.	P14*
Chang, Jen-Shih	61	Gupta, S. P.	P6, P7
Chen, Hongfei	54		
Chen, Tiehan	6*	Haigh, S. J.	24*, P15*
Chisholm, W. A.	61	Hardwick, C. J.	14*, 24*, 41*, 50*, P15*
Clerc, J. P.	25	Henderson, R. P.	17
Coffman, Steven	(withdrawn) 71	Hojo, J.	31*, 44*
Collier, Richard S.	13, 64	Holle, Ronald L.	66, 75
Cook, Bill	59	Honma, N.	44*, 57
Cooray, Vernon	48	Honnell, M. A.	P8
Covington, Donald R.	P3	Hoeft, Robert	4
Craven, J. D.	17	Hopf, Christian	32
Cummins, K. L.	76*	Horii, K.	P10
		Horii, Kenji	45
Decker, Dennis M.	66	Horwath, John C.	(withdrawn) 71
Devereux, R. Wayne	29, P13*	Hussein, A. M.	61
Donnet, G.	8*		
Dziurewicz, P.	61	Inculet, I. I.	22
		Ishii, M.	31*, 44*
Easterbrook, Calvin C.	74		
Eichenberger, C.	35	Jadhav, D. B.	30
Elkins, D. B.	17	Jafferis, William	7‡

* Paper printed in the Addendum

† Camera-ready copy not available

‡ Paper not submitted

Janischewskyj, W.	61	Patnaik, J. K.	73‡
Jennings, N.	41*	Paxton, Charles H.	66
Jolly, Jon B.	34	Perala, Rodney A.	13, 74
Jones, Philip J.	P14*	Pfeffer, Robert A.	69‡
		Plumer, J. A.	1, 19*, 52*
Kawasaki, Z-I.	60, 61	Puybras, B.	25
Kern, A.	43*	Podgorski, Andrew S.	46
Komuro, H.	44*, 57	Podgorski, Elizabeth M.	46
Krehbiel, Paul	6*		
Krider, E. P.	56, 76*	Reap, Ronald M.	49
		Reed, Jim	39
Labate, D.	47*	Reilly, John J.	34
Lee, T. S.	72	Richard, P.	60, 77
Lehmann, Monty R.	16, 18‡	Rigden, Gregory J.	15
Lemke, L. T.	9	Rison, William	6*
Liu, Xinzhong	54	Rompalla, John	7‡
Lopez, Raul E.	66, 75	Roohr, P. B.	58
LoVetri, J.	22	Roth, J. U.	43*
		Roy, T. E.	17
MacGorman, Donald R.	55*	Rudolph, Terence H.	74
Maier, Matthew R.	28		
Matsuura, K.	60, 61	Sanicandro, Rocco	7‡
Mauriello, A. J.	34	Sargent, Noel B.	36*
McCrary, Stephen	6*	Sawada, J.	31*
McDowall, Rosemarie L.	19*	Schaffar, A.	2
McKenna, Paul M.	62	Schnetzer, George H.	51
Merewether, M. O.	P9	Sebacher, Kurt	70
Morgenstern, Carolyn D.	55*	Serafin, D.	35
Morita, N.	23*	Setzer, T. E.	1
Morris, M. E.	P9	Shio, Hisashi	(withdrawn) 26
Mousa, Abdul M.	67	Shumpert, T. H.	17
		Shumpert, Thomas H.	P8
Nagamori, Yuki	45	Siddiqi, S.	1
Nakamura, K.	P10	Smith, Daniel L.	66
Nakamura, Kouichi	45	Smith, I.	35
Nanevich, J. E.	27*	Sone, Mototaka	45
Narita, K.	57	Spiller, Olaf	(withdrawn) 42
Neumann, W. T.	76*	Stahmann, J. R.	3*
Ng, Poh H.	21, 62	Steffen, Dale A.	74
Nial, Jack	16	Sumi, Shin-ichi	45
Ortiz, Robert	66, 75	Thompson, V. K.	50*

* Paper printed in the Addendum

† Camera-ready copy not available

‡ Paper not submitted

Trochet, P.	8*
Troncoso-Lozada, Oscar	63*
Tu, Yinggang	53, P1
Tuttle, John E. B.	P11
Vaughan, Jr., Otha H.	P12
Vecchi, G.	47*
Vonder Haar, T. H.	58
Wada, Masakazu	45
Wakefield, Charles	4
Walko, Lawrence C.	(withdrawn) 71
Watson, Andrew I.	66, 75
Weckman, E. J.	22
Weigel, Henry S.	20*
Wenzler, Carl J.	36*
Whitaker, Mike	16, 18†, 70
White, Jane	(withdrawn) 71
Wiedmann, J.	43*
Wilson, J.	40
Wohlman, Richard	7‡
Yamamoto, T.	31*
Yost, Charles A.	5
Zaima, E.	31*
Zischank, W. J.	33

* Paper printed in the Addendum

† Camera-ready copy not available

‡ Paper not submitted

LAUNCH PAD LIGHTNING PROTECTION ENHANCEMENT BY INDUCED STREAMERS

**J. R. Stahmann
Boeing Aerospace Operations, FA-48
Kennedy Space Center, Florida 32899
Telephone (407) 867-1400 FAX (407) 867-1087**

**E. R. Benti
NASA, TM-LLP-5
Kennedy Space Center, Florida 32899
Telephone (407) 867-8745 FAX (407) 867-3737**

ABSTRACT

Estimations of the effectiveness of launch pad lightning protection systems on protected points within the cone of protection usually ignore the effects of streamers that propagate out to meet downcoming lightning leaders. Multiple streamers develop when the lightning leader is close enough to cause high electric fields and air breakdown on the structures. The tips of the streamers propagate toward the leader tip; and the longest and fastest streamers capture the stroke. Improved operational television at the launch pads has produced TV pictures of this process. The lightning protection enhancement caused by this streamer extension of the protective systems can be estimated.

INTRODUCTION

For perspective, figure 1 shows Launch Complex 39A (LC-39A) at KSC as it might appear to an approaching lightning leader. As the stroke approaches, streamers from the catenary wire lightning protection system and other exposed points are produced by the high electric fields that go out to meet the downcoming leader. Figure 2 shows such a streamer formed on the lightning protection mast at Pad 39B with Space Transportation System-40 (STS-40) present. However, other streamers from the catenary wire successfully captured the stroke. This unusual lightning picture was obtained due to improved operational TV camera surveillance during thunderstorms as a result of actions taken by the KSC Lightning Safety Committee. The picture was taken from Pad 39A where lightning interference was minimal. The length and shape of the streamer can be inferred from video pictures as shown in figure 3 and in previous papers (1)(2).

The earlier papers estimated the probability of striking a point on the structure in the presence of other points by using the striking distance theory, which assumes that lightning strikes the nearest grounded point in its last jump to earth. The last jump to earth is called the striking distance, which is a function of the stroke charge and peak current. For convenience, all strokes were divided into deciles with striking distances and peak currents corresponding to the average for that decile.

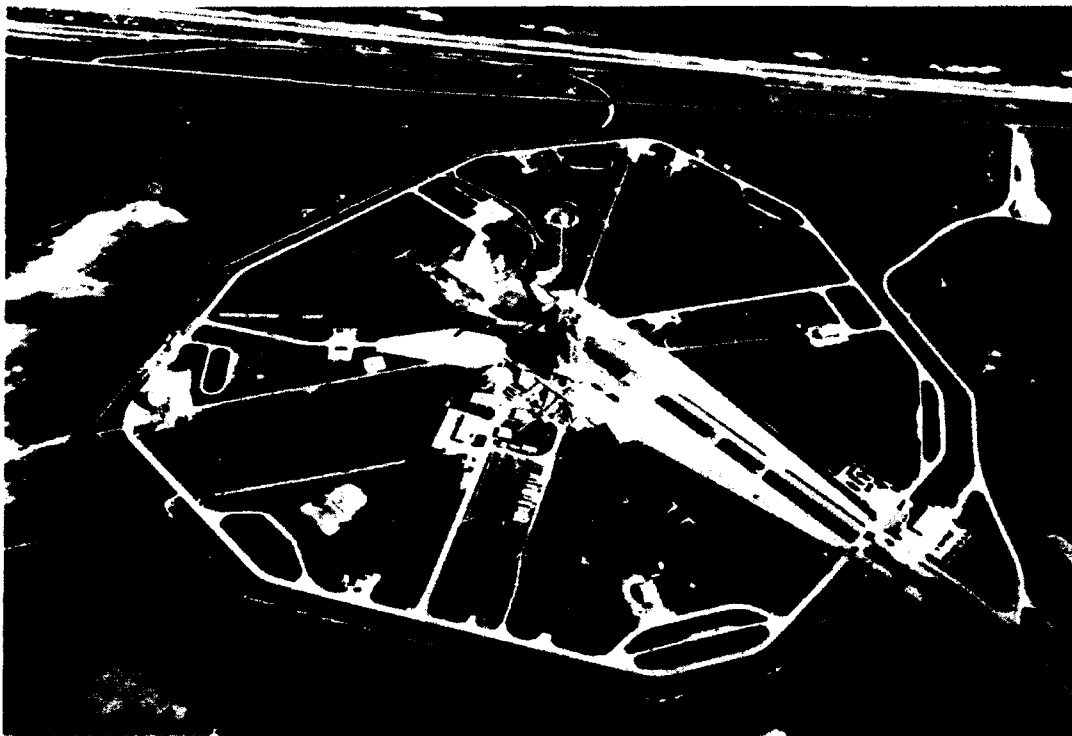


FIGURE 1. LIGHTNING'S EYE VIEW OF LC-39A AT KSC

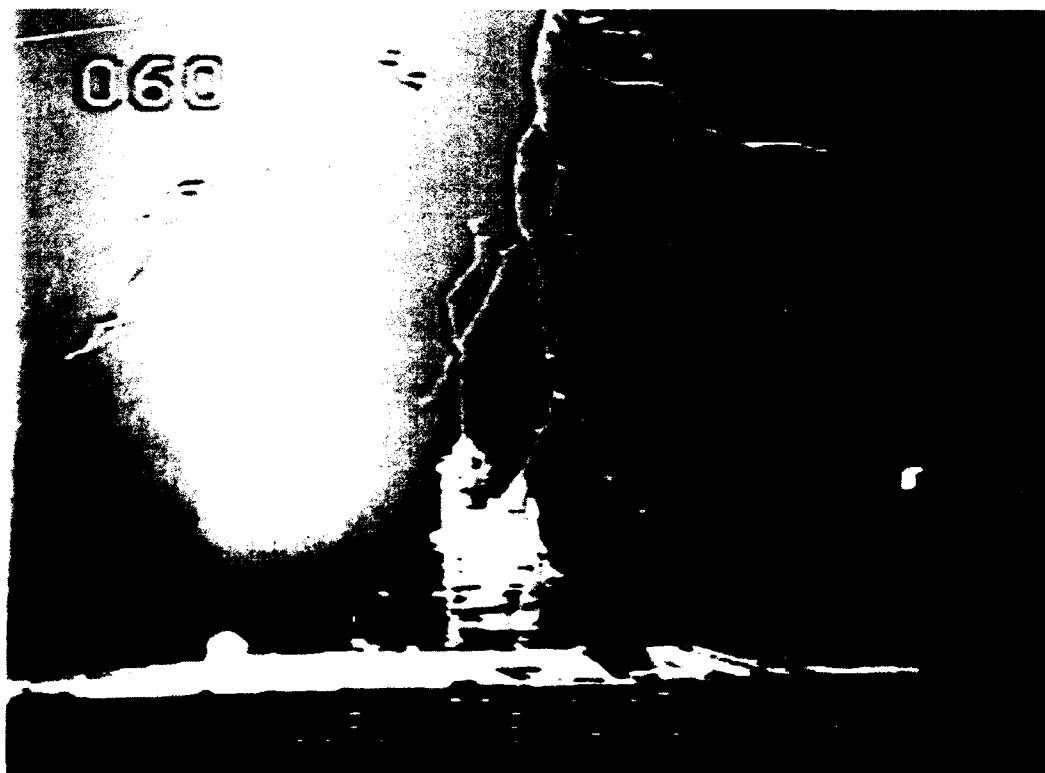


FIGURE 2. UPWARD-GOING STREAMERS GOING OUT FROM PAD PROTECTION SYSTEM TO MEET AND CAPTURE DOWNWARD-GOING LIGHTNING LEADERS (STROKE OCCURRED MAY 31, 1991, AT LC-39B WITH STS-40 PRESENT)

160



FIGURE 3. STREAMER LENGTH AND SHAPE CAN BE INFERRED FROM ABRUPT DIRECTION CHANGE AS STREAMER CAPTURES STROKE AT LC-39A, AUGUST 19, 1991

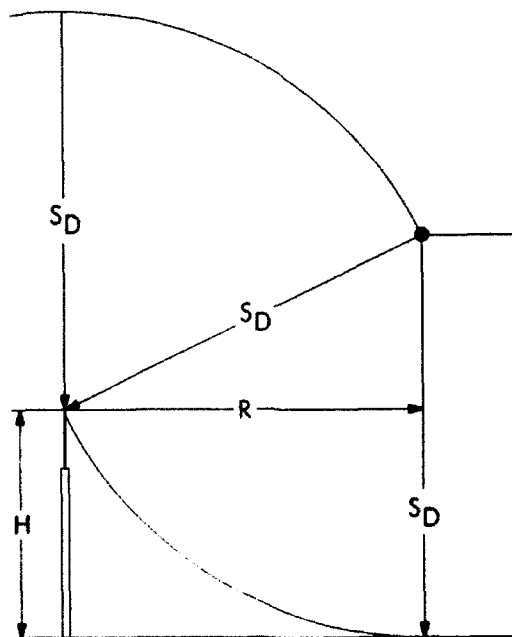


FIGURE 4. RADIUS OF ATTRACTION, R , IS A FUNCTION OF STRIKING DISTANCE, S_D , AND POINT HEIGHT, H

STRIKING DISTANCE THEORY

The assumption is that all leaders that approach a grounded point or plane will go to that point or plane when they are within the striking distance. This assumption results in a series of spherical surfaces around grounded points and planes above the ground plane, corresponding to the various striking distances. The basic geometry is shown in figure 4 for a single pole of height, H, above a ground plane. All strokes within the attraction radius, R, of the pole will hit the top of the pole if $S_D > H$. R can be calculated from the relationship:

$$R = \sqrt{2S_D H - H^2}$$

The area corresponding to this radius can then be multiplied by the stroke density for that area, assumed in this paper to be 2×10^{-6} strokes per square meter per decile per year, to obtain the probability of a stroke hitting the pole for each decile striking distance. Repeating the calculations for the ten deciles and adding the results give the hit probability in strokes per year. For those deciles where the striking distance is equal to or less than the pole height, the attraction radius is equal to the striking distance, and the stroke may hit the side of the upper end of the pole for a distance equal to the difference between the pole height and the striking distance. When the leader is closer to the ground than to the pole, the stroke is assumed to hit the ground.

When additional points are "protected" by a point or pole, the spheres with a particular striking distance intersect and result in "windows" of approach discussed in a previous paper (2) where the leader is closer to the protected point than the protecting point (figure 5). The probability of entering such a window and striking the protected point is determined by calculating the window projected area on the ground and multiplying by the decile stroke density, as in the case of the single pole. The upper edges of the windows are located on the perpendicular bisector of a line between the points, and the lower edges are on a parabola with its focus at the lower point and the earth as its directrix. The windows are also the locus of the center of a "rolling ball" with a striking distance radius that rolls over the points.

DOWN'S PROGRAM

When a number of points have to be considered, the calculations detailed in the previous paper (2) become too laborious to apply to most protection investigations. David Downs of Martin Marietta in Denver, Colorado produced a computer program based on the above concepts and the paper (2). This makes such investigations relatively quick and easy. This program was adapted for KSC Launch Pad use, and illustrations of this technique applied to upward-going streamers are presented in this paper. The program assumes a 400- by 400-meter area and a stroke density of one stroke per square meter (160,000 strokes). The program calculates and plots where each stroke will hit for each of the ten deciles and then prints out the percentage of strokes hitting each point. Finally, it sums all the deciles and gives the overall percentage averages for all deciles. For striking distances, the program uses Love's formula:

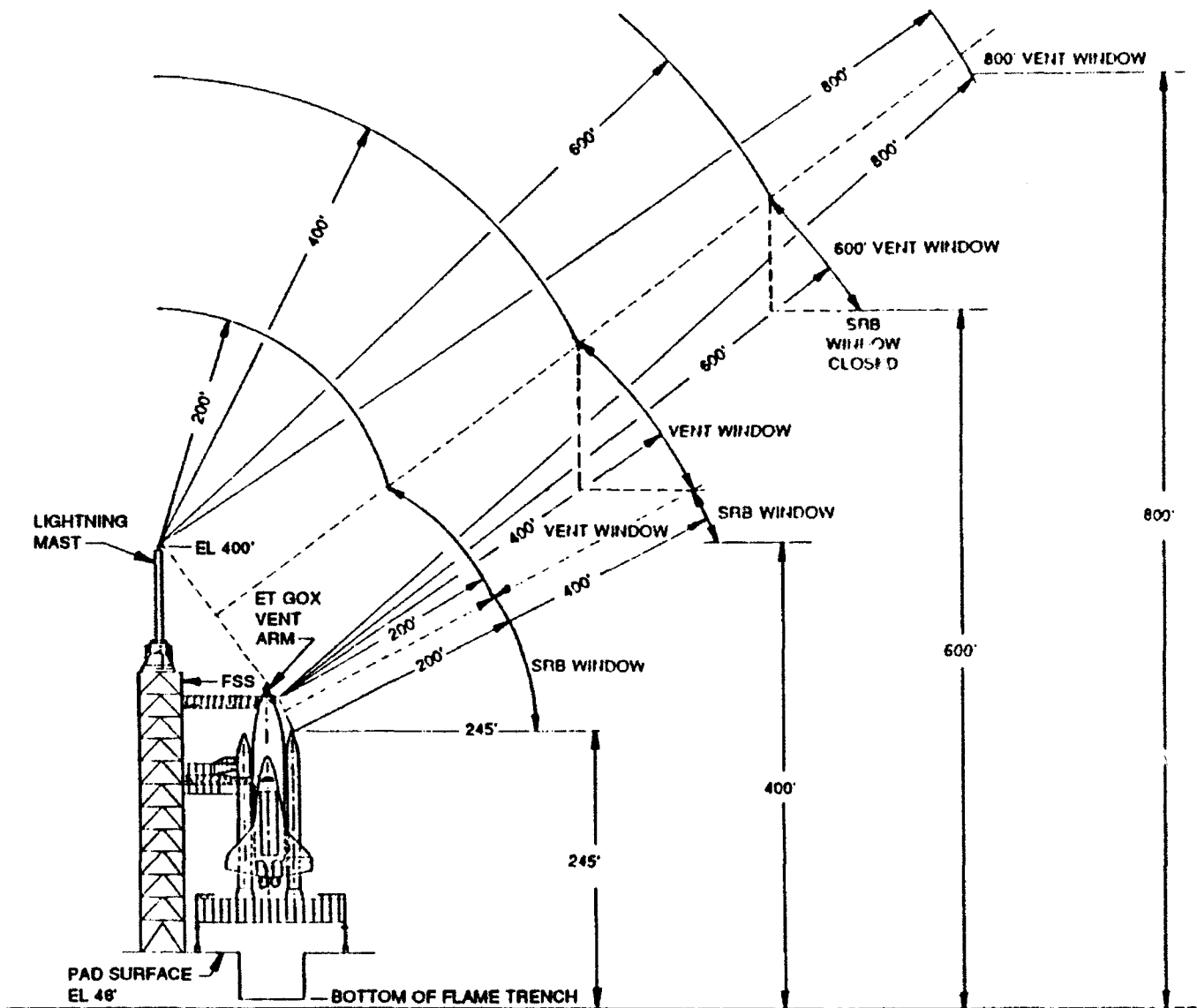


FIGURE 5. GOX VENT WINDOWS FOR STROKES APPROACHING DIRECTLY FROM THE EAST

$$S_D = 10I_{PK}^{0.65} \text{ Meters}$$

Another program, written by W.M. Jackson of Aerospace Corporation, Cape Canaveral Air Force Station, Florida, allows use of protecting lines as well as points and has a selectable stroke density using a Monte Carlo technique. The Down's program was modified for use at KSC to allow a larger area with the same number of strokes, generally one stroke for every 4 square meters in an 800- by 800-meter area. Points are identified by their x, y, z coordinates. The percentages of the total area can be converted to strokes per year for particular points by multiplying the stroke percentage by the stroke probability for the entire area [e.g., $(800 \times 800 / 1,000,000) \times 20$ strokes/kilometer x percent for the 800- by 800-meter area]. The program runs well on an IBM PC or compatible 386 with a math co-processor 387 chip and a VGA monitor.

For this study, streamers were added to the protecting points vertically and horizontally above the point. Since the streamers move horizontally toward the downcoming leader that may come from any direction, a circle of points was used to represent the tip of the streamer, as discussed in the next section.

SINGLE PROTECTING AND PROTECTED POINTS

To illustrate the technique, consider a 400-foot pole protecting a point 200-feet high and 100 feet from the pole. This places the protected point within the 1:1 linear cone of protection of the pole. This simple configuration is shown in figure 6. The window of approach shown closes at about 550 feet, corresponding to the striking distance of the ninth decile.

If we consider a pole by itself and use Love's formula for striking distance, the number of strokes attracted to the pole increases rapidly with its height (figure 7) but gradually tapers off as the height exceeds the striking distance of each decile in turn until the total probability of hitting the pole reaches a maximum of 0.881 stroke per year at the longest striking distance of 705 feet. This illustrates that, for striking distances in accordance with Love's formula, poles and towers with heights above about 400 feet do not offer much additional protection.

The computer tabulations shown and plotted in the next figures utilized the 800- by 800-meter total area used for the KSC Launch Pads. For this area, an average of 0.01 percent represents a probability of $12.8 \times 0.0001 = 0.00128$ stroke per year or one stroke every 781 years. For the 400- by 400-meter total area, 0.01 percent represents one stroke every 3,125 years.

Figure 8 shows a plot of stroke probability in percent area versus the decile striking distances for the single protecting and protected points assuming no streamers. As the striking distances increase, the protecting area increases; but the protected area probability first increases and then decreases until the window closes at the ninth decile (number 8 on the plot) at about 168 meters or 550 feet. The protecting point average area of 6.32 percent corresponds to 0.809 stroke per year, and the protected point average area of 0.39 percent corresponds to 0.05 stroke per year.

Figure 9 is a similar plot for a 600-foot protecting point, assuming that a 200-foot vertical streamer occurs on top of the pole. The results are very similar to those of figure

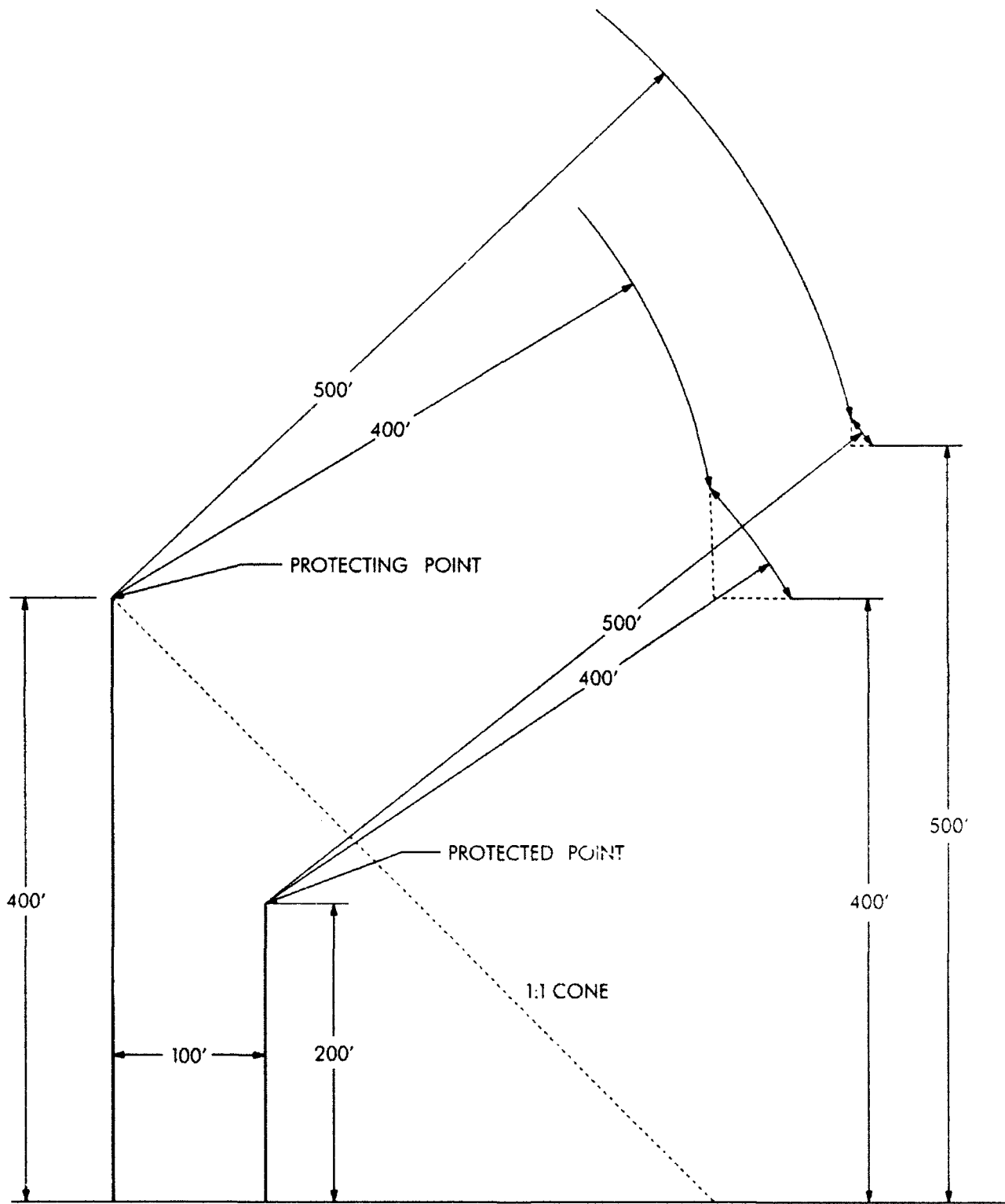
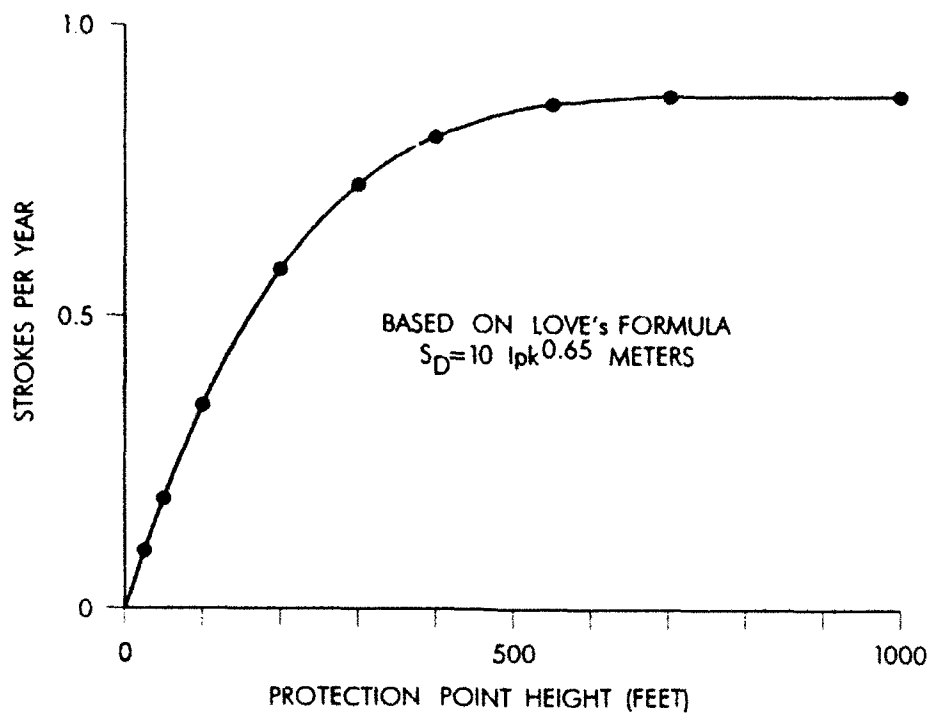
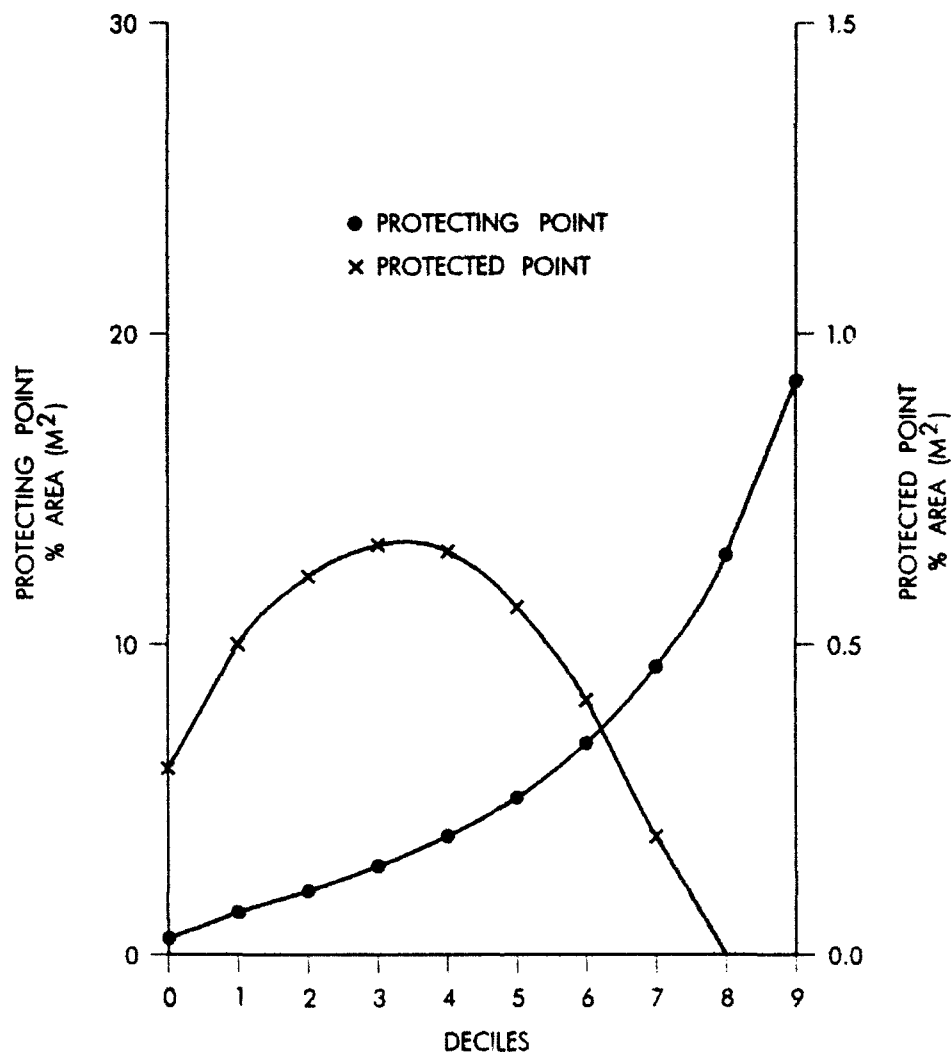


FIGURE 6. SIMPLE PROTECTION CONFIGURATION



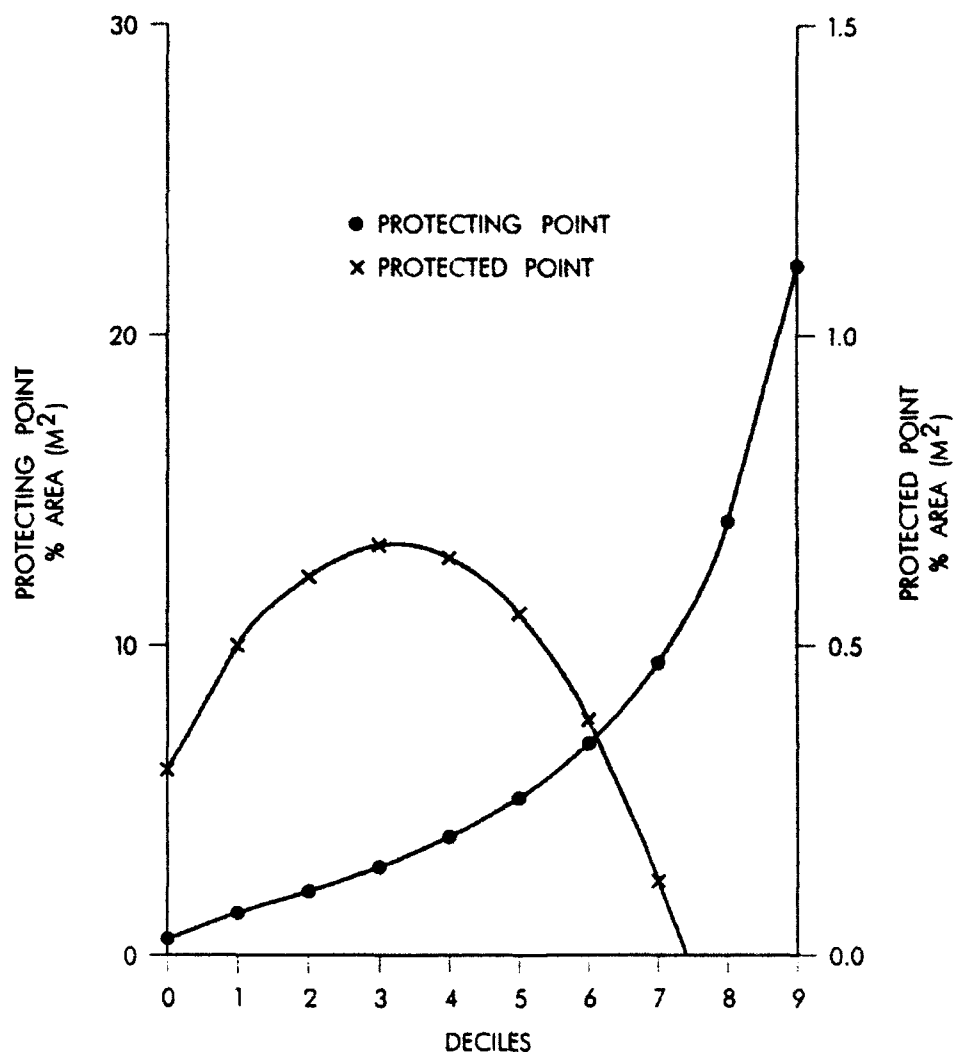
POLE HEIGHT (FEET)	STROKES/YEAR
25	0.099
50	0.188
100	0.348
200	0.582
300	0.728
400	0.810
550	0.867
705	0.881
1000	0.881

FIGURE 7. STROKE PROBABILITY VERSUS PROTECTING POINT HEIGHT



DECILE	SD(m)	lpk (KA)	PROTECTING POINT	PROTECTED POINT
0	32.7	6.2	0.53	0.30
1	52.7	12.9	1.37	0.50
2	64.5	17.6	2.06	0.61
3	76.1	22.7	2.85	0.66
4	88.0	28.4	3.82	0.65
5	101.2	35.2	5.05	0.56
6	117.9	44.5	6.82	0.41
7	138.5	57.0	9.29	0.19
8	168.4	77.0	12.90	—
9	214.8	112.0	18.50	—
AVERAGE			6.32	0.39

**FIGURE 8. PROJECTED AREAS VERSUS DECILES
(SIMPLE CONFIGURATION, NO STREAMER)**



DECILE	SD(m)	I _{pk} (KA)	PROTECTING POINT	PROTECTED POINT
0	32.7	6.2	0.53	0.30
1	52.7	12.9	1.37	0.50
2	64.5	17.6	2.06	0.61
3	76.1	22.7	2.85	0.66
4	88.0	28.4	3.83	0.64
5	101.2	35.2	5.06	0.55
6	117.9	44.5	6.85	0.38
7	138.5	57.0	9.45	0.12
8	168.4	77.0	14.00	—
9	214.8	112.0	22.25	—
AVERAGE			6.83	0.38

FIGURE 9. PROJECTED AREAS VERSUS DECILES (SIMPLE CONFIGURATION, 200-FOOT VERTICAL STREAMER)

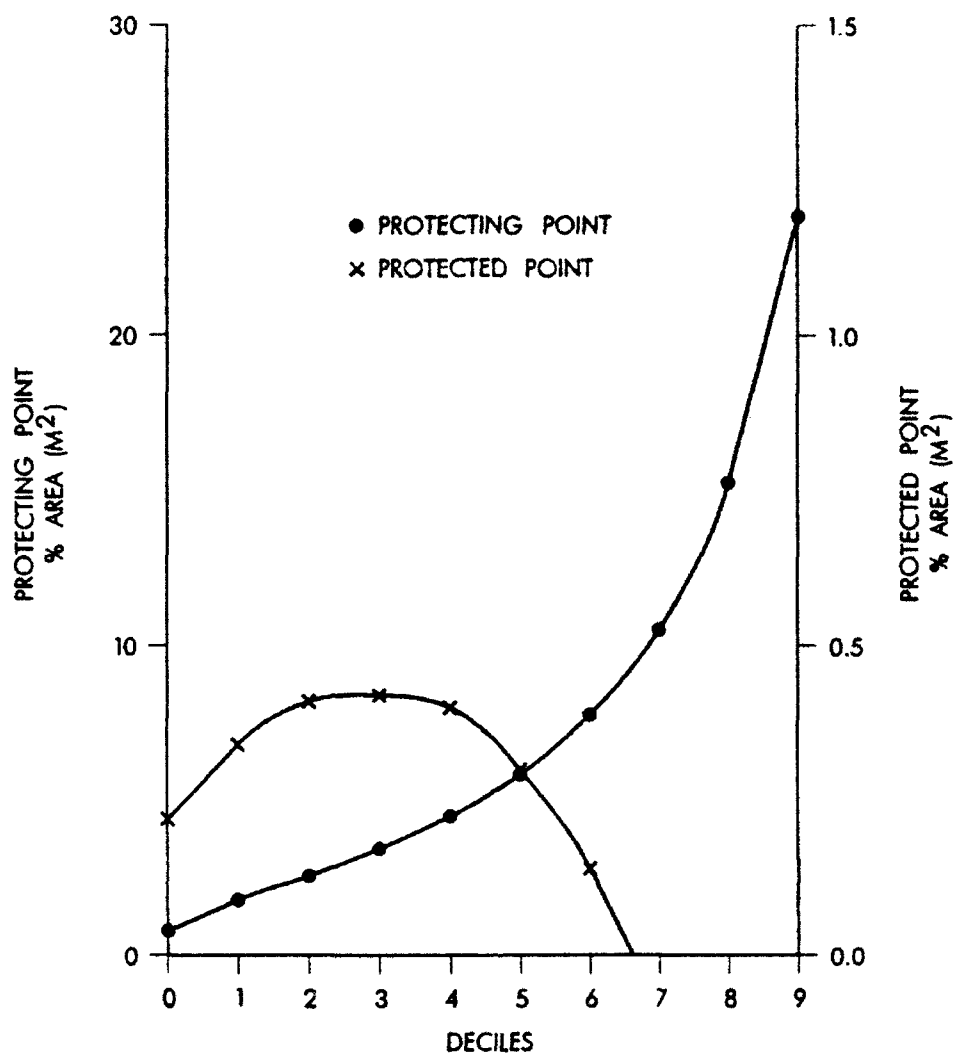
8 since the additional vertical height results in little additional protection above 400 feet, as discussed earlier.

However, if a 25-foot horizontal streamer is added (figure 10), the protection becomes more effective. The window closes between the seventh and eighth decile (about 125 meters or 410 feet). The protecting area average area of 7.64 percent corresponds to 0.98 stroke per year, and the protected stroke average of 0.22 percent corresponds to 0.028 stroke per year. Further, if the horizontal streamer length is increased to 75 feet (figure 11), the window closes between the fifth and sixth decile (about 94 meters or 308 feet). The protecting point average area increases to 9.44 percent corresponding to 1.21 strokes per year, and the protected point average area drops to 0.03 percent corresponding to 0.00384 stroke per year or one stroke every 260 years.

In addition to tabulating the areas of attraction, the computer program plots the areas associated with each point in color. Each point or group of points is assigned a unique color. Figure 12 shows a plot of the third decile of the simple single 400-foot protecting pole and the 200-foot protected pole. The outline of the 2.06 percent attraction area of the protecting pole can be seen, and the 0.61 percent attraction area of the protected pole can be seen in dark black at the right. When a 200-foot vertical and 75-foot horizontal streamer is added to the protecting pole, the third decile result is shown in figure 13. The top of the protecting pole is shown in the center, the tips of the horizontal streamers are shown as a circle of dots, and the top of the protected pole is shown at the right. The attractive area of the protecting pole is increased to 3.75 percent and that of the protected pole is reduced to 0.09 percent. It should be understood that figures 12 and 13 show only one decile and that all deciles must be averaged to obtain the total probability.

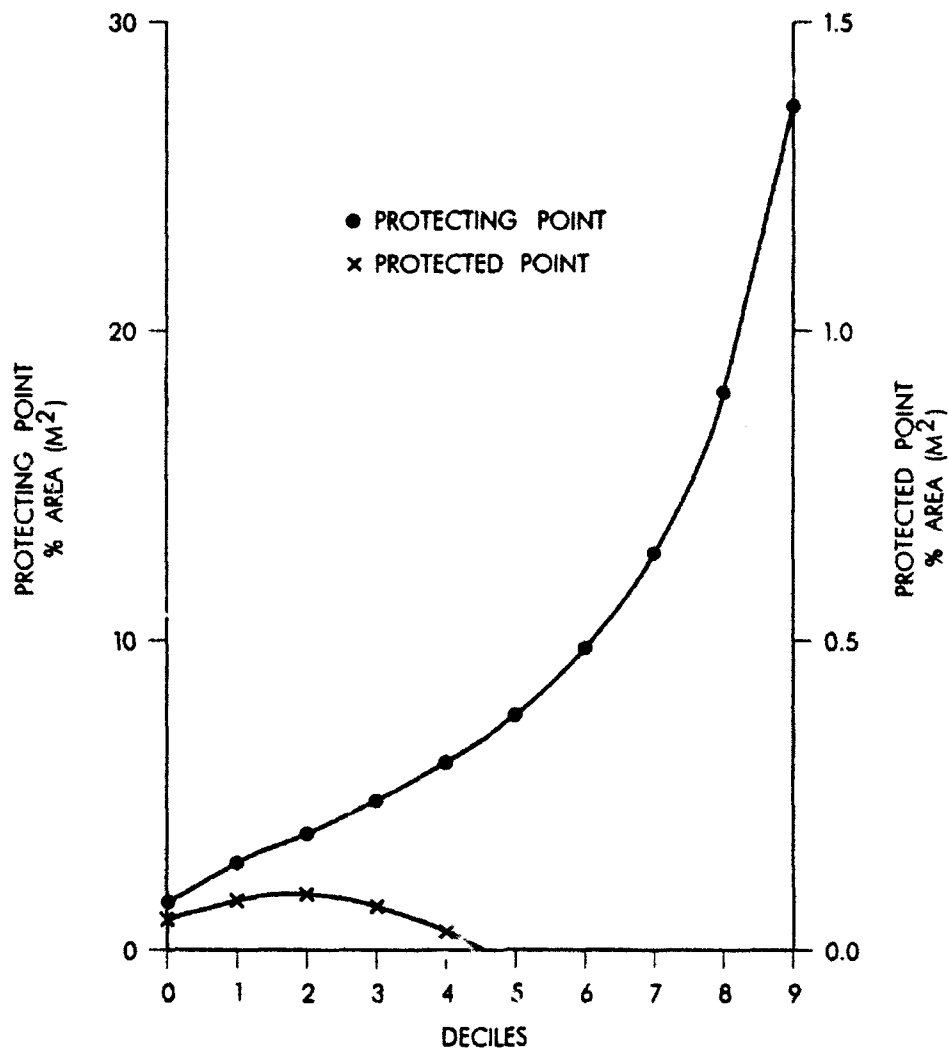
LAUNCH PAD APPLICATION

When the significant points corresponding to the lightning protection systems on Launch Complex 39 are entered into the computer program along with the points to be investigated, plots similar to those obtained with the simple configuration are obtained. The attractive areas of the lightning mast, catenary wire, tip of the crane, and gaseous oxygen (GOX) vent hood lightning rods are plotted in figure 14. The attractive area of the protection system, which includes both the lightning mast and catenary wire, totals $9.39 + 8.38 = 17.77$ percent, which corresponds to 2.27 strokes per year to the protection system. The crane tip attractive area of 0.07 percent corresponds to 0.009 stroke per year or one stroke every 112 years if the crane were stowed in the westerly direction. Actually, the crane is usually stowed under the catenary wire where it is very well protected. The GOX lightning rods have an attractive area of 0.09 percent corresponding to 0.01152 stroke per year or one stroke every 87 years. However, the GOX vent arm is extended toward the east only during operations so that this probability is much reduced. Since these points are exposed to high electric fields prior to the stroke, streamers could also enhance their attractive areas. The third decile plot of the attraction areas for the Launch Pads is shown in figure 15. As shown, the catenary wire is approximated by a series of dots. The crane tip area is shown in white at the left and the GOX vent rod area is shown in black at the right. This application is shown only as an illustration of the investigation of a practical structure.



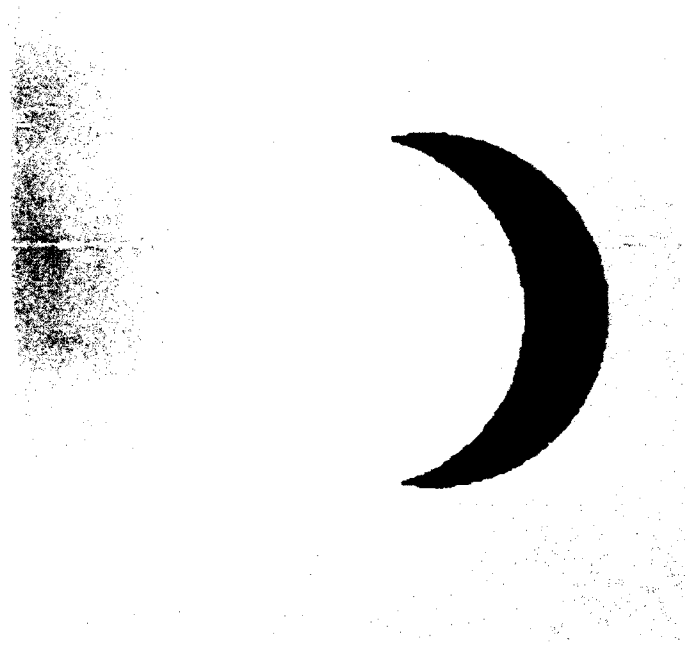
DECILE	SD(m)	lpk (KA)	PROTECTING POINT	PROTECTED POINT
0	32.7	6.2	0.80	0.22
1	52.7	12.9	1.80	0.34
2	64.5	17.6	2.57	0.41
3	76.1	22.7	3.46	0.42
4	88.0	28.4	4.50	0.40
5	101.2	35.2	5.85	0.30
6	117.9	44.5	7.77	0.14
7	138.5	57.0	10.53	—
8	168.4	77.0	15.27	—
9	214.8	112.0	21.36	—
AVERAGE			7.64	0.22

FIGURE 10. PROJECTED AREAS VERSUS DECILES (SIMPLE CONFIGURATION, 200-FOOT VERTICAL STREAMER PLUS 25-FOOT HORIZONTAL STREAMER)



DECILE	SD(m)	l _{pk} (KA)	PROTECTING POINT	PROTECTED POINT
0	32.7	6.2	1.51	0.05
1	52.7	12.9	2.81	0.08
2	64.5	17.6	3.75	0.09
3	76.1	22.7	4.82	0.07
4	88.0	28.4	6.06	0.03
5	101.2	35.2	7.58	—
6	117.9	44.5	9.75	—
7	138.5	57.0	12.82	—
8	168.4	77.0	18.01	—
9	214.8	112.0	27.27	—
AVERAGE			9.44	0.03

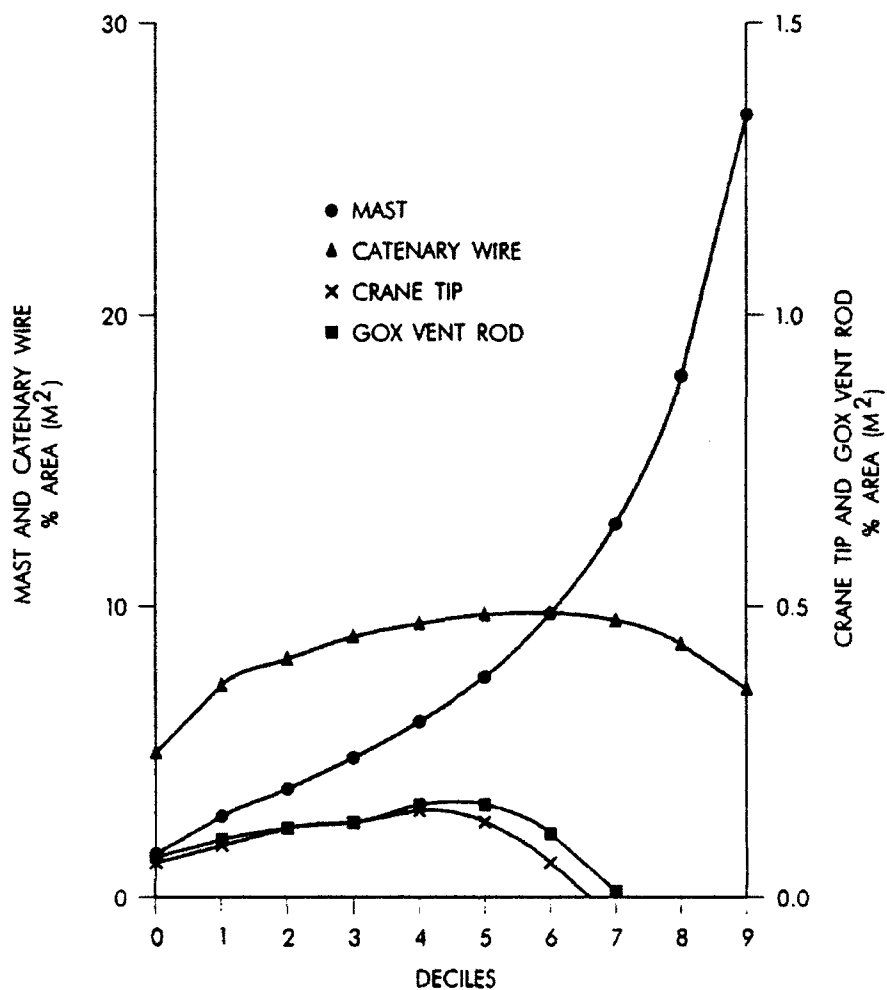
FIGURE 11. PROJECTED AREAS VERSUS DECILES (SIMPLE CONFIGURATION, 200-FOOT VERTICAL STREAMER PLUS 75-FOOT HORIZONTAL STREAMER)



**FIGURE 12. SIMPLE CONFIGURATION, THIRD DECILE PROTECTION,
NO STREAMER**



**FIGURE 13. SIMPLE CONFIGURATION, THIRD DECILE PROTECTION, WITH
200-FOOT VERTICAL STREAMER AND 75-FOOT HORIZONTAL STREAMER**



DECILE	SD(m)	l _{pk} (KA)	MAST	CATENARY WIRE	CRANE TIP	GOX VENT ROD
0	32.7	6.2	1.51	5.00	0.06	0.07
1	52.7	12.9	2.81	7.30	0.09	0.10
2	64.5	17.6	3.75	8.20	0.12	0.12
3	76.1	22.7	4.82	8.96	0.13	0.13
4	88.0	28.4	6.06	9.41	0.15	0.16
5	101.2	35.2	7.58	9.71	0.13	0.16
6	117.9	44.5	9.75	9.77	0.06	0.11
7	138.5	57.0	12.82	9.52	—	0.01
8	168.4	77.0	17.92	8.70	—	—
9	214.8	112.0	26.86	7.17	—	—
AVERAGE			9.39	8.38	0.07	0.09
PROBABILITY (STROKES/YEAR)			1.20192	1.07264	0.00876	0.01152

FIGURE 14. PROJECTED AREAS VERSUS DECILES (LC-39 CONFIGURATION, 200-FOOT VERTICAL STREAMER PLUS 75-FOOT HORIZONTAL STREAMER)

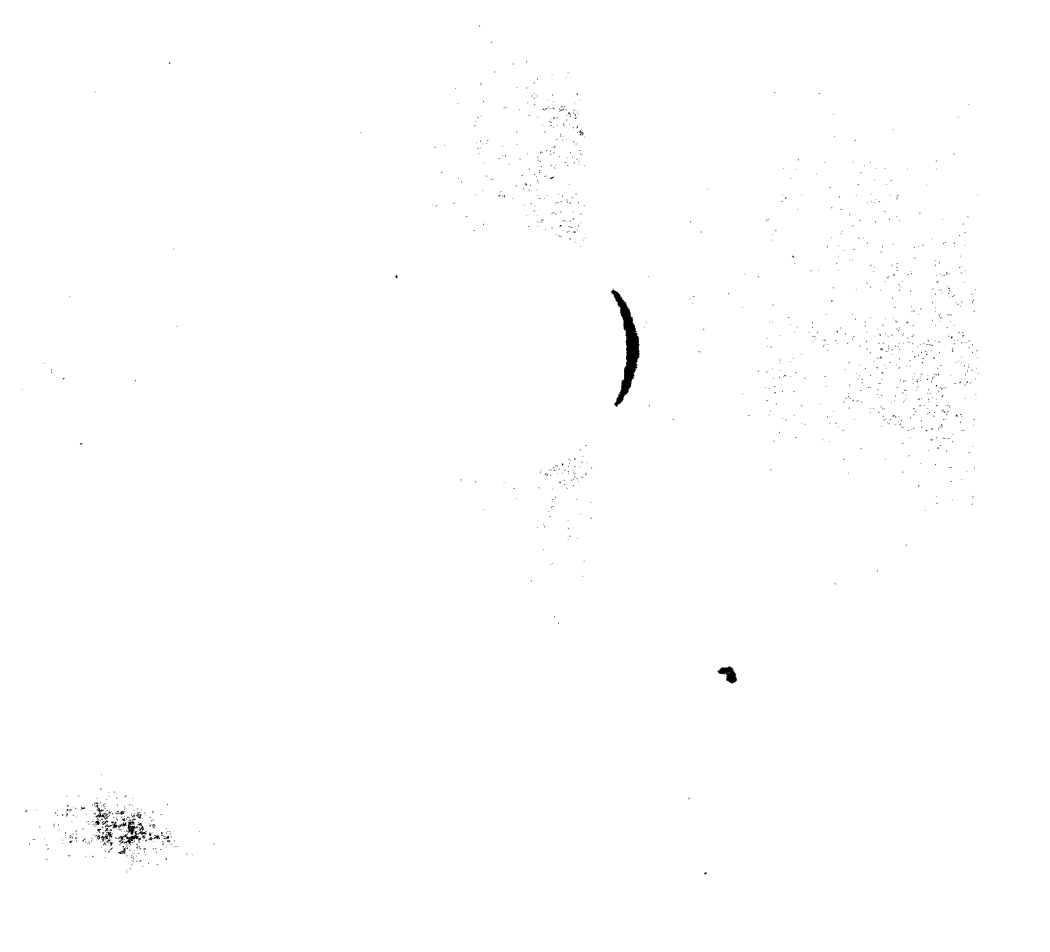


**FIGURE 15. LC-39 CONFIGURATION, THIRD DECILE PROTECTION, WITH
200-FOOT VERTICAL STREAMER AND 75-FOOT HORIZONTAL STREAMER**

CONCLUSIONS

TV surveillance of KSC Launch Pads during thunderstorms has resulted in pictures of upward-going streamers moving from the ground to meet one or more downcoming lightning leaders to complete the lightning stroke. The shape and length of these streamers can be inferred from the pictures, even after the stroke is completed. The techniques of a previous paper can be used to assess the lightning protection effectiveness of a system and its streamers, particularly when incorporated in a computer program that greatly speeds the computations so the effects of design changes can be quickly assessed.

The general effects of streamers are in a direction to enhance the lightning protection of a system designed for exposure to the high electric fields preceding a lightning stroke. This is especially true when the streamers move horizontally over the point to be protected. Since the striking distance theory results in windows of approach the leader must use to reach the protected point, high electric fields will be produced in a direction to produce streamers from the protecting system in such a direction that further protects the protected point. In the simple case discussed previously, a 75-foot horizontal streamer reduced the probability of hitting a protected point from once every 20 years to once every 260 years.

The techniques illustrated in this paper can be used to quickly estimate the effectiveness of lightning protection systems. When used by designers, both the protection and cost effectiveness of design changes can be quickly estimated.

REFERENCES

1. J.R. Stahmann, "Inside the Cone of Protection," International Aerospace and Ground Conference on Lightning and Static Electricity, Fort Worth, Texas, June 21-23, 1983, pp. 27-1 to 27-7.
2. J.R. Stahmann, "Launch Pad Lightning Protection Effectiveness," International Aerospace and Ground Conference on Lightning and Static Electricity, Cocoa Beach, Florida, April 16-19, 1991, pp. 31-1 to 31-12.

Lightning Precursor Signatures from Dual-Polarization Radar Measurements of Storms

Paul Krehbiel, Tiehan Chen, Stephen McCrary, William Rison, Grant Gray, Marx Brook

Langmuir Laboratory, Geophysical Research Center

New Mexico Tech, Socorro, NM 87801

Telephone: (505) 835-5215; Fax: (505) 835-5707

ABSTRACT

Real-time correlation and display of the co-polar and cross-polar radar returns from electrically active storms has provided dramatic indications of the buildup of electric stress in the storms, and of the collapse of the stress at the time of lightning. Following up on the pioneering work of Hendry and McCormick, strong correlations are observed above the 0 °C level in the middle and upper parts of storms that are indicative of the presence of electrically aligned particles. Regions of strong correlation are readily identified in scanning a storm and provide an excellent indicator of the potential for lightning in the storm. The correlation values have been used to predict the occurrence of individual lightning discharges in storms. In addition, they have been used to detect the onset of electrification in storms and to tell when a storm is finished producing lightning.

INTRODUCTION

In a pioneering study, Hendry and McCormick (1976) of the National Research Council in Canada reported radar observations which indicated that particles were being electrically aligned in the upper levels of thunderstorms. Their observations were made using a dual-channel circular polarization radar which operated at 16.5 GHz, and were obtained by coherently correlating the co-polar (e.g. RHC) and cross-polar (LHC) returns from a storm. Large correlation coefficients were observed in the upper parts of storms which they interpreted as indicating a high degree of common particle orientation. The correlation values decreased at the time of lightning discharges and regenerated between discharges. Lightning was sometimes also observed to increase the correlation or orientation.

In this paper we describe dual-polarization observations which confirm and extend Hendry and McCormick's results. Digital signal processors have been used to compute the co-polar-cross-polar correlation in real time and to display the correlation vs. position as the radar scanned through a storm. The resulting correlation 'signatures' have been found to provide an excellent indicator of the potential of a storm for producing lightning. The observations were made at Kennedy Space Center, Florida as part of the Convective and Precipitation/Electrification (CaPE) program conducted at KSC during the summer of 1981.

MEASUREMENTS

The radar used in this study was a polarization-diverse system in which the polarization of the transmitted signal was alternated from pulse to pulse, between either right- and left-circular polarization or, with a different orthomode transducer, between horizontal and vertical linear polarizations. The co-polar and cross-polar returns were simultaneously received, both coherently and incoherently, and the receiver outputs were digitized, processed and displayed in real time. The processing was accomplished with PC-based digital signal processors and the results were displayed on a high resolution monitor of the host PC. In addition, a high-density digital recorder was used to record complete time series data. The radar operated at 9.8 GHz (3 cm wavelength) and was a pulsed system having a 1 microsecond pulse length and 20 kW peak transmitted

power. It utilized a circularly-symmetric Cassegrain antenna with a corrugated feed to maximize polarization purity.

For detecting the presence of aligned particles, the simultaneous co- and cross-polar returns for a given transmitted polarization were coherently correlated to give the squared magnitude $|\rho|^2$ and phase ϕ of the correlation function. These and other quantities were displayed in PPI and RHI format as the radar scanned through a storm. All results presented in this paper are from circularly polarized transmissions, which were found to be more sensitive to alignment effects than linear polarization. Lightning occurrences were detected using an electric field change sensor and a directional optical detector attached to the radar antenna.

RESULTS

Figures 1a and 1b show vertical cross-sections of the various polarization variables in a storm on Day 278, 1991. (The scans do not extend down to ground level because radar transmissions at KSC were restricted at low elevation angles.) The two sets of cross-sections are from sequential scans just before and after an intracloud lightning discharge occurred in the storm, and were separated by less than 20 seconds in time. The figures show the co-polar and cross-polar reflectivity structure, the resulting circular depolarization ratio (CDR), and the squared magnitude and phase of the co-polar - cross-polar correlation. The storm was 15 to 27 km distant from the radar and extended up to 13 km altitude (MSL), with two cells being evident in the co-polar reflectivity.

In the scan just prior to the lightning (Figure 1a), two regions of strong correlation ($|\rho|^2 > 0.75$) existed at mid-levels (6-9 km MSL) in the far cell and in the upper part (9-12 km altitude) in the near cell. These were associated with local maxima in the cross-polar power and in CDR. After the discharge, the correlation regions had essentially disappeared and the associated cross-polar returns and CDR had diminished in intensity. The co-polar returns were unchanged in the two scans, as were the cross-polar returns and CDR values below the melting level, at about 4-4.5 km altitude.

Figure 2 shows how the polarization quantities change with time in a fixed direction through the electrically active region of a storm. The variables in the figure are the same as in Figure 1 but are displayed as a function of range and time over a 20 second time interval. Lightning occurred partway through the interval and caused sudden decreases not only in $|\rho|^2$ (lower left) but also in the cross-polar power and depolarization ratio (upper right and upper middle, respectively). The phase of the correlation was also observed to change (lower middle). No change was detected in the normal or co-polar return of the radar.

Over a longer time interval, the correlation $|\rho|^2$ was observed to regenerate gradually between lightning discharges and to decrease suddenly at the time of lightning, in a cyclical, 'sawtooth' manner. Figure 3 shows an example of the variation of $|\rho|^2$ over a two-minute time interval which illustrates this behavior. In this figure, range increases in the radial direction and time increases in the clockwise direction.

DISCUSSION

Regions of strong co-polar-cross-polar correlation are readily identified in scanning through a storm and appear always to be present in electrified storms. As noted by Hendry and McCormick (1976), the fact that the correlation values are affected by lightning and are observed above the 0 °C level indicates that they are indicative of the electrical alignment of ice particles. The effect of alignment upon the correlation is surprisingly strong, and produces 'signatures' as in Figure 1a which are found to be an excellent indicator of the potential for lightning in a storm. We have been able to predict the occurrence of numerous discharges from real-time correlation observations.

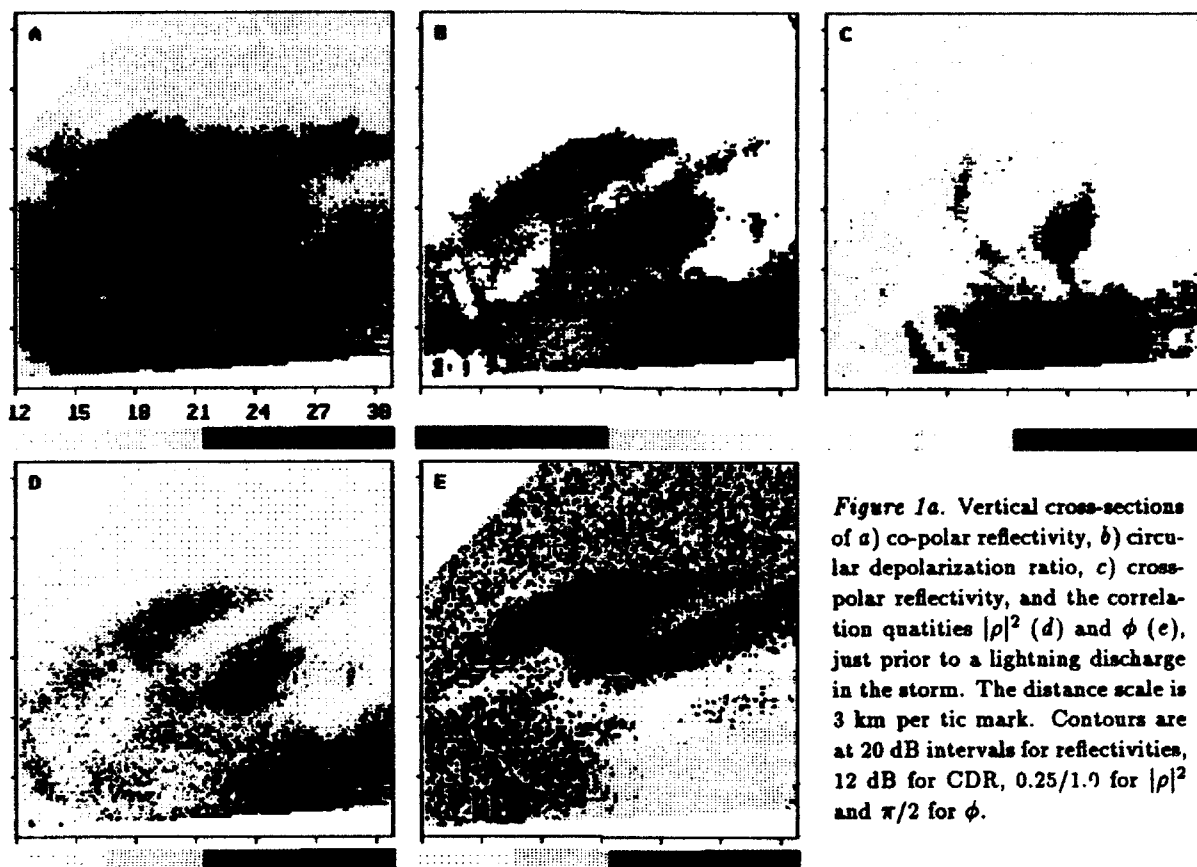


Figure 1a. Vertical cross-sections of a) co-polar reflectivity, b) circular depolarization ratio, c) cross-polar reflectivity, and the correlation quantities $|\rho|^2$ (d) and ϕ (e), just prior to a lightning discharge in the storm. The distance scale is 3 km per tic mark. Contours are at 20 dB intervals for reflectivities, 12 dB for CDR, 0.25/1.0 for $|\rho|^2$ and $\pi/2$ for ϕ .

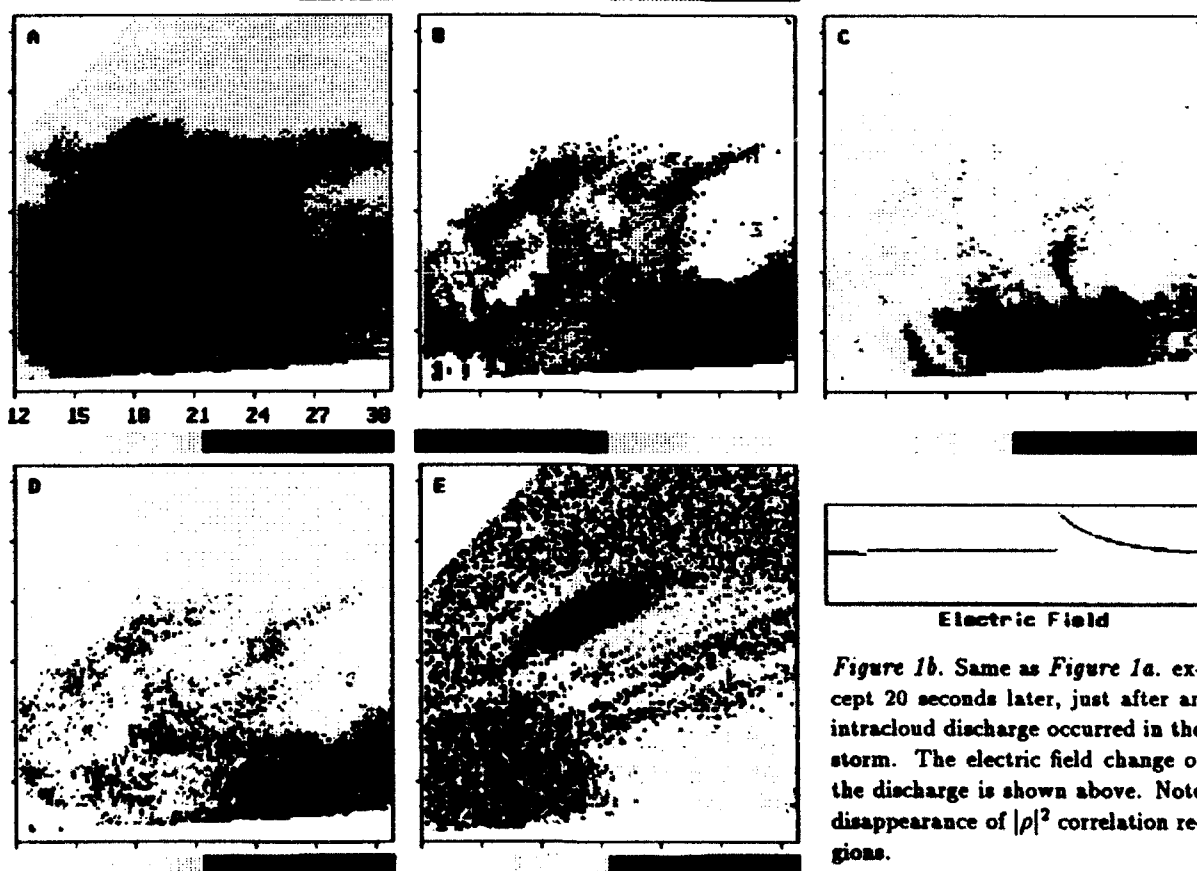


Figure 1b. Same as Figure 1a. except 20 seconds later, just after an intracloud discharge occurred in the storm. The electric field change of the discharge is shown above. Note disappearance of $|\rho|^2$ correlation regions.

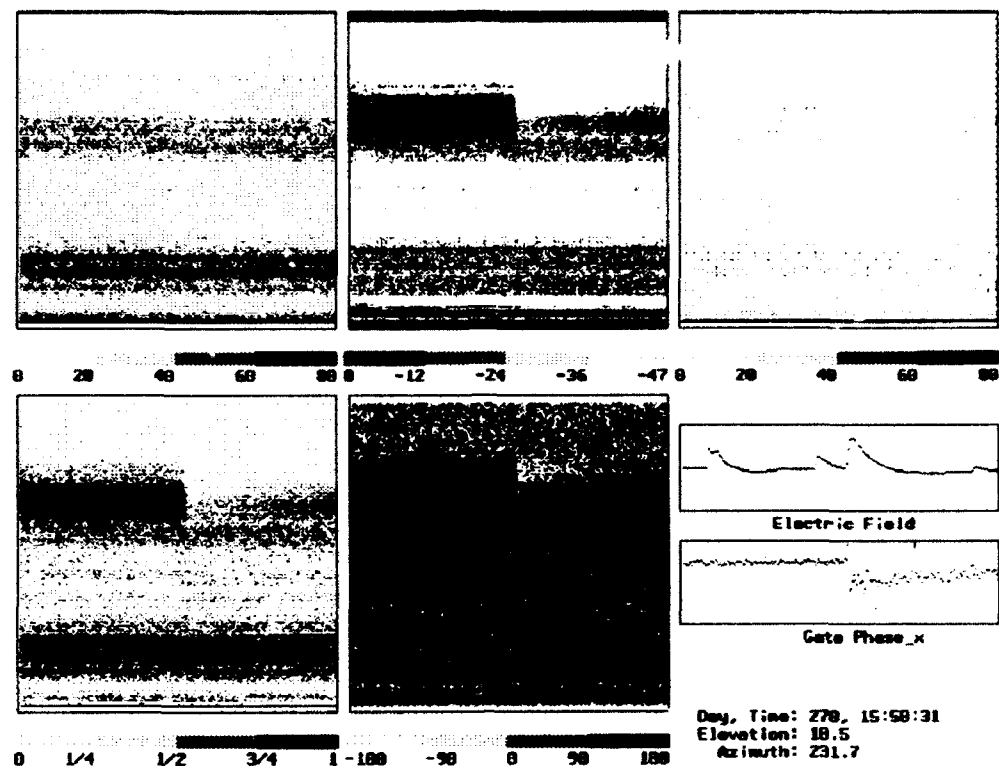


Figure 2. Variation of radar signals vs. range and time over a 20 second time interval around the time of lightning. Range is displayed vertically (0-37.5 km) and time increases from left to right. The radar signals are the same as in Figure 1.

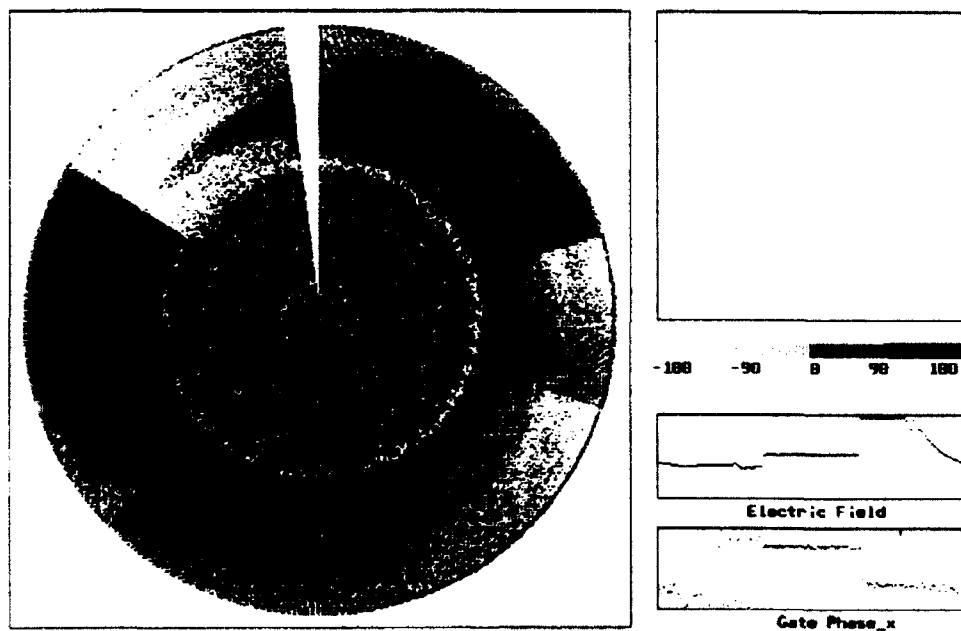


Figure 3. Variation of the squared magnitude $|\rho|^2$ of the co-polar-cross-polar correlation vs. range (radial) and time (clockwise) over a two-minute time interval, showing the build-up of electrification and its sudden decrease at the time of lightning.

The correlation measurements have also been used to detect the onset of electrification in several storms, prior to the first lightning discharge. In one instance a marginally electrified storm produced strong correlation values at mid-levels for several minutes before finally producing its first of only several lightning discharges. During the initial stages of storms, and often in later stages as well, the region of strong correlation is observed between about 6 and 8-9 km altitude MSL, and is co-located with the storm core. In one storm, the altitude of the correlation region was observed to decrease as the storm dissipated, down to just above the melting level. In several instances, storms which were decaying and had not produced lightning for several minutes were observed still to have large correlation values within them, and subsequently went on to produce additional discharges. Storms which are not electrified exhibit weak correlations above the 0 °C level.

Aligned particles would produce correlated co-polar and cross-polar returns for two reasons: First, orthogonal returns from the aligned particles themselves will be correlated. This would not produce large correlation values unless a large fraction of the particles are aligned (McCormick and Hendry, 1975). Second and more importantly, the circularly-polarized radar signal becomes progressively depolarized in propagating through a region of aligned particles, due to differential propagation effects. As the signal becomes depolarized, it is reflected by larger, non-aligned or non-depolarizing particles. This gives rise to a relatively strong cross-polar return that is perfectly correlated with the co-polar return, which explains why strong correlation values are observed. Hendry and McCormick (1976) demonstrated that the cross-polar signals were the result of a propagation-induced differential phase shift and inferred from this that the effect was produced by ice crystals. McCormick and Hendry (1979) and Hendry and Antar (1982) further documented the differential phase nature of the effect, and refined the interpretation of the cross-polar return as being due to reflections by non-depolarizing particles of the propagation-depolarized radar signal.

The observations of this study clearly indicate that the depolarization is propagation-induced, as indicated by the presence of large depolarization ratios and constant correlation phases on the far side of the correlation regions in Figure 1. These 'shadow'-type signatures are consistent with the interpretation proposed by Hendry and Antar (1982) that the depolarization is caused by propagation of the radar signal through a region of small, aligned particles that in themselves may not be particularly reflective of the radar signal, but whose presence is detected by reflections of the depolarized signal from larger, non-aligned particles in or on the far side of the aligned particles.

Liquid precipitation produces strong depolarization due to the aerodynamic flattening of large drops, and this effect has been studied by a number of investigators as a means of remotely sensing the rainfall (e.g. Holt, 1984; Sachidananda and Zrnic, 1986; Bringi *et al.*, 1991). In this case the depolarization is caused primarily by differential attenuation of the radar signal in the horizontal and vertical directions. The depolarizing effect of rain is partly evident below 4 km altitude in Figure 1, on the far side of the main precipitation shafts of the storm. It remains unaffected by lightning, confirming the non-electrical nature of the effect.

Alignment signatures are also observed with linearly polarized transmissions (horizontal and vertical) but are much less pronounced than with circular polarization. The depolarizing effects of aligned particles are independent of the orientation direction for circular polarization, but will have nulls when the particles are aligned parallel or perpendicular to linearly-polarized transmissions.

As seen in Figure 2, alignment effects are readily detectable from incoherent measurements of the cross-polar power and depolarization ratio. This was also observed by Hendry and McCormick (1976) and has previously been detected with the radar of this study using linear polarizations (Krehbiel *et al.*, 1991). As can be seen from Figure 1a, aligned particles produce a region or regions of locally enhanced cross-polar return and depolarization ratio above the 0 °C level in a storm. Thus, incoherent measurements by

themselves could be used to detect or indicate the presence of strong electric fields. The interpretation of incoherent measurements is less certain because of the possibility that the cross-polar return is produced by non-spherical particles, in which case it would not be correlated with the co-polar return. However, it appears likely that depolarization ratios above a certain threshold and having certain spatial structures or signatures would not be obtainable except when electrical alignment exists.

ACKNOWLEDGMENTS

This research was supported by the U.S. Air Force Office of Scientific Research under Grant AFOSR-89-0450. Earlier development of the radar was supported by the U.S. Office of Naval Research and by the National Science Foundation.

REFERENCES

- Bringi, V.N., V. Chandrasekar, P. Meischner, J. Hubbert, and Y. Golestani (1991): Polarimetric radar signatures of precipitation at S- and C-bands. *Proc. IEE*, **138**, 109-119.
- Hendry, A., and G.C. McCormick (1976): Radar observations of the alignment of precipitation particles by electrostatic fields in thunderstorms. *J. Geophys. Res.*, **81**, 5353-5357.
- Hendry, A., and Y.M.M. Antar (1982): Radar observations of polarization characteristics and lightning-induced realignment of atmospheric ice crystals. *Radio Sci.*, **17**, 1243-1250.
- Holt, A.R. (1984): Some factors affecting the remote sensing of rain by polarization diversity radar in the 3- to 35-GHz frequency range. *Radio Sci.*, **19**, 1399-1412.
- Krehbiel, P.R., W. Rison, S. McCrary, T. Blackman, and M. Brook (1991): Dual-polarization radar observations of lightning echoes and precipitation alignment at 3 cm wavelength. Preprints, 25th Conf. Radar Meteorology, Paris, Amer. Meteor. Soc., 901-904.
- McCormick, G.C., and A. Hendry (1975): Principles for the radar determination of the polarization properties of precipitation. *Radio Sci.*, **10**, 421-434.
- McCormick, G.C., and A. Hendry (1975): Radar measurement of precipitation-related depolarization in Thunderstorms. *IEEE Trans. Geosci. Elect.*, **GE-17**, 142-150.
- Sachidananda, M., and D.S. Zrnic, (1986): Differential propagation phase shift and rainfall rate estimation. *Radio Sci.*, **21**, 235-247.

APPLICATIONS OF TRIGGERED LIGHTNING TO SPACE VEHICLE OPERATIONS

William Jafferis (Retired)
National Aeronautics and Space Administration
Kennedy Space Center, Florida

Rocco Sanicandro
Boeing Aerospace Operations
Kennedy Space Center, Florida

John Rompalla
University of Wisconsin-Stout
Menomonie, Wisconsin

Richard Wohlman
Western Carolina University
Cullowhee, North Carolina

ABSTRACT

Kennedy Space Center (KSC) and the USAF Eastern Space Missile Center (ESMC) covering an area of 25 x 40 km are frequently called America's Spaceport. This title is earned through the integration, by labor and management, of many skills in a wide variety of engineering fields to solve many technical problems that occur during the launch processing of space vehicles. Weather is one of these problems, and although less frequent in time and duration when compared to engineering type problems, has caused costly and life threatening situations. This sensitivity to weather, specially lightning, was recognized in the very early pioneer days of space operations. The need to protect the many facilities, space flight hardware and personnel from electrified clouds capable of producing lightning was a critical element in improving launch operations. A KSC lightning committee was formed and directed to improve lightning protection, detection and measuring systems and required that all theoretical studies be confirmed by KSC field data. Over the years, there have been several lightning incidents involving flight vehicles during ground processing as well as launch. Subsequent investigations revealed the need to improve these systems as well as the knowledge of the electrical atmosphere and its effects on operations in regard to cost and safety. Presented here is how, KSC Atmospheric Science Field Laboratory (AFSL) in particular Rocket Triggered Lightning, is being used to solve these problems.

Paper not submitted.

NUMERICAL MODELLING OF INDUCED EFFECTS OF LIGHTNING STRIKE ON AN ALL COMPOSITE HELICOPTER

P.Gondot

**Centre Commun de Recherches LOUIS BLERIOT
AEROSPATIALE**

92150 SURESNES, FRANCE

Telephone 33 1 46 97 33 79 Fax 33 1 46 97 30 08

G.Donnet and P.Trochet

NUCLETUDES SA

91944 LES ULIS CEDEX, FRANCE

Telephone 33 1 69 07 10 20 Fax 33 1 69 07 21 01

ABSTRACT

The use of Carbon Fiber Composite in airframe construction arouses an increase of interest to protect sensitive avionic systems against indirect effects of lightning. In the SAE-AE4L recommendation, a long duration waveform is specified for equipment tests, especially in the case of an all composite structure. An all composite helicopter have been modelled with a FDTD method including internal structures and cables network. Then, the induced currents on shielded cables have been calculated for three lightning strike configurations. The purpose of this study is to discuss a specification for equipment tests based on calculations which permit us to distinguish typical waveforms, and levels of transient for every equipment.

1 - INTRODUCTION

The finite difference techniques in time domain(FDTD) were initially developed to study the response of aircrafts and missiles to electromagnetic illuminations such as NEMP. More recently they were adapted to study the coupling between lightning and aircrafts by modelling the injection of current on complex structures and by taking into account the resistivity of the materials (formalism of surface impedance).

During the last conference, various works [1][2] showed the capability of FDTD methods to predict in canonical cases the characteristics of the transient signals induced on the cables inside an aircraft subjected to a lightning strike.

The reliability of these methods and the calculation capability of computers allow today to model complex objects within the framework of an industrial program.

The application of this approach to an all-carbon composite aircraft is particularly interesting. Because of their low conductivity, the CFC have a low attenuation with respect to the magnetic field. So, one can thus expect high values of conducted transients. In the same way, the SAE-AE4L recommends a very severe test specification on equipment (waveform 5B, levels 4 and 5) for carbon aircraft. Nevertheless the application of this general specification would result in oversized protections to be installed in equipment and consequently increases in cost and weight. Therefore our objective is to determine by mean of FDTD modelling, a refined specification of electrical constrains for each equipment. This article presents the method implemented to define the lightning specification relating to an all composite helicopter. We describe here, essentially, a qualitative approach, a complete quantitative analysis will be published in a future paper.

2 - OVERVIEW OF THE NUMERICAL METHOD

2.1. Basic finite difference method

An effective technique to determine scattered electromagnetic fields 3D structures consists of solving Maxwell's equations in the time domain by finite difference approximations of the partial derivatives in space and time. The explicit method from YEE [3] is used for this purpose. For a given Ex component, finite differencing leads to:

$$E_X^{n+1}(i+1/2,j,k) = E_X^n(i+1/2,j,k) + \frac{\Delta t}{\epsilon_0} \left(\frac{H_Y^n(i+1/2,j+1/2,k) - H_Y^n(i+1/2,j-1/2,k)}{\Delta y} - \frac{H_Z^n(i+1/2,j,k+1/2) - H_Z^n(i+1/2,j,k-1/2)}{\Delta z} \right) \quad (1)$$

n : n° of iteration
 (i,j,k) : cell indices
 Δt : time step
 $\Delta x; \Delta y; \Delta z$: spatial step

The calculated EM field, which is the scattered field, derives from the application of the boundary condition $E_d = -E_i$ to the metallic surfaces of the object, where E_i represents the incident field and E_d the scattered field[4].

The finite difference code named DFTR initially designed to solve the diffraction of an electromagnetic wave by a perfectly conductive solid, was adapted to the problems of injection of a lightning current, of finite conductivity of materials and thin wires. The thin wire and the charge injection were modelled by introducing the following complementary equations :

$$\begin{aligned} \frac{\partial Q}{\partial t} &= -\frac{\partial I}{\partial k} \\ \frac{\partial I}{\partial t} + c^2 \frac{\partial Q}{\partial k} &= \frac{1}{L_k} \langle E_k \rangle \end{aligned} \quad k=x,y,z \quad (2)$$

I = current circulating on the wire element parallel with the direction k ,

Q = charge per unit of length on the wire element parallel with the direction k ,

c = speed of light

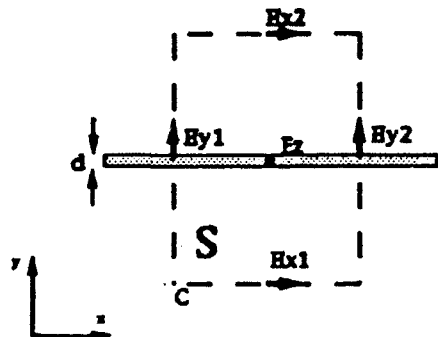
L_k = in-cell inductance

$\langle E_k \rangle$ = average value in the cell of the component k of the electric field.

The wires can locally simulate passive circuits (R, L, C) according to the formalism described by HOLLAND [5].

2.2. Taking account of the composite walls

For metallic structures, the effect of diffraction is obtained by writing the total electric field is zero on the external surfaces. At low frequencies, magnetic fields penetrate through the composite carbon. The determination of this diffusion would require to mesh carbon composite walls. The thickness of carbon panel is around one millimetre and for a 10 m long object that would lead to a number of cells too large for a realistic computing time. Specific formulations were added to the code to introduce the thin composite walls, while preserving the mesh criteria used for perfectly conducting objects [6]. Using Maxwell's equations in their global form and by considering an area C around a surface S crossing the thin composite wall of thickness d and conductivity σ , we obtain:



$$\int \int_S \left(\epsilon \frac{\partial \vec{E}}{\partial t} + \sigma \vec{E} \right) d\vec{s} = \int_C \vec{H} d\vec{l} \quad (3)$$

When the skin depth is significantly greater than the thickness of the carbon wall (in a low frequency domain), the tangential electric field on the composite wall can be considered to be the same on the two sides of the wall. The surface integral can be replaced by its average value at the point of calculation of E_z . Then, the formula (3) becomes :

$$\epsilon \Delta x \Delta y \frac{\partial E_z}{\partial t} + \sigma d \Delta x E_z = \int \vec{H} d\vec{l} \quad (4)$$

Let us note $E_n (I, J, K)$ and $H_{n+1/2} (I, J, K)$ values of fields E and H in the calculation cell (I, J, K) respectively at times $n \Delta t$ and $(n + 1/2) \Delta t$.

To simplify the notations, the mesh in ox, oy and oz are supposed to be uniform, of respective zone size Δx , Δy , Δz , and the equations are written in total field. By using the conventional scheme [3], the formula (4) becomes :

$$E_z^{n+1}(i,j,k) = \alpha E_z^n(i,j,k) + \beta ((H_x^{n+1/2}(i,j,k) - H_x^{n+1/2}(i,j-1,k)) \Delta y + (H_y^{n+1/2}(i,j,k) - H_y^{n+1/2}(i-1,j,k)) / \Delta x) \quad (5)$$

$$\alpha = \exp(-\sigma d \Delta t / (\epsilon \Delta y))$$

$$\beta = (1 - \alpha) \Delta y / (\sigma d)$$

Considering the value of conductivity for composite carbon, a thickness of a few mm, a cell size of a few cm and time steps of some ns, the term of (5), of $\exp(-10^3)$ or $\exp(-10^4)$ can be neglected. Let us note Z_s the surface impedance: $Z_s = 1/(\sigma d)$. The following formulation is finally obtained:

$$E_z^{n+1}(i,j,k) = \Delta y Z_s ((H_x^{n+1/2}(i,j,k) - H_x^{n+1/2}(i,j-1,k))/\Delta y \\ + (H_y^{n+1/2}(i,j,k) - H_y^{n+1/2}(i-1,j,k))/\Delta x)$$

This equation is programmed in DFTR to solve the case of thin composite walls.

3 - MODELLING

The helicopter to be considered is mainly made of composite carbon. Its characteristic dimensions are :

Length: 14 m Width: 1.1 m Height: 4 m

In our study, all harnesses of the helicopter are supposed to be shielded.

The lightning threat is component A (first return stroke current) defined in the SAE-AE4L revision B January 89 [7]:

$$I(t) = I_0 (\exp(-\alpha t) - \exp(-\beta t))$$

$$I_0 = 218810$$

$$\alpha = 11354 \text{ s}^{-1}$$

$$\beta = 647265 \text{ s}^{-1}$$

The analyzed stroke configurations are characterized by the following attachment points :

Configuration 1 - axis rotor/lower part of tail boom

Configuration 2 - axis rotor/ front gear.

Configuration 3 - noze/lower part of the tail boom.

3.2. Structures and cables.

Description of the helicopter structures.

For this helicopter, the compromise between a realistic model and an acceptable calculation time, imposes a mesh zoning of 5 cm in Y and Z, and of 20 cm according to the main axis of the helicopter (X axis).

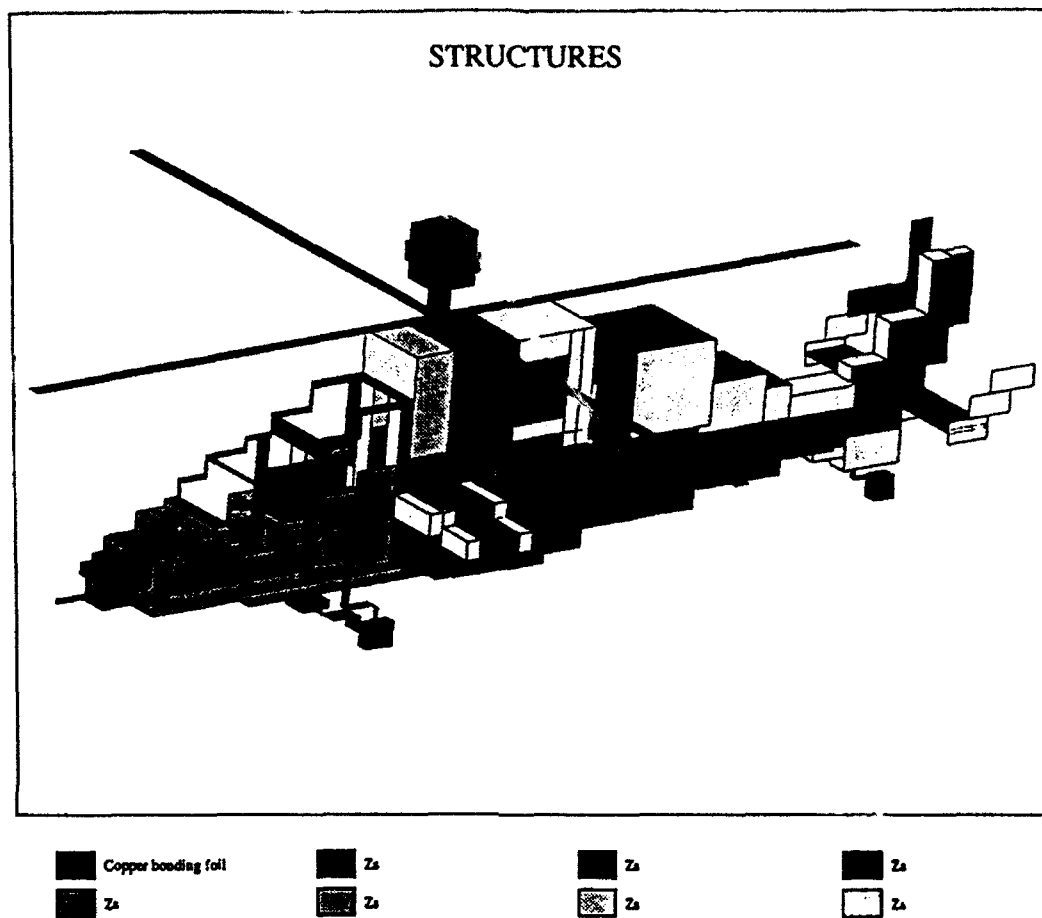
This modelling implies a number of elementary cells slightly equal to 900 000. Numerical stability imposes a time increment close to 90 ps; the determination of the electromagnetic fields and currents is carried out over 50 μs . This duration is generally sufficient to deduce the characteristics of the environment.

Six types of materials numbered from 0 to 5 are defined respectively with their surface impedance values. The helicopter can be divided into four main parts (see figure 1)

Front part and cockpit:

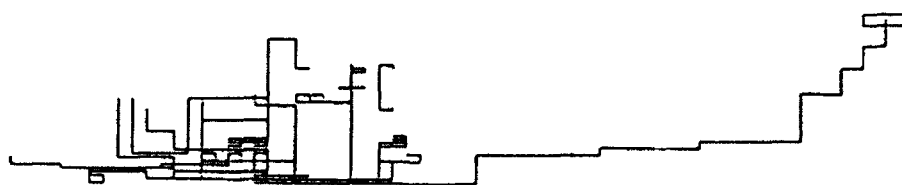
The external and internal structures of the front part are modelled: side walls with metallic, inspection doors, inside partitions, drive train support platform, front

FIGURE 1

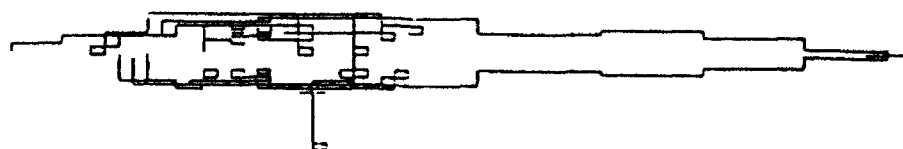


MODELLING OF THE REDUCED HARNESS

SIDE VIEW



TOP VIEW



gear. The cockpit is described with the metal frames of the canopies and the instrument panels.

Central part:

The central part consists of the fuselage with the metallic strips, the doors of the equipment racks, the fuel tank. In this part, one finds the two engines and their grounding, the main gear-box, the engine cowlings, the four blades of the main rotor.

Rear part:

The modelled structures are the aft fuselage with the metallic strips, the aft wings and their fins, the tail boom with the aft rotor and its four blades and various fairings.

Winglets and supports:

The two small wings are described with simple structures simulating embarked systems.

Description of the electric harnesses

The topological analysis of the harness network results in considering 10 main routes in the helicopter (see figure 1). These 10 main routes have been modelled with 28 elementary cables (or wires). One main route is modelled with several cables and also one cable can concern several main routes. In fact, cables or wires represent the shield of the harnesses. The effectiveness of the shielding of the harnesses is defined by their transfer impedance, here we choose a typical constant value of 15 mohm.m^{-1} . In the same way the connectors are supposed to have an transfer impedance equal to 2.5 mohm . The shield braid harness is connected on the back shell of connectors. The internal conductors of cables or bare wires are supposed to have an electrical resistance of 100 mohm.m^{-1} .

4 - RESULTS

4.1. Electromagnetic fields

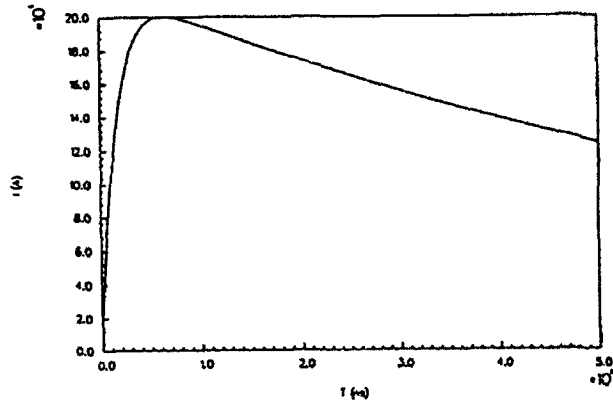
The amplitudes of the magnetic fields obtained by injection of lightning current on the external structure of the helicopter are high : a maximum of approximately 43 kA/m is calculated under the floor and on the engines cowlings. As a general rule, maximum values are obtained for the configuration 1 (rotor/tail boom). For the internal magnetic fields (cockpit, equipment racks, wings and fuselage), high levels (few kA/m) are observed. For most external points, waveforms are found, similar to the injected current waveform but, generally internal waveforms present a important low frequency content. A strong attenuation (50dB) is observed on electric fields inside the structure. Examples of waveforms are presented on figure 2.

4.2. Shielding Currents

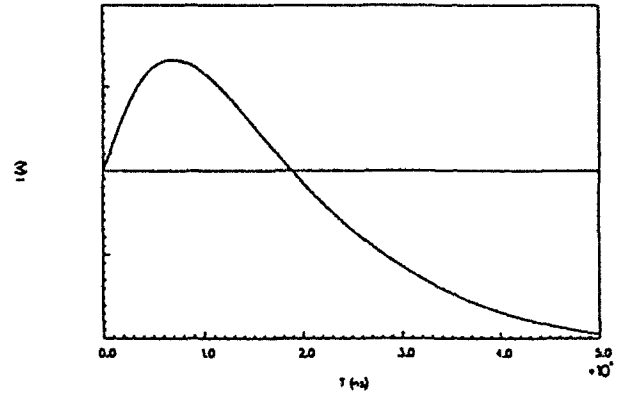
For a lightning injection of 200 kA , the maximum current values calculated on the 28 cables are around few kA . The highest values are obtained for the longest cables parallel with the flow of the injected current. The weakest currents are observed on the shortest cables and/or on cables directed perpendicular to the injected lightning current. Among the three scenarios of lightning strokes, the maximum amplitudes are found for the configuration 1. Various waveforms of the shielding currents are shown on figure 2. The maximum amplitudes of the shielding currents on the 28 cables among the three configurations are illustrated in figure 3. We note that distribution of shield currents presents a large extend (30dB) but the major part of values (70%) are 10dB below the maximum calculated value (C27).

FIGURE 2

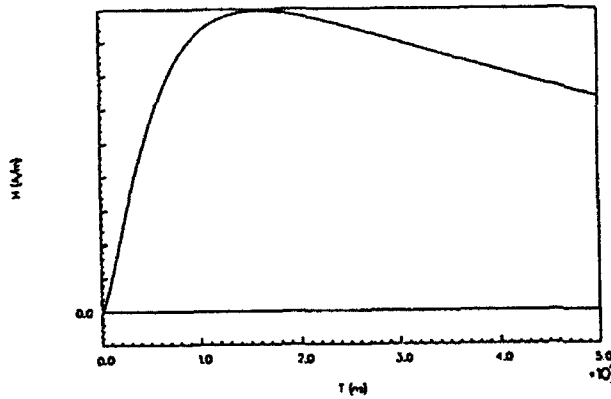
LIGHTING CURRENT



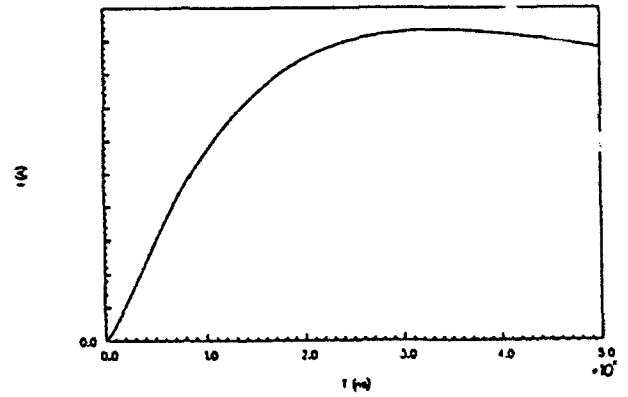
SHIELD CURRENT ON TAIL BOOM CABLE ROTOR AXIS-TAIL BOOM INJECTION



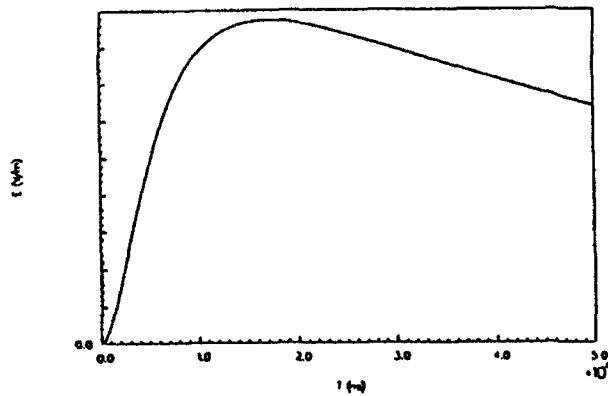
EXTERNAL MAGNETIC FIELD NEAR TAIL BOOM



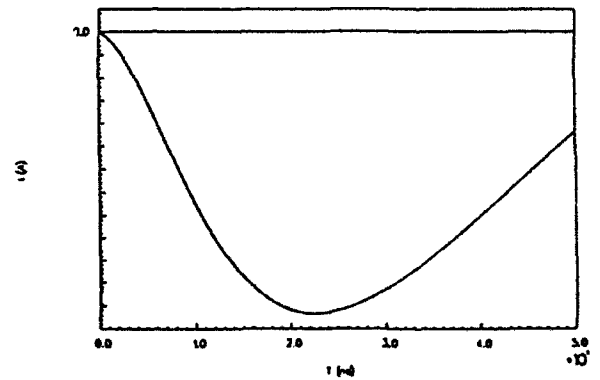
SHIELD CURRENT ON CENTRAL CABLE ROTOR AXIS-TAIL BOOM INJECTION



EXTERNAL ELECTRIC FIELD NEAR TAIL BOOM



SHIELD CURRENT ON CENTRAL CABLE NOSE-TAIL BOOM INJECTION



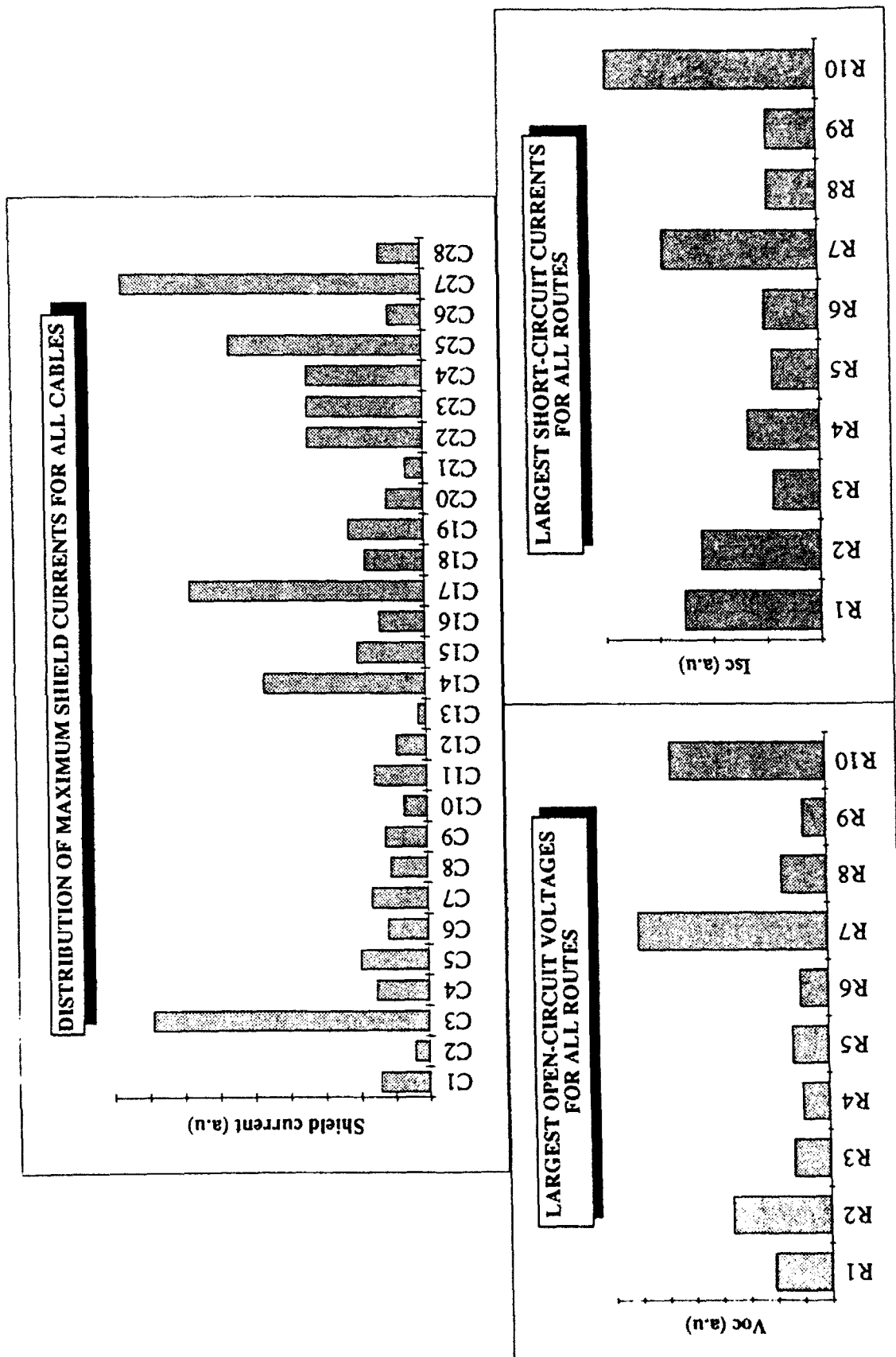


FIGURE 3

4.3. Electrical transients on loads

Open circuit voltages are deduced from the maximum shield current (I_s) and transfert impedance value of the harness (Z_t) : $V_{oc}=Z_t \cdot I_s$. In a low frequency domain , short circuit current can be deduced from V_{oc} and the lineic resistance (R_l) of the wires: $I_{sc}=V_{oc}/R_l$. The maximum amplitudes of open circuit voltages and short-circuit currents are presented in two histograms of figure 3. The associated waveforms are of double exponential type with rise time ranging between 15 and 50 μs (F.W.H.M. of 120 μs). Maximum open circuit voltages and short-circuit currents obtained on the 10 routes are characteristic of a severe electromagnetic environment.

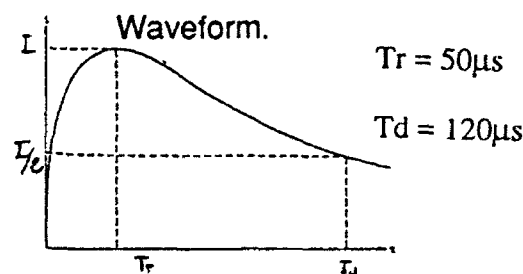
5 - SPECIFICATIONS OF THE ELECTRICAL STRESSES

Calculation results make it possible to cover the diversity of the signals induced by lightning . However amplitudes and waveforms are too different to be used easily during studies and demonstration of hardening.

5.1. Proposal for a specification of electrical transient

Generators are easily available to test equipments according to the SAE-AE4L recommendation. Considering the cost and the difficulty to build other generators, it seemed that it was desirable to keep the SAE-AE4L waveforms when possible. The results of all calculations were sorted out in four categories of different severities with only one associated waveform.

Amplitudes.		
- Level A :	300 V	500 A
- Level B :	300 V	750 A
- Level C :	750 V	1200 A
- Level D :	1500V	2000 A



5.2. Comparison with the SAE-AE4L

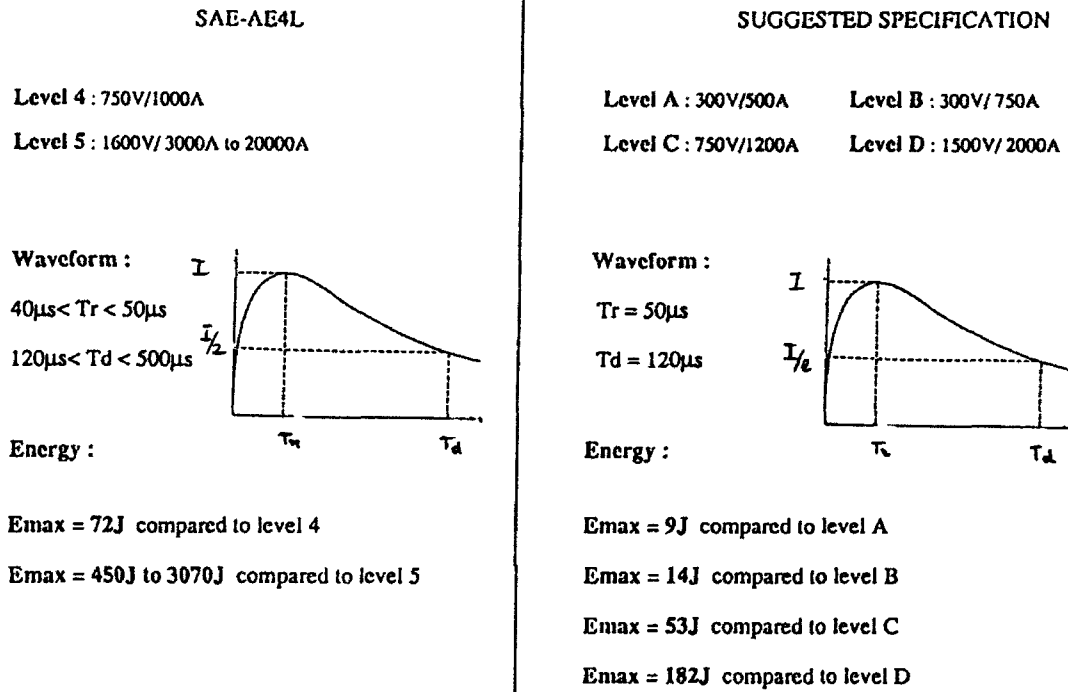
Figure 4 compares the draft specifications presented above with the recommendations of SAE-AE4L. It appears that taking into account a customized specification would reduce significantly the electric stresses for equipment input/output. The gain varies from:

- 2 to 20 in amplitude,
- 8 to 20 in energy.

It is then possible to define lightning protections best adapted to the real need. This would result in the optimization of volume and weight allocated to these devices and in a reduction in cost.

FIGURE 4

COMPARISON BETWEEN SAE-AE4L AND SUGGESTED SPECIFICATION



6 - CONCLUSION

We have shown that it was possible to model the coupling between a lightning and an all-carbon composite helicopter.

Modelling allow us to describe the structures of the aircraft and the routes of the various harnesses.

The DFTR code using the finite differences technique in time domain, was adjusted to simulate thin composite walls . It was then possible to determine :

- external and internal electromagnetic fields.
- electrical transients induced on cables.

The synthesis of the calculated transient signals allowed us to draw up adapted specifications for the major part of equipment. Also, modelling permit us to identify few routes and equipments which will require a special design or eventually a specific protection. In a such case, our theoretical approach would lead to a reduction in cost and weight of the protections to be installed.

REFERENCES

1. F. FLOURENS, T. MOREL, D. GAUTHIER and D. SERRAFIN, "A theoretical analysis of the electromagnetic environment of the AS 330 Super Puma Helicopter external and internal coupling" International aerospace and ground Conference on Lightning and Static Electricity, April, 1991.
2. J.C. ALLIOT, J. GRANDO, J.D. MULLER and X. FERRIERES, "FDTD numerical simulation of an entire lightning strike on the C160 aircraft" Inter. aero. ground Conf. on Lightn. and Stat. Electricity, April, 1991.
3. K.S. YEE, "Numerical solution of initial boundary value problems involving Maxwell equations in isotropic media" IEEE Trans. Antennas Prop, vol AP-14, pp.302-307, May 1966.
4. J.P. BERANGER, "Calcul de la diffraction à l'aide d'une methode aux differences finies" 2ème colloque national sur la compatibilité électromagnétique Trégastel Juin 1983.
5. R. HOLLAND and L. SIMPSON "Finite difference analysis of EMP coupling to thin struts and wires" IEEE trans. on EMC, vol 33, N 2, pp. 88-97, May 1981.
6. Y. LE GUILLOU "Calcul par une méthode aux différences finies du couplage de champs électromagnétiques avec des parois minces en composites C, en prenant en compte l'effet de peau" 6ème colloque international et exposition sur la compatibilité électromagnétique, Lyon-Ecully 1992.
7. Report of SAE committee AE4L "Protection of aircraft electrical/electronic system against the indirect effects of lightning" Originally Published 4 february 1987- Revision B January 1989.

Zoning of Aircraft: A Review Of The Definitions

By NATHANIEL G. BANKSTON

Space Systems Division, Rockwell International

ABSTRACT

The assignment of lightning strike zones to the surface areas of aircraft is a necessary first step in the protection design and certification process. Lightning strike zones are defined with respect to an external environment that has been synthesized from the important characteristics of natural lightning. Based on recent discussions in the Society of Automotive Engineers (SAE) AE4-L committee on lightning standards, it is apparent that the zone definitions are not intuitively clear. This paper presents a review of the zone definitions and discusses some of the problems associated with these definitions, including the problem of making probability statements in the definitions.

Introduction

In the Department of Transportation Aircraft Lightning Protection Handbook (1), paragraph 5.6 titled "Steps in Protection Design and Certification", suggests that the first step should be: Determine the lightning strike zones. In Federal Aviation Administration (FAA) Advisory Circulars (AC's) (e.g., ref's. 2,3) determining the lightning strike zones is the first step in the suggested outline of steps to follow in order to show compliance with Federal Aviation Regulations. Determining the location of the lightning strike zones before proceeding to the other steps, makes it possible to design and implement lightning protection for those areas where the lightning threat is greatest. This could be especially important when relocation of susceptible components is not practical or possible.

Lightning Strike Zones and the External Environment

In all of the documents where zoning is discussed and the lightning strike zone definitions are given, it is stated that lightning strike zones are the surface areas or points at which the external environment is applied to the aircraft. The external environment referred to is the lightning current flash model that has been synthesized from the important characteristics of natural lightning. This current model, with its associated test waveforms, has been designed for use in engineering applications. The lightning current components of the flash model required for each zone are shown in Figure 1. (Figure 1. not available)

The model represents the interactions which can occur when lightning approaches and attaches to an aircraft. While this current model is consistent with those aspects of the natural lightning environment that have significance in the engineering evaluation of the lightning threat to aircraft, the zoning of aircraft using this model recognizes that the current components of a lightning flash will produce different effects depending on where those components are applied.

From the late sixties until the present, the lightning strike zone definitions have gone through several changes. Most of the changes have resulted from an increased understanding of the interactions which take place when the external environment is applied to an aircraft.

It is important to remember that lightning strike zones on any aircraft are dependent on aircraft geometry, operational factors, and the materials with which it is constructed. This latter point is especially important when advanced composites are used in place of conventional metals.

Appendix A contains the complete text of the more recent lightning strike zone definitions from several sources. Figures 2. and 3. are typical examples of aircraft zoning schemes.

The Early Definition:

The original lightning strike zone definitions, first published in FAA AC 20-53 (4), included a swept stroke zone. Before and after their publication in AC 20-53, a large effort was underway to characterize the swept stroke phenomenon and quantify its effects on aircraft skins. Most of the results from this effort were presented at the Lightning and Static Electricity Conferences of the late sixties and early seventies. Several of these papers are listed in the references (5,6,7,8). They described the effects on aircraft surfaces due to a physically attached, moving current arc. They also investigated the mechanisms of attachment and reattachment of a moving current arc as a function of the types and treatments of surface materials. The result of all of this effort was to define surfaces in zone 2 as being in a swept stroke zone. They are still defined that way in recent zone definitions.

The original zone definitions as given in FAA AC 20-53 in 1967 are:

Aircraft can be zoned according to the probability of stroke attachment. Zone 1 is defined as a direct stroke zone, Zone 2 as a swept stroke zone, and zone 3 covers surfaces not identified in zones 1 or 2. The following are definitions of these zones.

Zone 1: All surfaces of the wingtips located within 18 in. of the tip measured parallel to the lateral axis of the aircraft and surfaces within 18 in. of the leading edge on wings having leading edge sweep angles of more than 45 degrees. Includes projections such as engine nacelles, external fuel tanks, propeller disk, and fuselage nose. In the tail group, zone 1 includes all surfaces within 18 in. of the tips of the horizontal and vertical stabilizers, trailing edge of the horizontal stabilizer, tail cone, and any other protuberances. Also, any other projecting part that might constitute a point of direct stroke attachment.

Zone 2: Surfaces for which there is a probability of strokes being swept rearward from a zone 1 point of direct stroke attachment. This zone includes surfaces that extend 18 in. laterally to each side of fore-and aft lines passing through the zone 1 forward projection points of stroke attachment. All fuselage and nacelle surfaces, including 18 in. of adjacent surfaces. Surfaces not defined as zone 1 are included in zone 2.

Zone 3: Surfaces other than those covered by zones 1 and 2. Ignition sources in these areas would exist only in the event of streamering.

Several points are worth noting:

first, zoning is based on "the probability" of stroke attachment;

second, concepts are introduced in the definitions as needed, e.g., streamering is mentioned as an ignition source in Zone 3;

third, each zone is provided with examples of the surface areas which are contained in that particular zone.

The First Change: Flash Hang-on

The accumulation of data which indicated that once the lightning stroke became attached to the trailing edges of an aircraft, that it was likely to remain there for the duration of the flash, led to the first changes in the zone definitions. It was decided to divide Zones 1 and 2 into A and B regions. An A region was defined as an area of Zones 1 or 2 where a lightning flash would be unlikely to remain after initial attachment. A B region was defined as an area of Zones 1 or 2 where a lightning flash would be most likely to remain after attaching to a surface in this region, either by initial attachment or by sweeping onto this surface from a forward initial attach point.

A look at the more recent zone definitions for both the A and B regions (see Appendix A) will show that the words "flash hang-on" have replaced "lightning channel hang-on". In the generally accepted usage of '(lightning)flash', the word 'flash' is taken to mean the total lightning event. In the present zone definitions, the only zones that are defined in such a way as to experience the total flash event are Zones 1B and 3. When used in the definition for Zone 2B, it must be understood that "flash hang-on" refers to those currents which occur after the first return stroke. These are the current components B,C,and D in the current flash model. The definition for Zones 1A and 2A is correct in that these zones are defined as having a low possibility of flash hang-on.

After the addition of A and B regions, the zone definitions remained basically the same until the mid to late eighties.

Probability or Possibility

Probability is a number between 0 and 1 which is assigned to or determined from the outcomes, or groups of outcomes, in a(an) sample(event) space. The discussion of the types of sample(event) spaces that are possible, with a description of their properties can be found in any of the referenced textbooks on the subject of Probability (9,10,11,12). With respect to the lightning strike zone definitions, an ongoing question has been whether to use the words 'probability' or 'possibility' when describing the probable or improbable initial attachment and flash hang-on locations or surface areas.

The difference between 'possibility' and 'probability' may need some clarification. The possibilities which can be postulated or realized as the outcomes of an experiment are distinct from their probabilities. For instance, from a shuffled deck of 52 cards it is possible to obtain four aces and one king by drawing five cards. The associated probability is 1/649,740. The event is possible, but it is not likely to occur. The real, or logical, possibilities that can be realized from any given experiment or trial are not required to have the same probability. The frequency interpretation of probabilities, used extensively in science and engineering, accepts the proposition that the probability to be assigned to the outcome of an experiment is the ratio of that outcome to the possible outcomes.

In the more recent zone definitions, the use of the phrases 'low possibility' and 'high possibility' to modify "initial attachment" and "flash hang-on" were questioned on the grounds that a thing (i.e., initial attachment or flash hang-on) is either possible or not possible. The use of the words 'low' and 'high' in the definitions were being used to distinguish between events that although possible to occur do not occur with the same relative frequency. Perhaps the intent of the definitions would have been easier to understand, if there had been a preliminary discussion explaining the difference between the possibility of occurrence and the probability of occurrence.

Although there are FAA documents that refer to probability values like 10^{-9} , it is not realistic to calculate such numbers to delimit areas of the aircraft which are in a particular zone. An attempt at such a calculation was done by Hardwick (13), with the result that 99.9% of the aircraft surface was in Zone 1A. To include probability statements in the zone definitions, without giving the probability values and the degree of confidence to be associated with those values would not improve the definitions.

The Department of Transportation Aircraft Lightning Protection Handbook Para. 5.2.3, discusses defining probabilities for lightning strike occurrences and concludes that such an approach is misleading and should not be accepted as evidence of compliance with FAA regulations. The reason is that the large number of possible lightning environments and modes of interaction with an aircraft render such calculations suspect. This same reasoning would also apply to any attempt at defining lightning strike zone boundaries with a probability.

Corbin and Cooley (14) describe the use of a statistical approach to determine probabilities to use in assessing the relationship between lightning criteria and aircraft susceptibility and vulnerability to

lightning attachment in critical areas. However, based on the assumptions that they used and the uncertainties they mentioned, this approach would not be likely to make defining lightning strike zones easier or more objective.

In order to produce numbers on the order of 10^{-9} by multiplying a sequence of probability values, it must be shown that the probabilities being multiplied are independent. It has not been shown in the case of lightning strikes to a particular area of an aircraft that all of the probabilities involved are independent. In fact, the ratio of lightning strikes to flight hours (the strike incidence rate) has been shown to vary between Europe and the U.S.A., and between military and civilian aircraft (15). This ratio is used in all calculations which attempt to determine the probability of a lightning strike to a particular area of an aircraft. It could then be argued that based on data supporting a geographic dependency of the strike rate, that the same aircraft should be zoned based on where it is to be primarily in service.

All of this is not to say that probability values (which have been properly bounded using statistical methods) cannot be calculated and used when reporting the results from determining initial and swept stroke attachment locations using one of the standard methods: rolling sphere, field enhancement computer simulation, long arc model tests, etc. In this case, the probabilities are being used to express the degree of confidence to be associated with the results which have been obtained. This could prove helpful in establishing the strike zone boundaries on an aircraft, but the lightning strike zone definitions could not be defined with these probabilities.

The Swept Leader

An aspect of the lightning attachment process that has been responsible for the more recent discussions relating to the lightning strike zone definitions is the swept leader. The phenomenon of leader sweep is simple to describe: after attachment to a moving aircraft, prior to first stroke arrival, the attached leader will sweep (usually aft) from its initial attach point, placing the initial attachment of the first return stroke a finite distance from the initial leader attach point. Figure 4. depicts this phenomenon. By definition, the location of a first stroke attachment to an aircraft is in Zone 1A. The result of leader sweep is to extend Zone 1A by the sweep distance.

To calculate the leader sweep distance requires a knowledge of aircraft operational factors and lightning leader characteristics. Lightning strike statistics for cloud-to-ground lightning indicate that most lightning strikes to aircraft occur at or below 15,000 ft. (16,17). One data base concluded that more probable altitudes for encountering cloud-to-ground strikes were below 10,000 ft. (18). This was attributed to the increase in exposure time to a lightning strike during the ascent from landing sites, and the descent and approach to landing sites.

Since leader sweep distances can vary 1-2 meters depending on the altitude of the aircraft and the value used for the leader velocity, most FAA documents give these two parameters as 15,000 ft. and

1.5×10^5 m/sec. Appendix B shows the effect that altitude and leader velocity can have in determining the sweep distance.

The previously cited paper by Hardwick discusses some of the natural lightning phenomena that should be considered when attempting to define the swept leader for all situations, e.g., what effects on leader sweep are due to differing charge structures in the cloud; and, what effects are due to whether the leader is propagating with positive or negative charge.

A tacit assumption that is made when discussing the swept leader is that one is talking about cloud-to-ground lightning having a negatively charged downward moving leader. This is not a bad assumption, considering that approximately 90% of all cloud-to-ground lightning has these characteristics (19). Approximately 10% of all cloud-to-ground lightning has a positively charged downward moving leader and is often associated with a more severe action integral. Naturally occurring cloud-to-ground lightning with upward moving leaders of either polarity is rare.

Besides the uncertainty in calculating the sweep distance due to uncertainties in leader velocity, and the altitude of most likely leader attachment and aircraft speed, the threat level which should be applied to areas which lie within the sweep distance also requires further discussion.

In the present draft of the User's Guide for FAA AC 20-136 which the SAE AE4-L committee is reviewing at this time, the swept stroke is given a detailed discussion which is then followed by the lightning strike zone definitions. Following the lightning strike zone definitions in the section discussing the location of these zones on transport category aircraft, the swept leader concept is introduced. This is then followed by guidelines on how to locate the lightning strike zones on other types of aircraft. Unlike the swept stroke discussions which precede the zone definitions, in all documents which address zoning, the leader sweep is invariably introduced after the zone definitions have been given.

The swept leader deserves as much consideration as the swept stroke; and all relevant aspects of the problem should be discussed, and the data which supports the need to include the swept leader in the lightning strike zone definitions should be given. The swept leader may require defining a new zone which overlaps portions of Zones 1A and 2A rather than just including it as an extension of Zone 1A.

Conclusions

1. The use of zoning to define where the external environment should be applied to aircraft surface areas should continue. It is cost effective in terms of both protection design and certification procedures.

2. The lightning strike zone definitions should be kept as simple as possible, and should not make reference to a probability. An example of a simple definition is found in FAA Advisory Circular 20-136: Zone 1A: Initial attachment point with low possibility of lightning channel hang-on. With

respect to the above discussion on the use of the word 'possibility', perhaps "where the possibility of hang-on is not likely to occur" would be clearer.

3. Differing operational conditions for the same aircraft, may require zoning the aircraft in more than one way. Operational flight conditions have a direct influence on the swept leader. For the Space Shuttle Program, zone definitions for the Orbiter were made for ground operations, launch, and landing (20). The cost of varying protection design based on operational zoning may preclude its general use, but the engineer who has to design protection may be interested in anticipated operating conditions for an aircraft that require special attention.

4. A recommendation is made that all zoning criteria and methodology be placed in one document dedicated to zoning. Such a document might include:

- a. A discussion of natural phenomena that affect zone boundaries, e.g., sweeping of both an attached leader and an attached stroke.
- b. A discussion of the affect that aircraft geometry, operational factors, and materials have on locating zone boundaries.
- c. A discussion of the methods available to establish initial attachment locations, e.g., long arc model tests, the rolling sphere, etc.
- d. A discussion of the zoning of different types of aircraft, e.g., rotorcraft, transport category aircraft, etc.
- e. A review of the lightning strike data bases with respect to meteorological and other factors which have an effect on zoning.

A document such as this would allow all of the documents where zoning is discussed to have a common reference for the lightning strike zone definitions with an explanation of the reasoning which resulted in the definitions.

References:

- (1.) F.A. Fisher, J.A. Plumer, and R.A. Perala, Aircraft Lightning Protection Handbook DOT/FAA/CT-89/22, Sept. 1989
- (2.) Protection of Aircraft Electrical/Electronic Systems Against the Indirect Effects of Lightning, FAA AC 20-136, Federal Aviation Administration, Washington, D.C., 5 March 1990
- (3.) Protection of Airplane Fuel Systems Against Fuel Vapor Ignition Due to Lightning, FAA AC 20-53A, Federal Aviation Administration, Washington, D.C., 12 April 1985
- (4.) Protection of Airplane Fuel Systems Against Fuel Vapor Ignition Due to Lightning, FAA AC 20-53, Federal Aviation Administration, Washington, D.C., 6 October 1967
- (5.) R.O. Brick, "A Method for Establishing Lightning-Resistance/Skin-Thickness Requirements for Aircraft," Proc. 1968 Lightning and Static Electricity Conference, Miami, Fla. Dec. 3-5
- (6.) R.O. Brick, L.L. Oh, S.D. Schneider, "The Effects of Lightning Attachment Phenomena on Aircraft Design," Proc. 1970 Lightning and Static Electricity Conference, San Diego, Ca, Dec. 9-11
- (7.) J.D. Robb, J.R. Stahmann, T. Chen, C.P. Mudd, "Swept Lightning Stroke Effects on Painted Surfaces and Composites of Helicopters and Fixed Wing Aircraft," Proc. 1975 Lightning and Static Electricity Conference, Culham Laboratory, Eng., April 14-17
- (8.) L.L. Oh and S.D. Schneider, "Lightning Strike Performance of Thin Metal Skins," Proc. 1975 Lightning and Static Electricity Conference, Culham Laboratory, Eng., April 14-17
- (9.) H. Reichenbach, The Theory of Probability, Univ. of California Press, Berkeley and Los Angeles, Ca, 1949
- (10.) W. Feller, An Introduction to Probability Theory and Its Applications, Vol. I, second ed., John Wiley and Sons, Inc., New York, N.Y., 1961
- (11.) E. Parzen, Modern Probability Theory and Its Applications, John Wiley and Sons, Inc., New York, N.Y., 1962
- (12.) A. Papoulis, Probability, Random Variables, and Stochastic Processes, McGraw-Hill Book Co., New York, N.Y., 1965
- (13.) C.J. Hardwick, "Background Information and Comments on AC 20-53B Zoning," Private in Confidence submittal to SAE AE4-L and EUROCAE WG31-3 committees, CLIC/DD-38, May 1991
- (14.) J.C. Corbin and W.W. Cooley, "Assessment of Aircraft Susceptibility/Vulnerability to Lightning and Development of Lightning-Protection Design Criteria," IEEE Transactions on Electromagnetic Compatibility, Vol. EMC-24, No. 2, May 1982

- (15.) J.A. Plumer and B.L. Perry, "An Analysis of Lightning Strikes in Airline Operation in the U.S.A. and Europe," Proc. 1975 Lightning and Static Electricity Conference, Culham Laboratory, Eng., April 14-17
- (16.) R.B. Anderson and H. Kroninger, "Lightning Phenomena in The Aerospace Environment Part 2. Lightning Strikes to Aircraft," Proc. 1975 Lightning and Static Electricity Conference, Culham Laboratory, Eng., April 14-17
- (17.) N.O. Rasch, M.S. Glynn and J.A. Plumer, "Lightning Interaction With Commercial Air Carrier Type Aircraft," Proc. International Aerospace and Ground Conference on Lightning and Static Electricity, Orlando, Fla, 26-28 June 1984
- (18.) R.B. Anderson, H. Kroninger, M. Smith, "Lightning Strikes to Aircraft - An Analytical Study," Proc. International Aerospace and Ground Conference on Lightning and Static Electricity, 1982
- (19.) M.A. Uman, "Natural and Artificially-Initiated Lightning and Lightning Test Standards," Proc. of The IEEE, Vol. 76, No. 12, December 1988
- (20.) NASA NSTS 07636 Rev. F, Appendix B, Space Shuttle Lightning Protection, Test and Analysis Requirements, Nov. 13, 1991

Appendix A: Zone Definitions

1. MIL-STD-1795A, June 20 1989:

The aircraft surface is divided into zones to define the relative likelihood of lightning strike attachment to the aircraft's exterior. Attachment zone 1 includes the surfaces on which lightning usually attaches. Attachment zones 2 and 3 would be inferred from ...

Zone 1A: Initial attachment point with low possibility of lightning channel hang-on.

Zone 1B: Initial attachment point with high possibility of lightning channel hang-on.

Zone 2A: A swept stroke zone with low possibility of lightning channel hang-on.

Zone 2B: A swept stroke zone with high possibility of lightning channel hang-on.

Zone 3: Those portions of the airframe that lie within or between the other zones, which may carry substantial amounts of electrical current by conduction between areas of direct or swept stroke attachment points. It includes those surfaces where attachment of the lightning channel is a very low possibility.

2. FAA AC 20-136, March 5 1990:

Zone 1A: Initial attachment point with low possibility of lightning channel hang-on.

Zone 1B: Initial attachment point with high possibility of lightning channel hang-on.

Zone 2A: A swept stroke zone with low possibility of lightning channel hang-on.

Zone 2A: A swept stroke zone with high possibility of lightning channel hang-on.

Zone 3: Those portions of the aircraft that lie within or between the other zones, which may carry substantial amounts of electrical current by conduction between areas of direct or swept stroke attachment points.

3. FAA AC 20-53B, April 22, 1991 (SAE AE4-L Committee Draft):

Zone 1A: All areas of the aircraft surfaces where there is a high possibility of an initial lightning attachment with a low possibility of flash hang-on. Those surfaces where first return strokes arrive by sweeping of the leader are also included in this zone.

Zone 1B: All areas of the aircraft surface where there is a high possibility of an initial lightning attachment and a high possibility of flash hang-on.

Zone 2A: All areas of the aircraft surface where there is a high possibility of a lightning attachment being swept on to it from a Zone 1A but having a low possibility of flash hang-on.

Zone 2B: All areas of the aircraft surface where there is a high possibility of a lightning attachment being swept on to it from a Zone 1A or 2A, but having a high possibility of flash hang-on.

Appendix A (Cont.)

3. FAA AC 20-53B, April 22, 1991 (Draft) (Cont.):

Zone 2B: All areas of the aircraft surface where there is a high possibility of a lightning attachment being swept on to it from a Zone 1A or 2A, but having a high possibility of flash hang-on.

Zone 3: Those surfaces not in zones 1 and 2 where there is a low possibility of any attachment of the lightning channel. Zone 3 includes those portions of the aircraft that lie within, beneath, or between the other zones and conduct substantial amounts of electrical current between direct or swept-stroke attachment points.

4. DO-160 Section 23:

Zone 1A: All areas of the aircraft surfaces where there is a high possibility of an initial lightning attachment with a low possibility of flash hang-on. For the purposes of this document, swept leader attachment areas are also included in Zone 1A. (In the future those surfaces where first return strokes may only arrive by sweeping of the leader may be separately designated.)

Zone 1B: All areas of the aircraft surface where there is a high possibility of an initial lightning attachment and a high possibility of flash hang-on.

Zone 2A: All areas of the aircraft surface where there is a high possibility of a lightning attachment being swept on to it from a Zone 1A but having a low possibility of flash hang-on.

Zone 2B: All areas of the aircraft surface where there is a high possibility of a lightning attachment being swept on to it from a Zone 1A or 2A, but having a high possibility of flash hang-on.

Zone 3: All areas of the aircraft surface not covered by all Zones 1 and 2. In Zone 3 there is a low possibility of a direct lightning attachment.

NOTE: All zones of the aircraft (including Zone 3) may be required to carry part or the whole of the total lightning flash currents flowing between two attachment points.

5. DOT/FAA/CT-89/22, Sept. 1989 (Lightning Protection Handbook):

Zone 1: Surfaces of the vehicle for which there is a high probability of direct lightning flash attachment or exit.

Zone 2: Surfaces of the vehicle across which there is a high probability of a lightning flash being swept by the airflow from a Zone 1 point of direct flash attachment.

Appendix A (Cont.)

5. DOT/FAA/CT-89/22 (Cont.):

Zone 3: Zone 3 includes all of the vehicle areas other than those covered by Zone 1 and Zone 2 regions. In Zone 3 there is a low probability of any direct attachment of the lightning flash arc, but Zone 3 areas may carry substantial amounts of electrical current by direct conduction between some pairs of direct or swept-stroke attachment points in other zones.

Zone 1A: Initial attachment point with low probability of flash hang-on, such as a nose.

Zone 1B: Initial attachment point with high probability of flash hang-on, such as a tail cone.

Zone 2A: A swept stroke zone with low probability of flash hang-on, such as a wing mid-span.

Zone 2B: A swept stroke zone with high probability of flash hang-on, such as a wing trailing edge.

6. Recent Proposal at SAE AE4-L meeting Feb. 1992:

Zone 1A: All areas of the aircraft surfaces where there is a high probability of a first return stroke during lightning channel attachment with a low probability of flash hang-on.

Zone 1B: All areas of the aircraft surfaces where there is a high probability of a first return stroke during lightning channel attachment with a high probability of flash hang-on.

Zone 2A: All areas of the aircraft surfaces where there is a high probability of subsequent return stroke attachment with a low probability of flash hang-on.

Zone 2B: All areas of the aircraft surfaces where there is a high probability of subsequent return stroke attachment with a high probability of flash hang-on.

Zone 3: Those surfaces not in Zones 1 or 2 where there is a low probability of any attachment of the lightning channel and those portions of the aircraft that lie beneath or between the other zones and conduct substantial amounts of electric current between direct or swept stroke attachment points.

Appendix B.

Lightning Leader Sweep Distance As A Function Of Leader Velocity

Aircraft Speed: 100 m/sec

<u>Altitude:</u>	$v_l = 1.5 \times 10^5 \text{ m/sec}$	$= 2.0 \times 10^5 \text{ m/sec}$
3000 m	2.0 m	1.5 m
2000 m	1.33 m	1.0 m

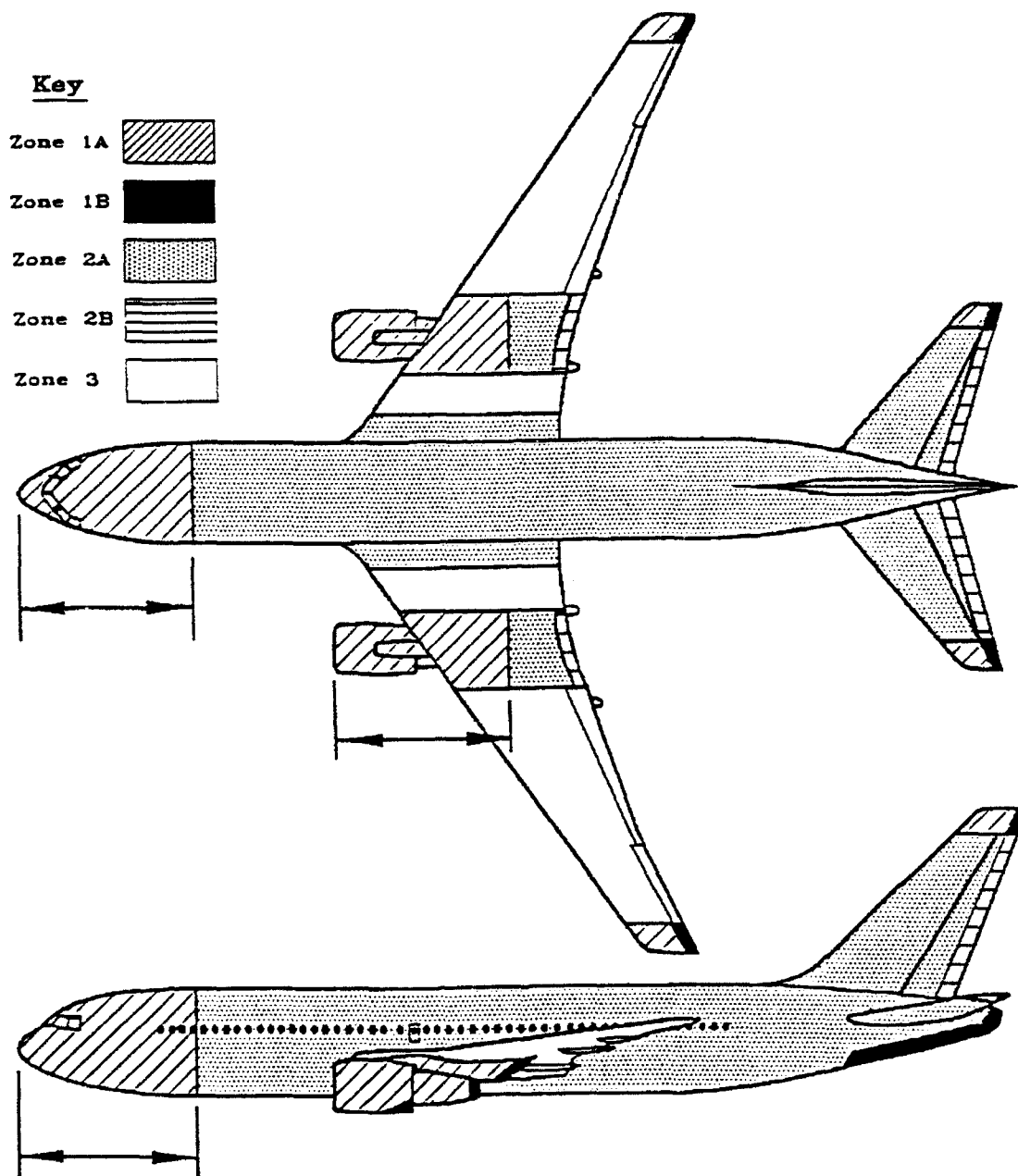


Fig. 2 Strike zones showing rearward extension of Zone 1A

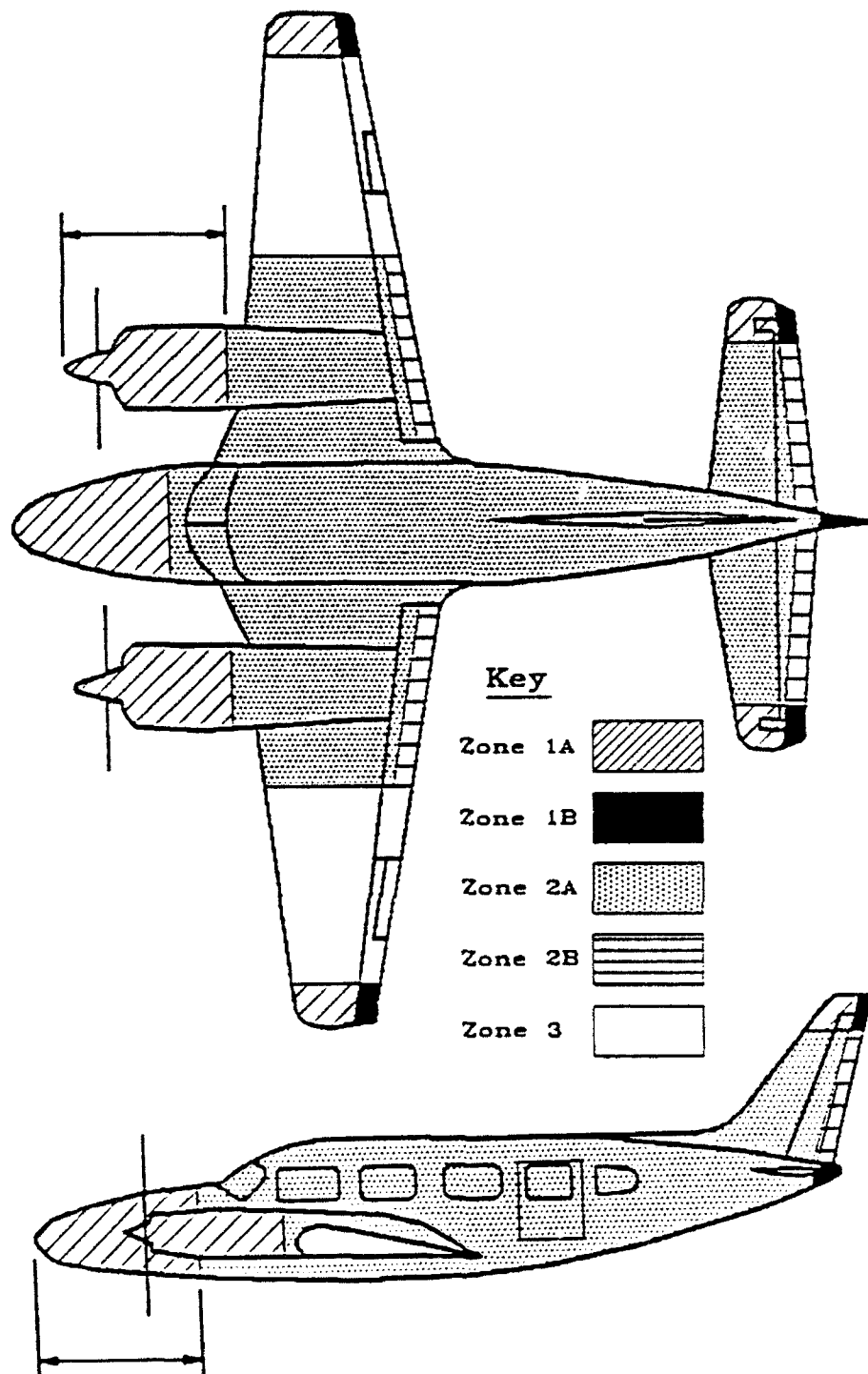


Fig. 3 Strike zones for a light twin turboprop aircraft

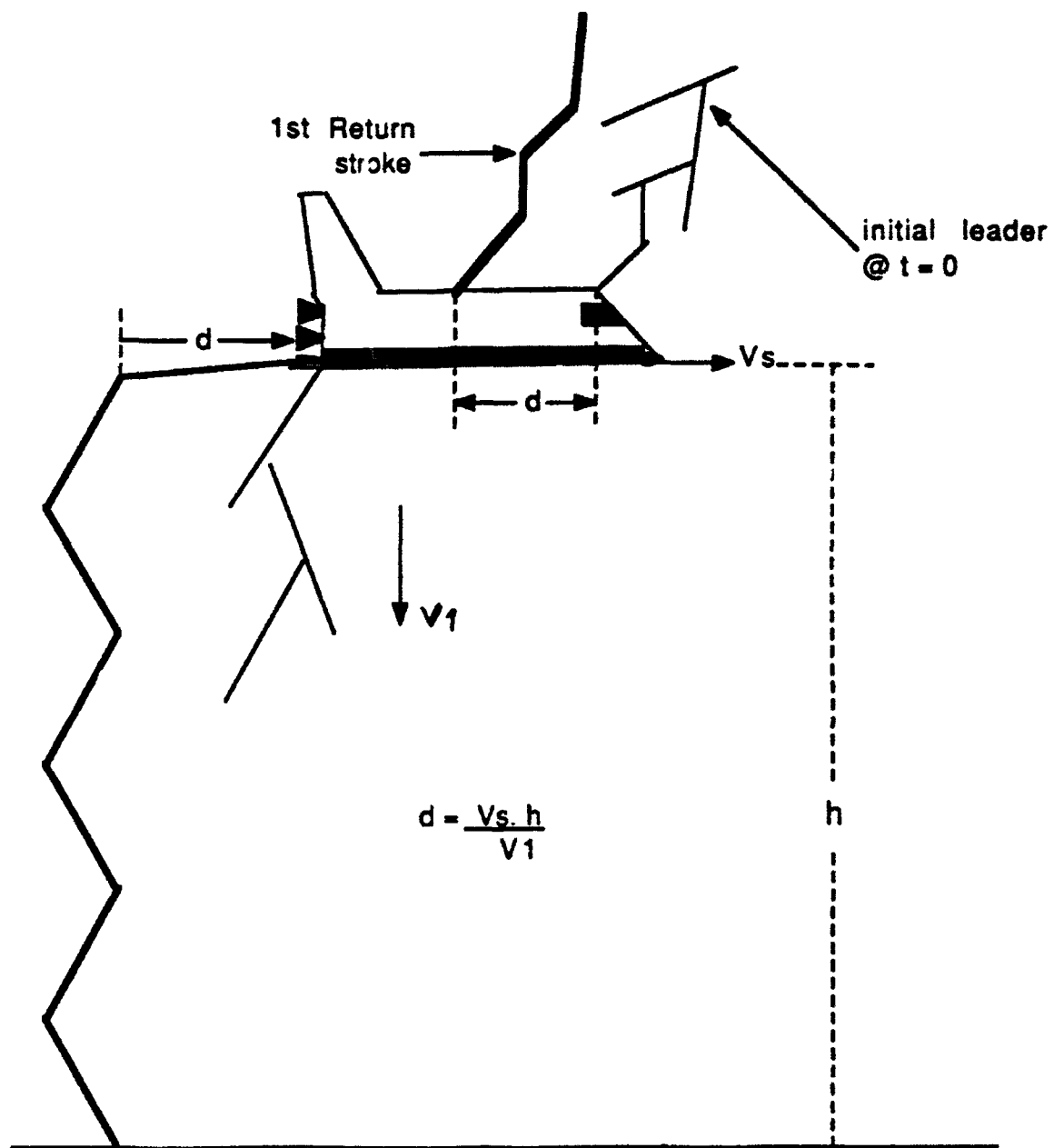


Fig. 4 Leader attachment and first return stroke arrival

EQUIPMENT TESTING WITH DAMPED SINEWAVES BETWEEN 1 AND 50MHz

C J Hardwick, R E Baldwin
Lightning Test and Technology, AEA Industrial Technology, Culham Laboratory,
Abingdon, Oxfordshire OX14 3DB, England
Telephone: +44-235-46-4264 Facsimile: +44-235-46-4325

ABSTRACT

Present lightning equipment test standards such as RTCA DO160C call for damped sinusoidal tests at 1 and 10MHz. There has been some discussion in the lightning community about extending these tests to 50 frequencies in the region 1-50MHz. This paper presents characteristics of such tests on cable bundles and notes the relationship between bundle current and injected voltage; important parameters are the cable loss and Q of the driving waveform.

1 INTRODUCTION

Much discussion at the EUROCAE WG31 and SAE AE4L committee meetings has occurred during the preparation of FAA AC20-136 and RTCA revised Section 22, issued as change 2 to DO160C/EUROCAE ED-14C in 1992 concerning equipment test methodology and test levels. The test levels and limits in the revised Section 22 are quite different from those used hitherto, in particular current test levels are substantially higher. There has been some concern as to whether the new levels will cause problems in practice and whether or not the revised current test levels are representative of those expected on aircraft cable bundles in a lightning strike.

The relationships between current and monitored voltage for the slower waveforms due to aperture flux (waveform 1 current, waveform 2 voltage) and redistribution current (waveform 5 current, waveform 4 voltage) were reported at the Cocoa Beach Conference, Reference 1. This paper reports investigations on the current level/monitored voltage relationship for 1MHz, 10MHz and variable frequency damped sinewaves from 6 to 100MHz (waveform 3) for a series of screened cable lengths varying from 3 to 6.5m long so that a reasonable spread of cable resonant frequencies was obtained.

Section 2 describes the experimental arrangement, section 3 introduces theoretical expectations, section 4 reports the experimental results, and compares them with the theoretical expectations and section 5 makes some conclusions and comments on differences between bench tests and those that might occur in an aircraft test or natural lightning strike.

2 EXPERIMENTAL ARRANGEMENT

A two centimetre diameter screened cable bundle was supported 5cm above an eight metre long aluminium ground plane. The cable was bonded securely at one end

to the ground plane. The other end of the cable was bonded at various points to the ground plane so that the length of the cable-ground plane loop could be varied by removal or reconnection of the various bonding straps. A transient generator to achieve the appropriate frequency range was used to inject the pulses via an injection transformer. The current induced in the bundle was measured with a current transformer; the voltage in a high impedance loop wrapped around the core of the injection transformer was also measured. The arrangement is illustrated in Figure 1.

3 THEORETICAL EXPECTATIONS

3.1 Theoretical Values – The relationship between voltage and current levels in equipment tests and aircraft tests below the first cable resonance has been discussed extensively elsewhere (Reference 1). The monitored voltage magnitude (which is the voltage driving the current around the loop under test) in the equipment test is essentially given by:

$$V = iR + L di/dt$$

which, for low resistance screened cables approximates to:

$$V \approx L \frac{di}{dt}$$

For damped sinewaves (waveform 3) $V \approx i\omega L$ where ω is the sinusoidal angular frequency and the V/i ratio increases with frequency up to near the first cable resonance. However, at the first resonance which is a $\frac{\lambda}{2}$ resonance, the V/i ratio goes through a minimum (ie, a current maximum, Figure 2) and the V/i is limited only by the loss in the cable/ground plane system. However because the sinewave is decaying and not a continuous wave (CW) large current standing waves cannot build up and the minimum ratio is much higher than that obtained in a CW test (Figure 3). The minimum value that the V/i ratio can reach is determined by the rate of decay of the exciting waveform and the loss in the cable/ground return system, ie the "Q" of both the exciting resonance and of the cable resonance.

In order to estimate the likely values of V/i ratio we consider the build up of a current standing wave in a loss-less cable system with a decaying sinusoidal driving waveform.

The minimum V/i ratio is only attained after the build up of the standing wave. During the first cycle, V/i is simply the surge impedance of the cable/return conductor assembly $\approx 100\Omega$. A current wave will build up but the magnitude will be given by:

$$i = I_0 (1 + k + k^2 + k^3 + \dots)$$

where I_0 is the current induced during the first cycle and k is the per cycle decay rate of the sinusoid.

Assuming the cable is lossless

$$i = \frac{I_0}{1 - k} \text{ (geometric series summation)}$$

For the limits of waveform 3 defined in AC20-136, we have Q values between 9 and 43 and hence k varies between 0.71 to 0.93 respectively and we obtain the following ratios:

Q drive	i	V/i	for $Z_0 = 100\Omega$
43	$I_0 \times 14.3$	$Z_0/14.3$	7Ω
9	$I_0 \times 3.45$	$Z_0/3.45$	16Ω

Hence for loss-less lines, rather than having a very small V/i ratio, the ratio is never lower than several Ω 's depending on the Z_0 (surge impedance) and the Q of the driving waveform.

For lossy lines the build up of the standing wave is even more restricted. The standing wave reaches its maximum level when the loss/cycle \approx the increment of energy added to the total by the subsequent oscillation. For cable resonances having Q's from 10-50 we estimate with the range of driving waveform indicated above (Q's from 9-43), V/i minimum ratios at resonance from 60Ω down to 14Ω .

3.2 Existing Values – The version of RTCA DO160C Section 22 issued in 1989 (Reference 2) has a limit of 25Ω , change 2 (Reference 3) has 5Ω .

The European Fighter Aircraft (EFA) spec. (Reference 4) has a V/i ratio of 100Ω which increases by 6dB from 30MHz to 50MHz. The 100Ω level is the traditional 25Ω level from various specifications increased to 100Ω as there is a V_i product limit of $\frac{1}{4} V_L I_L$, where V_L and I_L are voltage and current limits respectively.

Reference 5 based on circuit analysis but without losses suggests an increasing ratio of 5Ω to 25Ω from 1 to 5MHz as the current flowing is reduced by the increasing inductive reactance with frequency; the ratio then decreases again from 10MHz upwards to account for resonance effects.

These limits are illustrated in Figure 5.

4 EXPERIMENTAL RESULTS

The results are split into two sections; the first deals with the default frequency values suggested by DO160C, (1 and 10MHz) which for shorter cables, <15m, will tend to show inductive behaviour. The second deals with the higher frequencies where resonant behaviour is expected.

4.1 1 and 10MHz Damped Sinewaves – Measurements were taken at the maximum available capacitor charges for both frequencies. The generator used was a unit with an inbuilt output impedance of 25Ω . Results have been plotted as the current that would be obtained for particular lengths of the screened cable when the monitored voltage is 3.2kV, ie the highest level 5 of DO160C; see Figure 5. Also included as data points are the results obtained with a calibration loop of estimated self inductance of $\frac{1}{4}\mu H$ taken to be equivalent to a cable length of $\frac{1}{2}m$.

Also indicated on the Figure are curves fitted to the data following i/L as a function of length, where L has been estimated using the formula for the self inductance of a cable above a ground plane of $L = 0.2 \ln(2h/r) \mu\text{H/m}$ where h is the height of the cable above the ground plane (5cm) and r is the cable radius (1cm), giving $L \approx .46 \mu\text{H/m}$.

We note that as expected, for these frequencies below resonance the current drops off with increase of cable length due to the increase in inductive reactance.

The change 2 DO160C limit implies that at 1MHz only for the shortest cables would the current limit be reached before the voltage limit. For longer cables and 10MHz the voltage limit will always be reached first.

4.2 6-100MHz Damped Sinewaves – In contrast to the 1 and 10MHz discrete frequency data, the V/i ratio is now no longer dominated by the inductive reactance of the cable. The ratio is plotted as a function of frequency in Figure 6 for cable lengths of 3, 5 and 6.5m.

The general features are an initial fast increase with frequency due to inductance effects followed by a dip to the first resonance which roughly corresponds to the $1/2$ wavelength resonance associated with the particular cable length.

Above the first resonance the V/i ratio increases again. For the 5m length, sufficient frequency points were measured to detect a dip to the second resonance.

Also plotted in Figure 5 are the V/i limits from the EFA Spec. and a prediction based on circuit modelling without losses in the cable ground plane system (Reference 5). The actual values of V/i attained at resonance lie between the EFA Spec. and those of Reference 5.

As noted in Section 3 expected values of the limits are a function of the driving waveform Q and system loss but also depend linearly on Z_0 , the characteristic impedance of the cable-ground return system. By reducing the gap between the cable and ground plane, Z_0 will become smaller hence reducing minimum value of V/i obtained. The frequency scan for the 5m long cable was repeated with the 5cm spacers removed; Figure 6 compares the results, the minimum V/i ratio has dropped from about 90Ω to 40Ω .

Typical plots of monitored voltage and current waveforms are shown in plates 1-2. The effective Q of the driving waveform can be determined from the voltage waveform decay. Similarly the Q of the cable/ground plane system can be determined from the limited build up of the resonances; estimated values were 9 and 30 respectively. The measured V/i ratio is about 50Ω which is in accordance with expectations discussed in section 3.

We note that off resonance (Plate 1) the current follows closely the shape of the voltage waveform apart from a phase shift. However at resonance the current envelope builds up but at best the peak occurs at about the 9th $1/2$ cycle indicating a considerable loss in the cable-ground plane system. (If it were loss free, the amplitude of the oscillations would build up to a maximum and remain constant.) Also at resonance the particular generator used produces a fairly damped voltage waveform as the resonant current in the load produces a significant back EMF in the generator output stage. Hence the nature of the generator design can also limit the extent of resonance build up.

5 CONCLUSIONS

The data presented in Figures 5 and 6 and analysis of individual waveforms supports the theoretical expectations:

- 1) The V/i ratio is determined at resonance by:
 - a) the damping in the driving waveform
 - b) the loss in the cable-return circuit
 - c) the characteristic impedance of the cable-return system.
 - d) the effect of the resonant current in the load on the generator output.
- 2) For the examples studied, at resonance:
 - a) the damping of the driving waveform was large
 - b) the cable return system had a $Q \approx 30$
 - c) Z_0 of the cable was $60\text{-}130\Omega$ depending on proximity to the ground plane.
- 3) Values that might be expected in A/C depend on the same factors; but similar values might be expected. The following points have to be considered:
 - a) the driving waveform is the airframe resonance which could be damped by radiation resistance. It should be noted that substantially higher Q airframe resonances can be present in aircraft tests due to the enclosing return conductor system.
 - b) the cable airframe system loss might be lower in a more enclosed system such as inside the aircraft compared to an open bench test.
 - c) The Z_0 is a logarithmic function of the ratio of separation from ground return to cable radius which is a slow function and therefore impedances in the range $50\text{-}150\Omega$ are expected.
 - d) The effect of the cable resonance on the driving resonance.Points a), b) and d) require further study or data.
- 4) At resonance V/i ratios will be in the range of a few 10's to 100's of Ω , consequently the limit for waveform 3 testing in change 2 of DO160C Section 22 will always result in the voltage limit being reached first.

Below the first resonance V/i will be $\approx \omega L$. Only at 1MHz for short cables will the current limit be reached first. The new limit will not result in overtest provided the voltage threat level chosen is representative.

6 REFERENCES

- (1) C J Hardwick et al. A New Approach to Equipment Testing. ICOLSE Conference, Cocoa Beach, 1991.
- (2) EUROCAE WD-14C/RTCA DO160C, "Environmental Conditions and Test Procedures for Airborne Equipment", Issue 1989-12-12.
- (3) EUROCAE WG31/SAE AE4L December 1991 Draft Section 22/RTCA change 2 to DO160C, July 1992.
- (4) Eurofighter EFA-SP-J-000-2032. August 1988.
- (5) I Darney. Waveform 3—Current Limits. January 1991, BAe Airbus Div., B67-04.

7 ACKNOWLEDGEMENTS

The Culham Lightning Club comprising British Aerospace, the Civil Aviation Authority, CASA, Spain, Department of Trade and Industry, Rolls-Royce, SAAB Scania, Sweden, Short Brothers, Westland Helicopters provided the financial support for this work.

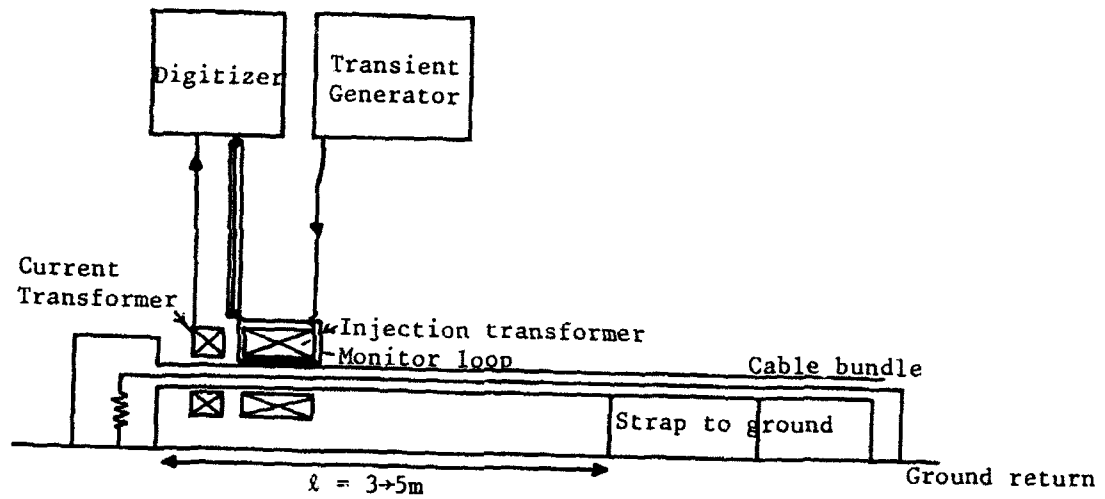


FIGURE 1
Schematic layout of test arrangement

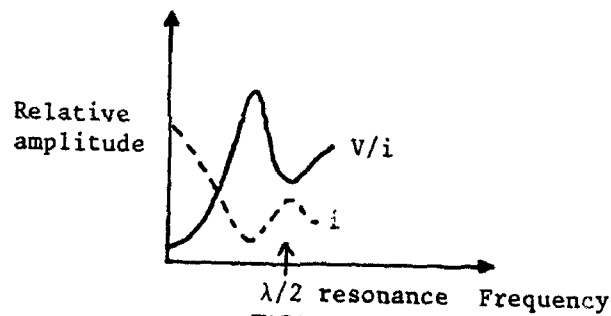


FIGURE 2

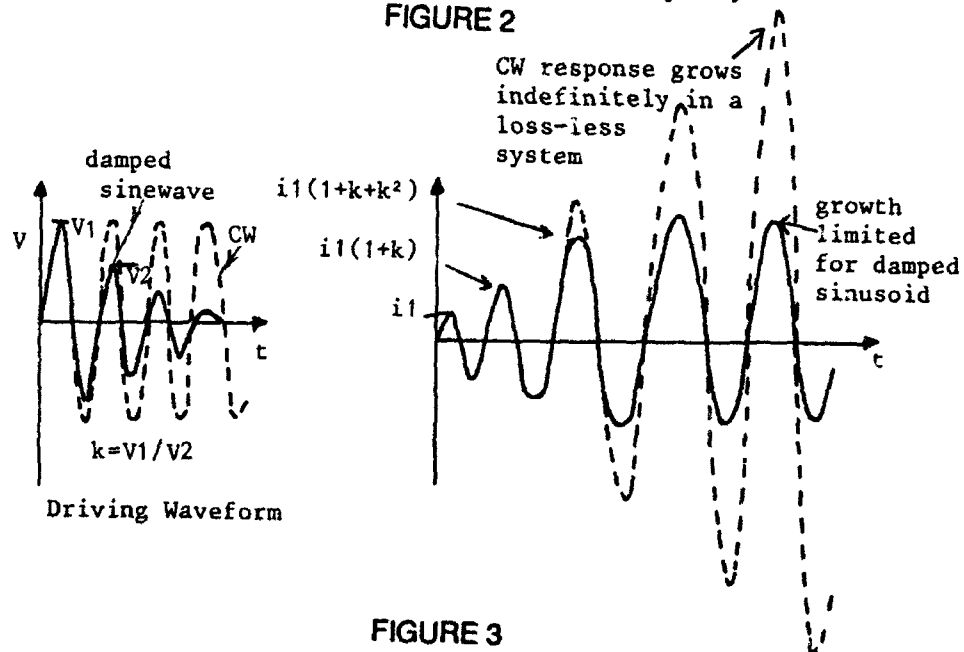


FIGURE 3

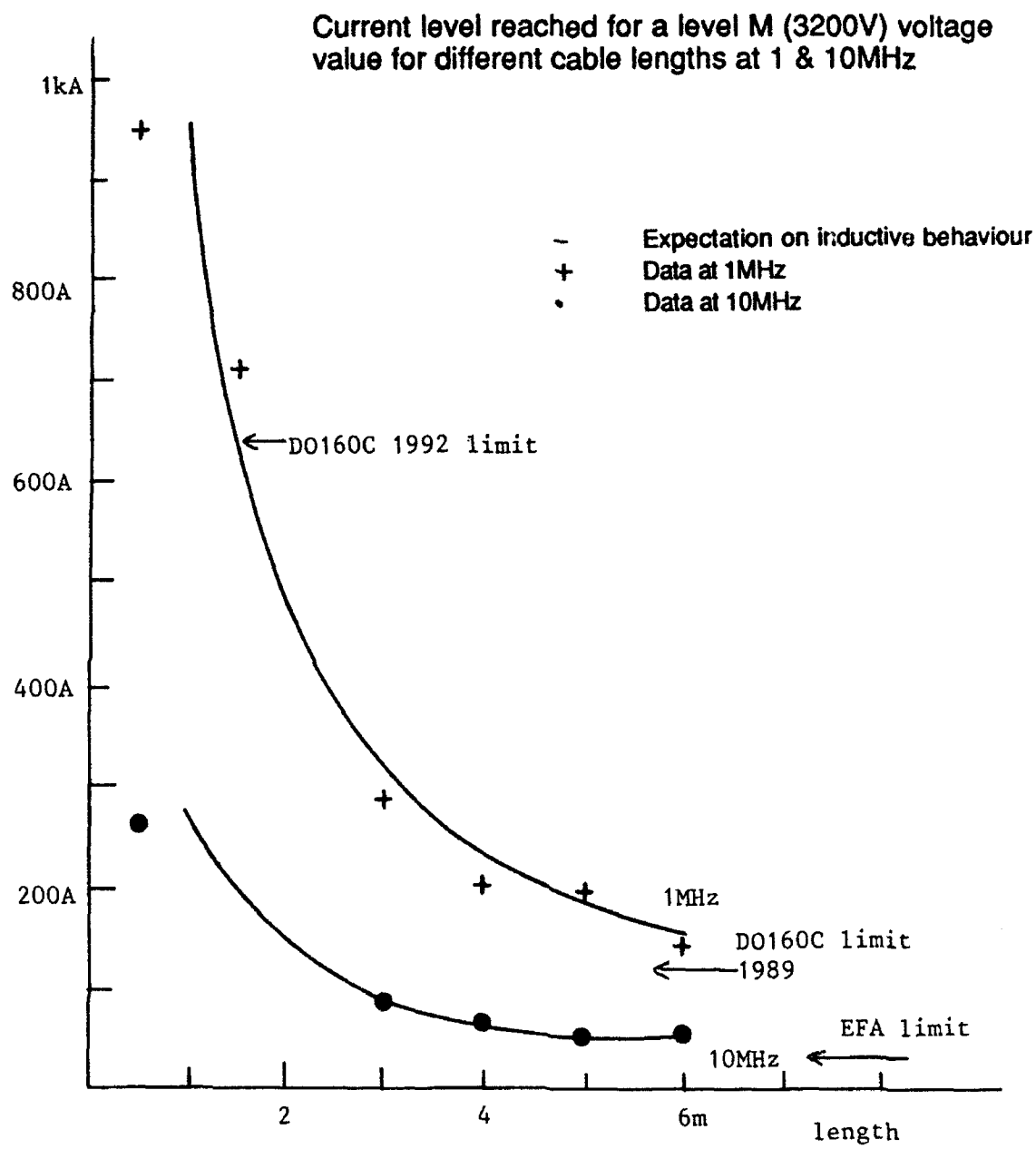


FIGURE 4

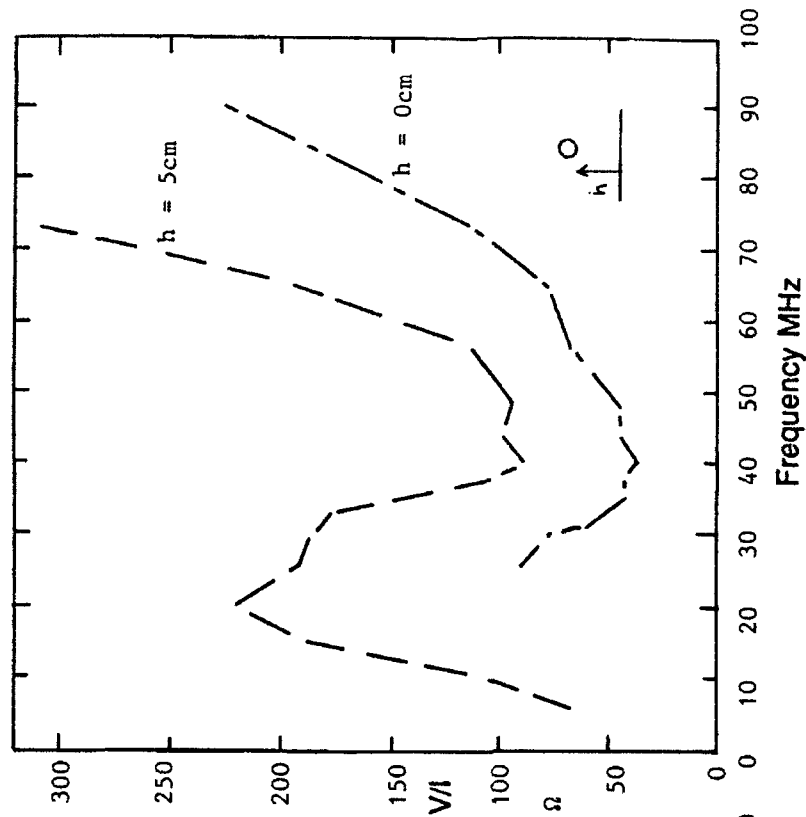


FIGURE 6
Effect on V/I ratio of displacement of cable from ground plane

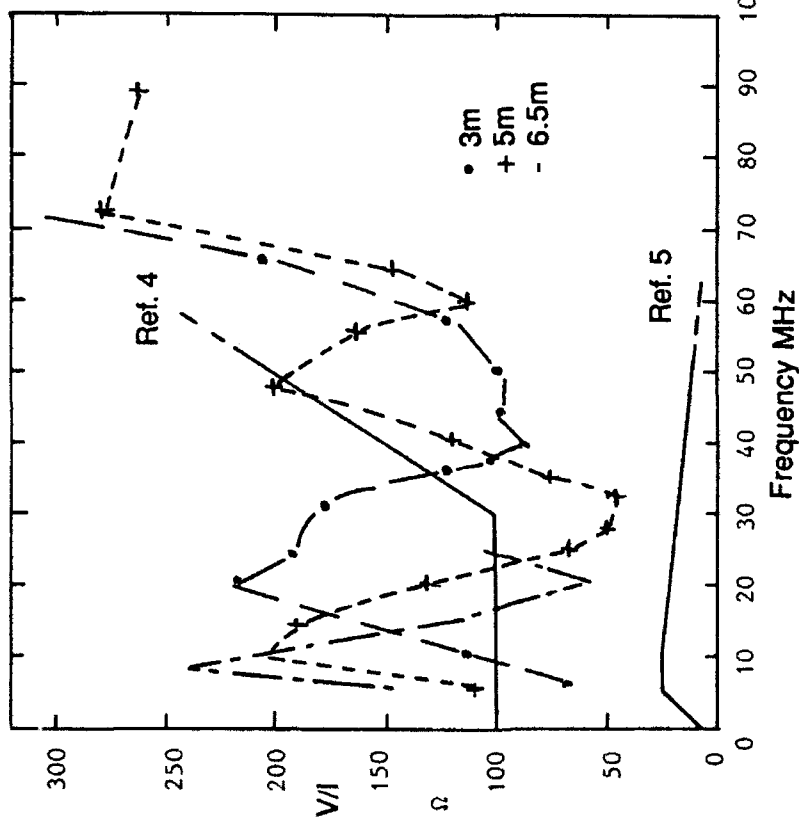
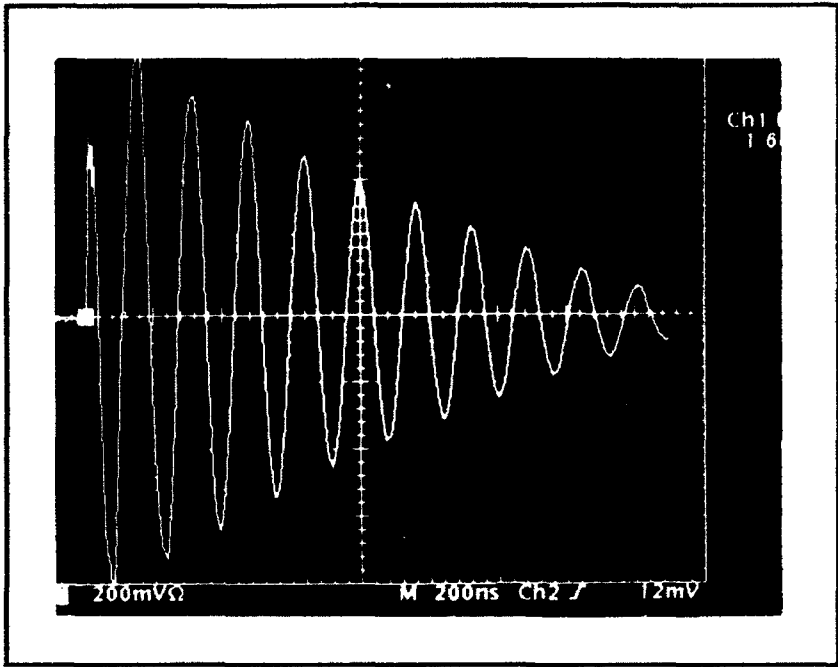


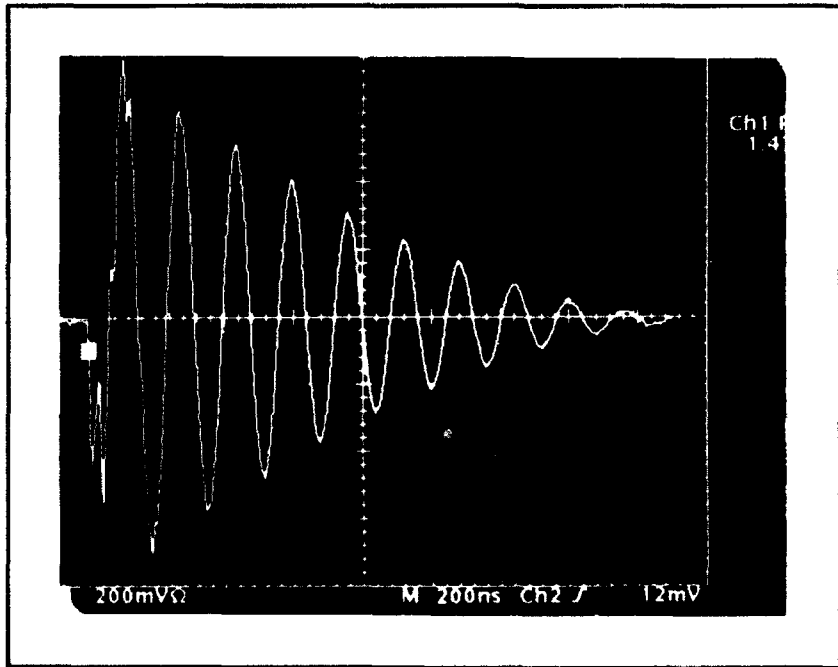
FIGURE 5
Variation of V/I ratio for various cable lengths against frequency and comparison with various test specifications

Cable Length 5m Frequency 6MHz
Condition Well below 1st resonance



Voltage Monitor Loop

Pk-Pk Voltage kV
 1.62

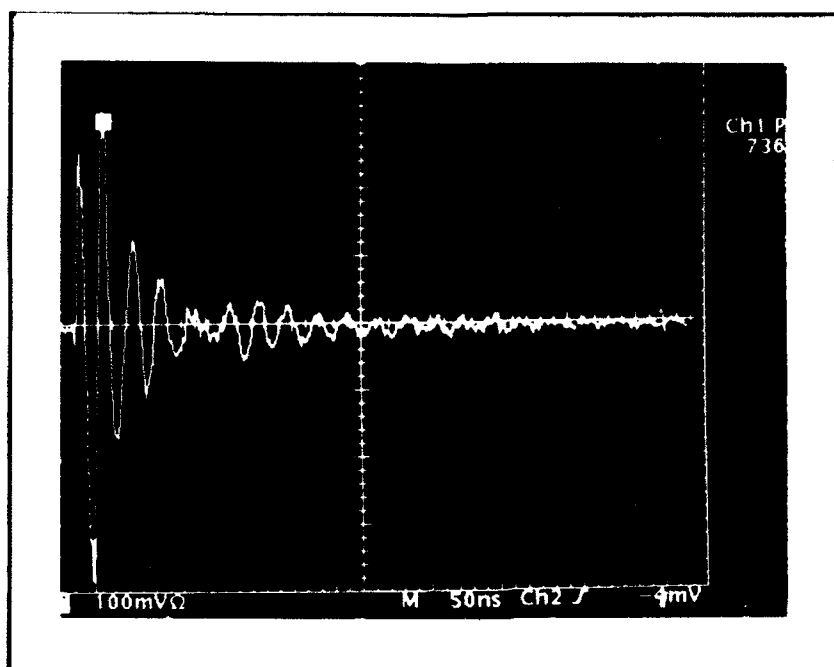


Current A

Pk-Pk Current
 1.47 + 20dB

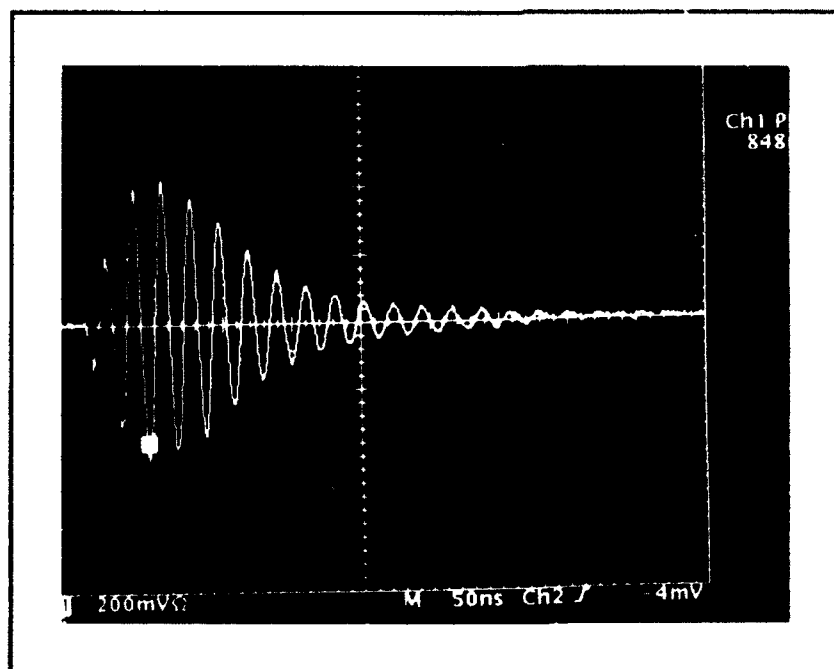
Plate No 1

Cable Length 3m Frequency 47MHz
Condition Resonance



Voltage Monitor Loop

Pk-Pk Voltage kV
0.736V



Current

Pk-Pk Current A
0.85 + 20dB

Plate No 2

**AN INTEGRATED APPROACH TO 300KV ELECTROSTATIC DISCHARGE
APPLICATION DURING COMPONENT TESTING THAT WILL SATISFY
MIL-STD-331B APPENDIX F**

**Monty R. Lehmann
Ktech Corporation
P.O. Box 70
Lexington Park, MD. 20653
Tel (301) 863-8607**

**Jack Nial 6720
Naval Surface Warfare Center
Indian Head Division 101-Strauss Ave.
Indian Head, MD. 20640
Tel (301) 743-4130**

**Mike Whitaker
Naval Air Warfare Center
Aircraft Division
Patuxent River, MD. 20670
Tel (301) 863-4598**

ABSTRACT

The widely differing methods of producing and applying a 300KV electrostatic stimulus to components during testing to satisfy MIL-STD-331B Appendix F has resulted in uncertainty about the validity of some test results data. Problems encountered in test methodology are examined and possible solutions are proposed. The resulting integrated systematic approach is presented; specific equipment is described and sample waveforms are shown. Test procedures are presented in a standardized format.

INTRODUCTION

Currently many different types of test sets and methods are used to apply an electrostatic pulse to bare and covered fuses to satisfy MIL-STD-331B Appendix F. These attempts to simulate the charge that builds up on hovering aircraft during vertical replenishment have led to questions about the validity of the test results. MIL-STD-331B Appendix F does not delineate the test methodology sufficiently so that the test can be repeated by different organizations or at different locations and still obtain the same

waveforms and test results. Figure 1 shows waveforms from two different test sets. Even accounting for time base differences, the disparity in the waveforms is apparent.

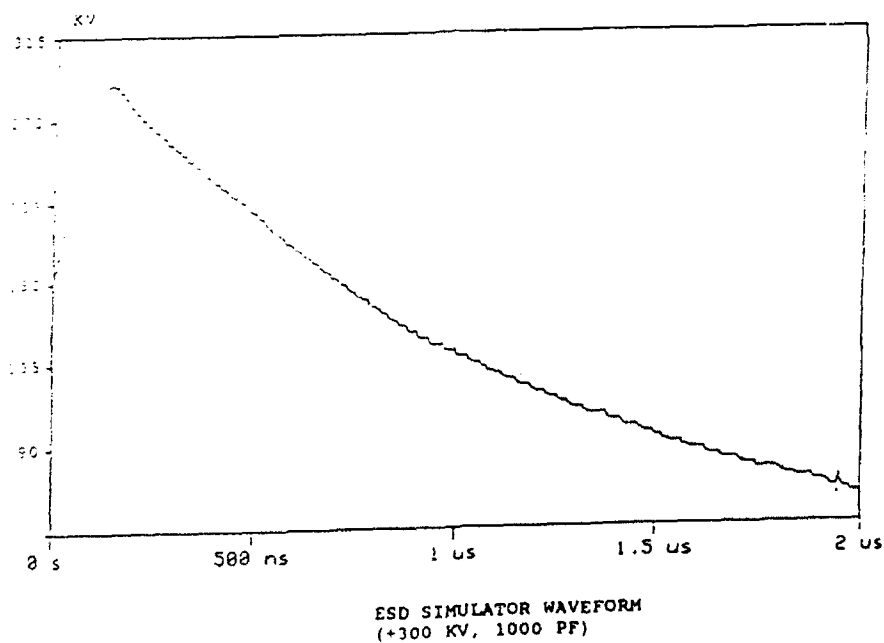
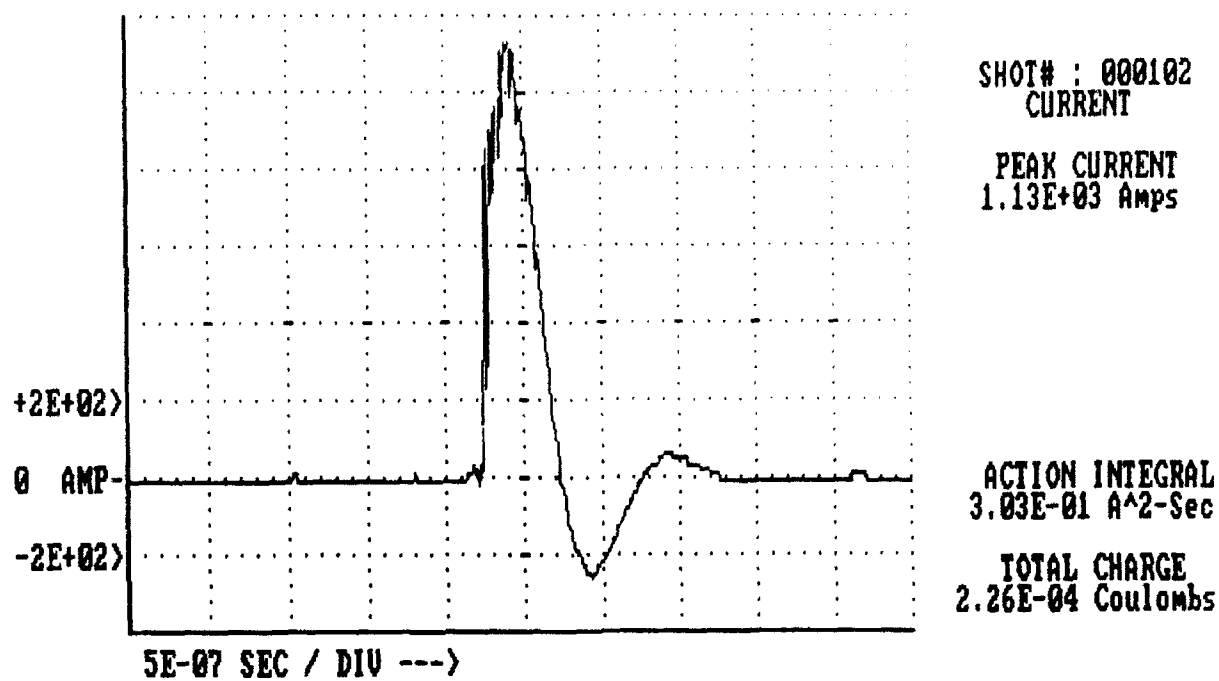


FIGURE 1

Not only are the test sets different, the test set-ups can vary greatly. The air gap between the test object and the pulser output electrode is not specified. This gap could be anywhere between 1 millimeter up to the breakdown distance of the 300 KV arc (as much as 300-400 millimeters). This alone leads to disparity between the energy package delivered to the test object. The gap requirements need to be quantified in a more exact manner by further research. Until this is done, we recommend a minimum air gap distance of 1". Also the specific type of output electrode is not specified. It could be a sharply pointed wire which would initiate gap closure far easier than if it was a sphere or hemispherical electrode which would result in a higher hold-off voltage before the air gap would break down. This air gap closure process would alter the waveshape and could result in questions about how much and of what type stress the particular test object was subjected to.

Since the inductance of a single arc is in the neighborhood of 1.4 nanohenries per millimeter, it can be seen the inductance of the gap could be drastically different. Although Appendix F lists discharge inductance at 20 microhenries it is unclear whether if this is an arc inductance or (most likely) a total circuit inductance. While this difference is not a large number, the addition of many variables into a test set-up is not conducive to a definitive answer.

With the inductance of the circuit varying between tests and test set-ups, it is also possible to deliver different waveforms to the test load, as the standard allows. The output from a capacitor or marx generator varies greatly with the load impedance, since the capacitance is fixed at 1000 pf, resistance at 100 ohm (cal.) and a 300 KV output is stated to be desired. It can be seen from (figure 2) that a load inductance of $1 \mu\text{h}$ results in a maximum delivered voltage of 250 KV to the load while an load of $20 \mu\text{h}$ (still within Appendix F specifications) results in a peak voltage in the region of only 130 KV. This is only $\approx 43\%$ of the stated 300 KV electrostatic impulse. With this variable test methodology

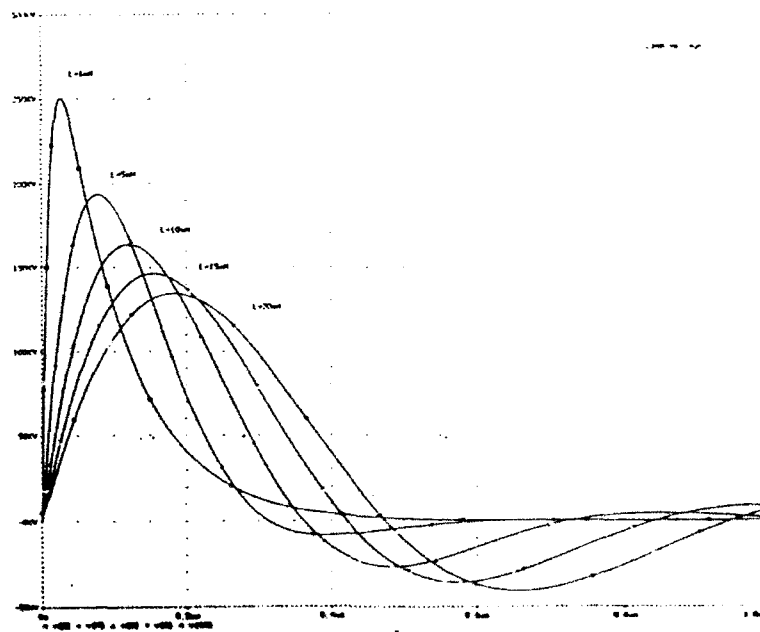


FIGURE 2

possible, it is very difficult to compare test results of any lot of fuses to any other lot, or even to separate sample tests within the same lot. This is especially difficult if the parameters of the test are not measured during the test.

In this paper, we propose a standardized method of producing, applying and measuring the applied waveform, before, during and after application of the pulse to the fuse sample/s under test.

So the question arises - is the desired impulse to be delivered to the test object 300 KV or the result after 300 KV is inserted into the test circuit with many possible parameters changing the properties of the delivered impulse?

DISCUSSION

Until MIL-STD-331B Appendix F is redefined further, we propose that a more standardized method of testing fuses be used.

The first step is to use a standard test set-up. Such a set-up is shown in (figure 3). It comprises a 300 KV marx generator, output probe, voltage and current monitors, with a data acquisition system to record the waveforms.

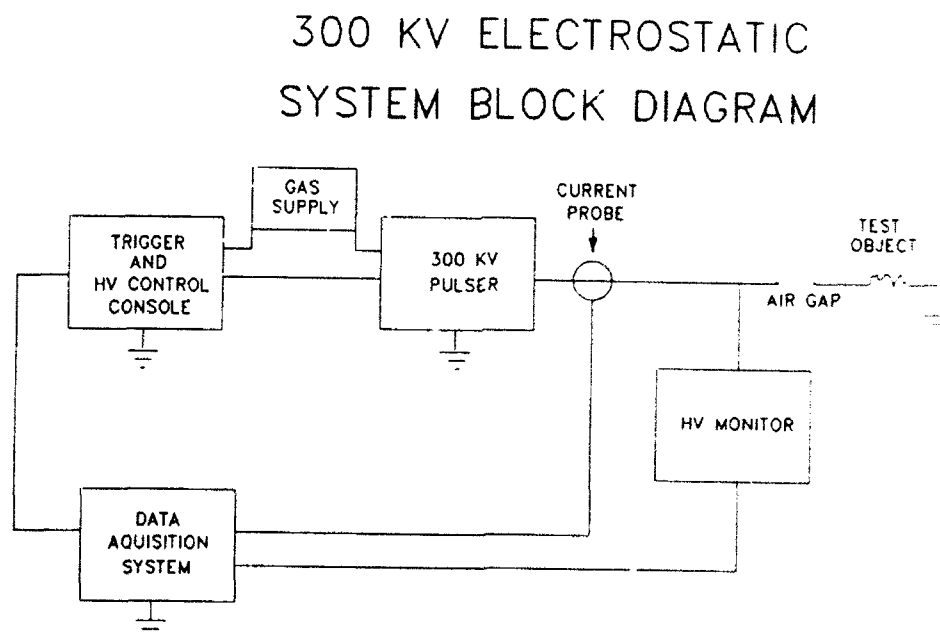


FIGURE 3

The 300 KV marx generator circuit diagram is shown in (figure 4). It is a portable, sulfur-hexafluoride gas insulated pulser. The marx generator has the following specifications:

300KV ESD

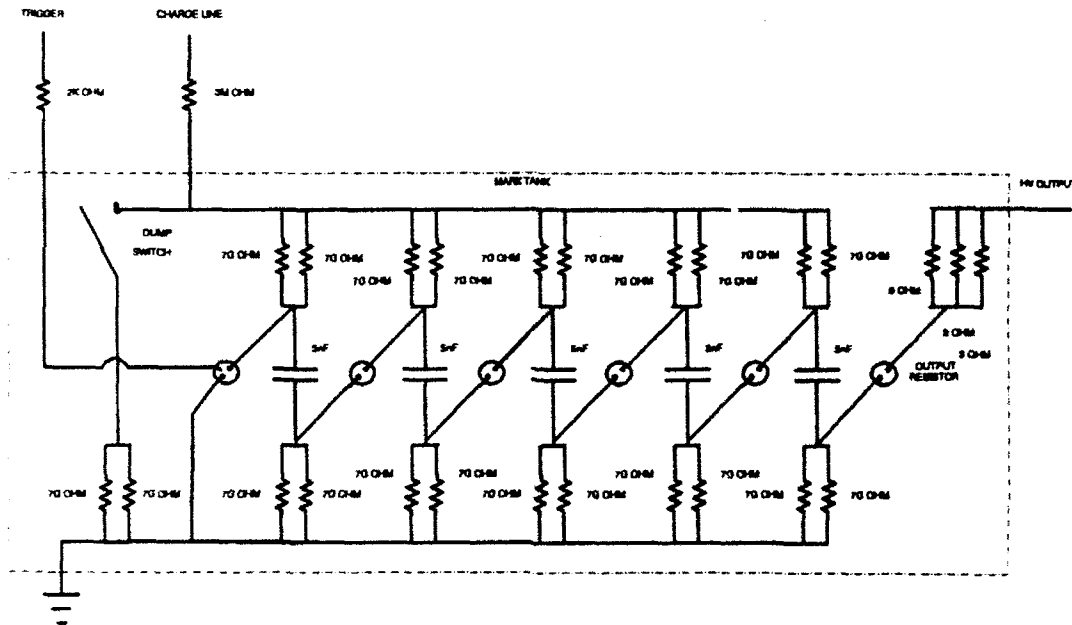


FIGURE 4

300 KV pulser specifications

TYPE OF PULSER:	5 STAGE MARX GENERATOR
CAPACITANCE EACH STAGE:	5 NANOFARADS
STAGE SEPARATION:	GAS INSULATED HIGH VOLTAGE SWITCHES
MARX TYPICAL RISETIME:	100 NANOSECONDS
CURRENT RANGE:	<3000 AMPS
REPETITION RATE:	3 MINUTES
REPRODUCIBILITY:	$\pm 10\%$
OUTPUT SECTION:	OUTPUT SWITCH W/3-3 OHM RESISTORS IN PARALLEL

MARX SPECIFICATIONS

OPEN CIRCUIT VOLTAGE:	150 TO 300 KV
ERECTED CAPACITANCE:	1 NANOFARAD
INDUCTANCE:	< 2 μ H
CHARGE VOLTAGE:	100 KV MAXIMUM

The output probe drawing (figure 5) is a cylindrical electrode with the excitation end being of a rounded cone design. The material for this probe is polished Monel 400 alloy. This particular electrode shape was chosen as a reasonable compromise between a sharp pointed electrode and a spherical electrode. The conical shape allows it to be directed towards the selected test point and avoids a sharp tip, which would initiate gap closure too quickly and which might erode with many pulse repetitions.

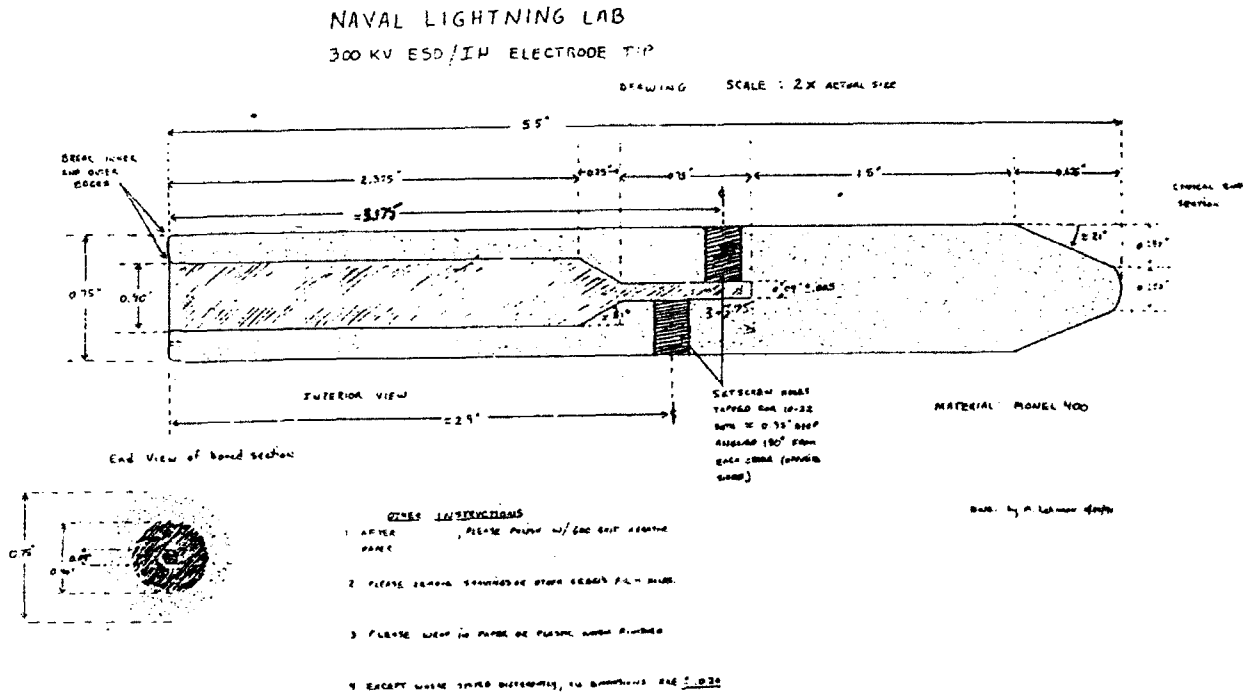


FIGURE 5

The current monitor on the pulser output is a Pearson probe (model #110) (essentially an insulated rogowski coil).

The voltage monitor is a Hipotronics model #CMD-400. It is a resistive-capacitance stack designed to influence the circuit as little as possible while registering

the output voltage. We selected the data acquisition components to be easy to use but still appropriate to the test parameters and data output desired. The following component list and data were taken from the operating system manual.

DATA ACQUISITION COMPONENTS

1. Compaq 386SX computer
2. HP Laserjet III printer
3. HP 54510A transient digitizer
4. GPIB interface card
5. Voltage and current monitors
6. *Software for system integration of reference data.

*Note: software was developed with the focus on producing a quick turn around time.

We propose that the following steps be used during the actual testing process.

1. Test the circuit with the 100 ohm calibration resistor as the load. Record both voltage and current waveforms.
2. Remove the 100 ohm calibration resistor, insert the object (fuze etc) under test, and pulse the circuit. Record both voltage and current waveforms.
3. Repeat step #1 after removing the test object and re-inserting the 100 ohm calibration test load.

Since the current and voltage monitors are part of the circuits, before, during and after the test their effect on the circuit can be accounted for and removed as a possible source of confusion as to their effect on waveforms.

SUMMARY

Since in the helicopter environment the physical factors can be significantly different due to different sizes of the aircraft, differing materials of construction and even the particular circumstances when an electrostatic discharge occurs; it is difficult to define the exact parameters of any one situation. Further research on providing answers to these complex questions is needed to enable the test parameters to be quantified in a more exact manner.

CONCLUSION

We have proposed a change to the current test methodology in an effort to place some boundaries on the uncertainties of test results. Without further research into the exact nature of the test parameters, we believe the procedures we have listed are to the best short term solution to assist in clarifying this problem area.

Ref (1) MIL-STD-331B Appendix F

Ref (2) "Detailed Operating Procedures Manual for the Electrostatic Discharge Simulator" EMP section (SY84) Systems Engineering Test Directorate, Naval Air Warfare Center, Patuxent River, Maryland.

**METHODS OF PRODUCING SIMULATED LIGHTNING PULSE WAVEFORMS
TO SATISFY MIL STD 1757A**

**Monty R. Lehmann
Ktech Corporation
P.O. Box 70
Lexington Park, MD 20653**

**Mike Whitaker
Naval Air Warfare Center
Aircraft Division
Patuxent River, MD 20670**

ABSTRACT

Practical methods used during the period 1989 - 1992 to produce simulated lightning pulse waveforms are described and documented. Circuits and equipment used in various testing modes are illustrated and explained and typical waveforms are shown. A novel type of hybrid marx generator developed and in service at the Naval Lightning Laboratory is described and its capabilities are discussed. Coaxial Current return arrays and their support structures used on full scale aircraft lightning tests are described as well as the design and construction of aircraft high voltage isolation test stands.

Paper not submitted.

LIGHTNING DATA ACQUISITION

**Rosemarie L. McDowall
Galaxy Scientific Corporation
2500 English Creek Avenue
Pleasantville, New Jersey 08232
(609) 645-0900**

**J. Anderson Plumer
Lightning Technologies, Incorporated
10 Downing Parkway
Pittsfield, Massachusetts
(413) 499-2135**

**Michael S. Glynn
Federal Aviation Administration
FAA Technical Center
Atlantic City International Airport, New Jersey 08405
(609) 484-4138**

ABSTRACT

Three data collection programs are being pursued to acquire data which may be useful in the Federal Aviation Administration (FAA) lightning databases. The Commercial Lightning Database (CLD) program solicits lightning strike data from commercial and general aviation pilots via a form filled out by the pilot when his aircraft is struck. Current airline participants are American and Delta. Another source of data is the Bureau of Land Management (BLM) which runs a network of lightning sensors covering the 11 western states of the United States. Data on approximately 13 million strikes between 1985 and 1990 have been reviewed. In addition to these two sources, the Organization of Flying Adjusters (OFA) and the Aircraft Owners and Pilots Association (AOPA) are starting to supply data from their files.

INTRODUCTION

The FAA continually addresses the potential adverse effects of lightning strikes to aircraft. As the proponent for advancing flight safety, the FAA has specified the threat which aircraft must be able to withstand. In addition, the FAA needs to verify that the built-in protection is working. As part of this verification, the FAA Technical Center is sponsoring programs to collect and review lightning strike data from various organizations including BLM, OFA, AOPA, and several commercial airlines.

COMMERCIAL LIGHTNING DATABASE

INTRODUCTION — The FAA's Commercial Lightning Database (CLD) is a continuation of the project started by Lightning Technologies, Incorporated (LTI) in 1972. Under this project, pilots of commercial aircraft were asked to fill out a form whenever their aircraft was struck by lightning. Five airlines — American, Braniff, Continental, Eastern, and United — participated in the first phase which lasted from 1971 through 1987.

The second phase of the project was initiated in 1992. American and Delta are the current participants, and it is expected that USAir, Trans World Airline, and United Airlines will also participate in the near future.

It must be emphasized that participation in this project is on a voluntary basis. Each airline places different amounts of emphasis or generates different levels of enthusiasm in their data collection efforts. As a result, the reader must bear in mind that the data collected is not random and the statistical variance of lightning strikes to all commercial aircraft may be appreciably wide.

PHASE I DATA — During the first phase of the CLD project, 1,101 strikes were reported. In 34 percent of the cases, damage was reported; in 16 percent of the cases, equipment interruptions were reported; and in 15 percent of the cases, effects on crew or passengers were reported.

PHASE II DATA — Phase II was initiated in January, 1992. One of the participating airlines continued to accumulate data using the original reporting form. The forms which they made available to the CLD cover the time period from June 1991 through December 1991. Use of the newly revised form began in 1992. Two airlines provided 170 reports, covering the time period between June 1991 and August 1992.

Damage was reported in only one percent of the cases. In 11 percent of the cases, equipment interruptions

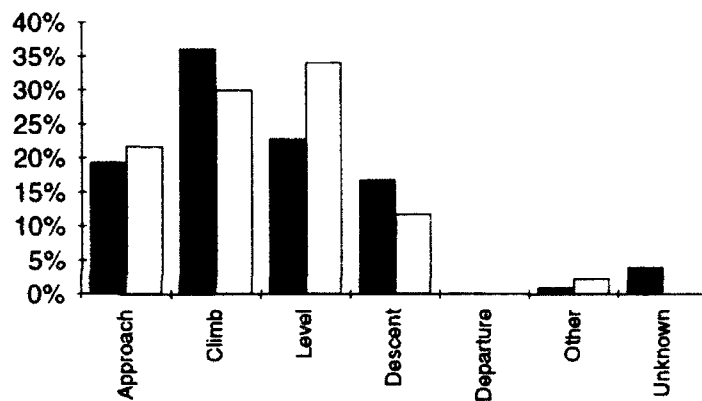


FIGURE 1. STRIKES BY ATTITUDE
■ 1971-1987 □ 1991-1992

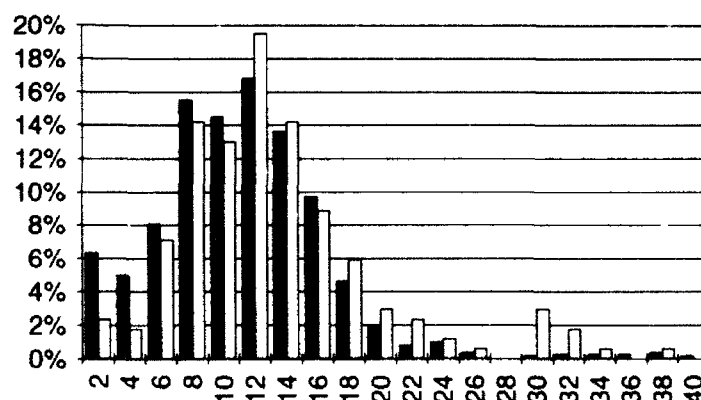


FIGURE 2. STRIKES BY ALTITUDE
■ 1971-1987 □ 1991-1992

were reported. In 12 percent of the cases, effects on crew or passengers were reported.

COMPARISON OF DATA FROM PHASE I AND PHASE II — Figures 1 through 6 show the normalized distribution of strikes reported during the first and second phases of the project. Each set of data was normalized to itself rather than to the whole data set. For example, in figure 1, 36 percent of the early strikes and 29 percent of the late strikes occurred during the climb phase of flight.

Figure 1 shows the percentage of strikes occurring to aircraft in different portions of their flight. Approximately 70 percent of strikes occurred while aircraft were on approach, climb, or descent phases of their flights. Figure 2 shows the percentage of strikes by altitude. It must be emphasized that the peak around 12,000 feet does not mean that there is more lightning at that altitude. During the cruise phase of flight, commercial aircraft are vectored around thunderstorms, so relatively few strikes are encountered at cruise altitudes.

Figure 3 shows the percentage of strikes versus cloud cover. The cloud cover is given in percentage of sky that is covered by clouds. Figure 4 shows the percentage of strikes occurring to aircraft in different locations with respect to clouds. Very few

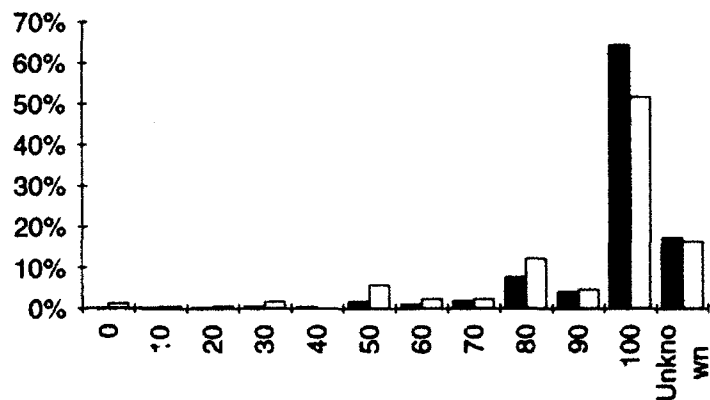


FIGURE 3. STRIKES BY CLOUD COVER
 ■ 1971-1987 □ 1991-1992

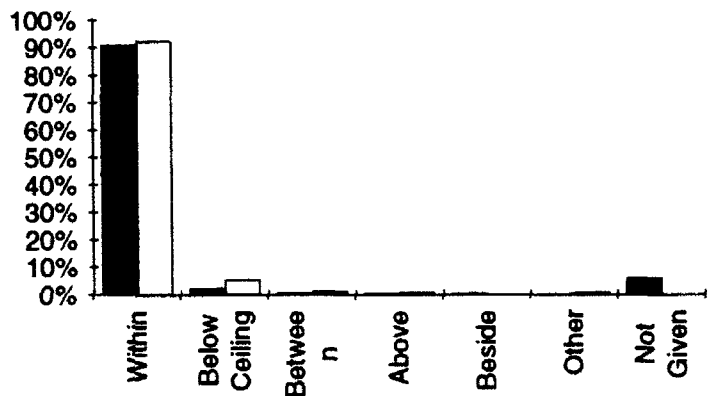


FIGURE 4. STRIKES BY LOCATION WITH RESPECT TO CLOUDS
 ■ 1971-1987 □ 1991-1992

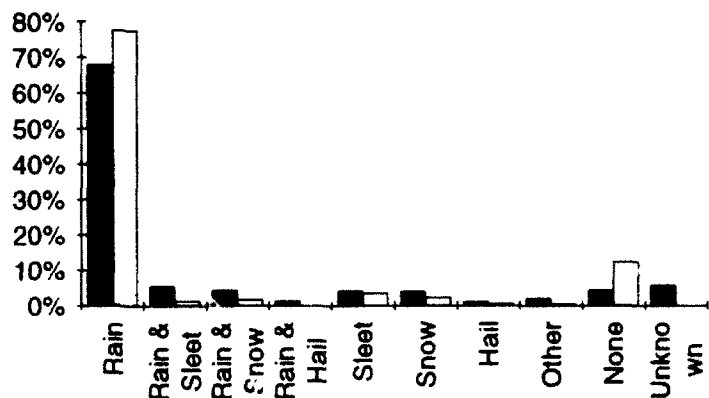


FIGURE 5. STRIKES BY PRECIPITATION
 ■ 1971-1987 □ 1991-1992

clear-air strikes were reported. Figures 5 and 6 show the percentage of strikes occurring under differing types of precipitation and levels of turbulence.

In addition to the general environment of the aircraft at the time of the strike, the data collection form asks the pilot to report on equipment interference or outage and damage to the aircraft.

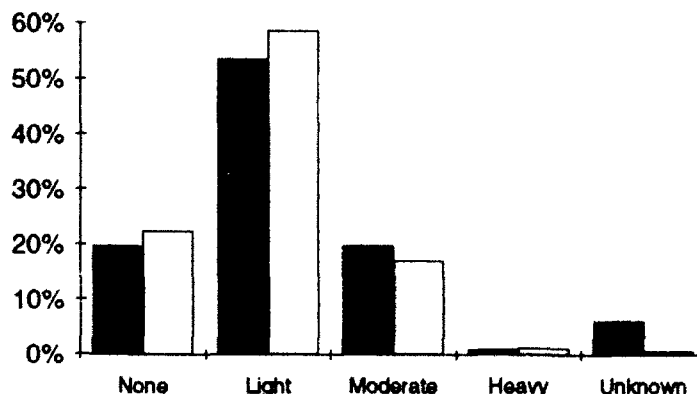


FIGURE 6. STRIKES BY TURBULENCE TYPE
 ■ 1971-1987 □ 1991-1992

TABLE 1. DAMAGE, INTERFERENCE, EFFECTS

Aircraft	Total	Int.	Eff.	Dam.
A300	3	1	0	0
B707	40	6	4	14
B727	720	93	104	91
B737	24	4	0	9
B747	39	9	5	8
B757	13	4	0	0
B767	23	1	5	0
DC10	205	53	27	21
DC8	50	9	7	10
DC9	53	8	14	3
FK-100	1	0	1	0
L-1011	2	1	0	0
L-188 ELECT	4	0	2	3
MD-11	1	0	0	0
MD80	25	2	6	1
MD88	6	0	1	0
MD80S	36	3	5	0
Other	18	4	3	5
Totals	1263	198	184	165

Table 1 shows the different aircraft types on which data were received. Phase I and II data are combined for this table. The total number of reports received for each aircraft type is listed under Total. The "Int." column shows the number of reports of equipment interference or outage. The "Eff." column shows the number of reports of effects, and the "Dam." column shows the number of reports of damage to an aircraft.

The data from Table 1 are represented graphically in figures 7 through 9. Please note that for some aircraft no damage, effects, interference, or outages were reported. Although these aircraft are included in Table 1, they have been deleted from the graphs for clarity. The figures show the percentage of reports for a given aircraft which indicate the presence of the relevant parameter.

ORGANIZATION OF FLYING ADJUSTERS

The OFA is an international organization of insurance agents whose specialty is aviation insurance and claims. Currently, there is no central repository of information, but the OFA is in the process of submitting questionnaires to its members concerning claims for damage due to lightning strikes. Where 71 percent of the respondents to the CLD report no damage, by definition, all of the strikes reported by the OFA will have associated damage. It is anticipated that the OFA may provide data which can correlate strike locations to damage sustained. Analysis of this data may guide further research into reducing the adverse effects of lightning.

BUREAU OF LAND MANAGEMENT DATA

The BLM manages a network of lightning detectors covering the 11 western states of the United States. The goal of this network is to pinpoint areas of intense lightning activity so that spotter airplanes can be sent out to look for signs of forest fire ignition. Although their system can record the intensity of each strike, the BLM is not interested in this parameter. As a result, their data are useful only for temporal and

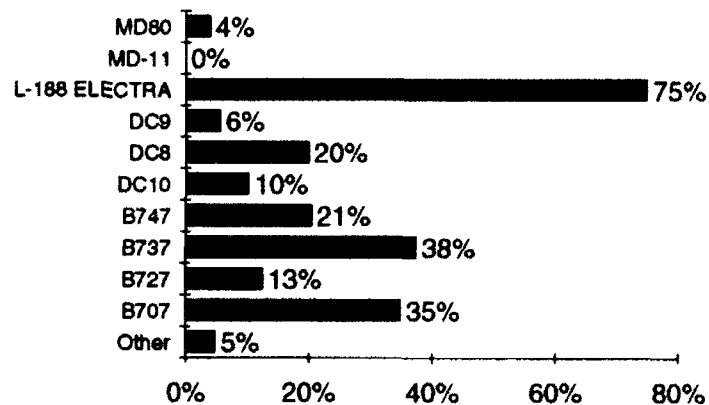


FIGURE 7. DAMAGE REPORTS, BY AIRCRAFT
■ 1971-1987 □ 1991-1992

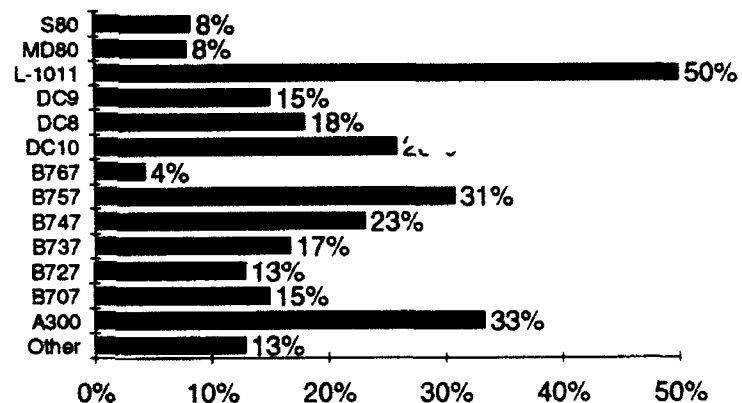


FIGURE 8. INTERFERENCE REPORTS, BY AIRCRAFT
■ 1971-1987 □ 1991-1992

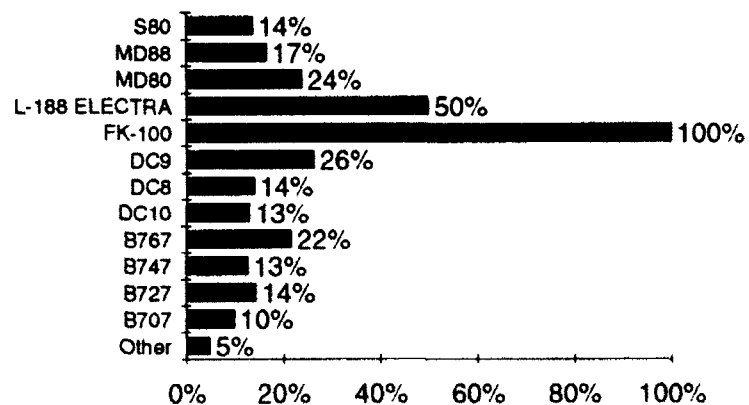


FIGURE 9. EFFECTS REPORTS, BY AIRCRAFT
■ 1971-1987 □ 1991-1992

spatial distributions of lightning strikes.

TABLE 2A. BLM DATA MATRIX

	125	124	123	122	121	120	119	118	117	116	115	114
49	0	1	1	0	0	4	1	1	4	3	5	0
48	376	501	1079	2063	3370	3885	5525	7639	6616	7476	9096	7509
47	253	570	1599	2539	2621	2957	4245	6436	8128	9898	12228	17583
46		401	862	1460	2863	3162	2268	2786	8096	12559	14679	18031
45		394	646	1578	3646	4498	5917	8939	14556	17625	19022	25321
44		1032	793	2436	7881	9582	11161	13614	12266	8822	14186	20223
43		988	1716	6365	11200	11746	12118	10563	10459	8409	11071	14958
42		1088	2753	6443	9911	13085	10861	10274	11080	14204	15710	20585
41	1	716	3753	10476	10803	12212	11315	7502	8985	16110	25846	38979
40	1	911	3204	7303	10237	14622	10437	8487	12166	20308	32682	50862
39		491	1613	4863	5558	16917	17364	11649	20486	41894	50950	58261
38		376	1592	2133	2481	8817	27220	20506	23751	44027	51852	72454
37		293	754	912	1939	2537	15690	18643	23032	30920	43917	83280
36		249	433	761	2747	2164	2407	14480	18609	22794	36770	52307
35		146	213	471	1209	1588	2525	14122	17410	22920	47632	55511
34		107	215	344	894	1688	4079	6507	13600	20620	21272	27471
33		64	140	336	1228	1554	867	1020	1977	7513	11850	26269
32		79	137	317	708	497	595	498	2086	6251	8909	15668
31		78	109	176	257	319	222	354	844	2925	15626	8825

TABLE 2B. BLM DATA MATRIX (Continued)

	113	112	111	110	109	108	107	106	105	104	103	102
49	0	1	2	3	4	3	1	4	4	2	0	49
48	11745	14932	17026	19177	20141	20448	21233	16922	10949	7597	1230	48
47	22908	25689	28612	28962	27138	31005	25936	21753	14943	10760	947	47
46	30959	36773	34268	36813	42478	38537	34071	26123	32317	24756	12938	1229 46
45	26421	32922	31109	36562	39340	34043	34823	40133	31439	23731	19202	1560 45
44	22860	26492	22603	28310	37028	31569	26412	36960	39657	35817	19304	1997 44
43	19006	20132	31041	32625	33142	29275	25089	35463	39660	31684	19984	1675 43
42	26556	39985	41492	40684	36839	25696	24569	27542	28727	22223	13117	1402 42
41	38239	38396	39360	45279	48656	30786	31362	27323	23821	17338	11278	1838 41
40	35497	51276	48227	57972	47376	46580	59238	46842	36526	23450	15310	1629 40
39	47230	45886	51540	65641	61545	65669	56180	38724	61195	40011	16920	1618 39
38	75707	61492	58264	57211	64549	73241	40731	41321	59727	40408	20445	2038 38
37	99494	77213	64814	51308	80606	94540	66992	52566	41436	53842	39939	4248 37
36	87577	72413	47877	58977	67018	73361	88389	100160	84688	117920	79061	6867 36
35	93338	85272	66167	45637	68839	95474	111460	128228	155837	170752	110094	8768 35
34	64754	91931	98195	82260	95743	117990	129142	122762	139835	162631	136502	7966 34
33	35982	51425	78152	110606	138881	131614	108420	102242	141998	129263	117789	11022 33
32	31557	56753	67998	122502	92501	102914	88233	81661	97264	74947	54881	8069 32
31	16390	52055	83208	109264	88182	65178	55040	58012	60838	44286	27167	3568 31

Data from this network was acquired for the time period from May, 1985, to September, 1990. During the time that the system was operating, approximately 13 million strikes were recorded. Strikes are counted in regions which measure one degree of longitude and latitude on a side. Table 2 is a matrix showing the number of strikes recorded in each longitude-latitude square. Unfortunately, review of this data indicates that it is not applicable to aircraft lightning strike problems.

AIRCRAFT OWNERS AND PILOTS ASSOCIATION

AOPA has an information processing center in Atlanta, Georgia which members can contact through a toll-free telephone number to solicit assistance in many areas. As an added benefit to the members, calls concerning lightning and static electricity will be forwarded to LTI to render assistance. In a continuing effort to statistically study the lightning-aircraft interaction, LTI will forward the standard Lightning Strike/Static Discharge Incident report form to the pilot/owner, requesting that information be submitted for inclusion in the CLD. In turn, this information will enable the engineers and statisticians to further understand the phenomenon of strike attachment and improve the protection offered to the airframe and avionics.

SUMMARY

The FAA is conducting on-going studies with various aviation organizations to collect data on lightning strikes to aircraft. It is anticipated that these studies will lead to improved understanding of the relationships among flight and environmental parameters in lightning strikes to aircraft. In addition, the FAA expects to learn about the relationship between the strike attachment/detachment points and the damage sustained by the aircraft. Additional data and analyses will be published as they become available.

ACRONYMS

AOPA	Aircraft Owners and Pilots Association
BLM	Bureau of Land Management
CLD	Commercial Lightning Database
FAA	Federal Aviation Administration
LTI	Lightning Technologies, Incorporated
OFA	Organization of Flying Adjusters
TWA	Trans World Airline

DIGITIZATION OF ANALOG DATA FROM IN-FLIGHT LIGHTNING STRIKES

**James R. Elliott and Henry S. Weigel
Electro Magnetic Applications, Incorporated
P.O. Box 260263
Denver, CO 80226, USA
Telephone (303) 980-0070 Fax (303) 980-0836**

ABSTRACT

Analog recorded data from inflight lightning strikes has been converted for installation in the FAA Research and Development Electromagnetic Database (FRED). One second of data associated with a lightning event is digitized for each of an ensemble of electromagnetic sensors. The digitization and conversion process, which yields as many as 4 million samples for a sensor, is described.

INTRODUCTION

At the 1988 International Aerospace and Ground Conference on Lightning and Static Electricity, plans for constructing a worldwide data base of information on lightning, under Federal Aviation Administration (FAA) sponsorship, were presented (1). Since then implementation of the database has begun (2). Primary objectives of the project are to collect, preserve and make available, in a unified format, information collected in a variety of different lightning research programs. It is expected that ready access to the combined data will be valuable to researchers investigating lightning formation and triggering as well as to those concerned with aircraft coupling and safety issues.

The first data to be incorporated in this FAA Research Electromagnetic Database (FRED) was obtained from flights of a CV-580 aircraft in 1984, 1985 and 1987 (3 and 4). The CV-580 program was a collaborative effort of several U.S. Government agencies (including the FAA) and France's ONERA. A variety of electromagnetic sensors were installed on the aircraft for the collection of information on inflight lightning strikes. The sensors outputs were recorded using both onboard digitizers and an analog recorder.

The analog record is particularly valuable in establishing the ambient conditions just prior to a strike. While lacking the fine time resolution of the onboard digitizers, analog records require no selection of a trigger signal/level and can extend much longer in time. The latter feature is important, for example, in characterizing the structure of lightning events in which electrical activity persists more than 0.5 seconds.

Although the analog format is useful when data is being acquired, it is extremely inconvenient when data is being installed in a central repository. It is difficult to avoid data degradation due to media deterioration and playback equipment must be maintained in good calibration for each analog format. It is much more convenient to excerpt the interesting time intervals of the analog data and to store them in a standard digital format. In this way playback, calibration and conversion of sensor signals to meaningful physical quantities need be done only once during the construction of the database instead of during

each user access. This paper will describe just such a digitization, processing and conversion of the CV-580 analog data for use in FRED (5).

ORIGINAL DATA

The sensors onboard the CV-580 were an assortment of commercial and custom units measuring quantities such as the time derivative of the normal electric field, the time derivative of the magnetic field, currents and other quantities. The sensor outputs fed into signal processing circuits which split the signals and set the levels for input to the digitizer and analog recorder as need. Some sensor signals were recorded on both direct and FM channels; some were recorded at both high and low levels and some derivative sensors were integrated.

The analog recorder onboard the CV-580 was a Honeywell 101 System whose key features are:

- 28 channels
- Ampex 795 tape (1 inch x 10,000 ft)
- speed selectable 1.87 -120 inches per second
- direct channels bandwidth 200 Hz-2 MHz Signal/Noise 23 dB
- FM channels bandwidth 0 - 500 KHz Signal/Noise 32 dB
- track to track timing skew 1.1 μ s

Each channel had an anti-aliasing filter and an adjustable input range. The nominal levels on tape corresponded to 0 - 1 Vrms upon playback. FM channels were used to capture accurately slowly varying quantities such as the ambient electric field; the number and configuration of direct versus FM channels varied from year to year. An IRIG B time code was impressed on channel 1. Channel 27 held a servo signal for tape speed control on playback. Another channel was devoted to the analog sum of the signals used in generating the onboard digitizer triggers.

DIGITIZING SYSTEM

A 1 second interval of the analog record for each strike was chosen for digitization. This length of time was deemed adequate based on the observed sensor responses during the inflight lightning strikes. In order to avoid loss of information for the highest frequency on the tape (2 MHz), a sampling rate of 4 MHz (sampling interval = 0.25 μ s) was required by Nyquist's theorem.

The heart of the digitizing system was the LeCroy 6810 Waveform Recorder configured with 4 Msamples of 12 bit memory. The clock used with the digitizer was an external 4 MHz unit whereas the input bandwidth of the digitizer extended to 2.5 MHz. A CAMAC crate with a GPIB 488 interface module housed the LeCroy 6810 and its memory modules. The digitizer was controlled by a local microcomputer running the ASYST data acquisition package. A GPIB bus extender linked both the CAMAC crate and the microcomputer to a remote VAX-11/780 with its own National Instruments GPIB 488 interface board. A trigger signal (described below) from the analog tape initiated the digitization. Figure 1 illustrates the instrumentation configuration.

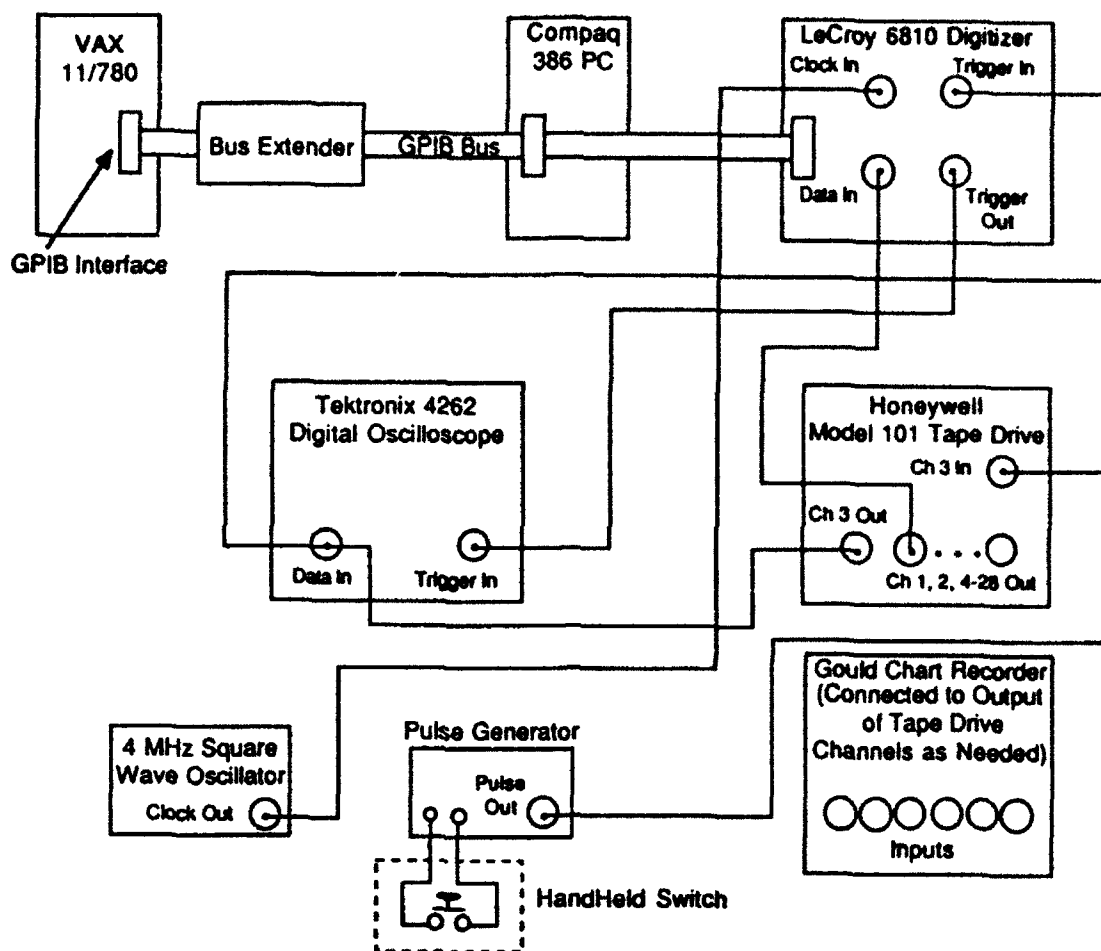


Figure 1 Digitizing System

DATA INTERVAL SELECTION AND CHANNEL SYNCHRONIZATION

The analog record for digitization was selected using the original researchers' time characterization of the inflight strikes. A strike on a tape was localized by using a time code translator to decode the information on channel 1. At this point the strike record from representative sensors was fed into a 6-channel chart recorder. From these plots it was observed that the waveform from the electric field sensor on the forward fuselage consistently had a sharp edge at the point of breakdown. This edge was selected as a coarse indicator of the lightning event.

It was desired to include some of the record previous to the strike as well as to maintain synchronization of all the analog channel and the onboard digitized data. Since the digital trigger signal on channel 3 was not consistent, it was decided to superimpose an additional pulse on this trigger channel. The additional pulse on channel 3 was used to trigger the LeCroy 6810 for the digitization of each of the analog channels. Digitizing the trigger channel itself permitted the time correlation with the onboard digitized data to be maintained. The procedure for adding the new pulse on the trigger channel was as follows

- play the tape at 1.87 ips until forward fuselage electric field sensor edge is observed,
- back up for 7 seconds at 1.87 ips,
- record 320 μ s squarewave pulse at 1.87 ips.

When the tape was played back at 120 ips the new pulse had a width of $\sim 5 \mu$ s and occurred approximately 100 ms before the breakdown feature of the forward fuselage electric field sensor. The 5 μ s pulse triggered the digitizer with a trigger to trigger variation of $\sim 0.5 \mu$ s, less than 1/2 of the dynamic time skew figure. A digital oscilloscope monitored the triggering waveform for the digitization of each channel.

DISCRETIZATION AND SAMPLING RESOLUTION

The noise levels from tape playback with no signal present are shown in Figures 2 and 3 for direct and FM channels respectively. The FM channel has a noise level of ~ 35 mV, slightly less than what might be expected from the Honeywell 101 specification of S/N ~ 32 dB and 0. - 1. Vrms signal range. The direct channel has a noise level of ~ 100 mV, consistent with the specification of S/N ~ 23 dB for 0. - 1. Vrms range. An input range of ± 5.12 V was chosen for the digitizer input. This corresponds to a discretization value of 2.5 mV, far more than required by the observed noise levels.

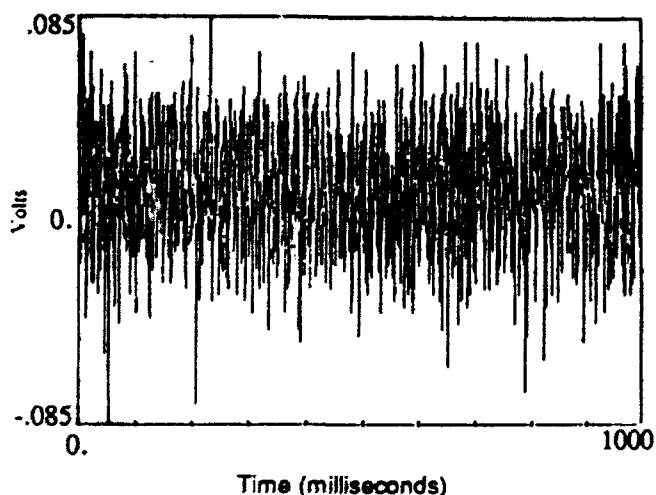


Figure 2 Noise Output of a Direct Channel

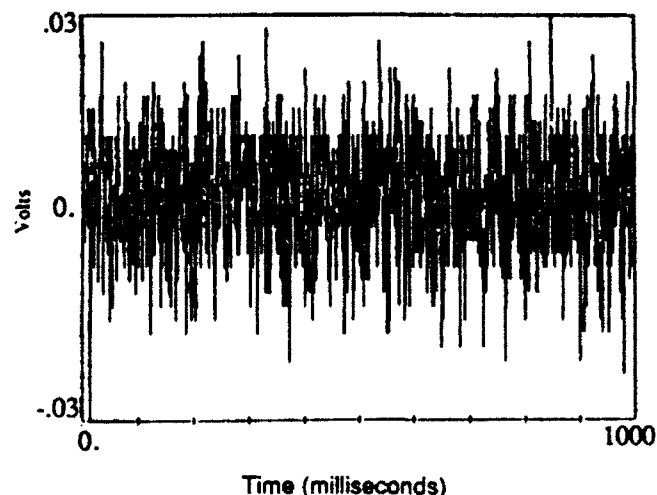


Figure 3 Noise Output of a FM Channel

To reduce the storage requirements for the direct channels, the data was truncated from 12 bit to 8 bits, giving a smallest level change of 40 mV. This is still less than 1/2 of the noise level. The full 4 Msamples were retained. To reduce the storage for the FM channels a different approach was taken. The full 12 bits of data were retained (with 4 bits of zeros padding to fill 2 bytes), giving a smallest level change of 2.5 mV; however, every other data sample was discarded. This was possible because of the 500 KHz bandwidth of the FM channels. Thus, 4 Mbytes of data is retained for either a direct or a FM channel.

strike number:	1
channel:	JNFF-L/FM
channel number:	5
year:	1987
timecode:	197:14:44:52
month:	Jul
day:	16
range (volts p-p):	10.24
offset (volts):	0.14168E-01
mode:	tape
velocity (ips):	120
period (ns):	500
transfer date:	04/09/89
transfer time:	12:31:20.70
comments:	
longitude(degrees):	N/A
latitude(degrees):	N/A
altitude(feet):	N/A
in air speed(knots):	N/A
turbulence:	None
in cloud?:	N/A
temperature (C):	N/A
weather:	
digital system OK?:	N/A
analog system OK?:	N/A
video system OK?:	N/A
sensor scale factor:	1.95E-6
record scale factor:	6.94
data scale factor:	1.
units of data:	C/m**2
sensor coupling:	dc
low freq limit(Hz):	0
high freq limit(Hz):	500000
derivative sensor?:	Y
integrated?:	Y

DIGITIZATION AND CONVERSION PROCEDURE

Using the new trigger signal for synchronization, the channels were digitized, one by one. After digitization of a channel, the data was transferred in 32 Kbyte blocks to the VAX-11/780 at ~ 100 Kbyte/s over the extended GPIB bus. On the VAX the 12 to 8 bit truncation of direct channel data and every other point deletion of the FM channel data was performed.

Two checks on data integrity were also performed. The first was a visual inspection of the 1 second waveform. The second was a checksum comparison between the VAX and the microcomputer on the first and last 32 Kbytes of data for each digitization. Only two checksum error were found in the VAX data in over 1000 waveforms. In each of these cases, a catastrophic failure dramatically corrupted the data in each data transfer block. For these waveforms, the data was retransmitted to the VAX. The statistics of the checksum errors estimate 75 data blocks with errors (of a possible ~ 160000) and the easily recognized form of the observed errors suggests no undetected errors in the entire data sample.

Once on the VAX, the digitized sensor data was written to 9-track magnetic tape in 4096 byte blocks. For the FM channels there were 2 bytes per sample and a total of 2 Msamples adding up to 1024 blocks of data. For the direct channels there was 1 byte per sample and a total of 4 Msamples, also adding up to 1024 blocks of data.

Figure 4 Sample Header Record

Calibration data including sensor and recording scale factors were obtained from the original CV-580 researchers. Knowledge of the scale factors allows the digitized voltage levels in the data blocks to be converted to physical units for each sensor, e.g., Amps for a current sensor or Coulombs per square meter for the integrated normal electric field sensors. These scale factors are included in a 4096 byte header block prepended to the data blocks. In addition, available flight data such as date/time, altitude, temperature, weather and related information was extracted from the flight logs and included in the header block. All of the information in the header is coded in ASCII in 80 character field-descriptor, field-value combinations. A sample header is shown in Figure 4.

The entire digitized analog data for the 1984, 1985 and 1987 CV-580 inflight lightning strikes represents 48 events, 1 per tape. On each tape there are 26 files of sensor data with >4 Mbytes implying > 104 Mbytes of data per tape.

DATA EXAMPLE

Figures 5-8 illustrate the digitized data for a pair of sensors on a single lightning event. The sensors are A) a normal electric field sensor on the forward fuselage (units used are surface current density) and B) a current shunt on the end of the left wing. Figure 5 shows the full digitized record with current sensor activity occurring between 0.2 and 0.3 seconds. Figure 6 is a blowup of this time interval revealing multiple correlated peaks in both the current and the normal electric field. Figures 7 and 8 covering intervals of 1 ms and 10 ms, respectively, are able to resolve details such as very fast risetimes and slow decay times which cannot be seen in Figure 5 and are only hinted at in Figure 6. From the information in Figures 7 and 8 it is possible to make accurate estimates of the maximum di/dt , as well the action integral and the number of current surges experienced by the aircraft.

SUMMARY

Analog data from 48 inflight lightning strikes to a CV-580 aircraft have been digitized. Synchronized records of 1 second of data from each 26 channels of electromagnetic sensors is available for each lightning event. The digitized data preserves both the sensitivity and the bandwidth of the original analog data recording. Calibration information is incorporated to transform the sensor data into directly usable, standard electromagnetic quantities. Additional information on sensor properties, weather and flight information is included for each lightning event. The entire data sample (over 5 Gbytes) is available to lightning researchers through the FAA Research and Development Electromagnetic Database.

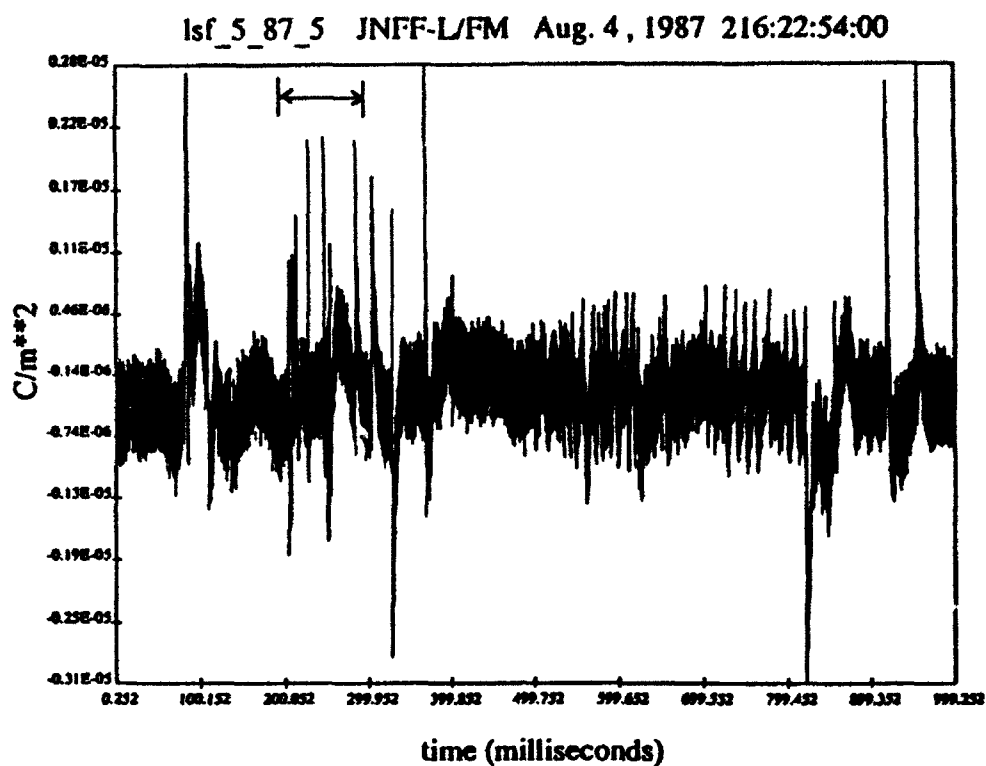
ACKNOWLEDGMENTS

The authors wish to thank Rosemarie McDowall, Mike Glynn, Jean Reazer, Pete Rustan and Brian Kuhlman for their unselfish support on this project. This work was performed under prime contracts DTFA03-86-C-60027-1 and DTFA03-C-00042 through subcontracts from Computer Resource Management, Incorporated.

REFERENCES

1. R.L. McDowall and M. Glynn, "Lightning Information Database," Proceedings of the 1988 International Aerospace and Ground Conference on Lightning and Static Electricity, NOAA Special Report, 1988.
2. R.L. McDowall, D.J. Grush, D.M. Cook and M.S. Glynn, "Implementation of the FAA Research and Development Electromagnetic Database." Proceedings of the 1991 International Aerospace and Ground Conference on Lightning and Static Electricity, NASA Conference Publication 10058.
3. P.L. Rustan, B.P. Kuhlman, H.D. Burket, J. Reazer and A. Serrano, "Low Altitude Lightning Attachment to an Aircraft," AFWAL-TR-86-3009, May 1987.
4. H.D. Burket, L.C. Walko, J. Reazer and A. Serrano, "In-Flight Lightning Characterization Program on a CV-580 Aircraft," AFWAL-TR-88-3024, June 1988.
5. J.R. Elliott and H.S. Weigel, "Digitization of CV-580 In-Flight Lightning Strike Data: Analog Data from 1984, 1985, and 1987", EMA Report EMA-90-R-35, May 1990.

A



B

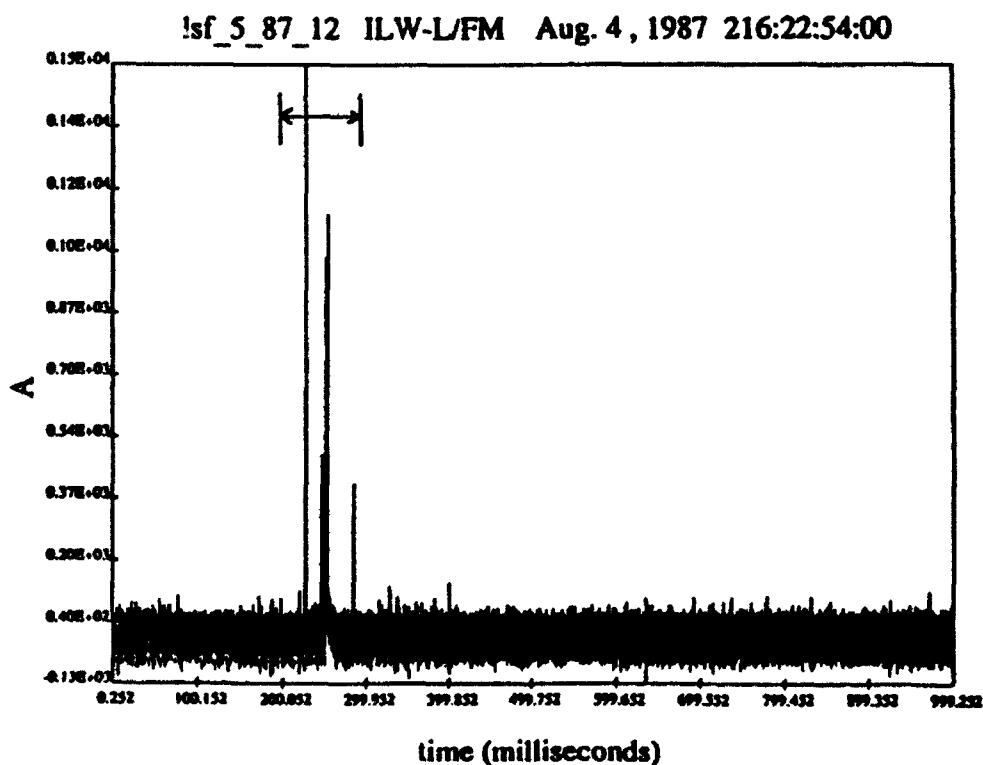
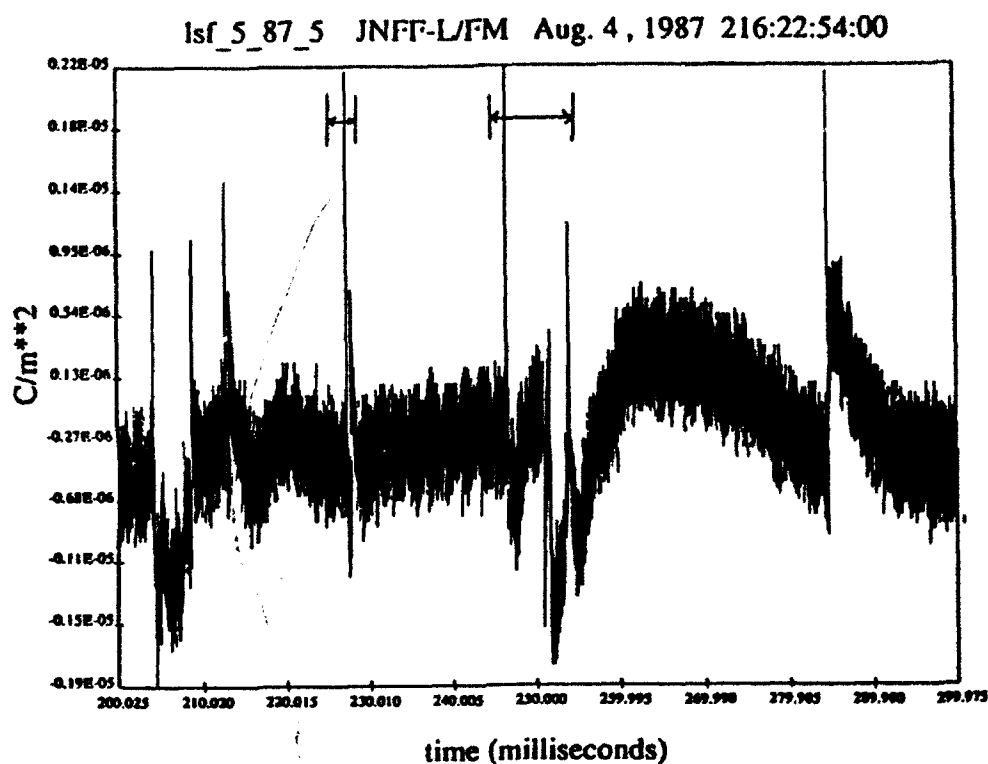


Figure 5 Full Digitized CV580 Analog Record for:
 A. Normal Electric Field Sensor on Forward Fuselage
 B. Current Shunt on Left Wing

A



B

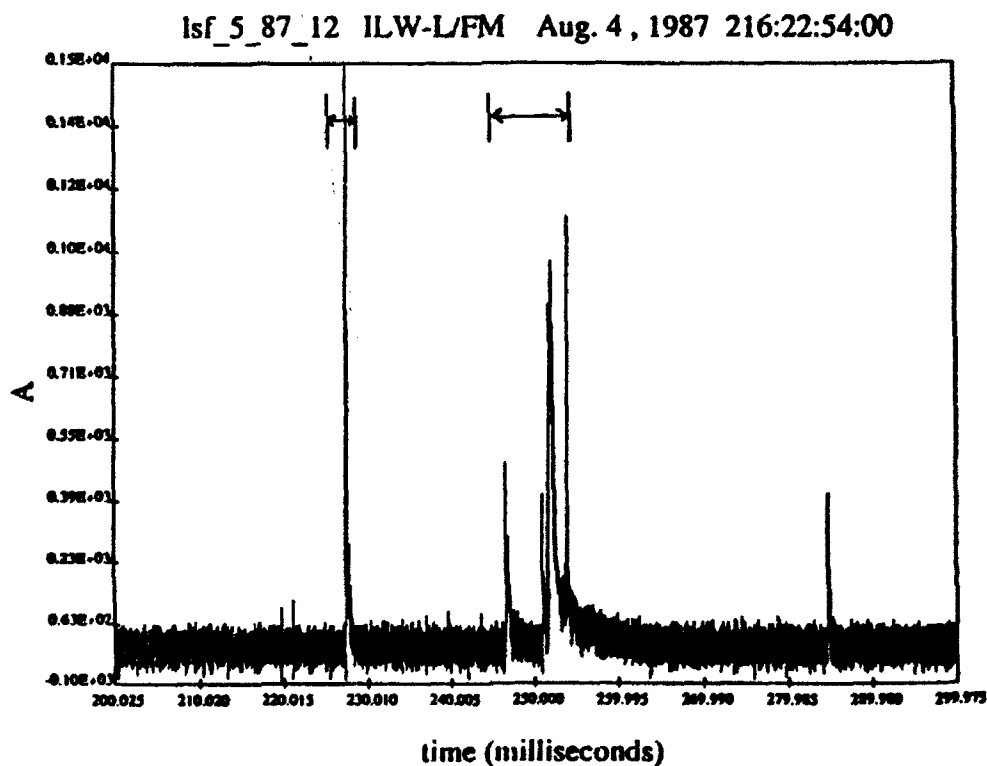
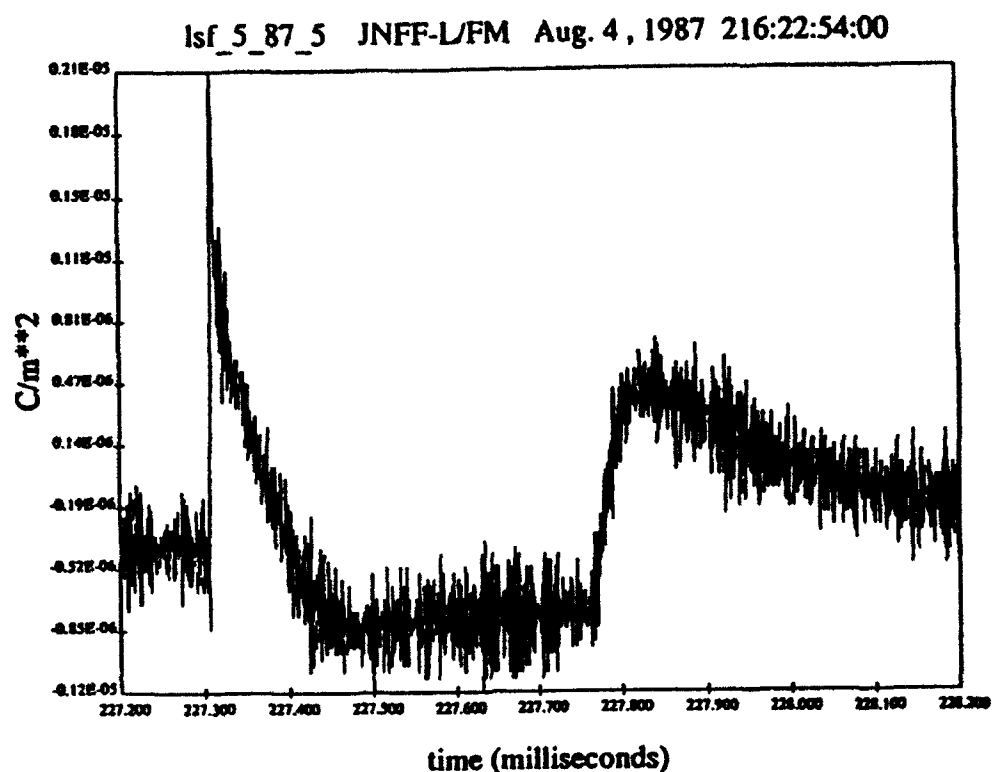


Figure 6 Blow-Up (0.2 - 0.3 Seconds) of Digitized CV580 Analog Record for:
 A. Normal Electric Field Sensor on Forward Fuselage
 B. Current Shunt on Left Wing

A



B

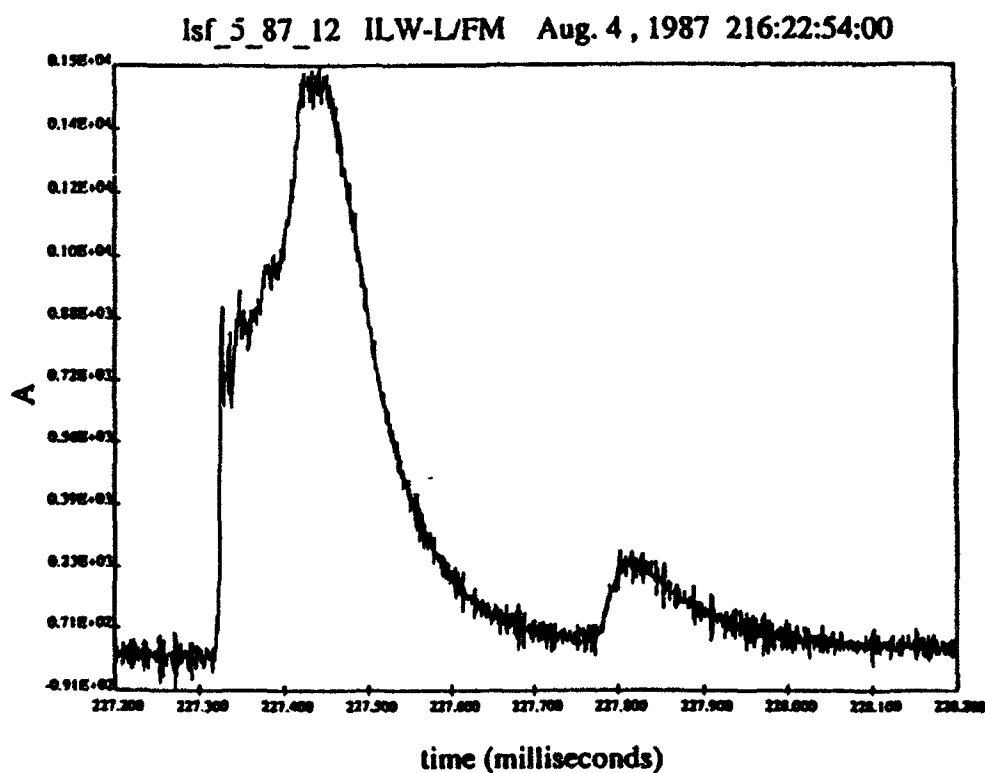


Figure 7 Further Blow-Up (.227 - .228 Seconds) of Digitized CV580 Analog Record for:
 A. Normal Electric Field Sensor on Forward Fuselage
 B. Current Shunt on Left Wing

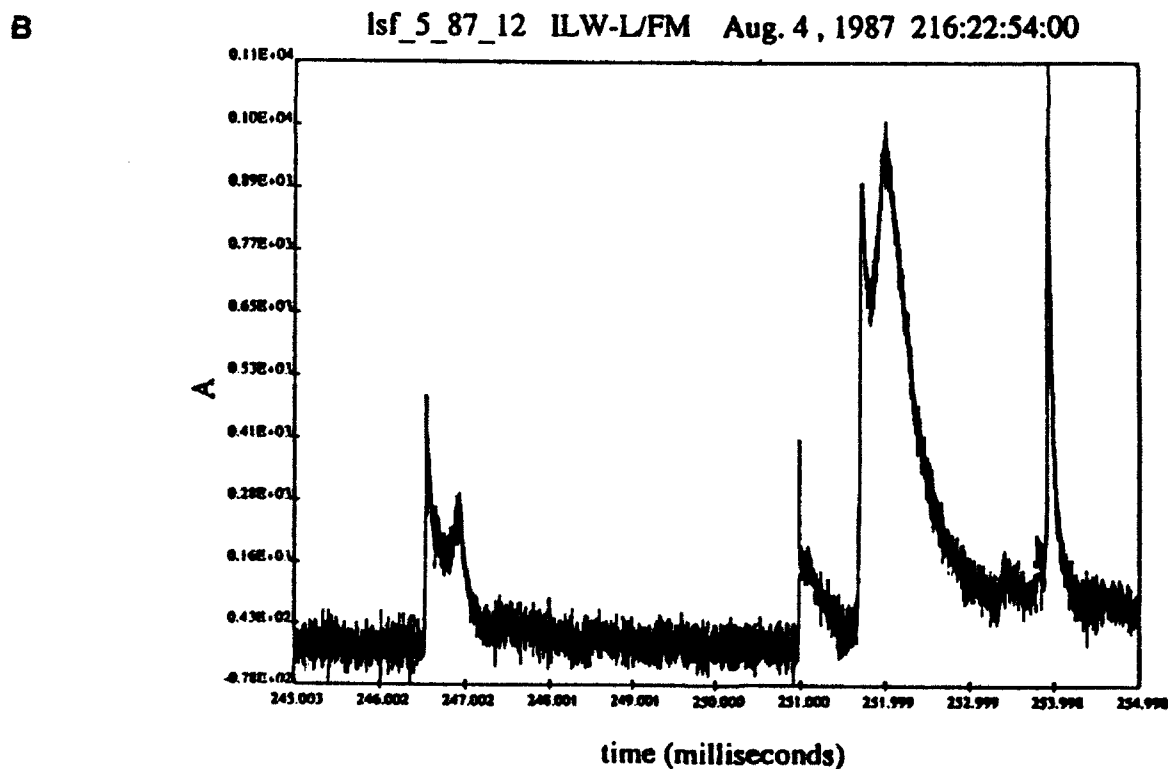
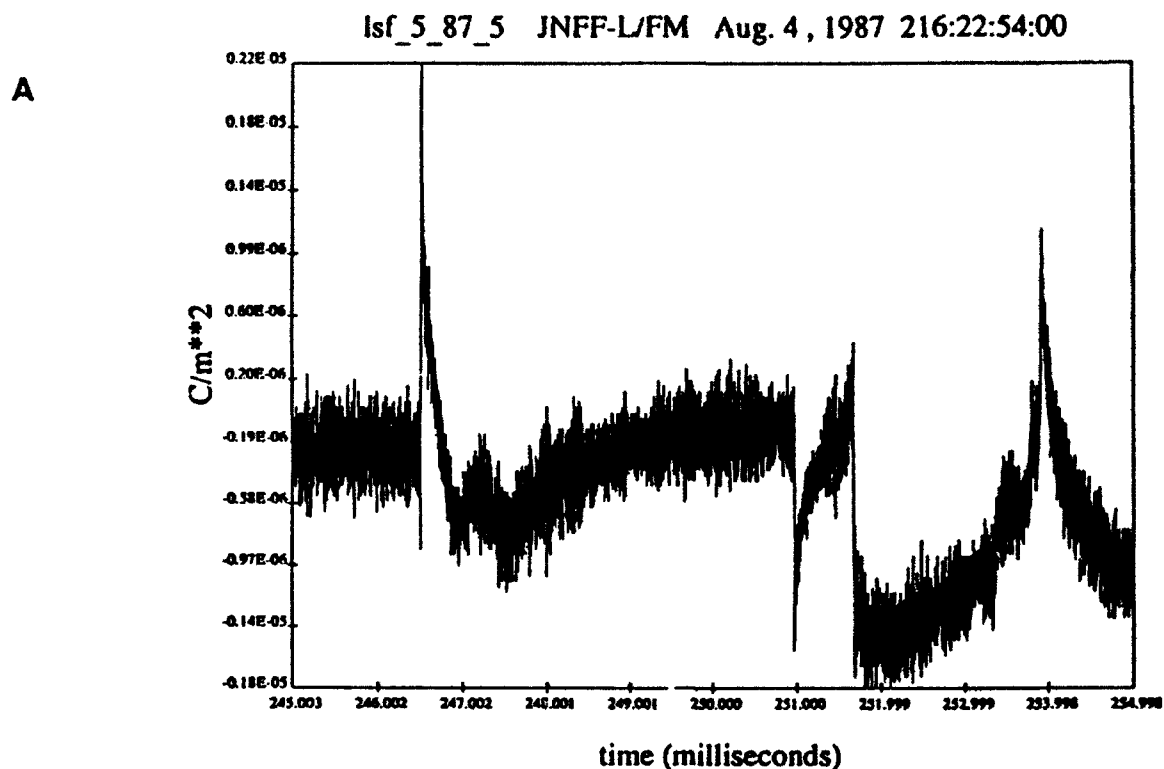


Figure 8 Further Blow-Up (.24 - .255 Seconds) of Digitized CV580 Analog Record for:
 A. Normal Electric Field Sensor on Forward Fuselage
 B. Current Shunt on Left Wing

A Procedure for Defining Lightning Risk to Air Vehicles

David Beeman

Naomi Morita

Northrop Corporation

Pico Rivera, CA

07 October 1992

Abstract

The risk of a lightning-induced failure is a function of the atmospheric conditions which produce lightning and the protective characteristics of the vehicle. Contemporary air vehicle designs – which incorporate “wet” wings and extensive composite skin and structures – require thorough consideration of this risk to balance performance of lightning protection measures against other performance parameters (*i.e.*, cost, weight, manufacturability, maintainability). An analytic procedure to investigate the risk of lightning-induced fuel vapor ignition is described in this paper. Sensitivity of the risk to various atmospheric and air vehicle design parameters was examined and is discussed.

1 Introduction

Although a significant body of knowledge and experience exists in the area of lightning protection of aircraft, [1] the advanced designs and materials require a reevaluation of that experience. Specifically, a thorough consideration of the currently understood protection requirements vis-à-vis the physics of the lightning problem is necessary. The work described herein was prompted by this very necessity: the design of an aircraft with many variations from conventional aircraft which compose most of the lightning strike experience. One major variation, discussed in [2], is the extensive use of composite materials, and how this influences the currently accepted zoning rules. The interaction of the electric field with a mostly-composite aircraft has not been characterized well enough to allow models to be built which accurately predict the likely strike areas, currents, and frequencies. Therefore, important experimental data such as that collected by the NASA F-106 [3] may not be relevant in the assessment of risk for composite aircraft.

The central issue of the study is the characterization of the lightning risk, which is defined as the probability that an aircraft fleet experiences one or more fuel tank ignitions over the life of the fleet. This risk is a function of vehicle "hardness" or protection configuration; the risk was evaluated under different assumptions of vehicle hardening. This parametric analysis, when combined with cost estimates to achieve those levels of hardness, forms the basis for a cost-effectiveness trade study. In addition to calculating the risk (of any ignitions), the probability of a large number of ignitions was also an important design consideration. To assure a robust design selection, critical parameters which drive the lightning risk were identified by conducting sensitivity studies of the input variables.

The second section of the report describes the background and the problem, which is to determine the sensitivity of risk to the design requirements for lightning protection. The third section defines the variables needed to determine risk and to verify their applicability this study. The fourth section describes the methodology used to quantify the risk. The fifth section discusses the results of the model for varying lightning protection configurations and the sensitivity studies which illuminated which input parameters were the driving factors to lightning risk. The last section summarizes observations and outlines some areas for further research.

2 Definition of the Problem

For conventional aircraft, the effects of lightning have been characterized well enough to allow thunderstorm avoidance and vehicle hardening to be effective in controlling the risk to these vehicles. Fisher and Plumer described the implications of advanced aircraft design and materials in [4]. An advanced design aircraft makes extensive use of composite materials in the skin and structure of the integral fuel tanks. Integral fuel tanks are "wet", that is, the inner surface of the wing is the fuel boundary - there is no separate structure for enclosing the fuel. The principal concern of this study is the lightning strike to the fuel tank, causing sparking inside the tank and the subsequent ignition of the fuel vapors. The problem addressed herein is to quantify the risk (number of aircraft which experience one or more of such ignitions) for various configurations of lightning protection and aviation fuel types.

3 Approach

Since lightning is usually modeled as a random event, a stochastic model was developed to utilize the probability distributions of each of the various events leading to fuel tank ignition. There are several papers describing similar approaches; Weinstock [5] uses a probabilistic approach to modify the requirements for lightning protection, while Corbin [6] advocates the use of a statistical approach to trade off risk for weight/cost/manufacturing penalties. A similar approach was used to define the risk for the A-6 wing [7] and the B-1 icing risk [8]; these studies derived an expected value for the risk. An expected value calculation produces a single number, such as the expected number of fuel tank ignitions, or the expected number of airplanes lost. A single expected value is inadequate for a design trade study because it cannot identify risk sensitivity to design parameters.

The basis for the analysis performed on this study was the calculation of the *distribution* of the number of catastrophic ignitions. One of the advantages of calculating a distribution (over an expected value) is that the effects of parameters which significantly alter the risk become obvious. Another aspect of the distribution is that it covers all possible options, giving detailed information about the probabilities of every event. This aspect of the distribution will be used to quantify (and minimize) the probability of any number of explosions.

The goal of this analysis is to construct a risk distribution for an advanced aircraft design. Building mission-specific risk requires evaluation of the entire distribution of all input parameters. The relevant domain must then be established for the aircraft's expected flight conditions, and the risk calculated from that portion only. For example, since strike rate has been correlated with altitude, it is important to use strike data that reflects experience of aircraft with similar flight profiles. (This becomes problematic when the form of the available data is considered.) The risk model then convolves the modified distributions to construct the mission specific risk.

4 Methodology

In order to provide an analysis of the complete distribution of risk, the expected conditions of the aircraft's lifetime and the random processes involved in a fuel tank ignition were simulated. The conditions at the time of the strike and consequent effects were modeled by a series of random draws, evaluated against the known (or estimated) distributions for the events. For example, the peak current amplitude of the strikes was a lognormal random variable; the random draw produced a current level from the lognormal distribution of test data. The aircraft's lifetime was simulated by constructing a set of mission profiles (*e.g.*, altitude, speed, fuel state) for several ambient conditions. The two aspects – the atmospheric and aircraft states – were combined to produce a stochastic risk model: a Monte Carlo simulation of the aircraft's exposure to lightning, executed over many lifetimes.

Historical data of strike frequency was used to define the number of lightning incidents to which the aircraft is subject. Scale model test results of lightning attachment areas determined the relative frequency of tank strikes. The use of these data is discussed in later sections. An offline analysis calculates the fuel system thermal performance for the missions representing the aircraft states under the MIL-STD-210B [9] standard day ambient

conditions with a 10% risk for hot day temperatures and a 10% risk for cold day temperatures. These thermal data consist of internal tank pressure, and six fuel temperatures (bulk fuel, ullage gas, top outer skin, bottom outer skin, top inner skin, bottom inner skin) for the fuel tanks as a function of mission time. A mission time is selected randomly for each strike to determine fuel tank conditions. The model compares this temperature/pressure data to the fuel flammability limits ([10], [11]) to determine if a flammable mixture exists in the struck tank.

There are four events which must simultaneously occur to endanger the aircraft; all are modeled using their observed or derived probability distributions. The fuel vapor ignition is the final state in a chain of events which starts with the lightning strike. The risk model therefore simulates the probability density of strikes. The next step is to identify those strikes which attach to the fuel tank areas. Although the consequences of striking other areas may be severe, the risk definition for this study is confined to the fuel tank. A fuel flammability assessment is then conducted to determine if the strike can ignite the fuel vapor in the tanks. Strike peak current amplitude is only calculated for the instances of flammable fuel tanks. Given a strike to a flammable fuel tank, the final calculation is made to decide if the fuel ignites.

4.1 Strike Frequency

The number of strikes and their probabilities are modeled via an event-driven simulation. The strike event generator uses strike rate and aircraft lifetime (in flight hours) to construct a binomial distribution of strikes. The density of the number of strikes is calculated using Equation 1 for the probability of a Binomial random variable X with parameters (n, p) :

$$P\{X=i\} = \binom{n}{i} p^i (1-p)^{n-i} \quad i = 0, 1, \dots, n \quad (1)$$

where:

$$\begin{aligned} n &= \text{number of hours per aircraft lifetime (10000)} \\ p &= \text{strike probability per hour (1/3000)} \end{aligned}$$

This relationship is used to compute the probability that an aircraft will experience i strikes in a 10000 hour lifetime (which is done for $i = 0, 1, \dots, 12$ in Table 1 and Figure 1). The above calculation produces the fraction of time an aircraft will see no strikes, one strike, etc., up to 12 strikes. (In this example, 0-12 covers 99.995% of the distribution.) The random strike calculation can be replaced by this distribution, with no loss of rigor. Using this approach, the variation of the number of strikes is accounted for, without incurring much of a computational time penalty.

4.1.1 Code Description

The strike generator provides the proportion of aircraft lifetimes which experience an arbitrary number of strikes. Combining this with the number of Monte Carlo iterations yields the fraction of iterations which experience i strikes. Following is a pseudo-code description of the implementation of the strike frequency.

Variable Definitions

Table 1: Sample Strike Rate Probability Density ($n = 10000$, $p = 1/3000$)

# Strikes	Probability
0	0.0357
1	0.1189
2	0.1982
3	0.2202
4	0.1835
5	0.1224
6	0.0680
7	0.0324
8	0.0135
9	0.0050
10	0.0017
11	0.0005
12	0.0001

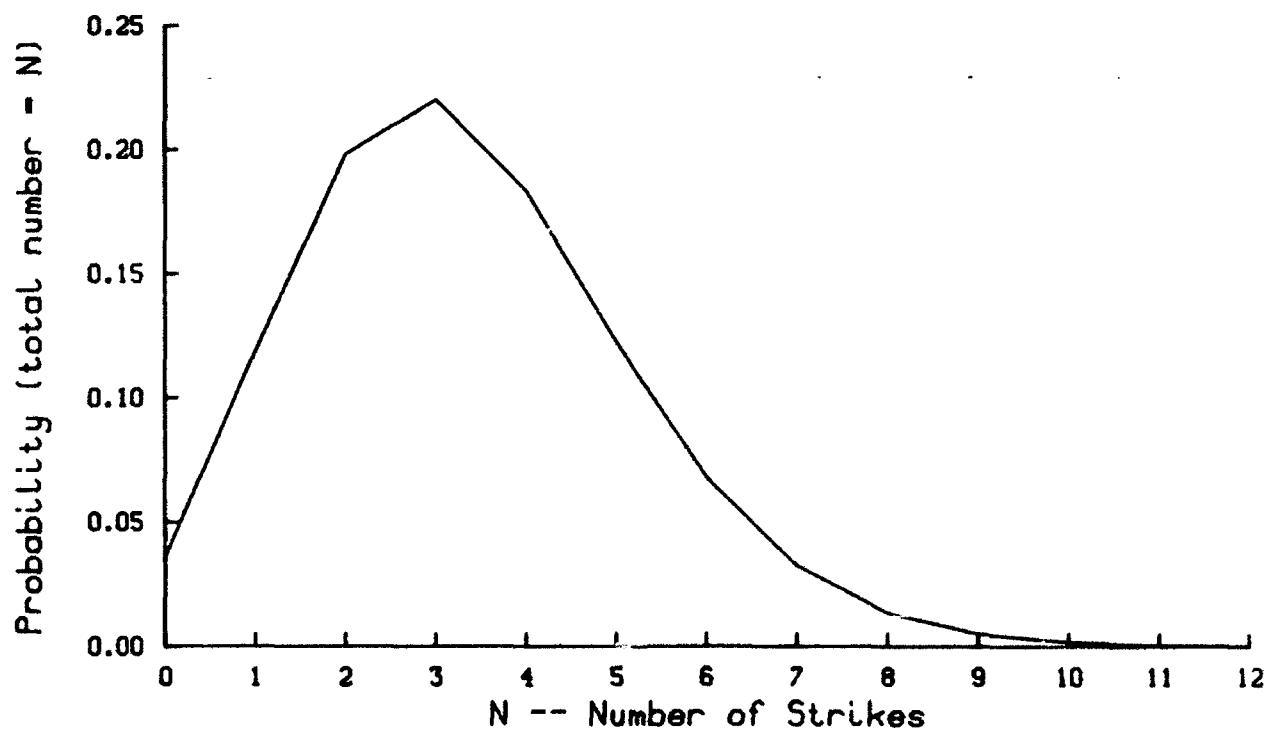


Figure 1: Sample Strike Rate Probability Density Function ($n = 10000$, $p = 1/3000$)

num_monte: number of Monte Carlo iterations of aircraft lives (something between 1000 and 10000)

p(i): probability of an aircraft seeing i strikes in one lifetime

mission_length(l): total length of mission l

p_mission(j): fraction of an aircraft lifetime mission j is flown

$$\sum_{j=1}^{nmissions} p_mission(j) = 1.0$$

sum_mission(k): range of probabilities for which mission k is drawn

Pseudo-Code

```
calculate the range of probabilities which produce each mission:
  sum_mission(0) = 0.
  do mission = 1, nmissions
    sum_mission(mission) = sum_mission(mission) + p_mission(mission)
  end do
calculate the risk for number of strikes between 1 and 12:
  do nstrike = 1, 12
    max_loop = p(nstrike) × num_monte
    loop_total = loop_total + max_loop
    do iterate = 1, max_loop
randomly select mission:
  draw uniform (0,1) random deviate, pdraw
  do mission = 1, nmissions
    if(pdraw > sum_mission(mission))then
      mission_run = mission
      mission_time = mission_length(mission) × (pdraw - sum_mission(mission))
      get out of mission loop
    end if
  end mission loop
  execute attachment routine for mission_run and mission_time
  execute flammability routine for mission_run and mission_time
  execute amplitude routine
  execute damage routine for configuration and strike_amplitude
  count up number of explosions, n_x
  end iterate loop
  histogram input (n_x)
  end nstrike loop
count the number of times there are 0 strikes:
  do loop = 1, p(0) × num_monte
```

Table 2: Lightning Strike Rate Data Summary

Source	Aircraft Type	Period	# Incidents	Strike Interval
Cummings	USAF	1965-1970	340	50000-200000
Corn	USAF	1969-1976	—	37900-81300
Abshier	USAF	1978-1988	530	145000
Plumer & Perry	US/UK Commercial	1959-1974	760	2490
Odam & Evans	UK	1972-1978	58	2703-3333
Ziegler	DKR	1973-1982	260	2564-9091
Newman	USA commercial	1950-1961	958	2970
Corbin	USAF	1970-1982	877	104000

```

        histogram input ( 0 explosions )
    end 0 explosion loop
normalize histogram:
    norm_histo(loop_total)

```

To determine the number of Monte Carlo iterations necessary, the number of iterations that would be required for zero strikes ("max_loop" in the pseudo-code above) was calculated. The number of iterations that caused max_loop to be statistically significant (greater than 20) was then used to exercise the model.

4.1.2 Strike Frequency Data

Strike frequency to aircraft is generally tabulated by flight hour. Unfortunately, databases often constrain reports to those incidents where a significant level of damage was incurred as a result of the strike. This practice biases reports towards the higher current amplitudes, especially when the experience is collected for metal-skinned aircraft. Commercial aircraft strike experience, often specified in terms of altitude, flight regime, attachment points and ambient temperature does not simultaneously provide the *a priori* probability of these states. For example, the Japanese carrier data tabulated by month of strike [12], shows the number of strikes experienced for each aircraft type. Using this information alone, one may (erroneously) assume that the lowest strike rate is observed by a specific type of aircraft. Without information describing the proportion of flight hours Japanese carriers flew this type, this data cannot be useful. The determination of mission specific lightning risk requires more than anecdotal strike data. Future research topics should investigate the probabilities of all conditions involved in each of these strikes in order to establish the risk to aircraft posed by lightning¹. In the survey of lightning strike experience, a wide range of observed strike rates was encountered, from a low rate of 1 strike every 200000 flight hours for USAF aircraft, to a high rate of one per 2490 flight hours (Table 2). This variability may be indicative of

¹It is important to establish the mission profiles and avoidance procedures used by the aircraft that were not struck, as well as those that were.

a minimum damage criteria on tabulated strike rate. However, for this study, a high strike frequency, 1 per 3000 flight hours, was used and the risk sensitivity to this parameter was examined. The density, shown in Table 1, is recalculated for each strike frequency that was run.

4.2 Attachment Model

To determine the proportion of strikes to vulnerable fuel tanks, scale model testing was conducted to determine where strikes are likely to attach to the aircraft structure. Capacitors were discharged to generate simulated lightning bolts on the aircraft model while the event was photographed from two orthogonal views. This procedure was repeated many times under various conditions to achieve confidence in the results.

A numerical count of the strikes attaching to the planform area around the fuel tanks in each wing was taken. Strikes attaching to the wing leading edge directly ahead of the tank planform were also added to account for the swept stroke phenomenon. Swept stroke refers to the situation when a strike attachment point sweeps backwards over the wing as the aircraft moves forward. The percentage of strikes that attach to fuel tanks is derived by dividing the number of strikes around the tanks by the total number of test iterations. Since the tank structure of most aircraft is broken down into separate, self-contained fuel tanks; the distribution of tank attachments is obtained by planform area ratio as follows:

$$p_i = P \times \frac{a_i}{A} \quad (2)$$

where:

- p_i = probability of attachment to fuel tank i
- P = fraction of strikes attaching to fuel tanks
- a_i = planform area of fuel tank i
- A = total area of the fuel tank structure

These attachment probabilities are combined for the left and right wings and for the top and bottom surfaces, assuming that the fuel tank structure is symmetrical. The data are input in decimal form to represent probabilities for a strike attaching to a particular fuel tank. If a fuel tank contains enough fuel to cover its bottom surface at the time the strike occurs, the probability of attachment is divided in half. This division models the assumption that half of the lightning bolts attach to the lower surface and an arc cannot form a spark across fasteners covered by liquid fuel. The mathematical attachment model then draws a uniform random number (between 0 and 1) to determine if a fuel tank has been struck and, if so, which one.

4.3 Fuel Flammability Model

After determining which fuel tank (if any) has been struck, a check is made to indicate the possibility of producing flame in the fuel vapors of the ullage. Ullage is a term used to denote the space not occupied by liquid fuel inside an aircraft fuel tank structure. This volume typically consists of a mixture of fuel and air vapors. If the fuel-to-air weight ratio of the ullage vapors is less than 0.035, the mixture will not ignite and is considered "too lean"

to burn. Conversely, if the fuel/air ratio is greater than 0.28, the mixture is "too rich" and will not support combustion.

A given set of static equilibrium temperature and pressure conditions inside a fuel tank produces a specific fuel/air ratio mixture in the ullage. Because of this, a lean flammability temperature limit can be defined (for a given fuel tank pressure) as the temperature required to produce a fuel/air ratio of 0.035. Similarly, the temperature that yields a 0.28 fuel/air ratio defines the rich flammability temperature limit.

Fuel flammability is primarily determined by aircraft operation (flight profile) and ambient conditions. However, flammability can also be affected by the presence fuel mists and sprays in the ullage. Fuel foam, mists, and sprays can exist in the ullage depending on: 1) fuel tank design, 2) operation of mechanical devices within the tank, 3) aircraft vibration, and 4) flight turbulence resulting in fuel sloshing and shaking.

4.3.1 Experimental Data

Reference [10] details the experimental setup and procedures used to test JP-8 (referred to as Jet A-1) and JP-4 (Jet B) aviation fuels for flammability. Tests basically consisted of subjecting a fuel specimen in a pressure vessel to a 20 joule spark and checking for the occurrence of ignition. Various equilibrium temperature and pressure conditions were tested to define a flammability envelope for each fuel type. While the relationship between the flammability temperature limits and the fuel tank pressurization is non-linear, the lean and rich limits are shown to vary linearly with the standard day pressure altitude.

Since the fuel refinement process cannot be duplicated exactly, individual batches of fuel can have different flammability characteristics. Test data in Reference [10] define flammability envelopes for several different fuel batches. Figure 2 shows a combined envelope which encompasses the envelopes for the individual fuel batches as well as the data presented in Reference [11]. The area between the lean and rich limit lines for each fuel shown in Figure 2 represents the flammable region for that fuel. Area to the left of the lean line represents nonflammable fuel states (too lean) as well as area right of the rich line (too rich). Note that an equivalent, standard day altitude must be determined from tank pressure to define flammability.

4.3.2 Theoretical Predictions

Appendix V of Reference [10] provides a detailed description of a method for calculating the flammability temperature limits for aviation fuels at any tank pressurization. Some simplifying assumptions were made in the derivation of the equations; and consequently, this theoretical method is not exact. The prediction method is more accurate for JP-8 than JP-4.

After inserting the appropriate fuel constants and reducing the equations, the method simplifies to a single equation for each fuel type. The flammability temperature limits are calculated for JP-8 fuel using the equation:

$$T = \frac{-247.30 \times \log(\lambda p) - 128.34}{1.15 \times \log(\lambda p) - 8.20} \quad (3)$$

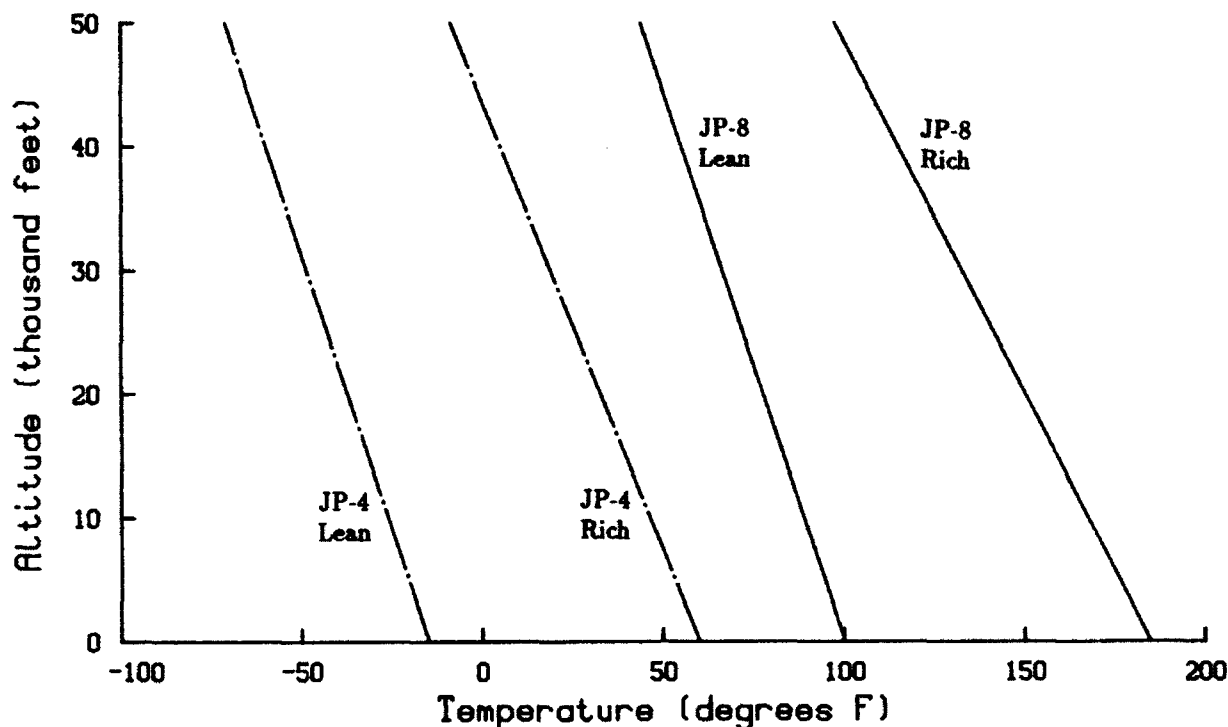


Figure 2: Static Flammability Envelopes for JP-8 and JP-4

and for JP-4 fuel using the equation:

$$T = \frac{-260.05 \times \log(\lambda p) + 338.65}{1.15 \times \log(\lambda p) - 8.03} \quad (4)$$

where:

- T = flammability temperature limit ($^{\circ}\text{C}$)
- p = fuel tank pressure (psia)
- λ = fuel/air weight fraction (in^2/lb)

The detailed calculations used to obtain the fuel/air weight fraction (λ) are shown in Appendix V of Reference [10]. Actual values used in the fuel flammability model are shown in Table 3. (Note: Since Equations 3 and 4 generate flammability limits in $^{\circ}\text{C}$, the limits must be converted to $^{\circ}\text{F}$ for comparison with the experimental data.)

A comparison of the results obtained from Equations 3 and 4 with the experimental data shown in Figure 2 reveals an offset due to the assumptions applied in the theoretical method. This is corrected by applying a "data bias" to the theoretical results. For JP-8 fuel, 5°F are subtracted from the calculated temperature limits. 15°F are subtracted from the JP-4 results. After this adjustment, the resulting calculated temperature limits provide close agreement with the experimental data.

4.3.3 Additional Flammability Factors

During flight operations, the ullage volumes of aircraft fuel tanks will rarely be at static equilibrium conditions. Although the exact conditions inside a fuel tank at any given moment

Table 3: Fuel/Air Weight Fractions for JP-8 and JP-4

Fuel Type	Limit	λ
JP-8:	Lean	0.39
	Rich	3.00
JP-4:	Lean	0.65
	Rich	4.80

cannot be known with certainty, some factors which have a significant effect on flammability have been tested and studied. The results of these studies are used to augment the methods for determining the equilibrium flammability temperature limits described in Sections 4.3.1 and 4.3.2.

Oxygen Enrichment As an aircraft climbs, air is vented from the ullage volume to equalize the pressure in the fuel tanks. The decreasing pressure in the fuel tanks causes the release of air contained in the liquid fuel. Because of the process in which air is absorbed into liquid fuel at sea level and subsequently released at a lower pressure, the trapped air added to the ullage tends to be oxygen rich. This sudden outgassing of oxygen-rich air changes the flammability characteristics of the fuel tanks.

Results of tests conducted to simulate this process are shown in Reference [10]. Oxygen enrichment of the ullage has the effect of increasing the flammability temperature limits. For JP-8 fuel, the lean flammability temperature limit is increased by $15^{\circ}F$ and the rich limit is increased by $7^{\circ}F$. Due to lack of data, no modification for oxygen enrichment is applied to the temperature limits for JP-4 fuel.

Air Ingestion During aircraft descent, air is ingested into the fuel tanks to equalize the pressure with the outside environment. This air intake lowers the fuel/air ratio of the ullage and increases the flammability temperature limits. To quantify the amount of air ingested, a pressure ratio is determined by dividing the pressure after descent by the initial pressure. New flammability temperature limits are then calculated by multiplying this pressure ratio by the fuel/air weight fraction (λ) before application into Equation 3 or 4 in Section 4.3.2 above.

Mists and Sprays Aircraft turbulence in varying severity occurs frequently in flight, especially when connected with the incidence of lightning strikes. Reference [13] shows that 21% of the reports indicated moderate turbulence at the time of a lightning strike and 1% reported heavy turbulence. Turbulence results in vibration and shaking of the fuel tanks; causing fuel to slosh, spray, and/or mist. An ullage with a fuel/air ratio that is too lean may become flammable with the introduction of a mist or spray.

Vibration test results given in Reference [10] show that mists and sprays have the effect of lowering the lean flammability temperature limits. A vibration with a displacement of

$\pm \frac{1}{16}$ in (inches) and a frequency of 10cps (cycles-per-second) reduces the lean flammability temperature limit of JP-8 by $10^\circ F$ and reduces the JP-4 limit by $55^\circ F$. A more severe vibration with a displacement of $\pm \frac{1}{8}$ in and a frequency of 15cps reduces the lean limit of JP-8 by $55^\circ F$ and effectively removes the JP-4 lean flammability temperature constraint. To mathematically model the removal of the JP-4 lean limit under severe vibration, a significantly large value ($155^\circ F$) is subtracted from the lean temperature limit.

Predetermined test conditions used to obtain the dynamic flammability data are controlled and repeatable. Conversely, the motion of aircraft fuel tanks during turbulent flight cannot be completely defined. In order to provide some measure of misting effects, the less severe vibration ($\pm \frac{1}{16}$ in, 10cps) is assumed to correspond to moderate turbulence (occurring for 21% of the lightning strike incidence) and the more severe vibration ($\pm \frac{1}{8}$ in, 15cps) corresponds to heavy turbulence (1% of the strikes). Note that the validity of this assumption has not been assessed and that other factors can lead to fuel tank misting (internal devices, tank design, etc.), leaving a fair amount of uncertainty in this portion of the flammability model.

4.3.4 Mathematical Modelling

The basis of the mathematical model is the static equilibrium flammability temperature limits as described in Sections 4.3.1 and 4.3.2. Using the mission flight time when the strike occurs, the mission profile is examined to determine the aircraft flight condition: level flight, ascent, or descent. If the aircraft is climbing or in a level flight condition, the experimental data of Section 4.3.1 is used to determine the flammability temperature limits. For cases when the aircraft are climbing, the experimental limits are modified for oxygen enrichment as described in Section 4.3.3. If the aircraft is descending at the time of the strike, the limits are calculated theoretically using Equation 3 or 4 of Section 4.3.2, modified for air ingestion as described in Section 4.3.3.

Regardless of flight condition, a check is made for the occurrence of random turbulence. A random number (between 0.00 and 1.00) is drawn from a uniform distribution to determine if the aircraft is experiencing turbulence and, if so, the severity of the turbulence. Numbers drawn between 0.00 and 0.01 indicate severe turbulence and likewise, numbers between 0.01 and 0.22 indicate moderate turbulence. The lean flammability temperature limit is then modified for the cases of severe and moderate turbulence as described in Section 4.3.3. No modification for turbulence is made when numbers are drawn between 0.22 and 1.00 indicating no turbulence.

Once the lean and rich flammability temperature limits have been determined, they are compared with the temperature of the fuel tank ullage gas. Ullage gas temperatures less than the lean temperature limit result in nonflammable fuel tanks regardless of the strike current level and the strike incident is discarded as being harmless. Likewise, ullages with gas temperatures greater than the rich limit will not ignite and no damage is assessed. In all other cases, the mixture is flammable and the fuel tank is at risk from the lightning strike. Note that flammability does not necessarily mean ignition or damage to the aircraft.

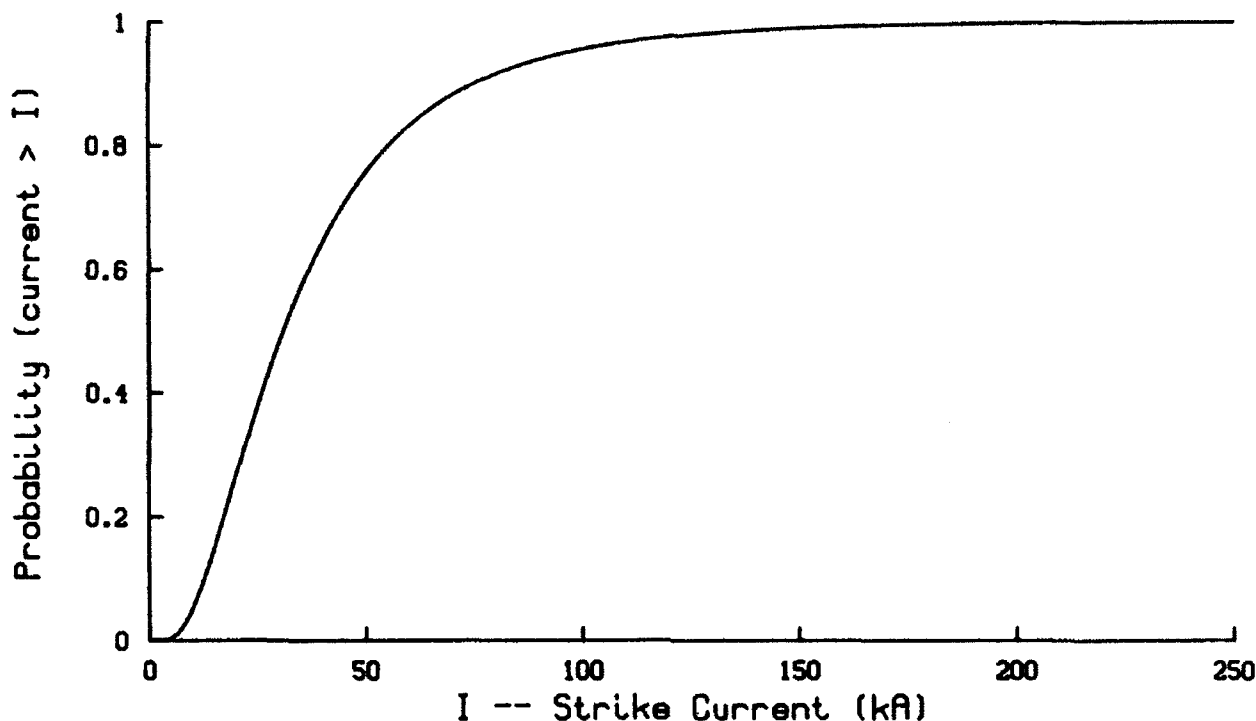


Figure 3: Distribution of Lightning Strike Peak Current Amplitude

4.4 Strike Amplitude Model

Given the occurrence of a lightning bolt attached to a fuel tank with a flammable ullage, the amplitude of the strike must be determined for damage calculations. Data collected in several independent tests has resulted in a distribution of expected values for peak current amplitude of cloud-to-ground lightning strikes as shown in Figure 3. According to Reference [1], the lightning strike to aircraft incidents that happen at or below 15,000 feet altitude are likely to be of the cloud-to-ground type. These cloud-to-ground lightning bolts are caused by an excessive accumulation of negatively charged electron particles being suddenly transferred to the earth's surface. Also presented in Reference [1] is an altitude distribution of reported strike incidents that indicates most strike events occur while aircraft are flying below 15,000 feet. The data in Figure 3 is represented as a cumulative density function that is lognormally distributed with a mean of 31kA (kilo-Amperes) and a lognormal deviation of 0.30.

To mathematically determine the peak current amplitude of a lightning strike, a number (between 0 and 1) is drawn randomly from a uniform distribution. This number is then applied to the lognormal distribution to obtain the current level of the strike. Experience has shown that a strike must have a certain minimum current level in order to be observed and submitted for data collection. For commercial aircraft this level is approximately 5kA to 10kA, depending on the aircraft structure and the established reporting criteria. Therefore, if the peak current amplitude for the strike incident is determined to be less than 10kA, the amplitude model will draw new random numbers and determine corresponding current levels until the result is greater than 10kA.

4.5 Ignition Model

The ignition model determines if the ullage vapors inside the fuel tank have ignited using the strike current amplitude and the fuel tank structural protection level. Initially, twelve different ignition functions were developed – three external protection configurations over four different internal fuel tank structure types. The three configurations of external protection are: 1) Secondary – consisting of secondarily-bonded fastener patches, 2) Cocured – consisting of cocured fastener patches, or 3) Inherent – defined as inherent fuel tank structural protection. The ignition function is selected for each strike event based on an output flag from the attachment model (fuel tank strike indicator) and the external protection configuration (input by the user).

The probabilities of ignition for a 200kA strike were determined from a limited amount of Light/No Light panel test data, extrapolations of that data, and engineering estimates. Visible light within the test structure (as detected by cameras) was used as the pass/fail criteria in the development of these ignition probabilities. Ignition functions were then developed by scaling the probabilities to other strike current levels using the action integral (defined as the integral of the strike current versus time function). Once the ignition probability for the given strike event has been determined, a uniform random number (between 0 and 1) is drawn. If the random draw is greater than the scaled ignition probability, the ullage gases have *not* ignited and negligible damage has been sustained by the aircraft. A random draw less than or equal to the scaled ignition probability indicates that the fuel tank has ignited.

More recent tests conducted at Lightning Technologies, Incorporated in Pittsfield, Massachusetts have refined the ignition probability estimates. The three configurations tested were: a thin composite section, a thick composite section, and a composite section with a metal substructure. No external protection was included on these test samples so this data represents the Inherent configuration only. Test data was reduced into ignition probability as a function of strike amplitude for each skin section as shown in figure 4.

5 Results & Sensitivities

The final product of the risk analysis is the determination of the probability of one or more fuel tank ignitions, p . A hypothetical distribution of risk is shown in Figure 5 as an example of program output. The important features of this distribution are a 50% chance of no ignitions during the fleet's lifetime and, therefore, a risk of $p = 0.5$. Also note that this distribution indicates a 4% chance of 3 ignitions and a 1% chance of 4 ignitions.

Risk is assessed using an agreed upon set of inputs considered to be a standard case. Input conditions are then varied to establish relative sensitivities among key parameters. A sample input set may consist of the following inputs:

- 100 aircraft in the fleet
- 10000 flight hour aircraft lifetime
- 3000 flight hour strike frequency
- JP-8 fuel
- No external lightning protection
- All strikes below 20000 feet altitude

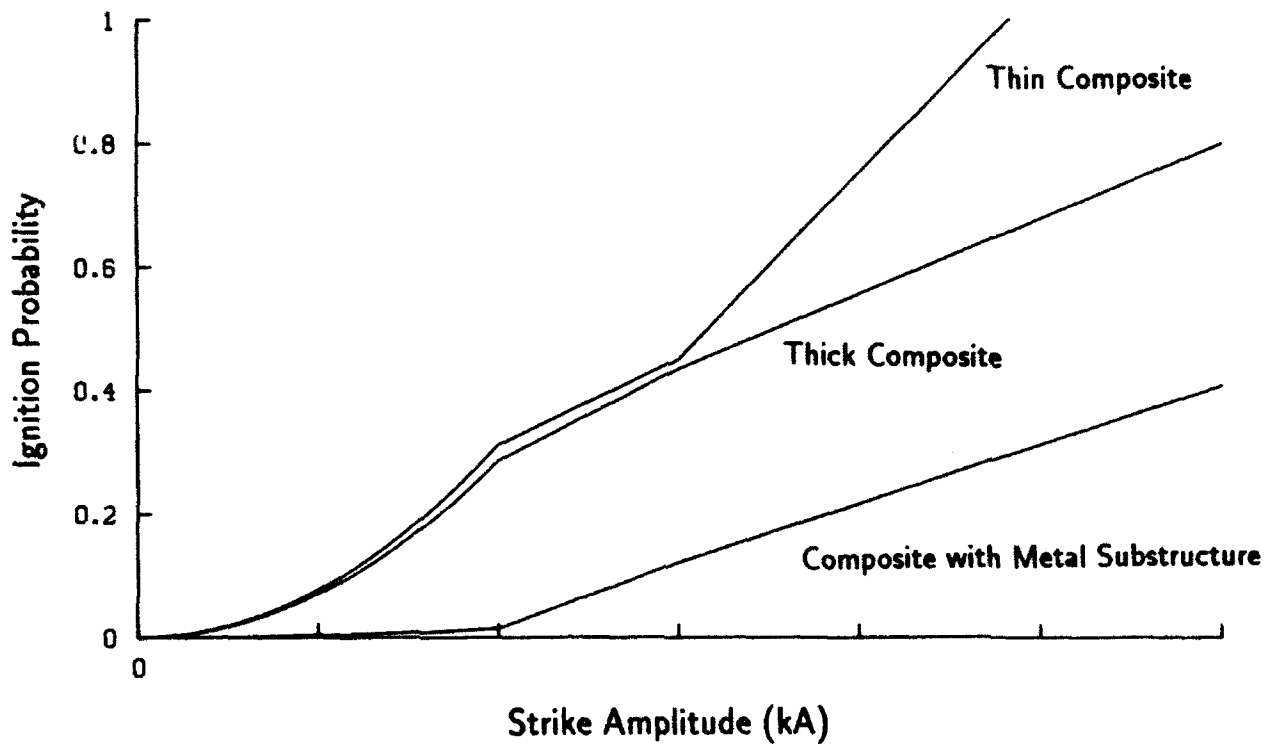


Figure 4: Ignition Probability Data for Inherent Protection

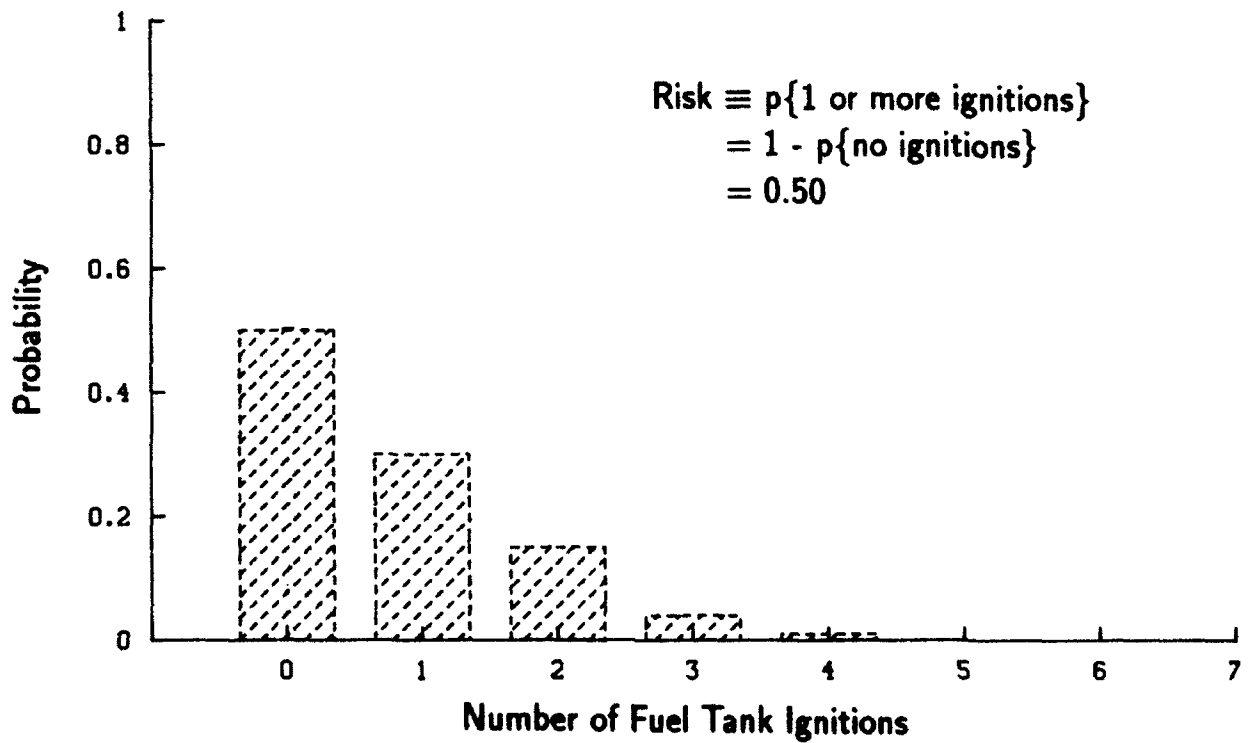


Figure 5: Sample Output - Number of Ignitions Distribution

- Standard day ambient temperature profile

In order to understand the risk well enough to design appropriate protection, sensitivities to the input parameters should be examined.

Strike Rate & Minimum Current The first comparison of interest is to alter the strike frequency value from the commercially-derived value of 1 strike per 3000 flight hours to something more representative of Air Force operations. The new value, 1 strike per 11000 flight hours, is considered a realistic value and, generally, produces a reduction in risk. This is not be surprising, considering that this parameter (along with strike amplitude) essentially defines the lightning threat; a lower rate implies a lower threat.

Another important input parameter, related to strike frequency, is the minimum strike amplitude. The impact of varying this parameter at the 11000 hour strike rate was explored by progressively increasing the minimum strike current from $5kA$ to $50kA$ and examing the impact to the risk. The effect of increasing the minimum current is to truncate the lognormal distribution of peak current described in Section 4.4. Since the number of strikes remains constant, the fraction of high amplitude strikes must therefore increase, thus increasing the likelihood of an explosion.

Configuration Effects One of the objectives of the risk assessment is to determine the relative merits of the three lightning protection configurations. The sensitivity study of this parameter shows how the risk analysis can be applied to design decisions. In addition to the standard case defined above, the other two configurations consist of a cocured patch and a secondarily bonded patch. The results are again intuitive since the risk decreases when the ignition functions (described in Section 4.5) are changed to reflect less structural protection.

Fuel Flammability There are several contributors to the fuel flammability within the tanks. The dominant effect is the ambient temperature; higher external temperatures drive the interior tank temperatures further into the flammability region (of JP-8). This effect can be examined directly by changing the thermal data to relect hot day ambient conditions.

Another factor that indirectly changes the flammability of the fuel is the dynamic mixing inside the tank (discussed in Section 4.3). Turbulent flight causes an effective lowering of the lean flammability temperature, which increases the opportunity for ignition. This effect is reflected in a reduction in risk when the inputs are changed to no turbulence (no alteration of the static flammability limits) for all strike attachments and an increase in risk when the aircraft is subject to "moderate" (see Section 4.3.3) turbulence during all strike events.

The effects of minor changes in the computation of fuel flammability are significant risk variations. Unfortunately, the issue of fuel flammability within an airborne vehicle has not been conclusively resolved; differences in fuel batch characteristics, aging effects, dynamic conditions, and internal tank construction can accumulate a great deal of uncertainty in any estimate of fuel flammability.

6 Conclusions

A modelling approach of this nature can be used to conservatively estimate the risk to a fleet of aircraft. In order to assure that the results are indeed conservative, each individual event associated with a fuel vapor ignition must be modelled with conservatism. Due to the complex interaction of events required to produce an ignition, the factors which have the most profound impact on the risk calculation will not be initially apparent. Once a standard set of inputs has been defined, parametrics may be performed to determine which events contribute the most to the risk estimate. Decisions on which events should be modelled with more fidelity or which tests should be performed can be made based upon these sensitivity studies.

The general procedure presented here can be applied to other aircraft systems or even other failure modes besides fuel vapor ignition. The fuel flammability data may be used in conjunction with other types of aircraft with little or no modifications. Strike rate distribution modelling and strike amplitude calculations apply directly to other problems. Only replacement the attachment point model and the damage functions will be necessary to define the lightning risk to other systems and components.

References

- [1] Franklin A. Fisher and J. Anderson Plumer, Lightning Protection of Aircraft, NASA Reference Publication 1008, October, 1977.
- [2] C. C. R. Jones, A. W. Hanson, G. A. M. Odam, "Zoning of aircraft for lightning attachment and current transfer", 1986.
- [3] Bruce D. Fisher, J. Anderson Plumer, "Lightning attachment patterns and flight conditions experienced by the NASA F-106B airplane from 1980 to 1983".
- [4] Bruce D. Fisher and J. Anderson Plumer, "Managing risks from lightning strikes to aircraft".
- [5] G. L. Weinstock, "A realistic approach to aircraft lightning protection".
- [6] John C. Corbin, "The risk factor in aircraft lightning protection"
- [7] Stan Schneider, briefing charts "A-6 Lightning Protection Approach - Wing Skin", 10 January 1989.
- [8] Colonel Tiegen, private communication.
- [9] "Military Standard: Climatic Extremes for Military Equipment." Department of Defense, MIL-STD-210B. 15 December 1973.
- [10] L. J. Nestor. "Investigation of Turbine Fuel Flammability Within Aircraft Fuel Tanks: Final Report." Naval Air Propulsion Test Center Report No. DS-67-7. Philadelphia, Pa., July 1967.
- [11] Coordinating Research Council, Inc. *Handbook of Aviation Fuel Properties*. Society of Automotive Engineers, Inc., Warrendale, Pa., May 1984.
- [12] Yukihiro Goto, Yoshihiro Murooka, "Statistics of lightning interaction with aircraft in Japan".
- [13] "Results of 851 Lightning Strikes to Commercial Transport Aircraft (from 1971 - 1984)", Lightning Technologies, Inc., Pittsfield, MS.

PARAMETERS INFLUENCING THE HOT-SPOT IGNITION OF AVIATION FUEL/AIR AND ETHYLENE/AIR MIXTURES

S J Haigh, C J Hardwick
Lightning Test and Technology, AEA Industrial Technology, Culham Laboratory,
Abingdon, Oxfordshire, OX14 3DB, England
Telephone: +44-235-46-3436 Facsimile: +44-235-46-4325

ABSTRACT

Lightning attachments to aircraft skins can lead to the creation of local areas of heating or 'hot-spots', which may be able to ignite fuel/air vapour mixtures contained within the skin.

The characteristic temperature/time histories of such hot-spots are very different depending on whether the skins are metallic or carbon fibre.

This report describes experimental work carried out under the Lightning Club programme to determine the ability of transient hot-spots in metal foil to ignite JP4/air mixtures. The influence of parameters such as hot-spot size and duration is considered, as well as fuel concentration and oxygen enrichment.

To establish the validity of simulation testing techniques in which ethylene is used to detect hot-spots, some experiments are also carried out using mixtures of this gas with air.

We make comparison of these with results with other reported work in this field.

1 GENERATION OF TRANSIENT HOT-SPOTS

For most of this test series the hot-spots were created by passing current through a thin stainless-steel sheet. The sheet was approximately 0.04mm thick and in the form of a single or double-parallel strip, each strip being 29mm x 21mm (Figure 1).

Current was applied in the form of a constant current of approximately 90 amps, but switched at ~35Hz so that the variable mark/space ratio controlled the power input.

The natural behaviour of the foil after current switch-on was for the temperature to rise rapidly initially and then to settle to its final value after 1 to 1.5 seconds.

Temperatures in the range of 700-900°C were the critical values for these measurements. Rise times were controlled so that temperatures for ignition were achieved between 0.25 seconds and 7 seconds, the faster rise-times tended to be linear to peak, and the slower values arising from an increase to a 'plateau value' which would then be held for several seconds (Figure 3).

2 TEMPERATURE MEASUREMENT

Temperature was measured primarily by the use of a thermocouple spot-welded to the stainless steel strip, but backed up by measurements of the infra-red/light-emission from the foil surface.

2.1 Thermocouple - To reduce the heat loss through the thermocouple wires, and to establish equilibrium quickly, care had to be taken in fixing the thermocouples. Each fine wire of the thermocouple was separately spot welded to the stainless steel strip, the copper wire (0.1mm dia) and the nickel wire (0.05mm dia) junctions being 0.5-1mm apart. The thermocouple wires were flattened down as closely as possible to the heating foil for several millimetres to minimise heat loss from the junction. New thermocouples had to be fixed fairly regularly, and occasionally new foils as well. Once the technique of fixing was established, reproducibility was better than $\pm 20^\circ\text{C}$. The results from one thermocouple, or from the light emission measurements, were consistent to better than $\pm 10^\circ\text{C}$.

Temperature measurement is only made during the 'space' parts of the switched drive current, since when current flows an offset voltage is injected into the thermocouple signal.

2.2 Thermocouple Calibration – The copper/nickel type thermocouple was cross-calibrated against a commercial chromel/alumel system - in this case with both thermocouples spot welded to a sheet of 0.2mm thick tinplate as above.

The outputs of both thermocouples fixed in this way were also cross referenced against the melting point of tin, and against some temperature sensitive coatings.

Some calibrations were carried out on the thin hot-spot foil itself as set up for a test, to check whether the foil in the proximity of the thermocouple junction could be slightly cooler than the surrounding foil, due to wire heat losses. (This heat loss would have led to a too low temperature measurement, a systematic measurement error which would not have shown up on the calibrations above). NaCl solution was painted thinly over the foil and allowed to evaporate leaving a thin white film. Temperature of the foil was increased, until the well defined melt at 801°C of the fine white film was observed. This gave good agreement with the other calibration results, and suggested that the systematic error was less than 10°C.

2.3 Temperature Response and Optical Measurements – With such a thermocouple system there will be an inertia to transient temperature changes, which limits the time response of the measurements.

For this reason the thermocouple measurements were supported by a photomultiplier/fibre optic system, measuring the emitted infra-red/visible radiation from the strip. The approach used was to cross correlate the thermocouple signal and the photomultiplier (PM) signal for a long duration hot-spot, and then for fast transient hot-spots to relate the measured PM signal back to an equivalent thermocouple signal.

The PM to thermocouple cross check was repeated to check for emissivity changes, although once the strip had been cycled to high temperature several times it appeared to change little.

3 GENERATION OF FUEL/AIR MIXTURES

3.1 Method – The many constituent components of aviation fuels exhibit various degrees of volatility and flammability and the collective product is then not as reproducible as a pure gas.

For these tests, in order to simulate flammable vapour generation in aircraft fuel tanks, a given volume of liquid fuel was allowed to come into equilibrium with a fixed volume of air in the test cell. Only a small proportion of the JP4 fuel evaporated and the remaining less volatile liquid was discarded after each test.

Care was taken to ensure that the large volume of JP4 fuel from which the test samples were drawn could not lose any of its volatile components by evaporation.

Figure 2 shows the apparatus built to create the equilibrium fuel/air mixture. An air circulator blows air over the surface of the fuel and recirculates it through the test cell, keeping the largely unevaporated liquid isolated from the test cell, and from the risk of ignition.

The system has the advantage that equilibrium is achieved quickly; a gas analysis system within the cell showed that the system reached 90% of its equilibrium richness within 60 seconds for a relatively weak equilibrium mixture. For these tests a standard equilibrating time of 10 minutes was used.

An earlier work (Reference 1) described how mixtures generated in this way were initially tested by ignition with voltage sparks of variable energy, to establish the most flammable mixtures and to verify that required ignition energies were in the accepted range.

4 EXPERIMENTAL TECHNIQUE

Once the vapour under test had been established in the test cell the pulsed current was switched on, either until ignition occurred or for a maximum of 7 seconds. Recordings were made of the photomultiplier signal and of the thermocouple output. Typical traces were shown in Figure 3 for both rapid and slow ignition.

On the time-scale of these hot-spots the appearance of ignition was normally virtually instantaneous, in that there was no gradual build up of light as the flame developed; its development to photomultiplier/scope saturation occurred within a few recording digitisations.

Exceptions to this were mixtures near to the flammable limits, particularly at the weak end where 'ignition' consisted of a very slow moving blue glow. With the fast rise-time hot-spots in particular greater care was taken in defining ignition point, since if there was a delay in detecting the ignition the temperature would continue to rise above the actual ignition temperature before ignition was detected.

Measurement of ignition temperature was therefore further supported by repeating the tests at successively lower temperatures until ignition did not quite occur.

These tests supported the supposition that detection of ignition was very fast, indicating that for mixtures well away from flammable limits the detection time was <15ms.

On completion of the test the fuel was drained, then the cell was partly dismantled, and the air circulator operated to flush out the vapour and ignition products.

The results of the tests are given in the sections below, each section describing the influence of a single parameter on ignition.

Most tests were carried out with the hot surface at the top of the test cell, since this tended to require lower temperatures for ignition (typically by 40°C). This does not necessarily have implications for upper and lower skins on aircraft however since the foil was held fixed 1cm away from the wall and ignition could have been generated on either side of it.

5 RESULTS

5.1 Introduction – Results are summarised graphically in Figure 4, in which the recorded temperature at ignition is plotted against mixture concentration for both ethylene and JP4/air mixtures.

The means of defining mixture concentration is necessarily different for these fuels, so that in this graph the X-axes have been contrived so that the weak limit for both occurs at approximately the same position.

Some measurements have been omitted from the figure for clarity (eg, effects of ambient temperature, humidity) since the trends are so weak that they do not show up on this graph.

5.2 Mixture Concentration and Oxygen Enrichment – Figure 4 shows that there was a remarkably constant ignition temperature over the wide range of mixture concentrations studied. At the very lean mixture end of the curve the required temperature rose slightly, but was only slightly higher for a mixture that could barely sustain an ignition than it was for a mixture which burned violently. It was not possible to investigate the upper (rich) limit for JP4/air mixtures, because of the limits to the quantity of fuel which could be contained in the mixture cell.

The injection of an additional 10% of oxygen, a quantity which would markedly reduce voltage spark ignition energies, had relatively little effect on the hot-spot temperature required for ignition.

5.3 Hot-Spot Duration – Long duration hot-spots were created by simply leaving the current on at a fixed setting, so that foil temperature rose to its equilibrium value in 1-1.5 seconds and then remained at this plateau value for several seconds more.

To create more transient hot-spots the current control is set so that the rate of rise of temperature is very high, so that the temperature for ignition is achieved in about 0.25 seconds. It is necessary however to immediately switch-off the current at the ignition point, otherwise the temperature continues to rise rapidly and the foil is destroyed. To do this the PM output signal is used to trigger a gate and deactivate the current pulse generation. The current is then immediately turned off when the temperature reaches a preset level or when ignition occurs.

The results of these measurements are plotted in Figure 5 as ignition temperature against 'hot-spot duration', where the duration is defined as being the time to ignition from current switch-on.

The difference in the temperature/time profile shape between the slow and fast hot-spot should be borne in mind for this data. For the fast hot-spots the temperature is near to ignition level for only a fraction of the 'hot-spot duration', whilst for the slow hot spots the temperature is high for most of the defined hot-spot duration (see Figure 3).

5.4 Hot-Spot Size – Hot-spot size was varied from 5.7 to 11.5cm² by having one or two foil strips, while very small hot-spots of 1.9cm² were generated by clamping brass strips as heat sinks over areas of a single strip. As expected the smaller the hot-spot the greater the temperature required for ignition, over the range of sizes below:

Hot Spot Area cm ²	Measured Temperature
1.9	870–890°C
5.7	780–800°C
11.5	710–730°C

Figure 6 includes results for these three sizes of hot-spots, which had similar time profiles (peak in 1-1.5s) and similar fuel concentrations near to the optimum.

Following these tests an attempt was made to extend hot-spot size to cover larger areas, such as might be achieved for a CFC hot-spot. A circular area of tinplate 85cm² was heated by a propane flame whilst the temperature at the centre of the opposite surface was measured by thermocouple, although temperature at the centre was higher than that at the edge. A large proportion of this area could be maintained at dull red heat without ignition occurring, and ignition only occurred when a more local area of ~20cm² was heated to a glowing orange, 750°C.

5.5 Ethylene/Air – Ignition of ethylene/air by hot-spots of 1.5 second rise-times occurred at consistently lower temperatures than did JP4/air, and as with the JP4/air, the ignition temperature was only slightly dependent on the mixture concentration (Figure 4).

This supports the use of ethylene/air as a diagnostic gas for ignition from lightning induced hot-spots in metallic skins, where hot-spot durations are short.

5.6 Humidity and Temperature – Other tests were carried out in which:

- (1) The ambient humidity was raised to saturation.
- (2) The ambient temperature was increased to 40°C, from the normal operating temperature of 17-23°C.

Neither of these parameter changes yielded any detectable change in ignition temperature, nor did any detectable changes occur by contaminating the foil with carbon dust, or metallic dust such as titanium.

6 TESTS TO PIPES

Results given so far on ignition of fuel vapour by hot-spots record temperatures far higher than those defined as auto-ignition temperatures.

In order to improve confidence in the measurements and methods, some tests were carried out to fuel enclosed totally within a heated pipe, as these should give measurements much closer to the auto-ignition temperatures, and far lower than the temperatures for flat single hot-spots.

The test rig was an insulated preheated copper pipe, 170mm by 40mm diameter with sealed ends and a small central hole into which fuel was injected by syringe/needle. Temperature was measured by Chromel/Alumel thermocouple fitted into a narrow hole drilled tangentially into the tube wall. During the test itself the temperature was decaying by approximately 2°C/s.

Results are summarised in the table below, for the optimum mixture.

Injected Fuel	Temperature	Ignition Delay
JP4	320°C	3 seconds
	310°C	3 seconds
	290-270°C	9 seconds
	260- °C	No ignition (too cool)
JP4 (volatile fraction only)	370°C	≤1 second
	340°C	≤1 second
	310°C	5 seconds
	300°C	7 seconds

Whereas earlier tests with small hot-spots effectively tested only the small proportion of the JP4 which is volatile enough to evaporate at room temperature, these tests use the evaporate of the whole of the fuel liquid. This could lead to lower ignition temperatures, since higher hydrocarbons are then involved and these are reported to be easier to ignite. Tests were therefore carried out injecting only the volatile components of JP4 into the heated pipe. These components had been previously produced by collecting the condensate which formed on a 0° surface directly above warmed JP4 liquid. Results in this test were similar, as shown in the table above.

7 DISCUSSION

These tests show that transient small hot-spots need to be at a much higher temperature than fully enclosing hot-vessels to cause ignition of JP4/air mixtures and that both decreasing size and decreasing duration of hot-spot independently lead to higher ignition temperatures. Oxygen enrichment and fuel concentration are both only weak factors in hot-spot ignition.

Similar trends have been observed by other workers in related fields. The results of such workers in relation to hot-spot size and hot-spot duration are discussed further below.

7.1 Hot-Spot Size – A great deal of data on the ignition of heavy hydrocarbon vapour by static hot-spots is quoted in Reference 3, and in this reference the ignition temperature varies as a logarithmic function of hot-spot area.

Cansdale (Reference 4) also studies aviation fuels including AVTAG (JP4) and AVTUR, and their ignition by hot pipes of constant temperature. The pipes run through the test cell containing the fuel vapour and it is the outside surfaces of the pipe which are the source of ignition. The pipes and hot spot areas in that study are relatively large and lead to lower ignition temperatures:

Pipes Dia × Length	Ignition Temperature
38mm × 0.45m	580°C
76mm × 0.45m	400°C
152mm × 0.45m	380°C

Cansdale, Reference 4.

So in both References 3 and 4 there is a clear trend of ignition temperature decreasing with hot-spot size, this trend is shown in Figure 6 along with the Culham data.

(Note that for Cansdale's data on pipes the hot-spot area used to plot Figure 7 is not that of total pipe external area, since that would be unrealistically large for such a long thin pipe. An arbitrary but 'reasonable' area of $d \times \pi d$ is chosen, where d is pipe diameter. An error bar on this of $\pm 50\%$ is included to indicate the arbitrariness of the value.)

Figure 6 shows that there is very good agreement between these data, which is perhaps surprising, given the fact that the data points at the lower end of the line are for rapid ignition, < 1 second, whilst at the top end ignition delays of tens of seconds are involved.

7.2 Hot-Spot Duration – Cutler (Refs 5 and 6) studied very fast heating of metallic strips of dimensions from :

5mm × 57mm to 13mm × 57mm

with rise-times of 0.1ms to 1ms, but with relatively slow decays of around 200°C per 100ms. This work yielded ignition temperatures of:

Ethylene (850°C)	Propane (1380°C)	Methane (1700°C)	for 5 × 57mm
	Propane (1270°C)		for 13 × 57mm.

Such ignition temperatures are much higher than those recorded by Culham for hot-spots of similar dimensions but of longer time duration. Both this data and the Culham data in Figure 5 shows a trend towards increasing temperatures for shorter durations.

7.3 Ignition Boundaries

Several data points from these results are plotted in the temperature/time curve (Figure 7).

It is proposed that the curves defining time/temperature ignition boundaries follow the form shown in Figure 8, for different sizes of hot-spot. However there are factors such as hot-spot shape and orientation which are not taken into account in such a series of curves, and such data should be used with a generous margin.

8 CONCLUSIONS

(1) Investigations show that for hot-spots in the range 2 to 12cm² in area and 0.25 to 7 seconds in duration, temperatures of around 750°C and above are required for ignition of aviation fuel vapour (JP4). The required temperature varies inversely with both hot-spot duration and hot-spot size.

(2) Very little change occurs in the required ignition temperature across the flammable range of the mixture, and oxygen enrichment has only a slight influence.

(3) Temperatures required to ignite the fuel in an enclosed heated copper pipe is far lower than those given in (1) above, and approach the auto ignition temperature.

(4) The results confirm the supposition that there is no ignition threat to JP4 from Aluminium hot-spots.

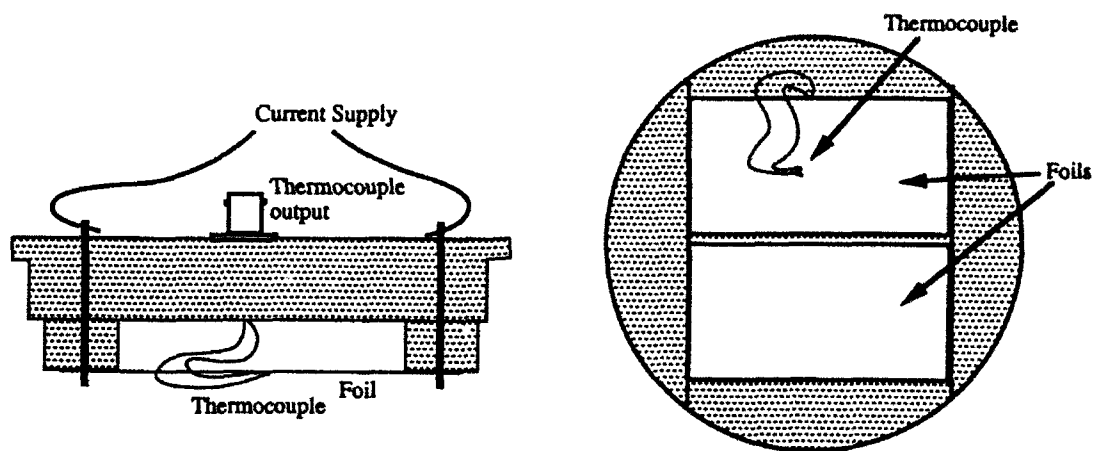
- (5) CFC hot-spots were not fully simulated - in that hot-spots of area 25-50cm² and duration 20 seconds were only investigated in one test using a metal plate. This test required ~750°C at the centre of the hot-spot to induce ignition. This test and extrapolation of the other results suggest that ignition will not occur at temperatures (<300°C) which the CFC could survive.
- (6) Hot-spots induced by lightning in metals of high melting point are known to be an ignition hazard. In such cases testing with ethylene/air gives a conservative test, since such a gas is more easily ignited by transient hot-spots than is aviation fuel.
- (7) It is proposed that temperature/time profiles for hot-spots of different sizes take the form of the curves in Figure 8.

9 REFERENCES

- 1 Haigh, Hardwick, Baldwin. "Measurements of Some Parameters of Thermal Sparks with Respect to their Ability to Ignite Aviation Fuel/Air Mixture". ICOLSE, Cocoa Beach 1991.
2. Crouch K. "Minimum Ignition Levels of Aircraft Fuel Constituents to Lightning Related to Ignition Sources". ICOLSE, Dayton 1986.
3. "Summary of Ignition Properties of Jet Fuels and other Aircraft Combustible Fluids". AFAPL-TR-75-70, US Bureau of Mines/Air Force Aero Propulsion Laboratory.
4. Cansdale J T and McDonald J A. "Spontaneous Ignition of Aircraft Fuel". RAE Technical Report 72059, 1972.
5. Cutler. "The Ignition of gases by Transiently Heated Surfaces". Combustion and Flame 22, 1974.
6. Cutler. "Further Studies of the Ignition of Gases by Transiently Heated Surfaces". Combustion and Flame 33, 1978.
7. "Propulsion and Energetics Panel Working Group 11 on Aircraft Fire Safety". AGARD Advisory Report No. 132.
8. Rae D, Singh B and Dawson R. "The Size and Temperature of a Hot Square in a Cold Flame Surface necessary for Ignition of Methane". Ministry of Power, Safety in Mines Research Establishment, Research Report No. 224.

10 ACKNOWLEDGEMENTS

This work forms a part of the Culham Lightning Club programme, and we are grateful for the continuing support of the Lightning Club members (British Aerospace, Civil Aviation Authority, CASA, Department of Trade and Industry, Rolls Royce, SAAB-Scania, Shorts Brothers).



Hot-Spot Device

FIGURE 1

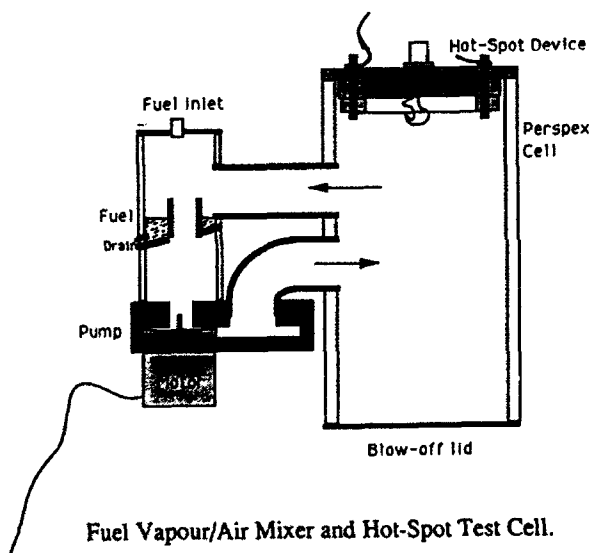


Figure 2

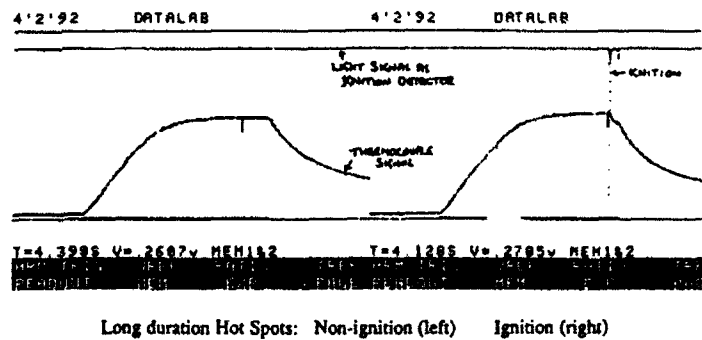
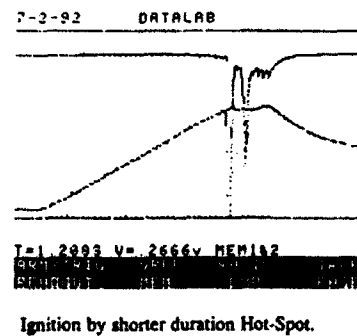


Figure 3



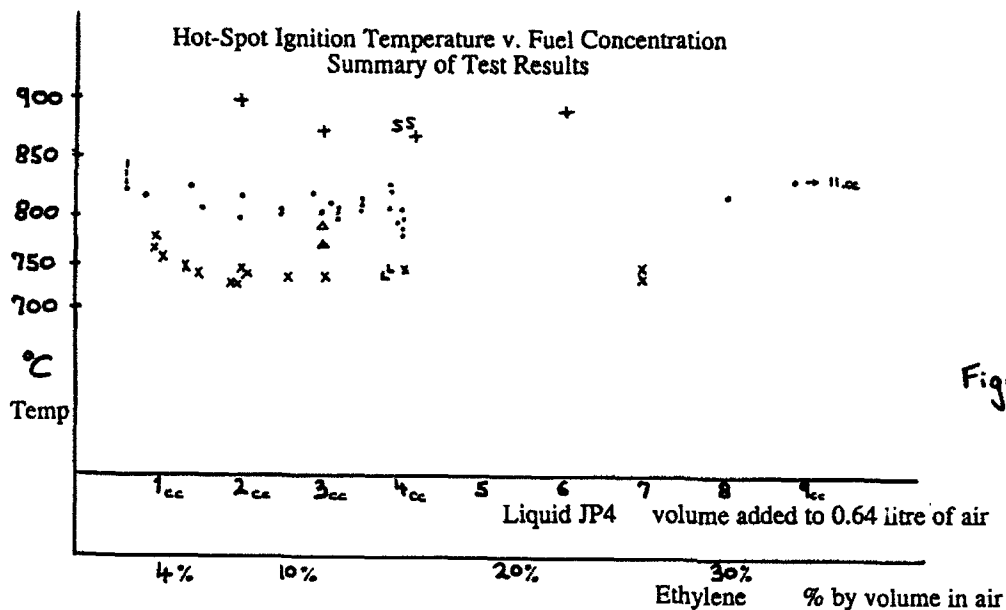


Figure 4

The default parameters in the graph above are for Hot Spots of 5.7cm² reaching peak temperature and ignition of JP4 vapour in 1.2-1.5 seconds. Changes to this parameter set are identified in the key below.

Key:

small, 1.9cm ² S	Ethylene/Air x	Q ₁ +5% Δ
5.7cm ² •		Q ₁ +10% ▲
large 11.5cm ² L		fast rise time (0.25s) +

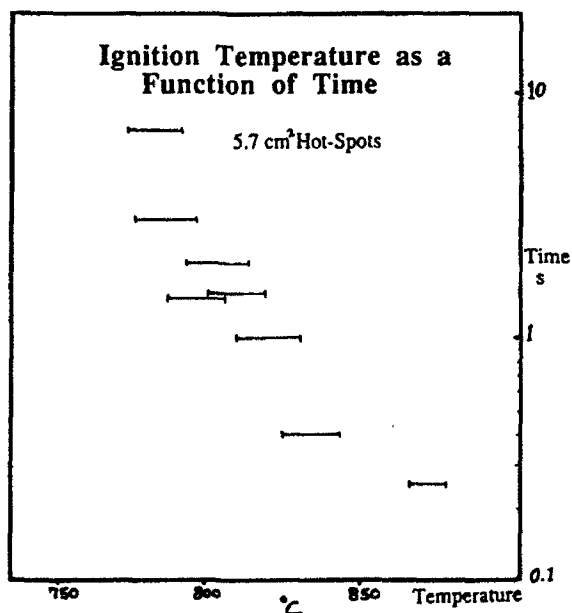


Figure 5

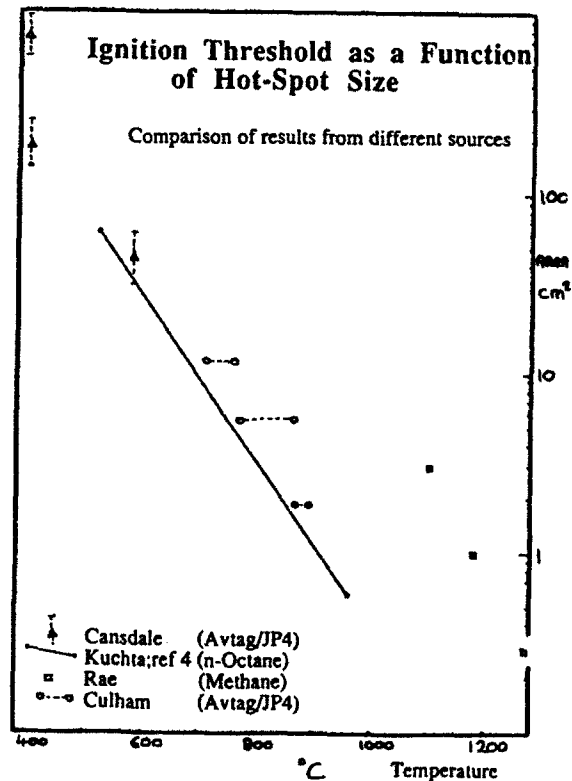


Figure 6

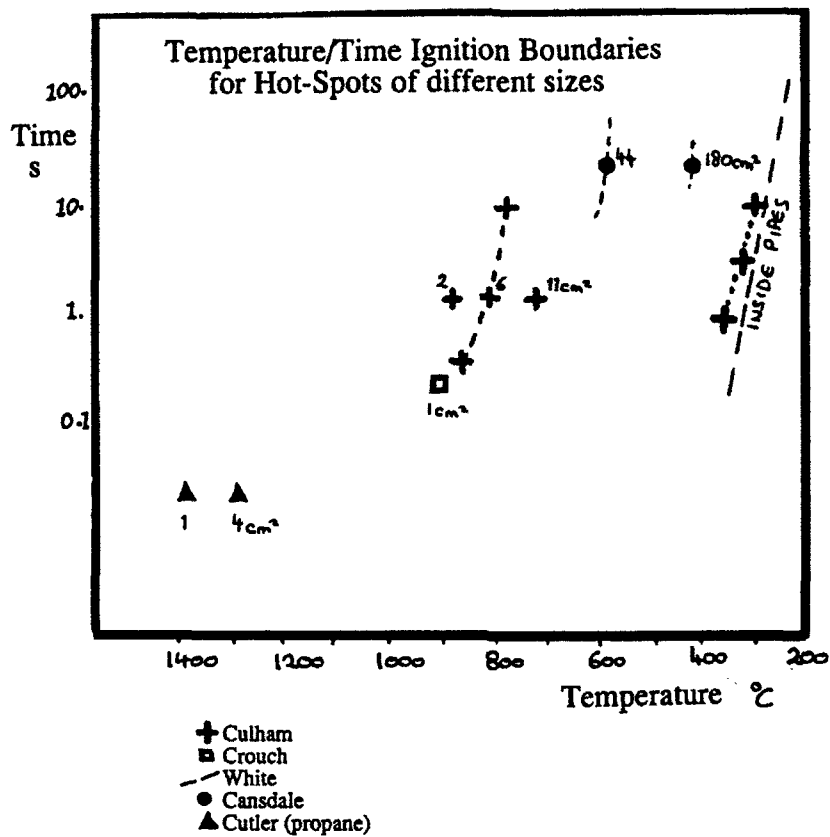


Figure 7

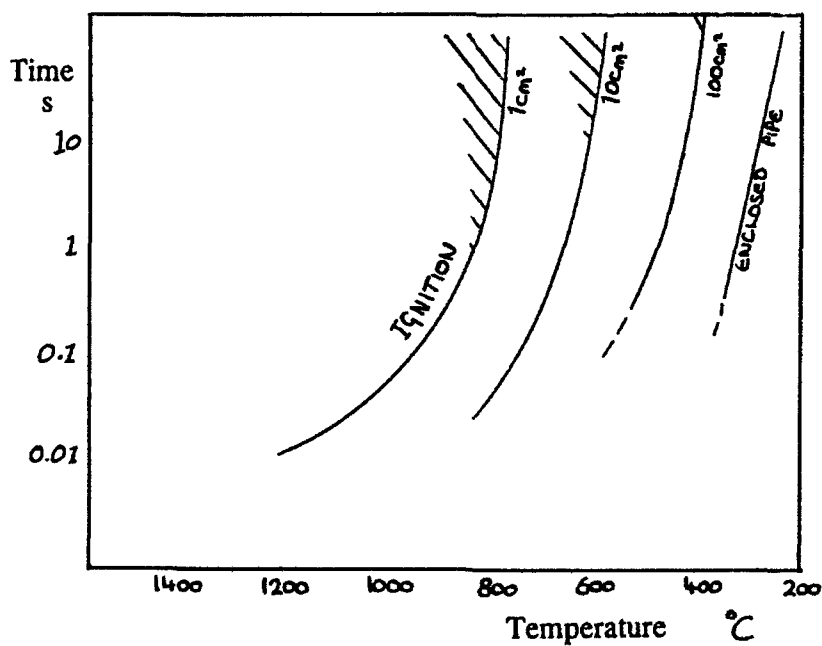


Figure 8

**Proposed Form of Ignition Boundaries
for Hot-Spots of Different Areas**

COMPARISON OF THE ELECTRICAL CHARGING AND DISCHARGING ENVIRONMENTS OF MULTIPLE AIRCRAFT-BORNE ELECTRIC-FIELD MEASUREMENT SYSTEMS

K. L. Giori and J. E. Nanevich
SRI International
Menlo Park, California, USA
Phone: (415) 859-3138, FAX: (415) 859-6259

ABSTRACT

Various aircraft and particle charging and discharging mechanisms can adversely affect the performance of aircraft-borne electric-field measurement systems. Samples of data collected both during coordinated flight maneuvers (T-28 and SPTVAR aircraft) and from similar flight environments (Learjets 24B and 36A) have been analyzed and compared. These comparisons help in the identification and interpretation of the possible effects of (a) charged particles, and (b) aircraft charging and discharging phenomena on the respective electric-field measuring systems. It was found that the SPTVAR generally became more highly charged than the T-28, and the Learjet 36A more than the 24B. Such comparisons offer a better understanding of the electrical characteristics and of the measurement accuracies of these systems.

INTRODUCTION

More than fifty years ago, researchers began studying the electrical charging of aircraft because of the noise problems it created for aircraft communications systems (a phenomenon known as precipitation static or p-static). The subsequent development of static dischargers helped alleviate these problems. At present, the charging characteristics of aircraft are an important issue for scientists who use these aircraft as platforms for conducting airborne measurements of the electric fields in or near clouds. Unfortunately, the use of dischargers is usually not sufficient to adequately control aircraft charging during penetrations of electrified clouds. Heavy aircraft charging makes it difficult to accurately measure a cloud's electric-fields (1) and, even if the net charge accumulating on the aircraft is kept small, large charging and discharging currents could still lead to a distorted local electric-field environment.

When an aircraft penetrates an electrified cloud, complex electrical charging of the aircraft and of impinging cloud particles occurs. The charging processes depend heavily on the type of aircraft, the type of cloud particles, and the strength and orientation of the cloud's electric-field. It has been shown that differences in engine types can greatly affect the rates of aircraft discharging (2). In this paper, variations in the charging characteristics and discharging rates between two propeller-driven aircraft and between two Learjets are discussed. Another cause of variations between aircraft is differences in aircraft skin materials. Although the skins of most aircraft in operation are made of conductive metal materials, many newly developed aircraft use mostly composite materials. Unless these composites are made to be electrically conductive, they too can limit the aircraft's ability to bleed off charge.

Particles that strike the airframe may cause triboelectric ("frictional") charging. Triboelectric charging is usually associated with direct impact of ice, graupel, snow, or other frozen particles. Even liquid water may cause charging of the aircraft when the particles are broken up with sufficient force by high-speed propeller or engine blades.

Finally, cloud electric-fields appear to affect both aircraft charging (through inductive charging processes between the airframe and cloud particles (3)) and aircraft discharging (through corona of a dominant polarity occurring at airframe extremities (4)). Rapid changes in the cloud electric-field can readily change the polarity of net aircraft charge as long as other charging mechanisms are less dominant.

COMPUTATION OF THE ELECTRIC-FIELD VECTOR

The electric-field is typically measured at multiple points on an aircraft using electric-field meters. All of the aircraft systems described in this paper flew rotating vane type meters known as field mills. The body of an aircraft enhances each component of the ambient field and any net charge on the aircraft creates a fourth additive field component. Each of the local enhancement factors must be known in order to derive the vector electric-field and aircraft charge (or potential) from the electric-field mill measurements.

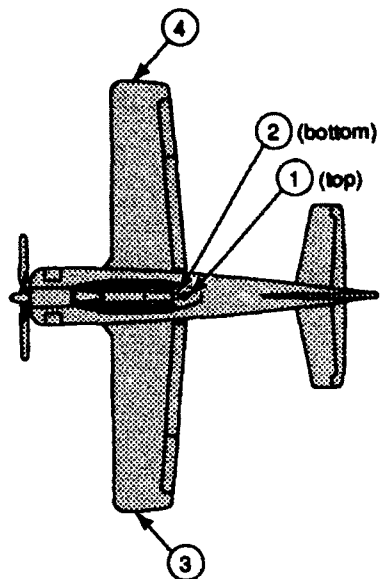
The electric-field vector \mathbf{E} (E_x , E_y , E_z , E_q or V) was computed by solving the equation $\mathbf{F} = \mathbf{A}\mathbf{E}$, where \mathbf{F} is an $n \times 1$ vector of the n field mill outputs, and \mathbf{A} is an $n \times 4$ matrix of aircraft enhancement factors (e.g., a_{1x} , a_{1y} , ..., a_{nz} , a_{nq}). The following lists the four \mathbf{A} matrices, one for each aircraft, that were experimentally determined and used to compute the data for this paper. The row numbers correspond to the field mill numbering systems shown in Figure 1. The columns correspond to x , y , z , and q (or V).

$$\begin{array}{l}
 \mathbf{A}_{T-28} = \begin{array}{cccc} 0 & 0 & 5.3 & 2 \\ 0 & 0 & -2.8 & 1 \\ 10 & 29 & -1 & 5.2 \\ 10 & -29 & -1 & 5.2 \end{array} \quad \mathbf{A}_{SPTVAR} = \begin{array}{cccc} -0.3 & 0 & 5.56 & 1 \\ -0.3 & 0 & -5.06 & 1 \\ -0.4 & 3.45 & 0 & 1 \\ -0.4 & -3.45 & 0 & 1 \\ -16.7 & 0 & 0 & 2.4 \end{array} \\
 \\
 \mathbf{A}_{24B} = \begin{array}{cccc} 1.6 & -0.9 & 1.6 & 0.17 \\ 1.1 & 0 & -1.6 & 0.18 \\ -0.8 & 0 & -1.6 & 0.21 \\ 1.6 & 0.9 & 1.6 & 0.17 \\ -0.08 & 0 & 1.6 & 0.28 \end{array} \quad \mathbf{A}_{36A} = \begin{array}{cccc} 2.2 & -0.08 & 1.9 & 0.3 \\ 2.1 & 0 & -1.9 & 0.29 \\ 2.2 & 1.3 & 0.9 & 0.28 \\ 2.2 & -1.3 & 0.9 & 0.28 \\ -0.02 & -0.13 & 1.5 & 0.17 \\ -1.4 & 0 & -1.8 & 0.26 \\ 1.0 & 0.9 & 0.9 & 0.17 \\ -0.3 & 1.1 & -1.3 & 0.34 \end{array}
 \end{array}$$

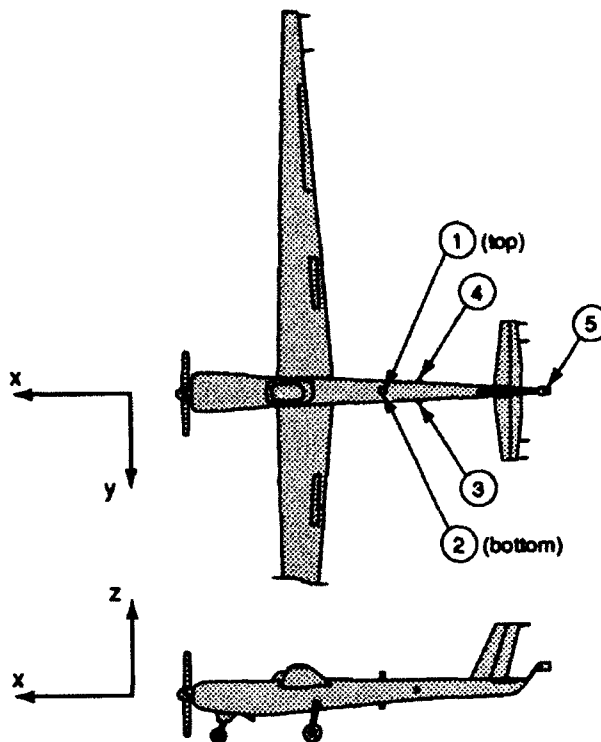
AIRBORNE FIELD MILL SYSTEMS

T-28 --The T-28 is a specially armored aircraft, operated by the South Dakota School of Mines and Technology, that can penetrate hailstorms while carrying a wealth of microphysical instruments. During the July 1990 flights it carried four field mills (top, bottom, and left and right wing). Figure 1(a) shows the field mill locations.

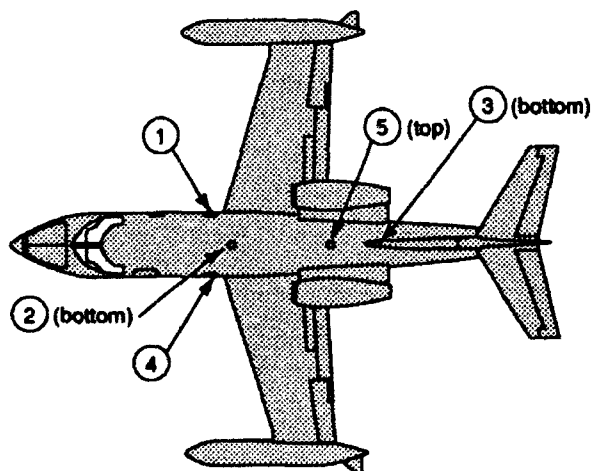
a. T-28



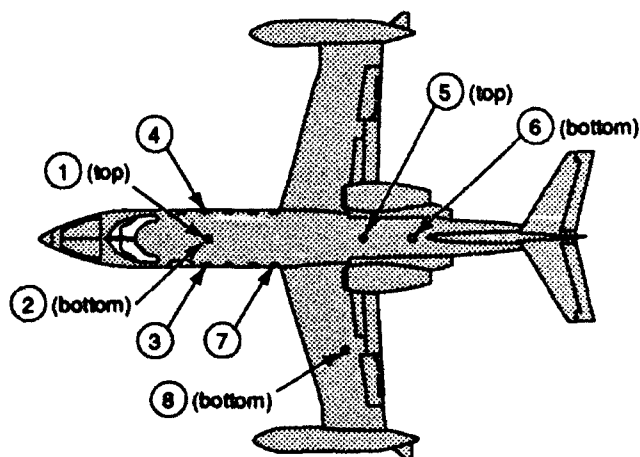
b. SPTVAR



c. Learjet 24B



d. Learjet 36A



p92-022/11

Figure 1 FIELD MILL LOCATIONS ON FOUR AIRCRAFT-BORNE ELECTRIC-FIELD MEASUREMENT SYSTEMS

The x-y-z coordinate system shown in b. is used by all aircraft.

SPTVAR --The Special Purpose Test Vehicle for Atmospheric Research (SPTVAR) is a Schweizer 845 airplane supported by the Office of Naval Research and operated for research purposes by the New Mexico Institute of Mining and Technology. During the July 1990 flights it was instrumented with five electric-field mills (top, bottom, port, starboard, and aft) as shown in Fig. 1(b).

LEARJET 24B --The NASA/Ames Learjet 24B was instrumented with five field mills by SRI and flown during 1987 and 1988. The field mill locations are shown in Fig. 1(c). The Learjet 24B is powered by two General Electric CJ 610-6 jet engines.

LEARJET 36A --Aeromet's High-Altitude Reconnaissance Platform (HARP), a Learjet 36A, was instrumented with eight electric-field mills by SRI (in addition to Aeromet's full complement of microphysical probes) and flown during the summer of 1989. Fig. 1(d) shows the field mill locations. The Learjet 36A is powered by two Garrett AiResearch TFE 731-2-2B turbofan engines.

COORDINATED FLIGHTS BETWEEN THE T-28 AND SPTVAR

SYNOPTIC SITUATION --The cloud studied on 25 July 1990 was an airmass thunderstorm located near Langmuir Laboratory in New Mexico.

FLIGHT REGIME --The T-28 and SPTVAR flew in formation (15 m diagonal separation) at an altitude of 3.4 km (which was below cloud base) and a speed of about 50 m/s. Both are propeller-driven aircraft. In order to fly together, the SPTVAR had to increase its usual flight speed, while the T-28 had to decrease its usual speed. Under cloud, the two aircraft occasionally passed through shafts of mostly rain and sometimes graupel.

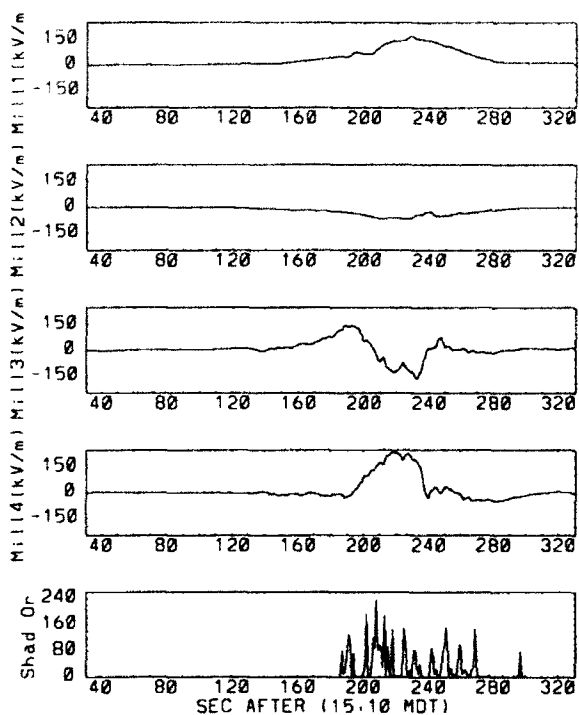
RESULTS--Six passes were made in formation between 15:12 and 15:42 MDT. The cloud was decaying in intensity during that half-hour interval. Data for the first two passes are shown in Figures 2 and 3. Parts (a) and (b) show individual field mill outputs for the T-28 and the SPTVAR, and parts (c) and (d) show corresponding computed electric-field components. Part (a) also includes "Shadow Or" particle counts (number of $> 25 \mu\text{m}$ particles per second) from the T-28's 2D-C probe.

The computed electric-field components for the aircraft are similar. E_z was the dominant intensity component (since the aircraft were flying below cloud base). For all six passes, E_z was positive, indicating negative charge above. E_x was much less intense, but generally followed a bipolar signature of + to - which agrees with the observation of negative charge above. E_y was generally the least intense component and varied in polarity.

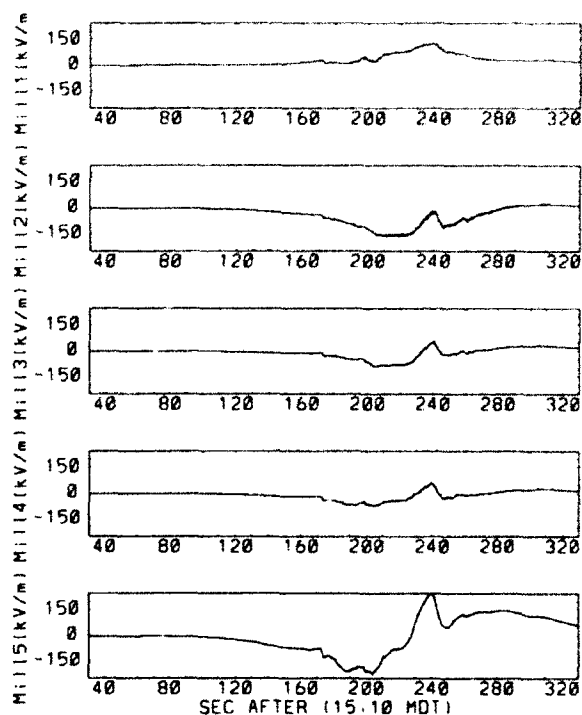
The charge on the aircraft (E_q) roughly correlated in intensity with the strength of the cloud's electric-field (E_m). The SPTVAR charge was generally 5-10 times greater than that of the T-28. In Figure 2, the large positive deviation in the field due to aircraft charge on the SPTVAR corresponds to a small negative deviation on the T-28.

DISCUSSION--The dominant E_z field was determined on each aircraft principally by top and bottom fuselage mill outputs. There is good correlation between the two measurements. The E_y components are also similar since the symmetry yields an accurate field measurement and any charged-particle effects should cancel. Additional coordinated flights in a stronger E_x field are needed before a complete system comparison can be performed, but the general polarity of the small E_x fields in Figures 2 and 3 is similar.

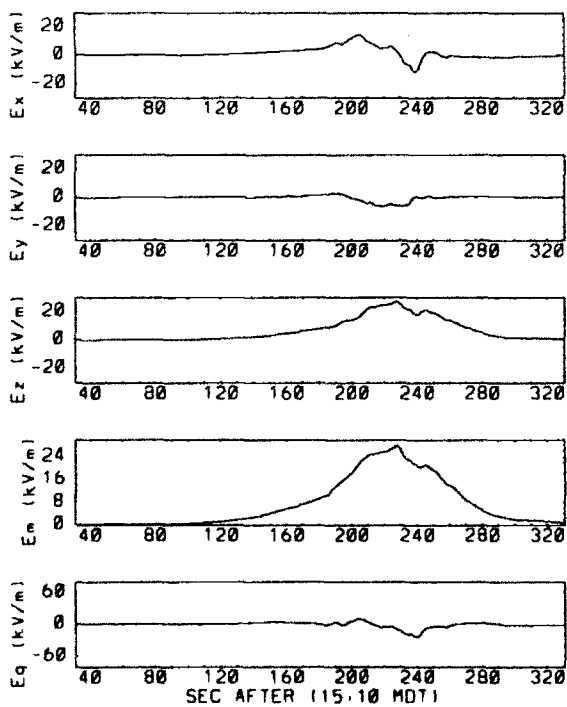
a. Individual mill outputs for the T-28



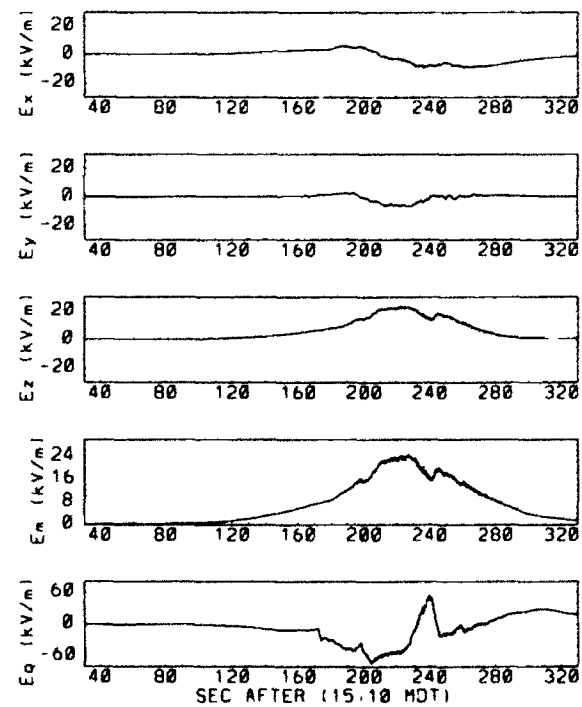
b. Individual mill outputs for the SPTVAR



c. Computed electric field for the T-28



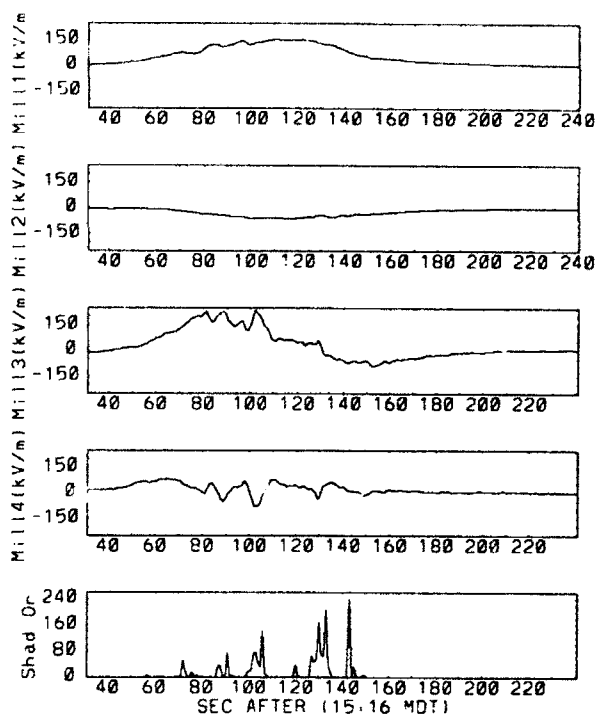
d. Computed electric field for the SPTVAR



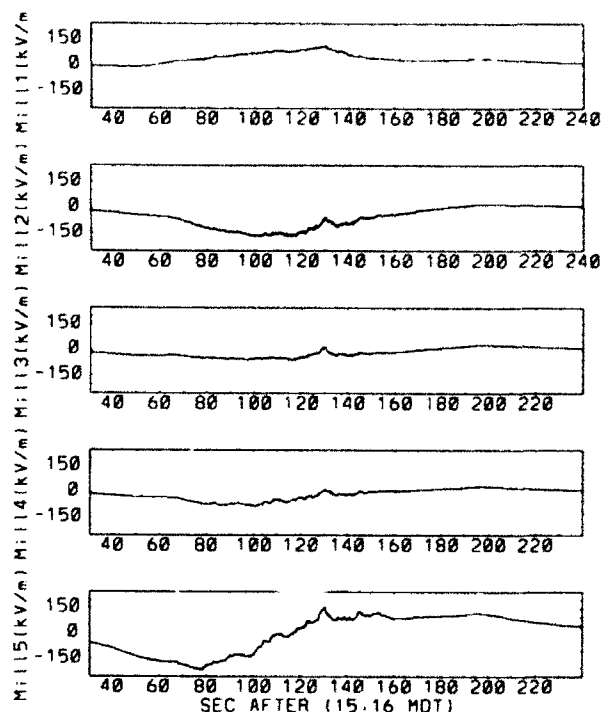
p92-022/12

Figure 2 PASS 1 OF COORDINATED FLIGHTS BETWEEN THE T-28 AND SPTVAR

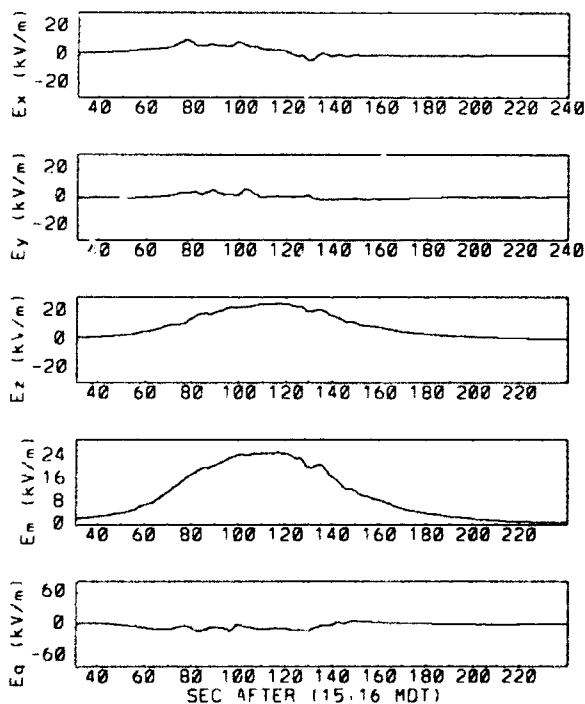
a. Individual mill outputs for the T-28



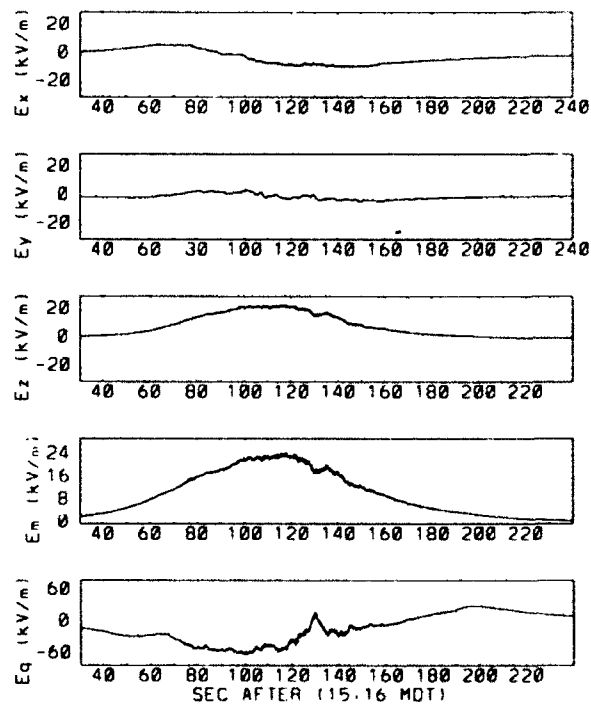
b. Individual mill outputs for the SPTVAR



c. Computed electric field for the T-28



d. Computed electric field for the SPTVAR



p92-022/13

Figure 3 PASS 2 OF COORDINATED FLIGHTS BETWEEN THE T-28 AND SPTVAR

A more prominent difference between the two systems is that the SPTVAR consistently shows greater charging levels than does the T-28, probably due to a lower rate of discharge by its engines. (The SPTVAR's lower discharge rate was determined by comparing the decay constants of E_Q for each aircraft after onboard artificial charging sources were turned off.) For the fairly mild charging environment existing under cloud, aircraft charging did not seem to significantly affect the accuracy of the computed cloud electric-fields. However, the small differences in the computed fields of Figure 2 (corresponding to the most dynamic changes in net aircraft charge) hint that if charging were much more significant, differences in the computed field response of the two aircraft systems might also become significant.

The degree to which computed field accuracy is affected by cloud penetrations is much more difficult to estimate if only the response one aircraft-borne system is known. Coordinated flights with two or more systems can reveal more about the effects of triboelectric charging, which is generally the most intense aircraft charging mechanism during penetration of clouds with high concentrations of ice-phase particles. Based upon the coordinated flight data presented here, it would be better to incrementally add more complexity to the aircraft charging environment during successive coordinated flights while trying to systematically understand the charging processes and their effects on these systems. Such an approach is preferable to diving into the worst-case charging environments and trying to sort things out.

SIMILAR FLIGHT ENVIRONMENTS OF THE LEARJET 24B AND LEARJET 36A

FLIGHT REGIMES --Data collected during three types of flight regimes will be described to highlight the differing responses of the two Learjet systems: (a) take-off, (b) artificial charging, and (c) penetration of small liquid-water-phase (un electrified) clouds.

RESULTS --Computed aircraft potential data are shown in Figure 4 for the takeoff and artificial charging flight regimes. The Learjet 36A charged to a higher degree than did the 24B (factor of about 3) during takeoff and discharged at a slower rate (15 seconds compared to 1 second) during decay of artificially applied aircraft charge. Also, the steady-state potential of the 36A was typically +4 kV (except at takeoff), as opposed to essentially zero for the Learjet 24B.

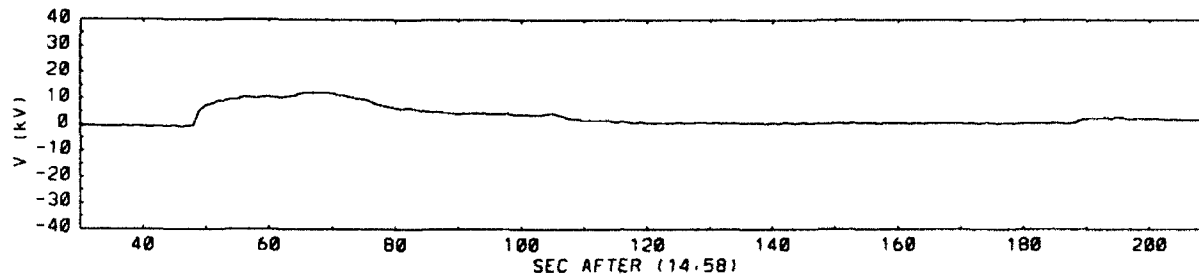
Individual field mill outputs and computed fields and aircraft potential are shown in Figure 5. During cloud penetration (the noise-like sections of each trace), the Learjet 36A fields were about 5-10 times greater than those of the Learjet 24B, while the 36A aircraft potential was about 2-4 times greater. Both Learjets charged negatively, while showing positive E_x , negative E_z , and an E_y of nearly zero.

DISCUSSION -- Other than the slightly larger size of the Learjet 36A, the main contributor to differences in aircraft charging for the 36A and 24B is likely to be the differences in their engine types. The 36A has turbofan engines, as opposed to the straight-jet design of the 24B. The fan contributes about 50% of the 36A's total rated thrust and the airflow through the fan duct completely bypasses the engine combustion chamber.

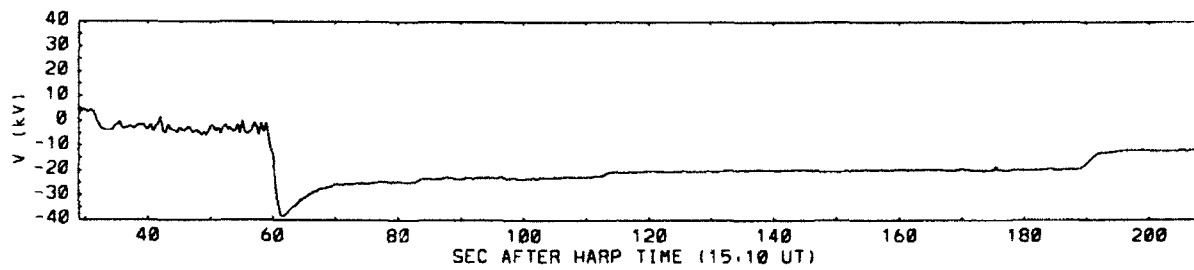
It is possible that the lack of heating or combustion chamber ionization of the fan duct air decreases the engine's effective discharge-current carrying capacity. Another possible scenario is that the high-speed fans rotate with enough speed to break up liquid water cloud or ice particles causing "Lenard-type" charge separation

TAKEOFF DATA

Learjet 24B

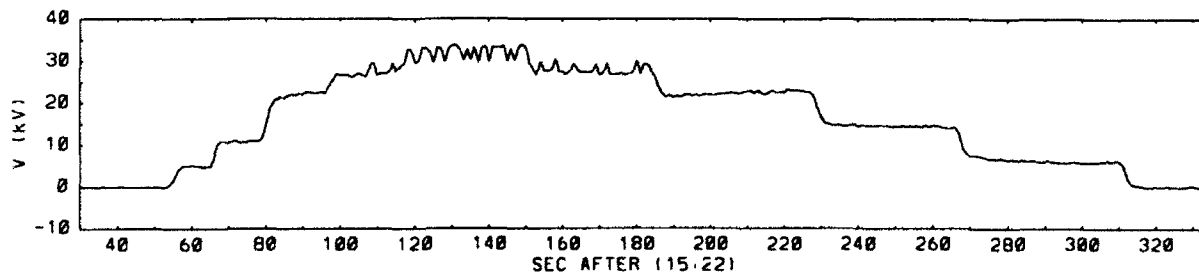


Learjet 36A

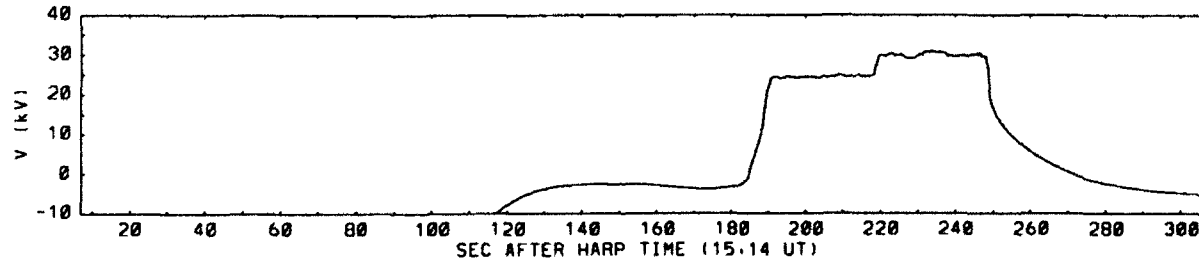


ARTIFICIAL CHARGING DATA

Learjet 24B



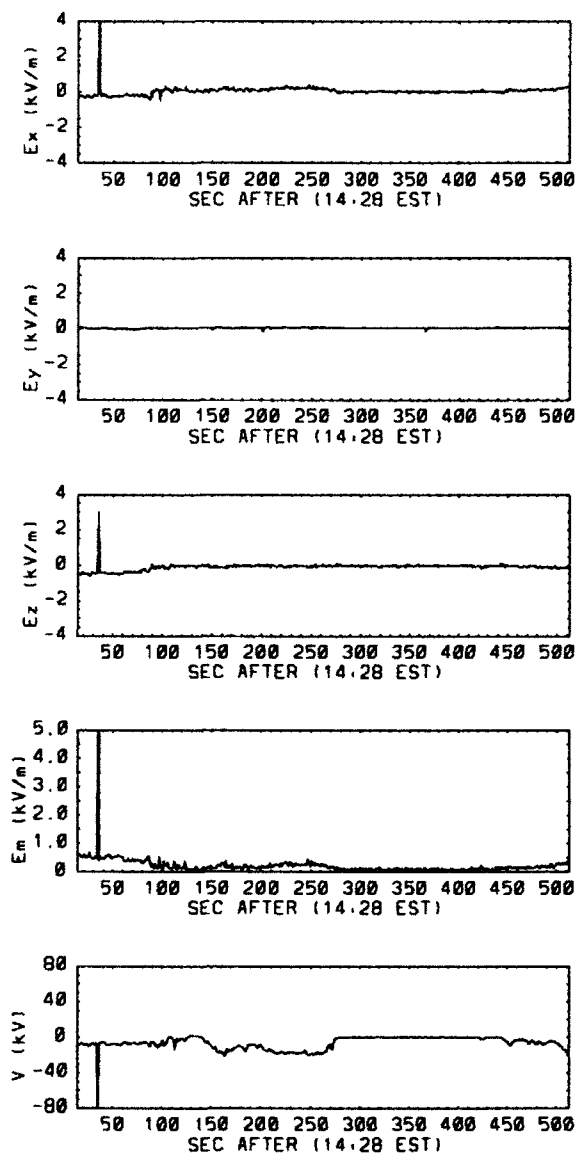
Learjet 36A



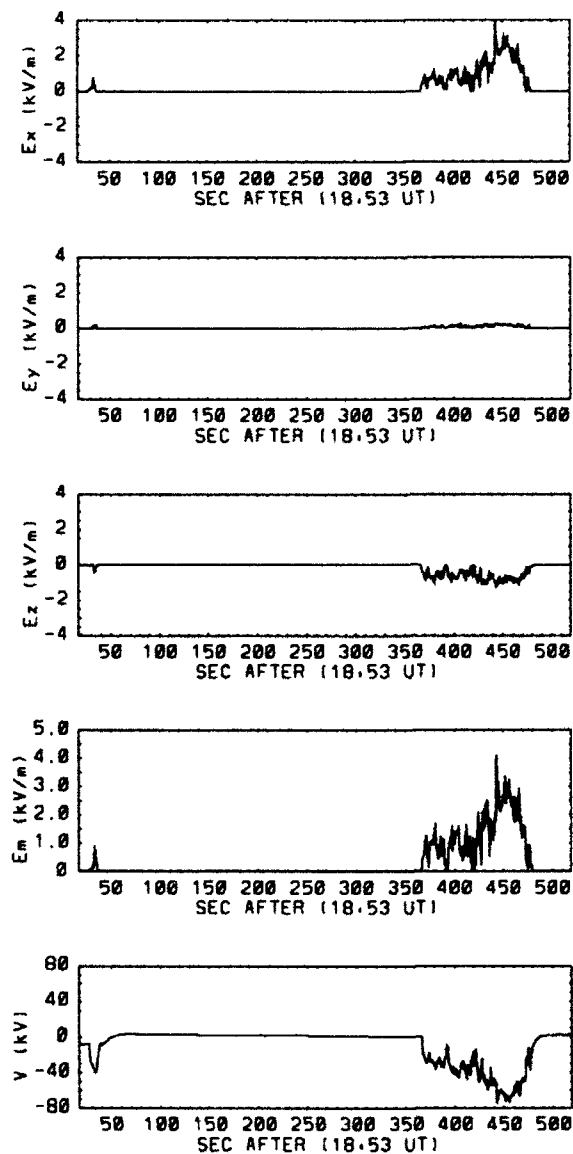
p02-022/14

**Figure 4 AIRCRAFT POTENTIAL OF THE LEARJET 24B AND 36A
DURING SIMILAR CHARGING CONDITIONS**

Learjet 24B



Learjet 36A



p02-022/15

Figure 5 COMPUTED ELECTRIC FIELDS AND AIRCRAFT POTENTIAL FOR THE LEARJET 24B AND 36A DURING SIMILAR PENETRATIONS OF A LIQUID WATER CLOUD

(5) resulting in equal-magnitude opposite-polarity current collection by the engine and its exhaust. Additional data relating to these issues would be available if electric-field measurement aircraft also carried instrumented dischargers to monitor airframe discharge currents.

CONCLUSIONS

Comparing results from different aircraft-borne electric-field measurement systems under similar flight conditions allows a glimpse into the complex charging and discharging environments that introduce errors in such systems. The T-28 and SPTVAR show good agreement between their field measurements even though the SPTVAR tends to charge 5 to 10 times more than the T-28 during passes through rain (and perhaps melting graupel).

Although the outside-of-cloud field measurement accuracies of the Learjets 24B and 36A are good (though not detailed here), the Learjet 36A shows significantly greater charging in cloud than does the Learjet 24B. Other charging differences and the slow rate of charge decay of the Learjet 36A point to their engines as the varying parameter between the two systems.

These results reinforce the fact that the aircraft itself is an important piece of any aircraft-borne electric-field measurement system and its effects on the local environment must be thoroughly understood for proper interpretation of acquired data. For all aircraft-borne electric-field measurement systems, it is recommended that at least one instrumented discharger be mounted near an aircraft extremity to provide additional data on aircraft charging and discharging characteristics under various flight conditions.

ACKNOWLEDGMENTS

We are grateful for the help and data provided by Andrew Detwiler of SDSMT and William Winn of NMIMT, for the efforts of the T-28, SPTVAR, NASA/Ames, and Aeromet aircraft crews, and for help from many at Aeromet and SRI.

REFERENCES

1. B.F. Evteev, "On Error Sources During Airborne Measurements of the Ambient Electric Field." Paper presented at 1991 International Conference on Lightning and Static Electricity, Cocoa Beach, Florida, 16-19 April 1991.
2. J.J. Jones, "Electric Charge Acquired by Airplanes Penetrating Thunderstorms," Journal of Geophysical Research, Vol. 94, No. D10, 1990.
3. J.J. Jones, "Electrical Emissions of Airplanes Flying in Electrified Clouds and Their Effect on Airplane Measurements of Cloud Electric Fields." Paper presented at 1991 International Conference on Lightning and Static Electricity, Cocoa Beach, Florida, 16-19 April 1991.
4. J. Kositsky, K.L. Giori, R.A. Maffione, D.H. Cronin, J.E. Nanevich, R.H. Harris-Hobbs, "Airborne Field Mill System Calibration Report." Final Report under USAF Contract F04701-90-C-0023, SRI Project 1449A, January 1991, 278 pages.
5. E.T. Pierce, "Waterfalls, Bathrooms, and -- Perhaps -- Supertanker Explosions." Paper presented at 1970 Lightning and Static Electricity Conference, San Diego, California, 9-11 December 1970.

OBSERVATION OF RADIATION FROM LIGHTNING DISCHARGES BY LPATS

M. Ishii and J. Hojo

Institute of Industrial Science, University of Tokyo
7-22-1 Roppongi, Minato-Ku, Tokyo 106, JAPAN
Telephone +81-3-3479-1949 Fax +81-3-3402-5078

T. Yamamoto, E. Zaima, J. Sawada and N. Fukiyama
Engineering Research Center, Tokyo Electric Power Co.
2-4-1 Nishi-Tsutsujigaoka, Chofu 182, JAPAN
Telephone +81-3-3300-2241 Fax +81-3-3305-2141

ABSTRACT

A lightning location system known by the name of LPATS was installed on the central region of the Honshu Island as its third system in Japan. Calibration of the sensitivity of this system was completed in 1991, and a function to distinguish electromagnetic field waveforms having small peak-to-zero times was added at that time. By these modifications, the system has almost become able to distinguish negative cloud-to-ground strokes in summer, but still misinterprets many cloud-discharge pulses in summer as positive return strokes. Majority of such misinterpreted field waveforms had rather small range-normalized signal strengths, and were identified as bipolar pulses originating from cloud-discharge processes. In winter, such a difference depending on the polarity of return strokes becomes remarkably less, suggesting seasonal variation in the occurrence of cloud-discharge pulses.

INTRODUCTION

A lightning location system called LPATS (Lightning Position and Tracking System, manufactured by ARSI) (1) is a widely used system of this kind, next to the magnetic direction finding system manufactured by LLP. LPATS receives electromagnetic pulses in about the same frequency range as that of the wideband magnetic direction finder, and may be used for the observation of electromagnetic radiation from lightning discharges. It is indispensable, however, to know the operating characteristics of LPATS, such as the detection efficiency and the absolute sensitivity, to produce lightning parameters from the output of the system, as have been done with the magnetic direction finding system (2).

A third network of LPATS in Japan was installed in 1990 to cover the area around Tokyo. The authors analyzed the output which was not too much processing by the system software, and revealed the essential operating characteristics of the system, except the location accuracy. Findings on the statistical characteristics of electromagnetic pulses associated with lightning discharges are reported in this paper, together with the operating characteristics of LPATS.

DESCRIPTION OF THE SYSTEM

GENERAL CHARACTERISTICS -- LPATS comprises 4 to 6 receivers located more than about 200km apart each other. If more than 2 or 3 receivers simultaneously receive electromagnetic pulses, they are regarded as radiated from a single source associated with a lightning discharge, and the location of the source is calculated two-dimensionally based on the differences of the time-of-arrival

of the pulses at the receivers. A receiver observes the electric field component of an electromagnetic pulse by using an electrostatic antenna. The frequency range of the wideband receiver is from about 2 to 500kHz, which is almost identical to the wideband magnetic direction finder manufactured by LLP. Therefore, a receiver of LPATS observes electromagnetic pulses having the duration of several tens of microseconds, and if the pulse is radiated from a return stroke, the peak current can be estimated, for example, by applying the transmission-line model (3).

Each receiver is triggered when the strength of the incoming electric field signal exceeds the threshold value, regardless of the polarity of the signal. The field waveform is digitized every $0.2\mu\text{s}$ with 8-bit resolution for about $100\mu\text{s}$, and each receiver transmits the time of the peak, the amplitude of the peak and the information on the peak-to-zero time of the waveform to a central analyzer through asynchronous communication lines. The central analyzer calculates the location of the source and the range-normalized signal strength. The synchronization between receivers is usually maintained through the broadcast of a satellite TV, and the accuracy is reported to be about $0.3\mu\text{s}$ on the average (1), which is usually smaller than the error introduced by the waveform distortion in the course of its propagation.

The manufacturer recommends the distances between receivers to be more than about 200km, which is closely related to the idea of how LPATS discriminates electromagnetic pulses radiated from return strokes. It was postulated that an electromagnetic pulse, powerful enough to be received by more than two or three receivers located widely apart each other, was associated with a return stroke. This design concept is based on the assumption that in-cloud discharge processes produce relatively weak signals in the observed frequency range, though this has not been statistically verified. According to this idea, if the distances between receivers are shorter, there will be more possibility for the system to accept signals originating from in-cloud discharge processes.

Later, a waveform discrimination criterion was added. When an incoming waveform has a short peak-to-zero time, the corresponding data set transmitted to the central analyzer is tagged by the receiver, and if at least one data, among the data sets producing a solution of the source location, has the tag, the corresponding source is not regarded as a return stroke.

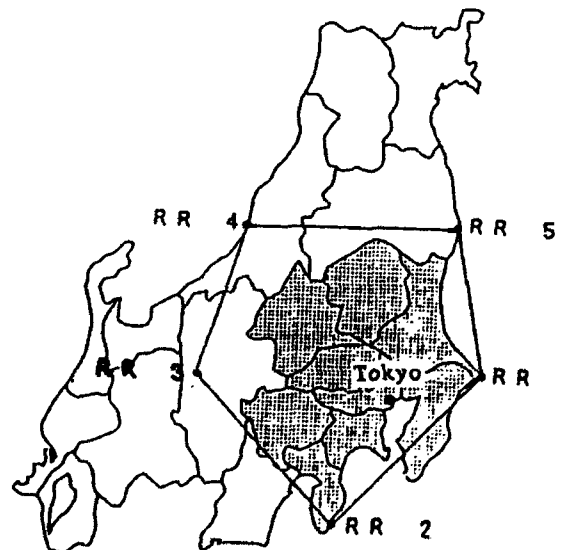


FIGURE 1. LPATS NETWORK AROUND TOKYO

NETWORK USED FOR THIS STUDY -- The configuration of the network is shown in figure 1. The distances between receivers might not be enough, but the configuration is better than the network in the Netherlands having shorter base-lines (1). At this network, digitized waveforms are also transmitted from all the receivers to the central analyzer, resulting in the slightly longer dead time, 20ms, of a receiver. The triggering level and the sensitivity of a receiver float depending on the frequency of triggering events, but do not become more sensitive than the initial values. This system regards an electromagnetic pulse having the peak-to-zero time of shorter than $10\mu\text{s}$ as originating from a cloud discharge process.

ESTIMATION OF RETURN-STROKE PEAK CURRENT

PRINCIPLE -- Regarding an electromagnetic pulse radiated from a return stroke, LPATS tries to locate the same position as the magnetic direction finding system does, that is, the position corresponding to the peak of the waveform immediately after the fast transition (4). The source corresponding to the peak of a waveform is thought to be very close to the lightning striking point on the ground. The peak current of a return stroke in the distance of more than about 100km can be estimated from the measured signal strength by using the transmission-line model (3). According to this model, the current waveform and the far-field waveform is the same, and the quantitative relationships are as follows.

$$B = I \mu v / 2 \pi c D \quad (1)$$

$$E = -I v / 2 \pi \epsilon c^2 D \quad (2)$$

where B and E are the magnetic field and the electric field intensity, respectively, and I is the current magnitude. v and c are the velocities of the return stroke current and the light, respectively. D is the distance between the source and the point of observation. μ and ϵ are the permittivity and the permeability of the air. For negative return strokes, the most appropriate value of v for observed results by a system like the magnetic direction finding system was reported to be about 10^8m/s (3).

LPATS observes the electric field, therefore, equation (2) is applicable to estimate the return-stroke current. In the current software of the LPATS, Cooray's model for attenuation of electromagnetic wave (5) is additionally incorporated, but such a complex model does not seem effective in the estimation of this kind (3,6), therefore, simply equation (2) is used in this paper.

CALIBRATION -- To use equation (2), the electric field intensity of an electromagnetic pulse needs to be measured. For this purpose, the sensitivity of each receiver has to be calibrated, which had not been tried for a network of LPATS. Especially, because the sensitivity of an electrostatic antenna is more influenced by surrounding objects than a magnetic field antenna, and the antenna of an LPATS receiver is usually set on the roof of a building, calibration of the sensitivity is an essential part of the present kind of the analysis.

The authors developed a method to calibrate an electrostatic antenna, through the simultaneous measurement of a broadcast standard signal at 40kHz with a reference antenna set on an open ground (7). By this method, the sensitivities of all the 5 receivers of the system were measured, and were adjusted within the accuracy of 5% by changing the length of the electrostatic antennas.

After this adjustment in May 1991, the dynamic range of each receiver can observe a return stroke of about 5 to 240kA at a distance of 200km. This sensitivity is less than a half of the initial setting of the system. The linearity of the analog part of an LPATS receiver was checked by comparing the waveforms, observed at the analog output terminal, with those simultaneously

measured by a fast antenna having a flat plate antenna and the frequency range of 0.4kHz~1.2MHz, and it turned out to be fairly flat.

RESULT OF THE OBSERVATION

As the statistics of the amplitude of electromagnetic pulses corresponding to first return strokes in Japan are well established (2), corresponding statistics are produced from the output of LPATS for comparison. LPATS does not distinguish first return strokes, so the first electromagnetic pulse in a group of pulses having small dispersions in the time and the location is subject to analysis. Lightning current amplitude is estimated by using equation (2) with $v=10^8$ m/s for both the polarities of pulses. The polarity of the return stroke is defined as the polarity of the charge neutralized.

The network tries to locate lightning when 4 or more receivers simultaneously receive electromagnetic pulses. Therefore, to see the influence of the distance to a stroke on the performance of the system, the distance to the farthest receiver from a stroke is the most important. Figure 2 shows the distributions of current peaks observed in July 1991. The data used in this figure are located in regions where the receiver RR1 is the farthest among the five receivers, and are processed depending on the distances from the receiver RR1, the location of which is shown in figure 1. Figure 3 shows similarly processed data observed in December 1991 and January 1992. The distribution curves denoted "LLP" in figures 2 and 3 were observed by a magnetic direction finder network in Japan (2), and the curve of LLP in figure 2(a) is almost identical to that measured in Switzerland by a current shunt.

DISCUSSION

APPARENT DISTRIBUTIONS -- Regarding the distributions corresponding to negative strokes in summer shown in figure 2(a), they are close each other in the region of current larger than about 40kA, and the distribution for 200-400kA is very close to the distribution observed by the magnetic direction finder network. The deviation in the low current region of distribution for 400-1000kA is due to the dynamic range of the receiver. When the true population of the return-stroke current amplitude does not depend on the range from a receiver, the observed distributions in different range bins should be somewhat like these distributions of figure 2(a), if not too much portions of the population are missed by the limited dynamic range.

It is reasonable to think that the negative first strokes observed in summer by the network of LPATS under investigation are mostly negative first return strokes. The difference in distributions for 100-200kA and 200-400kA in the low current region may be due to the misinterpretation of cloud-discharge pulses having lower amplitudes, but the portion of such data in the distribution for 100-200kA is less than 10%.

The distributions corresponding to positive return strokes in summer shown in figure 2(b) are quite different from figure 2(a). The electric field pulses corresponding to these data have negative initial polarity. If these distributions originate from a single population, the population has to have dual peaks in its histogram. The assertion that positive return strokes in summer belong to such population doesn't seem to be valid, because the number of these pulses, having the same polarity as positive return strokes, count up about 30% of recorded first pulses observed in the region of 100-200kA. Positive ground flashes in summer are known to be less than a few percents of total ground flashes according to the observation by a slow antenna. The number of observed

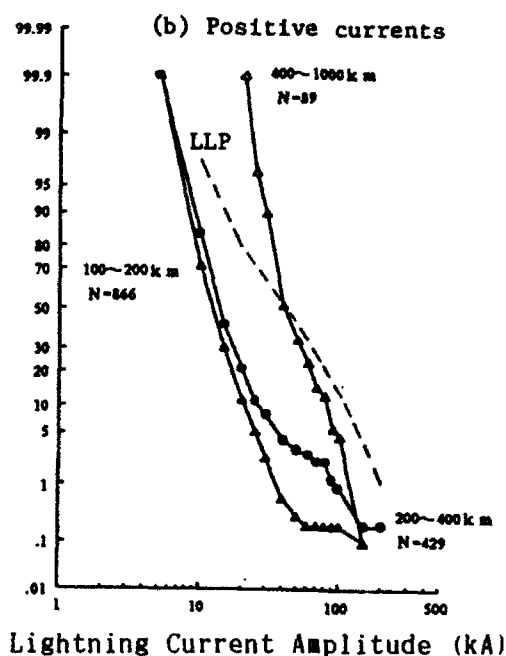
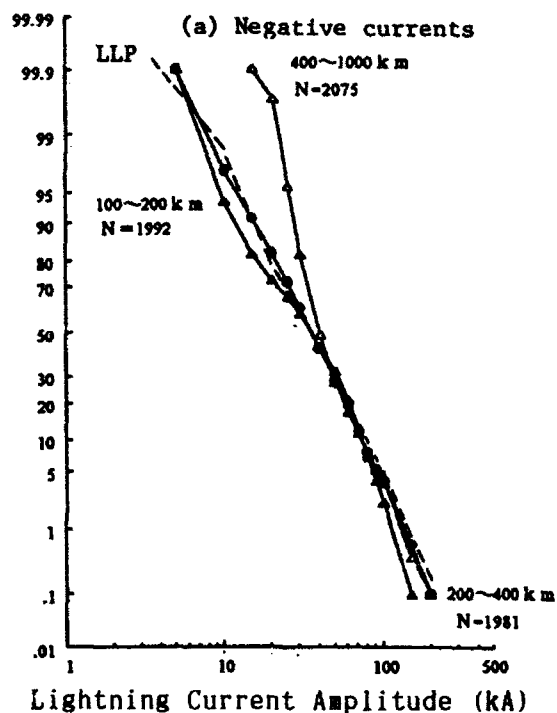


FIGURE 2. CUMULATIVE DISTRIBUTION OF LIGHTNING CURRENT OBSERVED BY LPATS IN SUMMER (NIIGATA, 1991)

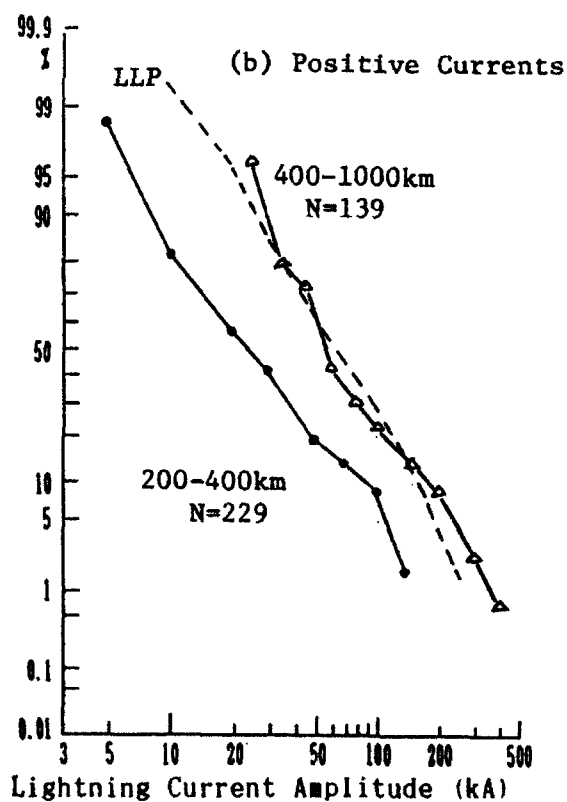
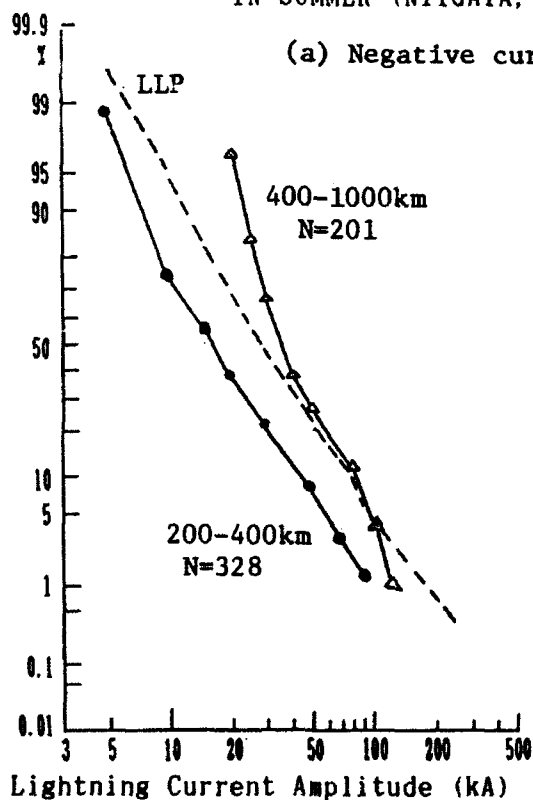


FIGURE 2. CUMULATIVE DISTRIBUTION OF LIGHTNING CURRENT OBSERVED BY LPATS IN WINTER (NIIGATA, 1991-1992)

pulses of negative initial polarity is too large, therefore, probably more than 80% of the recorded first pulses of negative polarity in the region of 100-200km are associated with in-cloud discharges, although there is a report about weak positive return strokes (8).

The apparent distributions in winter, shown in figure 3, are different from those in summer regarding the dependence on the distance. The distributions for the region of 400-1000km coincides with those observed by the magnetic direction finder network for currents larger than about 50kA. The lack of data in smaller current regions in the distributions for 400-1000km is obviously due to the limited dynamic range of a receiver. The simplest explanation of the dependence of the distributions on the distance to the sources of electromagnetic pulses is, this time too, the existence of a population of pulses having a peak at a smaller signal strength than the distribution observed by the magnetic direction finder network. In winter, the distribution for negative return strokes is also affected by such a population having smaller peak signal amplitudes.

CHARACTERISTICS OF ELECTROMAGNETIC PULSES -- The apparent distributions of positive return strokes in summer, figure 2(b), mean that there exist many field waveforms originating from in-cloud discharges which have the peak-to-zero time of more than $10\mu\text{s}$. Most of the magnitudes of the sources of them seem to be less than 20kA equivalent.

Many of recorded such waveforms different from return-stroke waveforms are bipolar pulses initially negative and having a duration of about 20-150 μs , which were called negative bipolar pulses by Weidman and Krider (9). Negative bipolar pulses are radiated from in-cloud discharge processes, and most of them have peak-to-zero time of longer than $10\mu\text{s}$. The initial half cycle is usually superimposed by narrow pulses and the overshoot into the opposite polarity after the peak is large, therefore, it is easy to identify if the waveform is recorded. An example is shown in figure 4. In summer, the polarity of the majority of the bipolar pulses radiated from in-cloud processes is initially negative (9), the same as that of positive return-stroke waveforms. This explains the difference between the apparent distributions for negative and positive return strokes in figure 2(a) and (b).

There are other kinds of in-cloud discharge pulses called narrow bipolar pulses (10,11). Figure 5 shows an example of such waveforms together with a waveform originating from a positive return stroke. The waveform of figure 5(b) more resembles figure 5(a) than a negative bipolar pulse, because of the smooth wavefront and smaller overshoot after the peak. According to the observation by Medellius et al. (11), the polarity of such pulses was mostly initially negative as is figure 4(b), and the ratio in the number was 16:1, where 1 corresponds to the pulses of the opposite polarity. Observation of summer in Japan by the authors agrees to these reports. Figure 6 shows the histogram of the peak-to-zero time of the narrow bipolar pulses having initially negative polarity. From this figure, it is obvious that narrow bipolar pulses are effectively removed by only accepting pulses having a longer than $10\mu\text{s}$ peak-to-zero time.

In winter, the difference in the distributions for positive return strokes in figure 3(b) is not so large as in summer, but is still obvious. Although there has not been a report on the negative bipolar pulses in winter, the cause of the difference will be the same as in summer. For negative return strokes, there is difference between the distributions for 200-400km and 400-1000km, which is not experienced in summer. It is likely that in winter, there may exist considerable number of positive bipolar pulses, which are not frequent in summer except being observed as characteristic pulses in negative ground flashes before return strokes (12).

From these results, it is likely that there is seasonal variation in the

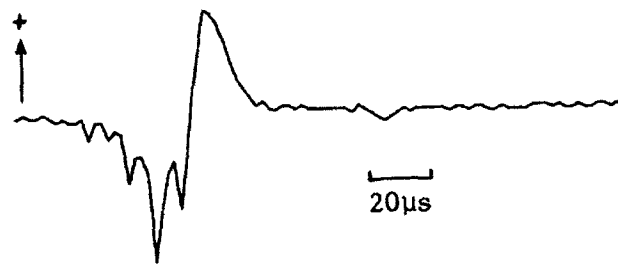
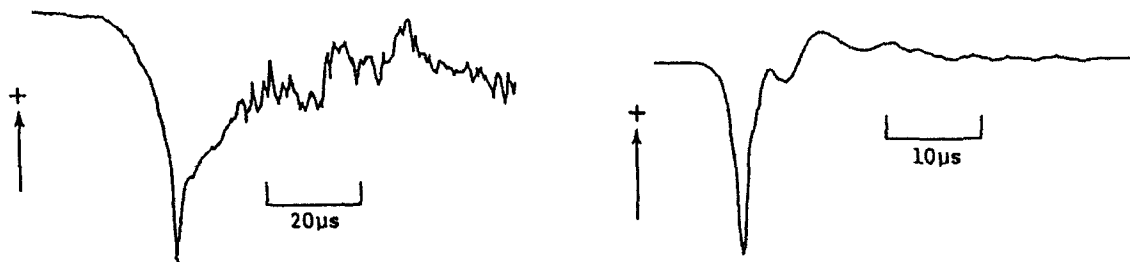


FIGURE 4. EXAMPLE OF NEGATIVE BIPOLAR PULSE (SUMMER, IN NIIGATA)



(a) Positive first return stroke (b) narrow bipolar pulse
FIGURE 5. EXAMPLES OF ELECTRIC FIELD WAVEFORMS (WINTER, IN NIIGATA)

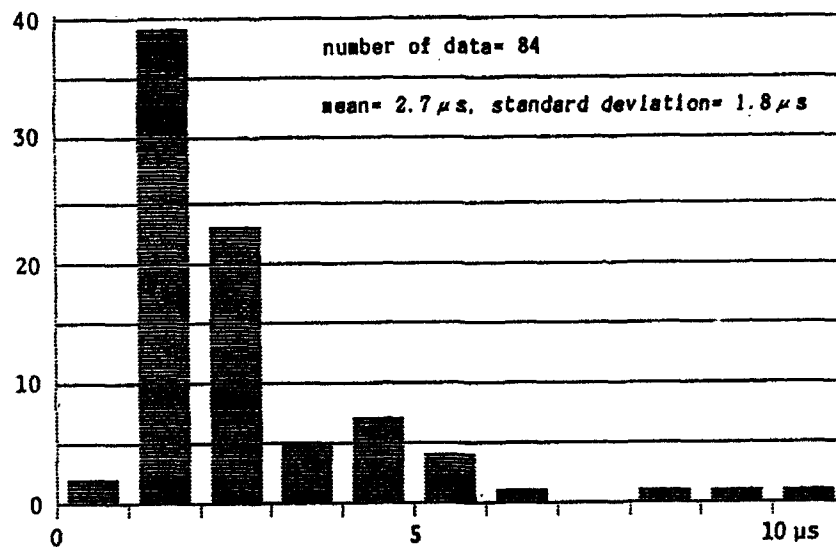


FIGURE 6. DISTRIBUTION OF PEAK-TO-ZERO TIME OF NARROW BIPOLAR PULSE HAVING NEGATIVE INITIAL POLARITY (SUMMER, IN NIIGATA)

occurrence of bipolar pulses radiated from in-cloud processes, as is observed for return strokes.

CONCLUSIONS

The sensitivity of the lightning location system called LPATS has been accurately calibrated. The normalized amplitudes of the first pulses among a group of electromagnetic pulses are estimated based on this calibration. The

distribution of negative first return-stroke current in summer, obtained by using the transmission-line model, agrees well with the observation by a current shunt, which demonstrates the accuracy of the calibration.

Other apparent distributions of range-normalized signal strengths lead to a conclusion that LPATS still accepts many pulses from in-cloud discharge processes as those from positive return-strokes, even after introducing the waveform criterion of the peak-to-zero time. In winter, similar phenomenon is experienced for distributions corresponding to negative return strokes, suggesting that there are seasonal variations in the occurrence of pulses radiated from in-cloud discharge processes.

The cloud-discharge pulses misinterpreted by LPATS are mostly negative bipolar pulses having the duration of about 20 to 150 μ s. Other kind of cloud-discharge pulses called narrow bipolar pulses, more resemble positive return-stroke waveforms than negative bipolar pulses, is effectively distinguished by the peak-to-zero time.

REFERENCES

1. M. J. G. Janssen, "The LPATS system in the Netherlands - critical evaluation of the results -", 20th ICLP, Interlaken, 6.7P, 1990.
2. J. Hojo, M. Ishii, T. Kawamura, F. Suzuki, H. Komuro, and M. Shiogama, "Seasonal variation of cloud-to-ground lightning flash characteristics in the coastal area of the Sea of Japan", J. Geophys. Res., 94, 13207-13212, 1989.
3. R. E. Orville, "Calibration of a magnetic direction finding network using measured triggered lightning return stroke peak currents", J. Geophys. Res., 96, 17135-17142, 1991.
4. C. D. Weidman, and E. P. Krider, "Submicrosecond risetimes in lightning return-stroke fields", Geophys. Res. Lett., 7, 955-958, 1980.
5. V. Cooray, and S. Lundquist, "Effects of propagation on the rise times and the initial peaks of radiation fields from return strokes", Radio Sci., 18, 409-415, 1983.
6. N. Herodotou, W. A. Chisholm, and W. Janischewskyj, "Distribution of lightning peak stroke currents in Ontario using an LLP system", IEEE PES Summer Meeting, 92 SM 452-3 PWRD, 1992.
7. Ishii, M., T. Kawamura, J. Hojo, and T. Iwaizumi, "Calibration of electrostatic antennas using broadcast signal", Res. Lett. on Atmospheric Electricity, 1, 45-48, 1981.
8. R. E. Lopez, M. W. Maier, and R. L. Holle, "Comparison of the signal strength of positive and negative cloud-to-ground lightning flashes in North-eastern Colorado", J. Geophys. Res., 96, 22307-22318, 1991.
9. C. D. Weidman, and E. P. Krider, "The radiation field wave forms produced by intracloud lightning discharge processes", J. Geophys. Res., 84, 3159-3164, 1979.
10. J. C. Willett, and J. C. Bailey, "A class of unusual lightning electric field waveforms with very strong high-frequency radiation", J. Geophys. Res., 94, 16255-16267, 1989.
11. P. J. Medelius, E. M. Thomson, and J. S. Pierce, "E and dE/dt waveshapes for narrow bipolar pulses in intracloud lightning", 1991 Int. Conf. on Lightning and Static Electricity, Cocoa Beach, 12, 1991.
12. W. Beasley, M. A. Uman, and P. L. Rustan Jr., "Electric fields preceding cloud-to-ground lightning flashes", J. Geophys. Res., 87, 4883-4902, 1982.

A System to Measure Lightning-Induced Transients on Spacecraft Umbilical Lines

**Jeffrey C. Brown
Noel B. Sargent
Carl J. Wenzler**

**National Aeronautics and Space Administration
Lewis Research Center
Cleveland, Ohio USA
Telephone (216) 433-3888 Fax (216) 433-6382**

ABSTRACT

Spacecraft electrical systems are potentially vulnerable during ground operations to damage from lightning-induced transients coupled onto umbilical cables. Limited data are available to compare spacecraft design protection levels with actual transient magnitudes. A system has been designed to accurately measure these transients and verify that spacecraft protection levels have not been exceeded. This paper describes the design and operation of the system and its installation at Launch Complex 36 on the Cape Canaveral Air Force Station (CCAFS).

INTRODUCTION

In November 1990, an industry-Government team held a consensus review of requirements for a system to measure lightning-induced transients on payload umbilical cables. This led to a feasibility study and conceptual design (1). That conceptual approach was modified and developed into a final design by NASA Lewis Research Center. The Lightning Transient Measurement System (LTMS) is a data acquisition system that provides continuous, unattended monitoring of unused wires in the spacecraft umbilical cable to sense lightning-induced voltage and current. The system is now in the final stages of fabrication and laboratory testing and is scheduled for installation at the launch site in March 1993. It will be used to support the launch of Government payloads.

METHOD

Lightning-induced transients on six unused umbilical wires are sensed by probes at the tower end of the umbilical cable. The analog probe signals are transmitted via fiber optics to a data collection system under the launch pad. There, high-frequency digitizers and peak detectors capture the waveforms and maximum voltages. A fiber optic data highway joins the data collection system with a dedicated data processing and storage system in the Blockhouse. The use of fiber optics for analog and digital signal transmission, transient protection of power lines, and EMI shielding of instruments make the LTMS nearly immune to the effects of the lightning event.

The LTMS consists of three sub-systems: the LTMS-Umbilical Interface Box (LUIB), the Lightning Data Acquisition System (LDAS), and the Lightning System Control Unit (LSCU). These components are installed at the launch facility as shown in Figure 1.

The probes are configured to measure common mode voltage and current and differential mode voltage. The system can fully digitize two inputs and can sample four for peak value only.

The system provides automatic self test and calibration, remote operation and data transfer via telephone modem, and operates autonomously. The system is entirely independent from other site data systems and provides its own emergency power to allow monitoring to continue in the event of a loss of site-supplied AC power.

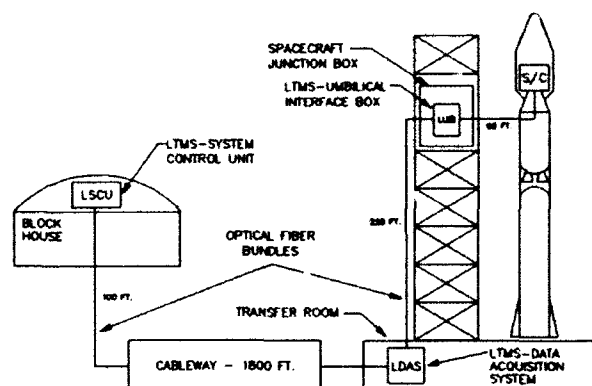


FIGURE 1-LTMS INSTALLATION AT LAUNCH COMPLEX 36, CCAFS

BACKGROUND

Missions on Expendable Launch Vehicles (ELV) are short in terms of exposure to lightning. Launch weather constraints also reduce the probability of damage from a significant nearby lightning occurrence. This accounts for the fact that many ELV payloads are not protected against the lightning threat to the extent of aircraft or manned launch systems.

The need for the LTMS grew from an earlier effort to upgrade the lightning protection and avionics design of the Centaur upper stage itself. Requirements derived from the Space Shuttle program (2) were employed to reduce the susceptibility of the ELV on stand. This activity reinforced the desire to assure that spacecraft interfaces were similarly adequately protected. It was felt that if the lightning induced transients on spacecraft GSE interfaces could be accurately measured and compared with design protection levels, an informed decision could be made to determine if the spacecraft had been compromised following a lightning event.

In the past, noise signatures on the vehicle digital data streams have been the only indication of possible upset or damage to avionics systems due to lightning-induced transients. Not knowing the magnitude of induced voltages and currents poses a costly and time-consuming launch delay to reconstruct the event and pursue vehicle checkout to assure nothing has been compromised.

The LTMS is expected to greatly reduce the uncertainty in providing a quick and accurate assessment of potential impacts to the launch director following a lightning event.

DESIGN REQUIREMENTS

During the consensus reviews and technical interchange meetings, several groundrules were adopted for LTMS design and operation. The system was designed to provide the following:

- Fully automated data recording and basic analysis
- Continuous, unattended operation
- No impact on payload design or operation
- Low impact on launch site operations
- Automatic self-test and calibration
- System hardened against lightning-induced fields

DATA REQUIREMENTS

MEASUREMENT TYPES--Electronic device damage is related to peak voltage, current and total energy from the lightning-induced cable-coupled transients. To define these parameters, common mode voltage and common mode current are measured. Differential voltage is also measured.

SIGNAL RANGES--Launch vehicle power interfaces are designed to withstand a common mode, 500 volt, 50 microsecond duration, 1 microsecond risetime pulse from a one ohm source. The maximum input ranges of the measurements were selected to be approximately twice that value. The differential voltage measurement was selected to be 20dB down from the peak or 100 volts full scale. The full scale value for the common mode current was set at 5 amps. Once bonding, grounding, and shielding interface characteristics are verified for the installation, full scale ranges are easily changed with a series of coaxial attenuators if higher or lower sensitivity is desired. The system will be set to trigger at levels well below the damage threshold.

SYSTEM BANDWIDTH--The end-to-end system bandwidth was chosen to accurately record the time domain response of the umbilical cable to a lightning event. With a digital sampling rate of 100 megasamples per second, the input signal conditioning was designed to maintain as broadband a characteristic as possible. Passive voltage dividers having a bandwidth exceeding 200MHz were developed for the common-mode measurement. Commercially available 100MHz coaxial shunts are used to measure common mode current. The differential mode measurement employs a wideband balun having a 3dB bandwidth of 1kHz to 15MHz and most importantly a volt-second product of 5000 volt-microseconds capable of reproducing the full scale pulse within its bandwidth. The end-to-end system bandwidth is approximately 6Hz-48MHz for the common mode measurements, and 1kHz-14MHz for the differential measurement.

UMBILICAL CONFIGURATION AND INTERFACE

The spacecraft umbilical consists of 106 conductors in a mix of twisted, shielded pairs and triples. The bundle has an additional overall shield and is approximately 90 feet long. The umbilical terminates in the Spacecraft Junction Box (S/C J-Box) at approximately the 190-foot level on the umbilical tower. Here the lines are connected to cables that run down the tower and through the cableway to the

blockhouse. Up to six umbilical lines which are not dedicated to payload functions are connected to the LTMS probes. Figure 2 illustrates the umbilical and probe configuration.

Since it is not practical to monitor the induced transients at the S/C interface, the next closest point (J-Box) was chosen. On the spacecraft side of the umbilical, at the vehicle's field joint (the distribution point for umbilical wires), both wires of each monitored pair are connected to structure to reflect the maximum induced voltages along the umbilical. Also, for each monitored pair, the wires that run to the blockhouse (1800 feet away) were disconnected at the J-Box terminal strips primarily to reduce distortion of the umbilical signals.

The umbilical signals must be conditioned to match the input requirement of the analog fiber optic transmission system. The common mode voltage signal is conditioned with a custom high voltage attenuator and several commercial coaxial attenuators. The balanced differential mode voltage signals are fed through a balun to provide an unbalanced output and then through coaxial attenuators to adjust the levels. The common mode and differential mode probes present the umbilical lines with impedances of approximately 500 and 1000 ohms respectively. The current shunts were selected to provide the required output signals without additional conditioning. Components in the input stage are easily changed should the need arise to adjust the input ranges. Tests were run on the probe components, individually and as a system, to verify acceptable frequency and pulse response (3).

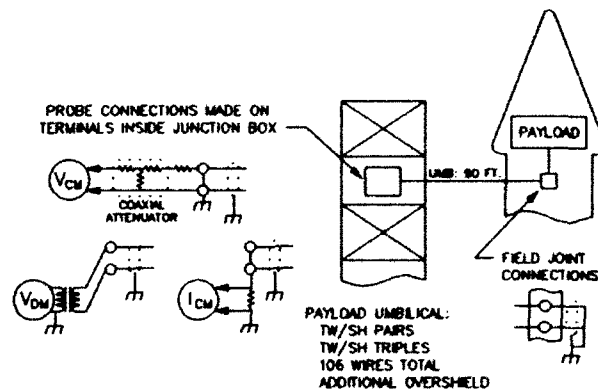


FIGURE 2-UMBILICAL CONFIGURATION AND PROBE INTERFACE

SUBSYSTEM DESCRIPTION

LTMS-UMBILICAL INTERFACE BOX--The LUIB houses the probes and signal conditioning equipment, the calibration pulse source, the analog fiber optic transmitters, as well as providing EMI shielding for these components. The LUIB is mounted inside the spacecraft junction box at the 190 foot level on the umbilical tower. A functional block diagram of the LUIB is shown in Figure 3, and its major components are described below.

Calibration Pulse Generator--To fulfill the requirements for end-to-end self tests and automatic recalibration of the analog fiber optic link, an accurate, stable pulse was required at the analog transmitter inputs. A signal generator was designed to provide pulses of selectable amplitude and polarity on command from the system controller. The pulses have rise times of 1 microsecond and are 10 microseconds in duration. A relay box disconnects the probe circuitry from the analog fiber optic transmitters during the self tests.

Digital Fiber Optic Link--The calibration pulse generator and the relay boxes are controlled from the LDAS via an eight channel, multiplexed digital fiber optic link.

Switching commands from the transmitter in the LDAS are sent via a single optical fiber to the receiver in the LUIB.

Power Filtering and Transient Protection--Power for the active components in the LUIB is provided by supplies in the LDAS via two, four-conductor cables. Four conductors supply power and four are used for sensing. These cables are routed through the duct which joins the spacecraft junction box and the Transfer Room, and because of their length, were considered to be susceptible to lightning-induced transients. To reduce the risk of damage or power upset to LUIB components, transient voltage suppressors with breakdown voltages just above the operating point are placed on each line to ground. Additionally, filters are used to reduce voltage pulses on the power lines to acceptable levels. Shielded cables and connectors are used on all power and sense lines.

LIGHTNING DATA ACQUISITION SYSTEM--The LDAS performs the collection of lightning event data, manages transmission of the data to the LSCU, and controls system self-tests and calibration runs initiated by the LSCU. The LDAS is installed in the Transfer Room, the under-pad signal conditioning and support system area. A block diagram of the LDAS is shown in Figure 4, and its major components are described below.

Data Acquisition and Control Mainframe--The modular Computer Automated Measurement And Control (CAMAC, IEEE Standard 583) system provides data acquisition and waveform sample storage, and discrete control capability for the LDAS. The system consists of a mainframe housing and various plug-in modules that perform the required functions. The CAMAC system communicates with the LSCU over the CAMAC byte-serial data highway (IEEE Standard 595), on a fiber optic link.

Waveform Digitizers--Two waveform digitizer modules and accompanying data memory modules are provided in the CAMAC mainframe, allowing digitization of two of the six input channels, or dual-speed cascade sampling of a single channel. The waveform digitizers provide 8-bit analog-to-digital (A/D) conversion at selectable sample rates up to 100 megasamples per second. Sufficient memory is provided to store up to one megasample of data per channel. The digitizers operate in a pre-trigger mode, continuously filling memory with input samples in a first-in, first-out manner prior to triggering. This allows the leading edge of a

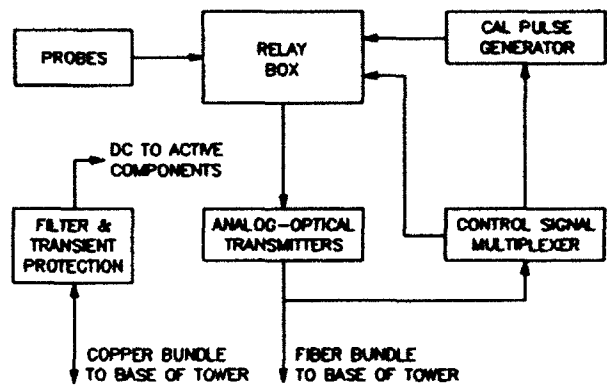


FIGURE 3--UMBILICAL INTERFACE BOX BLOCK DIAGRAM

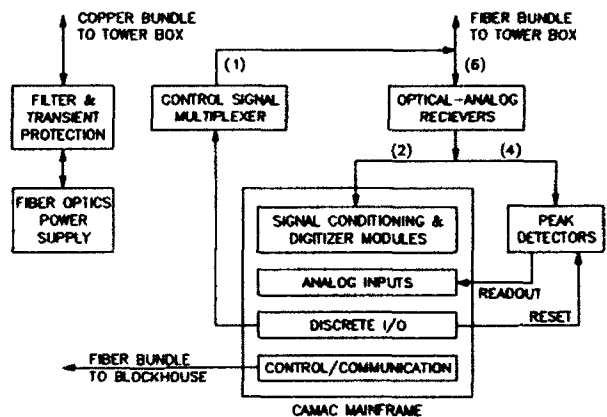


FIGURE 4--LIGHTNING DATA ACQUISITION SYSTEM BLOCK DIAGRAM

waveform to be captured prior to a system trigger. Signal conditioners ahead of the digitizer modules provide level adjustment and triggering.

Switching and Monitoring Functions--A discrete input/output (I/O) module provides switching functions required in the LDAS. The outputs are used to control (via the digital fiber optic link) the relay boxes and calibration pulse source in the LUIB. The inputs are used to monitor emergency power supply reserves and configuration switches in the LDAS.

Peak Detection and Readout--High frequency analog peak detectors provide detection and readout of the positive and negative peak voltages on four of the input signal lines. The peak detectors continuously monitor the signal lines and provide an analog voltage readout of the largest peak since last reset. Reset is commanded from the CAMAC system following each data transfer.

LIGHTNING SYSTEM CONTROL UNIT--The LSCU provides overall control and supervision of the LTMS. It sequences events, configures and arms the LDAS, schedules and executes system self-tests, gathers data following a lightning event, and handles all data processing, display, and storage. When the system is not collecting data, the LSCU can be used to analyze, process, and transfer previously collected data. A functional block diagram of the LSCU is shown in Figure 5.

The LSCU computer is an 80486-based, 33MHz PC equipped with a variety of expansion cards for I/O and communication, and sufficient hard disk storage for 250 recorded events. Operator interface is via the system keyboard, a high resolution color display, and a control panel. A timecode reader card provides timestamping of recorded events from the site timing signal, and a high speed modem allows remote control and data transfer. A CAMAC serial highway driver provides the interface between the fiber optic data highway and the computer system's General Purpose Interface Bus (GPIB, IEEE Standard 488) port.

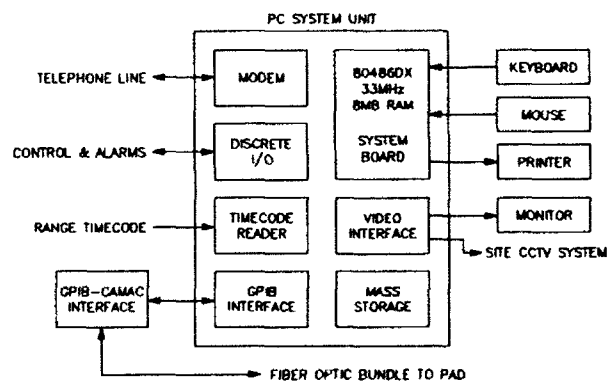


FIGURE 5-LIGHTNING SYSTEM CONTROL UNIT BLOCK DIAGRAM

ANALOG FIBER OPTIC LINK--Analog transducer data are carried from the probe enclosure to the data collection system via a six-channel, LED-based analog fiber optic transmission system. The system bandwidth of 6Hz-120MHz is sufficient to transmit the transient waveforms without any discernible distortion. Decay of the optical signal level due to LED aging, and variations in attenuation of optical fibers and connectors is monitored using the self test data, and corrected for by software.

SOFTWARE

Software running on the LSCU computer provides supervision and control of all system functions. Its three main tasks are to: configure and arm the data collection system, receive and store data after a trigger, and perform preliminary analysis of each received dataset. A multi-tasking operating system and Graphical

User Interface (GUI) support the LTMS application software. Functions which are not time dependant, such as operator input of setup information, are written in a graphics-based, high-level language, which provides a simple and intuitive interface. Assembly language routines provide high throughput for the data transfer operations, typically a bottleneck in a GUI environment. The software provides limited fault tolerance with automatic reconfiguration in certain failure situations.

DATA ANALYSIS

Preliminary analysis of collected data is performed immediately upon receipt of the data from the LDAS and provides an automatic "quick look" at the lightning event. Parameters of major interest such as peak voltage and current and total energy, are extracted at this time. This information can be used by the payload engineers to quickly assess the damage potential of the event. Additional analysis can be performed using the LSCU computer when the system is not armed to record data, or the datasets can be transferred elsewhere for study. Several signal analysis and plotting packages will be available on the LSCU.

OPERATION

Allocation of wires in the spacecraft umbilical is different for each mission, and probe connections must be made to the available spare wires. Prior to the start of monitoring, the system must be configured for the particular payload umbilical configuration by associating each monitored wire pair with a measurement type and scale factor. Several other parameters, such as digitizer sample rate, and trigger levels are selectable also, but will probably not be changed after their optimum values are determined during initial test phases. After configuration and checkout of the mission-peculiar probe connections, automatic monitoring can be started.

Following a system trigger, the LDAS alerts the LSCU that data are available for transfer. The LSCU then accepts the digitizer data, reads the peak detectors, re-arms the LDAS, and begins the quick look data analysis. The digitizers are off-line for a few seconds during data transfer operations, and indeed there are occasions when the digitizers could miss a significant transient. However, the peak detectors are never taken off-line or reset simultaneously, and provide a continuous record of peak voltage and current.

CLOSING REMARKS

The LTMS is designed as a practical tool for use by payload engineers and launch directors in assessing potential damage to spacecraft by nearby lightning events. Data from the LTMS is also expected to improve our understanding of the adequacy of lightning protection criteria currently imposed on ground support equipment interfaces. Its primary purpose is to record data from a potentially damaging strike rather than for every detectable event. The usefulness of the system will ultimately be measured by its ability to assist in making informed go/no-go launch decisions, and by our increased knowledge of lightning-induced transient phenomena at this launch site.

REFERENCES

1. Rodney A. Perala and Henry S. Weigel, "Instrumentation System for Lightning Transient Measurements on Atlas-Centaur Payload Umbilical Cable at Launch Complex 36B." Electro Magnetic Applications, Inc. Internal Report #EMA-91-R-016, prepared under Analex Corporation contract #AC-90-713, December 28, 1990.

2. NASA Johnson Space Center, "Space Shuttle Program Lightning Protection Criteria Document." #JSC-07636 Revision B, March 15, 1979

3. John C. Sturman, "Characterization of the Components for the Lightning Transient Measurement System." NASA Lewis Research Center; EMI Laboratory Internal Report #TEC-003, May 1992.

**RF ANTENNA AND LIGHTNING GROUNDING SOLUTIONS FOR
CLIMATIC AND GEOLOGIC EXTREMES BASED ON
EXTENSIVE MEASUREMENTS AND TDR MODELS**

**Burt J. Bittner
Harris Corp. ESD
2580 Clinton Dr. N.E.
Palmbay, FL 3205 - 2506
Telephone (407) 727-6440 FAX (407) 72 -2406**

ABSTRACT

Data is presented for our WENNER ARRAY 10 X 10 MATRIX conductivity measurements in Colo; N.Dak; 'Andesite' Volcanic Mountains and Alabama (chalk) $\sigma > 0.9$!!. The Andesite measures $\sigma < .00005$, $\epsilon > 8$, $\mu = 1.07$ rel Hy/M (due to the iron content) and N.Dak (deep winter) soil equivalent of TEFLON to 4 Meters.

RF and Lightning surge analysis and TDR, time domain measurements show that DC grounding (Sunde) solutions must be drastically altered AND in different ways to provide good Lightning protection and improved antenna efficiency in these various installations.

Grounding variations -- with useful solutions are provided -- including new graphite fiber grounds and rules for Biot-Savart, lowest forces and inductance connections from the lightning rod to the ground terminal.

Camera-ready paper not available.

A COMPUTATIONAL APPROACH TO PREDICTING THE EXTENT OF ARC ROOT DAMAGE IN CFC PANELS

N.Jennings

British Aerospace plc, Sowerby Research Centre,
Filton, Bristol, UK.

Telephone (0272) 366553 Fax (0272) 363733

C.J.Hardwick

Lightning Test and Technology, Culham Laboratory,
Abingdon, Oxon, UK.

Telephone (0235) 464264 Fax (0235) 464325

ABSTRACT

It is important to understand the mechanism of lightning arc root damage to carbon fibre composite panels in view of their increasing use in airframe construction. A computer model has been developed which contains coupled models of current and heat flow and predicts the extent of panel damage. Both initial stroke and continuing current components can be modelled, and the CFC parameters may be temperature dependent. Results and some comparisons with observations are presented.

1. INTRODUCTION

Experimental data on the effects of lightning arc attachments on CFC panels show a wide degree of variation, possibly due to the wide variety of make up of the panels. The use of computer modelling can assist in gaining an improved understanding of these data. Computer modelling of the heating effects of lightning arc attachment to aluminium sheets was carried out in the 1970s, and excellent agreement with experimental results was obtained. In recent years simple analytical and computational models of lightning current flow in CFC have been developed. This paper describes a computer code which contains linked numerical models of current flow and heating effects in a CFC panel due to lightning arc attachment.

Heating of the CFC panel will be due to current flow within the panel (Ohmic heating), and due to charge transfer across the arc attachment area (Coulomb heating). The code must therefore predict the distribution of current within the panel throughout the lightning strike event, and from this the heat produced due to Ohmic heating can be calculated. The Ohmic heating is input as a source term to the heat flow calculation. The current and heat flow calculations are also linked due to the electrical conductivity being a function of temperature. The anisotropic properties of the CFC panel were taken into account by using different values for the conductivities in directions within the plane of the panel, and across the panel. The detailed ply structure of the CFC was not modelled. The lightning arc attachment area was assumed to be circular in cross-section, and the flow of current and heat across this area was assumed to be normal to the panel. The problem to be solved then has cylindrical symmetry, and becomes two-dimensional, in cylindrical polar coordinates. This saved on computational resource requirements. The code can be used to predict the damage effects of lightning waveforms with varying action integral and charge transfer.

2. THE CURRENT FLOW SOLUTION

Different methods of solution for the current flow are appropriate depending on the phase of the lightning impulse. For the continuing current phase, determination of the current flow at each time step can be regarded as a steady state problem, and the electrostatic potential satisfies an equation closely related to Laplace's equation. For the fast initial stroke, inductive effects must be taken into account. For the particular problem under consideration it is convenient to work with the magnetic field which satisfies a diffusion-type partial differential equation. The current distribution can then be obtained from the magnetic field.

2.1. CONTINUING CURRENT—In this case we use the equations for steady-state current flow. The electric field \underline{E} can be derived from a scalar potential ψ using $\underline{E} = -\nabla\psi$, and the continuity equation becomes $\text{div} \underline{j} = 0$. We use an anisotropic form of Ohm's Law given by $j_r = \sigma_r(T)E_r$ and $j_z = \sigma_z(T)E_z$ where j is the current density and σ is the conductivity. The conductivities may be dependent on the temperature T .

Combining these equations we obtain the following equation for ψ which is expressed in cylindrical polar coordinates:

$$\sigma_r(T)\left(\frac{\partial^2\psi}{\partial r^2} + \frac{1}{r}\frac{\partial\psi}{\partial r}\right) + \sigma_z(T)\frac{\partial^2\psi}{\partial z^2} + \frac{\partial\sigma_r(T)}{\partial r}\frac{\partial\psi}{\partial r} + \frac{\partial\sigma_z(T)}{\partial z}\frac{\partial\psi}{\partial z} = 0$$

This may be transformed to Laplace's equation in the case where the conductivities are constants, by making the change of variable $z' = \left(\frac{\sigma_z}{\sigma_r}\right)^{\frac{1}{2}}z$ giving:

$$\frac{\partial^2\psi}{\partial r^2} + \frac{1}{r}\frac{\partial\psi}{\partial r} + \frac{\partial^2\psi}{\partial z'^2} = 0$$

Referring to figure (1), the boundary conditions for the solution are that there is no normal flow of current across the top and bottom faces of the panel except where the lightning arc attaches, and also there is no flow of current across the axis of symmetry. On the boundary AB, distant from the arc attachment area, the potential is assumed to be constant across the panel. Where the arc attaches, the appropriate boundary condition, derived from Ohm's Law is $-\sigma_z(T)\frac{\partial\psi}{\partial z} = j_{arc}$ where j_{arc} is the current density in the arc.

The equation for the potential was solved by means of the numerical scheme:

$$\begin{aligned} &\sigma_r(T_{i,j})\left[\psi_{i+1,j}\left(1 + \frac{1}{2i}\right) - 2\psi_{i,j} + \psi_{i-1,j}\left(1 - \frac{1}{2i}\right)\right]/h_r^2 + \sigma_z(T_{i,j})[\psi_{i,j+1} - 2\psi_{i,j} + \psi_{i,j-1}]/h_z^2 \\ &+ [\sigma_r(T_{i+1,j}) - \sigma_r(T_{i-1,j})][\psi_{i+1,j} - \psi_{i-1,j}]/4h_r^2 + [\sigma_z(T_{i,j+1}) - \sigma_z(T_{i,j-1})][\psi_{i,j+1} - \psi_{i,j-1}]/4h_z^2 \\ &= 0 \end{aligned}$$

where h_r and h_z are the space steps in the r and z directions respectively. Since the solution will vary more rapidly across the panel, h_z should be smaller than h_r and it is appropriate to take $h_z = \left(\frac{\sigma_z}{\sigma_r}\right)^{\frac{1}{2}}h_r$. The boundary conditions were also approximated by difference formulae. The numerical solution of the equation for the potential requires the solution of a system of linear equations. The components of current density may then be determined from the second order difference formulae $j_r = -\sigma_r(T)\frac{\psi_{i+1,j} - \psi_{i-1,j}}{2h_r}$ and $j_z = -\sigma_z(T)\frac{\psi_{i,j+1} - \psi_{i,j-1}}{2h_z}$. In general, as the temperature of the panel changes the conductivities will vary, and this steady

state current distribution must be recalculated at each time step.

2.2. FAST INITIAL STROKE- In this case, where inductive effects are important, we use Faraday's Law of induction which may be expressed as $\text{curl} \underline{E} = -\frac{\partial \underline{B}}{\partial t}$ where \underline{B} is the magnetic induction. The magnetic field \underline{H} , where $\underline{H} = \underline{B}/\mu$ and μ is the magnetic permeability (assumed isotropic), is given by Ampere's Law $\text{curl} \underline{H} = \underline{j}$. The displacement current has been neglected from this equation, since radiation effects are not significant in determining the current flow. Finally we have the anisotropic form of Ohm's Law $j_r = \sigma_r(T)E_r$ and $j_z = \sigma_z(T)E_z$. Since \underline{E} only has components in the r and z directions and is independent of θ , $\text{curl} \underline{E}$ only has a component in the θ direction. Hence from Faraday's Law, the only time-varying component of the magnetic field is in the azimuthal (θ) direction. Combining the above equations we find that H_θ satisfies the equation:

$$\begin{aligned} \mu \frac{\partial H_\theta}{\partial t} = & \frac{1}{\sigma_z(T)} \left(\frac{\partial^2 H_\theta}{\partial r^2} + \frac{1}{r} \frac{\partial H_\theta}{\partial r} - \frac{1}{r^2} H_\theta \right) + \frac{1}{\sigma_r(T)} \frac{\partial^2 H_\theta}{\partial z^2} \\ & - \frac{1}{\sigma_z^2(T)} \frac{\partial \sigma_z(T)}{\partial r} \left(\frac{\partial H_\theta}{\partial r} + \frac{H_\theta}{r} \right) - \frac{1}{\sigma_r^2(T)} \frac{\partial \sigma_r(T)}{\partial z} \frac{\partial H_\theta}{\partial z} \end{aligned}$$

This is a partial differential equation of diffusion type.

Similar boundary conditions to section 2.1 were used. A fully implicit numerical scheme was implemented, in which the solution obtained at each time step was fed into the equations to obtain the solution at the next time step. Solutions for the current density were found from the magnetic field using Ampere's Law. Details can be found in reference (1), but space precludes their inclusion here.

3. THE HEAT FLOW SOLUTION

The temperature T and heat flow \underline{q} satisfy a continuity equation $\text{div} \underline{q} + \rho c(T) \frac{\partial T}{\partial t} = S$, where ρ is the density of the CFC, $c(T)$ is the specific heat which may be dependent on temperature, and S is a source term. In this case the source of heat is Ohmic dissipation of energy, and S is given by $S = \frac{j_r^2}{\sigma_r(T)} + \frac{j_z^2}{\sigma_z(T)}$. The heat conductivity of the CFC is anisotropic and hence the heat flow is given in terms of the temperature gradient by $q_r = -k_r(T) \frac{\partial T}{\partial r}$ and $q_z = -k_z(T) \frac{\partial T}{\partial z}$. Combining these equations the temperature is found to satisfy the equation:

$$\begin{aligned} \rho c(T) \frac{\partial T}{\partial t} = & k_r(T) \left(\frac{\partial^2 T}{\partial r^2} + \frac{1}{r} \frac{\partial T}{\partial r} \right) + k_z(T) \frac{\partial^2 T}{\partial z^2} \\ & + \frac{\partial k_r(T)}{\partial r} \frac{\partial T}{\partial r} + \frac{\partial k_z(T)}{\partial z} \frac{\partial T}{\partial z} + \frac{j_r^2}{\sigma_r(T)} + \frac{j_z^2}{\sigma_z(T)} \end{aligned}$$

In this model we assume that there is no radiation of heat by the panel, and no absorption of heat as a result of heat radiated by the lightning arc. Similar boundary conditions to section 2.1 were used. The rate of flow of heat q_z across the arc attachment area is given by $q_z = j_{\text{arc}} V_{\text{arc}}$ where V_{arc} is the arc voltage drop. An explicit numerical scheme was used to solve the equation for the temperature. Methods can be found in reference (1), but space precludes their inclusion here. In practice it is expected that since the heat conductivity is low, the major contributor to increase in temperature at any point will be the Ohmic dissipation.

4. CALCULATION OF DAMAGE TO THE PANEL

Experimental results indicate that the onset of physical damage to CFC occurs when the matrix holding the fibres in place softens or is vapourized by heating. Our model calculates the temperature in cells within the panel. When the temperature in any cell reaches the vapourisation temperature T_{vap} there is no further increase of temperature and the model then calculates the heat released in that cell (due to Ohmic heating) plus the heat flow into the cell at each time step. That is $S - \text{div}q$ which will in general be positive due to the low heat flow within the CFC. When the sum of these quantities calculated over several timesteps, if necessary, exceeds the latent heat L of the epoxy then the cell of CFC material is considered to no longer exist. This implies that the boundary of the CFC panel will move during the lightning strike. The boundary conditions applied will then be complicated by changes in the direction of the normal to the damaged panel. In practice, since the damage is shallow and over a wide area, it has been assumed that the normal to the damaged panel remains in the z direction. Hence the original form of boundary conditions could be applied. These were applied at the current boundary cells of the damaged panel.

5. RESULTS

5.1. INPUT DATA- A 2mm thick panel was represented by a mesh of 40 cells of 1mm in the radial direction, and 32 cells of 0.0625mm in the axial direction. The radial size required is dependent on the penetration distance of current into the panel. This is given by Evans (2) to be $3D$ where $D = 0.4\sqrt{k}d$ where k is the ratio of the electrical conductivities, and d is the thickness of the panel. For the values of the parameters which have been taken the penetration distance is 3.8 cm, and therefore the extent of the mesh in the radial direction should be sufficient.

For the runs presented here, the following values for the parameters were chosen:

Density of CFC	1800kg/m ³	Vapourisation temperature of epoxy	300°C
Arc root radius	5mm	Latent heat of vapourisation	assumed zero
Arc voltage drop	80V	Heat capacity of CFC	1000.0J/kg/°C
Electrical conductivity in radial direction	25600.0S/m	Heat conductivity in radial direction	6.0W/m/°C
Electrical conductivity in axial direction	100.0S/m	Heat conductivity in axial direction	0.4W/m/°C

There is the option in the program to make the electrical and thermal conductivities and the heat capacity of the CFC functions of temperature.

5.2. CASES RUN- Lightning impulse components A, D, and C as defined in (3) were input to the panel. Component C was taken to be 400A for 0.5s, and this period was divided into 60 time steps. Components A and D had the standard double exponential form and were run for the first 200μs and 100μs with time steps of 3μs and 1.5μs respectively. The program had an option whereby cells that reached the vapourisation temperature of the epoxy could be removed from consideration or left intact.

For each run graphs of the temperature, radial current density, and axial current density along and across the panel were produced. The values of the temperature at the end of each run, close to the top face of the panel, and across the panel close to the centre line of the arc allow volumes of damage to be estimated.

5.3. INTERPRETATION OF RESULTS- As an example figures (2a) to (2f) show values of variables for Component C input with the cells left intact. Assuming that the panel consists of 16 plies, the volume of the panel which attains the temperature of 300 degrees is 6 plies deep, and extends to 1.6 cm from the centre of the arc root. The radial current density undergoes a very rapid increase from the centre line of the arc to the edge, as shown in fig. (2c). This shows that the current tends to flow along the top surface of the panel (due to the large anisotropy in the conductivities) and this gives a very large radial current density in the CFC at the edge of the arc attachment area. The values shown in fig. (2e) for the axial current density just under the arc attachment area are consistent with the values expected. Similar profiles were obtained with the other components. Volume of damage profiles for components A, D, and C are shown in figures (3a) to (3c).

For component C, if damaged parts of the panel were removed from consideration, the arc rapidly burned down into the panel. The run was stopped after only 12 time steps, that is 0.1s, by which time the arc had burned half way through the panel. The resulting damage profile is shown in fig. (3d). Had the program been run for the full half second, it is expected that burn-through would have been obtained.

6. CONCLUSIONS

The results obtained with the cells left intact indicate that damage will be deeper but less extensive than obtained in experiments, as reported in (4). For comparison the range of the extent of visible damage from reference (4) is shown in figures (3e) - (3g) for components A, D, and C respectively. The shape of the damaged area in the experiments is elongated presumably because of the linear nature of each ply. In the model the properties of the panel are assumed to be cylindrically symmetric.

The comparison with data indicates that the model gives the correct order of magnitude for the extent of damage, but more development and comparisons with experimental data are required. In particular:-

1. The too rapid ablation of plies predicted for component C when damaged cells are removed from consideration suggests that this procedure is incorrect. However, maintaining the cells intact with parameters appropriate to CFC at 300°C will also be a simplification and may account for the smaller extent of damage predicted, compared to experiment. A method of parameterizing the damage needs to be developed.

2. The temperature at the lower surface of the panel opposite the arc attachment point could be measured experimentally for different components; comparisons with predictions would then aid development of the model.

7. ACKNOWLEDGEMENTS

This work was funded by the Culham Lightning Club comprising BAe, Rolls Royce, CASA, SAAB, CAA, DTI, and Shorts.

8. REFERENCES

1. N.Jennings, "A Computational Approach to Predicting the Extent of Arc Root Damage in CFC Panels. Culham Lightning Club reference number: CLiC/16-1." British Aerospace, Sowerby Research Centre Report, JS 12008, March 1992.
2. R.H.Evans, "An Analysis of Effective Resistivity and Current Distribution in Composite Panels at Low Frequency." International Conference on Lightning and Static Electricity, 1989.
3. "Protection of Aircraft Electrical/Electronic Systems against the Indirect Effects of Lightning." Report of SAE Committee AE4L, 1988.
4. G.W.Reid et al. "Preliminary Lightning Arc Root Damage Investigation to Unprotected CFC." AEA Report, 1990.

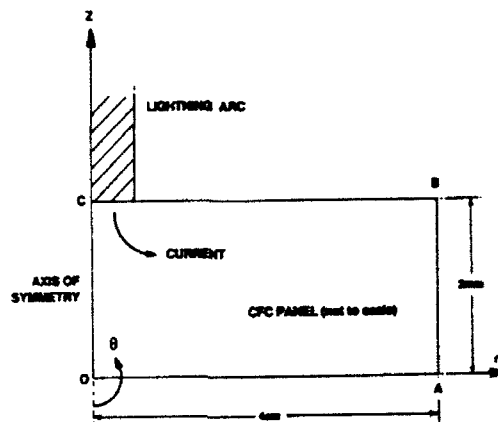


FIGURE 1: SECTION OF PANEL MODELLED AND CO-ORDINATE SYSTEM USED

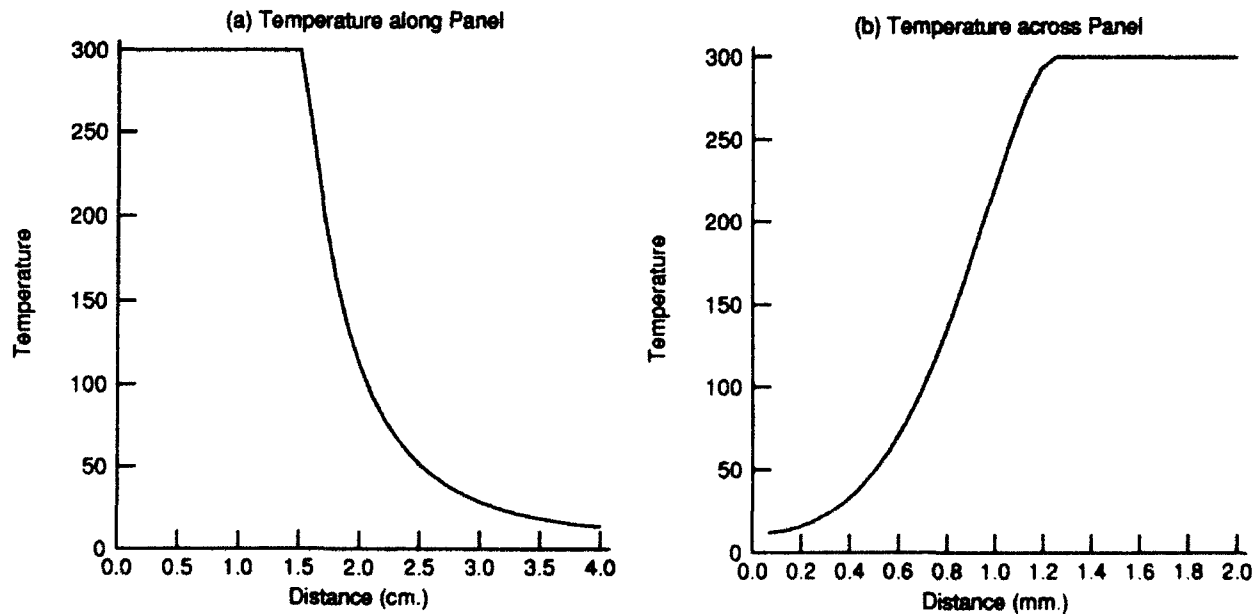


FIGURE 2: GRAPHS OF KEY VARIABLES AT THE END OF THE MODEL RUN - COMPONENT C INPUT

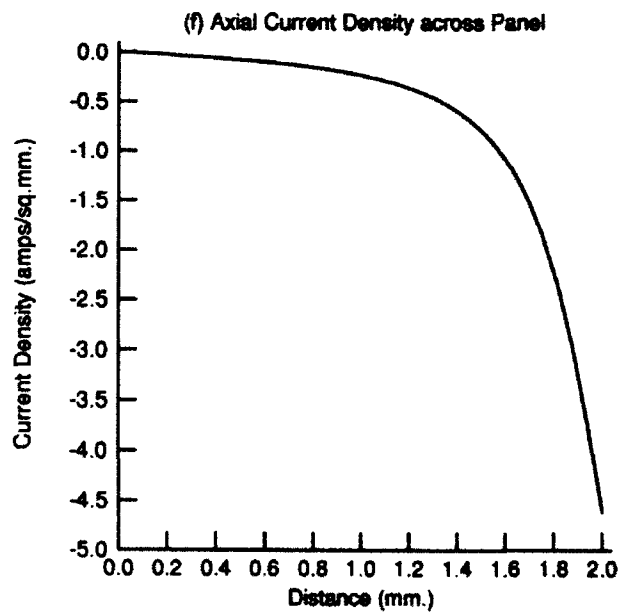
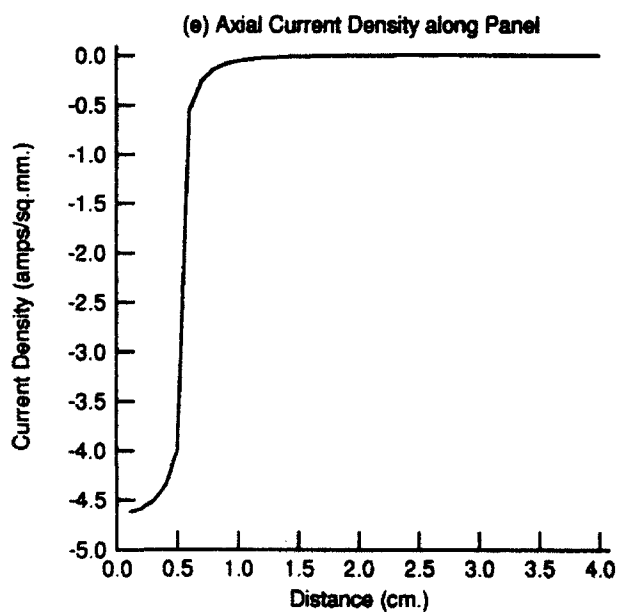
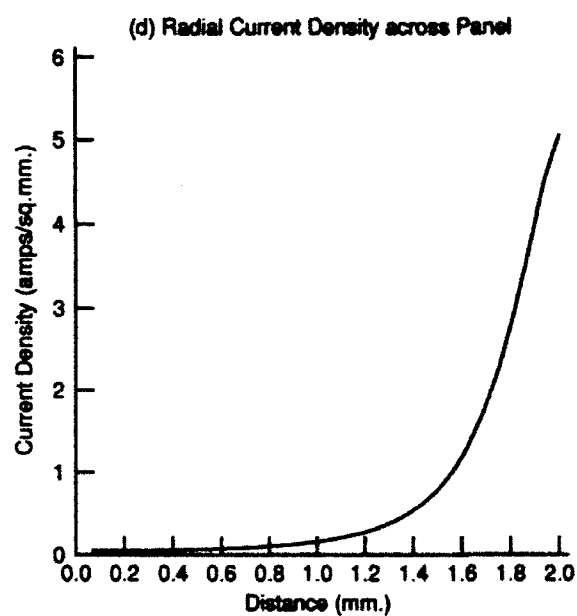
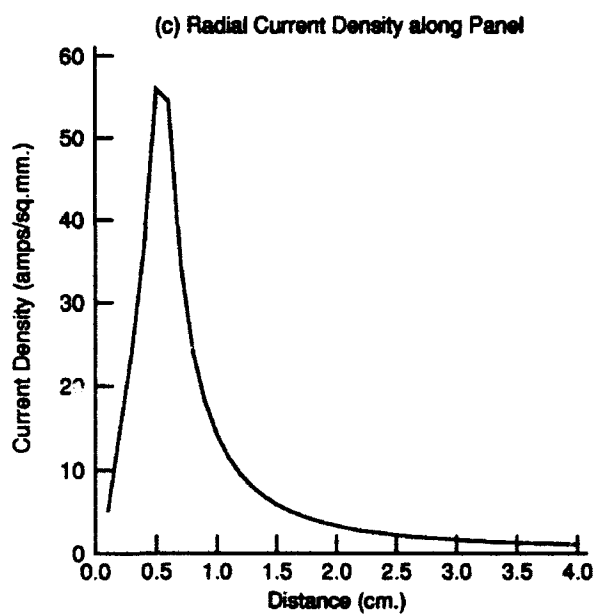


FIGURE 2 (cont'd): GRAPHS OF KEY VARIABLES AT THE END OF THE MODEL RUN - COMPONENT C INPUT

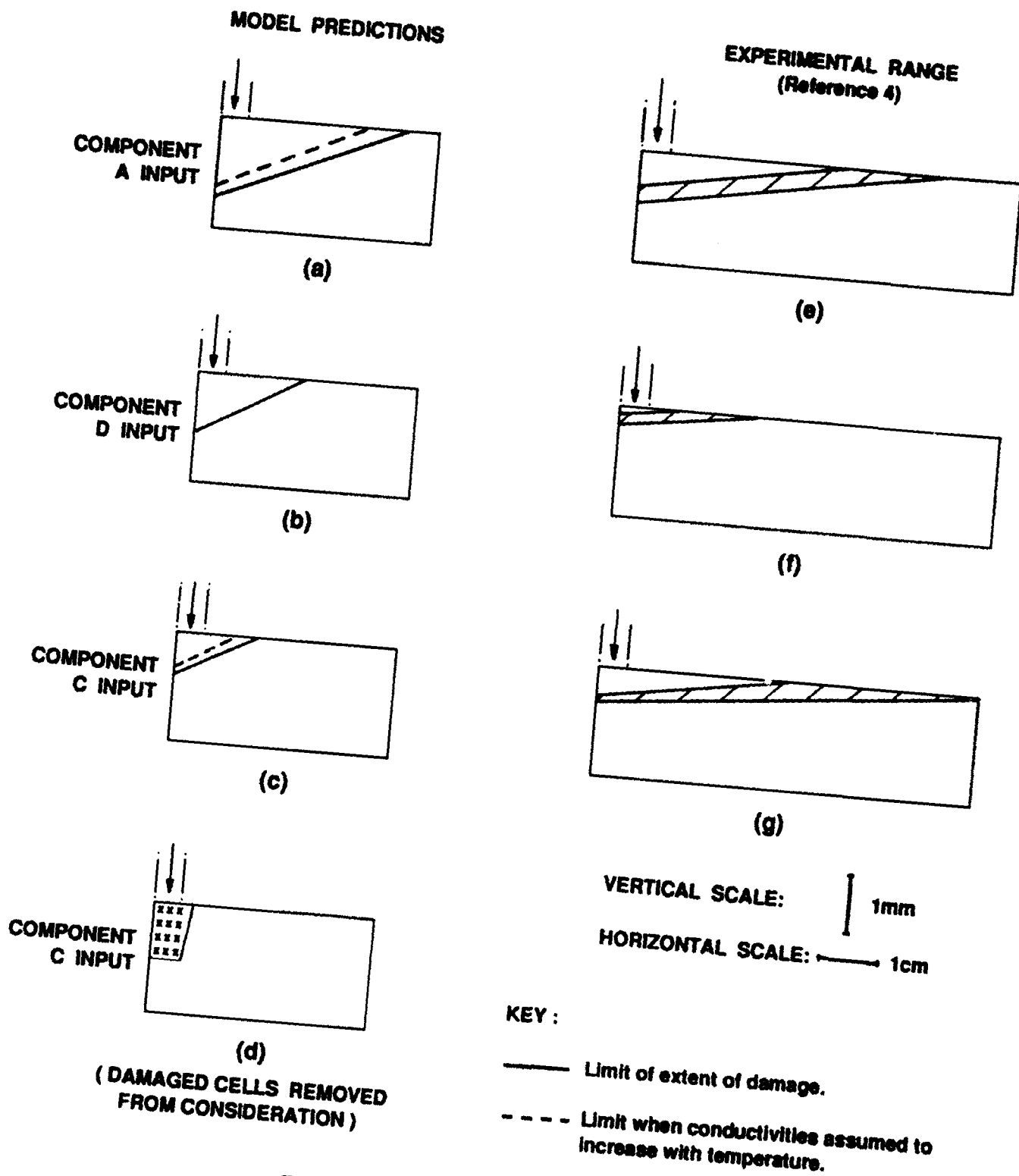


FIGURE 3: EXTENT OF DAMAGE

**COMPARISON OF THE DAMAGE FOR VARIOUS TYPES OF FIBRE
REINFORCED COMPOSITES DUE TO DIFFERENT LIGHTNING TEST STANDARDS
(MIL-STD-1757 A, GERMAN MILITARY VG-STANDARD 96903)**

J. Wiedmann and J.-U. Roth
Dornier Luftfahrt GmbH
P.O. Box 1303
D-7990 Friedrichshafen
Germany
Telephone (7541) 4961 or (7545) 84897 Fax (7545) 84411

A. Kern
Universität der Bundeswehr, München
D-8014 Neubiberg
Germany
Telephone (89) 6004-3940

ABSTRACT

This paper provides experimental results on the extent and nature of damage on various types of aircraft FRC (fibre reinforced composites) caused by lightning arc attachment. Two different lightning test parameter sets were applied corresponding to MIL-STD-1757A and the German military VG-standard 96903 part 71. Concerning direct effects, the VG-standard differs from MIL-STD especially in the higher action integral (10 MJ/Q), the most important damage parameter with respect to FRC. Lightning tests with VG-standard are not known yet. The various types of tested aircraft FRC comprise unprotected and protected CFC and SFC/CFC-hybrid structures as well as novel, multilayered electromagnetic structures. The visible damage areas caused by impulse currents are strongly correlated to the action integrals. Metal protection meshes seem to suffer more from higher action integrals than the underlaying structures. The protection effectiveness of a new homogeneous protection system is proved.

1. INTRODUCTION

The increasing use of nonmetallic materials in aircraft constructions in place of aluminium-structures is combined with a higher vulnerability to lightning threat. An overview to essential features of the damage behaviour of classical polymeric materials and composites caused by lightning stikes is given e.g. in [1-4]. Although the descriptions are based on a high number of laboratory tests, the analysis is limited as the tests are often not directly comparable due to different test apparatus, lightning simulations and test specimens. Nowadays, the international aerospace industry is testing uniquely according to MIL-STD-1757A. Recently [5] reported on extensive tests on a high number of unprotected and protected test panels made from different advanced aircraft materials and constructions. These tests showed that the damage behaviour is strongly dependent on applied materials and constructions. In [6, 7] investigations were performed on the dependance of visible damage in unprotected composites on lightning test parameters, especially the action integral, which is assumed in all reports to be the most important damage parameter with respect to FRC. A strong dependancy starting with a certain threshold level [7] could be shown. Although some attempts have been made in [1], [3] and recently in [8] to quantitatively describe the damage behaviour in FRC, no satisfying analysis and modelling is available. This is in contrast to the situation with metallic structures (compare e.g. [9] and [10]). A scaling to other than the special test conditions is not possible with FRC, and test parameters have been limited by the availability of suitable test benches to maximum MIL-STD-values.

Recently, for the equipment items and systems procured for or furnished to the German Federal Armed Forces, a new NEMP and lightning test standard has been defined [11]. Most important is a higher action integral (10 MJ/Ω) compared to MIL STD (2 MJ/Ω). A test bench for simulation of VG-standard lightning test parameters has been installed at German Federal Armed Forces University, Munich [9, 10, 16]. The VG standard refers to MIL-STD-1757 A as a minimum requirement for flying military aircraft.

The ongoing discussion about zoning and the tendency to extend the zone 1 region and to load further structural parts - occasionally made from FRC - with high lightning test parameters underlines the scope of this work.

The scope of this work is

1. To obtain some form of scaling factors for damage with increasing level of lightning threat parameters on unprotected and protected FRC, especially subjected to the severe VG lightning test standard. A direct comparison to the results in [5] will be provided.
2. To enlarge the knowledge about lightning damage to special unprotected electromagnetic aircraft structures used for low observability purposes.
3. To prove the efficiency of a novel homogeneous protection measure under severe VG 96903 test conditions.

2. LIGHTNING TEST STANDARDS

Standards for the simulation of lightning currents have to be based on the parameters of natural lightnings. For analysis and for classification of lightning currents, four threat parameters are defined, each characterizing specific effects of lightning:

- Peak current i_{max} , responsible for the ohmic voltage drops on stricken objects.
- Charge $Q = \int i \, dt$, leading to melting, vaporizing and welding by the electric arc at the point of stroke. Because of the different effects, the total charge Q_t has to be divided into the charge of the impulse current Q_i and the charge of the long duration current Q_l .
- Specific energy $W/R = \int i^2 \, dt$, also called the action integral, responsible e.g. for the heating and the electrodynamic forces of metal wires carrying the lightning current, or the disintegration of composites.
- Current rate-of-rise $\Delta i/\Delta t$ in the front of a lightning current, leading to electromagnetically induced voltages in installation circuits.

With respect to the subject of this paper, only three of these parameters have to be considered: i_{max} , Q (Q_i and Q_l) and especially W/R . The current rate-of-rise $\Delta i/\Delta t$ has no remarkable influence on meltings/evaporation and structural damage in FRC.

2.1 VG 96903 PART 71 - MIL-STD-1757A

The German military test standard VG 93903 part 71 [11], valid for planning and construction of systems and equipment for the "Bundeswehr", corresponds to the definitions of International Technical Commission (IEC), finally provided by the Technical Committee 81 (TC 81) of IEC [13]. Two test levels are determined here: level "high" covers about 99% of natural lightning, level "normal" about 95%.

The aerospace industry normally uses another standard for the simulation of lightning currents, the MIL-STD-1757A [12] or the SAE AE4L [14], respectively. These standards define a long duration current, which corresponds to the definitions of VG, but the impulse current shows remarkable differences. The parameters of the impulse currents and the long duration currents are listed in Table 1.

Table 1: Impulse Current Parameters of VG 96903 part 71, Level "high", and MIL-STD 1757A, Component A

Test Parameter	VG 96903 part 71 Level "high"	MIL-STD 1757A Component A
Peak Current i_{max}	200 kA \pm 10%	200 kA \pm 10%
Charge Q_i	100 C \pm 20%	1.)
Specific Energy $W/R = \int i^2 \, dt$	10 MJ/Ω \pm 35%	2 MJ/Ω \pm 20%

- 1.) Assuming an exponential decay of this impulse current, the impulse charge calculated with the values for i_{max} and W/R is given to $Q_i = 20$ C.

Table 2: Long duration current parameters of VG 96903 part 71, level "high", and MIL-STD 1757A, Component C

Test Parameter	VG 96903 part 71 Level "high"	MIL-STD 1757A Component C
Charge Q_1	200 C \pm 20%	200 C \pm 10%
Time T_1	0,5 s \pm 10%	0,25 s - 1,0 s

A comparison of VG 96903 part 71 and MIL-STD-1757A with natural lightning data is given in [10].

3. TESTHOUSES

The tests were conducted at two different testhouses. The tests in the former test programs [5] were conducted at the "Institut für Plasmaphysik (IPP)", University of Hanover (Germany) according to MIL-STD-1757A. A representative set of probe-types, subjected to MIL-STD peak current component A, was selected from the former programs. These probes were now reproduced and tested according to VG 96903 part 71 at the "Institut für Elektrotechnik" of the German Federal Armed Forces University in Munich. Additionally electromagnetic multilayer panels and a panel with a special protection system were tested at the Munich testhouse.

3.1 LABORATORY EQUIPMENT OF THE FEDERAL ARMED FORCES UNIVERSITY, MUNICH

3.1.1 Surge current generator

For the simulation of the impulse current according to VG 96903 part 71 and the exponentially damped impulse current according to MIL-STD-1757 A, a twin arranged surge current generator with crowbar sparkgaps has been recently realized by the "Institut für Elektrotechnik" at the Federal Armed Force University, Munich. A brief description with detailed information on test configurations, measurement tools and signal recording is given in [16]. Typical currents into metallic plates and protected FRC-panels obtained with this equipment and for proper choice of the internal resistance of the test bench are shown in fig. 1.

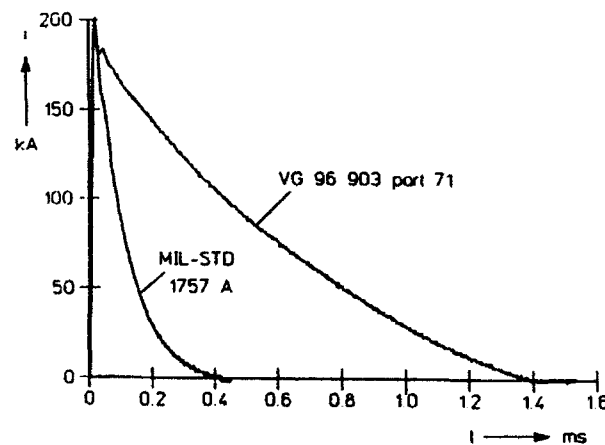


Figure 1: Typical Currents according to VG 96903 and MIL-STD-1757A for metal plates

The high VG-parameters, especially the impulse charge and the action integral of 10 MJ/Ω, could not be achieved in higher-ohmic panels, such as the unprotected CFC panels and the electromagnetic multilayer (EM) panels. In these cases the maximum achievable parameters were applied.

Due to the geometrical symmetry of the twin arrangement, the arc to the test sample burns uninfluenced by the external magnetic fields.

The test table with surrounding mounting frame limited the dimensions of the panels to 400 mm x 400 mm. Only one shot per panel was applied to prevent damage interferences. An insulated electrode was used with a spacing of about 45 mm.

3.1.2 Long duration current generator

The current of Fig. 2 with nearly rectangular wave shape is generated with the long duration current generator [10]. By means of an adjustable loading resistor different current amplitudes can be created. Lower conducting materials do not impose a restriction to these parameters.

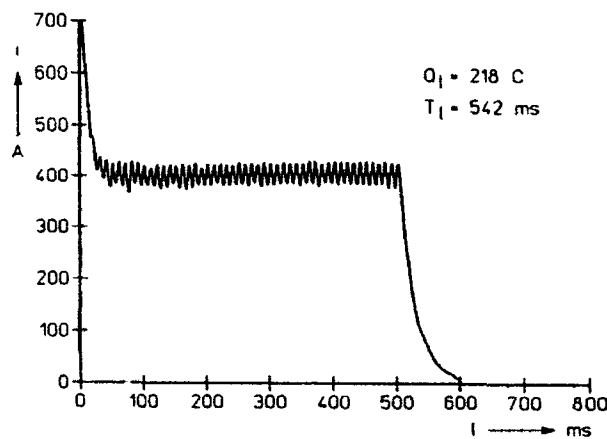


Figure 2: Typical long duration current

3.2 LABORATORY EQUIPMENT OF THE UNIVERSITY OF HANOVER

For impulse current simulation according to MIL-STD-1757A, component A, a capacitive surge current generator has been used, consisting of 96 capacitors, $4,6 \mu\text{F}/30 \text{ kV}$ each. Two capacitors are connected as a group in series. The maximum working voltage is 60 kV. The waveform of the impulse current is a damped sinusoidal oscillation with a basic frequency of about 8 kHz. Peak currents of 250 kA and specific energies up to $2,5 \text{ MJ}/\Omega$ can be achieved.

The test rig is similar to the one at the Munich testhouse.

A detailed description of the simulation of all current components according to MIL-STD-1757A is given in [15].

4. SPECIMEN DESCRIPTIONS

The tested specimens represent parts of typical aircraft fibre reinforced composite structures as well as novel multilayered electromagnetic aircraft structures.

The conventional structure test panels consisted of protected and unprotected CFC and SFC/CFC thermosetting hybrid specimens of 1 mm and 3 mm thickness.

The thermosetting electromagnetic structures (EM) test panels comprised different types of multilayered monolithic structures and three-to seven-layered sandwich structures. In this paper we report on two sandwich structures with total thicknesses of about 13 mm and 17 mm respectively, the other structures will be dealt with elsewhere.

The novel protection coating was applied to a 4 mm thick CFC test panel.

The specimens tested were flat panels with a dimension of 400 mm x 400 mm.

All tested panel-types are listed in Table 3.

Table 3: Overview of the tested specimen-types

Panel Type	Material	Protection Measure	Panel Thickness [mm]
1	CFC	Al-Mesh	1
2	CFC	Aramid Isolation Layer + Al-Mesh	1
3	CFC	unprotected	3
4	CFC	Al-Mesh	3
5	SFC/CFC	Al-Mesh	1
6	SFC/CFC	Al-Mesh	3
7	CFC	Electrolytic Copper Coating	4
EM 1	Sandwich	unprotected	13
EM 2	Sandwich	unprotected	17

4.1 CONVENTIONAL STRUCTURE TEST PANELS

The panels were designed using unidirectional prepreg layer systems. The prepreps consisted of carbon (CFRP) and aramid (SFRP) longfibre reinforced conventional epoxy resins.

The protected panels had an Al-mesh as protection measure. The Al-mesh used, was a 200 mesh type, which means that it has 200 wires each inch. The diameter of each wire is 0,077 mm and the specific weight of this mesh is 100 g/m².

The Al-mesh was always the first layer of the protected panels and was cocured with the structure. For panel type 2 an aramid mesh was used as an isolation layer between Al-mesh and CFRP.

The hybrid panels consisted of 50% CFRP and 50% SFRP.

All conventional structure test panels were painted on the front side with PUR primer and PUR finishing coat with a total thickness of about 120 µm. A 20 mm border around the test panels remained not painted.

4.2 MULTILAYERED TEST PANELS

The EM panels were designed according to structure mechanical requirements on aircraft and optimum radio-frequency performance.

The multilayer EM sandwich structures were fabricated using different types of fibres (quartzglass, SiC of different electrical conductivity, carbon) in either unidirectional or woven prepreg systems with conventional epoxy resins. Different types of honeycomb were applied: low dielectric constant Nomex honeycombs and gradient absorber honeycombs.

Figure 3 shows the principal structural design of the two sandwich structures considered here.

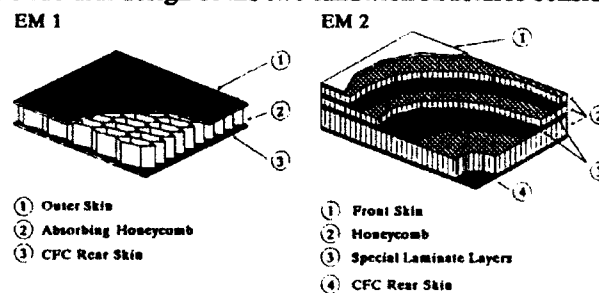


Figure 3: Principal structural design of the sandwich structures

The honeycombs were prepared around the plate with a 20 mm broad core-filling material so as to be able to fasten the test panels closely to the test rig grounding circuit.

Most of the EM panels were painted on the front side like the conventional test panels. Further EM panels were not painted, as in pretests it was found, that on behalf of the dielectric outer laminate layer in the EM panels, a thin aircraft paint has no identifiable influence on test triggering and the damage behaviour.

In the first test phase the dielectric first layer of some panels were drilled with a hole-diameter of 0,8 mm to ensure breakdown and to simulate the driving potential force in natural lightning. Later tests showed, however, that on the plate types reported here this measure was not necessary. Generally there was no influence of the holes to be observed on the damage behaviour.

4.3 SPECIAL PROTECTION SYSTEM

The protection system consisted of a multilayer coating with a homogeneous, electrolytically deposited Cu-layer with a thickness of about 14 to 20 μm . The CFC panel was first treated with gaseous SO_3 , a special primer and a very thin layer of a "chemically" deposited metal.

This coating should provide a very thin, efficient and weight-reduced protection layer compared to former plasma-sprayed or galvanically deposited Ni-coatings.

An additional paint was not applied.

5. LIGHTNING TESTS

TEST PANEL TYPES, TEST DATA AND DAMAGE

An overview of the tested panel types, the applied test standards and the current waveforms is listed in Table 4. The oscillating current waveforms of component A (MIL-STD-1757A) were tested in a former program.

Table 4: Overview of the test panels and the applied test standards

Panel Type	VG 96903 part 7: Impulse Current level "high"	VG 96903 part 71 Long Duration Current	MIL-STD-1757A Impulse Current Component A
1	X		oscillating current
2	X		oscillating current
3	X		oscillating current and unidirectional current
4	X		oscillating current and unidirectional current
5	X		oscillating current
6	X		oscillating current
7	X		
EM 1	(X)	X	
EM 2	(X)	X	

The charge data of these tests at the IPP in Hanover [5] were not registered. Based on the current recording an approximate value could be estimated (see below).

For the comparison of the conventional test panels in this paper, representative panels of each type were chosen. The listed damage in this paper is based on a visual analysis. Former programs and tests showed, that this procedure generally provides good results. More detailed damage investigations are still going on.

5.1 CFC TEST PANEL, 1 MM, PROTECTED WITH AL-MESH (TYPE 1)

This kind of panel is representative for aircraft fairing structures. It consists of 8 layers of CFRP, quasi-isotropically arranged and a layer of Al-mesh as protection system.

The test parameters according to component A (MIL-STD-1757A) and VG level "high" (VG 96903 part 71) and the structural damage of the panels are listed in Figure 4.

Test Parameter	MIL-STD-1757A Component A oscillating	VG 96903 part 71 "high" Impulse Current
Specific Energy W/R [MJ/Ω]	1,8	6,768
Charge Q [As]	≈ 20	63,03
Peak Current I _{max} [kA]	208	197,9

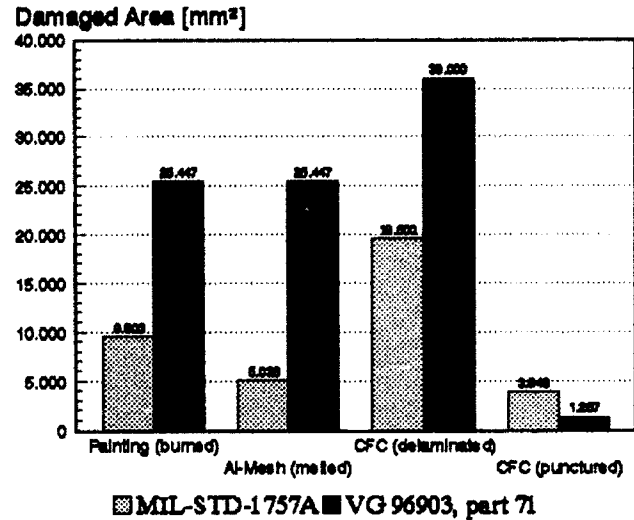


Figure 4: Test parameters and damage of panel type 1

5.2 CFC TEST PANEL, 1 MM, PROTECTED WITH AL-MESH, ARAMID ISOLATION LAYER BETWEEN CFC AND AL-MESH (TYPE 2)

This kind of panel differs from the test panels type 1 in chapter 5.1 only in an additional isolation aramid layer between CFC and Al-mesh. The reason for using such an isolation layer is the different electronegativity between CFC and Al, which causes corrosion of the Al.

Former tests showed that this configuration also has a damage reducing effect on the CFC, because the isolation layer prevents the current flow into the CFC-structure.

The test parameters according to component A (MIL-STD-1757A) and VG level "high" (VG 96903 part 71) and the structural damage of the panels are listed in Figure 5.

Test Parameter	MIL-STD-1757A Component A oscillating	VG 96903 part 71 "high" Impulse Current
Specific Energy W/R [MJ/Ω]	1,88	6,533
Charge Q [As]	≈ 20	62,56
Peak Current I _{max} [kA]	202	196,3

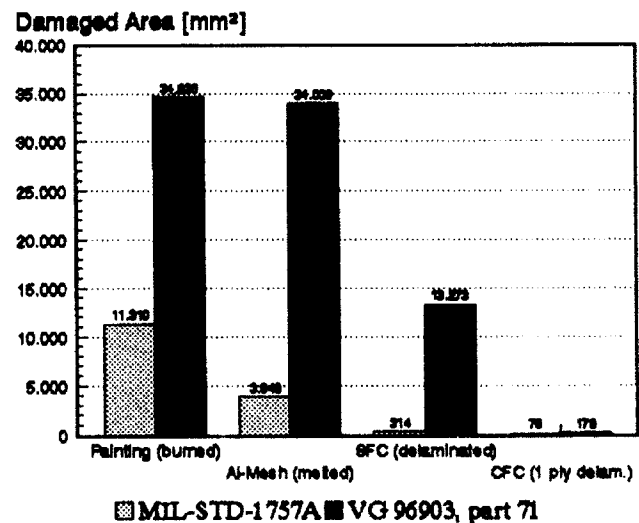


Figure 5: Test parameters and damage of panel type 2

5.3 CFC TEST PANEL, 3 MM, UNPROTECTED (TYPE 3)

This panel type is representative for an aircraft structure, whose damage by lightning strike is not flight-critical. An example for such a part is a CFC wing tip.

Additionally to the damage comparison between VG 96903, part 71 and MIL-STD-1757A (oscillating), a damage comparison between MIL-STD-1757A oscillating and unidirectional current waveforms was performed.

The test parameters and the structural damage of the panels are listed in Figure 6.

Test Parameter	MIL-STD-1757A Component A oscillating	MIL-STD-1757A Component A unidirectional	VG 96903 part 71 "high" Impulse Current
Specific Energy W/R [MJ/Ω]	1,8	2,39	3,97
Charge Q [As]	≈ 20	21,35	63,03
Peak Current I _{max} [kA]	215	199,5	196,7

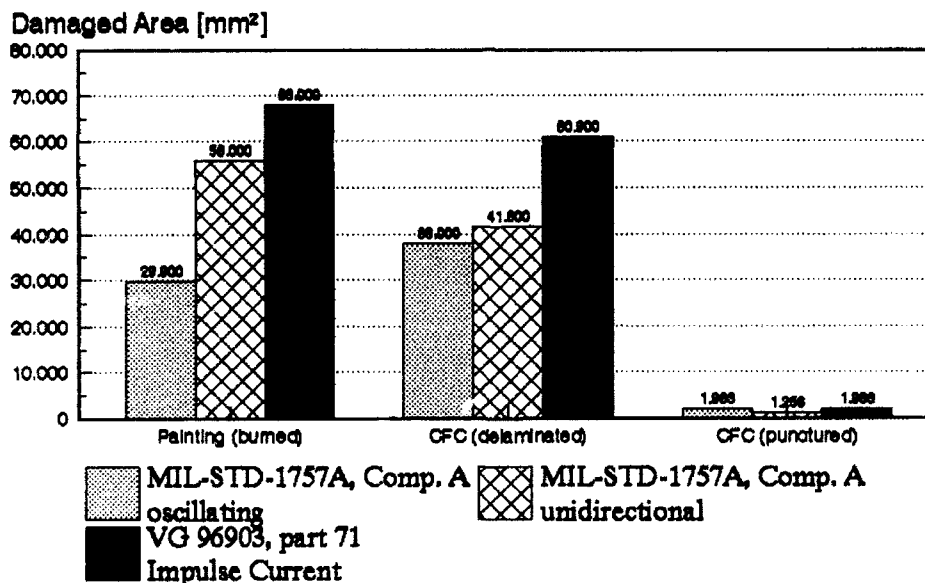


Figure 6: Test parameters and damage of panel type 3

5.4 CFC TEST PANEL, 3 MM, PROTECTED WITH AL-MESH (TYPE 4)

This panel type is representative for a primary aircraft structure, whose damage by lightning strike must be minimized, because a large structural damage could be flight-critical.

As with the tests with the unprotected CFC panels of 3 mm thickness, a comparison between MIL-STD-1757 A, component A, oscillating and unidirectional, and VG 96903, part 71 level "high" was performed.

The test parameters and the structural damage of the panels are listed in Figure 7.

Test Parameter	MIL-STD-1757A Component A oscillating	MIL-STD-1757A Component A unidirectional	VG 96903 part 71 "high" Impulse Current
Specific Energy W/R [MJ/Ω]	1,9	2,7	6,8
Charge Q [As]	≈ 20	25,43	66,58
Peak Current I_{max} [kA]	210	191,5	201,3

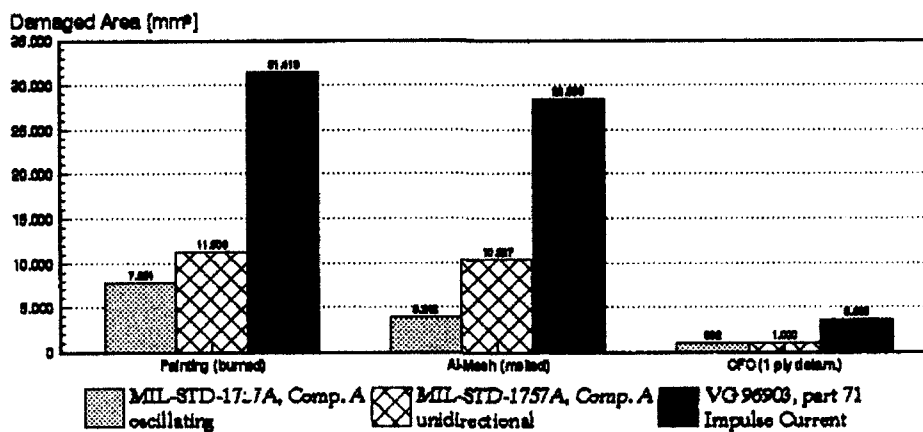


Figure 7: Test parameters and damage of panel type 4

5.5 HYBRID TEST PANEL, 1 MM, 50% CFRP, 50% SFRP, PROTECTED WITH AL-MESH (TYPE 5)

This panel type is representative for any kinds of fairings, which have no structural function but have to protect any underlying systems against lightning strike.

The test parameters according to component A (MIL-STD-1757A) and VG "high" (VG 96903 part 71) and the structural damage of the panels are listed in Figure 8.

Test Parameter	MIL-STD-1757A Component A oscillating	VG 96903 part 71 "high" Impulse Current
Specific Energy W/R [MJ/Ω]	1,98	6,959
Charge Q [As]	≈ 20	67,22
Peak Current I_{max} [kA]	200,5	203

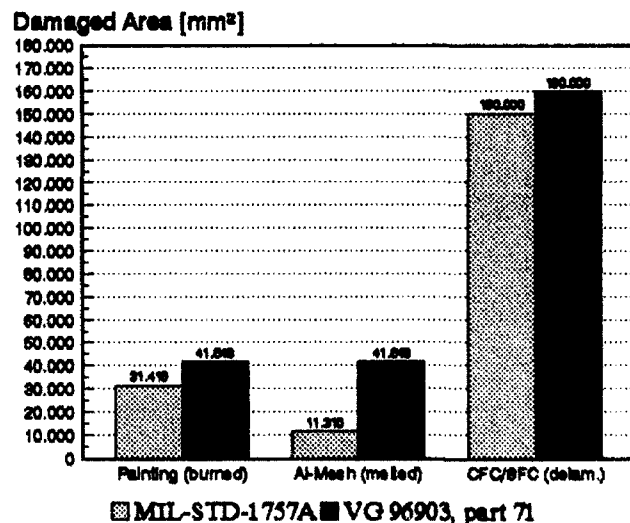


Figure 8: Test parameters and damage of panel type 5

5.6 HYBRID TEST PANEL, 3 MM, 50% CFRP, 50% SFRP, PROTECTED WITH AL-MESH (TYPE 6)

This panel type is representative for rudder or aileron structures, whose failure by lightning strike can be flight-critical. The test parameters and the damage are listed below. The test parameters according to component A (MIL-STD-1757A) and VG "high" (VG 96903 part 71) and the structural damage of the panels are listed in Figure 9.

Test Parameter	MIL-STD-1757A Component A oscillating	VG 96903 part 71 "high" Impulse Current
Specific Energy W/R [MJ/Ω]	2,0	6,714
Charge Q [As]	≈ 20	62,32
Peak Current I_{max} [kA]	200,5	201,3

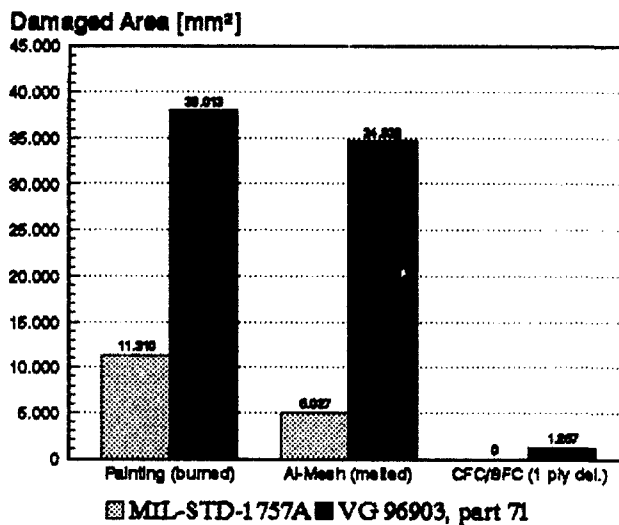


Figure 9: Test parameters and damage of panel type 6

5.7 CFC TEST PANEL, 4 MM, PROTECTED BY AN ELECTROLYTIC COPPER COATING (TYPE 7)

The novel Zone 1 protection system is especially applicable to complex contoured surfaces but also to FSS- (frequency selective surface) design, if lightning protection is of importance. It provides controllable, very thin, homogeneous copper layers.

Table 5: Test parameters of panel type 7

Test Parameter	VG 96903 part 71 "high" Impulse Current
Specific Energy W/R [MJ/Ω]	7,4
Charge Q [As]	75,2
Peak Current I_{max} [kA]	181,8

Test results:

- ◆ Copper coating
 - The coating is nearly totally evaporized within an area of about 28.000 mm²
 - Detached or peeled off parts of the coating in the outer region, within an area of maximum 57.000 mm²
- ◆ CFC panel
 - No visible damage
 - Microscopy: Some micro-delaminations only within first layer and within an area of about 4.000 mm²

5.8 ELECTROMAGNETIC SANDWICH STRUCTURE TEST PANEL, 13 MM, UNPROTECTED (TYPE EM 1)

Panel Type EM 1 represents a conventional constructional design (load-bearing) for low observability.

Table 6: Test parameters of panel type EM 1

Test Parameter	Impulse Current	Long Duration Current
Specific Energy W/R [MJ/Ω]	2,6	-
Charge Q [As]	44,3	155,0
Peak Current I_{max} [kA]	116,0	-
Time T_1 [s]	-	0,40

Test results:

1. Impulse Current (panel 1)

Catastrophic failure of the total panel

- Total separation of front-dielectric from absorber-honeycomb and rear skin
- big areal delaminations and failure/fracture of the skins
- front laminate: deep delamination and puncture within 25.000 mm², (hole-punctured area about 300 mm²)
- rear CFC-laminate: deep delamination and puncture within 14.000 mm² (hole-punctured area about 100 mm²)
- honeycomb: carbonized area of 11.000 mm². Honeycomb lifted from skins, only small remaining attachment areas on the panel borders.

2. Long Duration Current (panel 2)

- Small hole-punctures: front skin 15 mm², rear skin 1,3 mm² (corresponds to area of partial pre-drilling).
- Black smouldered traces in painting within 175 mm².

5.9 ELECTROMAGNETIC SANDWICH STRUCTURE TEST PANEL, 17 MM, UNPROTECTED (TYPE EM 2)

This EM sandwich structure panel represents an aircraft load bearing structure for broadband camouflage.

Table 7: Test parameters of panel type EM 2

Test Parameter	Impulse Current	Long Duration Current
Specific Energy W/R [MJ/Ω]	1,4	-
Charge Q [As]	15,1	157,0
Peak Current I_{max} [kA]	180,0	-
Time T_1 [ms]	-	500

Test results:

1. Impulse Current (panel 1)

Table 8: Test results with application of impulse currents

Panel-Layer	Damage
painting	no smouldering or colouring. Partly cracked away together with first layer segments
front skin	delamination of first layers, area 71.000 mm ²
first honeycomb	disintegration from front skin, partly damaged, area 14.000 mm ²
rear skin	vast delamination of last layers
deep delamination with puncture	area 12.000 mm ²

2. Long Duration Current (panel 2)

Table 9: Test results with application of long duration current

Panel-Layer	Damage
painting	smouldering within area of 3.800 mm ²
front skin	hole puncture 24 mm ² , small delaminations within 700 mm ²
rear skin	hole-puncture 12 mm ² , small delaminations within 1.900 mm ²

In impulse current tests, delamination areas and cracking of layers are observed to follow the unidirectional SiC-fibre orientation. Lift off and cracking has areal characteristics, single SiC fibre - and SiC filament - disintegrations cannot be found. A further analysis into non-visible damage is underway. Additional tests with lower action integrals show reduced damage areas in first honeycomb layer and especially in the deep delamination and puncture damage zones.

6. EVALUATION OF THE TEST DATA

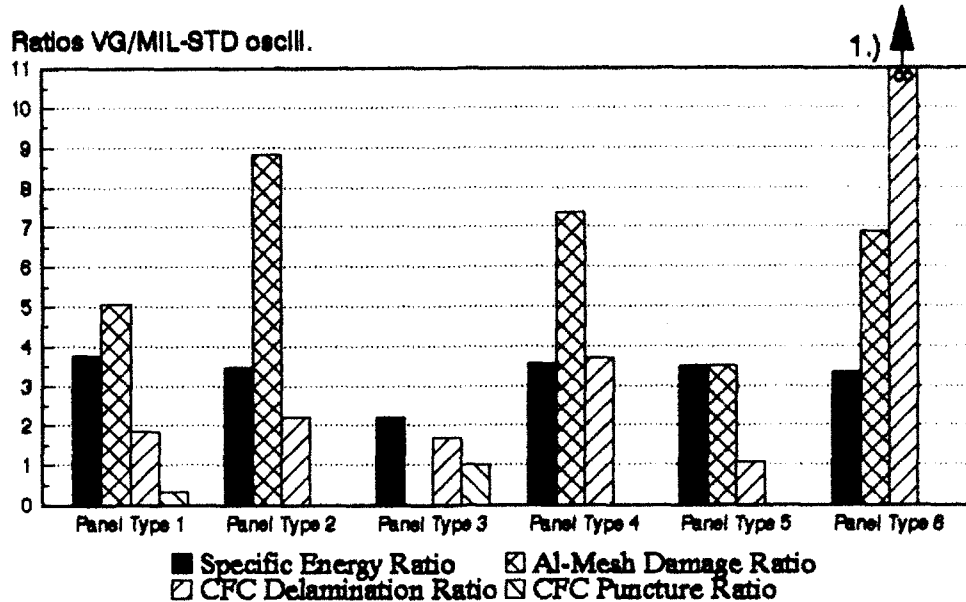
Panel types 1 - 6 were tested to compare the damage caused by the different impulse current test standards. For each of these conventional panel types, Fig. 10 shows the specific energy ratio and the resulting damage area ratios. The specific energy of the tests according to VG 96903 part 71 was standardized with the corresponding specific energy of the MIL-STD-1757A, component A tests. Just as the damaged areas due to the VG 96903 part 71 tests were standardized with the corresponding damaged areas due to the MIL-STD-1757A tests.

Fig. 10 shows that the specific energy of the VG-tests was between 2,1 and 3,8 times higher than the specific energy of the MIL-STD tests.

The ratios of the damaged Al-mesh areas had the same size or were even bigger than the corresponding specific energy ratios for the protected panel types.

For panel types 1 - 5 the ratios of the delaminated CFC or CFC/SFC damage areas show equal or smaller ratios than the corresponding specific energy ratios. Panel type 6 shows an infinite ratio. The reason for this misleading value is the undamaged SFC/CFC-structure (damaged area = 0) of the panel type 6 due to the MIL-STD test.

The ratios of the punctured structure areas of panel type 1 and 3 are smaller than the specific energy ratios.



1.) Infinite ratio of the delaminated CFC areas because the structure of this panel type did not show any damage after the test according to MIL-STD-1757A oscillating current waveform.

Figure 10: Specific energy ratios (VG/MIL-STD oscill.) and corresponding structural damage ratios (VG/MIL-STD oscill.) of the conventional test panels, type 1 - 6

The comparison between VG-standard and MIL-standard tests shows that especially the Al-mesh was over-proportionally damaged by the higher test parameters of VG. The delaminated areas of the CFC or SFC/CFC test panels also grew with the specific energy ratio, but maximally with the same ratio as the corresponding specific energy ratio. The number of delaminated plies remained virtually uninfluenced by the higher test parameters of VG. The punctured areas of panel type 3 did not show any dependance on the specific energy, while the punctured areas of panel type 1 were smaller although the specific energy was higher. In order to clarify the influence of the different lightning parameters on the damage the correlations between the parameters in the experiment seem to be important.

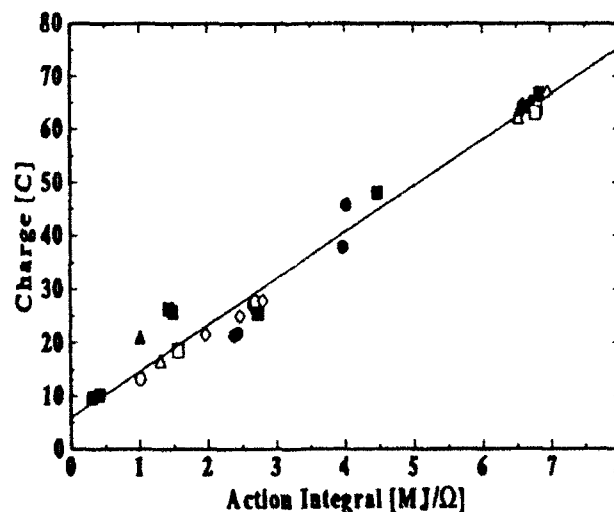


Figure 11: Dependency of the charge on the specific energy of the tests at the Munich testhouse

Fig. 11 shows a linear dependency of the charge on the specific energy in the tests according to VG and MIL-STD unidirectional current waveform (Munich testhouse). According to these standards we chose approximately the same maximum currents while varying the action integral. In consequence, these tests do not allow a discrimination between the influences of the charge and the action integral. In the experiment of Reid [6] the peak current seems to be correlated with the action integral.

Nevertheless, in both cases the damaged area is proportional to the action integral, thus stressing the importance of this parameter for damage behaviour of FRC.

Including additional tests Fig. 12 shows the dependency of the damaged area on action integral (exemplary) for protected and unprotected 3 mm CFC panels.

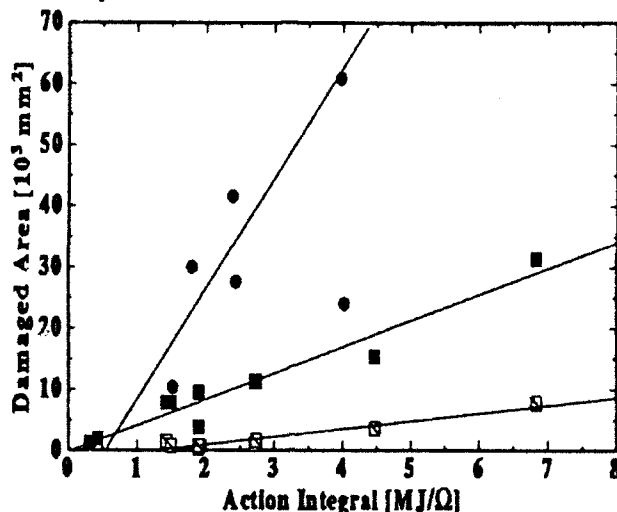


Figure 12: Dependency of the damaged area on action integral

• 3 mm CFC panels, unprotected
 □ 3mm CFC panels, protected: ■ Al-mesh, □ CFC

The data show that the mesh system of the protected panels seems to be most sensitive to an increasing action integral. A strong dependence is found for unprotected structures, too. The absolute values of the damaged area of course depend, on the type of materials and, in the case of EM structures, on the structural design.

The comparison between MIL-STD-1757A, component A, unidirectional and oscillating current waveforms (Fig. 13) shows the same trend as observed above. The higher specific energy of the unidirectional impulse current test had a strong influence on the damaged Al-mesh area (Panel type 4), while the structural damage of the CFC was nearly the same (Panel type 3 + 4). Having exactly the same specific energy, there seems to be no difference between a unidirectional and an oscillating impulse current waveform with respect to the structural damage.

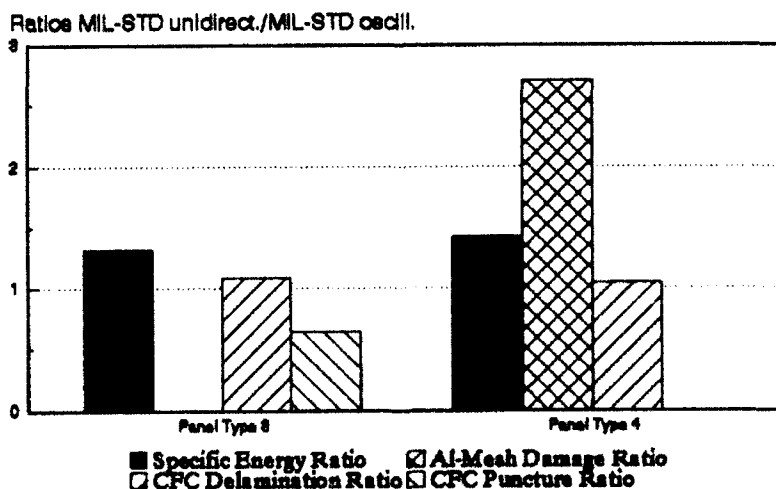


Figure 13: Specific energy ratios (MIL-STD unidirect./MIL-STD oscill.) and corresponding structural damage ratios (MIL-STD unidirect./MIL-STD oscill.) of the conventional test panels, types 3 + 4

The electrolytic copper coating panel shows an enlarged damage area of the protection system compared to conventional mesh-type systems, probably resulting from a higher isotropic current conduction ability combined with a wider areal spread of lightning energy.

The main advantage lies in the negligible effects of lightning on the basic CFC structure.

On basis of a comparable effective resistance, the electrolytic copper layer shows a certain weight-disadvantage with respect to Al-meshes, which could be overcome on the one side by even thinner and/or perforated copper-layers. On the other side it is known from copper meshes that a comparison of effective resistances alone may lead to wrong conclusions. Generally copper seems to have a better weight specific protection ability than aluminium.

If not protected, the multilayered electromagnetic aircraft structures are damaged by impulse currents to an unacceptable degree. The visible damage is strongly dependant on the type of multilayer structure. With honeycombs, big areal disintegrations and critical implosions of internally built gas-pressures may occur. There are also indications that damage areas are stronger correlated with the action integral. The deep damage areas with puncturing seem to be more extended within EM-sandwich structures than in unprotected 3 mm CFC panels under comparable test conditions.

The long duration current causes local small punctures of the EM sandwich panels with only small damage potential to the structure.

7. CONCLUSION

- ◆ The tests and their interpretation show that the damage of the conventional aircraft FRC test panels are strongly correlated with the action integral. Especially the protection system (Al-mesh) seems to be over-proportionally concerned by the much higher specific energy of VG 96903 test standard, whereas the damage in underlying CFC and SFC/CFC parts increases not in the same manner as the Al-mesh damage. But the damage of the Al-mesh is generally not critical for the structural integrity of the panel.
This leads to the conclusion that conventional FRC aircraft structures with sufficient thickness and protection measures can withstand an impulse current according to MIL-STD-1757A as well as an impulse current according to VG 96903 part 71 level "high" without flight-critical damage. However detailed investigations and tests have to be performed with respect to special applications.
- ◆ The electrolytic copper protection system demonstrates a very high protection effectiveness under severe VG test conditions. Its application to complex contours offers advantages over other conventional homogeneous protection systems.
- ◆ The multilayered EM structures suffer from intolerable impulse current damage, which also seems to be correlated the action integrals. Protection measures for Zone 1 and Zone 2 applications are inevitably necessary for those structures.
- ◆ Further investigations are necessary to fully understand the results on a microscopic level and to model satisfactorily the lightning attachment and damage processes.

8. ACKNOWLEDGEMENT

This study was funded by the German Ministry of Defence (MOD). The authors gratefully acknowledge the financial and administrative support of German MOD.

9. REFERENCES

- [1] F.A. Fisher and J.A. Plumer, "Lightning Protection on Aircraft", NASA Reference Publication 1008 (1977)
- [2] F.A. Fisher, J.A. Plumer, R.A. Perala, "Aircraft Lightning Protection Handbook", Report No. DOT/FAA/CT-89/22 (1989)
- [3] S.D. Schneider et al., "Vulnerability/Survivability of Composite Structures to Lightning Strike", Report AFFDL-tr-77-127 (1978)

- [4] S.D. Schneider, "Lightning Protection Considerations on Graphite/Epoxy Aircraft Structure", AGARD-Report 14 (1980)
- [5] S. Krause and T. Thiele, "Comparison and Estimation of Basic Tests at Different Lightning Strike Protection Measures..", Paper presented at 1989 ICOLSE, Bath, UK (1989)
- [6] G.W. Reid, "Investigations into the Damage for Various Types of Unprotected Carbon Fibre Composites with a Variety of Lightning Arc Attachments", Paper presented at 1991 ICOLSE, Cocoa Beach, Florida (1991)
- [7] A.V. Isakova et al., "Investigation of Damages Pattern in Dielectric Radomes of Flying Vehicles Struck by the Lightning", Paper presented at 6th European Electromagnetic Structures Conference, Friedrichshafen, Germany (1991)
- [8] V.A. Avrotsky et al., "Electrical Characteristics of Graphite Epoxy Composites and their Lightning Protection", Paper presented at 20th ICLP, Interlaken, Switzerland (1990)
- [9] A. Kern, "The Heating of Metal Sheets Caused by Direct Lightning Strikes - Model and Measurement", Paper presented at 20th ICLP, Interlaken, Switzerland (1990)
- [10] A. Kern, "Simulation and measurement of melting effects on metal sheets caused by direct lightning strikes", Paper presented at 1991 ICOLSE, Cocoa Beach, Florida (1991)
- [11] VG 96 903 part 71/08.89: "NEMP and lightning protection". Test methods, test equipment and limiting values
- [12] MIL-STD 157 A: "Lightning qualification test techniques for aerospace vehicles and hardware"
- [13] IEC TC 81; CO paper 15/91: "Protection against LEMP". Part 1: General principles
- [14] SAE AE4L, "Protection of aircraft electrical/electronic systems against the indirect effects of lightning", Committee report, Feb. 1987
- [15] K. Woihe (ed.), G. Boes, T. Thiele, "Entwicklung und Prüfung von Blitzschutzsystemen für faserverstärkte Kunststoffe", Berichts-Nr. SK80-119/82 (1982)
- [16] W. Zischank, "A surge current generator with double-crowbar sparkgap for the simulation of direct lightning stroke effects", ISH Braunschweig, Paper No. 61.07 (1987)

LIGHTNING CHARACTERISTICS IN THE NORTH-EAST PART OF JAPAN OBSERVED BY A MAGNETIC DIRECTION-FINDER NETWORK

N. Honma and H. Komuro
Electricity Technology Research and Development Center
Tohoku Electric Power Company, Inc.
Sendai, Japan
Telephone (022) 278-0356 Fax (022) 278-2176

M. Ishii and J. Hojo
Institute of Industrial Science, University of Tokyo
Tokyo, Japan
Telephone (03) 3479-1949 Fax (03) 3402-5078

ABSTRACT

Observations of lightning ground flashes have been made by a magnetic direction-finder network in the Tohoku region, located in the north-east part of the island of Honshu in Japan. The performance of this system has been evaluated and improved through close observations and ongoing analysis.

Based on the data obtained to date, the density and the polarity of ground flashes were analyzed, focusing on various geographical and seasonal variations. It was concluded that the surrounding sea was the primary factor affecting ground flash characteristics.

INTRODUCTION

Due to Tohoku Electric Company's need to monitor lightning activity in the north-east part of Japan, two magnetic direction-finder systems were installed along the coast of the Japan Sea, at Niigata in 1986 and at Akita in 1987. Each system then consisted of three direction-finders (DFs) and a position analyzer (PA). This system was capable of providing wide-area, real-time registration of lightning parameters along with the location of lightning flashes. The DF's installed were especially capable of identifying cloud-to-ground flashes based on electromagnetic waveform discrimination criteria.

From the experience with the above system, seasonal lightning characteristics along the coast of the Japan Sea were quantitatively identified (1). An IKL map was produced from the observation results, therefore providing the necessary basis for an improved design of lightning resistant transmission lines.

The original systems, however, could not always accurately sense the electromagnetic fields of winter lightning flashes and had a finite dynamic range. In order to solve this problem, we designed and reconstructed the Tohoku direction finder network in 1991.

In this paper, we describe the improvements made to Tohoku Electric's magnetic direction-finder network, and evaluate its performance. Based on our observations from

August, 1991 to May, 1992, the analysis of ground flash density and polarity reveal that geographical and seasonal characteristics in the region, especially those of the surrounding sea, are significantly related.

IMPROVEMENTS OF THE DIRECTION-FINDER NETWORK

Plans for improving the direction-finder network first targeted raising the detection efficiency of winter lightning. In addition, expansion of system coverage area was needed with increased location accuracy.

The detection efficiency of a system depends on the configuration of DFs, their sensitivity, dynamic range and electromagnetic waveform discrimination criteria which identify cloud-to-ground lightning flashes. The most influential parameters of the waveform discrimination criteria are overshoot against the reverse polarity after the peak (bp) and the peak-to-0 time (tz). We were able to improve the detection efficiency in winter by changing bp up to 1.0 and tz down to $6\mu\text{s}$ based on a history of electromagnetic wave forms recorded in Niigata. The dynamic range of the DF sensitivity was doubled by cutting the threshold level down to 50% of the standard of medium gain, thereby decreasing the minimum threshold of the combined system to 10kA. Thus the mean distance between DFs was extended from 65km to 135km.

Lightning location accuracy also depends on the configuration of the direction-finder network. Tohoku has many mountains, plains and basins scattered throughout the region. We installed nine DFs on plain areas, with low background noise levels, keeping a safe distance from rivers and transmission lines. Adjacent DFs were situated to form quasi-equilateral triangles, which was found to be their optimal configuration. Furthermore, the new direction-finder network was placed under the unified control of a new version of Advanced Position Analyzer (APA). Fig.1 shows the configuration of the new network.

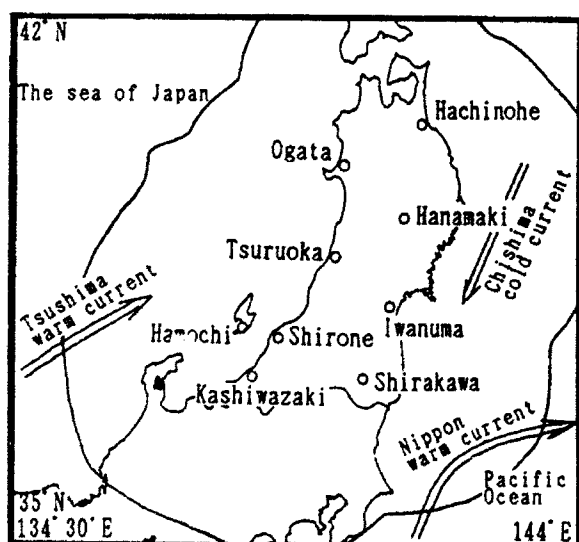


Fig.1. Configuration of the Tohoku direction-finder network. The solid line encloses the region where coverage of two or more direction-finders overlap.

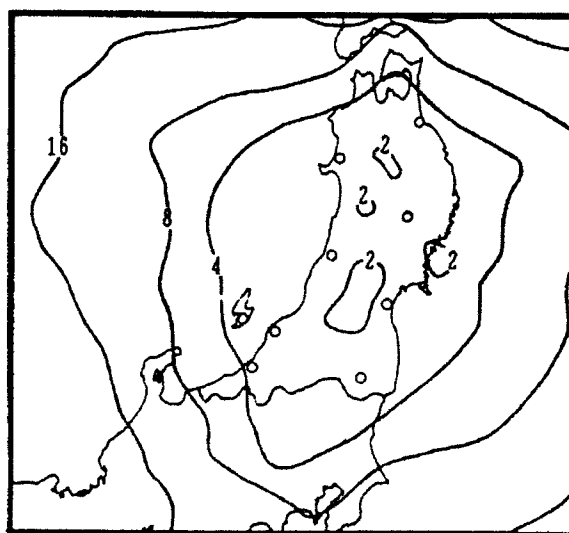


Fig.2. Projection of the flash location accuracy of the network. The solid line encloses the area where semimajor axis is less than the number of km.

LOCATION ACCURACY OF THE NETWORK

To improve the location accuracy of the system, it is necessary to reduce the site errors of DFs. In this paper, we assume that the true flash location is the same as that calculated by APA using the chi-square minimizing method. (2)

Optimizing parameters include the semimajor axis of the error ellipse, ratio of semimajor to semiminor axis and minimized chi-square. The error ellipse indicates a 50% range of the estimated error around the optimal flash location. We could evaluate the site error by assigning a correction value to change the flash bearing by DFs to the optimal location.

APA has the ability to recalculate flash locations from the stored DF data, based on the database in which site error correction values were decided.. By applying this APA function, we were able to get corrected flash location data, evaluate the effect of DF site error correction and calculate improved correction values. When the procedure was repeated, highly optimized flash location data was obtained.

In order to evaluate the practical flash location accuracy, we analyzed the distribution of semimajor axis, measured from August, 1991 to May, 1992. Fig.2 shows that most values of the semimajor axis of the error ellipse on land in the Tohoku region are 2 or 4km.

GROUND FLASH DENSITY

The observation period from August, 1991 to May, 1992 was, for our purposes, divided into three seasons: SUMMER - August/September, 1991; WINTER - from October, 1991 to March, 1992; and SPRING - April/May, 1992. The seasonal characteristics of ground flash density were then studied.

Figs. 3a, 4a and 5a show the seasonal contour lines of flash density over Tohoku, determined by subdividing each degree of latitude and longitude into quarters and counting the number of ground flashes in each quarter of the resulting grid.

Fig.3b, 4b and 5b show 1 °C-isotherms of sea surface temperature, per season, based on the observation data from the meteorological satellite on the 10th day of each month.

As shown in Fig.3a and b, summer lightning was rather inactive in the observation period due to unusually low temperatures for those months. The figures show that most ground flashes occurred over land, being clustered, especially, over more southern land areas where air temperature is higher and lightning activity greater (ground flash density of 1.0). This results from air temperature immediately over land being considerably higher than the sea surface temperature in summer.

Fig.4a and b show that winter lightning activity is quite different from that of summer lightning. Ground flashes rarely occurred above land except along the Japan Sea coast. Main flash areas are near the coast on the Japan Sea and off the southern coast of the Pacific Ocean.

In each area, a warm current is flowing with a higher sea surface temperature. In general, ground flash activity in winter is lower than summer with maximum activity of 0.04

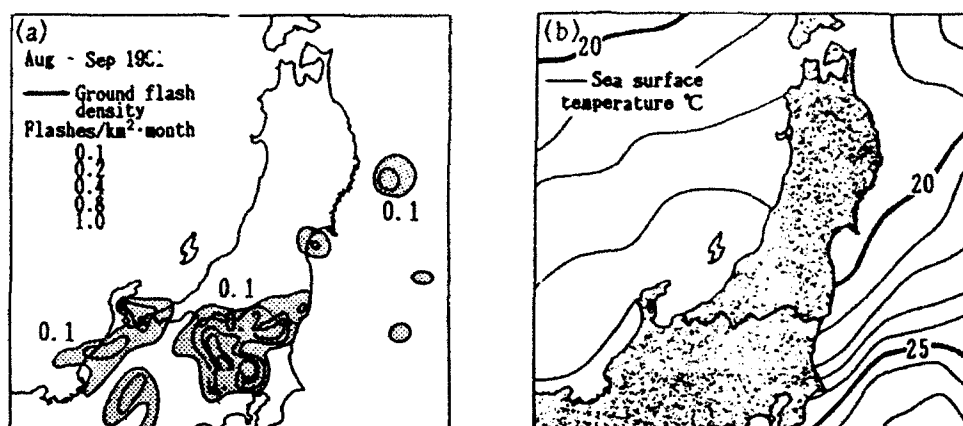


Fig. 3a,b. Distribution of ground flash density and sea surface isotherms in summer (August/September, 1991)

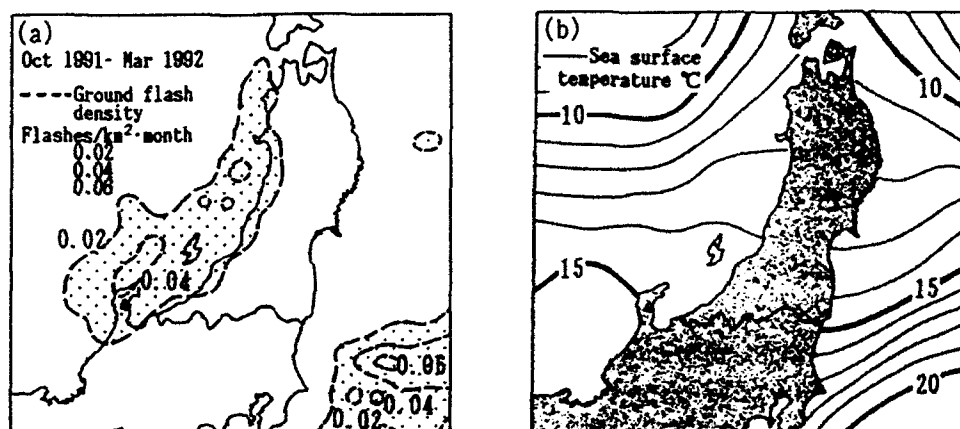


Fig. 4a,b. Distribution of ground flash density and sea surface isotherms in winter (October-December, 1991, January-March, 1992)

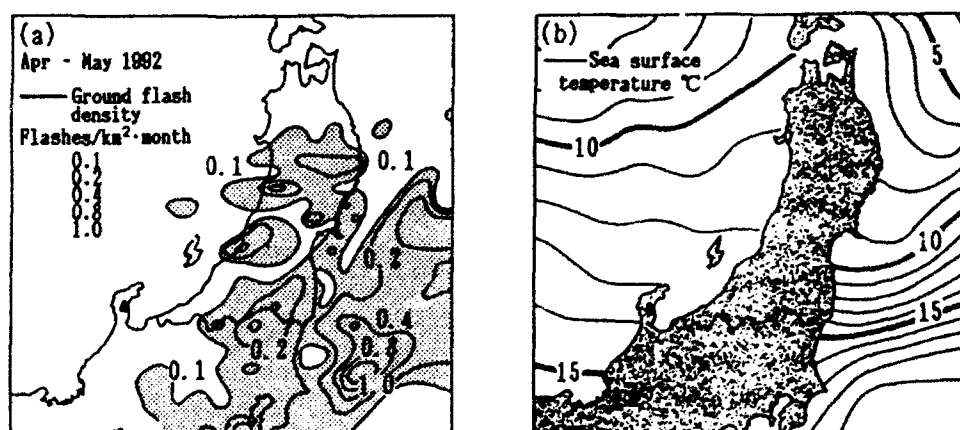


Fig. 5a,b. Distribution of ground flash density and sea surface isotherms in spring (April/May, 1992)

on the Japan Sea side and with maximum activity of 0.06 on the Pacific side. The values in winter are less than 10% of those in summer. In winter, a clustered ground flash characteristic, recognized in summer, is not seen, and broad contours appear.

These characteristics correspond to the results reported on the unique lightning behavior in winter on the Japan Sea side. As shown in Fig.4a, lightning area shifts 30km inland off the Japan Sea. This shift is explained as follows. In winter, the temperature above land is lower than that above the sea surface, which produces no lightning. On the other hand, the sea surface temperature is higher than the cold air mass passing over the sea and the air mass absorbs energy to generate lightning. Thunderstorms occurring over the sea are moved by the westerlies toward land. Above land, the energy required to generate lightning is not present and, therefore, lightning diminishes. This is the reason for winter lightning above land being in a diminishing stage.

As for the lightning occurring on the Pacific side, the lightning area is seen to shift 50km east. This is explained as follows. The cold air mass passes over the land and reaches the sea. This cold air mass absorbs energy from the sea where the sea surface temperature is higher and lightning is generated.

Thus, the 30km on-shore activity area is the distance where thunderstorms land, move inland and diminish. The 50km off-shore activity area is the distance where the cold air mass leaves the coast, and is moved by the westerlies until it generates lightning,

Fig.5a shows the mixed characteristics of both summer and winter lightning usually found in spring lightning. As for ground flash density, the southern Pacific side have maximum values that exceed 1.0/sq.km/month. It is notable that the ground flash density above sea, in some areas, exceeds that of summer above land. Over the Japan Sea, just off the coast, weak lightning activity occurs similarly to that in winter, but the contour line of the ground flash density is not indicated in the figure, because the activity is not significant when compared with that above land or over the Pacific. It is also shown that, on the Pacific side, there exists areas where lightning activity is very low. Perhaps this is due to the cold current that flows southward along the coast, and its very low sea surface temperature near the coast. In this observation period, lightning activity was unusually active due to the rapid development of the seasonal cyclone.

Fig. 6a shows the projection of the flashes in which the cyclone statically developed, swirled in the north, and its outer effect covered the whole of Tohoku region. Fig. 6b and c show meteorological maps.

It is concluded that the distribution of ground flash density in the Tohoku region has different profiles depending on the season and that these characteristic differences are greatly influenced by the surrounding sea.

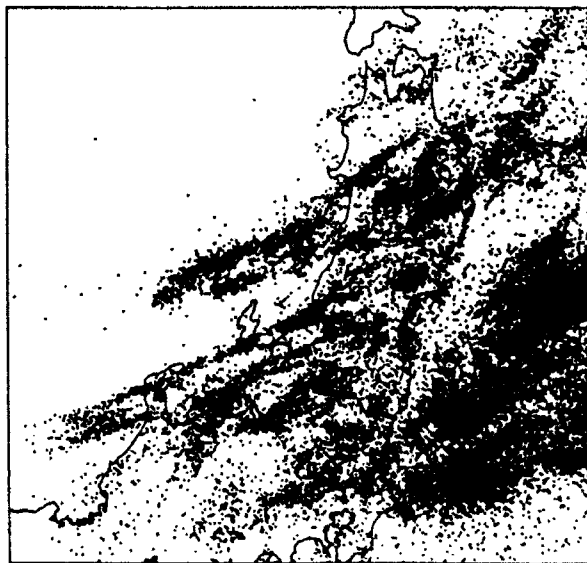


Fig.6a Projection of ground flashes, May 22, 1992. Note the concentration of flashes like spiral arms around the cyclone.

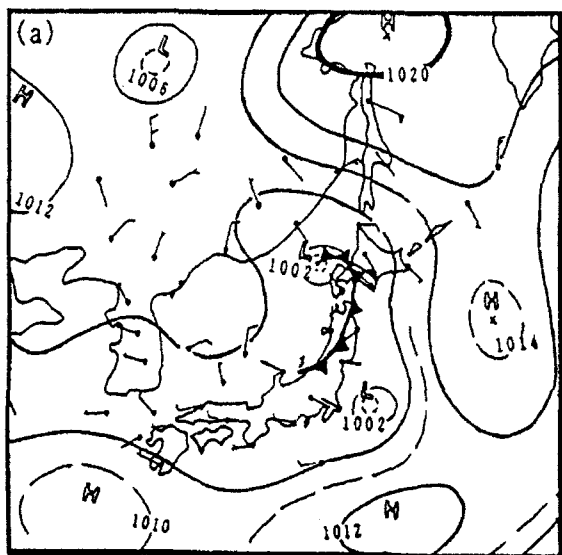


Fig.6b. The surface map for 1200 UTC, May 22, 1992. indicating the position of the cold front.

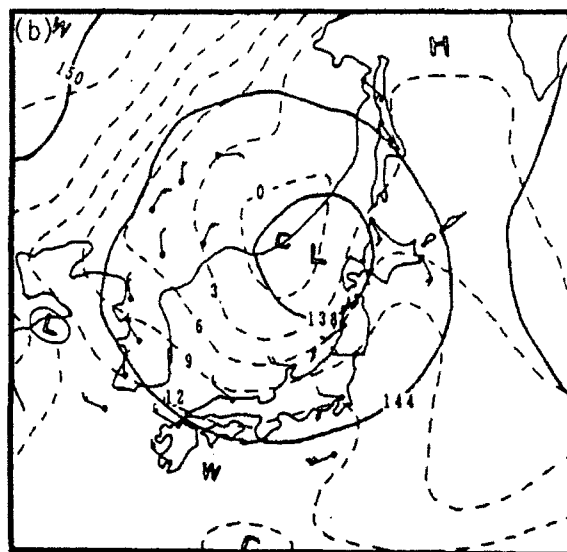


Fig.6c. The 850 mb map for 1200UTC, May 22,1992. Cold air is advecting over the region.

POLARITY

Fig.7 shows the high ratio region where positive lightning flashes exceed 20% in the observation period from August, 1991 to , 1992. However, it was too difficult to see any significant pattern. Further investigation was needed on a unique thunderstorm that could show the regional characteristics of polarity much more clearly.

Fig.8 (next page) shows such a thunderstorm. It occurred on November 3 and 4, 1991. The storm slowly developed along a cold front with minor lightning activity in the northern Japan Sea, 400km northwest of Tohoku. The storm was not highly active until about 2000 JST on November 3 when the number of flashes began to increase. As the front moved to the east and south, a clustered band of lightning activity became evident. By about 0000 JST, the cold front had moved further eastward to just off the coast with a small amount of lightning activity over parts of northern Tohoku.

Fig.9a shows the hourly change of the number of positive and negative flashes and the ratio of positive flashes per hour to total flashes per hour in the same thunderstorm of November 3 and 4. The highest frequency of negative flashes (1700 in the middle stage) was seen at 0000JST on

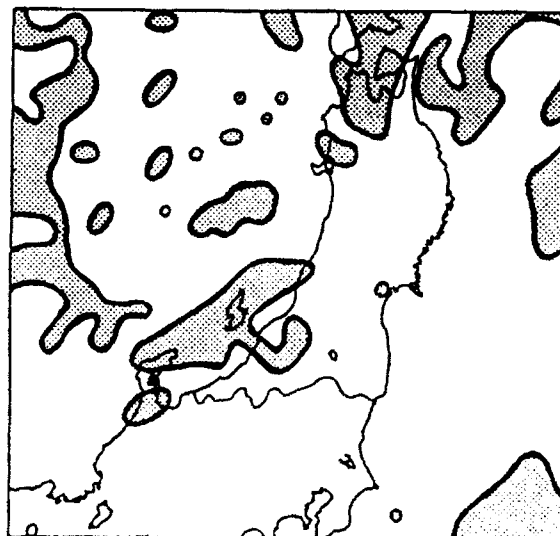


Fig.7. In the gray area, the ratio of positive flashes exceeds 20%.

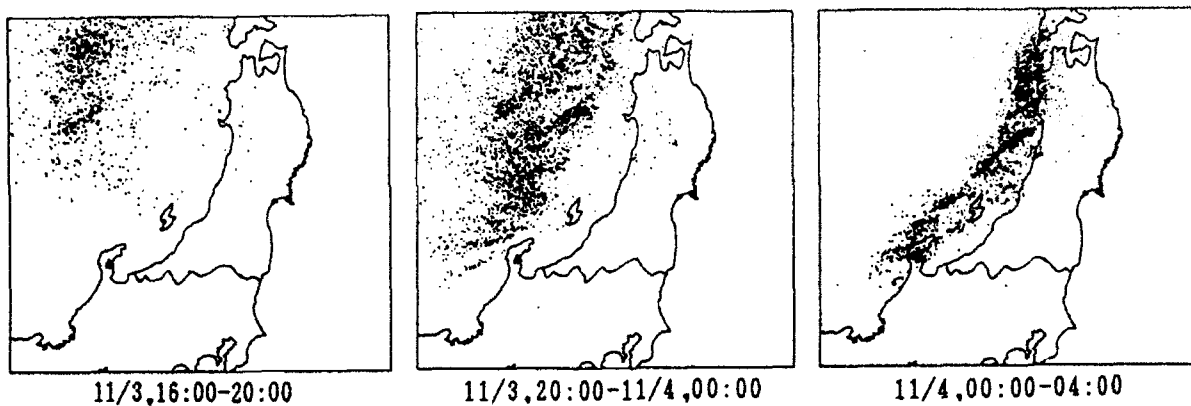


Fig.8. Projection of the progressing cold front of the November 3 and 4, 1991 thunderstorm.

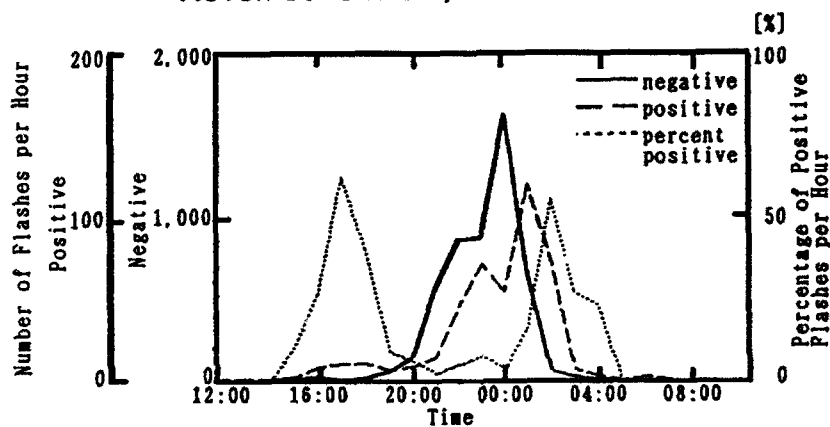


Fig.9a. Number of negative and positive flashes per hour (left axis) and percentage of positive flashes (right axis) for each hour of the November 3,4, 1991 thunderstorm.

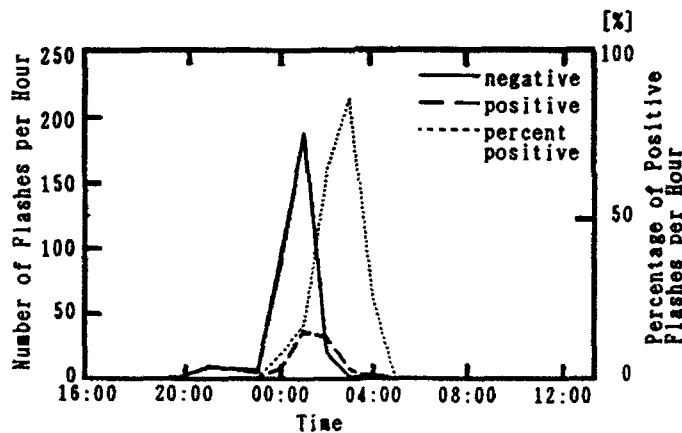


Fig.9b. Number of negative and positive flashes per hour (left axis) and percentage of positive flashes (right axis) on land for each hour of the November 3,4, 1991 thunderstorm.

November 4. Although the negative lightning was inactive in the initial and final stages of the storm, the percentage of positive flashes per hour during the same time was high. The pattern of hourly change for positive flashes was very similar to that of negative flashes, except for a delay of about 1 hour. If the positive and negative peaks had occurred simultaneously, the percentage of positive flashes would have peaked at only 10%, which is normal. In this case, however, the 1-hour delay clearly causes the percentage of positive flashes to occur after the negative peak and at the much higher level of 60%.

This storm suggests a hypothesis that winter lightning:

- characteristically shows positive activity of about 10% of negative activity,
- positive peaks occur after negative peaks,
- there is typically a one hour delay between the negative and positive peaks,
- this delay causes a subsequent percentage of positive flash peak.

Fig.9a presents all three stages of the November 3 and 4 storm. Fig.9b focuses on the data of lightning activity of only the final stage of the storm to investigate the winter lightning occurring over the land area. The number of positive flashes is considerably high at 20%. Furthermore, the 80% peak value for percentage of positive flashes is significant when compared to the overall storm's 60% level (in Fig.9a). Therefore, this data shows a typical picture of winter lightning.

Typically, only the diminishing stage of winter lightning activity is observed for the coastal area of the Japan Sea, because cells are driven by seasonal winds in winter and usually diminish after crossing the coastline. The observation data of other storms observed support this fact and agree with our analysis of flash density in the winter season (see p. 3).

The focus of Fig.9c is the initial stage of the November storm of 9a. The peak of the positive flashes occur one hour after the peak of the negative flashes, but with less activity. The peak value of the positive flashes are 50% of the negative flashes. In Fig.8, the flash activity area was located 400km from the coast, just outside the coverage area. Investigation of other storms was needed in order to obtain more accurate data.

An analysis was made of the thunderstorm shown in Fig.10 (November 17, 1991) in which a cold air mass, moving from west to east and passed overland, reached the warm Pacific Ocean and began to generate lightning flashes. Fig.11 shows the number of negative and positive flashes per 30 min. and the percentage of positive flashes. Two peaks of positive flashes occurred, the first coming about an hour earlier than the peak of negative flashes, the second positive peak coming an hour after. This is a different phenomenon from that indicated in the storm of Fig.9a. All of the conclusions resulting from the analysis of the storm in Fig.9a cannot be supported by the data of Fig.10.

CONCLUSION

The authors designed and reconstructed an improved magnetic direction-finder network in the Tohoku region of Japan. The system features strategically placed DFs and utilizes modified electromagnetic waveform discrimination criteria. During a recent observation period, actual data collected confirmed that the system could locate lightning

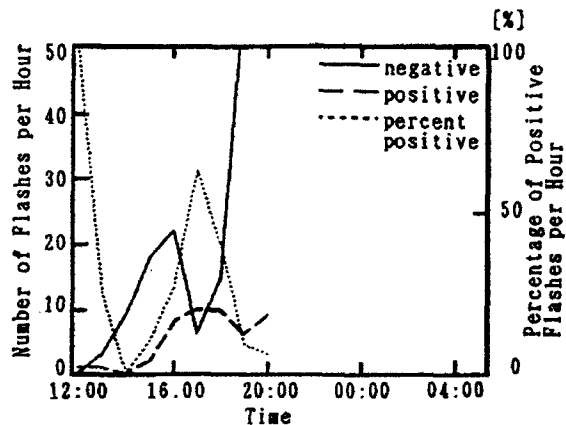


Fig.9c. Number of negative and positive flashes per 30 min. (left axis) and percentage of positive flashes (right axis) in the initial stage of the November 3,4, 1991 thunderstorm.

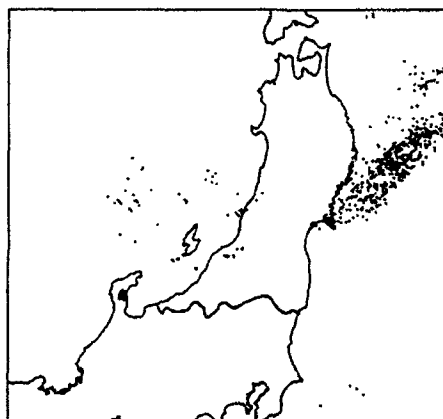


Fig.10. Projection of the thunderstorm of November 17,1991.

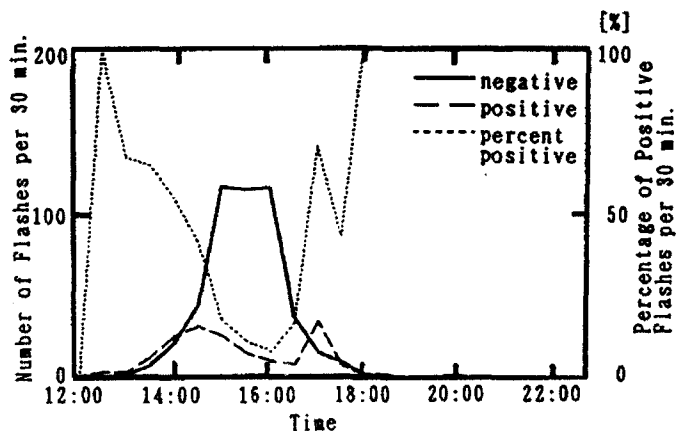


Fig.11. Number of negative and positive flashes per 30 min. (left axis) and percentage of positive flashes (right axis) of the November 17, 1991 thunderstorm.

positions with increased precision over a broader coverage area. For the first time, monitoring of the entire Tohoku area, as well as the adjacent area of the Japan Sea and Pacific Ocean, was possible. The improved network permits the analysis of flash density and polarity distribution including more accurate data on seasonal winds, surface temperatures, etc. that affect lightning activity in Japan.

The observation results of flash density show that the greatest lightning activity occurs over land in summer and over sea in winter, and in spring, the mixed features of both lightning types appear. In winter, the greatest lightning activity is over the high sea surface temperature areas where warm currents flow. Furthermore, winter lightning on the Japan Sea coast is believed to be caused by the partial shift of lightning activity area from sea to land pushed by seasonal winds from the west.

According to the observations of winter and summer lightning, positive ground flashes do not significantly depend on geographical differences even though the observation of the lightning activity caused by cold fronts showed that the rate of positive ground flashes tends to be high at the initial and final stages of lightning, where lightning activity is weak. Thus, it is difficult to assume the cause of these two peaks of positive ground flashes only on the basis of the observation data obtained from the direction-finder network.

Future observations will need to expand to include careful study of entire storm systems and the characteristics of individual thunderclouds.

References

1. Hojo, J., Ishii, M., Kawamura, T., Suzuki, F., Komuro, H. and Shiogama, M., "Seasonal variation cloud-to-ground lightning flash characteristics", J. Geophysics. Res., 94, 13207-13212, 1989.
2. Hiscox, W. I., Krider, E. P., Pifer, A. E. and Uman, M. A., "A systematic method for identifying and correcting "site errors" in a network of magnetic direction finders", Int. Aerospace and Ground Conf. on Lightning Static Electricity, Orlando, 7-1, 1984.

Fractal Determination of Parameters in Lightning and ESD model

G.Vecchi, D.Labate and F.Canavero

Dipartimento di Elettronica, Politecnico

I-10129 Torino, Italy

Abstract — *In this paper, the radiation from a geometrically fractal (i.e. arbitrarily irregular) discharge channel is investigated from the point of view of fractal geometry. Numerical results are presented for lightning return stroke radiation, which demonstrate that the time waveform of radiated field (in the Fraunhofer region) is a fractal with the same fractal dimension as the channel path. Some implications of this finding are discussed.*

I Introduction and motivations

The gross structure of the electromagnetic field generated by lightning has received considerable attention up to now, being the major responsible of the lightning-related hazards to systems (e.g., see the comprehensive review in [1], and the classical Uman's book [2]). Much less attempt of *modeling* has insofar received the fine structure of the field radiated by lightning discharges, whose time history however exhibits a jagged shape with remarkable spectral content in several bands of practical importance for communication, control, and generally consumer electronics. In addition, the VHF and UHF portions of the radiated field are presently regarded as the clues to the (insofar little understood) initiation region of the lightning (see Gardner's preface to [1]). Likewise, beside mechanical and thermal problems, electrostatic discharges (ESD) generate broad-spectrum electromagnetic fields (up to the GHz range) that interfere with proper operation of most types of electronic units, especially those hosted aboard satellites [3], [4]. Hence, a model capable of describing discharge radiated field would be of importance, e.g., for use in simulators of control or communication systems.

The fine-structure, higher-frequency noise due to discharges is most likely due to microscopical physical mechanisms of chaotic or almost-chaotic nature, whose microscopical description is very difficult. Therefore, a *macroscopical*, or phenomenological, model that bypasses the analysis at the microscopical level, would be of importance for practical simulation purposes.

At this macroscopical level, fractals should be appropriate descriptors, since fractal geometry is the natural framework for the description of chaos (eg. see [6], Ch. 4). Much like the moments of a statistical distribution that have a physical meaning and allow a good description of a stationary noise by any process sharing the same statistical characterization, fractals are characterized by some parameters that are intimately related to the physics of the phenomena. Therefore, fractals with the same parameters as those observed in experiments or measured discharges will give a good description of the fine structure of discharge-generated transient fields. The main interest in engineering application of fractals is the observation that very

complicated shapes can be described in a simple way by using fractals. More precisely, a complex shape can be described by a few parameters of a fractal object (e.g., an iterative generation algorithm), so that a complex shape can be represented, for a given degree of accuracy, with a small quantity of information.

Fractals in the description of discharge paths. Fractal description techniques have been successfully applied to the geometrical description of the discharges, i.e., for the description of the discharge *paths* [8], [9]. Confirming the intuitive expectation that the ragged, irregularly looking discharge paths be fractals, these recent research showed the usefulness of the fractal description and proved the fractality hypothesis for the tree-like shapes of discharge phenomena. The results have been obtained for inter-electrode discharges, but there is no reason against their application to lightning.

Fractals in the description of complex physical data. Besides the widely known use of fractals to computer *generate* real-looking pictures (e.g. [5]), it has recently been shown that fractal techniques can be employed to *represent* (that is, approximate) *real* complex patterns [6] (Ch. 5). In addition to that, the parameters of the fractal approximation of measured data contain information strictly tied to the physics of the phenomenon, as it has been shown for gas combustion [7].

Aim of this work. On the basis of the above considerations, one can suppose that fractals can be used to obtain good phenomenological models of the macroscopical quantities of interest.

This idea works in two directions. On the one side, the problem is that of tying together a fractal description of the discharge and a fractal description of the discharge-generated field. Once this is done, one can attempt to go in a reversed direction, using the so-obtained information to construct a phenomenological model of the discharge from *observed* data.

In this paper, we address the problem of finding the field radiated by a fractal-modeled discharge, and of analyzing such a field from the fractal point of view, in order to assess the fractality of the temporal field and seek the relationship between the fractal parameters of the model of the discharge and those of the field.

Because of the availability of reference data, in this paper we have restricted ourselves to *lightning*. As a representative of different physical mechanisms of discharge that may result in fractal objects, we have considered the example of a *tortuous* channel described by a fractal path. The effect of channel tortuosity on the return stroke radiation was investigated by LeVine and Meneghini [10], using a double-exponential current pulse form. It was then already known that channel tortuosity resulted in a jagged transient response that appeared very similar to typical measured field waveforms, and that increasing tortuosity could eventually obliterate the standard smooth waveform of the radiated field. Basing on this, we attempt a fractal-based description of the effect of channel tortuosity.

The problem can thus be stated as that of finding the transient field radiated by a pulse traveling along a fractal channel, and subsequently analyze the relationship between the fractality of the path and of the transient field waveform. Although fractal electrodynamics has been investigated by several researchers in the past years (e.g., see the recent review [11]), the authors are not aware of any other work addressing this problem.

II Transient radiation from a fractal current path

Frequency- and time-domain radiation of a tortuous channel. The lightning channel is assumed lossless, composed of N straight segments. Radiation is calculated without taking into account the possible lumped admittances at junctions between segments ("kinks"), so that the total field is the sum of the elemental fields radiated by each current segment. The ground is assumed flat and perfectly conducting. Corrections due to lossy earth can be inserted as detailed in [1] (Ch. 10), but these, as well as the effect of ionosphere do not appear to appreciably change the structure of the transient field. The above-listed approximations appear to yield a field response in good agreement with measured results [10]. Although the results are as in [10] and [17], we will briefly summarize them and the way they are obtained, in order to point out the simplicity deriving from the use of the Green's function for the fields, as contrasted to the use of potentials.

In view of the considerations above, the task reduces to that of evaluating (N times) the electromagnetic fields produced by a straight, arbitrarily oriented channel along which propagates a traveling wave current. This problem admits to a closed form solution in both frequency- and time-domains only if the current pulse propagates at a velocity $v = c$ (c being the speed of light) [13]. A closed-form solution in time domain is important to reduce computation times, control the errors inherent to discretization, and grant insight into the radiation mechanisms. Therefore, in the practically important case $v \neq c$, we will use the Fraunhofer (far-field) approximation, that allows the desired closed form solution.

We consider thus a straight segment with center located at \mathbf{r}'_i and extending for a length L_i along the direction \hat{s}_i , carrying a current $I(\ell, \omega)$, where $\ell \in [-L_i/2, L_i/2]$ is the rectilinear coordinate along the segment. We want to find the radiated electric field $\mathbf{E}_i(\mathbf{r})$ at the observer location \mathbf{r} , and denote $\mathbf{r}_i = \mathbf{r} - \mathbf{r}'_i$. Provided that $r_i \gg \lambda = c/f$ over the frequency band of interest, that $L_i/\lambda \ll 4\pi(r_i/L_i)$ and accepting a phase error bounded by $\delta\pi$, on use of the free-space dyadic Green's function (e.g., [12], Sec. 1.1b), after straightforward manipulations one can write the radiated electric field $\mathbf{E}_i(\mathbf{r}, \omega)$ as

$$\mathbf{E}_i(\mathbf{r}, \omega) = -j\omega\mu \frac{e^{-jk r_i}}{4\pi r_i} [A_i K_{r_i} \hat{r} + B_i (K_{\theta_i} \hat{\theta} + K_{\phi_i} \hat{\phi})] e^{jkb_i} \int_{-L_i/2}^{L_i/2} I(\ell, \omega) e^{jka_i \ell} d\ell, \quad (1)$$

where

$$A_i = \frac{2j}{k r_i} + \frac{2}{k^2 r_i^2}, \quad B_i = 1 - \frac{j}{k r_i} - \frac{1}{k^2 r_i^2}, \quad k = \omega/c$$

$$K_{r_i} = a_i = \hat{r} \cdot \hat{s}_i, \quad K_{\theta_i} = \hat{\theta} \cdot \hat{s}_i, \quad K_{\phi_i} = \hat{\phi} \cdot \hat{s}_i, \quad b_i = \mathbf{r} \cdot \mathbf{r}'_i.$$

The current on the channel is assumed to be a traveling wave with velocity v regardless of channel kinks,

$$i(s, t) = i_0(t - s/v), \quad \text{or: } I(s, \omega) = I_0(\omega) e^{-j\omega s/v} \quad (2)$$

s being the total arc-length along the (piecewise linear) channel path. Summing up all contributions from the N segments, one gets the total radiated field,

$$E_r(\mathbf{r}, \omega) = 2Z_0 I_0(\omega) \sum_{i=1}^N C_i^r \frac{1}{4\pi r_i} e^{-j\omega(r_i/c - T_i)} Q(r_i, \omega) (e^{j\omega\tau_i/2} - e^{-j\omega\tau_i/2}) \quad (3)$$

$$E_\alpha(\mathbf{r}, \omega) = -Z_0 I_0(\omega) \sum_{i=1}^N C_i^\alpha \frac{1}{4\pi r_i} e^{-j\omega(r_i/c - T_i)} (1 + Q(r_i, \omega)) (e^{j\omega\tau_i/2} - e^{-j\omega\tau_i/2}) \quad (4)$$

$$(5)$$

where α indicates either θ or ϕ , $Z_0 = \sqrt{\mu_0/\epsilon_0}$, $C_i^\alpha = K_{\alpha,i}/(c/v - a_i)$ and

$$\tau_i = (1 - a_i v/c) L_i/v, \quad T_i = \frac{b_i}{c} - \frac{s_i}{v}, \quad s_i = \sum_{n=1}^{i-1} L_n, \quad Q(r, \omega) = \frac{c/r}{j\omega} + \frac{(c/r)^2}{(j\omega)^2}.$$

The time-domain counterpart of (3) is obtained directly via Fourier inversion. Letting

$$t_i^{(1)} = r_i/c - T_i - \tau_i/2, \quad t_i^{(2)} = t_i^{(1)} + \tau_i,$$

the E_θ and E_ϕ components read

$$E_\alpha(r, t) = \frac{Z_0}{4\pi r} \sum_{i=1}^N C_{\alpha,i} \left\{ \left[i_0(t - t_i^{(1)}) - i_0(t - t_i^{(2)}) \right] + \right. \\ \left. + \left[i_1(t - t_i^{(1)}) - i_1(t - t_i^{(2)}) \right] + \left[i_2(t - t_i^{(1)}) - i_2(t - t_i^{(2)}) \right] \right\} \quad (6)$$

with

$$i_1(t) = \frac{c}{r} \int_0^t i_0(t') dt', \quad i_2(t) = \frac{c}{r} \int_0^t i_1(t') dt',$$

while E_r is obtained from (6) on substituting $\alpha = r$ and deleting the term in i_0 . By geometric considerations, one sees that each term in the sums in (6) appears as contributions originating from the lower and upper ends of each segment. Last, note that although v has been assumed constant, it may be let to have different values on different segments.

Pulse Shape. The current waveform assumed in this simulation is the standard model proposed by Uman [2] and modified by Le Vine and Meneghini [17]

$$I_0(t) = I_a[e^{-\alpha t} - e^{-\beta t}] + I_b[e^{-\gamma t} - e^{-\delta t}]$$

with the following parameters:

$$\alpha = 2 \times 10^4 \text{s}^{-1}, \quad \beta = 2 \times 10^5 \text{s}^{-1}, \quad \gamma = 10^3 \text{s}^{-1}, \quad \delta = 2 \times 10^4 \text{s}^{-1}, \quad I_a = 30 \text{kA}, \quad I_b = 2.5 \text{kA}$$

Fractal model of the channel. The channel is described as a function of the altitude z , i.e., $\mathbf{r}_c(z) = x(z)\hat{x} + y(z)\hat{y} + z\hat{z}$, and the $x(z)$ and $y(z)$ are two fractals curves. In order to keep closer to the probable random nature of the channel formation, $x(z)$ and $y(z)$ are two statistically independent fractal random processes. For the numerical generation of the channel path, we have employed here the random midpoint displacement algorithm ([14], Ch. 2), that builds up the fractal iteratively, starting from a straight segment and randomly displacing the midpoint, then proceeding on each of the two halves and so on. The variance of the independent discrete random variables used in the displacement process is a function of the fractal dimension D_c of the channel, which is the parameter to be specified. The so-constructed fractals appears to simulate the so-called 'fractal random walk' ([5], Ch. VIII). It is apparent that a 'true' fractal (i.e. an infinitely self-similar, infinitely detailed one) depends on the number m of iterations, which in turns fixes the number of segments, $N = 2^m$. The fact that the employed fractals are 'approximate' ones has to be kept into account when performing the fractal analysis of the field (Sec. III), because the latter will also be a fractal only within a certain range of time scales, and its fractal dimension will be subject to a certain uncertainty. Being essentially concerned with return stroke, in this work branching of the channel is not considered, because of the difficulty in modeling the return along secondary branches. In fact, the authors do not know of any work about this problem.

III Fractal Analysis of the Field

Typical plots of the transient radiated field are reported in Figs. 1, 2 and 3 for the most significant cases. Correctness of the results has been ensured through checks, for the case of a straight channel (not shown) and of a tortuous channel (obviously qualitative; not shown), against the simulated and measured data in [10]. In all cases, a channel with vertical (z) extension of 6 km has been considered; note that the actual *length* of the channel considerably varies with the degree of tortuosity (here related to the fractal dimension D : see below): as a result, also the flight time of the pulse along the channel, and the duration of the transient field waveform varies accordingly. The pulse velocity v is constant in Figs. 1 and 2; we have used the value $v = c/3$ which seems to (partially) account for the corona effect around the channel [15]. In Fig. 3, v is constant along each straight segment but variable with height z , with $v(z)$ exponentially decreasing from the value $v(0) = c$ at ground level, where we suppose the initiation to take place, to the asymptotic value $v = c/3$. This roughly simulates the variable corona along the channel [15], [16]. In all reported cases, the plots do not show the late part of the time response, consisting of a smooth pulse corresponding to the radiation from the top end of the channel [17], and all fractal-based considerations apply to the jagged portion which is shown here solely.

Fractal analysis of the radiated field is essentially based on the most important parameter of a fractal object, its *fractal dimension* D (e.g. see [6], Ch. 5, or [5], Ch. I). This is a (quantitative) measure of the "jaggedness" of a curve, or equivalently, of its space-filling property: a standard curve has $D = 1$, while a two-dimensional surface (e.g. a black square) has $D = 2$. Here, the fractal dimension has been computed using the box counting algorithm ([6], Ch. 5). Besides fractal dimension, Fig. 1 shows the *self-similarity* of the field, which is another key property of fractals ([6], Ch. 3, [5], Ch. IV).

In all of the reported cases, the field radiated by a fractal channel appears to be self-similar, and with fractal dimension $D_f > 1$, which allows to maintain that radiated field is, for a convenient time interval, a fractal itself. Moreover, within the confidence range of the box-counting algorithm, the radiated field appears to have the *same fractal dimension* as the channel ($D_f \approx D_c$). Also, it appears that the closeness between D_f and D_c increases as the D_c increases and as the resolution of the channel increases (numerical fractals are, obviously, not infinitely detailed).

Although not reported here for reasons of space, all of the examined cases showed the same result about fractality and fractal dimension, regardless of: location in the horizontal plane (ϕ), pulse velocity (v), fractal dimension of the channel, different and statistically independent realizations of the (random-based) channel, scale contraction of x and y (to reduce the horizontal occupation of the channel), and distance from the origin. Fields have not been computed in the near-field region, where the Fraunhofer approximation fails (in the present case the specification of an overall phase error of $\pi/10$ sets the minimum distance at about $r = 35$ km for the bandwidth of the input pulse). Note however that closer to the source, Fraunhofer approximation fails for the low-frequency component of the field spectrum, thus resulting in low accuracy in the *late* part of the transient response (see also [17]), which is essentially smooth. Therefore, fractality considerations extend below the Fraunhofer bound for distance. The results reported in this paper refer to a random-based fractal channel (see Sec. II); we have also tried a channel whose shape was generated through Von Koch's ("snowflake") curve [5] (Sec. II.6), which is a "canonical" deterministic fractal. The results, not shown here, are the same as with the random-based fractals as far as fractality and fractal dimension are concerned.

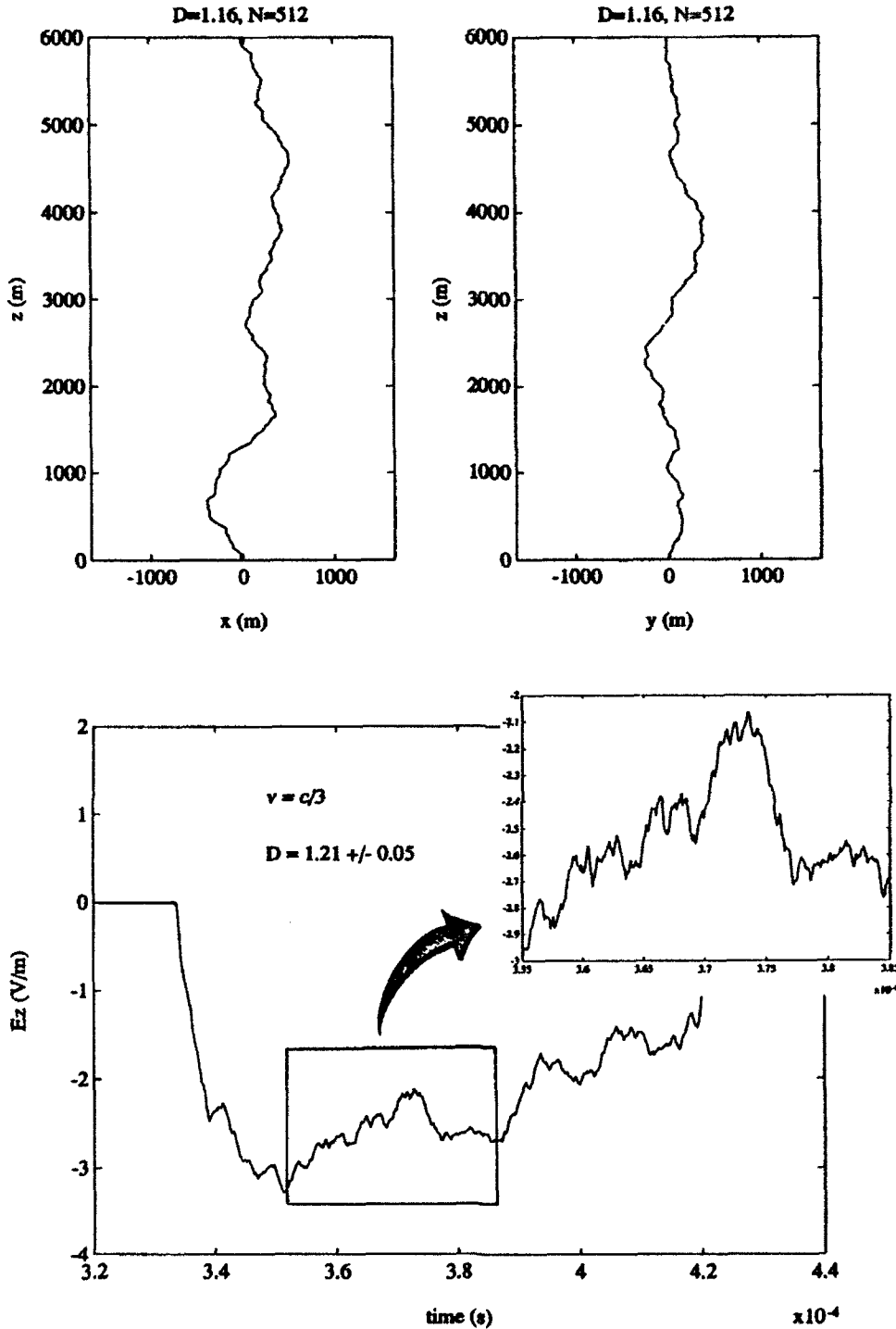


Figure 1: *Channel and field: fractality and self-similarity.* Top: (x, z) and (y, z) projections of the channel, with fractal dimension $D_c = 1.16$ and $N = 512$ segments. Current pulse velocity is $v = c/3$. Bottom: vertical component (E_z) of the radiated electric field at ground level ($z = 0$, or $\theta = 90^\circ$), $r = 100\text{km}$ away from the channel foot, along $\phi = 45^\circ$. The smooth, late-time part of the waveform is not shown on the plot. The inset shows an enlargement ("zoom") that reveals the same jagged structure (self-similarity). The computed fractal dimension of the field is $D_f = 1.21 \pm 0.05$.

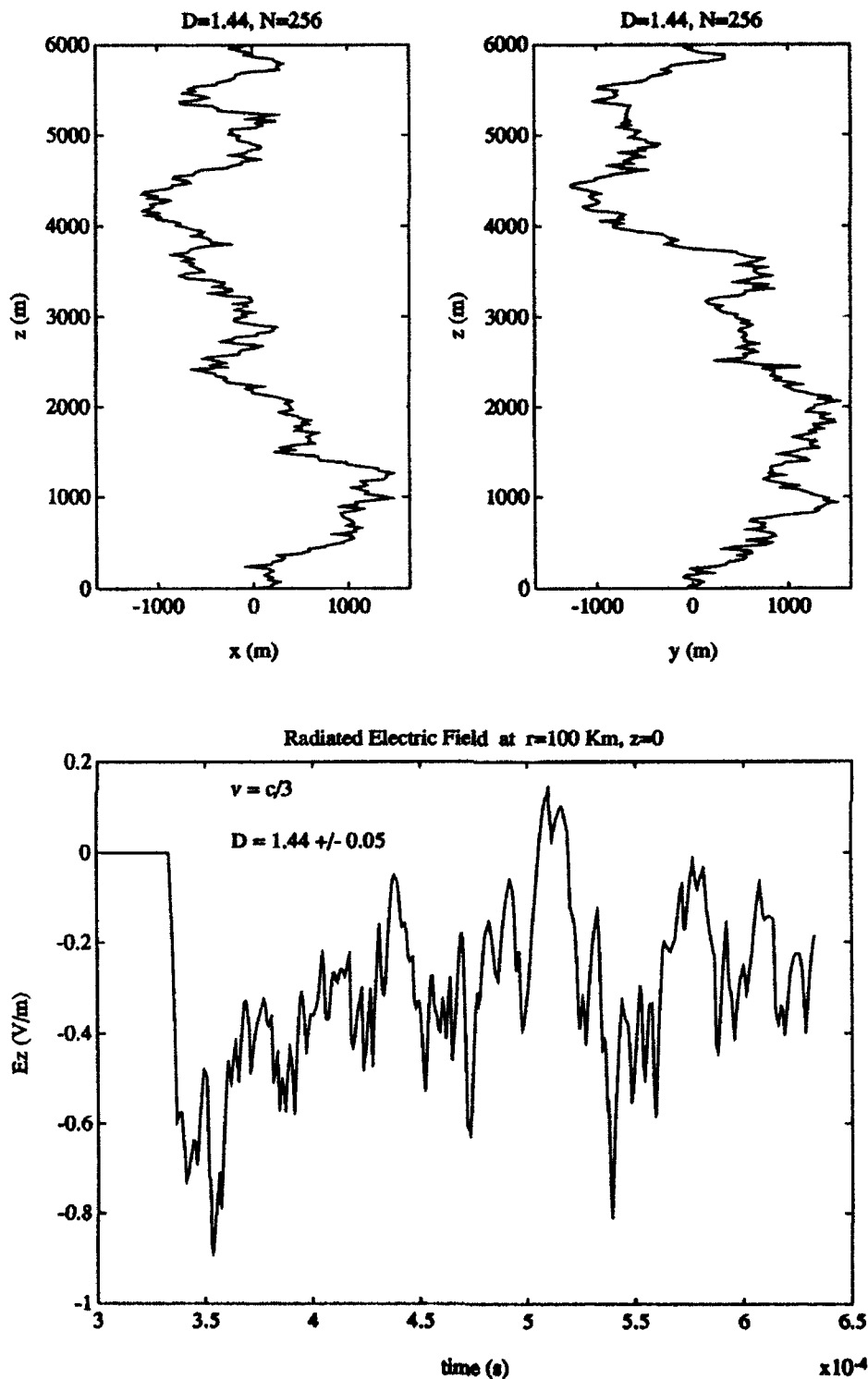


Figure 2: Higher fractal dimension. Top: (x, z) and (y, z) projections of the channel, with fractal dimension $D_c = 1.44$. Current pulse velocity is $v = c/3$. Bottom: vertical component (E_z) of the radiated electric field at ground level; horizontal location as in Fig. 1. Late times not shown on the plot. The computed fractal dimension of the field is $D_f = 1.44 \pm 0.05$.

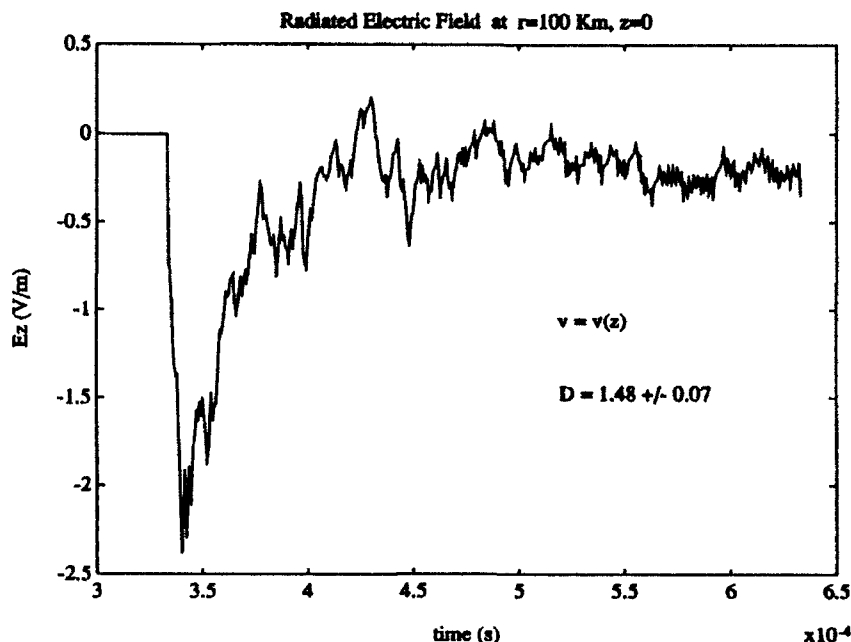


Figure 3: *Altitude-dependent pulse velocity. Vertical component (E_z) of the radiated electric field at ground level. Same observation location and channel ($D_c = 1.44$) as in Fig. 2, but pulse velocity depends on z (see text). Late times not shown on the plot. The computed fractal dimension of the field is $D_f = 1.48 \pm 0.07$.*

IV Summary and Conclusions

In this paper, we have investigated the fractality hypothesis on the field generated by a discharge. Although we have confined ourselves to the case of a lightning discharge, the analysis should apply directly to in-air ESD (while in dielectrics field computation is complicated by air-dielectric inhomogeneity). Specifically, we have considered the radiation from a return stroke pulse traveling along a fractally tortuous channel. Within the framework of the simplifying assumptions (non-dissipative channel, perfectly conducting ground), results demonstrate that the radiated field is a fractal, and has the same fractal dimension as the channel. This suggests that the fractal dimension of the channel, i.e., its tortuosity can be given a measure, and especially, that this information on the channel can be inferred from the *measured* field data. These results lend some substance to the fractal modeling of the (fine structure) of the discharge radiation, and indicate the importance of a fractal analysis of *measured* field data, which were not, however, available to the authors. Firstly, one can think of making a statistics of the fractal dimension of measured data, to be subsequently used in modeling. In fact, besides the importance of establishing the link between the fractal description of the source (discharge path) and of the field, this work serves also as a first step towards the development of a fractal model of discharges based on measured field data. From the more theoretical point of view, research is needed to prove (mathematically) the numerical evidence about the fractality and dimension of the radiated field. Work in this direction, along with extension to ESD is presently in progress.

Acknowledgments

This work was supported in part by the EEC Science Project under grant SC1*CT91-0690.

References

- [1] R.L.Gardner (Ed.), *Lightning Electromagnetics*, Hemisphere: New York (NY), 1990.
- [2] M.A.Uman, *The Lightning Discharge*, New York (NY): Academic Press, 1987.
- [3] C.R.Paul, *Introduction to Electromagnetic Compatibility*, J.Wiley: New York (NY), 1992; Ch. 12.
- [4] W.Boxleitner, *Electrostatic discharges and electronic equipments*, IEEE Press, 1989; Ch. 5.
- [5] B.Mandelbrot, *The fractal geometry of nature*, W.H.Freeman: New York (NY), 1982.
- [6] M.Barnsley, *Fractals everywhere*, Academic Press: San Diego (CA), 1988.
- [7] W.C.Strahle, *AIAA Journal*, **29**, no. 3, p. 409; March 1991.
- [8] L.Niemeyer, L.Pietronero and H.J.Wiesmann, *Phys. Rev. Lett.*, **52**, p. 1033; March 1984.
- [9] N.Femia, V.Tucci, *Proc. IEE Int. Conf. on Computation in Electromagnetics*, London (UK), p. 119; Nov. 1991.
- [10] D.M.LeVine and R.Meneghini, *Radio Science*, **13** no. 5, p. 801; 1978.
- [11] D.L.Jaggard, Ch. 6 in: H.N.Kritikos and D.L.Jaggard (Eds.), *Recent Advances in Eletromagnetic Theory*, New York (NY): Springer-Verlag, 1990.
- [12] L.B.Felsen and N.Marcuvitz, *Radiation and Scattering of Waves*, Engelwodd Cliffs (NJ): Prentice-Hall, 1973.
- [13] L.Fang and W.Wenbing, *IEEE Trans. Electromagn. Compat.*, **31**, no. 4, p. 404; November 1989.
- [14] H.O.Peitgen and D.Saupe. *The science of fractal images*. Springer Verlag, Berlin (1988).
- [15] C.E.Baum and L.Baker, Ch. 2 of [1]
- [16] C.E.Baum, Ch. 8 of [1], and private communication.
- [17] D.M.LeVine and R.Meneghini, *J. Geophys. Res.*, **83** , no. C5, p. 2377; 1978.

ZONING OF AIRCRAFT BY ELECTRIC FIELD MODELLING

C J Hardwick, V K Thompson*

Lightning Test and Technology, AEA Technology, Culham Laboratory;

*Engineering Projects,

Abingdon, Oxfordshire OX14 3DB, England

Telephone: +44-235-46-4264, Facsimile: +44-235-46-4325

ABSTRACT

The accurate determination of the zoning of aircraft has become more important with the increasing use of CFC materials in airframe construction. In-flight evidence suggests previous rules such as those given in the FAA AC20-53A are unsatisfactory. The proposed AC20-53B recommends substantially increased areas for Zone 1A. This paper presents an approach for calculating the initial attachment zones which, unlike the rolling sphere model, explicitly takes field concentration factors into account.

1 Introduction

Present standards for the protection of aircraft against lightning strikes such as the FAA AC20-53A and MIL STD 1757A give examples of the zoning of aircraft and in particular define zone 1 as the initial lightning attachment region. This zone has been taken as being restricted to aircraft extremities where electric field enhancement will tend to favour attachments to such sites. The region has usually been taken as the extremity plus a region .5m aft or inboard of it. Severe lightning strikes with currents and action integrals greater than 100kA, $.25 \times 10^6 \text{ A}^2\text{s}$ respectively should not occur outside zone 1 regions. Reported flight experience however indicates that occasionally very severe strikes do occur outside this zone. This has lead to new schemes for determining the initial attachment zone such as the "rolling sphere" method (Ref 1, 2) and the "swept leader" method (Ref 1, 3). These ideas have been taken up by the SAE AE4L committee and substantially larger zone 1 regions have appeared in a draft AC20-53B which has been submitted to the FAA by this committee.

Several methods for determining the initial attachment zone are proposed in this draft; they are analytical methods such as the rolling sphere and electrical field analysis; and test methods such as model arc attachment tests. However the detailed procedures to be applied have not been specified for the analytical methods.

This paper presents an approach to determine zoning based on electric field modelling. Section 2 outlines the necessary features of a zoning methodology, section 3 introduces the proposed method, section 4 describes the electric field modelling technique used and section 5 presents some results.

2 Requirements for a Zoning Methodology

Aircraft flight safety is sometimes discussed in terms of the probability of a catastrophic incident per flying hour. As an example, to illustrate aircraft zoning let us assume that the probability of a hazardous lightning strike has to be less than one in 10^9 flying hours, Assuming:-

- One strike every 1000 flying hours.
- The most severe damaging lightning strikes are associated with cloud to ground (c-g) strikes and there is only one strike to ground involved in every 10 aircraft strikes.
- Only one in ten of c-g strikes has severe parameters exceeding the protection levels appropriate to a swept stroke zone (zone 2).

This gives a lightning strike to aircraft exceeding zone 2 protection requirements every 10^5 flying hours. Hence, in order to achieve the required probability of a potentially hazardous strikes to a zone 2 region, zone 1 has to contain 99.99% of all cloud to ground strikes. Different assumptions will change this figure but it will remain large, for example if there is only one c-g strike involved in every 100 aircraft strikes it will be 99.9%.

The following observations can now be made on particular methodologies

- In flight service experience for a particular aircraft generally suffers from poor statistics - typically 100 strikes for one type and many of these will be triggered intra cloud strikes which are thought to have lower action integrals than cloud to ground strikes. Hence similarity arguments to zone aircraft should be used with caution.
- It is known that HV arc attachment tests to models yield different results depending on the shape of the applied HV pulse; the slower fronted impulses tend to give a wider spread of attachment points. Even so, an impractical number of shots and electrode orientations would be required to obtain the appropriate statistics.

For these reasons some lightning specialists have been developing analytical methods. The rolling sphere method is one such procedure and a probabilistic approach has been suggested by Jones (Ref 2) and King (Ref 4). A conservative value for the sphere radius of 25m is usually

taken; however striking distances for a 100kA return stroke are probably well in excess of this (Ref 5). Nevertheless Jones claims the results agree well with in-flight experience.

The other analytical model proposed - electric field modelling - can be used to determine likely points of attachment, for example stress raisers, but the question of how to obtain a probabilistic assessment arises. An approach to this problem is made in the next section.

3 Probabilistic Method

Parker and Kasemir presented a 3-D electric field computer analysis of an aircraft at the Orlando conference (Ref 6) and showed that significant field concentration factors of the order of 100 or so could occur at aircraft extremities for some ambient field orientations. However they also noted that the local field on the surface decays away rapidly with distance from the surface and hence the criterion by which corona at a point on the aircraft surface transforms into either a bi-directional leader for triggered lightning or an answering streamer for intercepted lightning is not clear. For our purposes we propose that the probability of streamer/leader formation is related to some complex function of aircraft surface curvature or local surface electric field.

Consider an aircraft immersed in a uniform electric field whose magnitude and direction are designated by the vector $E^{(i)}$. This will be a possible situation prior to triggered lightning where the local surface electric field is sufficient to initiate the formation of a bi-directional leader. For intercepted lightning the field will not be uniform but provided the approaching leader is not close we can assume that the field will not be divergent.

The electric field intensity at a region 'j' of the surface is proportional to the local charge density which is given by

$$\sigma_j^{(i)} = \sigma_j^{(x)} E_x + \sigma_j^{(y)} E_y + \sigma_j^{(z)} E_z$$

where $\sigma_j^{(v)}$ is charge density on element j for a unit field orientated in the direction (v). Hence if the charge density for 3 orthogonal directions of field are known the charge density distribution for any direction can be calculated. The probability of attachment to element of area 'j' for a particular field orientation (i) is given by

$$P_j^{(i)} = \frac{a_j f(\sigma_j^{(i)})}{\sum_j a_j f(\sigma_j^{(i)})}$$

where a_j is the area of element, $f(\sigma_j^{(i)})$ is an unknown function of charge density.

For example we might imagine a power law dependence such as $(\sigma_j^{(i)})^n$; $n \rightarrow \infty$ would be the same as choosing a probability of one for the element of area having the highest local field value; $n=0$ would correspond to no dependence on local field at all and the probability would be proportional to the element area.

In order to obtain a probability for all possible field directions and hence determine the areas of the aircraft that contains for example 99.9% of all strikes, the expression would have to be evaluated over an ensemble of N field orientations (i) and an average taken:-

$$\bar{P}_j = \frac{1}{N} \sum_i \frac{a_j f(\sigma_j^{(i)})}{\sum_j a_j f(\sigma_j^{(i)})}$$

The average value of such an ensemble is readily estimated by Monte Carlo methods (Ref 7). A Monte Carlo program was used which generated 10,000 angles (i) of the field randomly over a 4π solid angle. The value of \bar{P}_j was then evaluated for various objects for which σ_j could be evaluated analytically and for functions $f(\sigma_j)$; this allowed the method to be tested. For example Fig 1 shows a 2D illustration of the procedure applied to a "delta wing". Fig 2 shows the results for an oblate ellipsoid representing a wing. For $n \rightarrow \infty$ the attachment points are restricted to the leading edge, primarily the tip. Results similar to the rolling sphere model predictions are obtained when $n=5$ (Ref 8).

To determine the probabilities on an aircraft shape the charge distributions on the surface $\sigma_j^{(v)}$, for 3 orthogonal field orientations (v) have to be determined numerically. This is described in the next section.

4 Electric Field Model

4.1 Problem Formulation

The charge distribution over a conducting object immersed in an ambient electric field follows from solving Laplaces equation, $\nabla^2 V=0$, in the region exterior to the object (provided that the region has uniform isotropic dielectric properties). V is the voltage potential and the boundary conditions are a constant V on the conductor and a know uniform $\text{grad } V=E$ well away from the object.

4.2 Numerical solution

Many numerical codes are available for solving Laplaces equation for thermal problems. These codes can be used here as there is a direct analogy between thermal and electrostatic

problems where temperature T is equivalent to potential V and heat flux density q to electric field E . Most of these codes use the Finite Element (F.E.) method in which the space region to be modelled is divided into elements connected together at a Finite number of points (nodes). For the aircraft problem a F.E. mesh would consist of the 3D region bounded by the aircraft surface and some suitable remote boundary. For any reasonable attempt to model a real aircraft such a mesh would be prohibitively complex and an alternative method based on the less common Boundary Element (B.E.) approach is preferred here. The B.E. method derives a solution to Laplace's equation over a surface spanning the region. The properties within the region must be uniform and linear and the method has the advantage that only the surface of the aircraft has to be meshed; thus a 3D problem is reduced to 2D. The far field boundary must also be included as a second 2D surface, but the two surface meshes are not linked and the outer mesh can be arbitrarily remote and simple.

The PAFEC code contains a boundary element facility and is available on the Culham computer. For this problem an additional facility was added to the PAFEC models in order to find the distribution of heat flux (or equivalently the surface charge distribution) over the aircraft surface.

The numerical method was verified using the analytical solution for a 10m long prolate ellipsoid. An aspect ratio of 5:1 was chosen, the B.E. mesh used had about 100 elements, the outer boundary consisted of a centrally located cube of 100m side dimension with zero potential. This outer boundary is sufficiently remote to make this model equivalent to an isolated ellipsoid. The potential on the ellipsoid was set to a fixed potential and the numerical result for the charge was accurate to 4%, consistent with the limitations of a practical mesh. For the distribution of average charge density over each patch, which is required for the purposes of the Monte Carlo program, accurate results were also found.

The procedure used for the ellipsoid can be repeated for other shapes although with the complexity of an aircraft more care is needed in defining the mesh and computer storage and run times are considerably larger than for the ellipsoid.

The mesh for the aircraft, a BAC111, is illustrated in Fig 3.

5 Results

Charge density distributions on the aircraft for 3 orthogonal field directions were obtained and one of these is shown in Fig 4. The three directions chosen were wing tip - wing tip, nose to tail and up-down. As would be expected and as shown in the 2D studies of section 3, very different charge distributions are obtained for the different orientations and largest values occur at extremities aligned with the field. The charge densities associated with the different area patches were stored on a disk file for each field orientation. This allows the Monte Carlo program to be run with various trial probability functions.

As an example, Fig 5 shows the zone 1 elements using the criterion of the maximum local field for determining the strike point location (ie $n \rightarrow \infty$). We see that 99.96% of all strikes are restricted to a few regions of the aircraft. Interestingly the analysis shows .15% of strikes would occur to the rear underside; for a small number of field orientations which don't align with any stress raisers this region has the highest charge density. For triggered lightning however where a minimum electric field intensity would be required or for downward approaching leaders, this region might be excluded. Areas not having the minimum surface electric field value necessary for corona inception can be removed from consideration by applying a field concentration factor cut; for example a cut of about 10 would be required in an ambient electric field of $3 \times 10^5 \text{V/m}$.

Another example is shown in Fig 6, here we have used a probability function with $n=5$ and a field concentration factor cut of 3. The value of 5 has been chosen as this value gave results similar to those obtained with the rolling sphere method when applied to an oblate ellipsoid. We see that the regions are larger than the more simplistic scenario chosen for Fig 5 and not dissimilar from results that would be obtained with the rolling sphere method. Larger values of the field concentration factor cut necessary for triggered lightning will restrict the regions more to the extremities.

The correct zoning diagram probably lies between these two extremes. To progress further, microphysics input on the attachment process and hence on the probability function is required.

6 Conclusions

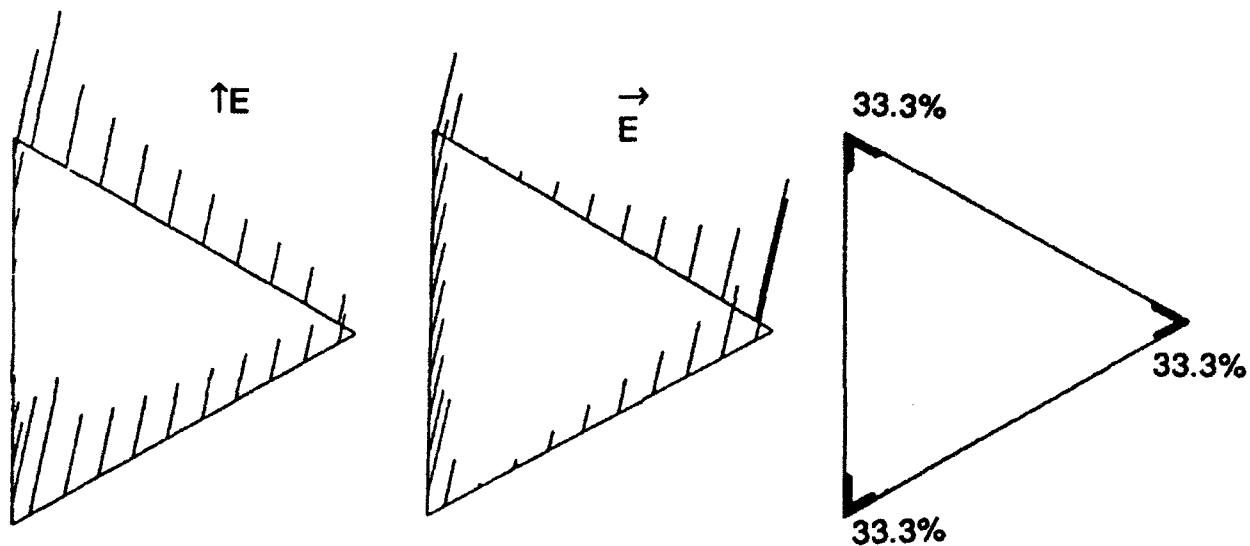
- 1) Considerations of probability suggest that data from in-flight experience or model tests to determine the zoning of aircraft should be used with caution.
- 2) The basis of a methodology based on electric field modelling and the Monte Carlo method is presented as an alternative approach to the rolling sphere method to determine the initial lightning arc attachment zones. More studies on the effect of the mesh granularity and accuracy of the electric field model are required.
- 3) The approach gives reasonable results in that the initial attachment zones tend to be restricted to but not exclusively to, stress raisers. The exact determination of probabilities requires further knowledge of the physics of leader/streamer inception so that the form of the dependence of strike probability on local surface charge density can be determined.

References

- [1] Jones Hanson and Odam. Zoning of aircraft for lightning attachment and current transfer. ICOLSE, 86 Dayton OH, USA
- [2] Jones, The rolling sphere as a maximum stress predictor for lightning attachment zoning. ICOLSE 90 Bath, UK
- [3] Plumer, Evidence of return stroke arrival of aircraft frontal surfaces and implications for protection design. ICOLSE, 90 Bath, UK
- [4] King and Ogden Analysis technique for lightning attachment zoning of aircraft. ICOLSE, 90 Bath, UK
- [5] Golde Vol II Lightning Pg 556
- [6] Parker and Kasemir, Predicted aircraft field concentration factors and their relation to triggered lighting. ICOLSE 84 Orlando F1, USA
- [7] Culham Lightning Club report CLiC/DD21 Cooke, Gimblett, Lightning strike risk assessment. Feb 89
- [8] Culham Lightning Club report CLiC/5-11 Hardwick, Marlow, Jones. Comparison of Rolling Sphere and Electric Field Models, July 91

Acknowledgements

The Culham Lightning Club comprising British Aerospace, CASA, Rolls Royce, SAAB Scania, Shorts, Westlands, the UK Civil Aviation Authority and the Department of Trade and Industry who provided financial support. John King of PAFEC for advice on the use of the BE facility. C Jones of BAe Warton for the use of his Rolling Sphere program.



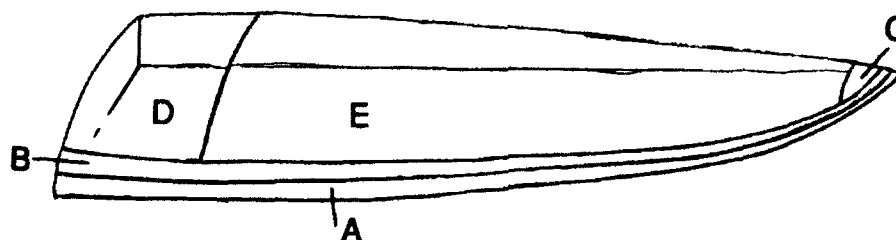
a) charge distribution
field vertical

b) charge distribution
field horizontal

c) resultant attachment
probability $n \rightarrow \infty$

(the length of the diagonal lines around the perimeter of the object are proportional to the local charge density)

FIGURE 1 2D Delta Wing Example



ZONE	E FIELD MODEL		ROLLING SPHERE
	$n \rightarrow \infty$	$n = 5$	
A	99.38	78.8	74.5
B	0.24	8.5	15.6
C	0.30	3.8	1.2
D	0.24	1.5	2.7
E	0.05	7.4	6.0

FIGURE 2

Results for 50:10:1 ellipsoid giving attachment probabilities for areas using different assumptions for n

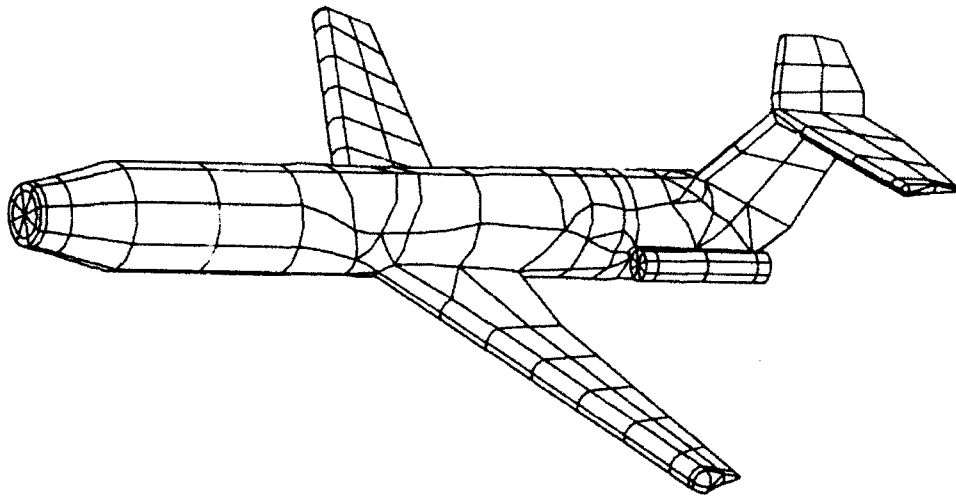


FIGURE 3 Boundary Element Mesh for Aircraft

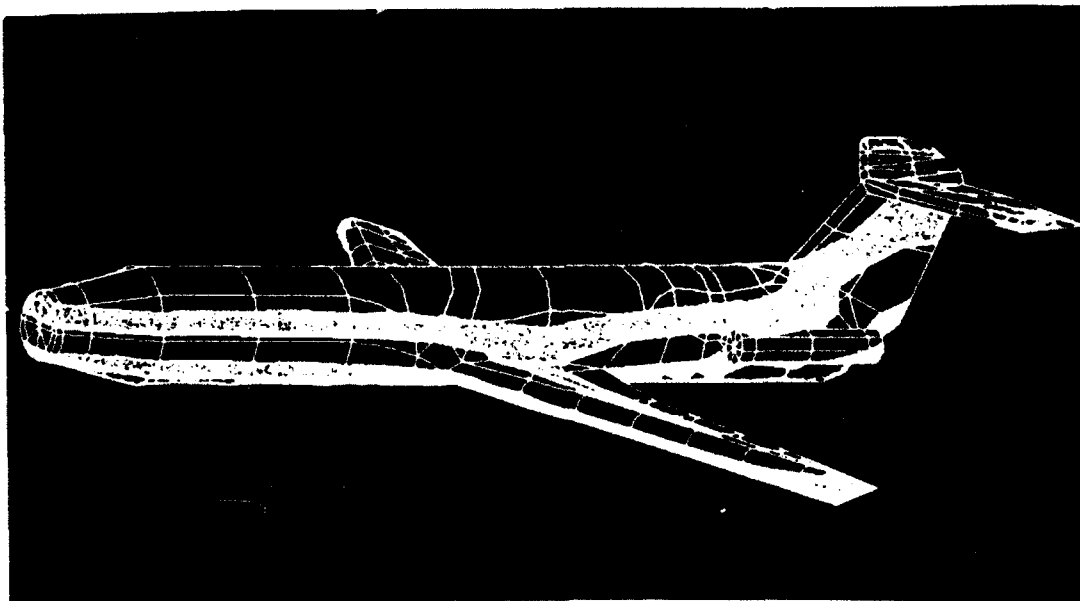


FIGURE 4 Contours of Local Electric Field for Aircraft situated in a Vertical Field

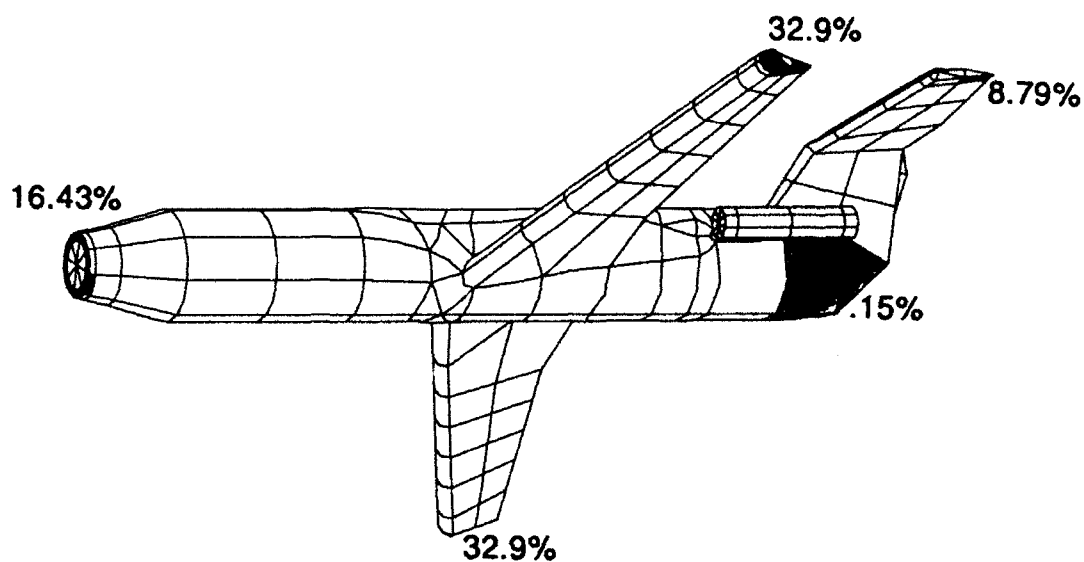


FIGURE 5
BAC111 Zoning Diagram, $n \rightarrow \infty$, 34 Patches Containing 99.96% of Hits

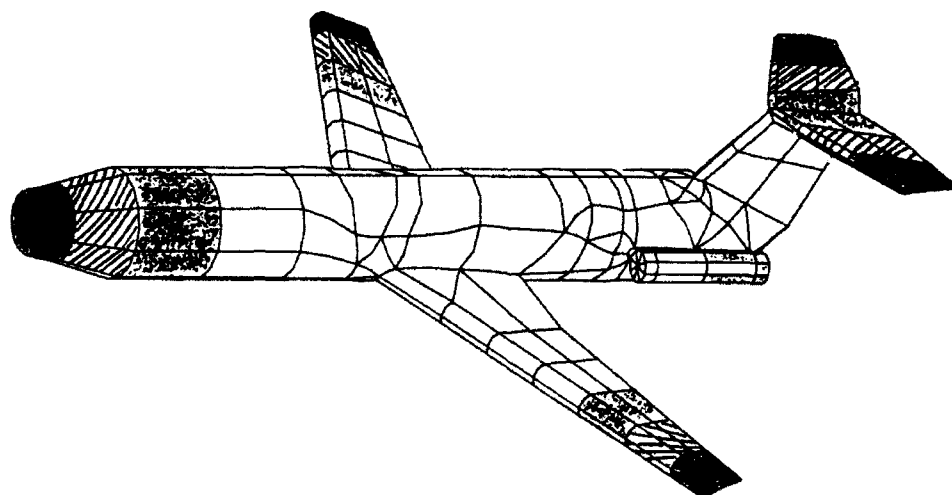


FIGURE 6
BAC111 Zoning Diagram, $n = 5$, Field Concentration Factor Cut = 3.
The three shaded zones include 90%, 99% and all attachments progressively from the extremities.

LIGHTNING PHENOMENOLOGY BASES FOR FULL THREAT RETURN STROKE OCCURRENCE FOLLOWING EXTENDED LEADER SWEEP AT FLIGHT ALTITUDES

J. A. Plumer
Lightning Technologies, Inc.
10 Downing Parkway
Pittsfield, MA USA
Telephone (413)499-2135 FAX (413)499-2503

ABSTRACT

It has been recognized that lightning leaders sweep aft from initial attachment points on aircraft forward extremities prior to arrival of the first return stroke, which, in a cloud-to-earth flash, is not initiated until a branch of the leader reaches the earth. This process has lead to more realistic procedures for locating lightning strike Zone 1A on aircraft surfaces, with the result that Zone 1A covers considerably more of the aircraft surfaces than previous zone location methods (i.e., "the 18-inch criteria") would indicate.

Some observers have suggested that, whereas the leader may indeed sweep a considerable distance alongside fast moving aircraft at flight altitudes, the intensity of the ensuing first return stroke will be less than it would be at the ground terminus of the lightning channel, because a portion of leader charge is below, not above, the airplane. Analytical models of lightning channels are often cited to support this, since such models often show reduction of the stroke intensity (i.e., peak current and action integral) with distance from the earth terminus. Physical damage on aircraft struck in flight belies this contention, however, as damage indicative of severe return strokes is often seen well beyond 18 inches aft of initial leader attachments.

This paper discusses the natural lightning characteristics that explain why severe first return strokes may arrive well aft of forward extremity tips of aircraft, and why zone location methods must account for this. It is the third paper in a series begun in 1980 by the author on the topic of swept leader and zone location methodology, and presented at these conferences.

BACKGROUND

Lightning strike zones have been defined to enable important aspects of the aircraft lightning strike environment to be allocated to aircraft surfaces and structures in the most realistic manner, so that protection may be designed which is commensurate with the lightning strike effects expected at specific locations on the aircraft. In this manner lightning protection features can be matched to the characteristics and intensity of the lightning strike effects associated with each zone. Surfaces exposed to the first return stroke, which has the highest action integral of the several current components of the aircraft lightning environment, for example, can be provided with protection capable of sustaining this current, while other surfaces, exposed to a subsequent stroke of lower

intensity, can usually have light-weight protective treatments, or no specific protection features at all.

Designers can utilize surfaces where lightning strikes are highly improbable to locate sensitive components, such as fuel tank vents and filler caps, or electrical devices.

Present zone definitions are found in a variety of standards (Ref. 1 and 2) and related publications, and are as follows (with minor variations):

- Zone 1A** Initial attachment point with low possibility of lightning channel hang-on
- Zone 1B** Initial attachment point with high possibility of lightning channel hang-on
- Zone 2A** A swept stroke zone with low possibility of lightning channel hang-on
- Zone 2B** A swept stroke zone with high possibility of lightning channel hang-on
- Zone 3** Those portions of the airframe that lie within or between other zones, which may carry substantial amounts of electrical current by conduction between areas of direct or swept stroke attachment points. It includes those surfaces where attachment of the lightning channel is a very low possibility.

At the time (1975) when the above definitions were first published by SAE Committee AE4L, an "initial" attachment point was considered to be the place where the first return stroke "struck" the aircraft and, first return stroke arrival was assumed to be coincident with initial leader attachment. The fact that the leader's journey is usually incomplete when it first contacts the airplane, and must continue propagating to earth (or another region of opposite polarity charge) prior to return stroke initiation, was overlooked. These "initial attachment points" were also assumed to occur only at or very near major aircraft extremities, such as wing and empennage tips, the nose, propeller tips, and tail cones, due to the electric field enhancement that occurs around such projections, and the initial attachment zones were assumed to be limited to the outermost (or forwardmost) 18 inches (0.5 m) of the major extremities. Observed marks, such as melted spots, pitting, splatter, small dents, and occasional holes in aluminum skins at surfaces aft and (less frequently) inboard of major extremities were attributed to "sweeping" of the lightning channel alongside these surfaces after first return stroke arrival. The "sweeping" effect is actually due to flight of the aircraft through the lightning channel. An aircraft zoned in such a manner is shown in Figure 1.

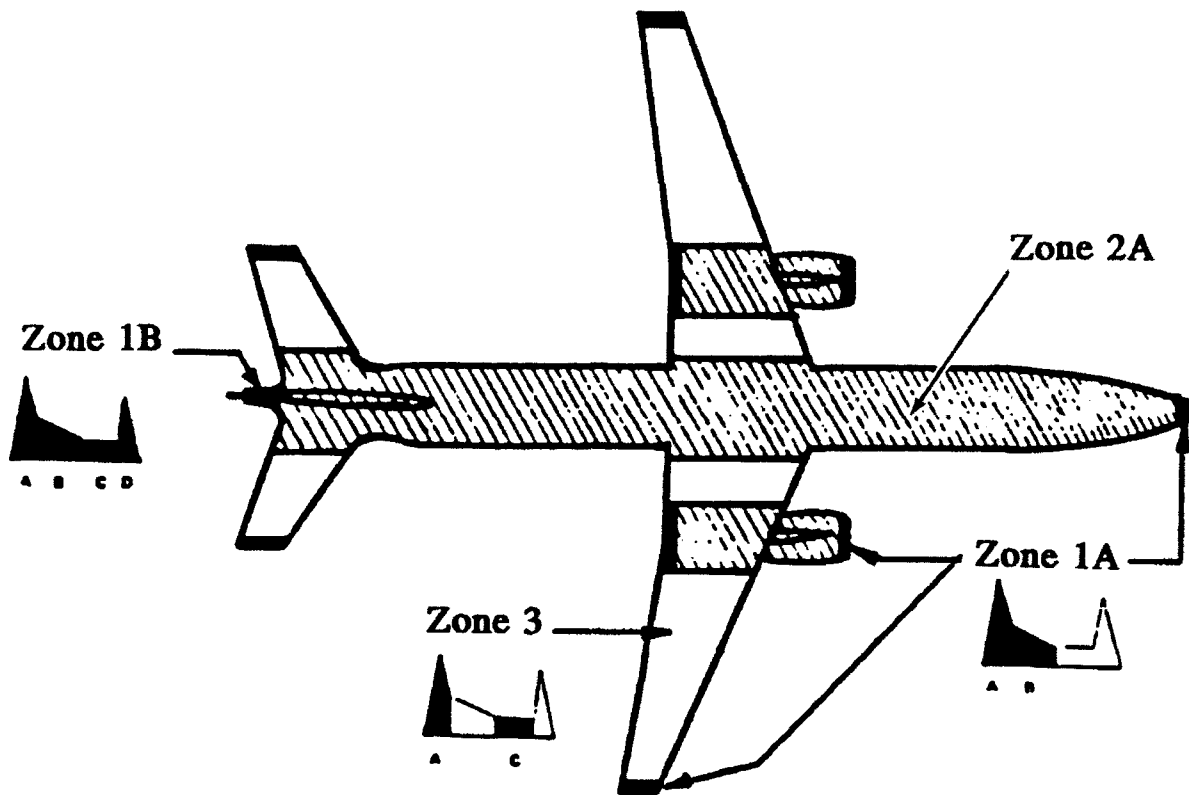


Figure 1 - Traditional aircraft lightning strike zones, based on 18-inch criteria
(Reference FAA AC 20-53A)

The observed "swept stroke" effects were attributed to small amounts of continuing current entering individual spots, or to occasional subsequent strokes, which have always been assumed to have lower peak currents and action integrals than the first stroke. Occasional evidence of more severe stroke currents having reached side surfaces attracted little attention, because this damage rarely proved a hazard to flight safety¹ and necessitated only minor repair. Aluminum aircraft skins are quite tolerant of lightning strike effects associated with any of the strike zones.

By the late 1970's, however, the regularity of severe strike effects, similar to those of a first return stroke (or at least the one defined in aircraft lightning standards) arriving aft of traditional Zone 1A locations, had become evident to this author and to others in a position to compare observed effects with simulated lightning test effects on similar skin materials and structures. The reasons for this had also become apparent; specifically:

- 1 An apparent exception was the crash of a DC-2 over Lovettsville, VA in 1940, attributed to shattering of the windshield by lightning shock wave. Occasional reports of lightning related flameouts of small, fuselage-mounted jet engines may indicate another potential hazard from first return strokes swept in front of intakes.

- An airplane may move a significant distance through the air between initial leader attachment and first return stroke arrival. This distance may depend on airplane speed and the time taken for the leader to complete its journey.
- The leader, being ionized air, will "sweep" alongside the airplane, and may reattach periodically to it. Reattachment is especially likely upon return stroke arrival at the airplane, because the electric field along the leader channel at this time is intensified.
- Not all leaders will initially attach to the forwardmost or outermost surfaces of major extremities. Some may attach to "flat" surfaces further aft or inboard of extremity tips. It is true that the highest percentage of leader attachments will occur at tips (etc.) where the electric field gradient is highest, but the random nature of air breakdown under high voltage stress assures that other leaders will attach to surfaces some distance inboard of extremity tips. Some aircraft, of course, do not have pronounced tips or noses of small radii of curvature, in which cases there are no particular extremities at all.

A more thorough discussion of the above factors is found in Reference 3 and examples of severe first return strokes having reached surfaces aft of traditional Zone 1A boundaries are described in Reference 4.

The advent of carbon fiber reinforced composite (CFC) fuselages, wings and other aircraft structures necessitated that account be taken of the extended Zone 1A to assure that adequate protection be provided, since unprotected CFC skins and structural elements are potentially more vulnerable to lightning strike effects than are aluminum skins. Lightning damage to CFC is most directly proportional to stroke current action integral, and the action integral of the first return stroke (Component A) applicable in Zones 1A (and also 1B) at $2 \times 10^6 \text{A}^2 \cdot \text{s}$ is eight times more severe than that of the subsequent stroke (Component D) associated with Zones 2A and 2B. Some CFC skins in Zone 2A need no additional protection, whereas CFC skins in Zones 1A and 1B nearly always do, if puncture, cracking, or deep penetration are to be avoided.

Considerable discussion of these factors followed in the technical committees (SAE AE4L and EUROCAE WG-31) in the U.S. and Europe, responsible for defining the aircraft lightning environment and test methods, and two changes were recommended by SAE AE4L for incorporation in U.S. FAA and Department of Defense (DOD) documents pertaining to aircraft lightning protection. These were:

1. Clarification of the zone definitions to make clear the association of the first return stroke arrival locations with Zones 1A and 1B, as follows:

Zone 1A All areas of the aircraft surfaces where there is a high probability of a first return stroke during lightning channel attachment with a low probability of flash hang-on.

- Zone 1B** All areas of the aircraft surface where there is a high probability of a first return stroke during lightning channel attachment with a high probability of flash hang-on.
- Zone 2A** All areas of the aircraft surfaces where there is a high probability of subsequent return stroke attachment with a low probability of flash hang-on.
- Zone 2B** All areas of the aircraft surfaces where there is a high probability of subsequent return stroke attachment with a high probability of flash hang-on.
- Zone 3** Those surfaces not in Zones 1A, 1B, 2A, or 2B where there is a low probability of any attachment of the lightning channel and those portions of the aircraft that lie beneath or between the other zones and conduct substantial amounts of electrical current between direct or swept stroke attachment points.

2. Improvement of the zone location guidelines to account for more realistic initial leader attachment possibilities and the leader sweep prior to first return stroke arrival at the aircraft. Leader attachment locations can be determined by prior experience, model testing, the "rolling sphere" method, or electric field mapping. Leader sweep distance (and thus the extension of Zone 1A aft of initial leader attachment areas) is based on aircraft airspeed, an assumption that the leader propagates straight to earth at 1.5×10^5 m/s, and the further assumption that severe first return strokes occur only in cloud-to-earth flashes and only at flight altitudes below 15,000 ft. (These latter assumptions have, for the most part, been substantiated by in-flight lightning experience.)

A typical zone diagram in accordance with this methodology is illustrated in Figure 2.

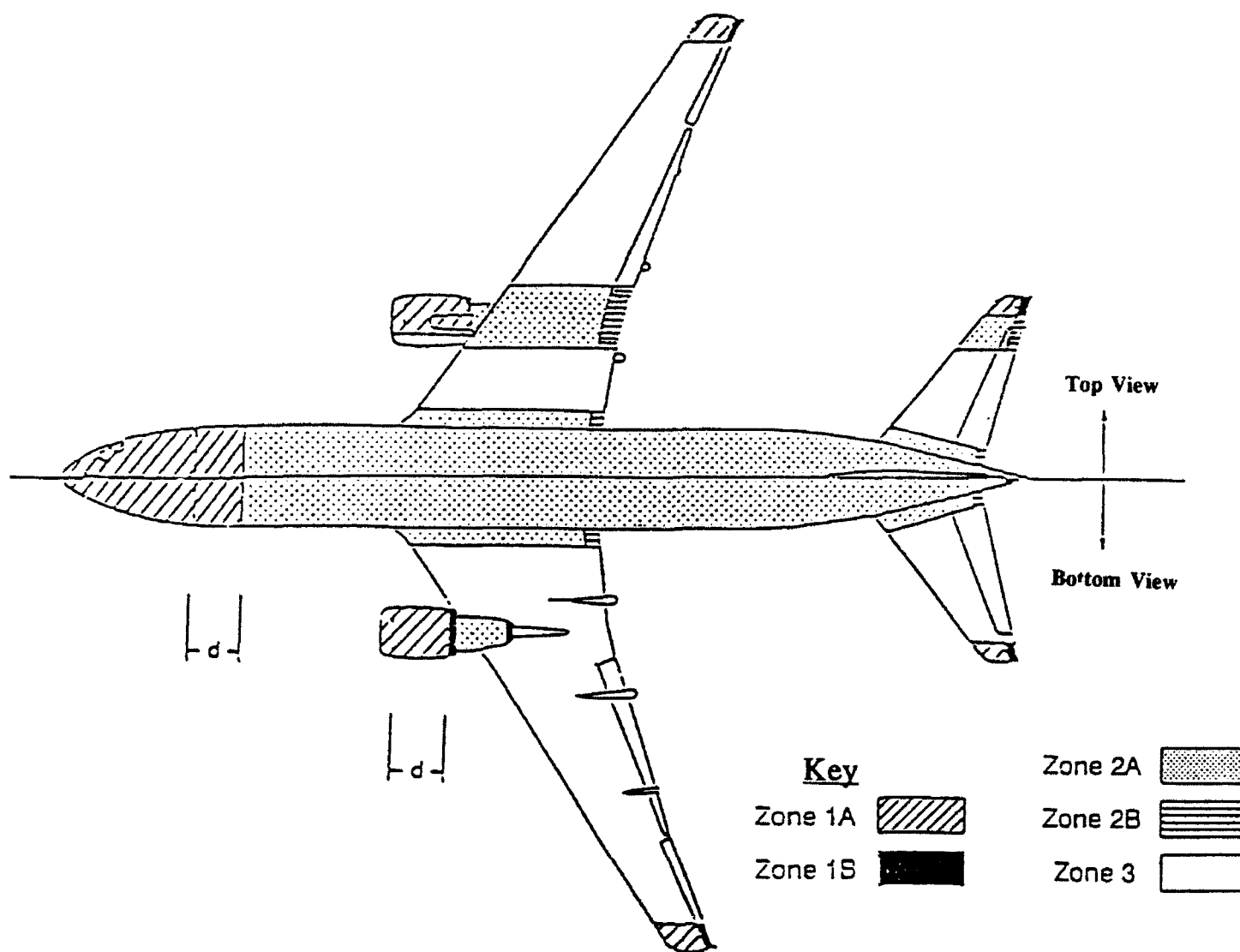


Figure 2 - Aircraft zones that account for leader attachment and sweep aft of forward extremities prior to return stroke arrival (Ref. FAA AC 20-53B, proposed)

The above changes have been documented in the proposed revision B of FAA Advisory Circular 20-53. Similar versions have already been incorporated in the U.S. Mil-Std-1795A (Ref. 5) and in the FAA Aircraft Lightning Protection Handbook (Ref. 6).

Understandably, the zone changes described above have prompted resistance from those who fear the impact of more extensive first return stroke zones (Zone 1A) on aircraft design, due to the weight and cost of assumed protection, or who disagree with the phenomenological or flight experience bases for the new zone location methods. Some of the latter contentions have been:

1. Leaders can initially strike only the outermost surfaces of major extremities.
2. Leaders do not "sweep" (i.e. the aircraft can not fly through or alongside a leader channel). Apparently, only a completed channel can sweep.

3. Leaders do sweep, but by the time they have swept very far alongside an aircraft (as from a frontal extremity like a nose or engine nacelle inlet) the amplitude and action integral of the first return stroke have diminished to levels similar to the subsequent stroke (i.e. Component D) associated with Zone 2A. This contention is based on analytical models of the cloud-to-earth lightning channel, which show maximum charge flow, peak current and action integral at ground level, and pronounced reduction of these parameters with altitude.
4. There has been no evidence of severe first return strokes having arrived at aircraft surfaces not within traditional Zone 1A/1B areas within 18 inches of "extremities."

The balance of this paper addresses each of the above contentions.

INITIAL LEADER ATTACHMENT POSSIBILITIES

It is well known that electric fields become highly intensified about sharp-edged conducting objects such as the tips of lightning rods on buildings, tall poles and towers, and other pointed objects, including sharp-edged wing and empennage tips of aircraft and nose-mounted pitot booms. Experience seems to confirm that when such well defined extremities are present on aircraft, leaders will originate there, whether they comprise an aircraft-triggered strike or whether the aircraft intercepts a leader that has originated elsewhere. The marks left by leader currents of 100 A (or so) amplitude and short duration ($\leq 50 \mu\text{s}$) are not easily discerned, and sometimes these initial attachments are overlooked. The behavior is not unlike that of a lightning rod on a rooftop, which serves as a preferential lightning attachment spot. The NASA F106B airplane, which received over 800 lightning strikes during six seasons of thunderstorm flying, for example, nearly always had an initial lightning entry (or exit) point at the radome-mounted pitot boom, whose tip is eleven feet forward of the fuselage. A typical strike to the NASA F106 airplane is illustrated in Figure 3 of NASA TP 2087 (Ref. 7). Some business jet airplanes and military fighter-type aircraft also have sharp extremities like the F106B, but many aircraft, including large, transport airplanes, do not have sharp extremities but instead have rather blunt noses, wing and empennage tips. In these cases there is simply no unique "extremity" and a lightning leader may attach to the general area of the extremity, at random. This behavior is commonplace in high voltage test laboratories where large diameter electrodes are frequently utilized for testing purposes and to inhibit the formation of unwanted streamers. In these situations any attempt to restrict initial attachment zones (i.e., Zone 1A) to 18 inches from a presumed "tip" makes no sense at all. The best example of such a case is the nose and forward cockpit area of a transport airplane, generally from the radome to well aft of the cockpit, where the fuselage sides become straight and its diameter is constant. Lightning junction leaders may originate, with near equal probability, from anywhere in this region.

The solid-bar type lightning diverters found on some radomes will provide local field intensification and attract some leaders, but others will attach elsewhere in the vicinity (not all radomes are equipped with diverters).

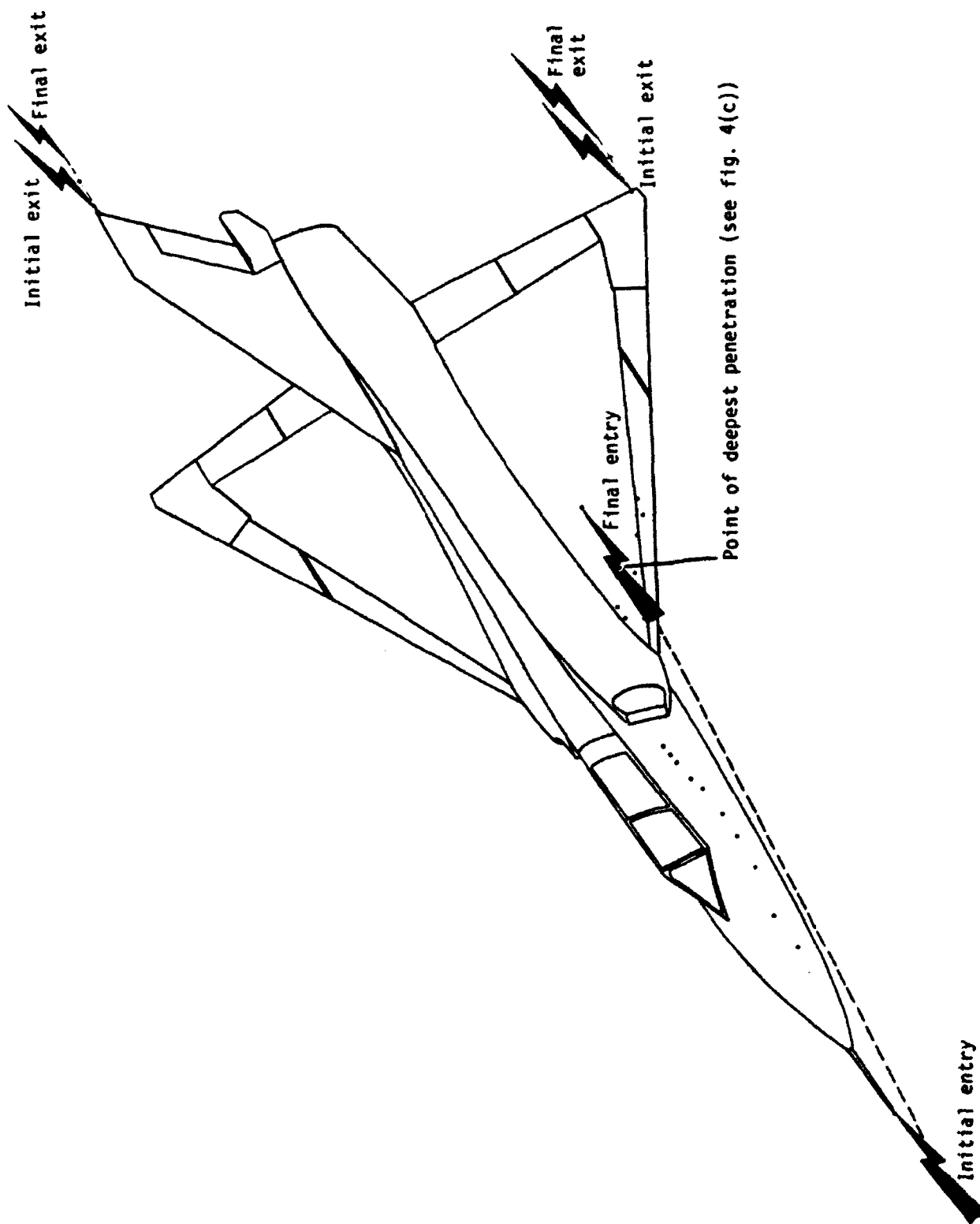


Figure 3 - Lightning attachment points for lightning strike 1, flight 80-018, June 17, 1980

Other extremities where random leader attachment is possible are rounded wing tips, empennage tips and tail cones. Whether lightning attachment occurs at the outermost region of an extremity depends somewhat on the direction of the electric field (i.e., the direction from which a naturally occurring leader is approaching), and also upon the rate of increase of the field intensity. Rapidly increasing fields cause a higher percentage of attachment to the "closest" or outermost regions, whereas slower rising fields give more time for ionization and streamer formation to occur at alternative locations, after which a "race" is run to see which streamer(s) contact the lightning leader or (if aircraft originated) which one(s) survive the race outward from the aircraft.

There is a somewhat lower probability of initial leader attachment to a "flat" surface of the aircraft well aft of the extremity regions described in the foregoing paragraphs, although it is known that this does happen now and then. It does seem likely that the first return stroke which follows such leader attachments will be of comparatively low intensity, and more similar to a subsequent (i.e., Component D) than a severe first return stroke (Component A) as defined in the aircraft design and test standards. Attachments to flat, aft surfaces would have to be associated with short striking distances, which, in turn, are due to lower charge in an approaching (or originating) leader tip. Upon discharge of this leader, a comparatively lower stroke current will occur. Interestingly, there appears to be more evidence of these "flat surface" attachments to upper surfaces rather than lower surfaces of airplanes. This may suggest that most naturally occurring leaders approach from above, not below, the airplane. The general relationship between striking distance and stroke current is illustrated in Figure 4.

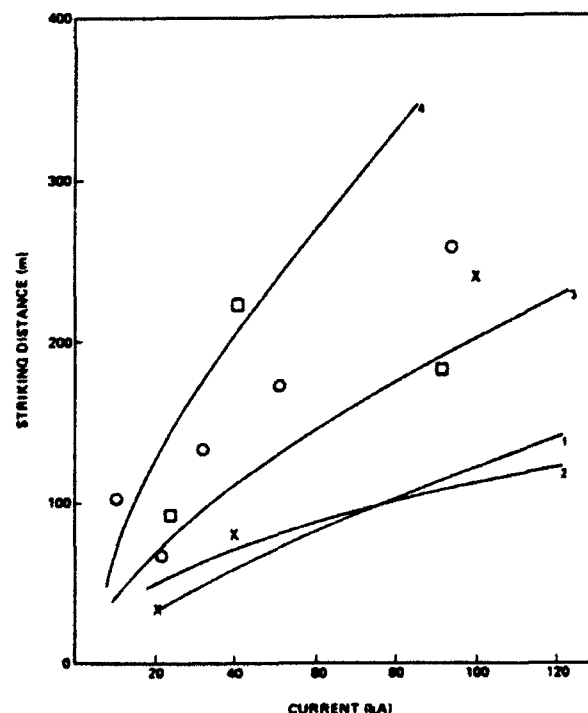


Figure 4 - Striking distance vs return stroke peak current for objects attached to ground [curve 1, Golde (1945); curve 2, Wagner (1963); curve 3, Love (1973); curve 4, Ruhling (1974); X, Davis (1962); O, estimates by Eriksson (1978); □, estimates from Eriksson from three-dimensional photography (1978)]. Adapted from UMAN (Ref. 8).

LEADER SWEEP

The contention that lightning leaders cannot sweep does not make sense. Leaders are well known to carry currents in the 10 A - 1,000 A range for periods of up to 20 ms, as the leader progresses from cloud to earth. Luminous leader channels have been measured photographically (Ref. 9) and they are, after all, ionized air. An airplane moving at 200 m/s would travel 4 m in 20 ms, and the leader channel would have to "sweep" alongside this aircraft in the same manner as virgin air. The leader will reattach to surfaces aft of the initial leader attachment or origination point at random locations, dependent on the locations of exposed (i.e., unpainted) conductive surfaces, or the occurrence of voltage pulses along the channel sufficient to break down the paint and establish a subsequent attachment point, whereupon the previous attachment will extinguish. This process has been simulated and studied repeatedly in laboratory tests by this author and others, in which test surfaces have been moved through stationary leader-type arc channels, or arc channels have been air-blown over test specimen surfaces. Formerly, it was thought that each new channel attachment spot on an aircraft was due to the arrival of a stroke; however, in most cases there can be found far more individual attachment spots than there are strokes in a typical lightning flash. Some intra-cloud flashes do not even contain well defined strokes; having lower amplitude, shorter duration current pulses, or just continuing currents instead.

REDUCTION OF STROKE INTENSITY WITH ALTITUDE

The third contention acknowledges that leaders do sweep aft of initial attachment points and reattach elsewhere prior to first return stroke arrival, but contends that the intensity of first return strokes at aircraft flight altitudes cannot be the same as that at the earth terminus of the flash. In particular, peak current and impulse charge and action integral diminish with height up the channel, since some leader charge then exists below, not above the airplane. This leads to the conclusion that strokes of intensity similar to that (200 kA, $2 \times 10^6 \text{ A}^2 \cdot \text{s}$) defined for the A-Component found in Zone 1A cannot occur far from initial leader attachment points.

Aircraft lightning strike experience belies this contention, as there have, in fact, been numerous instances where stroke currents at least as intense as Component A have arrived at aircraft surfaces considerably aft of forward extremities. This author described seven such incidents in an earlier paper (Ref. 4) and others not reported in that paper, are also known to him, and to other observers. Rough estimates of the magnitudes of the action integrals present in these incidents have been made by comparison with laboratory test effects on similar skin materials or other components and, in a few instances, these estimates have been corroborated by computation of temperature rise or magnetic forces occurring in objects, such as bond straps or control surface edges, of simple geometry.

These severe stroke effects have occurred as far aft as the aft fuselage on some airplanes and have clearly resulted from leaders having swept there from locations nearer the front of the airplane, though not always from a forwardmost part of an extremity.

The most common reason why these severe first return strokes do occur at airplanes at flight altitudes is simply that, whereas intensity of strokes in cloud-to-earth flashes does

diminish with altitude, the magnitude of charge remaining above the airplane is still sufficient to produce an A-type stroke, or even, upon occasion, a stroke of higher apparent action integral than that of Component A ($2 \times 10^6 \text{ A}^2 \cdot \text{s}$). In these instances, of course, the intensity of the stroke current at ground level is even greater. Records of strokes with action integrals far greater than $2 \times 10^6 \text{ A}^2 \cdot \text{s}$ have been reported by Berger et al (Ref. 10) and lightning current parameters from this reference have been listed in Table 1.

Table 1

Lightning Current Parameters*					
Number of events	Parameters	Unit	Percentage of cases exceeding tabulated value		
			95%	50%	5%
	Peak current (minimum 2 kA)				
101	Negative first strokes	kA	14	30	80
135	Negative subsequent strokes	kA	4.6	12	30
20	Positive first strokes (no positive subsequent strokes recorded)	kA	4.6	35	250
	Charge				
93	Negative first strokes	C	1.1	5.2	24
122	Negative subsequent strokes	C	0.2	1.4	11
94	Negative flashes	C	1.3	7.5	40
26	Positive flashes	C	20	80	350
	Impulse charge				
90	Negative first	C	1.1	4.5	20
117	Negative subsequent strokes	C	0.22	0.95	4.0
25	Positive first strokes	C	2.0	16	150
	Front duration (2 kA to peak)				
89	Negative first strokes	μsec	1.8	5.5	18
118	Negative subsequent strokes	μsec	0.22	1.1	4.5
19	Positive first stroke	μsec	3.5	22	200
	Maximum di/dt				
92	Negative first strokes	kA/ μsec	5.5	12	32
122	Negative subsequent strokes	kA/ μsec	12	40	120
21	Positive first strokes	kA/ μsec	0.20	2.4	32
	Stroke duration (2 kA to half-value)				
90	Negative first strokes	μsec	30	75	200
115	Negative subsequent strokes	μsec	6.5	32	140
16	Positive first strokes	μsec	25	230	2000
	Integral ($i^2 dt$)				
91	Negative first strokes	$\text{A}^2 \text{ sec}$	6.0×10^3	5.5×10^4	5.5×10^5
88	Negative subsequent strokes	$\text{A}^2 \text{ sec}$	5.5×10^2	6.0×10^3	5.2×10^4
26	Positive first strokes	$\text{A}^2 \text{ sec}$	2.5×10^6	6.5×10^5	1.5×10^7
	Time interval				
133	Between negative strokes	msec	7	33	150
	Flash duration				
94	Negative (including single-stroke flashes)	msec	0.15	13	1100
39	Negative (excluding single-stroke flashes)	msec	31	180	900
24	Positive (only single flashes)	msec	14	85	500

* Adapted from Berger et al. (1975).

Berger and others generally report that positive cloud-to-earth flashes occur 10% of the time (that is, 10% of all cloud-to-ground flashes are positive) and Table 1 shows that 5% of these have had peak currents exceeding 250 kA and action integrals exceeding $15 \times 10^6 \text{ A}^2 \cdot \text{s}$. This is over seven times more intense than the action integral of Component A. This, of course, was recorded at the ground terminus of the flashes (Berger's measurements were of currents entering a tower) so the intensity at any flight altitude would presumably have been less².

Attempts have been made to model the lightning leader and return stroke mechanism so as to calculate the intensities of current and action integral at various altitudes above ground and compare this with conditions at the ground terminus. Examples are found in References 11, 12 (etc.). Such models nearly always predict a substantial reduction in stroke current amplitude and action integral with distance above ground (for a downward going cloud-to-earth flash). None of the computed parameters have been verified by measurements of actual stroke parameters both at the ground and at some altitude up the channel (a formidable task), however, and in any case the computed results depend heavily upon assumed input parameters, such as leader charge distribution prior to stroke initiation. Most significant is the fact that none of the models account for charge stored in leader branches, of which there are a large number. This charge must feed into the cloud-to-earth channel upon return stroke arrival at respective junction points and must certainly increase stroke current amplitude and action integral at these points. A typical branched cloud-to-earth lightning flash is pictured in Figure 5.

-
- 2 Berger was consulted during the period when Component A was being defined (1972-75) by the responsible committees and did, as this author recalls, recommend a first stroke action integral of $5 \times 10^6 \text{ A}^2 \cdot \text{s}$. The advice was not taken and the lower value of $2 \times 10^6 \text{ A}^2 \cdot \text{s}$ was selected based on observed damage from in-flight strikes which, it appeared, were inflicting damage indicative of lower intensity strokes on the metal airplane skins prevalent at the time. In retrospect, it would appear that evidence of high action integral strikes on metal skins was as difficult then as it is now to distinguish from marks left by strokes and continuing currents of lower intensity, so high action integral effects would have gone unnoticed. Such effects show up much more dramatically on the composite skins and fairings found on more modern aircraft.

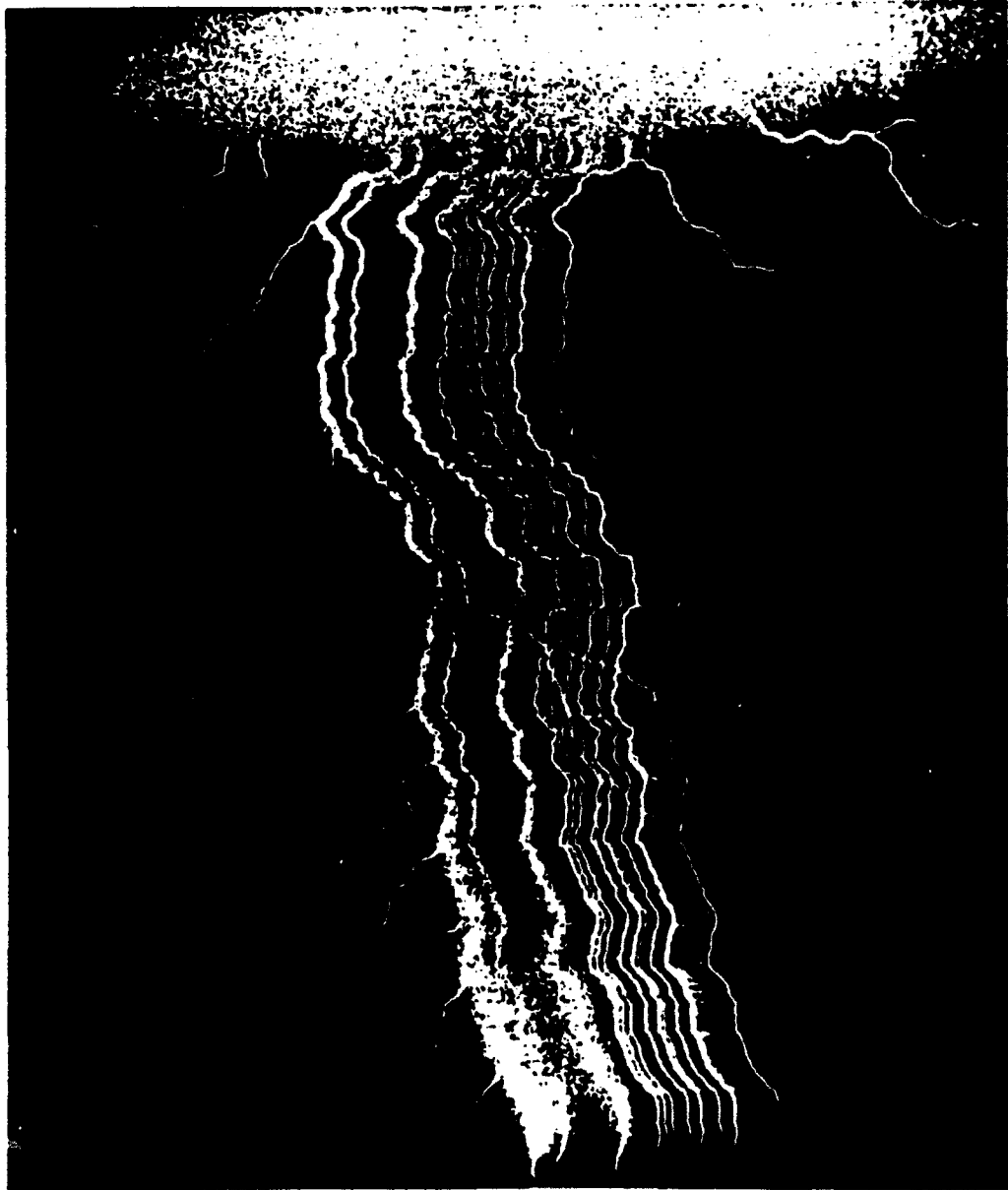


Figure 5 - Streak-camera photograph of 12-stroke lightning flash. The first stroke is on the left and is the only branched stroke. Photograph courtesy of M. Brook, New Mexico Institute of Mining and Technology (Ref. 13).

Other, recently published examples of very severe cloud-to-earth lightning discharges show peak currents in excess of 300 kA and action integrals of over $10 \times 10^6 \text{ A}^2 \cdot \text{s}$. Three such strokes, recorded on a tower near the Sea of Japan, are illustrated in Figure 6 (Ref. 14).

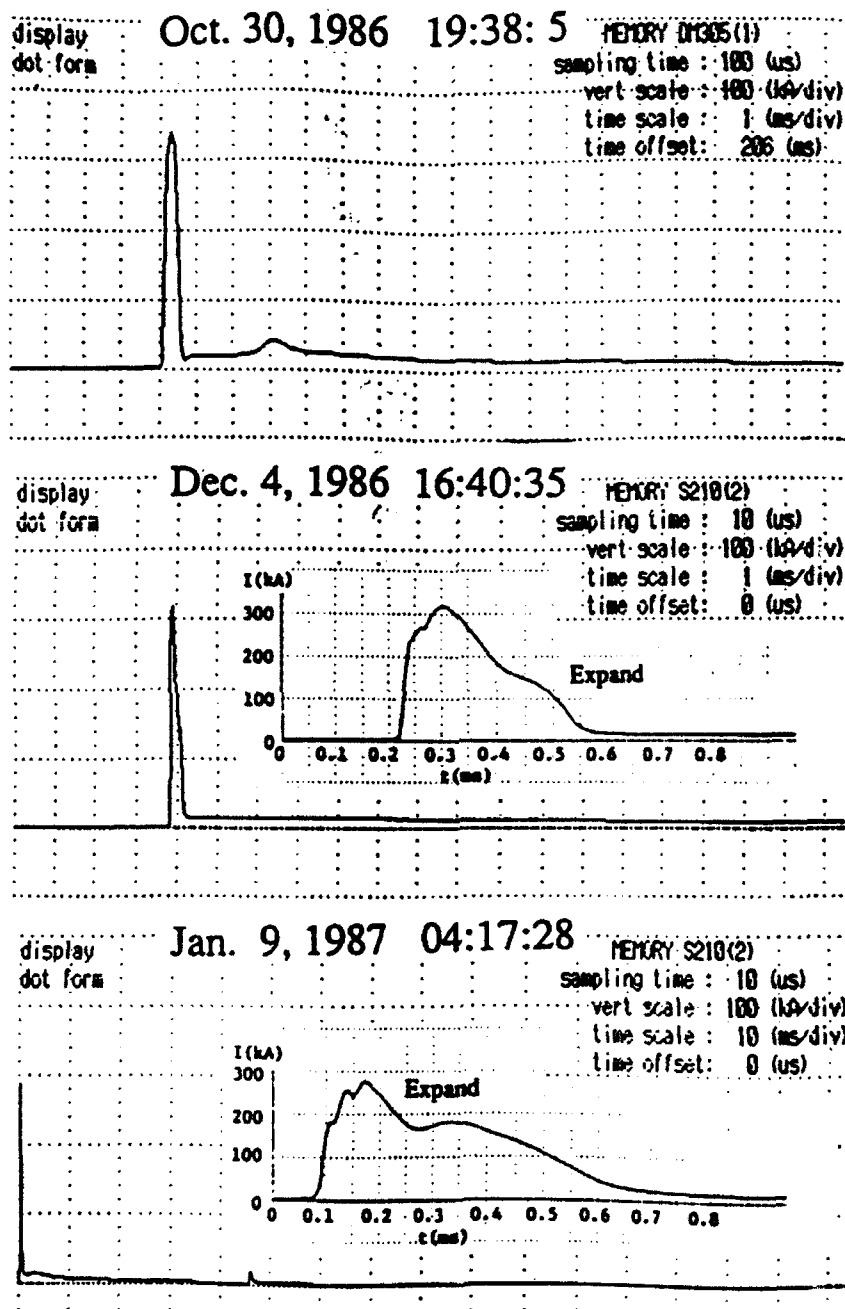


Figure 6 - Examples of severe positive lightning stroke currents recorded near the Sea of Japan (Ref. 14).

Two aspects of the positive flashes that produce these severe strokes are in order:

1. Flashes originating from storms over land or mountainous terrain originate from cloud anvils high (20,000-30,000 ft.) above the earth. Aircraft attempting to avoid flight through thunderstorms must frequently pass beneath (and occasionally through) anvils and are thereby exposed to positive flashes, even though they may be "in the clear." Pilot reports of strikes in these conditions confirm this.
2. Other severe positive flashes originate from low altitude clouds over water, and especially along sea coasts, often in winter, when thunderstorm conditions are not anticipated. Aircraft landing and taking off from coastal airports are exposed to these strikes, and the effects have indeed shown evidence of high action integral strokes. Typical examples have been noted at Seattle and Los Angeles on the western U.S. coast; Tokyo and other airports near the Japan coast; and London, England. This author is aware of unusually extensive damage, indicative of high action integral³ strokes at each of the above locations; though documentation of details of most of these encounters is not in the public domain.

The present Zone 1A lightning strike environment, which includes current Components A and B as defined in References 1 and 2, does not represent the most severe, or even an unduly severe environment for aircraft to be required to withstand safely. Arguments to the contrary would appear, as a minimum, to overlook the positive lightning stroke characteristics, and there is no way to assure that an airplane will not encounter positive, as well as negative, strikes.

PHYSICAL EVIDENCE OF SEVERE STRIKES TO AIRCRAFT

As noted earlier, it is possible to obtain some idea of the magnitude of action integral and electric charge entering (or exiting) an aircraft that has been struck by lightning in flight. This must usually be done by comparison of flight damage with damage inflicted by test currents of known description⁴ upon specimens of the skins, structures, and other

-
- 3 Physical damage to aircraft skins and structural elements is most directly relatable to action integral and charge transfer. Estimation of the peak current amplitude, or its rate of change, by comparison with laboratory tests, is not easily done. These latter parameters have more impact on lightning indirect effects than they do upon the direct effects on skins and structures that are the most important purpose of aircraft lightning strike zones.
 - 4 Comparison with test currents (i.e., Components A, B, C, and D) is, of course, legitimate in zoning considerations because the zones, in turn, establish which of these components are required for protection design and test purposes within each zone. From this point on it is the test criteria, not the natural environment, which must be satisfied.

airplane components that have been struck in flight. It is usually not possible to do this by other means. The author has described seven incidents (Ref. 4) where sufficient details were provided to make such comparisons, and he is aware of three or four times this number of additional cases not in the public domain. Some of these have involved severe strokes reaching extremities within "traditional" 18-inch Zone 1A areas, but at least an equal number of others have arrived well aft, and in some cases inboard, of the 18-inch regions on the extremities, and most have indicated action integrals well in excess of $2 \times 10^6 \text{A}^2 \cdot \text{s}$.

The fact is that marks left by a $2 \times 10^6 \text{A}^2 \cdot \text{s}$ stroke on a metal surface are not easily distinguishable from marks left by milder strokes and continuing currents. The effects of stroke currents include pitting and splatter of the outer 0.005 inches (or so) of aluminum skins, magnetic force crimping of light-weight trailing edges, and denting of thin, unstiffened skins. The intermediate currents produce deeper melting either within or quite close to the splatter or pitted area of the stroke. Surface finishes, including metal smoothness, primer and paint thicknesses have a great deal to do with resulting damage (the thicker the paint, the deeper the pitting, melting and denting), and the presence of rivets, fasteners, joints, edges, and seams of various sorts may alter the appearance of effects substantially from those appearing on "plain" skins. In most cases these effects are benign and have no impact on flight safety (the exception being integral fuel tank skins).

Fiberglass and CFC skins may be more extensively damaged by lightning stroke currents unless adequately protected. A review of examples of the damage mechanisms involved is found in Reference 6 (and elsewhere) and will not be discussed further here.

Examples of Zone 1A (Component A and B) effects on typical aircraft aluminum and composite skins, protected and unprotected, are available and will be displayed during the presentation of this paper at the International Aerospace and Ground Conference on Lightning and Static Electricity, 1992. Similar examples, of course, are described throughout the now vast literature on aircraft lightning testing.

Lightning effects on unpainted aluminum skins are sometimes indistinguishable to all but an experienced eye, as the dwell times at individual spots are shortened by the absence of insulating paints.

SUMMARY

The available body of natural lightning data does substantiate occurrence of severe action integral stroke currents at flight altitudes and in some cases these action integrals are unmistakably higher than the $2 \times 10^6 \text{A}^2 \cdot \text{s}$ incorporated in present airplane design and certification standards.

Well-known behavior characteristics of long, high voltage sparks in laboratory settings and physical marks left by lightning leaders attaching to airplanes confirm, without any doubt, that initial leader attachments may occur to airplane surfaces well away from outermost extremities or "tips." It is this author's opinion that this happens for both naturally occurring and aircraft triggered strikes (those that originate at the airplane) but there may be some differences in percentages of time "non-tip" strikes happen.

Since most aircraft are struck by lightning while in flight⁵, there must be "sweeping" of the leader channel as well as the lightning (i.e., post return stroke) channel following leader attachment. The "exit" channel will extend itself from aft surfaces or extremities while this happens, and after the aircraft has flown its entire length, both the entry and exit portions of the channel will hang on to the aircraft until the flash dies naturally.

The distance swept by the leader between initial leader attachment and first return stroke arrival will be determined by the aircraft airspeed and the time it takes the leader to reach the earth, typically 5 to 20 ms. This, in turn, depends on average leader velocity and path taken. Both of these parameters may vary widely in natural lightning, so the result will be a wide variation in actual return stroke arrival points, from strike incident to incident. Procedures used to estimate leader sweeping distance (known as "d") in the proposed B revision to U.S. FAA Advisory Circular AC 20-53 should therefore use mean or average leader distance and speed parameters and should be generally confirmed by the bulk of in-flight lightning strike experience, with the knowledge that some strokes will once in awhile fall beyond predicated Zone 1A/1B boundaries.

-
- 5 Occasionally airplanes and helicopters are struck while parked on the ground, or during take-off or landing. In these cases the uppermost extremity (i.e., the tail fin or main rotor blade) are most likely struck, and currents flash across wheels into the pavement. Unfortunately, several incidents of fatal injury to ground handling personnel have occurred, due to inadequate precaution during thunderstorm conditions.

REFERENCES

1. FAA AC 20-53A, *Protection of Fuel Systems*.
2. U.S. MIL-STD-1757A, *Lightning Qualification Test Techniques for Aerospace Vehicles and Hardware*, 17 June 1980.
3. Plumer, J. A., *Further Thoughts on Lightning Strike Zones for Aircraft*, Supplement to Lightning Technologies, NASA Conference Publication 2128, Washington, DC, 12 April 1985.
4. Plumer, J. A., *Evidence of Return Stroke Arrival Aft of Aircraft Frontal Surfaces and Implications for Protection Design*, 1990 International Conference on Lightning and Static Electricity, Bath, England.
5. U.S. Military Standard 1795A, *Lightning Protection of Aerospace Vehicles and Hardware*.
6. Fisher, F. A., Plumer, J. A., and Perala, R. A., *Aircraft Lightning Protection Handbook*, DOT/FAA/CT-89/22, September 1989.
7. Fisher, B. D., Keyser, G. L., Deal, P. L., *Lightning Attachment Patterns and Flight Conditions for Storm Hazards '80*, NASA TP 2087, December 1982.
8. Uman, M. A., *The Lightning Discharge*, Academic Press, Inc., 1987, p. 101.
9. Schonland, B. F. J., *The Pilot Streamer in Lightning and the Long Spark*, Proc. Royal Society, London, Ser. A, 220:25-38, 1953.
10. Berger, K., Anderson, R. B., and Kroninger, *Parameters of Lightning Flashes*, Elektra 80:23-37, 1975.
11. Strawe, D. F., *Non-linear Modeling of Lightning Return Strokes*, Proceedings of the FAA/FIT Workshop on Grounding and Lightning Technology, pp. 9-15, March 6-8, 1979, Report FAA-RD-79-6.
12. Uman, M. A., McLain, D. K., and Krider, E. P., *The Electromagnetic Radiation from a Finite Antenna*, Am. J. Phys., 43:33-38, 1975.
13. Uman, M. A., *The Lightning Discharge*, p. 15.
14. Goto, Y. and Narita, K., *Observations of Winter Lightning to an Isolate Tower*, Res. Let. Atmos. Elect., 12:57-60, 1992.

POSITIVE CLOUD-TO-GROUND FLASHES IN SEVERE STORMS

Donald R. MacGorman
NOAA/National Severe Storms Laboratory (NSSL)
Norman, OK 73069, USA
Telephone (405) 366-0405 Fax (405) 366-0472

Donald W. Burgess
WSR-88D Operational Support Facility
Norman, OK 73069, USA
Telephone (405) 366-6500

Carolyn D. Morgenstern
US Air Force and the University of Oklahoma
Norman, OK 73071, USA

ABSTRACT

We examine positive cloud-to-ground lightning in 25 mesoscale convective systems (MCSs) and in 15 severe storms. The signal amplitude distributions of positive ground flashes in MCSs that produced severe weather almost always either peaked at relatively large amplitudes or peaked at small amplitudes and decreased slowly with increasing amplitude. In the 15 severe storms we examined, cloud-to-ground flashes were dominated by positive flashes for periods ranging from 30 min to several hours. The geographic region in which positive or negative flashes dominated sequential storms on a given day appeared similar from storm to storm. In most cases observed by Doppler radar, storms dominated by positive flashes were low-precipitation or classic supercell storms. If negative ground flashes subsequently became dominant, the storm often became a classic or heavy-precipitation supercell storm. Large hail usually was reported during the period when positive ground flashes dominated, and the reported frequency and diameter of hail usually decreased after the dominant polarity of ground flashes switched to negative. In tornadic storms, the strongest tornado usually began after the positive ground flash rate decreased from its maximum value. Although many hailstorms and tornadic storms are dominated by negative flashes, tornadic storms and hailstorms comprise a small fraction of storms dominated by frequent negative flashes, but appear to comprise an overwhelming majority of storms dominated by frequent positive flashes.

INTRODUCTION

Although most cloud-to-ground flashes during the warm season effectively lower negative charge to ground (-CG flashes), cloud-to-ground flashes that lower positive charge (+CG flashes) have been observed to dominate in specific storm situations:

1. A few +CG flashes sometimes occur when storms previously dominated by -CG flashes begin to dissipate (e.g., *Fuquay* (1)).
2. Anvils of severe storms and the stratiform region trailing deep convection in mesoscale convective systems (MCSs) often contain a predominance of +CG flashes,

although adjoining regions of deep convection usually are dominated by -CG flashes (e.g., *Rust et al.* (2), *Rutledge and MacGorman* (3)).

3. +CG flashes sometimes occur in vigorous storms that produce tornados or large hail (diameter > 1.9 cm), and can either dominate CG lightning activity or occur in a pocket of a few +CG strikes (e.g., *MacGorman and Nielsen* (4), *Curran and Rust* (5)). Unlike other types of storms in which +CG flashes occur, severe storms can have +CG flash rates and densities of strike points comparable to those of -CG flashes in typical thunderstorms.

In this paper, we examine +CG data acquired by NSSL's direction-finder network (4) from severe MCSs and individual severe storms.

MESOSCALE CONVECTIVE SYSTEMS

We examined all MCSs that occurred in 1986 within the region covered by NSSL's network. There were a total of 25 MCSs, almost all of which produced severe weather. +CG lightning dominated CG activity in at least some region and period of 23 of these systems and appeared to occur in two modes:

(1) In the *convective mode*, the flash rate and strike point density of +CG flashes were large. In this mode, +CG flashes occurred in vigorous storms within an MCS, so the MCS's largest positive flash rate occurred early in its lifetime, usually before the peak -CG flash rate. This mode tended to occur during the spring and early summer, when severe storms are most likely in the region covered by NSSL's network.

(2) In the *stratiform/dissipating mode*, +CG strikes were scattered throughout either the stratiform region or a region of dissipating storms, while -CG strikes dominated in the vicinity of deep convective cells (similar to observations by *Rutledge and MacGorman* 1988). Our analysis combined cases having stratiform regions with cases having dissipating storms, because the two situations overlapped and had enough similarities that they were difficult to distinguish on lightning strike displays. In both cases, the maximum +CG flash rate occurred during the mature stage of the MCS, after or at the same time as the peak -CG flash rate. The maximum +CG flash rate usually occurred at about the same time as the peak in the area within contours of warmer cloud-top temperatures (e.g., -52°C).

We also examined the amplitude distribution of +CG flashes and found that the distributions tended to fit one of three categories:

(1) In the *low-amplitude* category (figure 1), most flashes had low amplitudes (median, 57 LLP units; 25% quartile, 37; 75% quartile, 115); there was a sharp decrease in the number of flashes at amplitudes above 50 LLP units. In five of the six MCSs in this category, +CG flashes occurred in the stratiform/dissipating mode. Only one case was in the convective mode. MCSs in this category tended to occur in April, May, and September.

(2) In the *high-amplitude* category (figure 2), the distribution peaked at much higher amplitudes and had few flashes at low amplitudes (median, 295; 25%, 189; 75%, 420). The majority of convective mode MCSs were in this category. Five of the nine cases in the high-amplitude category were in the convective mode; four were in the stratiform/dissipating mode. MCSs in this category occurred throughout the warm season.

(3) In the *middle* category (figure 3), the distribution peaked at low amplitudes, as in the first category, but decreased much more slowly at larger amplitudes (median, 183; 25%, 93; 75%, 317). Of the eight MCSs in this category, five were in the

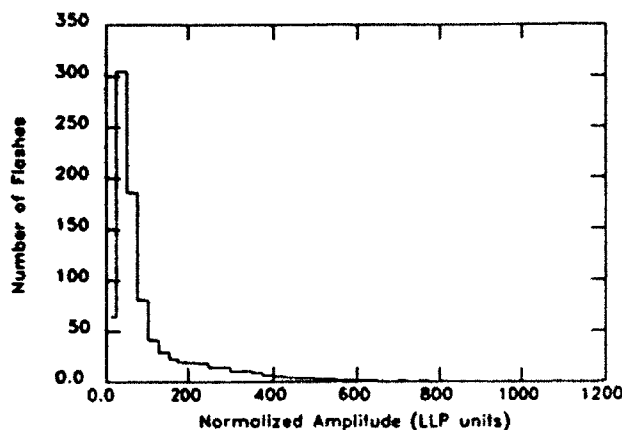


Figure 1. Signal amplitude distribution for low-amplitude category.

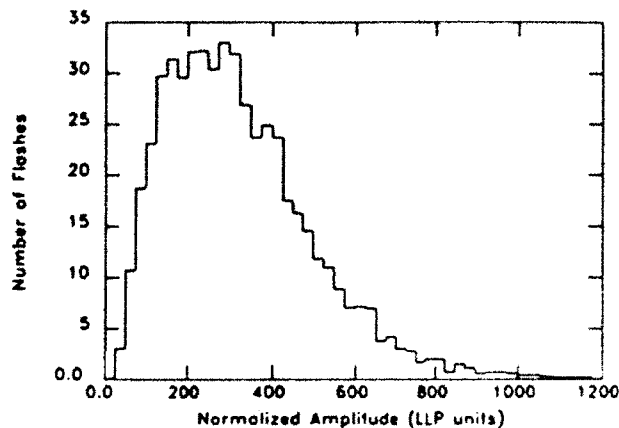


Figure 2. Signal amplitude distribution for high-amplitude category.

stratiform/dissipating mode; three were in the convective mode. Storms in this category occurred from June through August.

We examined briefly whether these different categories were a result of the decrease in the minimum amplitudes detected by the direction-finder network at increasing ranges. Although the low-amplitude category was detected only within roughly 150 km of stations in the network, several MCSs within this range were in the other two categories. Furthermore, we analyzed one MCS to examine the evolution of the amplitude distribution. As the MCS aged, there was a similar increase in the proportion of +CG flashes at small amplitudes for any range interval out to 200 km (the maximum range examined).

An analysis of representative soundings from each amplitude category suggests some tendencies that might be expected from the seasonal preferences. For example, soundings for low-amplitude MCSs tended to have cooler atmospheric temperatures and less precipitable water than soundings for middle category MCSs, since low-amplitude MCSs occurred in cooler months. Although high-amplitude MCSs occurred throughout the warm season, their soundings also tended to have cooler temperatures and less precipitable water. However, the average temperature lapse rate for high-amplitude MCSs was larger than for the other two categories (e.g., -7.97°C between 700 mb and 500 mb for the high-amplitude category, versus -6.29°C for the low-amplitude category, and -6.74°C for the middle). Both the larger lapse rate and the domination of the high-amplitude category by the convective mode suggest that the high-amplitude distribution is more likely in vigorous convection.

MCSs that produced +CG flashes in the convective mode, such as the storms we will examine in the next section, were more likely to have higher lightning signal amplitudes. Of the nine MCSs in the convective mode, five were in the high-amplitude category, and three were in the middle category. Only one was in the low-amplitude category.

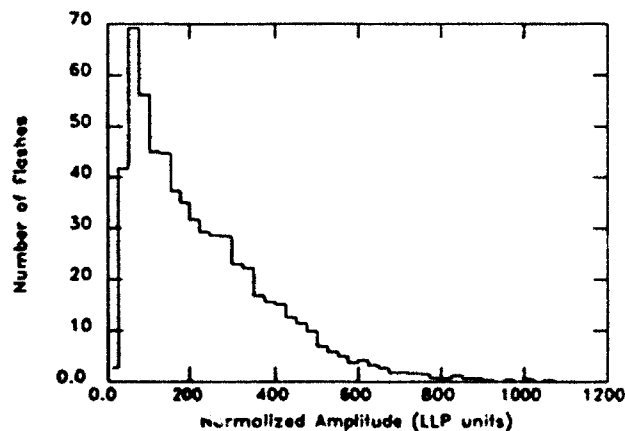


Figure 3. Signal amplitude distribution for middle category.

To test *Williams'* (6) prediction that amplitude tends to decrease with increasing flash rate, we examined median amplitude versus +CG flash count for 30-min periods in each amplitude category. Figure 4 shows all +CG categories combined. In all categories, the distribution of median amplitudes was almost random over a range of 400 LLP units during periods of low flash rates. However, for 30-min periods having >100 +CG flashes, the low-amplitude category had small median amplitudes (30-60 LLP units), while the other two categories had much larger median amplitudes (between 200-350). The median amplitudes of -CG flashes clustered around 140 and varied little with flash rate.

ISOLATED SEVERE STORMS

Although many hail or tornadic storms do not have large numbers of +CG flashes, early studies suggest that, when high flash rates and densities of +CG lightning occur, they are accompanied by severe weather. *Reap and MacGorman* (7) reported that a high density of +CG flashes was correlated with severe weather, particularly large hail, in a climatological study. *Curran and Rust* (5) and *Branick and Doswell* (8) found that +CG flashes dominated CG activity in low-precipitation supercell storms on two days.

We have examined fifteen severe storms in which CG activity was dominated by +CG flashes for periods ranging from a few tens of minutes to several hours. +CG strike points often occurred in dense clusters, much like the clusters of -CG strikes observed in most electrically active storms. In some of the storms, +CG flashes dominated CG activity throughout the lifetime of the storm, including all tornadic activity. An example of these storms is shown in Fig. 5a. Note that the storm produced hail and tornados throughout much of its life. The most violent tornado occurred after the maximum +CG flash rate.

In the majority of storms, +CG flashes dominated ground flash activity for only part of the storm's lifetime. Figure 5b shows an example of such a storm. This storm produced several tornados, including an F5 tornado near Plainfield, Illinois. Prior to the F4 tornado, when the storm was a classic supercell storm, CG activity was dominated by +CG flashes. This included periods when large hail and weaker tornados were produced. Note that there was a decrease in CG flash activity shortly before and during the F5 tornado, much as has been described previously for -CG flashes during some violent tornados.

At about the time that the F5 tornado began, the dominant polarity switched, and essentially all subsequent CG flashes were negative. This switch occurred at

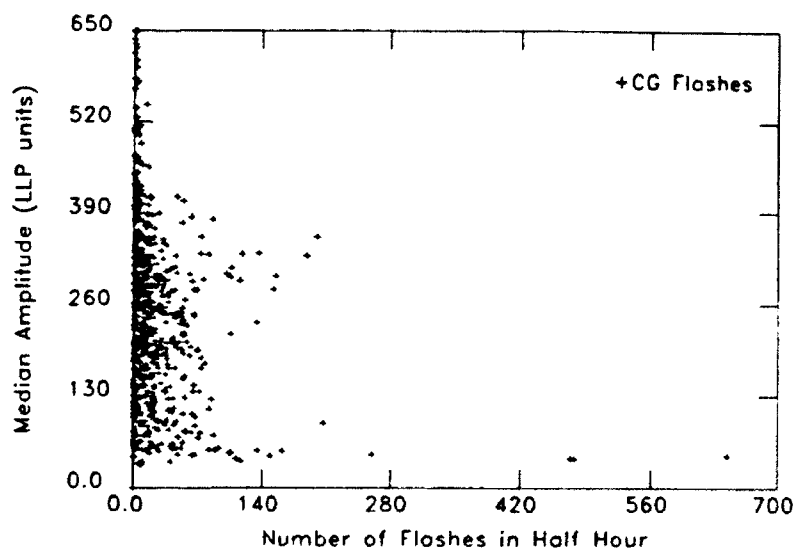


Figure 4. Median amplitude versus number of flashes per 30-min period for all +CG flashes in 25 MCSs.

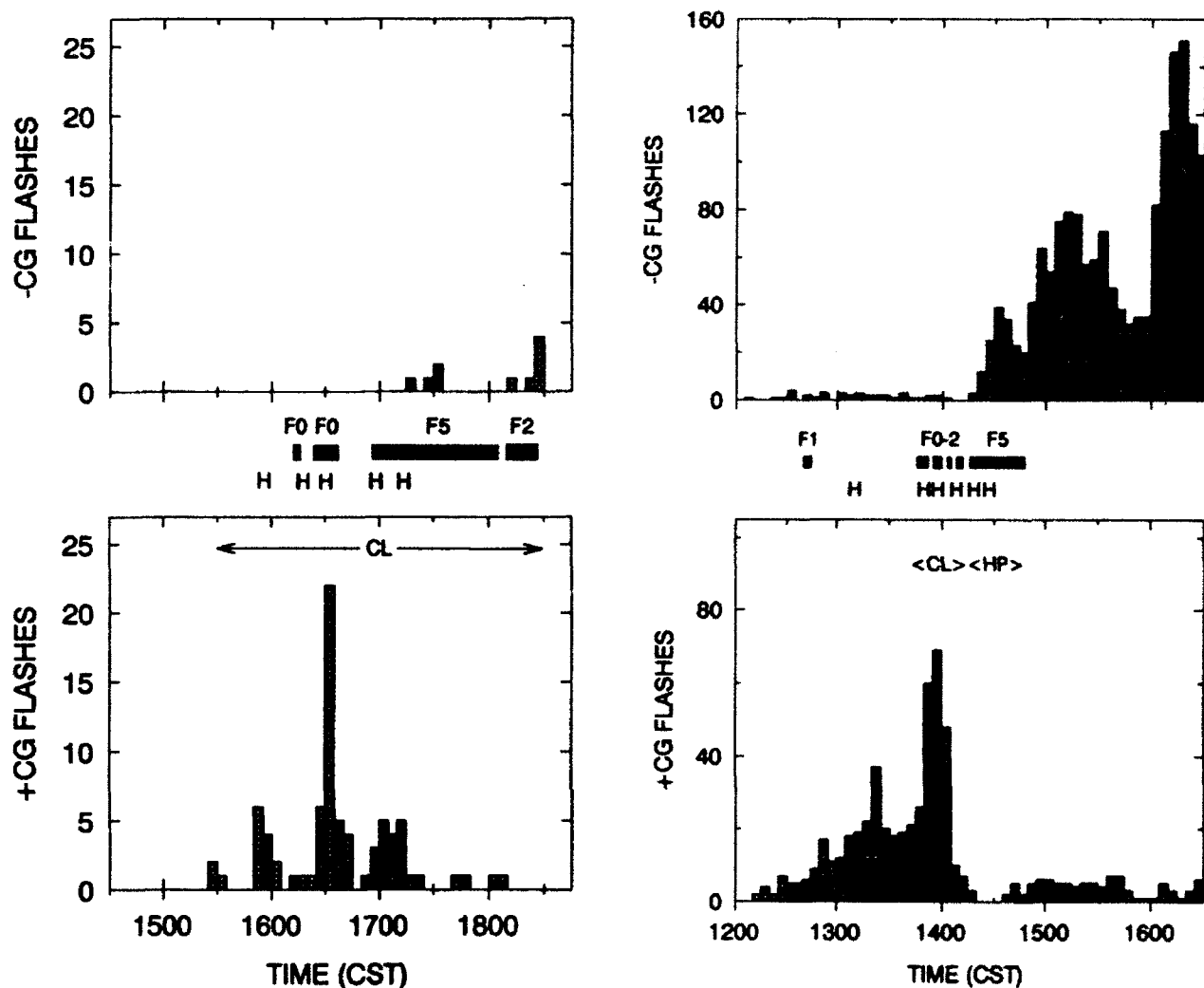


Figure 5. Number of +CG flashes per 5-min period for storms that passed through (a) Wichita, Kansas, on 26 April 1991 and (b) Plainfield, Illinois, on 28 August 1990. H's indicate the times of large hail reports; bars, the times of tornados, labelled with their F-scale ratings, F5 being most violent. Brackets around CL and HP indicate when the storms were classic and heavy precipitation supercells, respectively.

about the time that the storm evolved from a classic to a heavy-precipitation supercell storm. Shortly after the change in CG polarity, large hail reports ceased entirely. It appears that the transition in the dominant CG polarity of the Plainfield storm was related to fundamental changes in the storm's character. A similar transition was observed by Curran and Rust (5).

We observed high densities of +CG flashes in low-precipitation and classic supercell storms and in two hailstorms that had no mesocyclone. There are no reports of +CG lightning dominating in high-precipitation supercell storms or in weaker, multicellular tornadic storms. We infer from the two hailstorms with no mesocyclone that storm rotation cannot be a necessary condition for +CG flashes to dominate during intense convection.

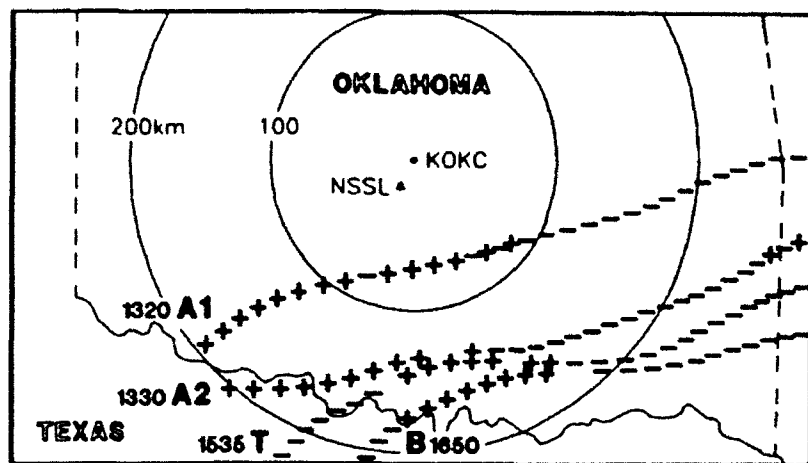


Figure 6. Storm tracks on 21 March 1991. Pluses indicate when +CG flashes dominated; minuses, when -CG flashes dominated; and zeros, when there were no CG flashes.

ground flashes occurred, but some of this overlap was caused by a gradual eastward shifting of the regions where each polarity dominated. Since the specific geographical pattern of this tendency shifted eastward in time and was different on other storm days, it appears that the explanation for the tendency most likely involves the regional properties of the atmosphere, possibly through systematic effects on other storm properties related to severe weather.

We suggest two possible causes for the domination by +CG flashes in these storms: (1) The horizontal displacement of precipitation from updrafts generally observed at lower-to-middle levels of supercell storms may create a tilted-bipole charge distribution such as has been observed in winter storms (e.g., by *Brook et al.* (9)). (2) If sufficient graupel and hail particles circulate through a region between roughly 0° and -15°C, they may create a region of lower positive charge. Several investigators have suggested that a lower positive charge could be formed by particle interactions at temperatures warmer than the charging reversal temperature studied, for example, by *Takahashi* (10) and *Jayaratne et al.* (11).

SUMMARY OF SEVERE STORM OBSERVATIONS

Many hailstorms and tornadic storms are dominated by negative flashes. However, tornadic storms and hailstorms comprise a small fraction of storms dominated by frequent negative flashes, and appear to comprise an overwhelming majority of storms dominated by frequent positive flashes. Although there was considerable variability in the details of the evolution of positive ground flash rates and of the relationship of positive ground strikes to severe weather, there also were tendencies toward some patterns:

1. The geographic region in which positive or negative ground flashes dominated on a given day appeared to be consistent from storm to storm on a given day; the dominant polarity switched in roughly the same region for sequential storms following similar tracks.
2. Most storms dominated by positive ground strikes were supercell storms (either classic or low-precipitation). In all storms with frequent positive flashes within range of a Doppler radar, some rotation was detected, although in two of the fifteen storms,

Large hail was present in all storms for which reliable hail verification was available.

Sequential storms that followed similar tracks on the same day tended to be dominated by +CG flashes in similar regions. Figure 6 shows that positive ground flashes tended to dominate in southwestern and south-central Oklahoma, west of a north-south line roughly 75 km east of KOKC, on 21 March 1991. There were some regions of overlap where both polarities of

the rotation did not meet criteria for a mesocyclone, and two weaker storms were beyond the range of the radar for radial velocity measurements. Storms often changed from low-precipitation supercell to classic supercell or from classic supercell to heavy-precipitation supercell at roughly the same time as the dominant ground flash polarity switched.

3. The majority of storms dominated by positive ground flashes produced tornadoes. In all tornadic storms in which positive ground flash rates had a prominent peak greater than 1.5 min^{-1} , the storm's most damaging tornado began after positive ground flash rates decreased from their peak value and before or near the time when negative flashes became dominant.
4. Sometimes ground flash rates decreased to near zero for tens of minutes or more after positive ground flash rates decreased from their peak and before negative ground flashes began to dominate ground flash activity. During this interval, storms generally appeared to remain strong and sometimes intensified, large hail continued to be reported, and sometimes the most violent or longest-lived tornado began.
5. All storms with frequent positive strikes in regions where we have greater confidence in hail verification produced large hail during the period when positive ground flashes dominated ground flash activity. If the dominant ground flash polarity subsequently switched to negative, the diameter and frequency of large hail reports usually decreased.

ACKNOWLEDGMENTS

The staff of NSSL provided valuable assistance in data acquisition and analysis, particularly Dennis Neilson, David Rust, Kurt Nielsen, Charles Doswell, and Dave Keller.

REFERENCES

1. Fuquay, D.M., 1982: Positive cloud-to-ground lightning in summer thunderstorms. *J. Geophys. Res.*, **87**, 7131-7140.
2. Rust, W.D., W.L. Taylor, D.R. MacGorman, and R.T. Arnold, 1981: Research on electrical properties of severe thunderstorms on the Great Plains. *Bull. Amer. Meteor. Soc.*, **62**, 1286-1293.
3. Rutledge, S.A., and D.R. MacGorman, 1988: Cloud-to-ground lightning activity in the 10-11 June 1985 mesoscale convective system observed during the Oklahoma-Kansas PRE-STORM Project. *Mon. Wea. Rev.*, **116**, 1393-1408.
4. MacGorman, D.R., and K.E. Nielsen, 1991: Cloud-to-ground lightning in a tornadic storm on 8 May 1986. *Mon. Wea. Rev.*, **119**, 1557-1574.
5. Curran, E.B., and W.D. Rust, 1992: Positive ground flashes produced by low-precipitation thunderstorms in Oklahoma on 26 April 1984. *Mon. Wea. Rev.*, **120**, in press.
6. Williams, E.R., 1985: Large-scale charge separation in thunderclouds. *J. Geophys. Res.*, **90**, 6013-6025.
7. Reap, R.M., and D.R. MacGorman, 1989: Cloud-to-ground lightning: Climatological characteristics and relationships to model fields, radar observations, and severe local storms. *Mon. Wea. Rev.*, **117**, 518-535.
8. Branick, M.L., and C.A. Doswell III, 1992: An observation of the relationship between

- supercell structure and lightning ground strike polarity. *Weath. and Forecasting*, in press.
9. Brook, M., M. Nakano, P. Krehbiel and T. Takeuti, 1982: The electrical structure of the Hokuriko winter thunderstorms. *J. Geophys. Res.*, **87**, 1207-1215.
 10. Takahashi, T., 1978: Riming electrification as a charge generation mechanism in thunderstorms. *J. Atmos. Sci.*, **35**, 1536-1548.
 11. Jayaratne, E.R., C.P.R. Saunders, and J. Hallett, 1983: Laboratory studies of the charging of soft hail during ice crystal interactions. *Quart. J. Roy. Meteor. Soc.*, **109**, 609-630.

STUDY OF ATMOSPHERIC ELECTRICAL EVENTS ABOVE COMPLEX TERRAIN

OSCAR TRONCOSO-LOZADA
CENTER FOR ATMOSPHERIC SCIENCES, UNAM
CU-MEXICO CITY, D.F., 04510 MEXICO
FAX: 525-548-9781

1. INTRODUCTION

From the middle of 1982 there has been, in our institution, an interest in thunderstorm studies, aided greatly by advances in instrumentation and data processing. As a result several cloud systems were analyzed and studied, and results are presented in this paper. The emphasis of the study was to investigate when and where the electrical discharge typically occur in relation to the lightning detection network. The sensor system consisted of two punctual discharge detectors, three radio noise detectors at frequencies of 10, 27 and 100 kHz and a tipping-bucket rain-gauge adjacent to the sensors. The instrumentation used in this study has been described by Troncoso (1987).

2. OBSERVATIONAL SYSTEMS AND ANALYSES

The point-discharge detector data were obtained mainly from the needle corona sensor installed at a height of 11.25 m. Also, a second identical sensor was located 8 m below and 48 m from the first sensor. Both sensors are placed in a flat rooftop 8.5 m in height. The data were collected during the entire day on a routine basis on strip-chart recorders. Radio-noise antennae are installed over the same rooftop as the rain-gauge, and both data sets were used as a complementary observational data. Finally, we used a set of rainfall data reported by some of the 45 active meteorological stations established in Mexico's Valley.

In particular, we show a prototype data set that was obtained by a highly sensitive detector system designed and operated at the National University campus in Mexico City. As Kasemir (1978) noted, the electric charge released from or to the earth by point discharge during a typical thunderstorm plays a dominant role in charge transfer between thunderclouds

and ground. The radio noise obeys the same laws as those controlling the propagation of conventional radio signals. At frequencies between 3 and 300 kHz the lower ionosphere (layer D) has the dominant influences in the propagation and is particularly important because of its practical significance in long range atmospheric detection of storms. As a result we now have better information on storm behaviour than previously available and our study supports the idea that these discharge features are fairly representative of severe storms in the southern region of the Mexico's Valley. We have in Fig. 1. point discharge data from corona current detection networks from the storm of July 18, 1990, as an example of one of the most common type of thunderstorm systems formed early in the diurnal convective cycle (1100 to 1300), beginning usually north of the southern mountain slopes. These clouds are small in area with a main convective center at the beginning. But, two hours later, the system of cells seems to be strengthened into a larger area and a more intense region. The system generally consists of several convective centers that form at different times and are active simultaneously together for some part of their lives. The current pulses measured by the point discharge detector grows in time. Notice that during this period the center of the main lightning activity overlies a region of positive and negative CG discharges. At this time (1515) occurred a heavy rain (265 mm/h) 26 km far east from our station. The southern region of the Valley was cloudy but clustered to the east side of the observation place. After 20 min precipitation decreased to a level of 5 mm/h for 75 min. Fig. 4 portrays the distribution of rain during the life cycle of this large convective system, the shaded area referring to the cloudy area. Numerals indicate the initial time of rainfall as was registered by the meteorological station. At 1645 an intense and violent precipitation, with an average rainfall rate of 305 mm/h was computed for two closed meteorological stations located 8 km north from our observatory. As we can see in the corona current records (Fig. 1), the electric field suddenly fluctuated during this time, the number of point-discharge currents increased to the highest values at this interval, both in number as in strength. Once the convective activity of the system ceased or moved to the north, as indicated by the weakening (Fig. 2) or absence of high lightning activity after 1800, some discharge

occurs in the weak and widespread region of the rain left behind.

3. DISCUSSION AND CONCLUSION

The air-flow over the southern border of the Mexico's Valley shows evidence that supports the existence of an air-current, passing over the mountain ridge, that is subjected of various kinds of deformations as described in a report by Durran and Klemp (1983). One of the effects often occurring is the development of a definitive wave pattern which is stably stratified in relation to the ground. Its existence and characteristics have been observed in our mountainous regions. Under certain weather conditions, during the rainy season, if the humidity in the upstream flow is favorable, these waves will produce visible clouds. The cloud pattern over the valley southern region is characterized by such trapped lee waves and such finding has significant implications for the reliable short and long-term prediction of rainfall. The storm on 18 July, 1990, used in this study contained at least two distinct regions associated with high lightning activity. This storm is shown in Fig. 4 as an example of this type. They could be identified and tracked throughout their lifetimes in view of the overall shape and relative position in the active electrical field. These regions lasted for 25 min in the precursor, and the nearby thunderstorm began abruptly with a rapid rise to peak at 1730 and then decayed regularly (Fig. 2 and 3). The rain data were recorded in two meteorological stations. The electric fields radiated from these abrupt events tended to have characteristic shapes which permit the events to be identified some hours before the beginning of the event (Fig. 3).

There is a need for research emphasizing the relationships and interactions between the smooth ascent of the orographic airflow and the effects of forced release of convective instability that substantially affects, on the windward slope, the airflow structure and precipitation processes (Marwitz, 1983). Also, as pointed out by Piepgrass et al (1982), there are relatively few detailed studies of the relationship between lightning and rainfall in the literature. Many questions about the electric activity processes of the different type of cloud systems arises from these observations. So, as we have few storms studied, these questions cannot be

answered from the present data, although some ground truth has been provided for testing some hypothesis. A satisfactory theory of cloud electrification must therefore explain why the electric field fluctuates so violently during a typical thunderstorm and field changes owing to lightning occur so frequently so some storms produce substantial rain, much more than had been forecasted. Also, it appears to be rather little correlation between either the character of the precipitation and the intensity of electrification as indicated by the lower frequency of lightning strokes during intense rain than usually last a short time, when observed with conventional on-site sensors.

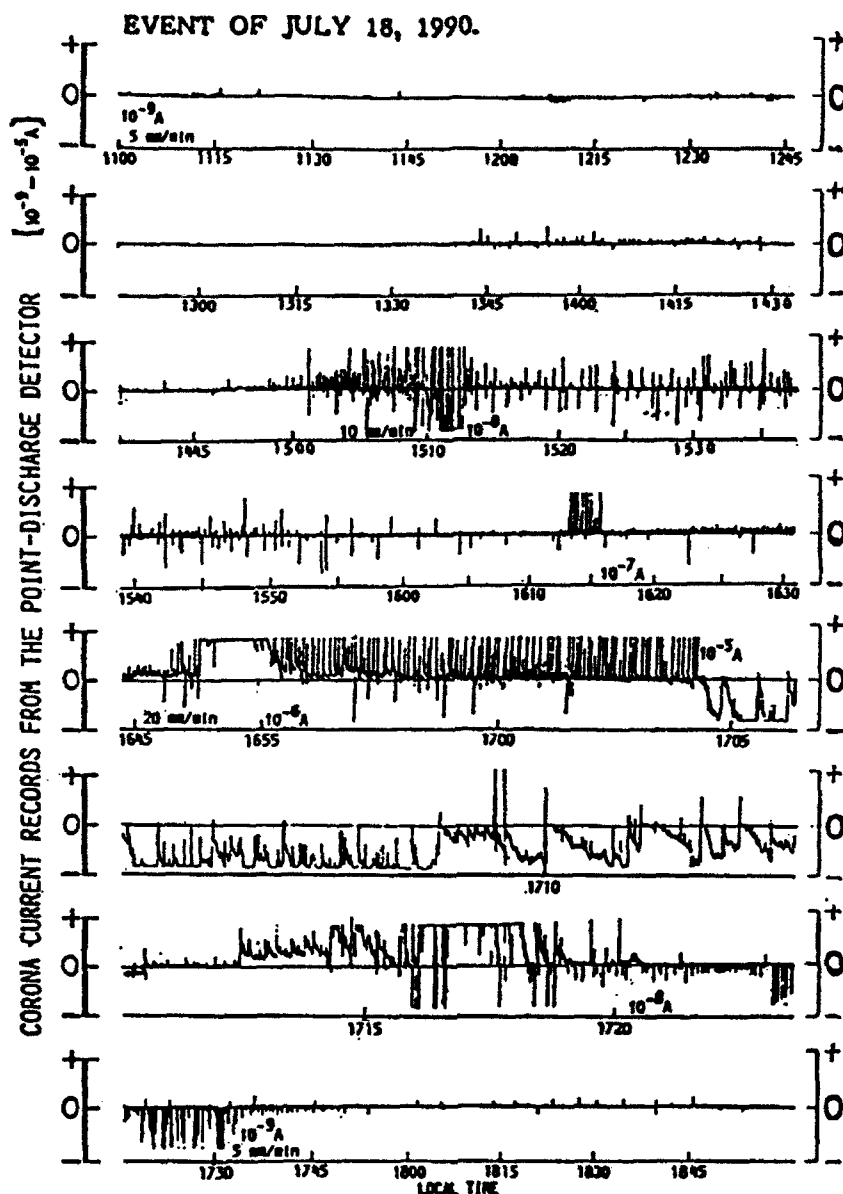
One might therefore expect that vigorous convective motions in storms will enhance the electrification process rather than interfering with it. Electrical storms occurring during a summer day in the southern Mexico's Valley area develop early in the day along the northern slopes of the Cuautzin-Ajusco-Las Cruces ranges in response to the upslope mountain circulation. Small systems containing only one or two convective cells develop to larger multicellular ones that arise later in the afternoon on the southern plains to produce orographic storms over the region.

Acknowledgements

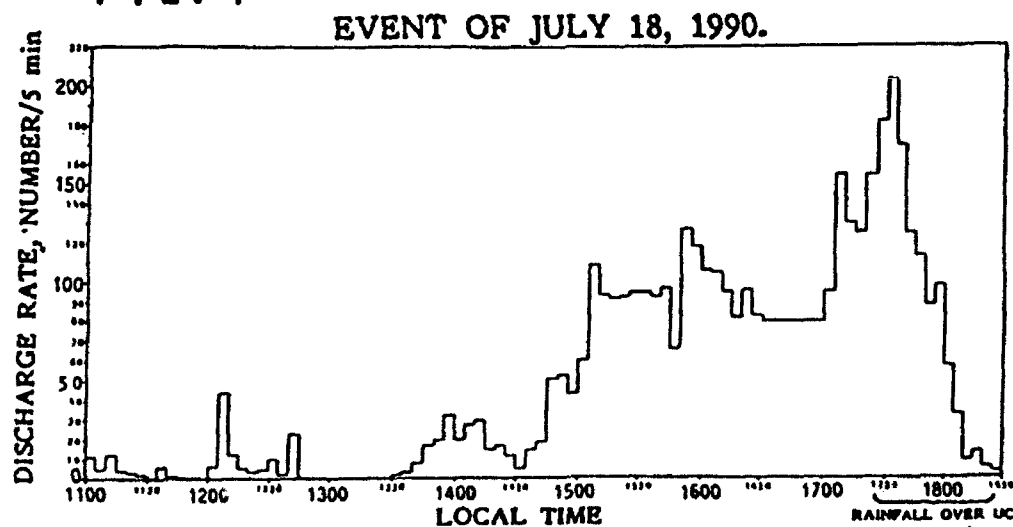
I wish to thank S. Arzak for operating and providing the rain gauge at the UC campus. I gratefully acknowledge to the National Service Meteorological Observatory in Mexico for the rainfall data of the 45 stations, and G. Zarraga for typing the manuscript.

References

- Durran, D.R. and J.B. Klemp. 1983. A Compressible Model for the Simulation of Moist Mountain Waves. *Mon. Wea. Rev.* 111, 2341-2361.
- Kasemir, H.W. 1978. Corona Discharge and Thunderstorm Fields. *Am. Meteor. Soc., Proc. Conf. on Cloud Physics and Atmos. Electricity*, 569-573.
- Marwitz, J.D., 1983. The Kinematics of Orographic Airflow During Sierra Storms. *J. Atmos. Sci.*, 40, 1218-1227.
- Piepgrass, M.P., E.P. Krider, and C.B. Moore, 1982. Lightning and Surface Rainfall During Florida Thunderstorms. *J. Geophys. Res.*, 87, 11, 193-11,201.
- Troncoso, O.L., 1987. Study of Electric Field Changes Accompanied by Atmospheric Radio Noise at 10 kHz at Mexico Valley. *Rev. Mex. Fis.* 33, 247-263.

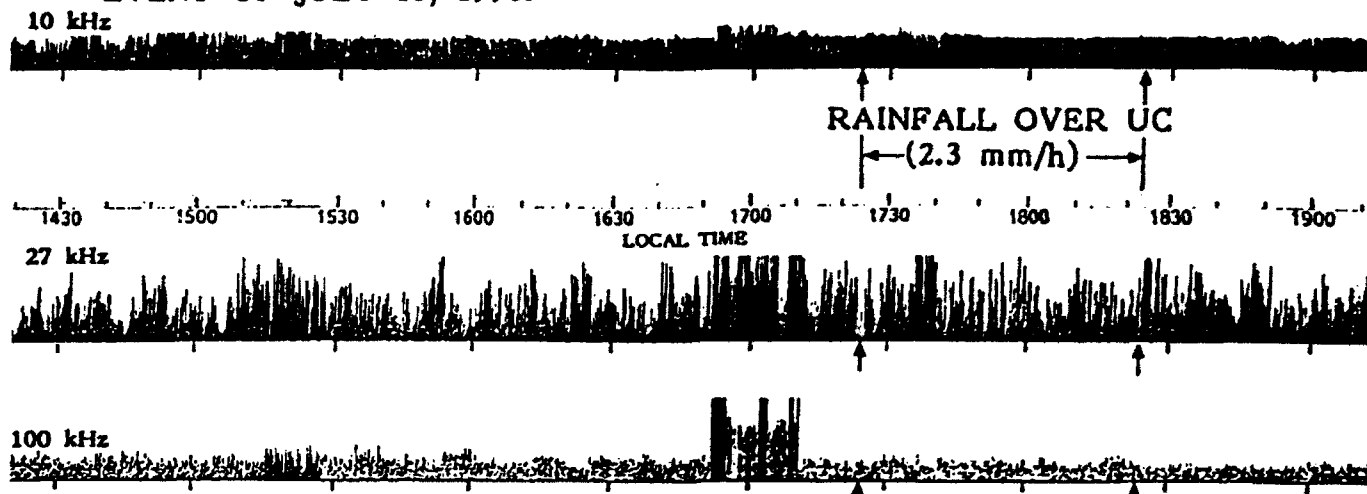


ANALOG RECORDER DATA CAPTURED IN PAPER CHARTS
FIG. 1



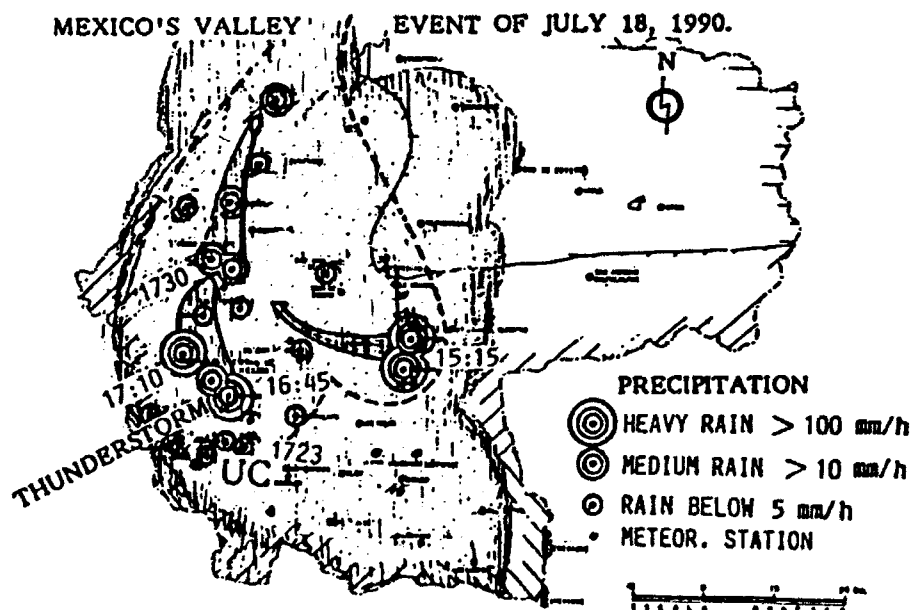
TOTAL NUMBER OF LIGHTNING DISCHARGES IN
FIG. 2 SUCCESSIVE 5 MIN INTERVALS

EVENT OF JULY 18, 1990.



DATA CAPTURED IN PAPER CHARTS

FIG. 3 MEASUREMENT OF ATMOSPHERIC RADIO NOISE



CLOUDY AREA AND PRECIPITATION

FIG. 4

APPLICATIONS OF STRESS ENVELOPE CONCEPTS TO AIRCRAFT EMP AND LIGHTNING SURVIVABILITY

Mr. Sam Frazier

**Naval Air Warfare Center Aircraft Division, SY84
Patuxent River, Maryland 20670-5304
Telephone (301) 863-3868 FAX (301) 863-3871**

ABSTRACT

The Naval Air Warfare Center Aircraft Division is conducting research into the modeling of aircraft electromagnetic transient response data. One result has been the development of a test point stress waveform which combines multiple responses. This single stress waveform bounds the test point stress responses collected during different test phases; each contributing waveform contains coupling response data from various polarizations, orientations and configurations relative to the external threat environment. This new waveform, termed the "Stress Envelope", has significant applications in the area of inductively coupled direct-drive, reducing test uncertainties, and permitting better estimates of system margins.

INTRODUCTION

This paper investigates the application of a waveform envelope to bound the measured system responses to electromagnetic transient environments. Significant improvements in current assessment capabilities may be possible by using existing data acquisition and processing capabilities and recently developed composite waveform direct-drive technology. The purpose of this research is: to reduce uncertainty by better bounding of the system-environment interaction; to use all of the available measurements of system response; and, to improve the current survivability Research, Development, Test, and Evaluation (RDT&E) process.

SYSTEM SURVIVABILITY

Survivability is dependent upon the interaction of threat, scenario and system. Each environmental scenario will result in a theoretically unique response for the system at a given measurement point.

The characteristics of a particular test point response varies based on the frequency range of the threat environment and how the environment is coupled to and into the system under test. Figure 1 identifies the aircraft stress mechanisms resulting from exposure to electromagnetic transient environments. When the system is exposed to simulated lightning and electromagnetic pulse (EMP) environments, it responds based on its structural resonance. These transient waveforms can be characterized and combined using accepted analysis techniques. Therefore, the transient threats are the focus of this research.

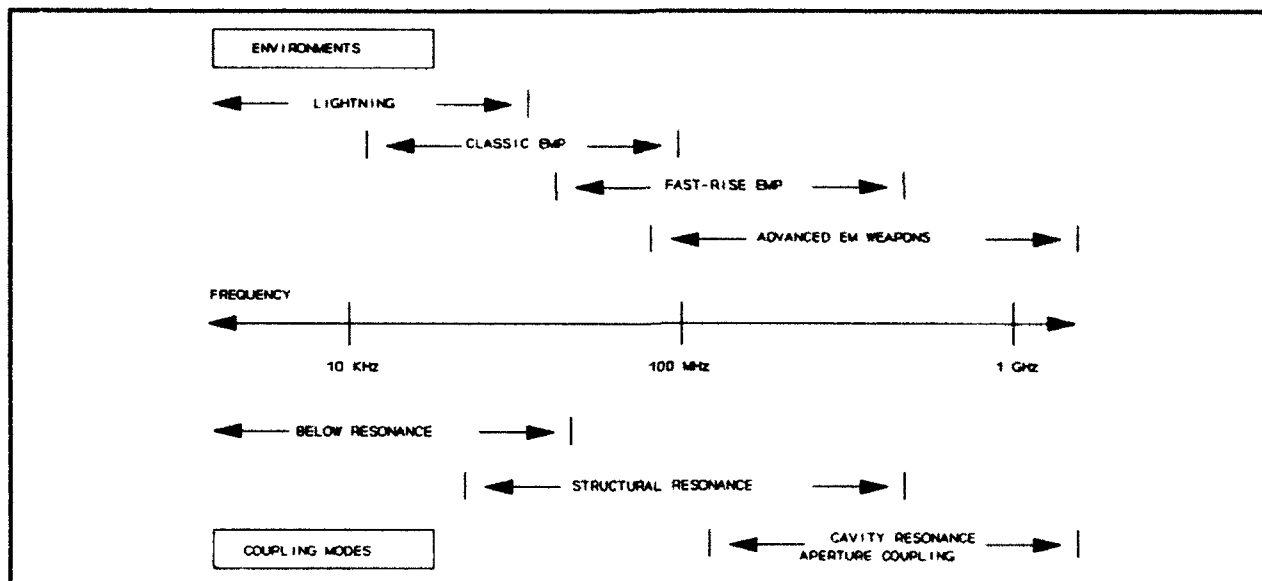


FIGURE 1
EM TRANSIENT ENVIRONMENTS VS. AIRCRAFT STRESS MECHANISMS

BACKGROUND

Electromagnetic transient effects testing seeks to determine the systems margin of survivability. One approach, depicted in figure 2, is to determine the stress placed on a system and then compare to the system's inherent strength.

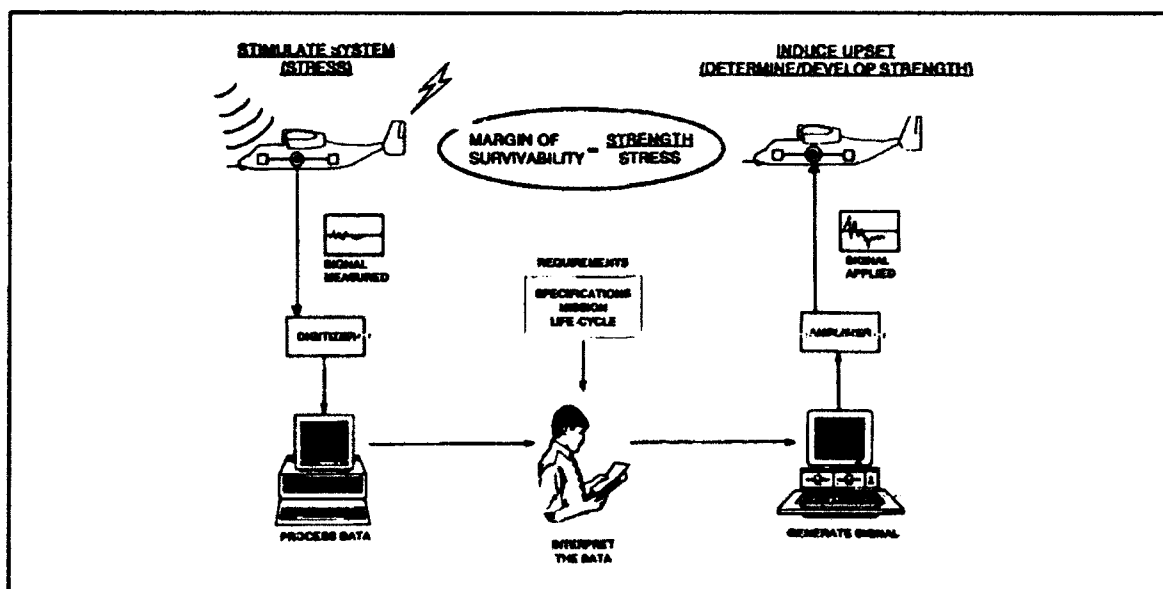


FIGURE 2
THE ELECTROMAGNETIC TRANSIENT EVALUATION PROCESS

The stress is determined by exposing the system to a simulated, external electromagnetic environment. Internal responses are measured at numerous locations on cables or individual wires. The measurements are then extrapolated to predict the full threat responses for the system. The system response, or stress, establishes the system level electromagnetic susceptibility to the external threat. In EMP testing, an aircraft can be tested in different configurations and orientations, while exposed to both horizontally and vertically polarized environments. Therefore, a test point may have several measurement records. Traditionally the highest peak current measurement is selected to represent the stress response at a test point. All other data is considered supplemental and ignored when determining the system margin and retains a very limited role in further aircraft survivability or electromagnetic assessments. In this approach, signal processing techniques have been restricted to correcting data.

Next, while the system is operating, the selected test point response is amplified and, using inductively coupled direct-drive, reinjected into the equipment at the same test point until the system upsets, fails, or a reasonable level of protection is demonstrated. This process establishes the system's strength and quantifies the system's vulnerability to an external threat.

STRESS ENVELOPE RESEARCH OBJECTIVES

It is proposed that by using basic signal processing techniques, all of a test point's response measurements can be efficiently combined to determine its overall stress envelope. The objective is to develop a worse case waveform from measured data at the black box level.

The electromagnetic stress envelope represents the system's maximum internal electromagnetic response at a physical location due to an external electromagnetic threat. Since the system under test is assumed linear, the initial stress envelope is developed by combining each of the multiple response measurements at an individual test point into a single threat response waveform as shown in figure 3. An envelope is not constrained to one parameter or attribute, but can be configured from multiple measured waveforms or system responses. This can include measurements from high level pulse and low level CW sources and from different orientations or stimuli. The resulting envelope bounds all information into a single worse-case waveform. This stress envelope can then be used in direct-drive testing to provide a better margin estimate.

METHODS FOR DEVELOPING ENVELOPES

A number of methods are available for developing envelopes. The two methods considered in this research are autoregression and damped sine characterization.

Autoregression methods are a linear way of using a correlation coefficient to estimate the average value of the dependent variable for each value of the independent variable. In other words, any regression technique is a linear means of developing an average from a group of weighted values or averages. When a number of scattered waveform points are involved, the regression line is a smoothed version of the graph of averages from as many sources as are available. Each point is weighted according to the number of cases it represents.

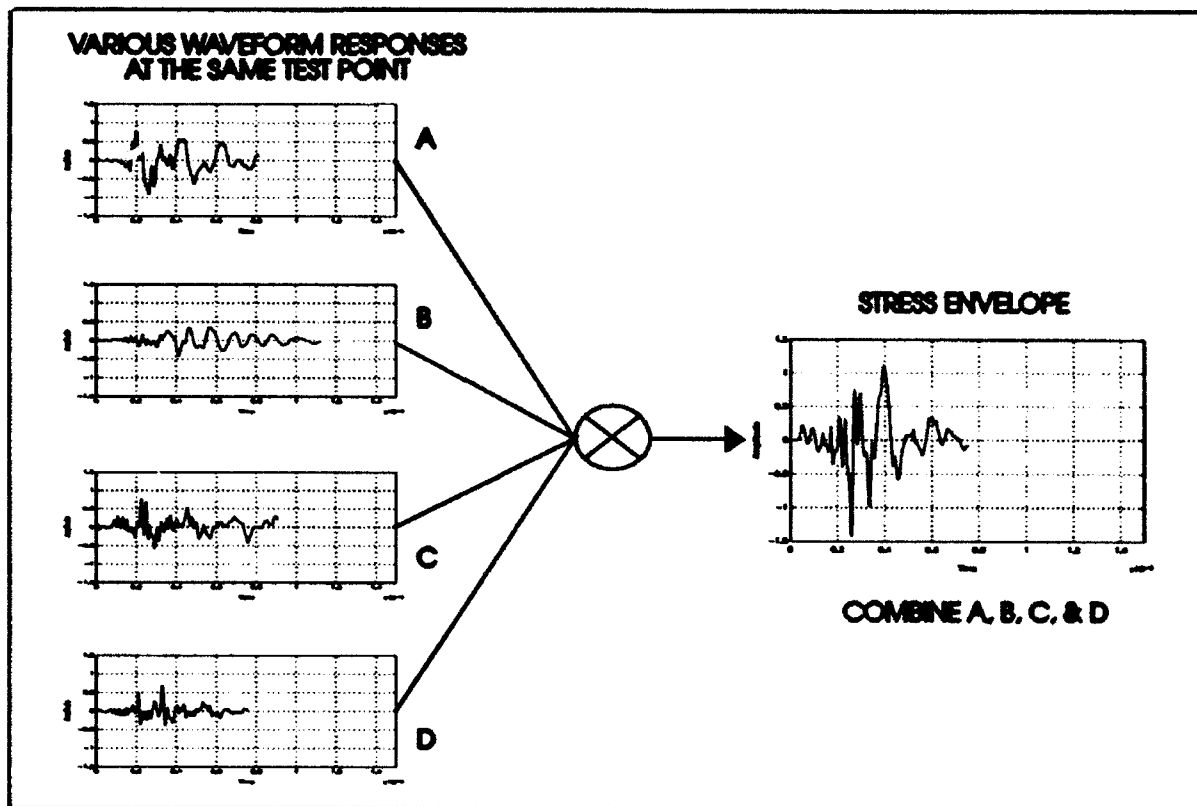


FIGURE 3
WAVEFORM CONVOLUTION PROCESS

Two autoregression techniques are being evaluated. One autoregression approach, AR, uses a weighted average technique. The second, ARMA, uses a moving average technique. Either method progressively fits each measured test waveform into a single polynomial equation. Each method further reduces the multiple waveform polynomials into single envelopes.

Damped-sine characterization (DSC) is a non-linear means of using the spectrum to characterize a test measurement as a sum of a small number of individual damped-sine waveforms. The DSC decomposes a waveform into multiple poles. The resulting poles from all data are placed in a table and reduced by eliminating smaller poles located close to larger poles. This method eliminates poles which would otherwise have no individual contribution. A single envelope is then constructed from the poles that remain.

PRELIMINARY ENVELOPE CHARACTERIZATION

Figure 4 depicts the current research effort. The approach to characterizing a stress envelope uses the standard data measurement techniques. All test point measurements from various orientations are obtained by measuring the system response to threat level EMP excitation at discrete test points using current probes. This data is

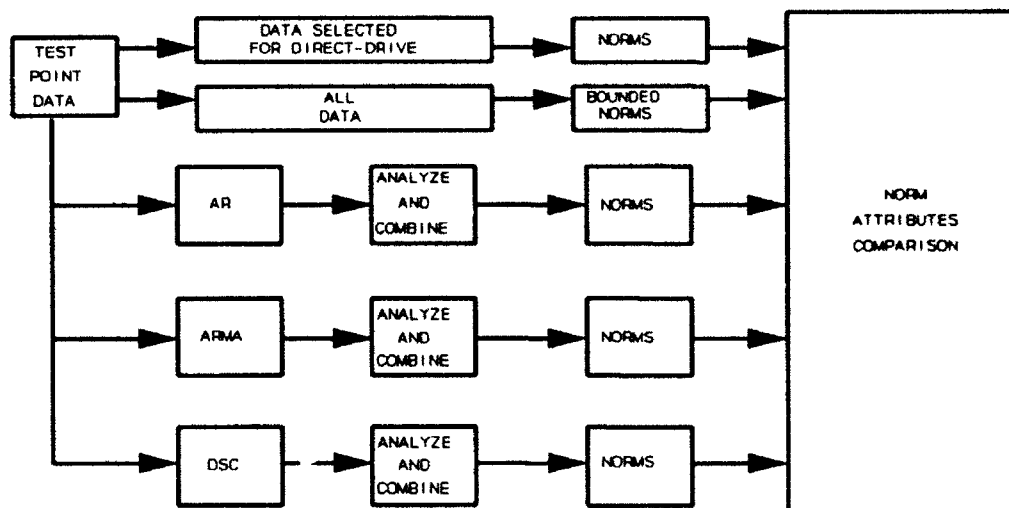


FIGURE 4
STRESS ENVELOPE ANALYSIS

combined using the techniques described to develop stress envelopes. The next step is to compare time domain attributes of the resulting stress envelopes. Norm attributes have been selected as a technique for making this comparison.

The norm attributes that are derived from various measured and developed waveforms provide a statistical comparison to characterize the difference between the new approach and current approaches. The results quantify the goodness of each envelope algorithm. This process will also be used to investigate envelope optimization.

FUTURE ENVELOPE RESEARCH

NAWC-AD has developed a direct-drive test capability that can provide a tailored stress waveform. We also plan to extend the bandwidth and power output ranges of our direct-drive capability along with other instrumentation improvements. These improvements in simulators, instrumentation, and test techniques plus the new stress envelope approach are expected to provide long-term, high-gain reduction of test assessment uncertainties. Such future improvements also highlight the possibility of extending into new applications and expanding the stress envelope technique to include additional threat environments.

Possible new applications for future research include circuit analysis and frequency-domain analysis. Computer aided circuit analysis techniques allow for predicting responses based on specific inputs. If the input can be modeled as the stress envelope, the potential to better identify actual threat response characteristics may significantly improve margin predictions.

Time domain analysis is used for this research. Future research will be extended to analyze frequency domain attributes. This additional information could allow better characterization of the system responses to a specified threat.

As previously noted, the stress envelope technique can be applied to other electromagnetic transient environments, such as lightning. Environments which contain higher frequencies where cavity resonances and aperture coupling are the dominant stress mechanisms are also of interest. All of these environments may be combined to create a more inclusive electromagnetic transient stress envelope. Research is needed to determine the viability and limitations of such an approach. The result could be a more cost effective and comprehensive system test approach.

BENEFITS

The stress envelope approach uses all measurements to provide a better estimate of system margins. The environment and hence the stress envelope contains significant components that do not interact with or affect certain aircraft equipment. The system's coupling modes and any system degradation or failure responses observed while acquiring stress measurements can be evaluated to identify the critical frequencies or poles in the stress envelope. The non-critical waveform components can then be deleted and only the critical ones used during direct-drive testing. This allows the limited direct-drive capability to focus on driving an optimized waveform to determine the margin. The "smart" margin approach using existing direct-drive capability is a practical approach to determine margins. This approach can extend the range of present test capabilities. This is an important benefit since new threat information continually requires upgrades in direct-drive capability.

CONCLUSIONS

The stress envelope concept has important applications in aircraft electromagnetic transient testing. The technique has the potential for significant improvements in current survivability assessment test capabilities by reducing test and assessment uncertainties. The stress envelope approach provides the maximum stress waveform regardless of the actual aircraft-threat scenario. It also allows waveform construction from multiple sources such as high-level pulse, low-level CW and analysis. Because of its flexibility, the stress envelope approach may support further research into unifying electromagnetic environments and test capabilities. Most importantly, this approach creates a more complete characterization of the electromagnetic transient stress and strength.

INTEGRATING ARMY AVIONICS HARDENING

Robert A. Pfeffer
U.S. Army Nuclear and Chemical Agency
ATTN: MONA-NU
7500 Backlick Road
Bldg. 5073
Springfield, VA 22150-3198
Telephone (703) 355-7256 FAX (703) 355-7284

ABSTRACT

The non-ionizing electromagnetic environments in which modern aircraft must operate are complex and potentially lethal, often consisting of transient and/or CW sources having a spectral content from nearly DC to tens of Ghz. The most cost effective hardening method of choice against all these environments is shielding and penetration control. The purpose of this paper is to detail the rationale and approach in integrating non-ionizing electromagnetic protection of modern avionic systems.

Paper not submitted.

LIGHTNING FREQUENCY AND ASSOCIATED CLIMATIC PROCESSES

J.K. Patnaik
Department of Meteorology & Oceanography
Andhra University
VISAKHAPATNAM-530003, INDIA
Telephone 52627

ABSTRACT

Using many years data (about 45 years) of Thunderstorm days, the lightning frequency maps are prepared for Africa, Europe, and India. The areas of maximum of lightning occurrences are pointed out. The associated climatic processes with the occurrences are discussed through Tropical, Sub-tropical and Equatorial Processes. An inter comparison between the occurrences are also carried.

Paper not submitted.

Development of Models for Predicting the Triggering of Lightning by Launch Vehicles

**Rodney A. Perala, Terence H. Rudolph, Calvin C. Easterbrook,
Dale A. Steffen**

Electro Magnetic Applications, Inc.

12567 W. Cedar Drive, Suite 250

Lakewood, Colorado 80228

Phone: (303) 980-0070 FAX: (303) 980-0836

ABSTRACT

As evidenced by incidents on Apollo 12 and AC-67 launches, the threat to launch vehicles from triggered lightning is real. Even in the absence of naturally occurring lightning, it is possible for a launch vehicle with attached plume to amplify atmospheric electric fields to an extent such that an electrical discharge can happen. Therefore, launch rules which are based on the presence of natural lightning in the vicinity may be inadequate to ensure that a triggered strike cannot occur. In order to develop adequate launch guidelines with respect to triggered lightning, it is necessary to first thoroughly understand the physical mechanisms leading to the triggered strike. To this end, we have begun to develop a triggered lightning model which will allow one to predict in advance the conditions under which a lightning strike will occur to a launch vehicle during ascent. The purpose of this paper is to describe the project and the technical issues, and to present some preliminary results.

1.0 INTRODUCTION

Vehicle triggered lightning is that which is caused by the vehicle itself, and would not otherwise occur. The basic requirement for its occurrence is that the local electric field exceeds air breakdown levels at some locations on the vehicle and that the ambient thunderstorm field is large enough to create and propagate a leader.

There are many factors which may affect the triggering of lightning by launch vehicles. These factors are illustrated in Figure 1 and are listed as follows:

1. Microphysic of air breakdown
2. Thunderstorm particles
3. Dynamic air pressure
4. Plume effects
5. Electric field enhancement factors

In this paper we describe a research program whose objective is to develop a methodology and construct a model which will accurately forecast the occurrence of triggered lightning for the Titan IV launch vehicle, given the atmospheric electrical environment and the Titan IV specifications.

Previous studies [1, 2] have described some of the factors listed above. In the present program, the following areas are being researched:

- Air pressure effects
- Rocket plume effects (charge density model)
- Form factor effects
- Corona vs. arc initiation conditions

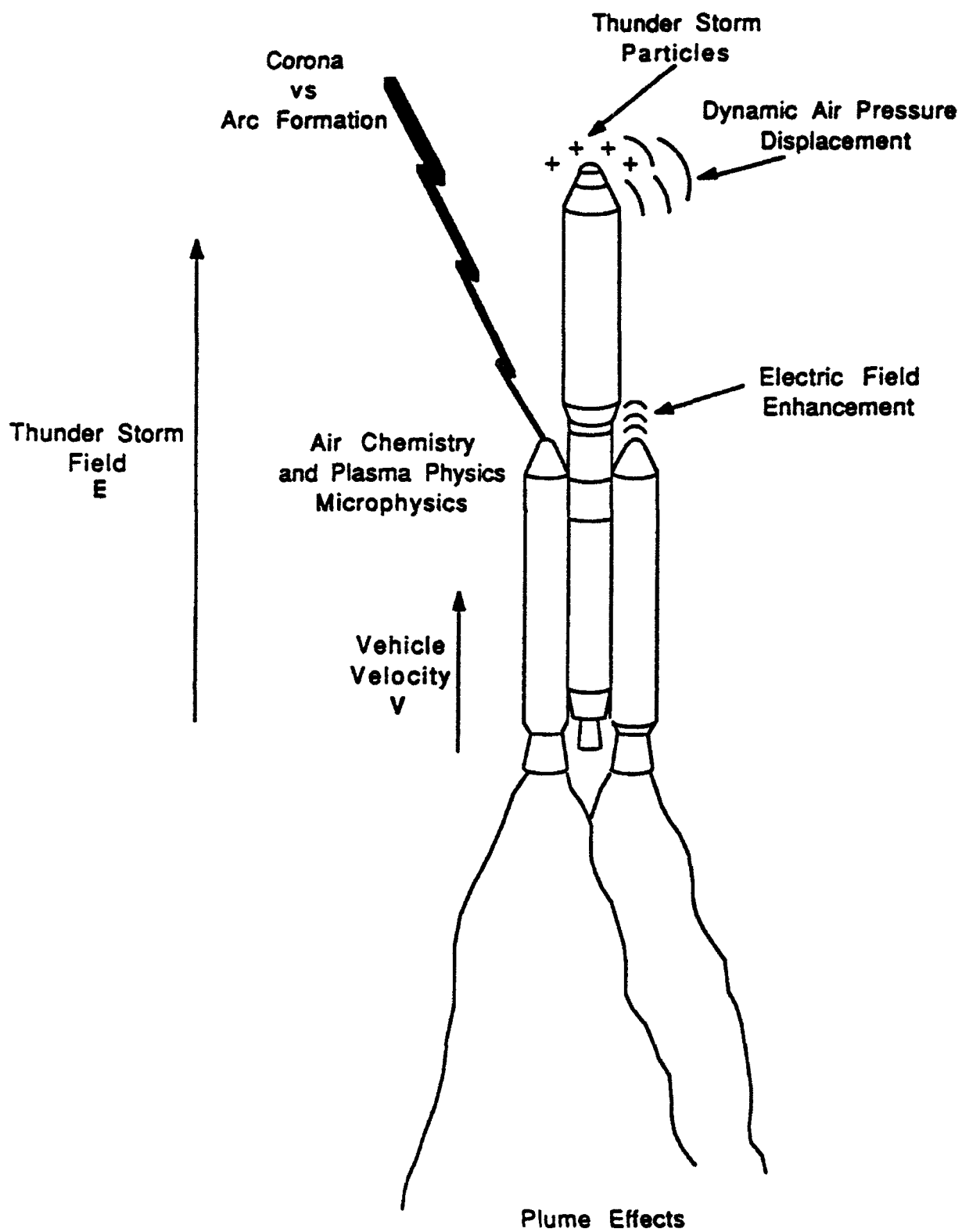


Figure 1 Summary of Triggering Issues

In this paper, we report results which have been obtained thus far. We describe first the experimental aspects, followed by the analytic aspects.

2.0 EXPERIMENTAL EFFORTS

There are three basic experiments of interest:

1. Laboratory flame experiments
2. Forty pound rocket motor tests
3. Corona/arc transition experiments

2.1 Laboratory Flame Measurements

This experiment has been completed, and the test set up is shown in Figure 2. The objectives of this experiment were to determine the following:

1. Does a flame from an electrically floating nozzle charge up the nozzle in the presence of a static field, as described for a rocket motor in Reference 1?
2. How can plume conductivities be measured?
3. What is the best way to instrument the forty pound motor tests?

As shown in Figure 2, an isolated flame/torch head is inserted in an electric field between two plates. The upper plate is movable so that the screen can intersect various parts of the flame. Equivalent circuits for the set up are shown in Figure 3. By moving the plate, the value of R is changed, and thus the circuit RC time constant. The transient voltages as measured by the electrometer are shown in Figures 4 and 5, with and without a flame, respectively. Without a flame, of course, the voltage immediately rises to a constant value determined by capacitive division, as shown in Figure 4. With the flame on, a time constant as shown in Figure 5 is observed. Moving the plate up or down changes the time constant, and one can thereby determine the flame conductivity profile as a function of height.

The results indicate that a net charge is acquired by the nozzle when a static field is applied. This supports the rocket charging scenario described in [1]. The conductivity profiles were measured as a function of height.

2.2 Forty Pound Rocket Motor Tests

These tests have not been completed at the time of this writing, and are summarized in Figure 6. The objectives are:

- Measure fields around the rocket motor and plume immersed in static field.
- Predict charge distribution on small rocket - plume system by fitting field measurements to parameterized static model.
- Adapt model to dynamic cases with specific motion, flow, temperature distribution, chemical content, etc.

The solid rocket contains 40 pounds of fuel, and burns for about 10 seconds. The potential of the grid is switched from 0 to $\pm 5\text{kv}$, and the 5 sensors on the support pole measure the vertical and radial components of the static electric field. Another sensor (#6) measures the voltage of the motor, which is electrically floating. The sensors are manufactured by EMA, and the data is acquired via fiber optics and a computer with a digitizing card, which time multiplexes all of the data. Although not shown, the data also in-

In this paper, we report results which have been obtained thus far. We describe first the experimental aspects, followed by the analytic aspects.

2.0 EXPERIMENTAL EFFORTS

There are three basic experiments of interest:

1. Laboratory flame experiments
2. Forty pound rocket motor tests
3. Corona/arc transition experiments

2.1 Laboratory Flame Measurements

This experiment has been completed, and the test set up is shown in Figure 2. The objectives of this experiment were to determine the following:

1. Does a flame from an electrically floating nozzle charge up the nozzle in the presence of a static field, as described for a rocket motor in Reference 1?
2. How can plume conductivities be measured?
3. What is the best way to instrument the forty pound motor tests?

As shown in Figure 2, an isolated flame/torch head is inserted in an electric field between two plates. The upper plate is movable so that the screen can intersect various parts of the flame. Equivalent circuits for the set up are shown in Figure 3. By moving the plate, the value of R is changed, and thus the circuit RC time constant. The transient voltages as measured by the electrometer are shown in Figures 4 and 5, with and without a flame, respectively. Without a flame, of course, the voltage immediately rises to a constant value determined by capacitive division, as shown in Figure 4. With the flame on, a time constant as shown in Figure 5 is observed. Moving the plate up or down changes the time constant, and one can thereby determine the flame conductivity profile as a function of height.

The results indicate that a net charge is acquired by the nozzle when a static field is applied. This supports the rocket charging scenario described in [1]. The conductivity profiles were measured on a function of height.

2.2 Forty Pound Rocket Motor Tests

These tests have not been completed at the time of this writing, and are summarized in Figure 6. The objectives are:

- Measure fields around the rocket motor and plume immersed in static field.
- Predict charge distribution on small rocket - plume system by fitting field measurements to parameterized static model.
- Adapt model to dynamic cases with specific motion, flow, temperature distribution, chemical content, etc.

The solid rocket contains 40 pounds of fuel, and burns for about 10 seconds. The potential of the grid is switched from 0 to ± 5 kv, and the 5 sensors on the support pole measure the vertical and radial components of the static electric field. Another sensor (#6) measures the voltage of the motor, which is electrically floating. The sensors are manufactured by EMA, and the data is acquired via fiber optics and a computer with a digitizing card, which time multiplexes all of the data. Although not shown, the data also in-

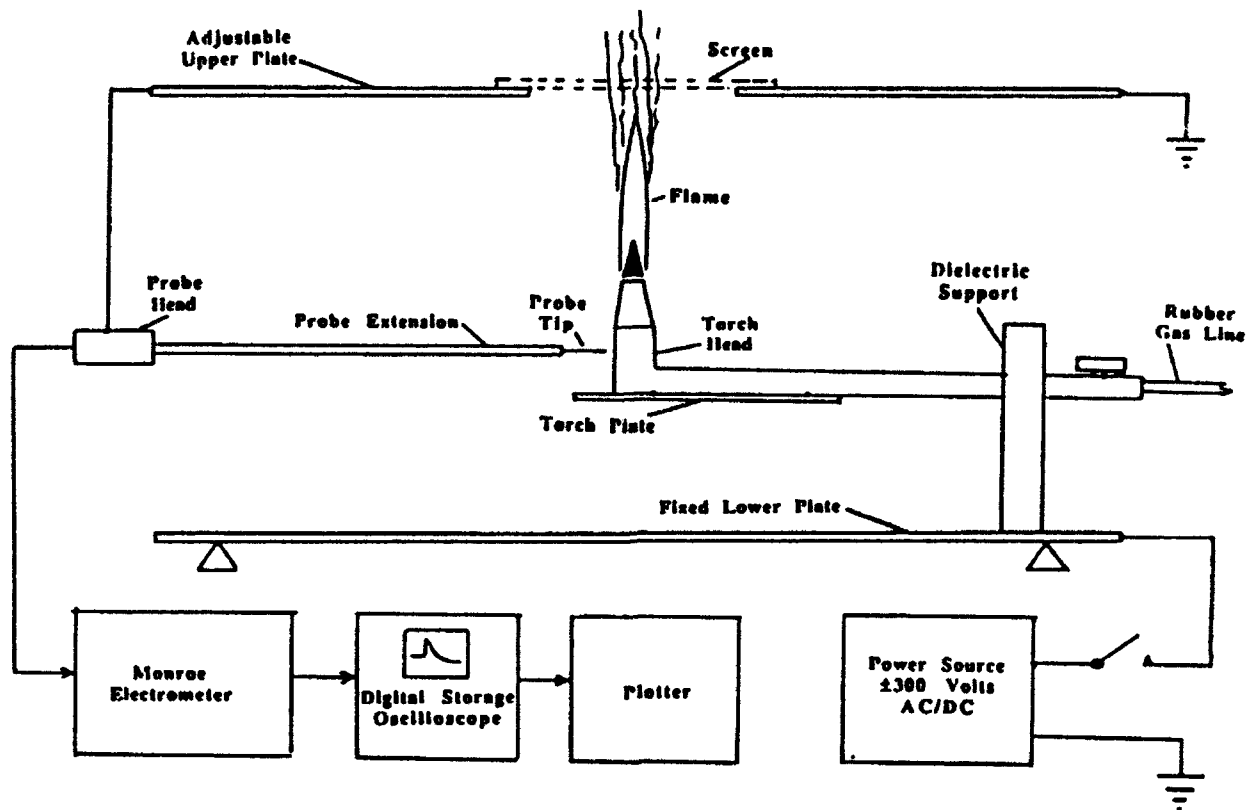
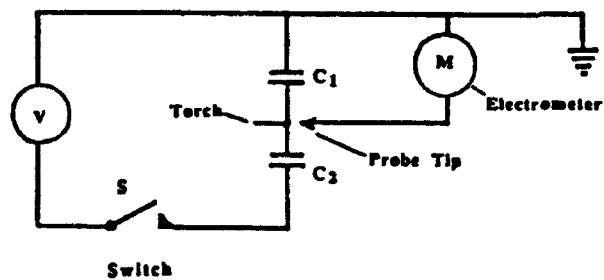


Figure 2 Block Diagram Showing Basic Equipment Set-Up for the Flame Tests

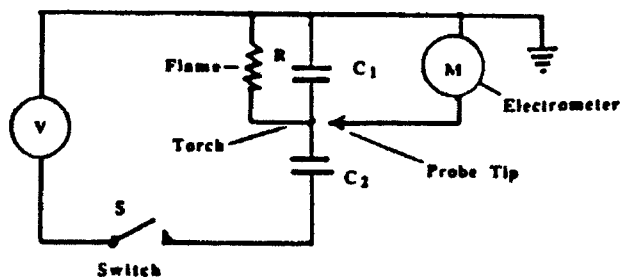


Upper Plate

C_1 = Torch Head Capacitance to Upper Plate

C_2 = Torch Head Capacitance to Bottom Plate

(a) No Flame



R = Resistance of Flame

(b) Flame On

Figure 3 Equivalent Circuits for the Tests

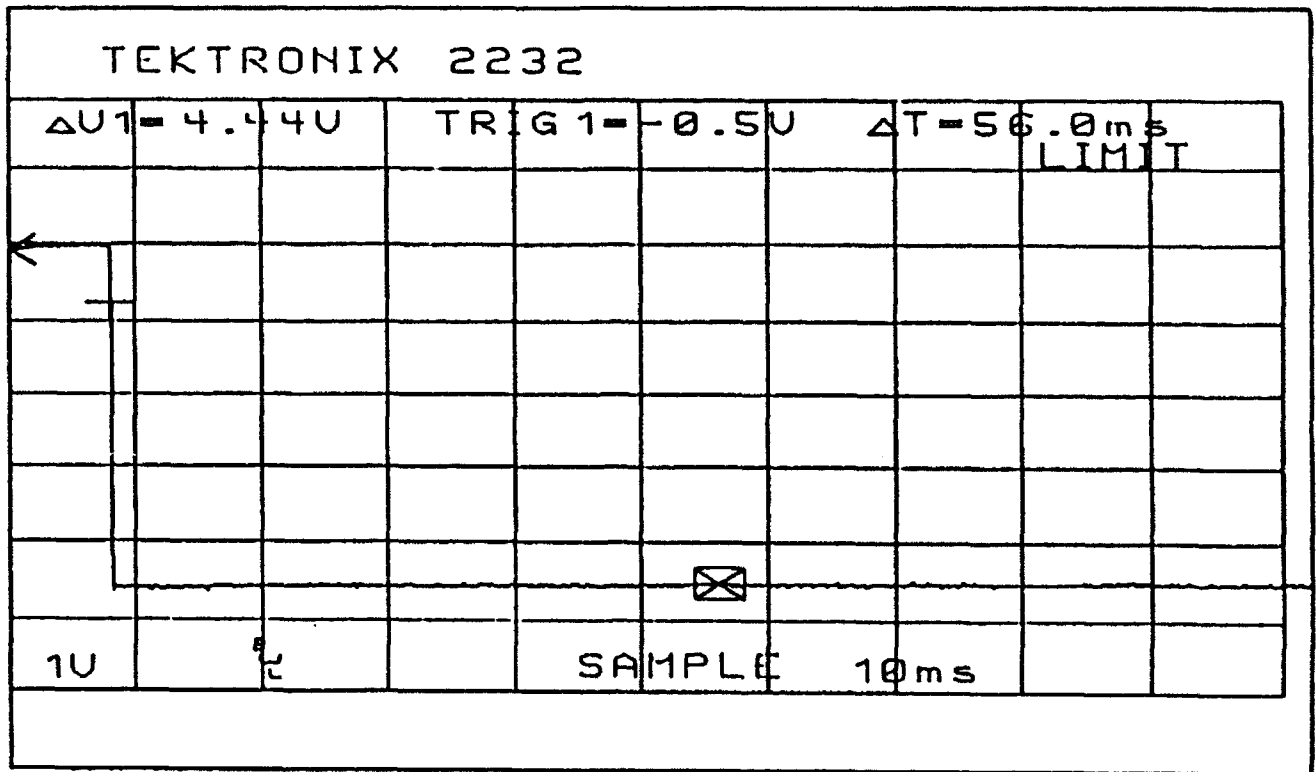


Figure 4 Torch Voltage Transient - No Flame, Plate Hieght 11 Inches, Top Plate Positive

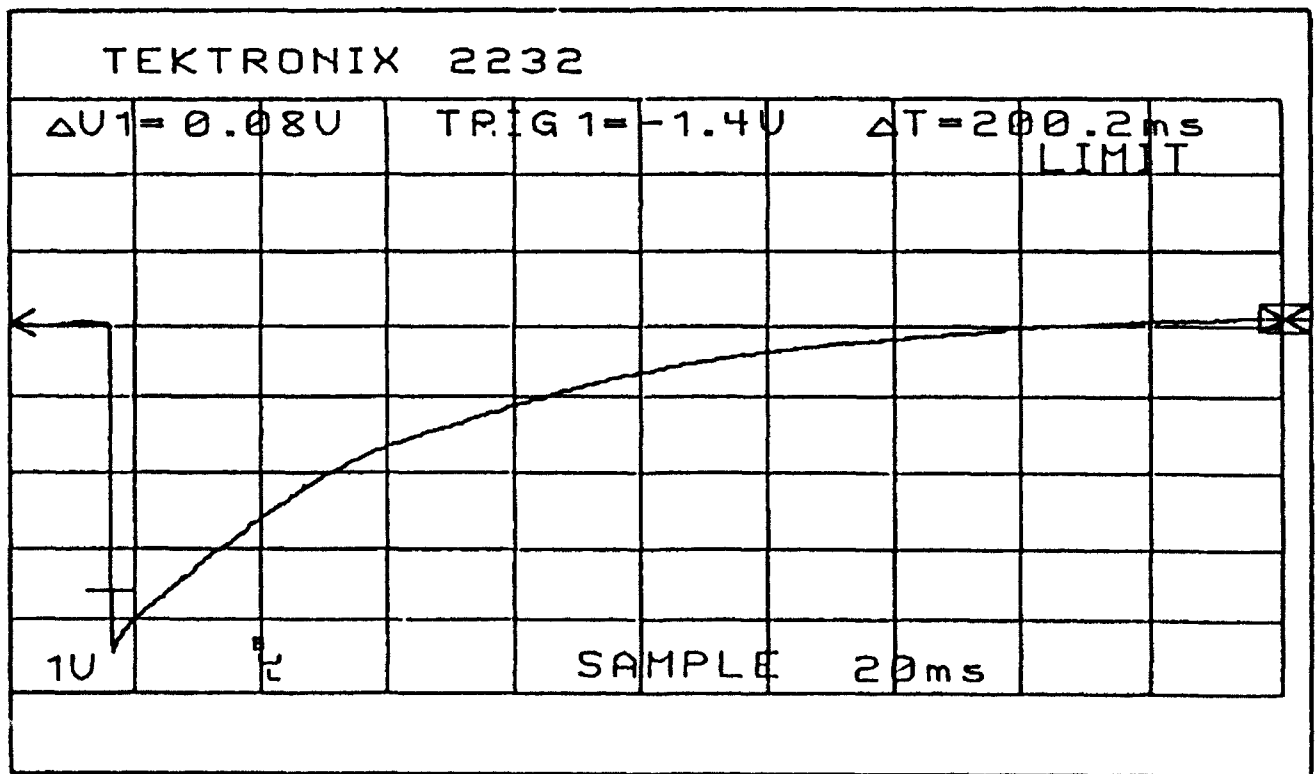


Figure 5 Torch Voltage Transient - Flame On, Plate Hieght 11 Inches, Top Plate Positive

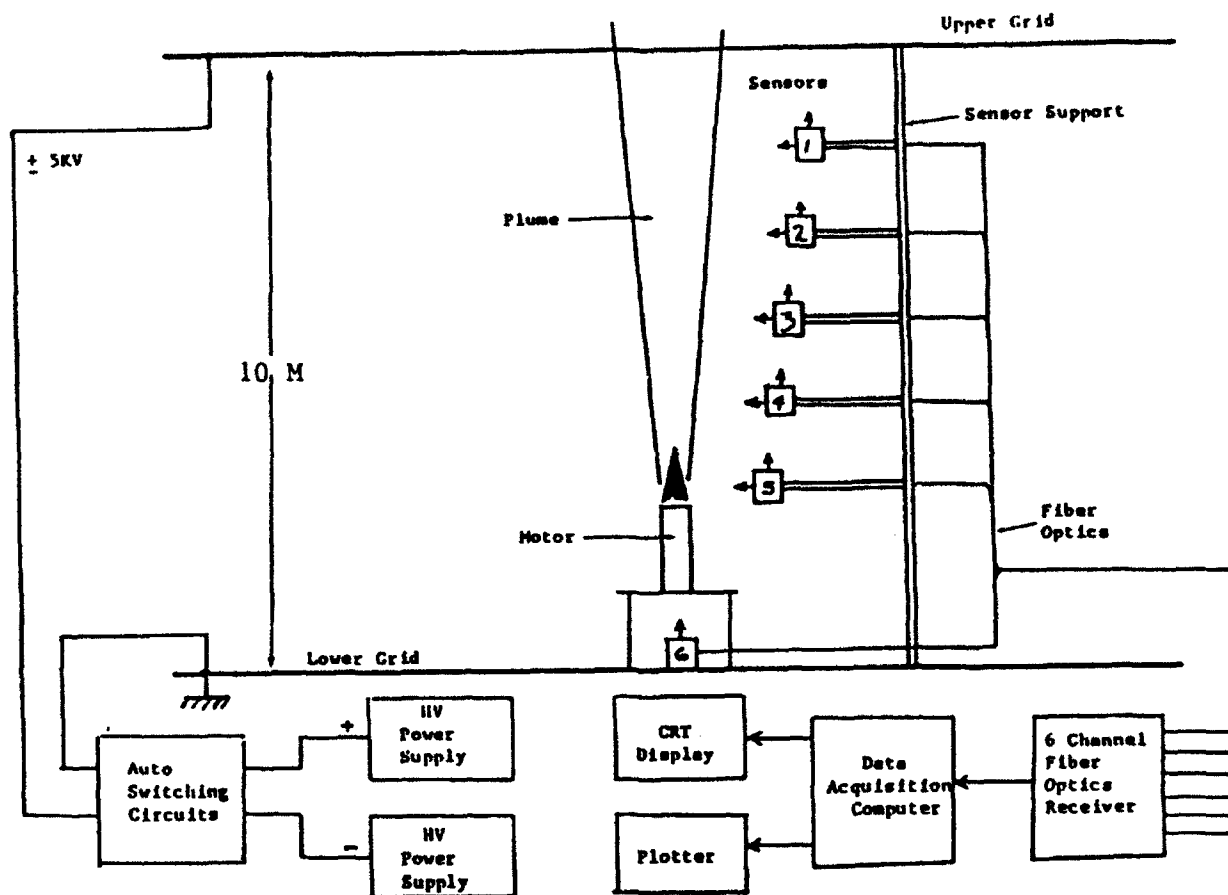
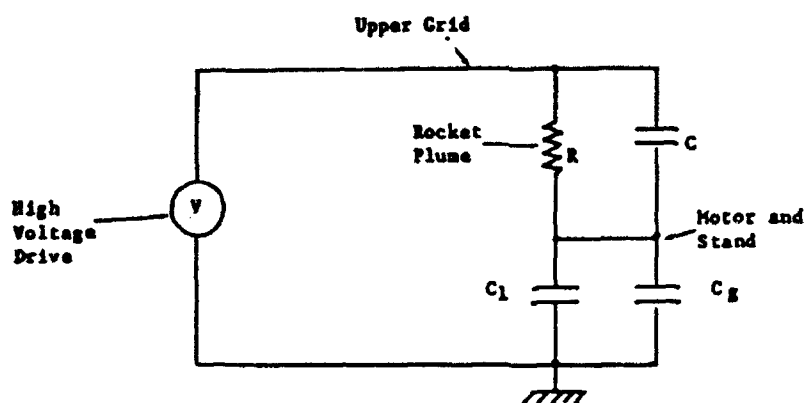


Figure 6 Small Rocket Motor Test Set-Up



C = Motor and Stand Capacitance to Upper Grid

C_2 = Motor and Stand Capacitance to Ground

C_1 = Added Capacitance to Adjust Experimental Time Constant

R = Effective Resistance of Rocket Plume (Determined by Plume Conductivity Near Upper Grid)

Figure 7 Equivalent Circuit of Small Motor Test

cludes the rocket chamber pressure and the RF transmission loss of a 10 GHz beam which is passed through the plume.

EMA has also engaged the services of Propulsion Science Technology, of Princeton, NJ, to calculate the flame dynamics and conductivity. An example conductivity profile for the forty pound motor is shown in Figure 8.

2.3 Corona/Arc Transition Experiments

The objective of these experiments is to characterize corona/arc transition conditions for floating electrodes of various shapes and sizes. The work is basically an extension of Hermstein's [3], whose experiment is shown in Figure 9. An inner sphere was raised to a high potential with respect to an outer hemisphere having fixed radius. The inner sphere was interchangeable in order to see the effect of changing radius of curvature on the breakdown. As the size of the inner sphere was varied, the maximum spatial derivative of the field between the sphere and the hemisphere changed, with smaller spheres producing larger spatial derivatives. Hermstein assumed that the field distribution between the inner sphere and the outer hemisphere was the same as that between two concentric spheres, and from that distribution calculated a spatial derivative in the absence of space charge. He recognized several different types of breakdown, ranging from glow (corona) to streamers to complete arc breakdown between the electrodes. These occurred in different ranges of inner conductor radius and for different potential differences. Hermstein was able to quantify the ranges over which each type of discharge took place in terms of the maximum electric field spatial derivative between the electrodes.

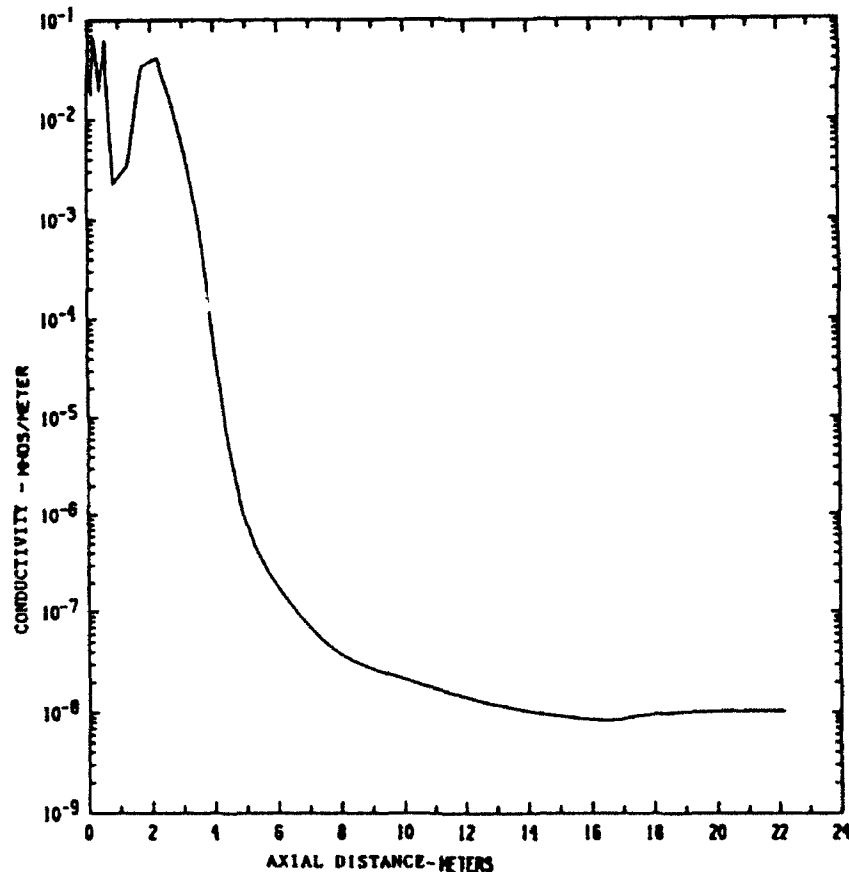


Figure 8 PST Model Output - Conductivity on Plume Axis

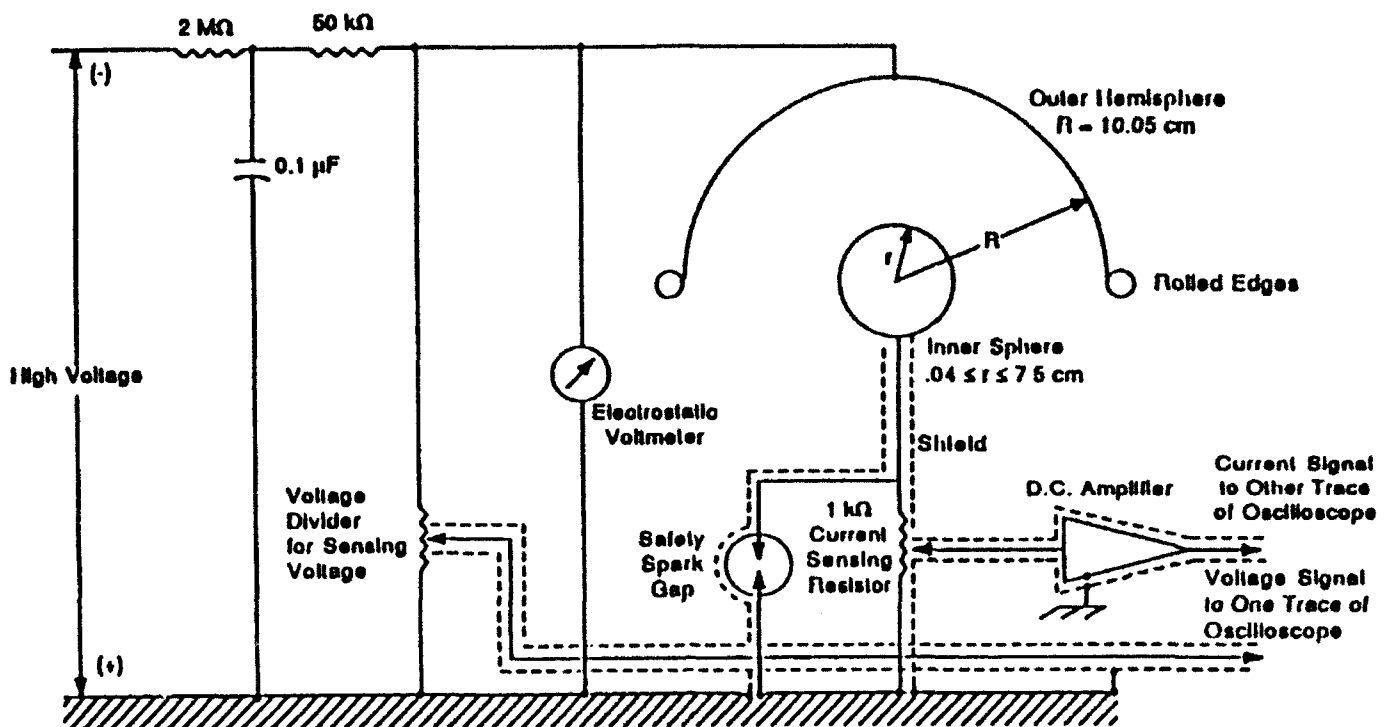


Figure 9 Experimental Set-Up Used by Hermstein to Investigate Conditions for Arc Formation

The experimental procedure was to slowly increase the voltage between the electrodes until breakdown occurred. Initially, small amplitude current spikes were seen, which Hermstein identified with streamer growth. If the voltage continued to increase, a slowly growing continuous current was seen which eventually led to complete breakdown and a large current flow as a discharge bridged the gap between the electrodes. If the rise in voltage was stopped, the discharge would not necessarily proceed through all phases, but could stop in the streamer or glow stage.

The key result of his work is illustrated in Figure 10 which shows the absolute value of the electric field spatial derivative as a function of the inner sphere radius. E_a for the plot is that achieved just before breakdown of any kind occurred, derived from the potential difference between the electrodes at that time. On the graph four regions were marked. The first, ranging from A to B, is the region for which only glow (corona) occurred. The ranges from B to C and from C to D represent the appearance of glow and streamers or only streamers, respectively. In the range above D, the absolute value of the spatial derivative is less than $2.5 \times 10^8 \text{ V/m}^2$, for which case Hermstein saw only arc breakdown between the electrodes. He therefore concluded that this condition was necessary for arc formation to occur.

3.0 MODELING ACTIVITIES

There are several numerical modeling activities which are not yet completed and will be reported in a later paper.

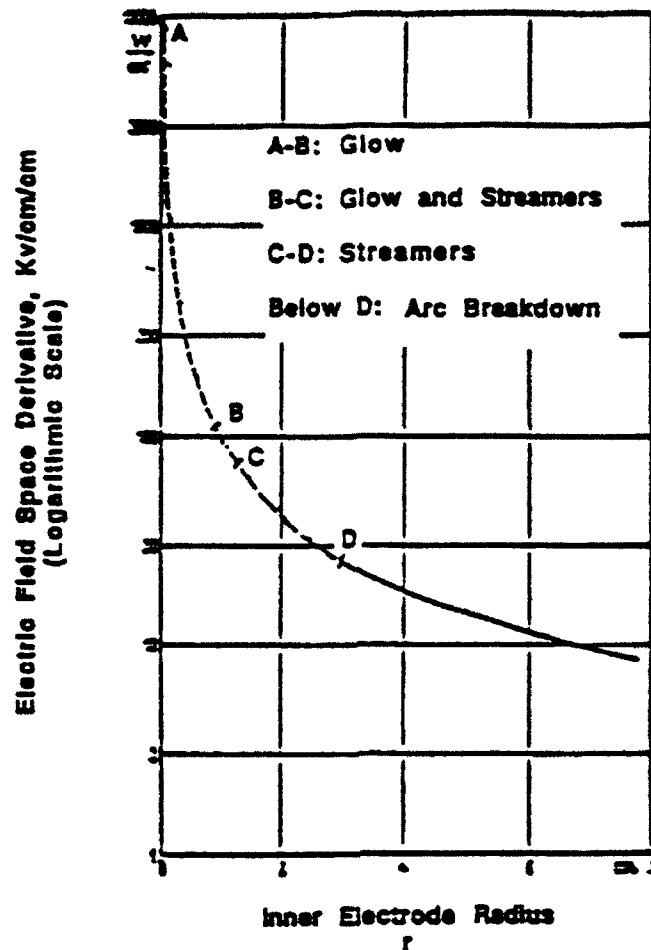


Figure 10 Maximum Spatial Derivative of the Electric Field before Breakdown Given as a Function of Inner Sphere Radius r (Outer Radius = 10.05 cm)

The first activity is modeling the plume dynamics and electrical properties. The plume dynamics in the absence of a static electric field is modeled by PST as described earlier. EMA is using the output of this model to develop the model when the plume is inserted in a static electric field. The objective is to determine the charge distribution in the rocket/plume configuration, so that electric field enhancement factors can be calculated.

The second activity is to build an electrostatic model of the rocket/plume configuration. This is basically a 3D solution of Poisson's equation, and the objective is to determine the system's enhancement factors. In addition, the dynamic air pressure distribution/profile about the vehicle will be folded into the model, in order to identify air pressure effects on the air breakdown levels.

4.0 CONCLUSIONS

We have described a variety of activities that will allow us to develop an overall model of the launch vehicle static electric configuration in a thunderstorm environment. Although presently limited to the Titan IV vehicle, we expect that the model could be applied to other launch vehicles as well. It shows that this type of model will be used to successfully relax launch criteria so that expensive launch delays can be safely avoided.

REFERENCES

1. Eriksen, Frederick J., Terence H. Rudolph and Rodney A. Perala, "The Effects of the Exhaust Plume on the Lightning Triggering Conditions for Launch Vehicles," presented at the International Aerospace and Ground Conference on Lightning and Static Electricity, Cocoa Beach, Florida, April 16 - 19, 1991.
2. Perala, R.A., T. Rudolph, F.J. Eriksen, M.C. Erie and G.J. Rigden, "Investigation of the Triggering of Lightning by Launch Vehicles During Ascent," EMA-89-R-61, August 1989.
3. Hermstein, W., "Die Stromfaden-Entladung und ihr Übergang in das Flimmen," Archiv für Electrotechnik, XLV Band, Heft 3, 1960.

A SINGLE-POINT WARNING SYSTEM FOR THUNDERSTORMS AND ELECTRIC FIELDS

W.T. Neumann and K.L. Cummins
Lightning Location and Protection, Inc.
Tucson, AZ, USA

Telephone (602) 741-2838 Fax (602) 741-2848

E.P. Krider
Institute of Atmospheric Physics
University of Arizona
Tucson, Arizona, USA
Telephone (602) 621-6831 Fax (602) 621-6833

ABSTRACT

In this paper, we describe a single-point warning system that combines a single-station thunderstorm warning sensor with a static electric field sensor. This integrated system monitors nearby cloud-to-ground lightning and overhead electrification, allowing a wide variety of potentially hazardous meteorological conditions to be monitored. The paper discusses relevant sensing technologies, public safety and aviation applications for the system, recent field experience, and future development options.

INTRODUCTION

While cloud-to-ground (CG) lightning is, perhaps, the most spectacular form of natural electrical activity, a wide variety of meteorological conditions can present a hazardous electrical environment for public safety, aviation, and aerospace operations. In addition to the threat of a direct cloud-to-ground lightning strike to equipment or personnel, near or overhead electrified clouds can produce serious threats at the ground. Static-sensitive operations, such as refueling, must consider all electrical activity when developing a comprehensive risk assessment plan for static discharge.

In most instances, monitoring the potential danger presented by electrical activity requires the use of specialized weather sensors. While such sensors typically offer a view of some aspect of atmospheric electrical conditions, the information they provide is limited to one particular field or field change parameter. In this setting, the weather or risk assessment officer must integrate the information from several independent field or field change sensors to assess hazards. One weakness, however, of using independent sensors is that the integration of information is a manual and, often, visual process. Therefore, the quality of the risk assessment depends on an

individual recognizing the need to collect the data, doing so in a timely fashion and analyzing the data to identify potential threats.

Since personnel involved in weather-related risk assessment cannot be expected to continuously monitor weather conditions, the issue of recognizing when conditions have changed sufficiently to require data to be collected is an important one. Human factors experts have long recognized that humans do a poor job monitoring systems that change slowly, due to the fatigue, disinterest, or distraction (1). In order to assist the person monitoring the system, many weather sensors incorporate some form of visual or audible alarm to obtain attention. However, multiple alarms from several independent sensors can themselves become a distraction, and autonomous sensors cannot identify when conditions, considered collectively, represent a dangerous situation.

Recognizing the specialized need to monitor all electrical activity at a site, Lightning Location and Protection, Inc. (LLP) of Tucson, Arizona, has developed a single-point warning system to monitor these hazardous atmospheric electrical conditions. The LLP Thunderstorm Sensor Model 440 is an integrated warning system that monitors electrical activity using an electric field sensor and a single-station thunderstorm warning sensor. In the following sections, we describe the capabilities of the two sensors -- the LLP Thunderstorm Sensor and the Mission Instruments Electric Field Mill -- and discuss how a personal computer-based display system is used to display and analyze the information from these sensors.

LLP THUNDERSTORM SENSOR MODEL 420A

The LLP Thunderstorm Sensor Model 420A (TSS) is a single-station thunderstorm warning system that provides real-time information about the occurrence of CG lightning around the sensor site. The sensor is based on the gated, wideband, magnetic direction finder (DF) technology used within LLP's lightning locating networks as described by Krider, Noggle and Uman (2) and Krider, Pifer, and Uman (3). The TSS incorporates patented waveform discrimination logic to identify return stroke signatures of CG lightning from other atmospheric discharges. For properly sited and operated sensors, the reliability of the CG events reported by the TSS is quite good, with less than 1 percent of all events reported as CG lightning being from other sources, including cloud discharges. For most installations, the TSS has an effective range of approximately 150 km, and a per-flash angular accuracy within ± 2.5 degrees.

With only a single station, locating the CG contact point is not currently practical using triangulation techniques. However, the range-dependent features in the lightning waveform can be used to provide a coarse estimate of the range, as described by Pifer, et al. (4). Depending on the distance from the sensor to the CG flash, the Thunderstorm Sensor will use one of three different techniques to estimate the range. First, if the incoming field saturates the sensor's measurement electronics (i.e., the waveform cannot be properly measured due to the signal exceeding the dynamic range of the sensor), the flash is considered to be within 5 km of the sensor. Second, if the sensor is able to process the waveform of a stroke and a significant

electrostatic field is present, a range estimate is made using the ratio of the peak of the radiated electric field and the electrostatic field measured 170 microseconds after the radiation peak. However, this ranging technique is only effective within approximately 20 km of the sensor because the strength of the electrostatic field attenuates at a rate that is inversely proportional to the cube of the range. Finally, beyond 20 km, range is estimated using a model based on the distribution of the peak radiation field of a "typical" 30 kA flash. This last method is fairly inaccurate for individual flashes, but improves dramatically when flashes beyond 30 miles are considered as a group.

The Thunderstorm Sensor is an intelligent weather instrument that uses a microprocessor-based controller to perform much of the signal processing and waveform analysis within the sensor itself. After a given waveform has been identified as a lightning stroke by analog signal processing circuits, digital measurements of key waveform parameters are recorded by the microprocessor. By comparing the temporal and spatial characteristics of recent strokes, the Thunderstorm Sensor groups discrete strokes into flashes for reporting. For each flash, key characteristics of the first return stroke of the flash, such as a peak measured B-field amplitude, multiplicity, and E-field measurements, are transmitted to the personal computer system in digital form as an ASCII-encoded character string over an RS-423 data link.

MISSION INSTRUMENTS FIELD MILL

The electric field sensor used for this product is a shuttered electric field mill (EFM) developed by Mission Instruments of Tucson, Arizona, and incorporates a continuous precision rectifier design, which produces a stable and precise measurement. The EFM sensor is physically placed in the field in an inverted orientation which reduces contamination and noise induced by charged raindrops impacting sensing surfaces of the mill. The EFM has an effective operating range of 10-15 km, and can report static fields in the range of ± 20 kV/m with an accuracy of 2% for fields over 1 kV/m, although extended field ranges are available.

In contrast with the Thunderstorm Sensor, an EFM produces an analog voltage output that is proportional to the measured field without any filtering or other signal processing. Since analog voltages can only be reliably transmitted a fairly short distance (on the order of a few meters) and the personal computer display system requires digital interface, a data conditioning unit, the D-1141, manufactured by DGH Corporation of Manchester, New Hampshire, converts the analog voltage produced by the EFM into a digital numeric value. Once each second, the personal computer system requests that the D-1141 transmit a digital sample encoded as an ASCII-encoded character string over an RS-485 data link.

PERSONAL COMPUTER SYSTEM

The IBM-PC/AT-compatible personal computer performs several key functions for the integrated Thunderstorm Sensor Model 440. Using the appropriate serial

interfaces, the personal computer system communicates directly with both sensors. In addition to managing the ongoing task of collecting data from the sensors, the personal computer is also responsible for configuring the operating parameters of the sensors, monitoring periodic diagnostic tests on the sensors to ensure their proper operation, and reporting equipment failures to supervising personnel. Beyond its data collection responsibilities, the personal computer system also presents the information from the sensors in several formats, including a graphical color display, printed warnings, and an audible alarm.

CLOUD-TO-GROUND LIGHTNING INFORMATION --

The cloud-to-ground lightning reports from the single-station thunderstorm sensor are presented in two forms. As shown in Figure 1, recent CG lightning activity is presented using a "dart board" format that allows even a casual user to identify the direction, distance and the number of CG flashes that have occurred within a user-defined moving time window that is usually 15 minutes. Also, the number of flashes is used to select a warning color for each sector using the fairly intuitive color scale of green (all clear), yellow (intermittent activity), orange (moderate activity), and red (frequent activity). Since a logarithmic range scale was used to improve the visibility of the inner sectors, sector size does not reflect the actual area. Therefore, the flash count ranges used for each warning color have been normalized to maintain a consistent flash density for all sectors.

Along with the recent activity display, a one hour trend histogram displays all CG lightning activity detected on a minute-by-minute basis, as shown in Figure 2. The purpose of this display is to provide the system operator with a general (omni-directional) assessment of thunderstorm activity in the vicinity (within 150km) of the site. Since this display presents general trends (increasing or decreasing ground discharge rate) over a longer interval, a system operator can use this information to decide when to resume normal operation.

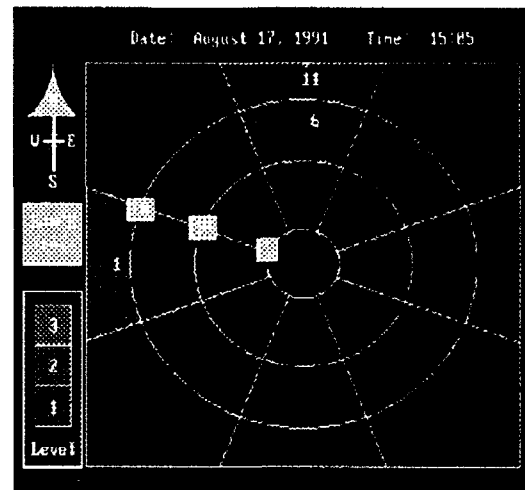


FIGURE 1. Dart Board Display



FIGURE 2. Trend Display

ELECTRIC FIELD INFORMATION -- As with the CG lightning information, the system presents the electric field information in several forms as well. As shown in Figure 3, three different views of the electrical activity are displayed. In the upper section of

the window, the most recent one-second reading is displayed as an "instantaneous" measurement of the field. However, when lightning activity is nearby, this reading can change rapidly, so the system also reports an arithmetic mean of all measurements within the last 60 seconds, shown as a "60 Sec Avg" below the trend chart. Using the same time scale as the CG histogram, the trend chart reports the minimum, maximum, and mean electric fields measured for each minute within the last hour. The field range is shown as vertical bar, using a three-color code (green, yellow and red), while the mean is shown as a white dot on the vertical bar. The yellow and red color codes are used to highlight fields over 1000 V/m and 2000 V/m, respectively, although these level can be adjusted to meet local site policy. In order to maintain the prominence of the data within the chart, the chart's scale is periodically changed to keep the largest peak data value near full scale.

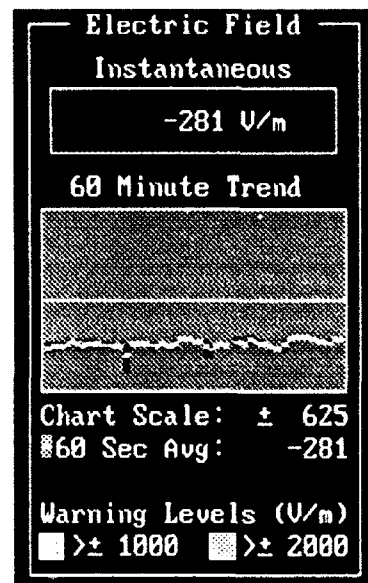


FIGURE 3. EFM Display

PUBLIC SAFETY AND AVIATION-RELATED APPLICATIONS

The Thunderstorm Sensor Model 440 has several applications related to the management of ground-based operations. With the accurate and timely warning of CG lightning activity and electric fields near the site, personnel can manage ground operations safely and efficiently. For example, suspending ground operations that support commercial aviation due to nearby lightning or high electric fields can have a significant impact on airline schedules and travellers. While this system cannot prevent ground operations from being suspended, it can provide enough advance warning to allow operations personnel to prepare for an interruption in service. Perhaps more importantly, though, the system also provides a clear indication of when electrified clouds have moved away or have diminished electrification, thereby allowing operations to resume as soon as possible without compromising safety.

The Thunderstorm Sensor Model 440 can also be used by pilots as a part of their pre-flight weather briefings. Especially for general aviation, the knowledge that thunderstorms are in the area is often significant enough to represent a go/no-go decision for take-off. Similarly, if thunderstorm information is available via radio, the pilot in route can decide whether to select an alternate airfield.

FIELD EXPERIENCE: A CASE STUDY

On August 17, 1991, a Thunderstorm Sensor Model 440 monitored the development of a thunderstorm over the Canadian Airlines maintenance facility in Toronto, Canada. Although CG lightning activity had been reported over a wide area throughout the day, a strong thunderstorm cell developed directly overhead with little advance warning.

As shown in Figure 4, although thunderstorms had been in the area, no imminent threat of lightning at the site was seen or heard. However, the presence of overhead electrical activity is clearly indicated by the electric field sensor. For most of the previous hour, normal fair-weather field had been reported by the electric field sensor, as shown by the narrow line of field measurements below the center line in the 60 minute trend display. Then, as the electrified cell built up over the site, the electric field reading rapidly increased. Shortly after this figure was recorded, an overhead CG flash was detected. In this case, the electric field sensor not only provided the operations personnel important information about dangerously high electric fields but also provided them with a five minute advance warning of an overhead CG lightning event.

In Figure 5 (40 minutes later), the overhead thunderstorm was very active, producing nine CG flashes within 3 mn of the site over the last 15 minutes. Below the CG lightning dart board, a thunderstorm alarm is shown. When CG lightning represents a clear and present threat to the site, the computer generates a warning message on the display screen and an audible tone. The warning is maintained until the operator acknowledges the warning or the CG lightning moves out of the area. In addition to the CG information, note the electric field trend display. As a result of the nearby lightning activity, the electric field trend display shows a rapidly changing field, with the last 20 minutes showing a full-scale swing of ± 20 kV/m.

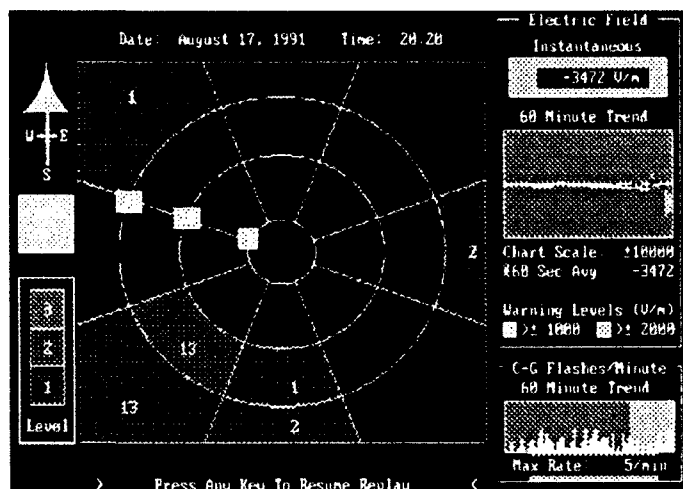


Figure 4. Overhead Development

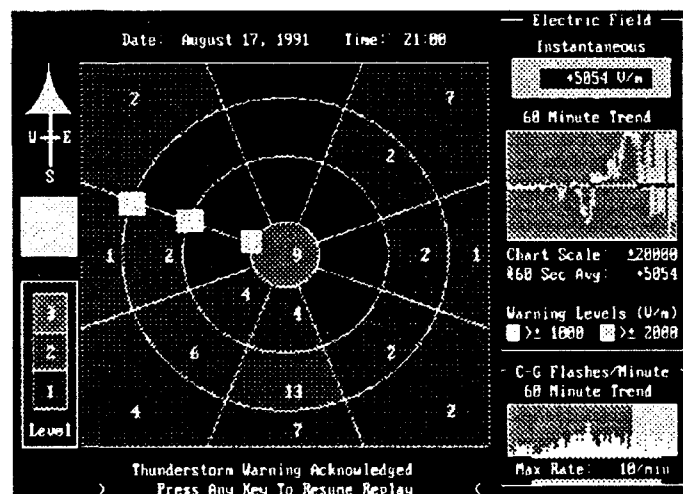


FIGURE 5. Overhead Thunderstorm

FUTURE WORK

We are investigating other synergistic benefits of using these two sensors. Our further evaluation will be focused on two important areas: identifying nearby cloud lightning and improving system fault tolerance and reliability.

In the discussion of Figure 5, it was noted that nearby lightning results in large, rapid changes in the local electric field measurements. Since the CG lightning is already known to be dangerous, the electric field data are typically ignored by the user under these circumstances. However, it may be possible to combine the reports from the electric field sensor and the thunderstorm warning sensor to identify cloud discharges with the Thunderstorm Sensor Model 440 as follows: In Figure 6, the electric field measurements, displacement currents and time coincident CG lightning events (shown as tic marks on the bottom axis of the displacement currents) for an overhead thunderstorm are shown. Note that each CG event can be directly associated with a significant and rapid change in the signal amplitude. Also, note that there are other large changes in displacement current that are not associated with CG lightning. It is likely they were produced by cloud discharges.

In the Thunderstorm Sensor Model 440, the electric field sensor can identify these large changes in signal amplitude between successive electric field measurements. We think that by further correlating these electric field sensor events with time coincident CG lightning reports from the Thunderstorm Sensor, cloud lightning can be identified. In cases where cloud discharges precede CG lightning, their detection may provide useful additional advance warning.

With regard to improving the Thunderstorm Sensor Model 440's system fault tolerance and reliability, the focus of this effort will be primarily directed towards exploiting the significant advantage of using two independent sensors. Since both sensors provide coverage in the immediate vicinity of the site (with 10km -15km), failure of either sensor would not result in the system being unable to provide some information on the local conditions. Likewise, having two sensors also provides some redundancy of information. By comparing the reports of one sensor to the other, reliability of the system could be improved by allowing system-level diagnostic checks to be performed.

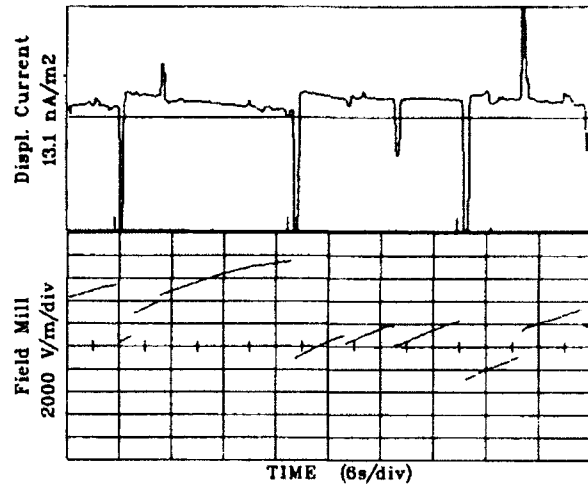


FIGURE 6. Field Mill Measurements

REFERENCES

1. Colquhoun, W.P., "Evaluation of Auditory, Visual, and Dual-mode Displays for Prolonged Sonar Monitoring in Repeated Sessions," *Human Factors*, 1975, Volume 17, pages 425-437.
2. Krider, E.P., Nogge, R.C., and Uman, M.A., "A Gated Wideband Magnetic Direction Finder for Lightning Return Strokes," *J. Appl. Meteorology*, 15, pages 402-405, 1976.
3. Krider, E.P., Pifer, A.E., and Uman, M.A., "An Automatic Locating System for Cloud-to-Ground Lightning," *Lightning Technology, Proc. of Technical Symposium held at NASA Langley Research Center, Hampton, VA, April 22-24, 1980*, NASA CP-2128, FAA-RD-80-30.
4. Pifer, A.E., Hiscox, W.L., Cummins, K.L., and Neumann, W.T., "Range Estimation Techniques in Single-Station Thunderstorm Warning Sensors Based on Gated, Wideband, Magnetic Direction Finder Technology," *Proc. International Aerospace and Ground Conference on Lightning and Static Electricity*, pages 21-1 - 21-10, Cocoa Beach, FL, April 16-19, 1991.

COMMERCIAL PRECIPITATION STATIC (P-STATIC) TEST EQUIPMENT

**R. Wayne Devereux
Veda, Incorporated
300 Exploration
Lexington Park, Maryland 20653
Telephone (301) 862-2100 Fax (301) 862-2530**

ABSTRACT

The aircraft industry requires commercially available, safe and reliable, test equipment to support Precipitation Static (P-static) Research, Development, Test and Evaluation (RDT&E). The test equipment must be able to simulate the in-flight P-static charging environment and acquire the P-static interference data for analysis of specification compliance. Using P-static test equipment the aircraft industry can locate P-static problem areas, compare these results to specification limits, identify potential fixes, and evaluate fixes effectiveness. This paper describes the commercially available portable P-static test equipment designed, from a "Users" perspective, to meet the Royal Australian Navy's (RAN) aircraft ground support equipment's (GSE) needs.

INTRODUCTION

The ruggedized P-static Simulator, Model PS/60P, is used to simulate the in-flight P-static charging environment during simulated P-static testing of aircraft. The automated P-static Database and Acquisition System (PDAS) is used to measure an aircraft's RF receivers' responses, in the form of RF and audio interference. Together, these test equipment were used successfully to perform specification compliance testing of RAN S-70B-2 helicopters in Australia, and were used to analyze and characterize the aircraft deficiencies and quantify the fix effectiveness of all problems areas corrected.

RUGGEDIZED P-STATIC SIMULATOR

The portable, ruggedized 60 Kilovolt (kV) P-static Simulator (PS/60P-491) was developed to meet military aircraft GSE specifications. The P-static Simulator design is smaller than two cubic feet, weighs less than 60 pounds, is highly reliable and very easy to maintain, and above all is very safe, see Figure 1. To generate the high voltage necessary to charge the aircraft during simulation, the Simulator uses a solid-state 60 kV DC power supply with built in high voltage control and output measurement circuitry. The P-static Simulator is designed as a modular, self contained, highly reliable simulation system that can be put into operation in a few minutes and can be disassembled for maintenance checks, with all test points easily accessed for measurements, also within a few minutes [1]. The PS/60P consists of a Control Module, a Hot Stick Storage Compartment, a Cable Storage Compartment, and standard accessories, as shown in figure 2.

CONFIGURATION -- The PS/60P's Control Module includes the Control Panel which houses all the necessary GSE controls, including, MIL-26482 Series Type I connectors, sealed indicators, sealed switches and circuit breakers, ruggedized MIL-STD meters and control knobs, handles which provide switch and knob protection upon roll over, an elapsed time meter, an anti-corona high voltage output connector, a remote Monitor and Control panel connector, and embossed safety instructions. The PS/60P's Control Module accepts standard 120 VAC (240 VAC optional), 50 to 400 Hz input power and houses an electromagnetic interference (EMI) power filter (for MIL-STD-461C compliance), a MIL-STD-810D sealed power distribution system, a ruggedized positive polarity 60 kV 1 milliampere (mA) high voltage power supply, and MIL-STD-810D sealed output control and metering circuitry. All components are mounted inside a sealed MIL-STD-810D approved container to avoid environmental fowling of the High Voltage modules.

Beyond the Control Module, the PS/60P's container houses the Hot Stick Storage Compartment where the dielectric Hot Stick, all High Voltage attachments, and the PS/60P's Operations and Maintenance Manual are stored. The Hot Stick Storage Compartment is a sealed compartment to minimize contamination of the High Voltage attachments and ease the attachments storage problems. Each section of the Hot Stick is securely stored while each High Voltage attachment is screwed onto a threaded mount to secure during transport. Lastly, the PS/60P's container houses the Cable Storage Compartment where the High Voltage Transmission Line cable, Ground cable, AC Power cable, and optional Remote Monitor and Control cable are stored. The Cable Storage Compartment is also a sealed area to ease cable contamination and storage problems.

SPECIFICATION -- The PS/60P is designed to meet the temperature (0-55°C), humidity (95%), vibration (Basic Carrier), shock (Vehicle Crash Hazards), and flammable atmosphere (explosive vapor operation) requirements of MIL-STD-810D and the Conducted Emissions and Susceptibility as well as the Radiated Emissions and Susceptibility requirements of the FCC Class A equipment and MIL-STD-461C for Class A1C GSE. The PS/60P's wiring and parts are designed to meet the MIL-STD-454L requirements for safety and workmanship. Each component's environmental specifications have been chosen to exceed those required by the system. The High Voltage power supply has been shock mounted to ensure reliable operation during transport and operation. The electrical components chosen are sealed to prevent arcing which can cause an explosion in a flammable atmosphere around aircraft fuel and to prevent problems during operation in high humidity conditions.

To meet the EMI requirements, the input power line is protected with an EMI filter having a superior insertion loss at very low frequencies for common mode and differential mode protection, and with transient protection devices. The High Voltage power supply's control circuitry has a shielded 25-pin D subminiature connector having good shielding effectiveness and uses shielded twisted wire. The AC Power cable is a shielded cable and the optional Remote Command and Control cable is also shielded twisted wire, both with MIL-26482 Series Type I connectors and EMI Backshells. The High Voltage Output connectors are the highest quality High Voltage anti-corona connectors made and are tested up to 75 kV to reduce radiated EMI from the connectors. The High Voltage Transmission Line is a shielded cable to reduce radiated EMI and electrostatic effects from the cable.

To meet the MIL-STD-454L safety requirements, the PS/60P has a sealed circuit breaker and power On indicator light, uses properly rated insulated wire and terminal blocks, and is built with proper workmanship practices. Additionally, the High Voltage Transmission Line is a 30' long flexible High Voltage cable, which is protected by a layer of insulation, a complete layer of shielding, and another layer of insulation, and has been tested to 75 kV. The double insulated shielded cable offers the best level of safety available, providing the cable with a direct path to ground for any High Voltage short circuit fault that may occur, and a tough outer jacket to keep the inner shield fully intact. The Safety Ground cable and clamp meets MS3493-4 requirements for grounding clamps and cables. Finally, the PS/60P has the appropriate High Voltage warning labels, Caution labels, and operator's instructions required by MIL-STD-454L.

P-STATIC DATABASE AND ACQUISITION SYSTEM (PDAS)

The automated PDAS, shown in Figures 3 and 4, is used to acquire broadband RF interference and audio signals during ambient conditions and P-Static charging of identified problem areas. While acquiring the interference signals, the PDAS generates and transmits an RF reference signal for the aircraft's radios to receive. This received reference signal's frequency, amplitude, and modulation is automatically set to test the radio's Minimum Sensitivity during P-static conditions [2].

During each PDAS measurement, the RF signal into the aircraft receiver is measured to define the broadband received RF environment. Also, the audio signal output of the receiver is measured to acquire audio Signal to Noise (S/N) and audio Signal to Noise and Distortion (SINAD). The S/N and /SINAD readings are then compared to the receiver's Minimum Sensitivity specification limits, for a given received reference signal level. Once measured, the severity of interference caused by the problem area can be compared to the ambient and to the aircraft RF receivers Minimum Sensitivity specification. These problem areas are measured before and after applying a fix, allowing a before and after fix comparison which provides an accurate evaluation of fix effectiveness. The PDAS stores and prints the spectrum analyzer's display, S/N and SINAD data, Problem Area Identification (PAID) numbers and definitions, aircraft configurations, and other associated test parameters. In this way, the effectiveness of each fix is measured accurately and recorded for a final test report.

CONFIGURATION

Hardware -- The automated PDAS uses a Wavetec 2500A RF Signal Generator, Hewlett-Packard (HP) 8590B RF Spectrum Analyzer, HP 8903B Audio Analyzer under GPIB computer control, and an A. H. Systems SAS-200/542 (30 - 330 MHz) Biconical or other antenna. The PDAS software is hosted on a Compaq 386s/20MHz CPU PC-AT clone with 2 Megabytes of RAM, using a Compaq VGA Color Monitor. For report quality data and graph printouts an HP-IIP LazerJet printer and a HP LaserJet Super Cartridge 1 with 55 Fonts is used. The PDAS instrument's power is protected by a SPC Technology LR62645 Surge Suppressor, a Staco GSD-1500 1500 'Vatt Transformer, and a Pulizzi Engineering Inc. Z-Line TPC-884 Power Controller. The PDAS instruments are packaged for portability and protection in an Anvil 17S Portable Equipment Rack.

Software -- The new PDAS software, Version 2.1, was developed using Professional Basic (ProBasic) to implement instrument control and data acquisition under relational databases. These databases relate all setup, configuration, and calibration data to the acquired RF and audio interference data and PAID numbers. The PDAS Version 2.1 software was written in modules for easy updating and maintenance, provides more accurate and efficient data acquisition, requires less operator interaction, and is fully automated. The PDAS software was written with ProBasic, Version 4.5, which allows easy development of relational databases. Because of the flexibility of ProBasic's database development architecture, our new version of the software includes a completely new automated P-Static Problem Area Tracking Database which is integral to the PDAS's function of acquiring data. The PDAS's databases includes Aircraft and Radio Configuration Tables, Equipment Calibration Data Tables, Problem Area ID Tables, Test ID Parameter Tables, and Test ID Data Tables [2].

Problem Area Tracking -- All P-static problem areas are tracked in the PDAS Problem Area Database by a three character alphanumeric PAID number scheme which uses a letter to denote the problem area's general location on the fuselage and a two digit number to denote the sequence in which it was found. The P-static problem areas are typically localized by Bottom, Front, Overhead, Port, Starboard, and Tail areas. All P-static problem areas, localized during the power-off testing of any model aircraft tested and for each BuNo or tail number tested, is entered into the PDAS's Problem Area Database and issued as the aircraft model Problem Area Report. This report includes the PDAS PAID code used to track each problem area, a Work Unit Code (WUC) for location of the physical problem area by aircraft maintenance work areas, and a brief description of the problem area [2].

PDAS OPERATION

PDAS Pre-requisite Tests -- The PDAS is operated in accordance with it's Operator's Manual [2]. During any type of PDAS test, a sequence number, date, and time is assigned to the data point for easy tracking of the data acquired. The PDAS requires four mandatory pre-requisite tests be performed prior to allowing the automatic acquisition of P-static interference data. These four tests are, Calibration, Free Space Loss, Radio Minimum Sensitivity, and Ambient Background. The Calibration (CAL) test acquire PDAS measurements for all PDAS and ARC-182 coaxial cables and RF splitters RF attenuation over a specified frequency range. If a cable or splitter is replaced it must be calibrated or have an existing calibration file. Calibrations are run before the test, and are checked and updated at various time during the test. The PDAS uses the CAL data to automatically normalize all PDAS data with the coax cables' and splitter's frequency response.

Free Space Loss (FSL) -- FSL acquires PDAS measurements for each discrete test frequency and aircraft configuration to be used during the test and accounts for all RF losses between the PDAS RF Signal Generator and RF Spectrum Analyzer. The FSL data, figure 5, accounts for the free space attenuation between the PDAS's transmit antenna and the aircraft's receive antennas, the RF losses in the aircraft's antenna cables and RF switches, and the RF losses of the PDAS coax cables and RF splitters. The FSL test must be run when a cable or physical arrangement of the antennas has changed, or when the RF losses are affected by other means, such as equipment in the vicinity.

Minimum Sensitivity (MinSens) -- MinSens acquires PDAS measurements for each discrete test frequency and modulation configuration for comparison to the radios specification limits. The Minimum Sensitivity level is the weakest RF signal strength that the receiver is specified to receive. Most aircraft receivers should have a minimum SINAD of 10 dB at the Minimum Sensitivity signal levels and modulation of each band. The MinSens test is run by generating a RF signal with the proper frequency and modulation and injecting this signal, the reference received signal, into the front end of the radio's receiver while measuring the radio's output audio SINAD for comparison to the radio's specification. The MinSens tests are usually only run before beginning PDAS data acquisition in order to determine whether or not the radio is performing within specification limits. If the audio SINAD is less than 10 dB, the received signal is affected by the noise.

Ambient -- Ambient test acquires PDAS measurements for each frequency, and aircraft configuration planned to be tested, prior to acquiring actual P-static interference data. The Ambient data, figure 6, is identical to the P-static interference data, except that the P-static Simulator is not used to excite the aircraft's P-static problem areas. Ambient RF data, as well as Post-fix P-static RF data, typically does show predominant, discrete, RF signals above the noise floor from local RF transmitting sources. It should be cautioned that these predominant, discrete, RF signals should not be mistaken for P-static RF interference during Post-fix P-static testing.

P-static -- Once all the PDAS pre-requisite tests are performed and the radio is found to be within the MinSens specification limits, the PDAS is used to acquire the RF and audio signals for each test frequency and aircraft configuration planned. During each PDAS ambient and P-static interference data measurement the RF signal is measured into the radio's receiver to define the broadband received RF environment which is a combination of ambient background noise, the PDAS receiver reference signal, and P-static RF interference if any is present. The radio's audio signal output is also measured to acquire audio SINAD (and S/N, if selected) data which is compared to the radio's specification limits, for a given received reference signal level. The PDAS RF and audio SINAD measurements are acquired during normal ambient background conditions and during P-static Simulator charging of all the identified problem areas. The method of acquiring P-static interference data is identical to acquiring Ambient data, except that the P-static Simulator is not used to excite the aircraft's P-static problem areas.

Pre-fix and Post-fix Test Data Comparison -- Using this method, the severity of interference caused by the problem areas during charging can be directly compared to the ambient data and to the receivers' Minimum Sensitivity specification limits. Additionally, PDAS RF and audio SINAD measurements are acquired before and after applying a temporary or permanent fix to the problem areas being tested. This allows a direct comparison of the data before (figure 7) and after (figure 8) applying a fix, which provides an evaluation of the fix's effectiveness.

ACCURACY -- To ensure the PDAS measures the RF interference and audio SINAD data accurately, while the P-static Simulator's operator is manually charging the aircraft's problem areas, the RF and audio measurements are acquired over a predetermined period of time. In order to preserve accurate narrowband resolution the RF spectrum analyzer is operated with a sweep speed based upon the RF bandwidth selected by the PDAS operator. The spectrum analyzer is operated in the Peak Hold mode to acquire the peak amplitude of the existing RF interference over a large number of sweeps.

The number of spectrum analyzer sweeps are determined by the desired fidelity of the audio SINAD and S/N measurements. The fidelity of these measurements is determined by the number of samples of SINAD (and S/N) measurements the operator has selected, which also determines the finite time required to measure the samples. During the time required to measure the audio SINAD (and S/N) data the PDAS continues to sweep the RF spectrum and holds each sweep's peak amplitude data.

To acquire the most accurate audio SINAD (and S/N data, if it is chosen by the operator) data for an intermittent, pulsed, noise source, such as P-static, the PDAS acquires several SINAD (and S/N if selected) data samples. The number of audio SINAD (and S/N) samples is chosen by the operator, and is typically 15 SINAD samples (and 10 S/N samples, if chosen by the operator). The audio analyzer takes approximately 1 second to acquire one sample of SINAD (or S/N) data, thus it requires approximately 25 seconds to acquire 15 SINAD samples and 10 S/N samples. Once all the audio analyzers' data is acquired, the PDAS uses the number of SINAD (and S/N) samples and all the SINAD (and S/N) data acquired to calculate the SINAD's (and S/N) statistical mean (AVG), maximum (MAX) reading, minimum (MIN) reading, average deviation (AVDEV), and standard deviation (STDEV). In this way each audio SINAD (and S/N) value used to evaluate a P-static problem area is actually the statistical mean (or average) of all the SINAD (and S/N) measurements acquired. The operator can evaluate the other statistical data (i.e. MAX, MIN, AVDEV, and STDEV) to determine how stable and realistic the measurement was, and decide to keep the data or repeat the test again.

SUMMARY

The ruggedized P-static Simulator, PS/60P, has been successfully used to locate problem areas and perform basic P-static Quick Look tests, similar to EMI scrubs. The P-static Simulator has also been successfully used with the PDAS data acquisition system to perform P-static Detailed tests to measure the degree of EMI caused by each problem area, compare the EMI measured to specification limits, and to quantify the degree of effectiveness for fixes. Veda, Inc. supported the U. S. Navy in using a prototype P-static test set and data acquisition instrumentation system to record and measure simulated and actual in-flight P-Static environments on a P-3B aircraft [3]. This inflight data successfully substantiated the test methodology, P-static test set simulation charging levels, and the accuracy of using a P-static test set and P-static data acquisition system [3].

REFERENCES

1. W. Devereux; "Precipitation Static Simulator, Model PS/60P-491 Operator's Manual"; Veda Report Number 75556-91U/P070006; August 1991
2. W. Devereux; "Precipitation Static Database and Acquisition System (PDAS) User's Manual, Version 2.1"; Veda Report Number 75450-91U/P070006; August 1991
3. M. Whitaker; "Results of the Recent Precipitation Static Flight Test Program on the Navy P-3B Antisubmarine Aircraft"; IAGC on Lightning and Static Electricity Proceedings; April 1991

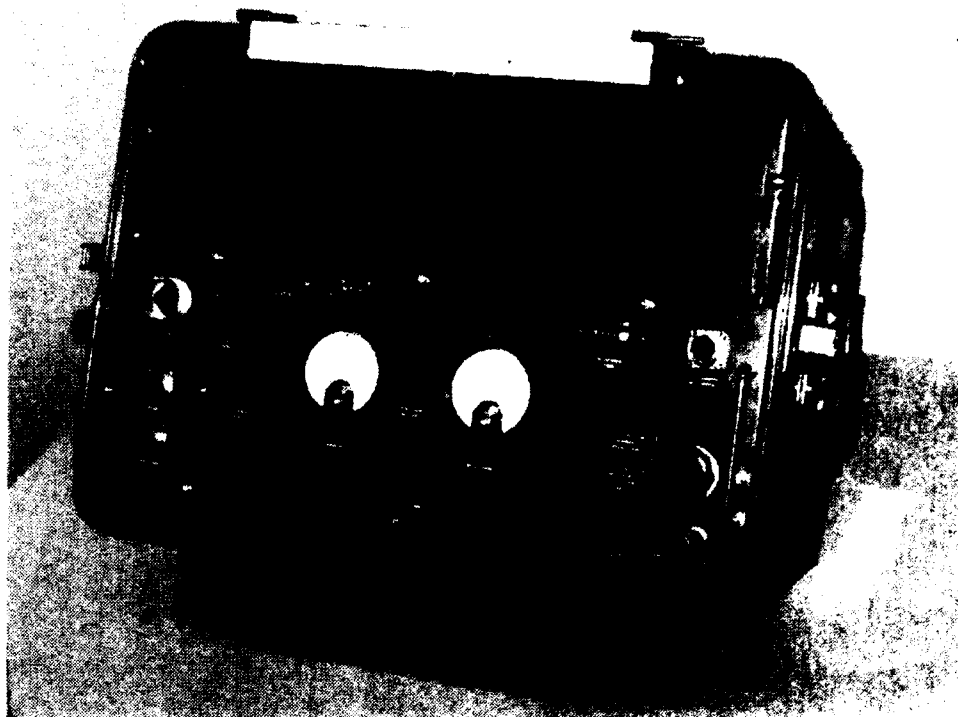


Figure 1
RUGGEDIZED P-STATIC SIMULATOR

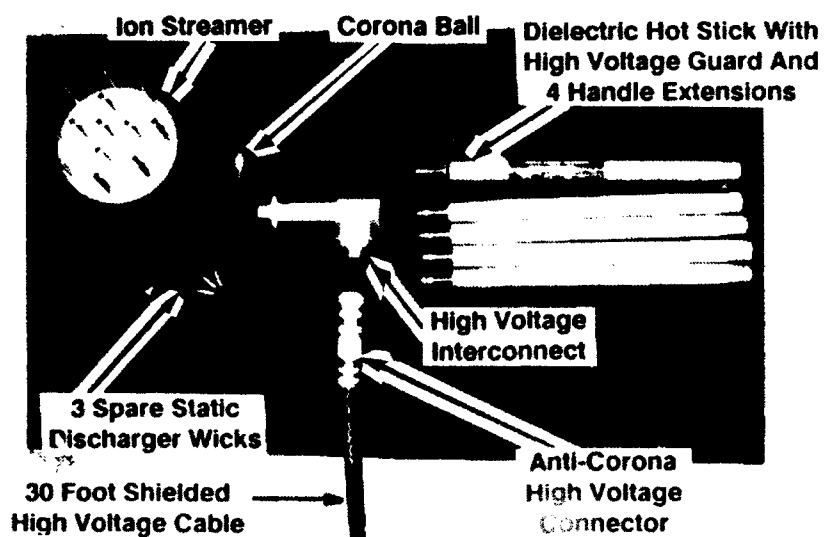


Figure 2
P-STATIC ACCESSORIES

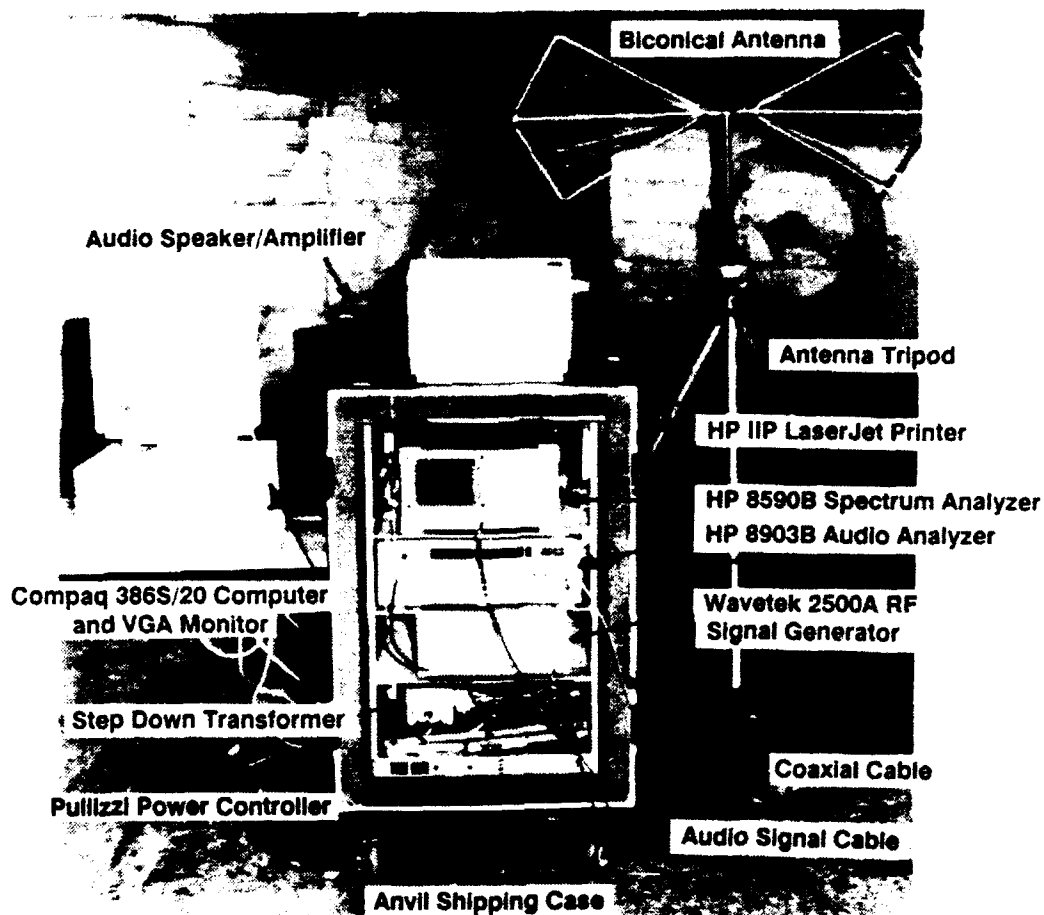


Figure 3

P-STATIC DATABASE AND ACQUISITION SYSTEM (PDAS)

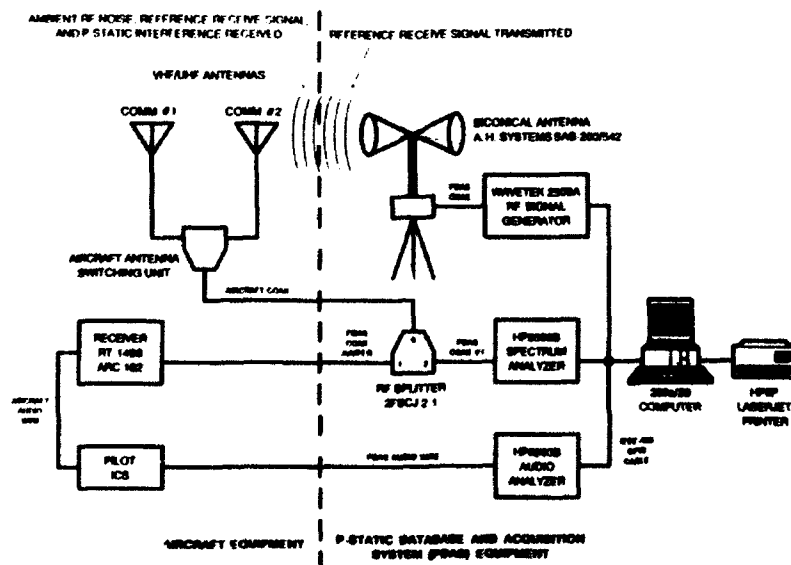


Figure 4

PDAS INSTRUMENTATION CONFIGURATION

TEST SEQ#: 108
 TEST TYPE: FSLOSS
 TEST DATE: 08-30-1991
 TEST TIME: 13:16:58
 OPERATOR: SCD
 A/C MODEL:
 BUREAU #:

RES BW: 10 KHz
 VIDEO BW: 10 KHz
 ATTENUATION: 0 dB
 REF OFFSET: 1.27 dB
 FREQ OFFSET: 165 KHz

CFGID: 16 COM: 1 FREQ MHz: 118.5 XMIT Ant: A.H. SYSTEMS BICONIC
 MOD: OFF REC V ANT: LOWER
 CALID: 7 CALREV: 1
 CABLE: RG223 30' #2 RADIO MODEL: ARC-182 REC V LEVEL dBm: -47.50
 COUPLER: ZFSCJ-2-1 #1
 PREAMP: NONE

FREE SPACE LOSS dBm: -47.5

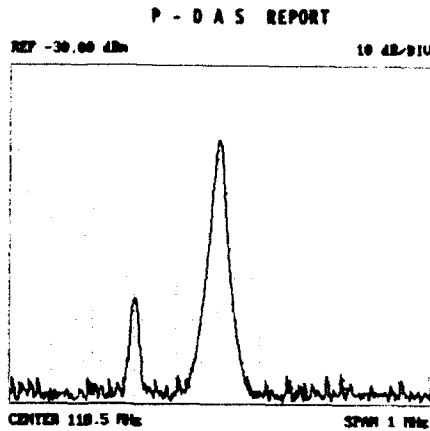


Figure 5
PDAS FREE SPACE LOSS DATA

TEST SEQ#: 110
 TEST TYPE: AMBIENT
 TEST DATE: 08-30-1991
 TEST TIME: 13:20:31
 OPERATOR: SCD
 A/C MODEL:
 BUREAU #:

RES BW: 300 KHz
 VIDEO BW: 100 KHz
 ATTENUATION: 0 dB
 REF OFFSET: 0 dB
 FREQ OFFSET: 0 KHz

CFGID: 16 COM: 1 FREQ MHz: 118.5
 MOD: AM (AM: 30 FM KHz:) REC V ANT: LOWER
 CALID: 7 CALREV: 1
 CABLE: RG223 30' #2 RADIO MODEL: ARC-182 REC V LEVEL dBm: -103
 COUPLER: ZFSCJ-2-1 #1 MIN SINAD dB: 10 MIN SENS dBm: -103
 PREAMP: NONE AUDIO FILTER: 30 KHz L-P AUDIO FREQ Hz: 1000

FREE SPACE LOSS SEQ#: 108 FREE SPACE LOSS dBm: -47.5

MIN SENS TEST SEQ#: 109 MIN SENS AVG SINAD: 10.23

AMBIENT AVG SINAD: 10.33

SINAD#: 15 AVG: 10.33 MAX: 11.00 MIN: 10.00 AVDEV: 0.36 STDEV: 0.39
 SIG/NO: 10 AVG: 9.10 MAX: 9.50 MIN: 8.50 AVDEV: 0.32 STDEV: 0.37

Figure 6
PDAS AMBIENT DATA

TEST SEQ: 131
TEST TYPE: PSTATIC
TEST DATE: 08-30-1991
TEST TIME: 14:17:58
OPERATOR: SCO
A/C MODEL:
BUREAU #:

RES BW: 300 KHz
VIDEO BW: 100 KHz
ATTENUATION: 0 dB
REF OFFSET: 0 dB
FREQ OFFSET: 0 KHz

START 20 MHz STOP 200 MHz

CFID: 16 COM: 1 FREQ MHz: 118.5 XMIT ANT: A.H. SYSTEMS BICONIC
MOD: AM (AMW 30 FM KHz:) RECV ANT: LOWER
CALID: 7 CALREV: 1 SQUELCH ON: 1 GUARD ON: 1
CABLE: BG223 30' #2 RADIO MODEL: ARC-182 RECV LEVEL dBm: -103
COUPLER: ZFSC-1-2-1 #1 MIN SINAD dB: 10 MIN SENS dBm: -103
PREAMP: NONE AUDIO FILTER: 30 KHz L-P AUDIO FREQ Hz: 1000
FREE SPACE LOSS SEQ: 100 FREE SPACE LOSS dBm: -47.5
MIN SENS TEST SEQ: 100 MIN SENS AVG SINAD: 10.23
AMBIENT TEST SEQ: 110 AMBIENT AVG SINAD: 10.31
SINAD: 15 AVG: 1.27 MAX: 2.00 MIN: 0.50 AVEDEV: 0.38 STDEV: 0.44
SIG/NO: 10 AVG: 0.15 MAX: 1.00 MIN: 0.00 AVEDEV: 0.24 STDEV: 0.32

P-STATIC WA: 20 P-STATIC KV: 60 P-STATIC PROBE: 10M STREAMER
PAID: PAID FIXED: 0 WORK UNIT CODE: 10.5
PAID DESCRIPTION: HANDHELD

Figure 7

PDAS PRE-FIX P-STATIC DATA

TEST SEQ: 284
TEST TYPE: PSTATIC
TEST DATE: 09-12-1991
TEST TIME: 12:14:14
OPERATOR: SCO
A/C MODEL:
BUREAU #:

RES BW: 300 KHz
VIDEO BW: 100 KHz
ATTENUATION: 0 dB
REF OFFSET: 0 dB
FREQ OFFSET: 0 KHz

START 20 MHz STOP 200 MHz

CFID: 16 COM: 1 FREQ MHz: 118.5 XMIT ANT: A.H. SYSTEMS BICONIC
MOD: AM (AMW 30 FM KHz:) RECV ANT: LOWER
CALID: 7 CALREV: 1 SQUELCH ON: 1 GUARD ON: 1
CABLE: BG223 30' #2 RADIO MODEL: ARC-182 RECV LEVEL dBm: -103
COUPLER: ZFSC-1-2-1 #1 MIN SINAD dB: 10 MIN SENS dBm: -103
PREAMP: NONE AUDIO FILTER: 30 KHz L-P AUDIO FREQ Hz: 1000
FREE SPACE LOSS SEQ: 257 FREE SPACE LOSS dBm: -47.33
MIN SENS TEST SEQ: 222 MIN SENS AVG SINAD: 9.80
AMBIENT TEST SEQ: 258 AMBIENT AVG SINAD: 9.20
SINAD: 15 AVG: 9.20 MAX: 9.50 MIN: 8.50 AVEDEV: 0.18 STDEV: 0.40
SIG/NO: 10 AVG: 8.50 MAX: 9.50 MIN: 7.50 AVEDEV: 0.50 STDEV: 0.63

P-STATIC WA: 20 P-STATIC KV: 60 P-STATIC PROBE: 10M STREAMER
PAID: PAID FIXED: 1 WORK UNIT CODE: 10.5
PAID DESCRIPTION: HANDHELD

Figure 8

PDAS POST-FIX P-STATIC DATA

COMPARATIVE PERFORMANCE OF LIGHTNING AIR TERMINALS UNDER NATURAL STORM CONDITIONS

J.R. (Rick) Gumley
International Protection Consultants Pty Ltd
Technopark, Hobart, Australia.
Telephone (6102) 730824 Fax (6102) 731871

Philip J. Jones
Lightning Protection International Pty Ltd
Technopark, Hobart, Australia.
Telephone (6102) 730133 Fax (6102) 730399

ABSTRACT

During August 1992, a test site was established in Florida USA to assess the upward leader initiation capability of air terminals under natural storm conditions. Five types of air terminals were mounted independently on 10m masts and grounded through one ohm resistors to sense emission currents. Two terminals were corona forming types, and three were spherical in design. Coaxial feeders conveyed the derived voltages to digitiser cards located in a Personal Computer with hard disc and tape drive storage. The two types of events described were recorded from very close lightning. The first showed marked differences in the emission currents of the spherical and corona forming terminals at the commencement of the return stroke. The latter exhibited strong negative polarity while the 3 Spheres simultaneously produced a strong positive deflection. Several events displayed this type of characteristic. The second type of event recorded pulse currents of 10-15 amperes with polarity consistent to that expected for upward streamer initiation. These emissions were generated from the floating spheres 30-150 microseconds ahead of the return stroke. No significant or similar emissions were recorded in the same period from the conventional Sphere or from the Franklin Rod. The reference Franklin Rod showed the lowest predischage activity in 75% of recorded events.

GENERAL

The experimental data gathered in Florida this year is a progression on previous attempts to record upward streamer emissions from air terminals of differing electrical and geometric concepts. The test site layout is shown in Figure 1. The air terminals and electrical arrangements for recording are shown in Figures 2 & 3.

Five masts supported air terminals at 10m height with each mast separated by 20m. The five air terminals configurations were named Franklin, Broomstick, Sphere, Dynasphere and Megasphere. The Franklin and Sphere were designed to be control or reference terminals from which relative performance of other configurations could be

measured. The connecting coaxial cables to the recording station were all 90m length to ensure identical transmission time delay. The cables terminated in a protection module containing surge divertors and impedance matching components.

New recording equipment replaced the older custom designed digitisers. The previous equipment triggered on the signal amplitude of the various input signals, and was very prone to false triggering. The effect was to fill the hard disc with useless information whenever a storm was in the general proximity.



Figure 1 – Site Layout Showing 5 Air Terminals

The digitisers for the 1992 season were triggered from signals derived from the E-field collapse on the occasion of a return stroke. This method proved very successful with only near events being recorded. Due to an inverting amplifier at the sensor plate, E-field recordings in the following results show positive for a negative approaching leader.

The digitiser had 8 inputs of which 7 were ultimately used. Five air terminal inputs were compared with a slow field mill and fast field antenna. Memory on each input was 8K and with sampling at 2 MHz, provided 4 milliseconds of record. The digitiser was set to record 2 milliseconds each side of the return stroke. Previous data had shown that this interval was adequate to record both the exponential rise in E-field and the onset of activity from the test terminals.

The recording equipment was located in a Recreational Vehicle which was self contained with power generator, UPS and long term battery backup. A camera platform

was available in the vehicle and video recordings were taken during storms. A Lightning Warning System was used to disconnect and isolate commercial power for extended battery operation during a storm. Modem connection was used to transfer data to Australia. This was successfully trialled in the short time available at site this year, and supports the concept of unattended operation with remote interrogation, including an ability to rapidly assess results and remotely change recording parameters when necessary. Figure 2 shows the Test Terminal Configurations. The broomstick comprised 35 radially fanned rods to 300mm diameter. The Sphere and Dynasphere were 350mm diameter, the Megasphere was 900mm diameter. Both Dynasphere and Megasphere shells were grounded by a very high impedance.

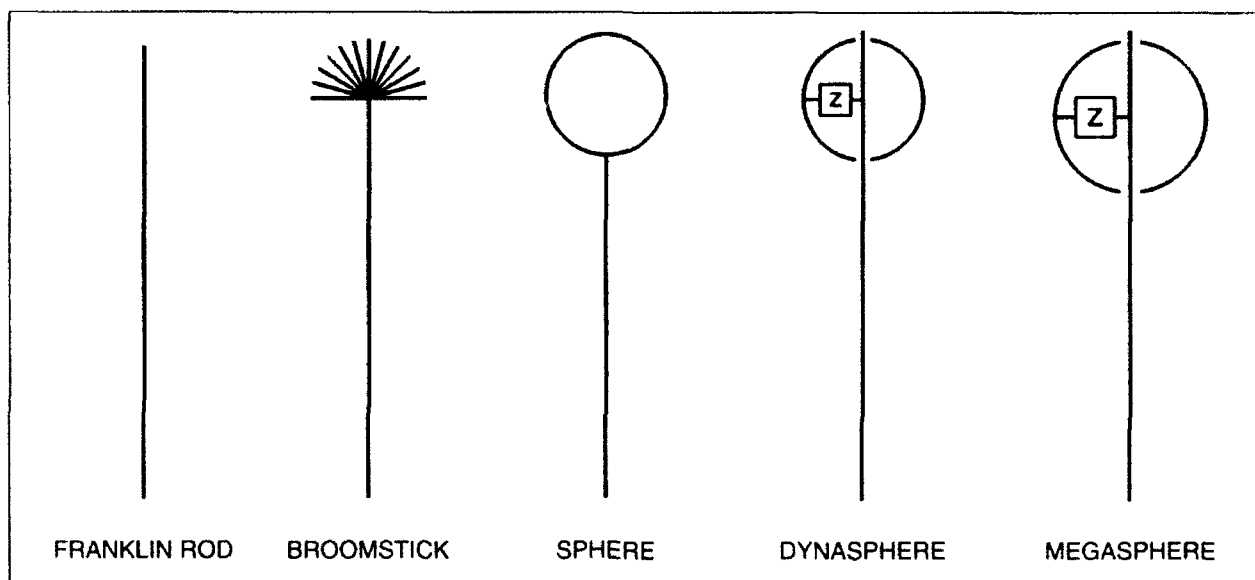


Figure 2 – Test Terminal Configurations

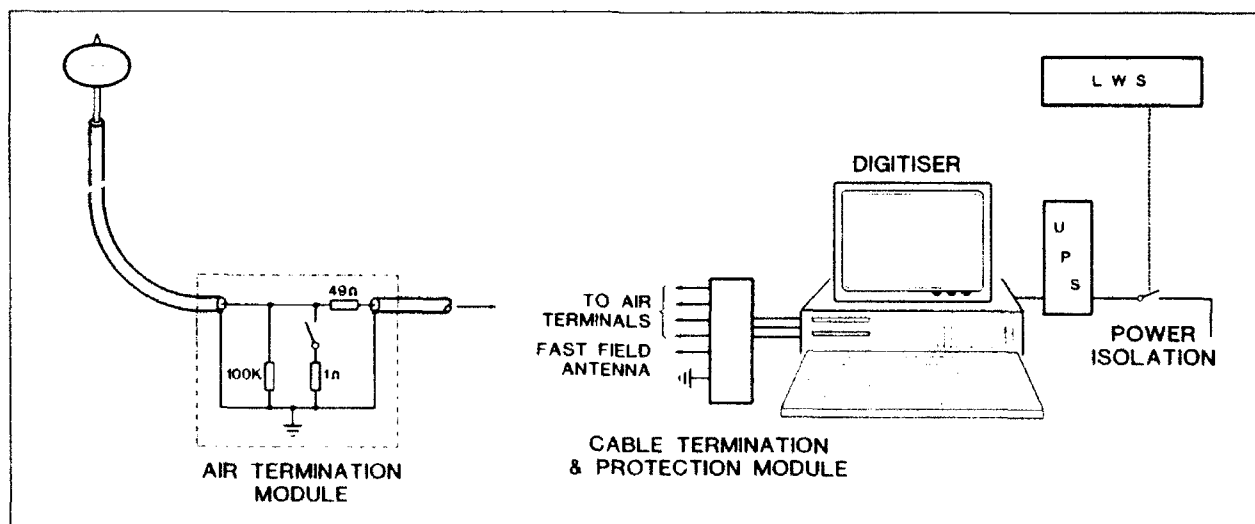
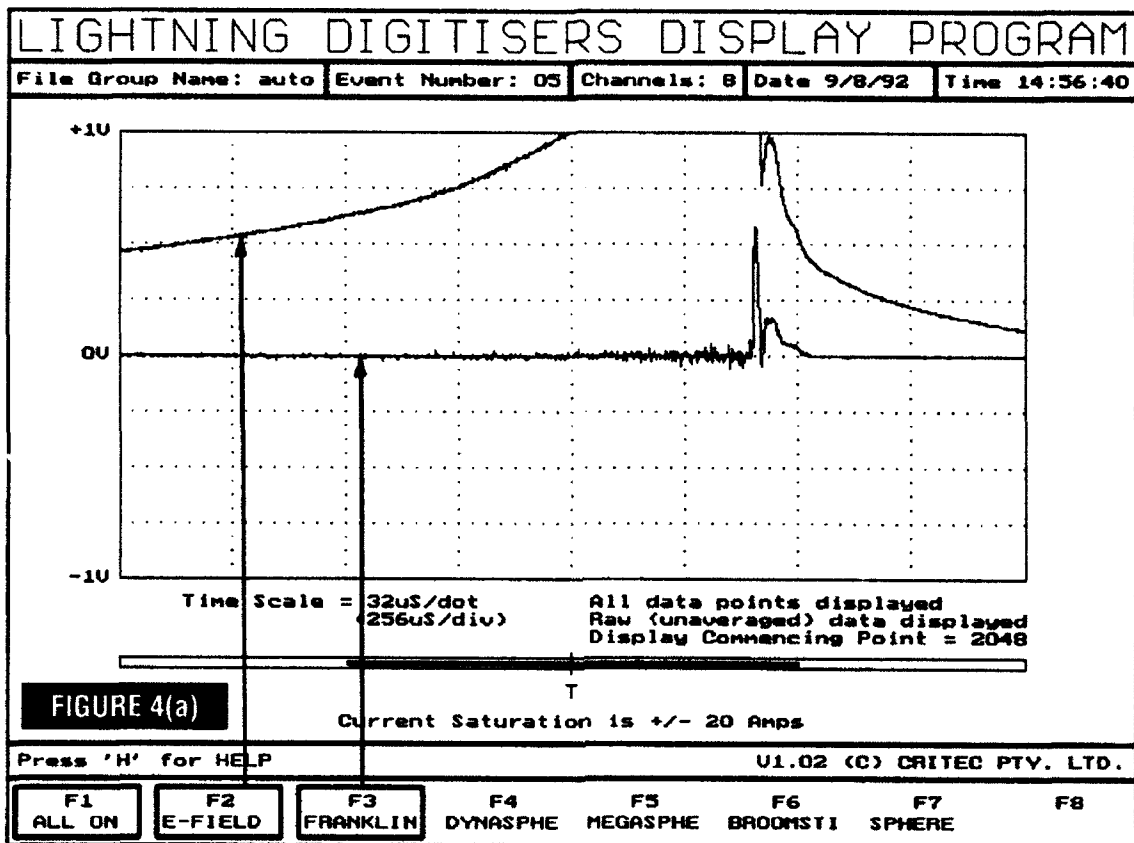


Figure 3 – Air Terminal Grounding and Recording System

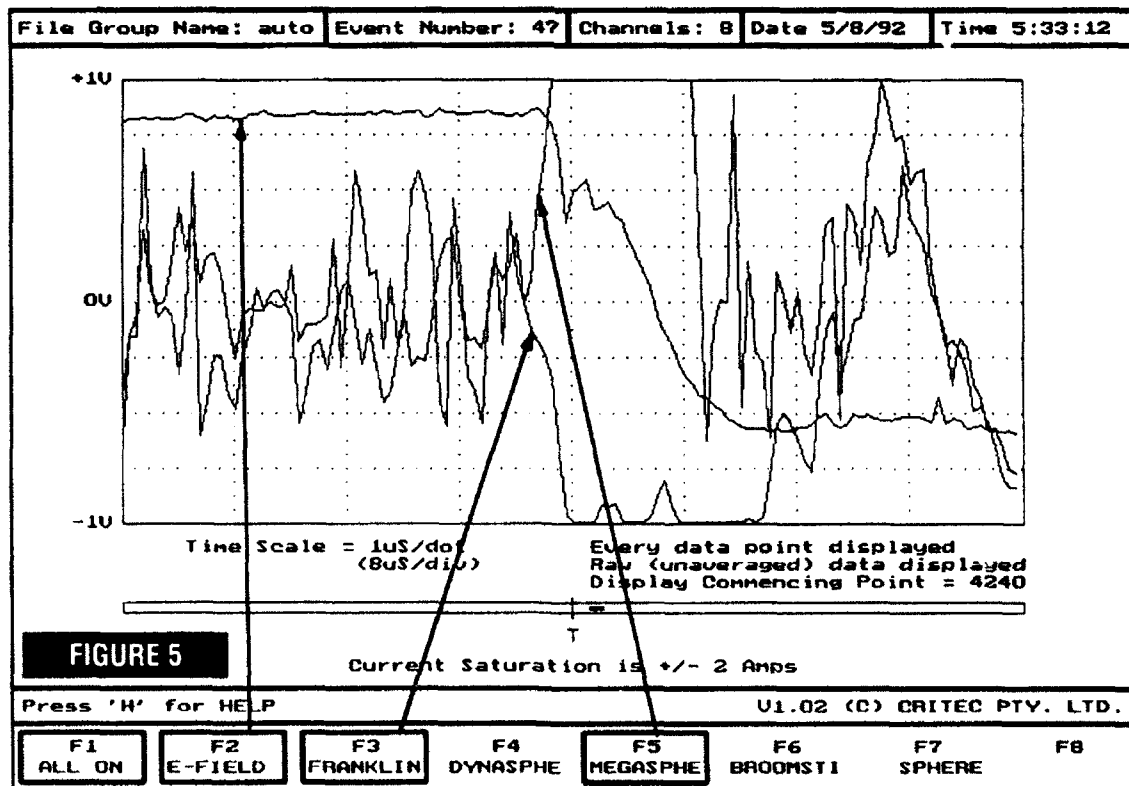
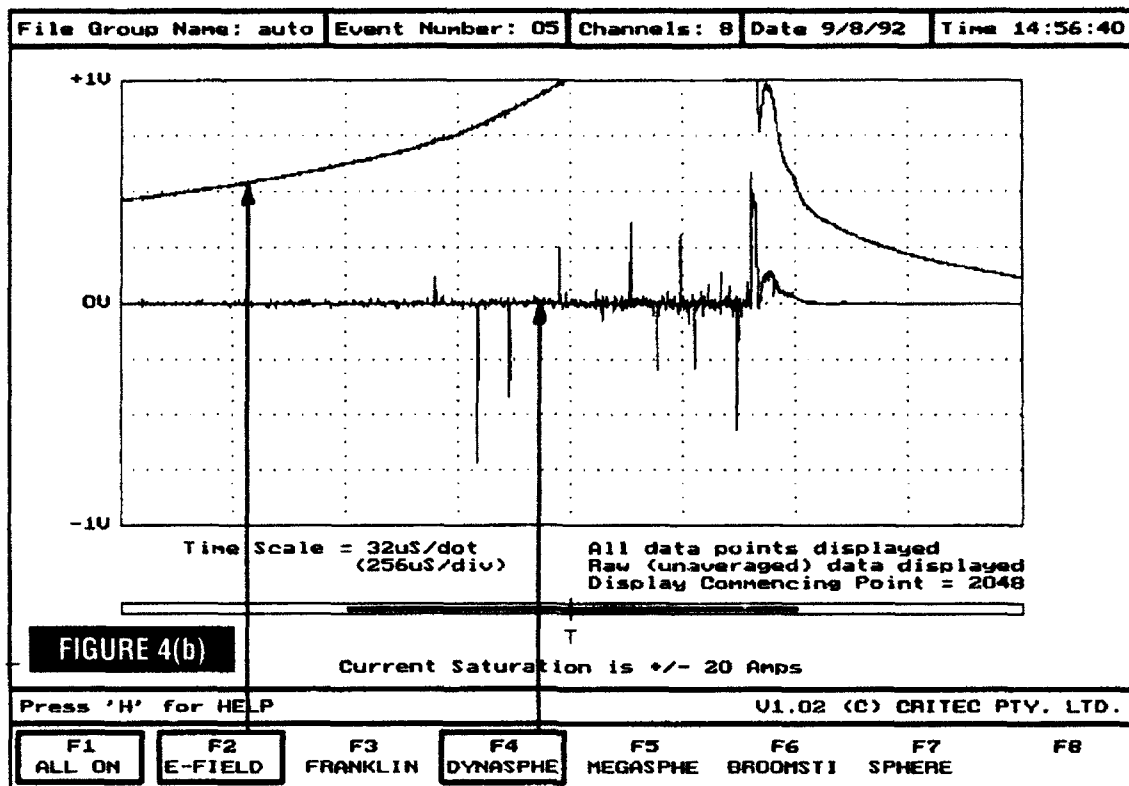


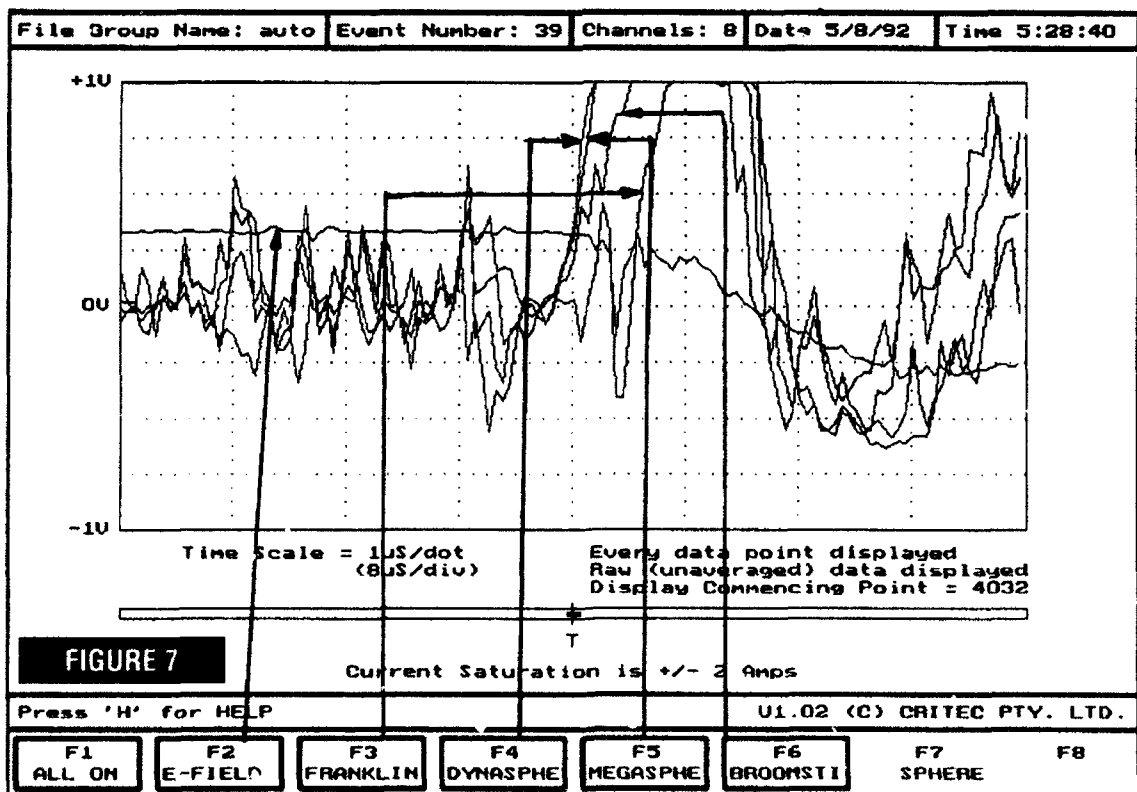
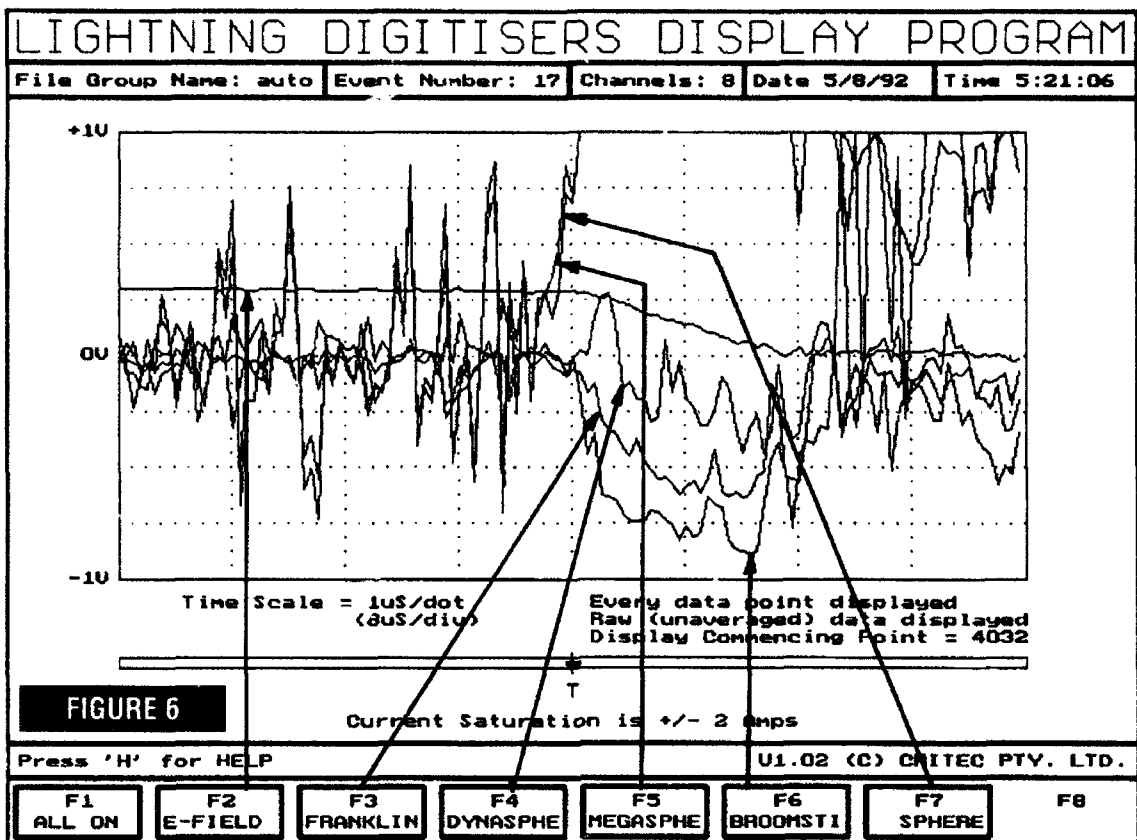
RESULTS

Figure 4 shows Event No 05-8/9/92, a typical result from near lightning. The saturation level for these recordings was set at ± 20 Amps. Notable, is the complete absence of pre-discharge emissions from the Franklin Rod compared with the Dynasphe which produced 10-15 Amp impulse emissions prior to the discharge. In this event, the two floating spheres produced virtually all activity. The conventional sphere had similar response to the Franklin Rod except that the pre-discharge activity in the final 400 microseconds before the return stroke reached levels of 2-3 Amperes.

Figure 5 shows Event No 47-4/8/92, a very close discharge with flash and sound and occurring in synchronism. This event shows a remarkable disparity between the corona and spherical terminals. All 3 spherical terminals showed the positive excursion usually associated with E-field collapse. However, both corona terminals showed strong negative displacement into saturation. In this instance, saturation occurred at ± 2 Amps. Note that the divergence in current in all cases is concurrent with the first indication of E-field collapse due to the return stroke. Fig 6 of Event No. 17-5/8/92 is another case where a similar disparity occurred, but with a lower E-field change. In this instance, due to the rapid onset of the storm, the Sphere and Megasphere gain settings were some 50 times that of the remainder. The figure should only be interpreted on the basis of divergence in response.

Figure 7 shows event 39-5/8/92 where divergence in response did not occur. In this instance both corona terminals exhibited a later response of lower magnitude.





After the events shown in Figs 5, 6 & 7 a polarity check was carried out on all air terminals at the completion of the storm. However, the return to tracking of the signals near the completion of the return stroke is clearly evident. This further discounts the possibility of polarity error.

A check was made to confirm the corona emissions of the various terminals under steady field conditions. The 1 ohm grounding resistor at the air terminals was removed to leave a residual 100K ohm as the ground connection. Current was measured with a meter placed across this resistor. The measurements were conducted at the end of the storm when long periods of relatively steady charge remained in the atmosphere. As was to be expected, the corona terminals in fields of 3kV/M exhibited some tens of microamps of discharge current, with the broomstick emitting 10-20% more than the Franklin Rod. The emission of the spherical terminals was below our measuring threshold.

CONCLUSION

This preliminary report covers an experiment which is of a continuing nature. Equipment is already being re-established in Darwin, Australia for the Southern Hemisphere lightning season, October 1992 through March 1993. The new recording equipment and triggering technique has proven very satisfactory. Although insufficient data has been recorded to lead to firm conclusions, some remarkable disparities were observed in air terminal response. Three spherical terminals and two corona terminals produced opposite polarities on a number of occasions. Other events recorded significant levels of upward emissions on floating spheres, with virtually no emissions on other terminals. The traditional Franklin Rod appeared the least responsive to pre-stroke electric fields. These early results suggest that it is incorrect to assume all air terminals, irrespective of geometric shape, have the same efficiency in generation of upward leaders. This assumption is currently present in all Lightning Protection Standards and Codes of Practice.

ACKNOWLEDGEMENTS

The authors wish to thank Mr William Jafferis and Prof Earl Williams for their assistance in locating and establishing the experimental site.

ALTERNATIVE EQUIPMENT TEST PROCEDURES FOR SIMULTANEOUS CURRENT INJECTION ON MULTIPLE CABLE BUNDLES

C J Hardwick, S J Haigh, R E Baldwin
Lightning Test and Technology, AEA Technology, Culham Laboratory,
Abingdon, Oxfordshire OX14 3DB, England
Telephone: +44-235-46-3436 Facsimile: +44-235-46-4325

ABSTRACT

Simple equipment tests can be accomplished by injecting currents into interconnect cables and adjusting the voltage injected into the loop under test or current in the cable until the ETDL is reached. However for more complicated systems with several cables this simple procedure is inadequate. This paper compares measurements made on cable bundles in a fuselage with both injection into the fuselage and injection on bundles to illustrate the problem and proposes alternative test methods.

1 INTRODUCTION

Cable bundle injection is one method of qualifying avionics equipment and systems to the lightning threat. Cable bundle currents measured during whole aircraft tests or predicted by analysis are injected into the appropriate cable bundle during the equipment or system tests at the same level or a higher level after the application of an agreed margin. For a single cable interconnecting two equipments an identical current distribution between the different individual cables within the bundle are obtained for both the aircraft test and equipment tests. However the question arises as to how these distributions will differ between the two tests when a more complex cable bundle connects the two equipments: one that includes "T" junctions or branches. As the whole of the bundle may no longer follow the same path between the two equipments, different parts of it may be exposed to different levels of electromagnetic threat in the aircraft test whereas in an equipment test the threat is generally only injected at a single point.

This report investigates these differences for simple branched and "T"ed cables interconnecting two equipments.

Section 2 describes differences that would be expected from circuit analysis theory, section 3 gives results and compares this with theory. Section 4 makes some recommendations to overcome the problems that can occur with single point injection.

2 THEORETICAL EXPECTATIONS

Consider the configuration of Figure 1 which shows a fuselage with two apertures. There are two cable looms tightly bound together; one spans both apertures and the other only the first aperture ie, it can be considered as a single cable bundle that branches after the first aperture; one branch is connected to airframe

immediately, the other is routed over the second aperture before being bonded to airframe. Both bundles have good screens which are bonded at each end.

For reference a "T"ed cable is also shown in Figure 1 - this is defined as a topologically continuous screen that splits into two after the first aperture.

Figure 2 and 3 show equivalent circuits for both current injection into the fuselage (Whole Aircraft Test or WhAT) and for injection into the cable bundle (equipment test). The elementary analysis initially assumes that both apertures are identical, that the self inductance for equal lengths of each cable bundle are identical and that cable loom 2 is twice the length of cable loom 1.

2.1 Aircraft Test

The aperture coupling is represented by 3 voltage generators inserted as shown in Figure 2. The variables are defined in the diagram. An analysis is made as follows:

For reference, if Circuit 1 only was connected, neglecting resistance

$$V = L \frac{di}{dt}$$

Therefore $i_1 = \int \frac{Vdt}{L}$, for future reference denote this value as I

For both circuits connected:-

Circuit 1

$$V = L \frac{di_1}{dt} + M \frac{di_2}{dt} \quad (1)$$

Circuit 2

$$2V = 2L \frac{di_2}{dt} + M \frac{di_1}{dt} \quad (2)$$

$$(1) \times 2 \quad 2V = 2L \frac{di_1}{dt} + 2M \frac{di_2}{dt} \quad (3)$$

$$(3) - (2) \quad 2L \frac{di_1}{dt} - M \frac{di_1}{dt} = 2L \frac{di_2}{dt} - 2M \frac{di_2}{dt}$$

$$\text{Integrating we obtain } (2L - M)i_1 = (2L - 2M)i_2 \quad (4)$$

But as $L \approx M$, if looms tightly bound.

$$i_1 \approx 0$$

$$\frac{di_2}{dt} \approx \frac{V}{M} \text{ from (1).}$$

$$i_2 = \int \frac{Vdt}{M}$$

$$\approx 1$$

2.2 Cable Loom Injection - Equipment Test

As the equipment test injects at a single joint the equivalent circuit now can be represented by a single voltage generator V , acting on both circuits as shown in Figure 3.

Circuit 1

$$V = L \frac{di_1}{dt} + M \frac{di_2}{dt} \quad (1)$$

Circuit 2

$$V = 2L \frac{di_2}{dt} + M \frac{di_1}{dt} \quad (2)$$

$$(1) - (2) \quad (L - M) \frac{di_1}{dt} = (2L - M) \frac{di_2}{dt}$$

Again $L \approx M$, if looms are tightly bound.

Therefore $i_2 = 0$

$$i_1 = \int \frac{Vdt}{L} = 1$$

Hence in the example considered where the parameters have been chosen to make the analysis simple, for the WhAT bundle 2 sees most of current; in the equipment test however, bundle 1 sees most of current.

To summarise:

WhAT	$i_1 = 0$	Equipment	$i_1 = 1$
	$i_2 = 1$	Test	$i_2 = 0$

Hence for tightly bound cables which branch and are exposed to distributed coupling, WhAT's and Equipment Tests will result in entirely different current distributions!

2.3 Other Configurations - In general, the length of cable over the two apertures and the coupling from the two apertures will not be equal. The following expressions are for the general case.

$$\left(M \frac{V_1}{V_2} - L_1 \right) \frac{di_1}{dt} = \left(M - L_2 \frac{V_1}{V_2} \right) \frac{di_2}{dt}$$

Where V_1 and V_2 are the total EMFs driving cable bundle 1 and 2 respectively and L_1 and L_2 are the total inductance of these bundles.

The same formulae apply for both aircraft and equipment tests, but for the equipment test:

$$V_1 = V_2$$

3 RESULTS AND DISCUSSION

Branched and "T"ed cable bundles of various lengths were installed in a Hawker Hunter fuselage in a similar configuration to that illustrated in Figure 1. A 3kA unipolar pulse of 6 μ s rise time was injected into the fuselage and the currents measured on the cable bundles. These current measurements were then repeated using the same installation but injecting current between the box A of Figure 1 and the fuselage by ground plane injection. Further details can be found in Reference 1. The inductance of the various branches were measured with a bridge and the relative strength of coupling via the two apertures was also determined by closing one of them off. These measurements allowed predictions of current partition to be made using the formula of section 3.

The results are summarised in Figure 4. The distribution of currents between the different parts of the cable loom is shown in the histograms as a % of the total current in the complete cable before the branch or "T" for both aircraft and equipment tests. We note good agreement between the circuit analysis predictions and the results.

The current partition is different in the branched and "T"ed set since the length of cable in the short run of the two configurations (i_1 and i_3 runs respectively) are quite different. For equal lengths similar current partitions would have been achieved.

In general we note that when multiple bundles have different exposure quite different results will be obtained in aircraft and equipment tests.

4 SYSTEM TEST PROPOSAL

Single point cable injection tests therefore normally simulate the 'real event' well only in the case of two boxes with a single interconnecting cable.

In cases involving very complex systems comprising many cable looms and LRU's a series of single point injection tests could either underestimate the threat, since the aircraft strike scenario involves simultaneous currents flowing on all bundles or overstress some wires and understress others even if the total current in a particular bundle is correct as discussed in section 3.

We propose that in these cases a test procedure could often be invoked which would inject current at the correct level simultaneously along all cable bundles.

This sort of test would be advantageous in being both more realistic and less time-consuming to carry out, than many repeated single point injections.

As an example of this technique we consider an engine system with an EEC unit and an assortment of sensors and other engine mounted units.

The 'environment' around the engine during the passage of a 200kA strike to the aircraft is influenced by the presence of carbon-fibre cowl, metallic structure and apertures and was calculated using the code INDCAL (Reference 2) for an idealised installation of evenly spaced conduits around the engine (Figure 5).

The approach is then to simulate this environment on a flat test bed on which the system under test has been laid out, roughly as it would be as an 'uncurled' engine. With the help of INDCAL computer analysis a disposition of forward/return conductors is designed, so that on application of a test waveform an array of evenly spaced conductors will carry similar current waveforms as those predicted for the engine installation (Figure 6). Figure 6 shows a comparison of the predicted waveforms around both the test bed and the actual engine installation; the test bed design has concentrated on providing good reproduction of the most exposed areas of engine so that it is the higher level waveforms which show best agreement. The method would in any case include an adequate margin on all the waveforms.

Essentially the flat test bed is recreating the engine environment during a lightning strike, so that here the injection of the current pulse of 65kA/20 μ s into the flat bed and its mounted components provides a good simulation of the current flow along the cable bundles, that would have occurred during a 200kA strike to the aircraft with a 6dB margin.

The approach could be used more generally where predictions can be made about the environment to which parts of the system will be subjected, and that environment simulated. The level of threat to which different cable bundles will be subjected can be adjusted by the position of return conductors and forward shielding conductors, and the distance of the cable bundles from the ground plane.

5 SUMMARY AND CONCLUSIONS

- 1) Results from either direct injection of current into an airframe or tests using single point cable injection for non simple configurations will give current distributions whose trend can be estimated from simple circuit analysis considerations.
- 2) The only way that aircraft tests and equipment tests using injection at discrete points will generally give the same voltages on each individual core wire is if simultaneous cable bundle injection of appropriate amplitude and wave shapes are made.
- 3) An alternative philosophy for equipment tests is to use more powerful generators and drive current waveforms through a special ground plane on which the equipment and cable bundles under test are mounted. Partition of currents into the cable bundles can be adjusted by appropriate positioning of the return conductors.

6 REFERENCES

- (1) C J Hardwick, V P Dunkley, B J C Burrows, I Darney. "A New Approach to Equipment Testing". ICOLSE Conference, Cocoa Beach, 1991.
- (2) C J Hardwick, S J Haigh, B J C Burrows. "A Filamentary method for Calculating Induced Voltages within Resistive Structures in either the Frequency or Time Domain." ICOLSE Conference, Oklahoma City, 1988.

7 ACKNOWLEDGEMENTS

This work forms a part of the Culham Lightning Club programme, and we are grateful for the continuing support of the Lightning Club members (British Aerospace, Civil Aviation Authority, CASA, Department of Trade and Industry, Rolls Royce, SAAB-Scania, Shorts Brothers).

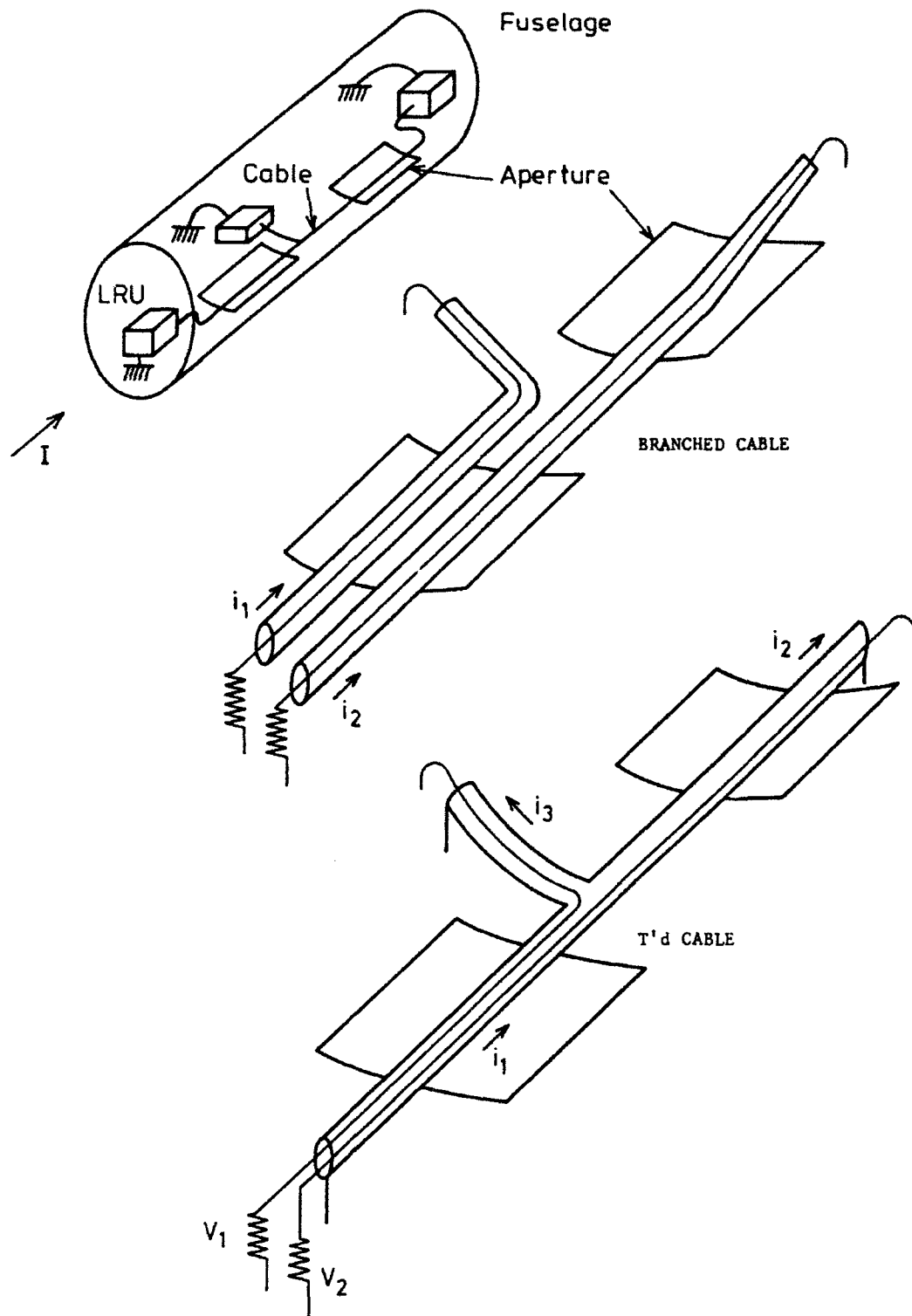
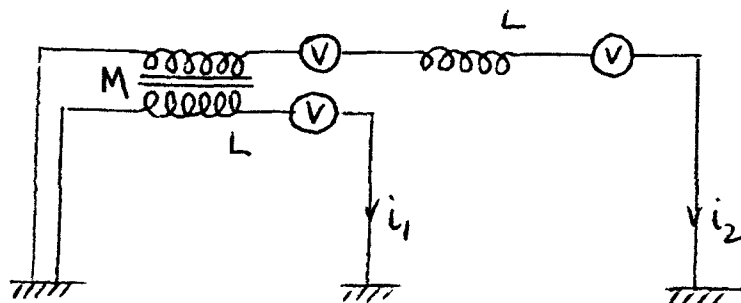


FIGURE 1
Schematic Drawing of Test Configurations Showing
Both Branched and 'T'ed Cable Installations.



L is inductance from each bonding point to half way along cable.
M is the mutual inductance along their common route, $1/2$ way along cable.
 i_1 is current/flowing in the short branch; i_2 that flowing the longer branch. V is the voltage source due to the aperture flux coupling.

FIGURE 2
Equivalent Circuit WhAT

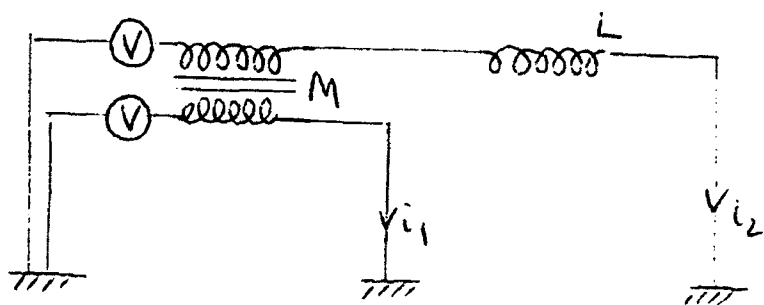


FIGURE 3
Equivalent Circuit of Equipment Test

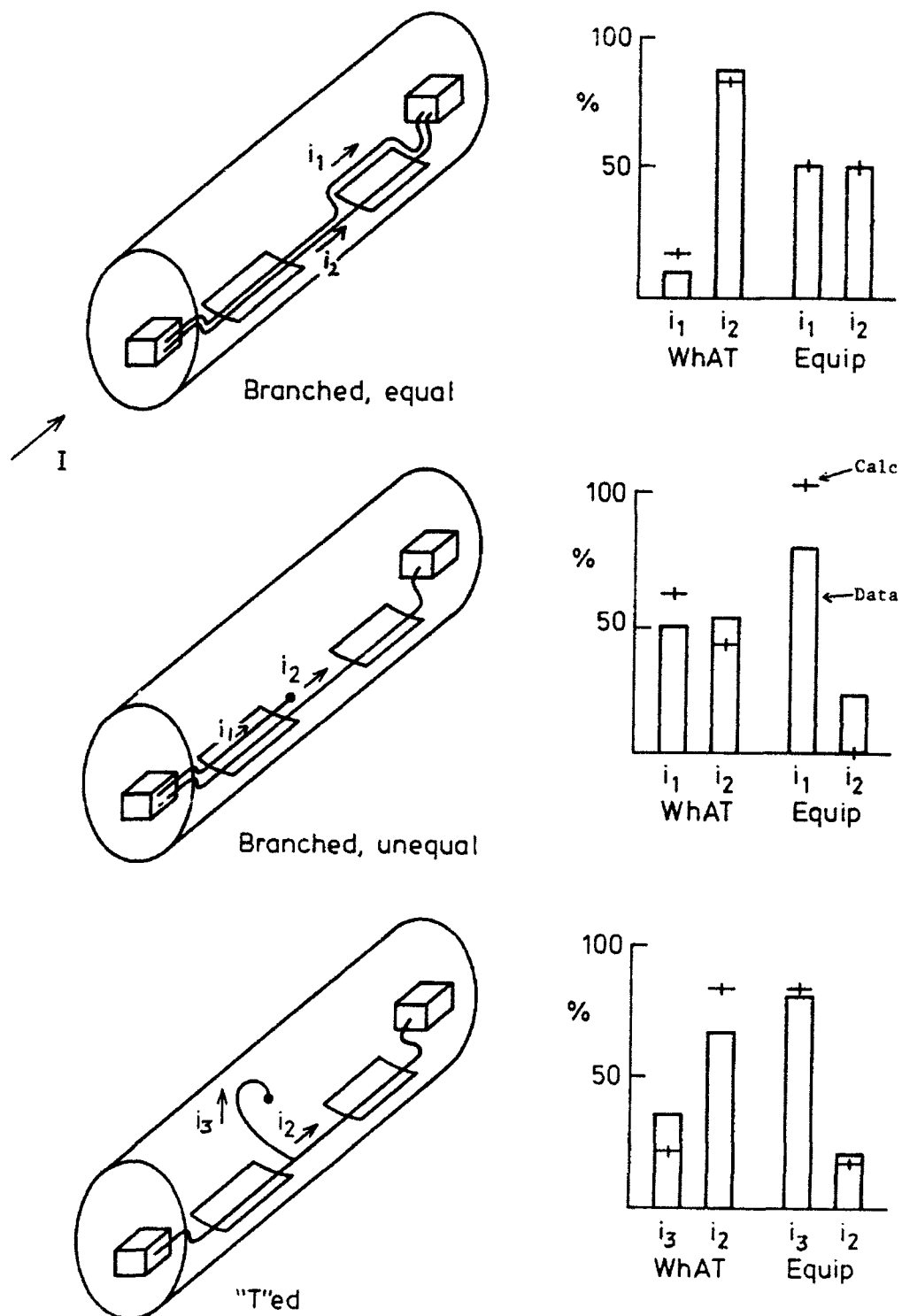
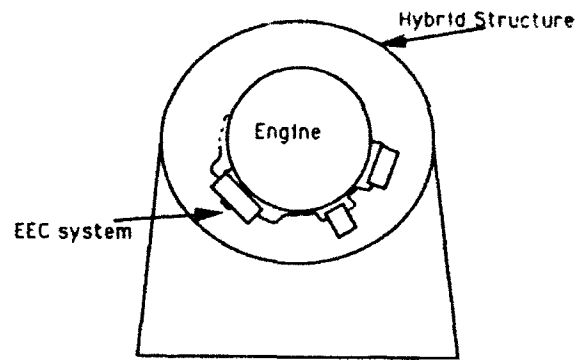
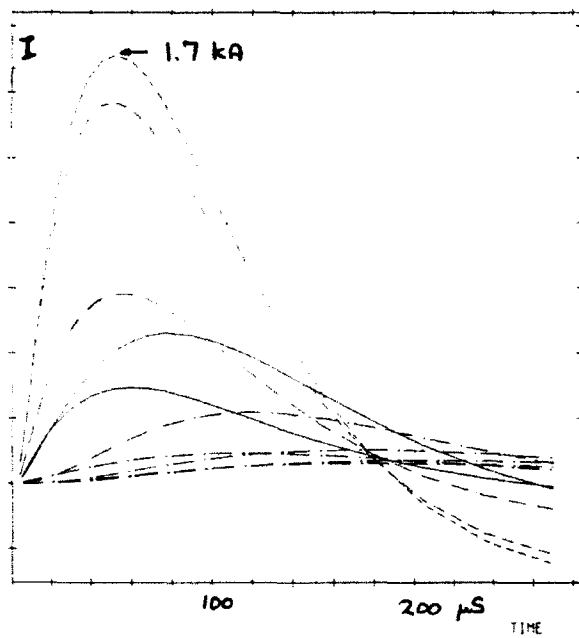


FIGURE 4
Histograms of Current Partitions between Different Branches and T's from Both Analysis and Measurement for Different Configurations

27-JUL-92

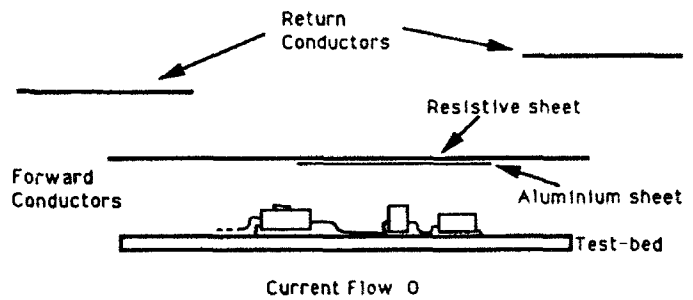
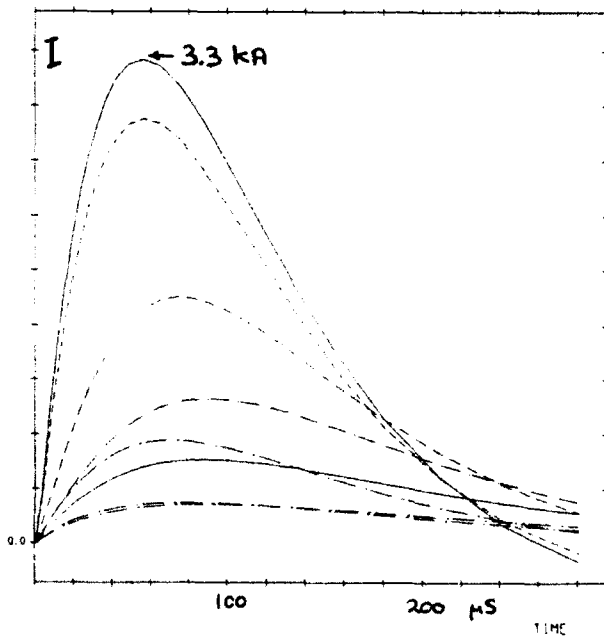


Engine Installation
on Aircraft

Figure 5

Indcal predictions of conduit currents on the engine
during a 200kA/6.4us strike to the aircraft.

GD. SET 30-JUL-92



EEC system installation on test bed.

Figure 6

Indcal predictions of conduit currents on the flat
test bed during a 65kA/20us simulation shot.

NAME	ORGANIZATION	ADDRESS	PHONE	FAX
Sam Abdelmalek	Bell Helicopter Textron	12800 Rue de L'Avenir Mirabel QB J7J 1r4 Canada	(514) 437-2768	(514) 437-6382
Richard C Adamo	SRI Int'l Bldg 408-65	333 Ravenswood Ave 404 Menlo Park CA 94025 USA	(415) 859-2370	(415) 859-6259
Gita Agustina	IPN - Co	Bandung Indonesia	633-900 (3097)	022-631-873
David L Albright	US Army Aviation System Command	4300 Goodfellow Blvd AMSAV-ESE St Louis MO 63120-1798 USA	(314) 263-1634	(314) 263-1622
M. Antley	United Int'l Engineering, Inc.	2201 Buena Vista Dr SE Suite 207 Albuquerque NM 87106 USA		
Kevin Bailey	Lightning Technologies, Inc.	10 Downing Parkway Pittsfield MA 01201 USA	(413) 499-2135	(413) 499-2503
David E Baker	Battelle-Pantex	PO Box 30020 M/S 12-107 Amarillo TX 79177 USA	(806) 477-3324	(806) 477-5613
Nathaniel G Bankston	Rockwell International, Inc.	12241 Lakewood Blvd Mail Stop FC27 Downey CA 90241 USA	(310) 922-2456	(310) 922-0472
Don L Barker	Aerospace Corporation	PO Box 21205 Kennedy Space Cntr FL 32815 USA	(407) 853-6666	(407) 853-3690
Alfred E Barrington	US DOT (Volpe Cntr), DTS-75	Kendall Square Cambridge MA 02142 USA	(617) 494-2018	
Dennis F Baseley	US Air Force ASD/ENACE	Wright-Patterson AF Base OH 45433-6503 USA	(513) 255-5078/5986	(513) 255-8777
Len M Baublitz	Boeing Commercial Airplane Group	PO Box 34125 Seattle WA 98124-1125 USA	(206) 266-8651	(206) 342-8445
David M Bayliff	FAA	4400 Blue Mound Rd Ft Worth TX 76193-0454 USA	(817) 740-3167	(817) 740-3298
Amaud J Bazin	Centre d'Etudes de Gramat	135 S 31st St Boulder CO 80303 USA	(303) 497-5575	(303) 497-6665
Georgia T Beckwith	Northrop T242	One Northrop Ave Hawthorne CA 90250 USA	(310) 332-6648	(310) 332-6794
Dave Beeman	Northrop Corporation	8900 E Washington Blvd Pico Rivera CA 90660-3783 USA	(310) 948-8287	(310) 942-6478
Hagen Beens	LBA	Haberweg 8 Braunschweig D-3300 Germany	0531-23550	0531-2355-254
Ron Benetti	NASA/Kennedy Space Cntr	TM-4P-5 Kennedy Space Cntr FL 32899 USA	(407) 867-8745	(407) 867-3737
Gérard M Berger	CNRS/LPD/ESE Plateau du Moulon	91190 Gif-sur-Yvette France	33-1-69-41-80-60	33-1-69-41-30-60
Carl W Bergman	G. Will Inc.	PO Box 549 Rainier WA 98576 USA	(206) 446-7750	(206) 446-7750
Burt J Bittner	Interstellar, Ltd.	2580 Clinton Dr NE Palm Bay FL 32905-2506 USA	(407) 766-2366	(407) 729-2406
C. Dale Bleakney	FAA Acft Certification Office	1801 Airport Rd Rm 100 Wichita KS 67209 USA	(316) 946-4135	(316) 946-4407

NAME	ORGANIZATION	ADDRESS	PHONE	FAX
Peter H Bootma	de Havilland Inc.	Garratt Blvd MS N46-05 Downsview On M3K 1Y5 Canada	(416) 375-4365	(416) 375-4537
Jean-Louis Braut	Alcatel Cable Dpt HF et Electroniqu	35 Rue Jean Jaures Bezons 95877 France	34236266	34236325
Ernst H Brehm	ABB Management Services GmbH, EFP	7 Scheresberg 6943 Birkenau Germany	0621-3813518	0621-3817480
Richard Briet	Aerospac Corporation	PO Box 92957 Mail Stop M4-934 Los Angeles CA 90009-2957 USA	(310) 336-1912	(310) 336-5581
Alfred O Britting, Jr.	Aerospac Corporation	5508 W 119th St Inglewood CA 90304 USA	(310) 336-9253	(310) 336-5581
Bill Brown	Self	GAS Anderson Ct Satellite Beach FL 32937 USA	(407) 777-0265	
Jeffrey C Brown	NASA Lewis Research Center-Avionic	21000 Brookpark Rd MS 86-5 Cleveland OH 44135 USA	(216) 433-3868	(216) 433-6382
Richard Brzostek	Woodward Governor Co.	5135 35th St Rockford IL 61109 USA	(815) 624-2499	(815) 874-1534
Brian J. C Burrows	Culham Lightning Test & Technology	Culham Laboratory Abingdon Oxon OX14 3DB United Kingdom	44 235 46 41 00	44 235 46 43 25
Heinrich Busse	Bundesakademie fur Wehrtechnik	Seckenheimer Landstrasse 8-10 6800 Mannheim 1 Germany	011 49 621 41 80 91	011 49 621 418483
Leon G Byerley	Lightning Protection Technology	2744 E 5th St Tucson AZ 85716 USA	(602) 741-2838	(602) 741-2848
Joseph Calabria	ARC	928 Jaymor Rd Southampton PA 18966 USA	(215) 322-7444	
Jason C Chai	Aerospac Corporation	PO Box 92957 Mail Stop M4-934 Los Angeles CA 90009-2957 USA	(310) 336-8341	(310) 336-5581
Jen-Shih Chang	McMaster University	Dept of Engineering Physics Hamilton Ontario L8S 4M1 Canada	(416) 525-9140x4924	(416) 527-5222
Alain Charoy	Cntr d'Essais Aeronautique Toulouse	86 Rue de la Liberte Seyssins 38180 France	76-49-76-76	76-21-23-80
Honglei Chen	Beijing Lightning Trigger Lab	PO Box 2851 Beijing 100085 China		
Yung G Chen	Maxwell Laboratories, Inc.	8888 Balboa Ave San Diego CA 92123 USA	(619) 576-7852	(619) 576-7661
Al Clark	FAA, ACE-115	601 E 12th St Kansas City MO 64108 USA	(816) 426-3102	(816) 426-3694
J. Pierre Clerc	Cntr d'Essais Aero. de Toulouse	23 Av. Henri Guillaumet Toulouse 31056 France	31/61-58-71-98	31/61-58-71-20
Jay D Cline	Dayton Granger, Inc.	PO Box 350550 Ft Lauderdale FL 33335 USA	(905) 483-3451	(905) 761-3172
William O Coburn	US Army Research Laboratory	2800 Powder Mill Rd Adelphi MD 20783 USA	(703) 490-2320	(703) 491-8809
Richard L Cohen	Panamax	150 Mitchell Boulevard San Rafael CA 94903 USA	(415) 498-3900x3918	(415) 472-5540

NAME	ORGANIZATION	ADDRESS	PHONE	FAX
Richard S Collier	Electro Magnetic Applications, Inc.	12567 W Cedar Dr Suite 250 Lakewood CO 80228-2091 USA	(303) 980-0070	(303) 980-0836
John M Collum	McDonnell Douglas Corp.	PO Box 516 Mail Code 1066267 Saint Louis MO 63166 USA	(314) 233-4216	(314) 233-6740
Dale Cook	EG&G Idaho, Inc.	PO Box 1625 Idaho Falls ID 83415-2408 USA	(208) 526-1615	
Vernon Cooray	Institute of High Voltage Research	755 92 Uppsala Uppsala 75592 Sweden	018 533636	018 502619
John Covell	Rockwell International	400 Collins Rd N.E. Cedar Rapids IA 52498 USA	(319) 395-5905	(319) 395-3661
Jim Crane	Simmonds Precision, Inc.	100 Oakdale Rd Chester NJ USA	(908) 879-5151	(908) 879-4563
Jeffery D Craven	Redstone Technical Test Cntr	ATTN: STERT-TE-F-EM Redstone Arsenal AL 35898-8052 USA	(205) 842-2952	(205) 842-9637
Rich Cuplin	Woodward Governor Co.	5125 35th St Rockford IL 61125 USA	(815) 624-2499	(815) 874-1534
Daniel Custis	Institute of Atmos Science	570 Forest Service Rd Spearfish SD 57783 USA		
Mike D'Angelo	GE Aircraft Controls	600 Main St Johnson City NY 13790-1888 USA	(607) 770-2796	(607) 770-3561
Amin R Daehne	Bundesaut fuer Wehrtechnik/Berchaff Vennad-Adenauer-Ufer 2-6D 5400 Koblenz Germany		261-4007779	261-4007964
Mike Dahl	FAA	601 E 12th St Kansas City MO 64106 USA	(816) 426-6941	(816) 426-2169
Michael Dargi	Lightning Technologies, Inc.	10 Downing Parkway Pittsfield MA 01201 USA	(413) 499-2135	(413) 499-2503
Josh M Doan	FAA ACD-230	Atlantic City Int'l Airport NJ 08405 USA	(609) 484-4468	(609) 484-4005
Edward Dunlap	Nuclear Effects Directorate	Commandear US Army WSMR WSMR NM 89002-5158 USA	(505) 679-6631	(505) 679-6670
Ervin E Dvorak	FAA ACE-111	601 E 12th St Kansas City MO 64106 USA	(816) 426-3102	(816) 426-3694
Gene Eley	Aerospace Corporation	PO Box 21205 Kennedy Space Cntr FL 32815 USA	(407) 853-6666	(407) 853-3690
David B Elkins	Redstone Technical Test Cntr	Director, RTTC Redstone Arsenal AL 35898-8052 USA	(205) 876-3965	(205) 842-9637
James R Elliott	Electro Magnetic Applications, Inc.	12567 W Cedar Dr Suite 250 Lakewood CO 80228 USA	(303) 980-0070	(303) 980-0836
Jean-Luc Emanoely	Centre D'Essais Aero. de Toulouse	23 Ave Henri Guillaumet Toulouse 31056 France	31 61 58 71 98	31 61 58 71 20
Alan Engisch	Simmonds Precision, Inc.	100 Oakdale Rd Chester NJ 07930 USA	(908) 879-5151	(908) 879-4563
Frederick J Erikson	Electro Magnetic Applications, Inc.	7605 Park Dr Suite 200 Omaha NE 68127 USA	(402) 592-0232	(402) 592-0065

NAME	ORGANIZATION	ADDRESS	PHONE	FAX
R. Ertman	Lockheed Aeronautical Systems Co.	Marietta GA 300663-068 USA	(404) 494-8355	
Boris F Erstev	Main Geophysical Observatory	Karbyshcheva St 7 St Petersburg 194018 Russian Federation	(812) 247-01-03	(812) 247-88-61
Patrick Farfal	Aerospatiale Espace et Defense	BP No. 96 Les Mureaux 78133 France	33-1-34-92	33-1-34-92-13-11
Greg Fawthrop	Lightning Prevention			
Gary L Fenical	Instrument Specialties Company Inc	PO Box A Delaware Water Gap PA 18327 USA	(717) 424-8510/177	
Charles Field	Sandia National Labs	Div. 9332 Box 5800 Albuquerque NM 87185 USA	(505) 845-7204	(505) 845-7602
Joseph F Fischer	Fischer Custom Communications, Inc	3121 W 139th St Unit F Hawthorne CA 90250 USA	(310) 644-0728	(310) 644-2452
Virginia D Fischer	Fischer Custom Communications, Inc	3121 W 139th St Unit F Hawthorne CA 90250 USA	(310) 644-0728	(310) 644-2452
Franklin A Fisher	Lightning Technologies, Inc.	10 Downing Parkway Pittsfield MA 01201 USA	(413) 499-2135	(413) 499-2503
Richard J Fisher	Sandia National Laboratories	PO Box 5800 Div 2754 Albuquerque NM 87185-5800 USA	(505) 844-2046	(505) 844-7857
Nicolas Floret	Helita	16 Rue Berlin-Poiree Paris 75001 France	33-1-45084747	33-1-40265623
Sam Frazier	Naval Air Warfare Cntr	Commander NAWCAD Patuxent River MD 20670-5304 USA	(301) 863-3868	(301) 863-3871
Charles A Freyre	Galaxy Scientific	2500 English Creek Ave Pleasantville NJ 08232 USA	(609) 645-0800	(609) 645-2881
Sam K Frick	FAA	3229 E Spring St Long Beach CA 90806 USA	(310) 988-5250	(310) 988-5210
Marselle Fritz	Nuclear Effects Directorate Commander	US Army WSMR WSMR NM 88002-5158 USA	(505) 879-6631	(505) 879-6870
Michael F Funya	Naval Air Warfare Cntr	Bldg 144 Patuxent River MD 20670 USA	(301) 863-4681	(301) 737-0305
Erik J Galis	American Cyanamid	1300 Revolution St Havre de Grace MD 21098 USA	(410) 939-1910	(410) 939-0930
Dider D Gauthier	Centre National d'Etudes Spatiales	18 Ave Belin Toulouse 31055 France	33 61 28 26 11	33 61 28 21 69
Richard C Gaynor	Dayton T. Brown, Inc.	Church St Bohemia NY 11716 USA	(516) 589-6300	(516) 589-3848
Bill Geitz	Atmospheric Research Systems, Inc.	2350 Commerce Park Dr NE Palm Bay FL 32905 USA	(407) 725-8001	(407) 725-7918
Roy Gillespie	Fairchild Aircraft, Inc.	PO Box 130490 San Antonio TX 78279 USA	(512) 824-9421	(512) 824-3869
Kathy L Giori	SRI International	333 Ravenswood Ave MS 408-80 Menlo Park CA 94025 USA	(415) 859-3138	(415) 859-8259

NAME	ORGANIZATION	ADDRESS	PHONE	FAX
Michael S Glynn	FAA Technical Cntr	AJD 230 Flight Safety Res Atlantic City Int'l Airport NJ 08405 USA	(609) 484-4138	(609) 484-4005
Thomas Goebel	Bundesamt Fur	Wehrtechnik Und Beschaffung Koblenzwehr Germany	2614008816	2614007360
Pascal Gondot	Aerospatiale	12 Rue Pasteur 92150 Suresnes France	33 1 46 97 33 79	33 1 46 97 30 06
Yukihiko Goto	Tohoku Gakuin University	1-13-1 Chuoh Tagajyo Miyagi 985 Japan	81-22-368-1115	81-22-368-7070
Kenneth M Grachen	Bendix/King	400 N Rogers Rd M/S 37 Olathe KS 66062-1212 USA	(913) 768-2353	(913) 791-1302
Kenneth Grass	Astroseal	6 Custom Dr Old Saybrook CT 06413 USA	(203) 399-7916	(203) 399-6499
Matt Z Grenis	Naval Air Systems Command	Air-51641F Washington DC 20361-5160 USA	(703) 692-8600	(703) 748-7897
Francois W Guay	Canadair	9800 Cavendish Blvd Montreal Qu Canada	(514) 744-1511	(514) 956-0746
Rick Gurnley	International Protection Consultant	Technopark Hobart TASM 7010 Australia	61-02-730066	61-02-730399
Stephen Haigh	LTT Culham	Agingdon Oxon OX143DR United Kingdom	44235463436	44235464325
Sigit Hardjanto	IPTN Ltd.	Bandung Indonesia	022-633900 x2433	022-631873
John Hardwick	Lightning Test & Technology	Culham Laboratory, Abingdon Oxon OX14 3DB United Kingdom	+44 235 46 4264	+44 235 46 4325
Richard J Hasbrouck	LLNL	PO Box 806 L-154 Livermore CA 94551 USA	(510) 422-1256	(510) 423-3144
Kevin A Hendricks	Dayton-Granger, Inc.	3299 SW 9th Ave Ft Lauderdale FL 33315 USA	(305) 473-3451	(305) 761-3172
Hugh A Heritage	Aerospace Corp, M5-596	PO Box 92957 Los Angeles CA 90009-2957 USA	(310) 336-1160	(310) 336-0425
Richard Hess	Honeywell, Incorporation	21111 N 19th Ave Phoenix AZ 85027 USA	(602) 436-1285	(602) 436-5151
Hubert Hibbler	Naval Air Warfare Cntr (NAWC)	6000 E 21st St Indianapolis IN 46219-2189 USA	(317) 353-3683	(317) 351-4949
Robert Hoefft	Indian Head Div	101 Strauss Ave Indian Head MD 20640-5035 USA	(301) 743-4758	(301) 743-4299
Axel Hohl	Lockheed Space Operations	Mail Stop LSO-415 Kennedy Space Cntr FL 32815 USA	(407) 861-6339	(407) 861-5750
Junichi Hojo	University of Tokyo	22-1 Roppongi-7-chome, minatu-ku Tokyo Japan	03-3479-1949	
Ronald L Holle	National Severe Storms Laboratory	1313 Halley Circle Norman OK 73069 USA	(405) 366-0614	(405) 366-0472
Everett D Holmes, Jr.	Los Alamos National Laboratory	PO Box 1663 M/S P-947 Los Alamos NM 87545-0001 USA	(505) 667-2973	(505) 665-2650

NAME	ORGANIZATION	ADDRESS	PHONE	FAX
Noriyasu Honma	Electricity Tech Research Cntr	2-1, Nakayama 7-Chome, Aoba-Ku Sendai 981 Japan	022-278-0356	022-278-2176
Christian Hopf	University of Federal Armed Forces	Werner-Heisenberg-Weg 39 Neubiberg BA 8014 Germany	49 89 60 04 37 21	49 89 60 04 3680
Melvin C Hudson	Indian Head Div. Naval Surface Welf	101 Strauss Ave Indian Head MD 20640-5035 USA	(301) 743-4484	(301) 743-6533
Masaru Ishii	Institute of Industrial Science	7-22-1 Roppongi, Minato-Ku Tokyo Japan	81 3 3479 1949	81 3 3402 5078
James Jacqueline	Grumman Aircraft	Mail Stop B25-35 Bethpage NY 11714 USA	(516) 575-9031	(516) 575-7428
William Jafferis	BUC, Inc.	4140 Hickory Hill Boulevard Titusville FL 32780- USA	(407) 269-8943	(407) 867-1603
Lai Hing Jeir	Naval Air Warfare Cntr- AC Div	SY 82 Patuxnt River MD 20670 USA	(301) 863-4681	(301) 737-0305
Nicholas Jennings	British Aerospace plc	Sowerby Res Cntr, PO Box 5 Filton Bristol BS12 7QW United Kingdom	02 72 36 65 53	02 72 36 37 33
John P Johnson	Sandia Labs - Div 9332	PO Box 5800 Albuquerque NM 87185 USA	(505) 845-7399	(505) 845-7602
Jon B Jolly	Jon B. Jolly, Inc.	5416 California Ave SW Seattle WA 98136-1596 USA	(206) 938-4166	(206) 938-4166
Christopher C. R Jones	British Aerospace	Warton Aerodome (W7G) Preston Lanc PR4-1AX United Kingdom	772-855262	772-855262
David T Jordan	UK Defence Research Agency	Flight Sys Dept. Q153 Bldg Farnborough Ha GU21 4SE United Kingdom	44 (0)252 24481	44 (0)252 377247
Isabelle Junqua	Service AEM	Centre d'Etudes de Gramat 46500 Gramat France	33 65 10 53 09	33 65 10 54 09
Edward J Kachmar	USAF 45 SPW/SEM	3313 Hadleigh Crest Orlando FL 32817 USA	(407) 494-7037	(407) 494-6535
Zan-Ichiro Kawasaki	Osaka University	Yamadacka 2-1, Faculty Engineer Suita Osaka 565 Japan	81-6-877-5111x4553	81-6-875-0506
Alexander W Kem	University of Federal Armed Forces	Werner-Heisenberg-Weg 39 Neubiberg BA 8014 Germany	49-89-6004 3940	49 89 6004 3560
Keith Kerr	Martin Marietta	PO Box 321399 Cocoa Beach FL 32932 USA	(407) 853-9775	(407) 853-9110
Lewis Keyser	Battelle Memorial Institute-Pantex	PO Box 30020 Amarillo TX 79177 USA	(806) 477-3324	(806) 477-5613
Charles H King	Boeing Commerical Airplane Group	PO Box 3707 Mail Stop: 9R-39 Seattle WA 98124 USA	(206) 393-8322	(206) 393-3638
Delip Kohli	American Cyanamid Company	1300 Revolution St Havre de Grace MD 21078 USA	(410) 939-1910	(410) 939-0930
Larry E Kozak	New Jersey Bell Telephone	16 Hancock Dr Kendall Park NJ 08824 USA	(201) 649-5180	(201) 494-8748
E. Philip Krider	University of Arizona	Room 542 PAS Bldg, Physics Tucson AZ 85721 USA	(602) 821-8631	(602) 821-8633

NAME	ORGANIZATION	ADDRESS	PHONE	FAX
Sandip Lal	EG&G	BOC 130 Kennedy Space Cntr FL 32899 USA	(407) 861-2103	(407) 861-2100
Calvin D Le	US Army Research Laboratory	2800 Powder Mill Rd Adelphi MD 20783 USA	(703) 490-2303	(703) 491-8809
Tom S Lee	University of Minnesota	4-174 Electrical Engineering Bldg 200 Union St Minn MN 55455 USA	(612) 625-2346	(612) 625-4583
Monty R Lehmann	KTech Corporation	PO Box 70 Lexington Park MD 20653 USA	(301) 883-8807	(301) 883-7278
Lee Lemke	Northrop Corporation T235/AP	8900 E Washington Blvd Pico Rivera CA 90660-3737 USA	(310) 942-4540	(310) 948-8068
Alma P Levy	Aerospace Corporation	PO Box 92957 Los Angeles CA 90660-3737 USA	(310) 418-7306	(310) 418-7331
Jack Lippert	Computer Science & Application	2 Clifford Dr Shalimar FL 32579 USA	(904) 651-4991	(904) 651-2816
Axel W Lohninger	US Army	25 High Crest Dr Sparta NJ 07871 USA	(201) 724-3208	
Jeffrey B Lorens	US Air Force	45 Weather Squadron Patrick AFB FL 32925 USA	(407) 494-5915	
Joe LoVetri	University of Western Ontario	London ON N6B5B9 Canada	518-679-2111x8342	
Donald MacGorman	National Severe Storms Laboratory	1313 Halley Circle Norman OK 73069 USA	(405) 366-0405	(405) 366-0472
Ben Mackenzie	Norton Performance Plastics Corp.	335 N Diamond St Ravenna OH 44266 USA	(216) 298-9948	(216) 298-7955
Ernest A Magyar	Magyar & Associates, Inc.	PO Box 6027 Wheaton MD 20806 USA	(301) 451-3246	(301) 431-3268
Matthew R Meier	Naval Air Warfare Cntr	Acrft Div, Bldg 2100, SY84 NAWC/A D Patuxent River MD20670 USA	(301) 863-4598	(301) 863-3786
Robert A Meijner	Sikorsky Aircraft, M/S Z108A	6900 Main St Stratford CT 06601 USA	(203) 383-3896	(203) 383-3306
Kartik C Mejjumdar	LLNL	7000 E Ave PO Box 808 L-1 Livermore CA 94550 USA	(510) 422-5060	(510) 294-6889
T. Howard Manning	FAA	4400 Blue Mound Rd Ft Worth TX 76193-0454 USA	(817) 740-3170	(817) 740-3298
Mark H Mar	US Army Research Laboratory	2800 Powder Mill Rd AMSRL-WT-ND Adelphi MD 20783 USA	(703) 490-2303	(703) 491-8809
Paul Marks	US Aviation Underwriters	199 Water St 1 Seaport Plaza New York NY 100 USA	(212) 952-0100	(212) 349-8226
Patrick Mattei	STPA French Airworthiness Authority	STPAIN 4 Ave de la Porte D'issy 75015 Paris France	33 1 45 52 43 15	33 1 45 52 61 76
William J Meyer	Los Alamos National Laboratory	PO Box O Mail Stop: J-900 Mercury NV 89023 USA	(702) 295-3600	(702) 295-3615
Jerry W McCormack	McDonnell-Douglas	PO Box 516 St Louis MO 63166 USA	(314) 232-8841	

NAME	ORGANIZATION	ADDRESS	PHONE	FAX
Rosemarie L McDowell	Galaxy Scientific Corporation	2500 English Creek Ave Pleasantville NJ 08232 USA	(609) 645-0900	(609) 645-2881
Steve McRae	AeroJet	1 NASA Dr Iuka MS 35630 USA	(601) 423-0672	
R. R Meek	EMI Consultant (Self-Employed)	1125 Wiley Bridge Rd Woodstock GA 30188 USA	(404) 926-7407	(404) 926-7407
K. Merewether	Sandia Natinal Laboratories	PO Box 5800 Albuquerque NM 87185 USA	(505) 844-7796	(505) 844-7857
Joseph R Milella	US Army Research Laboratory	2800 Powder Mill Rd AMSRL-WT-ND Adelphi MD 20783 USA	(703) 490-2303	(703) 491-8809
Jean-Patrick Moreau	Dassault Aviation/DGT/BEAME	78 Quai Marcel Dassault CEDEX 300 Saint Cloud 92552 France	33-1-47114707	33-1-47 11 42 94
Randy Moses	BF Goodrich Flight Systems	6878 Alloway St W Worthington OH 43085 USA	(614) 825-2001	(614) 825-2037
Abdul M Mousa	British Columbia Hydro	6911 Suuthpoint Dr (e06) Burnaby BC v3n 4x8 Canada	(604) 528-2328	(604) 528-2944
Bob Moyhner			(203) 383-3896	
Tapas Mukulmoni	Douglas Co. Dept 1x5: M/C 36-48	3855 Lakewood Blvd Long Beach CA 90846 USA	(310) 496-6469	(310) 593-0648
G. R Nagabhushana	Dept. of High Voltage Engineering	Indian Institute of Science Bangalore 560 012 India	812-344411	812-341663
Koichi Nakamura	Nagoya Institute of Technology	Gokiso, Showa, Nagoya 466 Japan	81 52 732 2111	81 52 733 6589
Poh H Ng	Electro Magnetic Applications, Inc.	12567 W Cedar Dr Suite 250 Lakewood CO 80228 USA	(303) 980-0070	(303) 980-0836
Michael O'Hara	Shaw Aero Devices, Inc.	PO Box 80 Wainscott NY 11975 USA	(516) 537-1404	(516) 537-1768
John H O'Kuma	Nuclear Effects Directorate	Commander US Army WSMR NM 88002-5158 USA	(505) 679-6631/6631	(505) 679-6670
J. A Oda	Lockheed Aeronautical Systems Corp.	8650 Cobb Dr Marietta GA 30063 USA	(404) 494-1097	(404) 494-5207
E. Carl Olson	Beech Aircraft Corp.	9709 E Central Wichita KS 67201 USA	(319) 676-6755	
Bill H Panesar	Bell Canada	483 Bay St F8N Toronto On M5G 2E1 Canada	(416) 581-3786	(416) 348-0383
Willie Papich	US Army Redstone Tech Test Ctr.	Redstone Arsenal Huntsville AL 35898 USA	(205) 876-1790	(205) 842-9637
Rodney A Parala	Electro Magnetic Applications, Inc.	12567 W Cedar Dr Suite 250 Lakewood CO 80228-2091 USA	(303) 980-0070	(303) 980-0836
Robert A Pfeiffer	US Army Nuclear and Chemical	7500 Backlick Rd Bldg 5073 Springfield VA 22150-7284 USA	(703) 806-7556	(703) 806-7814
Larry Pinkston	Rockwell International	350 Collins Rd NE Mail Sta. 106-183 Cedar Rapids IA 52498 USA	(319) 395-1938	(319) 395-5429

NAME	ORGANIZATION	ADDRESS	PHONE	FAX
Felix L Pitts	NASA-Langley Research Cntr	Mail Stop: 130 Hampton VA 23685-5225 USA	(804) 864-6186	(804) 864-4234
J. Anderson Plumer	Lightning Technologies, Inc.	10 Downing Parkway Pittsfield MA 01201 USA	(413) 499-2135	(413) 499-2503
Andrew S Podgorski	NRC-Canada	Montreal Rd Ottawa Ontario K1A 0R6 Canada	(613) 993-4198	(613) 952-7998
Elizabeth Podgorski	Transport Canada	Place de Ville, Tower C, 9th Floor Ottawa Ontario Canada	(613) 957-6947	(613) 957-6882
Rudy Popiela	Simmonds Precision, Inc.	100 Oakdale Rd Chester NJ 07830 USA	(908) 879-5151	(908) 879-4563
Christopher F Porter		17 Redcliffe Rd London SW10 9NP United Kingdom		071-352-0427
James Press	R & B Enterprises	20 Clipper Rd W Conshohocken PA 19428 USA	(215) 825-1960	(215) 825-1684
Denys Pugliese	Simmonds Precision, Inc.	100 Oakdale Rd Chester NJ 07830 USA	(908) 879-5151	(908) 879-4563
Ronald M Reap	Techniques Development Laboratory	1325 E-W Highway WOOD2 Silver Spring MD 20910 USA	(301) 713-1772	
Dale R Reed	Boeing Commerical Airplane Group	PO Box 3707 MS 60-MJ Seattle WA 98168-2207 USA	(206) 237-7260	(206) 234-8434
John Reed	FAA	329G Schooner Lane Sweetwater NJ 08037 USA	(609) 484-4135	(609) 484-4005
Andrew W Revay, Jr.	Florida Institute of Technology	150 W University Blvd Melbourne FL 32901-6988 USA	(407) 768-8000x7231	(407) 984-8461
Ronald J Reyzer	US Army Research Laboratory	2800 Powder Mill Rd AMSRL-WT-ND Adelphi MD 20783 USA	(703) 490-2303	(703) 491-8809
Ed Roberts	FAA	800 Independence Ave SW ANS-230 Washington DC 20591 USA	(202) 267-8382	(202) 267-5784
Randy Robinson	Lightning Technologies, Inc.	247 W 54th St South Wichita KS 67217-9967 USA	(316) 522-2803	(316) 529-2354
Peter B Roehr	HQ, AWS/XTR	AWS/XTR Scott AF Base IL 62225-5008 USA	(618) 256-5731	(618) 256-2417
Jan-Uwe Roth	Domier Luftfahrt GmbH	PO Box 1303 Friedrichshafen 1 7990 Germany	7545-84897	7545-84411
Michel Salaun	Dassault Aviation/DGT/BEAME	78 Quai M. Dassault CEDEX 300 St Cloud 92552 France	331-4711-3149	
Andre Schaffar	Aerospatiale Espace et Defense	BP No. 96 Les Mureaux 78133 France	(33) 1 34 92 27 45	(33) 1 34 92 1311
George H Schnetzer	Sandia National Laboratories	PO Box 5800 Div 2754 Albuquerque NM 87185 USA	(505) 844-6185	(505) 846-8123
Jack E Schroeder	Lightning Diversion Systems	17851 Jamestown Lane Huntington Beach CA 92647 USA	(714) 841-1080	(714) 841-5095
Kurt Sebecher	Naval Air Warfare Cntr	Acrft Div, Bldg 966, SY64 Patuxent River MD 20670-5304 USA	(301) 863-3872	(301) 863-3763x671

NAME	ORGANIZATION	ADDRESS	PHONE	FAX
Richard H Satchell	Wisconsin Electric Power Company	333 W Everett St A226 Milwaukee WI 53203-2046 USA	(414) 221-2345	
Xuan-Min Shao	New Mexico Tech	Physics Dept Socorro NM 87801 USA	(505) 835-5137	
Richard E Singer	ERICO, Inc.	34600 Solon Rd Solon OH 44139 USA	(216) 248-0100	(216) 248-0728
Joachim Skiba	Wehrtechnische Dienststelle fuer	Luftfahrzeuge, D 434 Flugplatz, Manching 8072 Germany	08459 80-2306	08459-802022
Victor Sokolowski	FAA	601 E 12th St Kansas City MO 64106 USA	(816) 426-3102	(816) 426-3694
George Soteropoulos	FAA Aircraft Engineering - AIR-120	800 Independence Ave SW Washington DC 20590 USA	(202) 267-9796	(202) 267-9562
Michael P Squires	Naval Air Warfare Cntr	Acrft Div, Bldg 966, SY84 Patuxent River MD 20670-5304 USA	(301) 863-4598	(301) 863-3766/3571
Paul St. Jean	Thiokol	PO 707 M.S.L.-62 Brigham City UT 84302-0707 USA	(801) 863-4082	(801) 863-4330
James R Stahmann	Boeing Aerospace Operations	Mail Stop: FA-48 Kennedy Space Cntr FL 32899 USA	(407) 867-1400	(407) 867-1087
Bill Stewart	Miliken Research Corp.	PO Box 1927 M-405 Spartanburg SC 29304 USA	(803) 573-2676	(803) 573-2417
James G Stobie	AF Force of Scientific Research	AFOSR, Incorporated Bolling AF Base DC 20332 USA	(202) 767-5021	(202) 404-7475
Graham W Strauss	Naval Air Warfare Cntr - AC Div	Route 1 Box 126 Lexington Park MD 20653 USA	(301) 863-4681	(301) 737-0305
Dennis Sutton	NAWC Warminster	Warminster PA 18974 USA	(215) 441-3453	(215) 441-1358
B. Tagliana	Eurocopter, Inc.	Marignane 13725 France	33-42-85-85	33-42-85-85-00
Russ Tagliarini	Florida DOT Aviation Office/MS 46	605 Suwannee St Tallahassee FL 32301 USA	(904) 498-8444	(904) 922-4942
Les Taylor	FAA, ACE-115	601 E 12th St Kansas City MO 64106 USA	(816) 426-3102	(816) 426-3694
Michael Taylor	Hercules Aerospace	4393 S Ashford Dr Salt Lake City UT 84124 Magna UT 84044 USA	(801) 251-5317	
Larry Thackray	Lightning Prevention System	PO Box 173 Chalfont PA 18914 USA	(215) 538-7700	
Herman Tharrington	FAA, AND-3	800 Independence Ave SW Washington DC 22182 USA	(202) 267-8218	(202) 267-3552
Patrick Trochet	NUCLETUDES	Ardu Hoggar Les Ulis 91944 France	33-1-69-07-10-20	33-1-69-07-21-01
Oscar Troncoso-Lozada	Cntr of Atmospheric Sciences UNAM	UNAM CU-Mexico City, D.F. D. 04510- Mexico	550-622-4056	525-05-48-9781
Yinggang Tu	Lightning Eliminators & Associates	6687 Arapahoe Rd Boulder CO 80303 USA	(303) 447-2828	(303) 447-8122

NAME	ORGANIZATION	ADDRESS	PHONE	FAX
Eric Tuttle	Harry Diamond Lab	2800 Power Mill Rd/Att:SLCHD-NW-E Adelphi MD 20783-1197 USA	(703) 490-2513	(703) 490-2334
Gene Vandermolen	FAA	1601 Lind Ave SW Renton WA 98055 USA	(206) 227-1100	
Giuseppe Vecchi	Politecnico, Dip. Elettronica	Corsa Duca degli Abruzzi, 24 Torino I-10129 Italia	+39-11-564-4055	+39-11-564-4015
J. L. Norman Violette	Violette Engineering Corp	120 E Broad St PO Box 639 Falls Church VA 22040-0639 USA	(703) 532-1355	(703) 538-3810
Masakazu Wada	Musashi Institute Of Technology	Setagayaku Tamazutumi Tokyo Japan	03-5706-3402	
Charles L Wakefield	US Navy	Naval Surface Warfare Cntr Indian Head MD 20640-5000 USA	(301) 743-4130/4466	(301) 743-4004
William H Walker	Code 7021 NAVAIR WARCEN/AD	Warminster PA 18974-5000 USA	(215) 441-3453	(215) 441-1358
John H Walker, Jr.	Northrop Aircraft	One Northrop Ave Hawthorne CA 90250 USA	(310) 331-5657	
Lawrence C Walko	USAF Aero Propulsion Lab	WL/PooX-2, Wright Lab Wright-Patterson A F Base OH 45433-6563 USA	(513) 255-8634/9189	(513) 476-4095
Mike Whitaker	US Navy	NAWC-AD PAX Patuxent River MD 20670 USA	(301) 863-4598	(301) 863-3786
Bill White	BF Goodrich Flight Systems, Inc.	2001 Polaris Parkway Columbus OH 43240-2001 USA	(614) 825-2001	(614) 825-2037
Johnnie White	FAA	4400 Bluemound Rd Ft Worth TX 76183 USA	(817) 740-3120	(817) 740-3287
Juergen Wiedmann	Domier Luftfahrt GMBH	PO Box 1303 Dep SY30 D-7990 Friedrichshafen 1 SY30 Germany	07541-4961	07541-43964
Stephen Williams	Abroyd Communications Limited	682 Colby Dr Waterloo Ontario n2v1a2 Canada	519-746-1743	519-746-0091
Ron Wojtasinski	STC Corporation	375 Dorset Dr Cocoa Beach FL 32931 USA	(407) 799-9164	(407) 799-9164
Carroll R Wright	FAA	4400 Bluemound Rd Ft Worth TX 76183-0111 USA	(817) 824-5120	(817) 740-3376
Charles A Yost	Dynamic Systems, Inc.	Route 2 PO Box 1828 Leicester NC 28748 USA	(704) 683-1280	(704) 683-3511
Wolfgang Zischank	Federal Armed Forces University	Werner-Heisenberg-Weg 39 Neubiberg 8014 Germany	49 89 60 04 37 21	49 89 60 04 3580